

Sustainable Control

A new approach to operate wind turbines

Final public report

Stoyan Kanev, Tim van Engelen, Wouter Engels (ECN) Xiukun Wei, Jianfei Dong and Michel Verhaegen (TUD)

June 2012 ECN-E-12-028

Abstract

This final report summarizes the work performed in the framework of the long-term EOS research project "Sustainable Control. A new approach to operate wind turbines", partially financed by the Dutch agency governmental AgentschapNL under number EOSLT02013. Within this project, a novel approach to operate wind turbines more efficiently has been developed, that integrates wind turbine control, monitoring and supervisory control into one concept: "Sustainable Control" (SusCon). The SusCon concept reduces extreme and fatigue loads on the main wind turbine components by means of combining the four major components: (1) Optimized Feedback Control (OFC) for reduction of the wind turbine costs and the limitations for upscaling by means of decreased wind turbine loads under normal operational conditions, (2) Fault Tolerant Control (FTC) for prevention of unnecessary standstill by means of an integration of self-adaptive controls and detection methods for component degradations, (3) Extreme Event Control (EEC) for reduction of turbine costs and increase of the certainty of electricity production by means of reduced turbine loads during extreme operating conditions, and (4) Optimal Shutdown Control (OSC) for avoidance of accumulation of damage during shutdowns resulting from a serious defects by means of condition-specific shutdown control. These concepts have first been developed in theory, and next verified by Proof-of-principle experiments. These experiments demonstrate significant reduction of fatigue during normal operation conditions, and extreme loads during strong wind gusts and/or serious system failures.

Keywords

Sustainable control, wind turbine control, load reduction, extreme event control, fault tolerant control, optimal shutdown control, system identification

Acknowledgment

Many people have contributed directly or indirectly to the success of this project, and risking to forget somebody, we do want to make an attempt here to mention all involved people.

First of all, Jaap 't Hooft and Andre de Boer (Agentschap NL) are acknowledged for making this project possible, the continuous interest therein, and support thereof, and the understanding they showed on several occasions when different bottlenecks were faced. Thank you for giving us the possibility to bring this utmost important project for us, ECN, to a good end, and hope you are just enthusiastic of the results reported here as we are ourselves.

DotX Control Solutions, and in particular Jan Schuurmans, have been subcontracted for preparing and performing the field experiments. Jan, we thank you so much for all your work; with your pragmatic approach and creative ideas you helped us bring the SusCon project to a good end. On those many occasions you were at the premises of ECN in Petten, you were always able to create a pleasant and relaxed working environment, and even people that you were not directly working with were happy to have you around here.

The industrial project partners Mitsubishi Heavy Industries (MHI), ALSTOM Wind, GL Gerrad Hassan and Nordex, are acknowledged for their interest and support during the project; collaborating with you has given the project a practice-oriented character, increasing the relevance of the achieved results and shortening the process needed for further developments of the methods to products ready for the market.

In particular, MHI has played a very important role in the project by being constantly involved in discussions on defining control objectives, performing Bladed simulations, and supporting the field tests. The following people are acknowledged in particular: Yoshiyuki Hayashi for his leading role, Akihiro Nakamura for his project-wide support, Wakako Ariki for her support in the

Bladed calculations and suggestions to improve the controller, Ikawa Yoshikatsu and Takahiro Naka for programming the SUSCON control systems in the wind turbine PLC, and Manabu Yamanaka and Masakazu Okumura for their assistance during the tests on the prototype wind turbine. The SusCon project would not have succeeded without your help.

And last, but certainly not least, many thanks to the project partner ALSTOM Wind who was deeply involved with the work on system identification, performing field tests and promoting the obtained results. In particular, we want to thank Michele Rossetti for the project support, Iciar Font for the many technical discussions, doing the field tests and presenting the results on two conferences, and to Carlo Carcangiu for promoting the results in two other conferences.

Many thanks to our ECN colleagues, and ex-colleagues, who have also indirectly contributed to the project by discussing control problems and ideas, giving feedback on the developed algorithms, and creating a pleasant working sphere and a motivating team feeling. In particular, I want to mention Koen Boorsma, Eric van der Hooft, Koert Lindenburg, Feike Savenije, Pieter Schaak, Kausihan Selvam, and Dennis Wouters.

The management of ECN deserves also an important place here for the continuous support it offered during the acquisition and through the course of this project. In particular, many thanks to Ben Hendriks, Aart van der Pal and Michiel Houkema.

Contents

Abstract and acknowledgment							
Lis	st of a	bbreviat	ions	10			
Su	mmar	у		12			
Sa	menva	atting		22			
Ι	Intro	Introduction					
II	Opt	ptimized feedback control (OFC)					
1	Mult	i-rotatio	nal mode individual pitch control	39			
	1.1	Introdu	ction	39			
	1.2		l design model	40			
	1.2	1.2.1	Linearized aerodynamic conversion	41			
		1.2.2	Periodic linear model equations	41			
	1.3		vidual pitch control	43			
	1.5	1.3.1	Linear time-invariant model	44			
		1.3.2	Feedback laws for IPC-1p	46			
	1.4		harmonics control	48			
	1.4	1.4.1	Feedback loops for IPC-2p	48			
	1 5	1.4.2	Feedback loops for IPC-3p	50			
	1.5		-loop analysis	52			
		1.5.1	Feedback laws in output equations	52			
		1.5.2	Rotational modes in control signals	53			
		1.5.3	Controlled blade root flap moments	55			
			tion results	55 56			
			Model for stability analysis				
	1.8	1					
	1.9	Conclu	sion	65			
2	Feed	back-fee	edforward IPC	67			
	2.1	.1 Introduction					
	2.2	Wind turbine model					
	2.3	Controller design					
		2.3.1	Conventional SISO control approach	69			
		2.3.2	Feedback-Feedforward multivariable control approach to IPC	70			
			2.3.2.1 Design of optimal LOG controller	70			

			2.3.2.2	Feedforward estimated wind disturbance rejection	72			
	2.4	in analysis	74					
3	Cons	Constraints handling in IPC 77						
	3.1	Introdu	action		77			
		3.1.1	Multi-bla	ade pitch limits	77			
			3.1.1.1	Position limit: $J(\psi, \theta_{cm,2}, \theta_{cm,3}) \leq \theta^{rest}$	78			
			3.1.1.2	Speed limit: $\dot{J}(\psi, \theta_{cm,2}, \theta_{cm,3}) \leq \dot{\theta}^{rest}$	79			
			3.1.1.3	Acceleration limit: $\ddot{J}(\psi, \theta_{cm,2}, \theta_{cm,3}) \leq \ddot{\theta}^{rest}$	80			
		3.1.2	Anti-win	dup scheme	81			
		3.1.3	Limits ur	nder blade speed control	82			
	3.2	Nonlin	ear simula	ation study	82			
		3.2.1	Simulation	on model	82			
4	Stab	ility ana	lysis using	g Floquet theory	85			
	4.1	Floque	t stability	analysis	85			
		4.1.1	Time-inv	ariant vs periodic systems	85			
		4.1.2	Applying	g Floquet theory	86			
		4.1.3	Modal an	nalysis with Floquet	90			
	4.2	Floque	et stability	analysis of 1p+2p controller	92			
5	Mod	Modeling external wind conditions in relation to IPC						
	5.1	Introduction						
	5.2	Definition of blade-effective wind speeds						
	5.3	CPSD between two blade elements						
	5.4	Realization algorithm for blade-effective wind speed signals						
	5.5	Model	ing oblique	e inflow	103			
		5.5.1		aries				
		5.5.2	The inter	polation algorithm	104			
		5.5.3	Numerica	al implementation	108			
		5.5.4	Numerica	al example	109			
III	Fa	ult-tole	rant contr	ol (FTC)	111			
6	GLR	T for de	etecting bla	ade moment sensor faults	113			
	6.1	Introduction						
	6.2	Problem Statement						
	6.3	Wind Turbine Modeling via Closed-loop Subspace Identification						
	6.4	and Isolation	117					
		6.4.1	Fault Mo	deling	117			
		6.4.2	Residue (Generation by Kalman Filters	118			

		6.4.3	Additive fault detection based on mean value observation	121
		6.4.4	Additive abrupt jump fault detection based on Generalized Likelihood	
			Ratio Test (GLRT)	
		6.4.5	Multiplicative fault detection based on residue variance observation	126
		6.4.6	Sensor Fault Isolation Logic and Recombination	126
		6.4.7	Fault detection from difference outputs based on GLRT (concepts)	127
	6.5	Simula	ation Results	128
	6.6	Conclu	usion	128
7	Acco		ation of yaw motor failures using IPC control	135
	7.1		ary	
	7.2	Introdu	uction	135
	7.3	TURB	U wind turbine model	136
	7.4	Detect	ing yaw motor failure by robust detection observer	137
		7.4.1	Modeling yaw motor failure as an additive fault	137
		7.4.2	Optimal observer design method	138
			7.4.2.1 Stability conditions	140
			7.4.2.2 Robustness conditions	140
			7.4.2.3 Sensitivity conditions	140
			7.4.2.4 Summary of the design method	141
		7.4.3	Implementation of the design method	141
		7.4.4	Simulation results	142
	7.5	Contro	ol reconfiguration via IPCs	145
		7.5.1	Control objectives	145
		7.5.2	Control design	145
		7.5.3	Simulation results	148
	7.6	Conclu	usions	148
IV	Ex	treme l	Event Control (EEC)	151
8	Dool	ina witl	h wind gusts in combination with wind direction changes	153
O	8.1	•	uction	153
	8.2		on and Symbols	155
	8.3	Turbine Simulation Model		
	0.3	8.3.1		156
		8.3.1	Structural dynamics system (SDM)	156
				157
		8.3.3	Aerodynamic module (ADM)	157
		8.3.4	Conventional controller	158
	0.4	8.3.5	Problem Formulation	159 160
	8.4 Extreme Event Recognition			

		8.4.1 Simplified model	160
		8.4.2 Augmented-state extended Kalman filter	161
		8.4.3 CUSUM test for Extreme Event Detection	163
	8.5	Extreme Event Control	164
		8.5.1 Rotor Overspeed Prevention	164
		8.5.2 Blade load reduction	165
	8.6	Simulation	168
9	Fast	wind gust detection with GLRT	175
	9.1	Brief method description	175
V	Opt	imal shutdown control (OSC)	179
	1		
10	Intro	duction	181
11	Cont	rol-oriented model for OSC design	183
	11.1	Modeling structural dynamics and aerodynamics	183
	11.2	Blade effective wind model	184
	11.3	Fatigue modeling	185
		11.3.1 Summary of control-oriented fatigue model	185
		11.3.2 Derivation of the control-oriented fatigue model	185
	11.4	Control-oriented model parameters for TTURB	186
12	Shute	down control	189
	12.1	Shutdown analysis	189
		12.1.1 Optimal shutdown	190
	12.2	Improvement on the Conventional Shutdown Control method	192
	12.3	Closed Loop Shutdown with classical control	193
	12.4	Optimal Shutdown with Nonlinear Model Predictive Control (NMPC)	193
13	Simu	lation results	195
	13.1	Normal wind speed variations	195
		13.1.1 Grid loss	195
	13.2	Pitch actuator stuck	196
	13.3	Shutdown during a strong gust	196
14	Conc	lusions	201
VI	Ex	perimental methods	203
15	Wind	I turbine model identification: method development	205

	15.1	5.1 Introduction				
	15.2					
		15.2.1	Nonparar	metric model identification using spectral analysis	. 210	
		15.2.2	Parametri	ic model identification	. 212	
			15.2.2.1	Direct ARX identification	. 212	
			15.2.2.2	Instrumental variable method	. 215	
			15.2.2.3	Indirect identification	. 216	
			15.2.2.4	Joint input-output identification	. 217	
			15.2.2.5	Two-stage method	. 217	
			15.2.2.6	Tailor-made instrumental variable method	. 218	
			15.2.2.7	Closed-loop N4SID method	. 219	
			15.2.2.8	Combined open and closed-loop identification using CL-N4SI	D 225	
	15.3	Individ	ual pitch i	dentification	. 226	
		15.3.1	Individua	al pitch identification in open-loop setting	. 226	
		15.3.2	Individua	al pitch identification in closed-loop setting	. 230	
1.0	E		1		237	
10	•	rimenta		t compoint		
	10.1			t campaign		
				data		
	16.2		•	I validation methods		
	10.2					
				pop identification methods		
				n of modal parameters		
	16.2			If mode identification		
				o-side mode identification		
				node identification		
				recommendations		
	10.0	Conciu	sions and	recommendations	. 244	
VI	I In	tegratio	on of meth	nods: Sustainable Control concept	247	
17	Intro	duction			249	
1,	muo	auction			2.0	
18	Susta	ainable c	control		251	
			_	latform		
	18.2	Produc	tion contro	ol platform	. 252	
	18.3	Shutdo	wn control	l platform	. 253	
VI	II C	Conclusi	ions		255	

References 257

List of abbreviations

3D 3-dimensional

ADM Aerodynamic Conversion Module ARX Auto Regressive with eXogenous inputs

ARMAX Auto Regressive Moving-Average with eXogenous inputs

BEM Blade Element Momentum theory CDT Control Design Tool of ECN

CL-N4SID Closed-loop N4SID
CPC Collective pitch control
CUSUM Cumulative sum test
DLC Dynamic load case

DEFL Damage Equivalent Fatigue Load

ECN Energy research Center of the Netherlands

EDC Extreme direction change EEC Extreme Event Control

EG&DR Extreme wind gust and wind direction change

EOG Extreme Operating Gust EKF Extended Kalman Filter

FLOW "Far and Large Offshore Wind Innovation" programme

FDI Fault Detection and Isolation

FTC Fault Tolerant Control

GCP Gust class evolution prototype

GH GL Gerrad Hassan

GLRT Generalized log-likelihood ratio test
GLR Generalized log-likelihood ratio maximum

HAWT Horizontal axis wind turbine IPC Individual pitch control IV Instrumental variable LMI Linear Matrix Inequality LTI Linear Time-Invariant system

LQ Linear Quadratic

LQG Linear (model) Quadratic (cost function) Gaussian (noise) control design

MHI Mitsubishi Heavy Industries
MIMO Multi-input-multi-output system
MOESP an open-loop SMI method
N4SID an open-loop SMI method

NMPC Nonlinear Model Predictive Control

OFC Optimized Feedback Control
OSC Optimal Shutdown Control

PARSIM Closed-loop PARSIMonious subspace identification method

PLC Programmable Logic Controller

PoP Proof-of-principle

PRBS Pseudo-Random Binary Signal

RUC Rotor Unbalance Compensation algorithm

SISO Single-input-single-output system SA Spectral analysis (estimate) SDM Structural Dynamic Model

SDMI Stable Dynamic Model Inversion SMI, SID Subspace Model Identification

SSARX Closed-loop SMI method using output prediction

SVD Singular Value Decomposistion

SusCon Sustainable Control

TUD Delft University of Technology
TTURB Test turbine model in TURBU
VAF Variance Accounted For

Summary

Background

For the sake of nature and future generations, the Dutch government is aiming to make the energy supply on short term more sustainable by means of wind energy. The government has defined for this purpose an ambitious goal to achieve 6000MW offshore wind energy (2020). However, offshore wind energy will only become economically viable if the price of energy drops and the investment risks are acceptable.

The break-even point for offshore wind energy generation is expected to take place around the year of 2025. To this end, upscaling of the wind turbines to 10MW and more is required due to the high foundation and installation costs offshore. In addition, due to the bad accessibility offshore (in the North See around 60%), it is necessary to seriously improve the reliability of the wind turbines to achieve high enough availability. This means that the offshore wind energy generation should be able to keep on operating under most environmental conditions, and in spite of small defects. An increase of the availability from 70% to 85% can be expected by a substantially higher reliability. Such an increased reliability results in much less unplanned maintenance and the supply certainty is significantly improved. Replacing a quarter of the unplanned maintenance by planned maintenance would lead to a reduction of mainenance costs of around 10%; a serious amount, bearing in mind that the maintenance costs offshore are at present about 25% of the total costs of wind energy.

Control is going to play increasingly important role being a viable way to realize cost reductions. During the past years, almost all wind turbine manufacturers have moved over to the so-called "controlled wind turbine concept", meaning that the blades can be actively adjusted and the rotational speed can vary. These degrees of freedom offer excellent opportunities for:

- reducing extreme and fatigue loads (blades, tower, nacelle, transmission),
- adaptation of the operation to all changing and extreme situations (wear, small defects, seasonal influences, etc.).

Due to the relatively recent transition to this turbine concept, these possibilities are yet not fully exploited. This project makes these opportunities accessible for the new generation wind turbines with a size of 10MW and larger. The focus is on new control concepts for the individual turbine, which will contribute to a large extend to enabling efficient manufacturing techniques that are part of the needed breakthrough technology for upscaling. The development of fundamentally other techniques for operating individual wind turbines and parks will increase the availability significantly and reduce the grid integration problems. The approach *Sustainable Control* (Sus-Con), chosen for this purpose, has a strongly innovative character with respect to other current research, both national and international. SusCon integrates control, condition monitoring and safety, which fundamentally differs from the conventional "isolated" approach.

Goal and collaborating parties

The main problem in the EOS reserach theme "Generation and Integration", topic "Offshore wind conversion", is formed by the price and the energy supply certainty of electricity generated offshore from wind. This is to a large extend due to a too low an availability. Furthermore, much larger wind turbines are needed (up to 10MW and larger). This requires a substantially lower loads, while retaining stability becomes more and more difficult as the wind turbine natural frequencies come closer to each other and closer to the excitation frequencies from wind and waves. This issue can be attributed to a large extend to the current state-of-the-art way of wind turbine operation.

The aim of this project is, by means of improved operation, to contribute substantially to the solution to the following specific problems:

- 1 unnecessary standstill due to the current isolated approach of wind turbine control and supervisory control,
- 2 high costs and limitations for upscaling due to high wind turbine loads and stability problems.
- 3 uncertainty of electricity production and high loads during extreme weather conditions,
- 4 accumulation of damage during turbine shutdown due to a serious defect.

This aim is realized by the development of an integrated approach, SusCon, for operating offshore wind turbines. In this approach, the following four components can be distinguished, which will are made available in the form of methods:

- 1 Optimized Feedback Control (OFC), to reduce wind turbine costs and the limitations for upscaling by means of decreased wind turbine loads under normal operational conditions,
- 2 Fault Tolerant Control (FTC), to prevent unnecessary standstill by means of an integration of self-adaptive controls and detection methods for component degradations.
- 3 Extreme Event Control (EEC), to reduce turbine costs and increase of electricity production certainty by means of turbine loads reduction during extreme operating conditions,
- 4 Optimal Shutdown Control (OSC), to avoid of accumulation of damage during shutdowns resulting from serious defects by means of condition-specific shutdown control.

The project consortium consists of the following six parties:

- Energy research Center of the Netherlands (ECN): ECN is coordinator of the project and performs the planned research together with TUD, and to a lesser extend with GH.
- Delft University of Technology (TUD): The TUD is involved in this project with research in the field of fault detection and fault tolerant control.
- Garrad Hassan & Partners Ltd. (GH): The consultant GH was involved in this project for reviewing and advice.
- Nordex Energy GmbH (Nordex): Nordex, a German wind turbine manufacturer, was involved in this project for supporting experiments on a N80 wind turbine located on ECN's test field in Wieringermeer (EWTW). Nordex withdrew itself from the project; the planned experiment were preformed on a Mitsubishi wind turbine.
- ALSTOM Wind (ALSTOM): ALSTOM is a Spanish wind turbine manufacturer which, due to the synergy between this project and ongoing research performed by ALSTOM itself, supported system identification experiments on an Eco100 wind turbine in Spain.
- Mitsubishi Heavy Industries, Ltd (MHI): MHI is a Japanese wind turbine manufacturer which is much interested in control methods that can reduce the wind turbine loads. For this reason, MHI provided a prototype wind turbine for for experimental verification of the OFC, EEC and OSC methods.

Description of the results, bottlenecks and application perspective

Results

OFC (Part II)

Within OFC methods have been developed to design feedback control focussing on the reduction of fatigue loads (Section 1). "Individual pitch control" (IPC) around multiples of the rotational frequency (multi-mode IPC) appeared to be a promising option for loads reduction on both rotating (blades and shaft) and non-rotating (nacelle, tower) components. For this purpose, algorithms have been developed for IPC-1p, IPC-2p and higher, making use of so-called multi-blade transformations. Time domain simulations have shown that a combination of IPC-1p, IPC-2p and IPC-3p can make it possible to realize a reduction of fatigue loads on different components, up to 20-30%. To achieve that, however, it appeared that a significant effort is required from the pitch actuators, which is often the limiting factor in practice for the application of higher mode IPC (IPC-2p and higher). Furthermore, it is shown in Section 2 that an even further loads reduction is achievable when above-mentioned feedback control algorithm is combined with so-called "feedforward IPC control" based on estimated blade effective wind speeds.

To get the most out of the pitch actuators, a procedure has been developed in Section 3 to manage in an optimal way hardware limitations on blade pitch angle, speed and acceleration. To this end, the available actuator capacity gets first transformed to multi-blade coordinates and next distributed between the different IPC loops, thereby giving always priority to the collective pitch control (CPC) algorithm. In this way, the CPC gets the possibility to use all needed actuator capacity (within given limits) for controlling the rotor speed, while the IPC is allowed to consume the remaining actuator capacity to reduce loads.

Further, attention has been paid to algorithms for compensation of aerodynamic imbalance, which can have such a disturbing effect on the IPC that (mostly) tower loads can significantly increase. A quasi-static algorithm has been developed that can compensate the effect of static aerodynamic unbalance completely under the conditions that offset-free blade root moment measurements are available. This condition cannot be satisfied with the currently available sensors. Therefore, attention has also been paid on different alternatives which use tower top acceleration measurements instead of blade load measurements. An additional drawback of these alternatives is that their operation can be disturbed by possibly present mass imbalance, the influence of which is also (just as with aerodynamic imbalance) visible in the measured tower top accelerations. Due to this, it gets very difficult to make a clear distinction between aerodynamic and mass imbalance, and as a result the alternative algorithms also (partially) compensate for the mass imbalance, which could be undesired due to the fact that the loads can, in theory, increase. Detailed simulation studies, however, show that the advantages outweigh this drawback. The results are, however, confidential and are not described in this public report.

Concerning stability analysis, the existing methods for linear systems in the literature are in most cases sufficient due to the fact that often linearized control models are used in the controller design. An exception to this is IPC-2p, which involves an intrinsic nonlinear, periodic model. For stability analysis of IPC-2p loops, a method is developed in Section 4 based on Floquet analysis of periodic systems.

For the purpose of performing simulations with the different control algorithms of the SusCon concept, and more specifically with IPC, a model is developed which has as inputs fictive, blade-effective wind speeds. These 3 signals (for a 3-bladed wind turbine) are realistic in the sense that they are designed in such a way that the resulting aerodynamic moment on the rotor has the same spectral characteristics as the moment that results when the rotor rotates in a 3-dimensional wind field. A procedure for the generation of blade-effective wind speeds is developed in Section 5, which speeds up the simulation, and thus also the whole controller design process. However, for a reliable verification of the performance of the IPC algorithms with respect to loads, a much

more detailed modeling is required. The current Blade Element Momentum (BEM) based models, used standardly in commercial aeroelastic simulation tools such as Phatas and Bladed, have shortcomings in the description of the unstationary aerodynamics on the one hand, and the different working conditions of the blades on the other hand, which are typical when individual blade pitching is used as in IPC control. A so-called "free vortex wake" model is considered a better alternative for loads analysis when an IPC controller is used. In this project, some improvements are made to the "free vortex wake" model which form an important contribution to the development of the model for detailed loads analysis of IPC algorithms. This model will be further developed in the continuation project "Improvement of advanced design tools" (see Section "Application perspective" below).

FTC (Deel III)

Fault tolerant control, considered in Part III of this report, aims at avoiding standstill in cases of minor sensor and actuator faults by means of fault detection and reconfiguration of the controller. In relation to IPC control, a failure of a blade sensor can be seen as a minor fault. Depending on the available instrumentation, it is possible to either switch off the IPC controller (if the blade sensors are not redundantly implemented), or replace the faulty measurement by a healthy one (if the blade sensors are doubly implemented). In the former case it suffices to detect the sensor fault (fault detection), but it is not strictly necessary to point the sensor that has failed (fault diagnosis). In the later case, however, fault diagnosis is preferred as this offers the possibility to accommodate numerous sensor faults before maintenance needs to take place. This makes it possible to better plan the maintenance, which can significantly reduce the O&M costs related to IPC control.

In Section 6 an algorithm is described that has been developed for the detection and diagnosis of faults in blade root moment sensors, in pitch and yaw actuators. The algorithm is based on an advanced observer that has the property that it is almost insensitive to disturbances from the wind, but at the same time is sensitive to sensor and actuator faults. By adding a realistic wind model to the wind turbine model, it becomes possible to employ a so-called Kalman filter for reconstruction of the state of this augmented model. The residual of the Kalman filter, i.e. the difference between the measured signals and the estimate of the filter, has the properties of a white noise process during normal operation. In case of a fault, however, the mean value of this residual signal undergoes a significant change to realize the fault detection with a GLRT test within a second.

A comparable approach is also used in Section 7 for the detection of faults in the yaw motor. The mechanism of controller reconfiguration is, however, completely different in this case: after yaw motor failures detection, a specially developed IPC controller becomes active which generates a yawing moment on the rotor. It is shown that this IPC yaw controller can be designed in such a way that it has approximately the same properties as the conventional yaw controller. Wind turbine yawing with individual blade pitching is, however, always accompanied with additional blade loads which are unavoidable for the generation of a yawing moment.

EEC (Part IV)

Extreme wind gusts and wind direction changes can give rise to heavy loads on different wind turbine components, as well as to unnecessary standstill. Aiming at increasing the certainty of energy production during extreme operating conditions, an algorithm has been developed in Section 8 for the detection and control of extreme excitations. The algorithm uses an estimator of the blade-effective wind speeds, which estimates are used in a CUSUM test for the detection of abrupt changes in the mean value of these signals. This results in a rather rapid recognition of coming wind gusts and changes in the wind direction, which in turn makes it possible to intervene on time by pitching the blades fast to feathering position. Detailed aeroelastic simulations with the software tool TURBU demonstrate that the EEC can be designed in such a way that it does not trigger during normal production, but triggers timely during severe gusts, which makes it possible to prevent shutdowns due to rotor overspeed. This research is further extended to a procedure that allows to differentiate between the following six different types of wind gust classes: (1) rotor-

coherent wind speed variations, (2) sudden height-dependent rotation of the wind ("backing and veering wind"), (3) jet stream, (4) wind direction variation, (5) sudden wind shadow in front of a side of the rotor plane of the wind turbine ("partial wake condition"), and (6) a sudden coherent vertical component in the wind speed ("sloping wind"). For this approach, a Dutch patent is granted [79].

Furthermore, model-based alternatives for the signals-based CUSUM test, and more specifically the so-called "Generalized Likelihood Ratio test", have been investigated in Section 9. By making use of a linearized model of the wind turbine and a linear model of the "wind disturbance" is this approach capable to distinct certain wind gusts (e.g. the well-known "Mexican hat") somewhat faster than the CUSUM test. However, this algorithm is still in a very preliminary stage of development, and it is more specifically not trivial to extend the GLRT such that it can apply to different mean wind speeds within the operating region of the wind turbine. The simplicity of the model-free CUSUM test, and the possibility of extending this relatively easy to the full wind region (this has already been done in the framework of the continuation project FLOW-CDTup, see Section "Application perspective"), has larger practical value than GLRT.

OSC (Part V)

OSC has to do with bringing the wind turbine to standstill as a result of serious system failures. This topic is treated in Part V, where the focus lies on specific situations, namely pitch actuator faults and the electrical moment dropping to zero (as a result of, e.g., net loss or shaft fracture). The aim is to guide the shutdown process in such a way that the loads remain as low as possible. Methods of different complexity have been developed and compared, from which it becomes clear that an advanced control algorithm based on "Nonlinear Model Predictive Control" yields the best result at the price of significant increase of the computational complexity. On the other hand, a simple shutdown solution based on a standard "pitching of the blade to feather as fast as possible", extended with a notch filter on the tower first frequency to prevent its excitation by the fast pitch action, results in an excellent trade-off between computational complexity and loads reduction.

The developed OSC methods are further improved and fine-tuned for application on the prototype wind turbine of MHI (see also "Proof-of-principle experiments" below).

Experimental modeling (Part VI)

The experimental modeling is related to the formation of models based on measurement data. In order to obtain useful data, specific experiments on the wind turbine during normal operation are necessary, whereby the dynamics relevant for control design and analyses gets carefully excited with test signals that are designed specially for that purpose. In Section 15 is described how these signals can be designed such that no natural frequencies get excited in order to prevent undesired resonances and unacceptable loads. These test signals are then added to the control actions blade pitch angle and generation torque, which are computed and sent out by the wind turbine controller at each controller cycle. Further, a number of methods for system identification are developed, with the focus on identification in closed-loop due to the fact that the wind turbine controller cannot be deactivated during the experiments. These techniques are first validated in simulation studies, and later in Section 16 applied to real-life measurement data from the Eco100 wind turbine of the partner ALSTOM Wind. The obtained models are then first validated using model validation methods, developed specially for that purpose in Section 15, and later using detailed aeroelastic model obtained with Bladed. The results show that the developed algorithms for system identification should be seen as accurate enough for controller design. The involved partner in these experiments, ALSTOM Wind, was satisfied with the results and took the initiative to publish the results at four different international conferences ([9, 10, 22, 23]).

Proof-of-principle experiments

PoP experiments are performed with the SusCon algorithms OFC, EEC and OSC. The preparation for these experiments, and specifically the fine-tuning of the algorithms, the experiments themselves, and the results, are strictly confidential and are excluded from this public report. All

these PoP experiments are performed on a MHI prototype wind turbine in two different measurement campaigns: first the IPC algorithm was tested as part of the OFC in April 2010, and one year later experiments were performed with EEC and OSC. These last experiments contain also tests with the combination OFC-EEC-OSC, which represents the largest part of the SusCon concept. The PoP with FTC is performed using the measurement data obtained during the second measurement campaign (no separate PoP experiments with FTC could be performed, see "Bottlenecks"). The results from all experiments are received very positively by the project partner MHI, and demonstrate that a reduction of fatigue loads on the blades of up to 17% can be realized with OFC, while the extreme loads in certain cases drop by as much as 50% with EEC and OSC.

Bottlenecks

During the course of the project, the following bottlenecks have arisen:

- The contractual end date of December the 31, 2009, is shifted in 2008 to December the 31, 2011, due to strong personnel undermanning during the first part of the project, as well as a substantially longer throughput time of the industrial parties for the Proof-of-Principle experiments,
- The industrial partner Nordex withdrew itself from the consortium on November the 17, 2009. Nordex has come to this decision on the basis of a long internal discussion and detailed presentations, that were held by ECN on May the 28, 2009, at the premises of Nordex in Norderstedt (Hamburg), over aspects related to the content and the execution of the experiments related to the integral SusCon concept. The main reasons were personnel shortage and a very tight time-to-market schemes for new developments. As a results, it became unacceptable to make available enough staff for setting up wind turbine experiments for execution of the PoP of the SusCon-concept. Shortly after, MHI was requested to perform the SusCon concept PoP experiments, and luckily MHI appeared to be happily surprised with this request, which made the execution of all planned PoP experiments possible.
- At the end of 2011, the end date of the project was shifted again to June the 30, 2012, due to the long absence of the original project leader Tim van Engelen due to illness on the one hand, and the fact that the FTC experiments could not be performed on time on the other hand. In the first half of 2012, due to a large operations planned to the nacelle of the wind turbine of MHI, it subsequently became clear that the FTC PoP experiments could anyway not take place. In the beginning of 2012 it was agreed upon with Agentschap NL that the PoP experiments will be done based on simulations with the software Bladed and using the measured data obtained during the other PoP field tests.

Application perspective

The developed methods, and the integrated SusCon control approach, will be further developed after the termination of the project in mutual coherence with the product development in the area of measurements. The focus lies on the development of algorithms that can be integrated into the process controllers of prototype wind turbines. The purpose of this is, by performing tests of a much larger duration than in this project, to undo the SusCon concept from its teething troubles and make the market enthusiastic about it. The later is to be done chiefly by presenting the concept as a "proven technology". To this end, already before the actual termination of this project, two continuation projects have been defined within the "Far and Large Offshore Wind Innovation" programme (FLOW):

- "Control Design Tool Upgrade" (CDTup), number P201101-014-ECN: This project represents the first phase of a large-scale upgrade of the Control Design Tool (CDT) of ECN, a tool for the design of industrial wind turbine controllers. During this first phase, the algorithms OSC and EEC, as developed in the SusCon project, will be further improved and implemented into the CDT.
- "Improvement of advanced design tools", number P201203-006-ECN: In this continuation project, representing the second phase, the remaining SusCon algorithms (namely, OSC and FTC) will be improved and added to the new tool, and the complete controller (incl. the whole SusCon concept) will be extensively tested on a 2-bladed prototype wind turbine of the Dutch wind turbine manufacturer 2-B Energy.

Furthermore, at the moment of writing of this report, it is being worked on a third related FLOW project proposal with the wind turbine manufacturer XEMC-Darwind as partner. This project will aim at improvement of the new tool by means of verifying it on a 3-bladed wind turbine . The market introduction of the new control tool is expected in the year of 2013.

After that, the advantages of SusCon will be taken into consideration in the design of the next generation wind turbines, so that these are calculated for lower loads. This will firstly concern turbines of the current size, and after that much larger ones of up to the optimal size of 10 MW or larger for offshore wind energy generation.

Description of the contribution to the governmental goals

Contribution to the sustainable energy economy

The project contributes to the main aim of making offshore wind energy competitive with fossil energy production on land in 2020 by means of increasing the availability and reduction of the structural loads, or making these more uniform. The latter makes a further upscaling possible, at powers of up to 10 MW or even more. A size of 10MW or more is needed to finally bring down the costs for offshore wind energy to the required level. The new control concepts have a central position in this, and will contribute to a large extend to making efficient building techniques possible that take part of the required breakthrough technology for upscaling.

The development of fundamentally other operation concepts for individual wind turbine and clusters will strongly increase the availability and reduce the problems related to the grid integration. The "Extreme event control" method strongly increases the certainty of energy generation during storm fronts. Due to "Fault Tolerant Control" the wind turbines can, in spite of small defects, continue its operation, resulting in less standstill and a better planning of maintenance.

It is expected that, due to SusCon, the costs of offshore wind conversion will decrease by about 16%: 11% due to increased availability, 2.5% due to reduced loads, and abother 2.5% due to less mainenance costs. Concerning the offshore wind conversio in the Netherlands, this boils down to the avoidence of usage of primary energy of around 8.2PJ per year in 2020.

Strengthening the knowledge position of the Netherlands

Wind conversion offshore is a spearhead in the LT-EOS programme, with design knowledge as research area. Concerning both the spearhead and the research area, ECN Wind Energy belongs to the world top of the research institutes, as becomes clear from its role in the European Academy of Wind Energy (EAWE), the role as coordinator of the Integrated Project "UpWind" within the European 6th Framework Programme, and the involvement in the European projects STABCON and DOWNVIND.

At the TUD, department Delft Center for Systems and Control (DCSC), under the leadership of Prof. Michel Verhaegen, there is high-quality technical knowledge in the field of Fault Tolerant Control and classical control theory. The affinity with wind energy is high.

This project delivers knowledge in the area of methods for operating offshore wind energy generators with a strong innovative character:

- control, monitoring and supervision and integrated for the first time in such a way, that the availability of the wind turbines substantially increases;
- pioneering control algorithms are developed in the field of fatigue load reduction and control during extreme wind conditions as strong wind gusts;
- for the first time attention is being payed to stopping the wind turbine due to serious failure with minimum subsequent damage.

This is very favourable for the knowledge position of the Netherlands because this knowledge cannot easily be made operational without the expertise that is built up during the execution of this project. The strengthened knowledge position in the field gives possibilities for substantial knowledge export, given the enormous potential of wind conversion and the applicability of the methods on both offshore and onshore wind energy.

To protect the developed knowledge, the following patent applications have been submitted:

- [79] van Engelen, T., L. Machielse and S. Kanev (2010): Method and system for wind gust detection in a wind turbine. Publication number NL C 2005400.
- [77] van Engelen, T. (pending): System and method for compensating rotor imbalance in a wind turbine. International publication number WO 2010/016764 Al.
- [42] Kanev, S., J. Schuurmans and T. van Engelen (pending): Apparatus and method for Individual Pitch control in Wind turbines. Publication number P6029490US.

Spin off inside and outside of the sector

A product/market combination is formed by control systems for offshore wind turbines for the electricity market. The wind turbine manufacturers play an important role here. Because SusCon will appear interesting also for the onshore wind energy conversion, the market is expected to take a worldwide size, but will mostly be concentrated in Europe, North America and Azia.

The developed integral control approach can lead to new product development in the field of measurement equipment and actuation after termination of the project, with the emphasis on the adaptation of the pitch actuators to make multi-mode individual control possible, as well as on improvement of the quality and reliability of the load measurement devices for IPC.

Overview of publications

In the list below, all publications related to this project are listed, where the numbering corresponds to that in the Bibliography at the end of this report.

- [9] Carcangiu, C., I.F. Balaguer, S. Kanev and M. Rossetti (2011): Closed-Loop System Identification of Alstom 3MW Wind Turbine. Proceedings of IMAC XXIX. Jacksonville-FL, USA
- [10] Carcangiu, C., S. Kanev, M. Rossetti and I.F. Balaguer (2010): System Identification on Alstom ECO100 Wind Turbine. Proceedings of the POWER-GEN International Conference.

- [22] Font, I., S. Kanev and M. Rossetti (2010): System identification on the ECO 100 wind turbine. poster in the European Wind Energy Conference.
- [23] Font, I., S. Kanev, D. Tcherniak and M. Rossetti (2010): System identification methods on Alstom ECO 100 wind turbine. Proceedings of The Science of Making Torque from Wind Conference. FORTH, Heraklion, Crete, Greece.
- [38] Kanev, S. (2009): Dealing with actuator constraints in multi-mode blade load reduction control. Report ECN-Wind Memo-09-069, ECN Wind Energy.
- [39] Kanev, S. (2009): System identification from BLADED simulations with the Ecotècnia 100 wind turbine. Confidential report ECN-X-09-026, Energy Research Centre of the Netherlands (ECN).
- [40] Kanev, S. (2009): System identification from field measurements on Ecotècnia 100 wind turbine. Report ECN-X–09-089, Energy Research Center of the Netherlands.
- [41] Kanev, S. and T. van Engelen (2009): Exploring the Limits in Individual Pitch Control. Proceedings of the European Wind Energy Conference (EWEC). Marseille, France.
- [42] Kanev, S., J. Schuurmans and T. van Engelen (pending): Apparatus and method for Individual Pitch control in Wind turbines.
- [43] Kanev, S. and T. van Engelen (2008): Wind Turbine Extreme Gust Control. Report ECN-E-08-069, ECN Wind Energy.
- [44] Kanev, S. and T. van Engelen (2010): Wind Turbine Extreme Gust Control. Wind Energy, 13(1):18-35.
- [65] Selvam, K., S. Kanev, J.W. van Wingerden, T. van Engelen and M. Verhaegen (2009): Feedback-feedforward individual pitch control for wind turbine load reduction. International Journal of Robust and Nonlinear Control, 19(1):72-91.
- [75] van Engelen, T. (2006): Design model and load reduction assessment for multi-rotational mode individual pitch control (higher harmonics control). Proceedings of the European Wind Energy Conference. Athens, Greece.
- [76] van Engelen, T. (2007): Control design based on aero-hydro-servo-elastic linear models from TURBU (ECN). Proceeding of the European Wind Energy Conference. Milan, Italy.
- [77] van Engelen, T. (pending): System and method for compensating rotor imbalance in a wind turbine.
- [79] van Engelen, T., L. Machielse and S. Kanev (2010): Method and system for wind gust detection in a wind turbine.
- [81] van Engelen, T. and P. Schaak (2007): Oblique Inflow Model for Assessing Wind Turbine Controllers. Proceedings of the 2nd Conference on The Science of Making Torque From Wind. Lyngby, Denmark.
- [82] van Engelen, T., J. Schuurmans, S. Kanev, J. Dong, M. Verhaegen and Y. Hayashi (2011): Fault tolerant wind turbine production operation and shutdown (Sustainable Control). Proceedings of the EWEA Conference. Brussels, Belgium.
- [96] Wei, X. (2009): Fault Detection of Large Scale Off-shore Wind Turbine Systems. Report 09-044, Delft University of Technology.

- [97] Wei, X. and M. Verhaegen (2008): Fault Detection of Large Scale Wind Turbine Systems: A mixed H_infinity/H_ Index Observer Approach. Proceedings of the 16th Mediterranean Conference on Control and Automation. Ajaccio, France.
- [98] Wei, X. and M. Verhaegen (2008): Mixed H_infinity/H_index Fault Detection Observer Design for LPV systems. Proceedings of the 47th IEEE Conference on Decision and Control. Cancun, Mexico, pages 1073-1078.
- [99] Wei, X. and M. Verhaegen (2009): Mixed H_/H_infinity Dynamic Observer Design for Fault Detection. Proceedings of the European Control Conference. Budapest, Romania, pages 1913-1918.
- [100] Wei, X. and M. Verhaegen (2009): Robust Fault Detection Observer Design for LTI Systems Based on GKYP Lemma. Proceedings of the European Control Conference. Budapest, Romania, pages 1919-1924.
- [101] Wei, X. and M. Verhaegen (2009): Robust Fault Detection Observer for LTI Systems with Additive Uncertainties. Proceedings of the 7th IFAC Symposium on Fault Detection, Supervision and Safety of Technical Processes (SAFEPROCESS). Barcelona, Spain, pages 756-761.
- [102] Wei, X., M. Verhaegen and T. van Engelen (2008): Sensor Fault Diagnosis of Wind Turbines for Fault Tolerant Control. Proceedings of the 17th World congress of IFAC. Seoul, Korea, pages 3222-3227.
- [103] Wei, X., M. Verhaegen and T. van Engelen (2010): Sensor Fault Detection and Isolation for Wind Turbines Based on Subspace Identification and Kalman Filter Techniques. International Journal of Adaptive Control and Signal Processing, 24(8).

Project data

Project number: EOSLT02013

Project title: Sustainable Control. A new approach to operate wind turbines

Coordinator: ECN

Partners: TU-Delft, Mitsubishi Heavy Industry, ALSTOM Wind, Nordex, Gerrad Hassan

Period: 1 January 2006 - 30 June 2012

Contact: S. Kanev (ECN), email: kanev@ecn.nl

This project is carried out with subsidy from the Ministry of Economic Affairs, Agriculture and Innovation, regulation EOS: Long Term carried out by Agentschap NL.

Samenvatting

Samenvatting van uitgangspunten

Omwille van het milieu en toekomstige generaties, heeft de Nederlandse overheid zich ten doel gesteld om de energievoorziening op korte termijn te verduurzamen door middel van windenergie. De overheid hanteert hierbij een ambitieuze doelstelling van 6000MW offshore (2020). Economische offshore windconversie is echter pas mogelijk als de kostprijs omlaag gaat en de investeringsrisico's aanvaardbaar zijn.

Het break-even point voor offshore windconversie zou rond 2025 liggen. Hiervoor is opschaling nodig van de windturbines tot een vermogen van 10MW of meer, in verband met de hoge fundatie- en installatiekosten offshore. Ook is het noodzakelijk om de betrouwbaarheid van de windturbines sterk te verhogen door afdoende beschikbaarheid vanwege de slechte toegankelijkheid offshore (Noordzee: ca. 60%). Dit betekent dat een offshore windturbine moet kunnen doordraaien onder nagenoeg alle omstandigheden en ondanks kleine mankementen. Een beschikbaarheidverhoging van 70 naar 85% mag worden verwacht bij een substantieel verhoogde betrouwbaarheid. Zo'n verhoogde betrouwbaarheid heeft ook tot gevolg dat veel minder ongepland onderhoud nodig is en dat de zekerheid van levering veel groter is. Vervanging van een kwart van ongepland door gepland onderhoud leidt tot verlaging van de onderhoudskosten met zo'n 10%. Dit, terwijl offshore de onderhoudskosten nu zo'n 25% van de totale kosten van de opgewekte windenergie bedragen.

Regeling gaat een steeds belangrijkere rol spelen en vormt een aangrijpingspunt om kostenreducties te realiseren. De afgelopen jaren zijn nagenoeg alle windturbinefabrikanten overgegaan op het zogenaamde "geregelde windturbine concept". Hiermee wordt bedoeld dat de bladen actief versteld kunnen worden en het rotortoerental kan variëren. Deze vrijheidsgraden bieden uitstekende mogelijkheden tot

- reductie van vermoeiings- en extreme belastingen (bladen, toren, gondel, transmissie),
- aanpassing van de bedrijfsvoering aan alle wisselende en extreme omstandigheden (slijtage, kleine defecten, seizoensinvloeden, enz.).

Door de recente overgang naar dit turbineconcept worden deze mogelijkheden nog weinig benut. Dit project maakt de mogelijkheden toegankelijk voor de nieuwe generaties windturbines met een schaalgrootte van 10MW of meer. De nieuwe regelconcepten voor de individuele turbine staan hierin centraal en zullen in hoge mate bijdragen aan het mogelijk maken van efficiënte bouwtechnieken die deel uitmaken van de vereiste doorbraaktechnologie voor opschaling. De ontwikkeling van fundamenteel andere bedrijfsvoeringconcepten voor individuele turbines en clusters daarvan, zal de beschikbaarheid sterk doen toenemen en de problemen van de netinpassing doen afnemen. De hiervoor gekozen benaderingswijze *Sustainable Control* (SusCon) is sterk vernieuwend ten opzichte van al het lopende onderzoek, zowel nationaal als internationaal. In SusCon worden regelen, bewaken en beveiligen geïntegreerd, hetgeen een doorbraak betekent.

Doelstelling en samenwerkende partijen

Het hoofdprobleem in het onderzoeksthema "Opwekking en Inpassing", speerpunt "offshore windconversie", wordt gevormd door de kostprijs en zekerheid van levering van offshore opgewekte elektriciteit uit wind. Dit is voor een groot deel te wijten aan een te lage beschikbaarheid. Verder zijn veel grotere turbines nodig (tot 10MW of meer). Dit vereist aanzienlijk lagere turbinebelastingen. Het behoud van stabiliteit wordt daarbij ingewikkelder omdat de trillingsfrequenties van de turbine dichter bij elkaar komen te liggen en ook dichter bij de aanstootfrequenties van

wind en golven. Deze problematiek is voor een aanzienlijk deel toe te schrijven aan de huidige stand der techniek voor wat betreft de bedrijfsvoering.

Het doel van dit project is om via de bedrijfsvoering een substantieel deel van de oplossing te bereiken voor de volgende specifieke problemen

- 1 onnodige stilstand door geïsoleerde benadering van regeling en turbinebeveiliging,
- 2 hoge kosten en opschalingbeperking door hoge turbinebelastingen en stabiliteitsproblemen,
- 3 onzekerheid van levering en hoge belastingen bij extreme weercondities,
- 4 opstapeling van schade bij turbine shut-down als gevolg van ernstig mankement.

Dit doel wordt gerealiseerd door een integrale benaderingswijze, SusCon, voor de bedrijfsvoering van offshore windturbines te ontwikkelen. In deze benaderingswijze zijn vier onderdelen te onderkennen die in de vorm van methoden beschikbaar worden gesteld:

- 1 Optimized Feedback Control (OFC), voor reductie van de turbinekosten en verlichting van de opschalingbeperking door verlaagde turbinebelastingen onder normale bedrijfscondities:
- 2 Fault Tolerant Control (FTC), ter voorkoming van onnodige stilstand door integratie van zelf-aanpassende regelingen met detectiemethoden voor componentdegradatie.
- 3 Extreme Event Control (EEC), voor reductie van de turbinekosten en het verhogen van de zekerheid van levering door verlaagde turbinebelastingen onder extreme bedrijfscondities;
- 4 Optimal Shutdown Control (OSC), ter voorkoming van opstapeling van schade bij turbine shut-down als gevolg van een ernstig mankement door conditiespecifieke regeling naar stilstand.

Het projectconsortium bestaat uit de volgende zes partijen:

- Energie onderzoekcentrum Nederland (ECN): ECN is aanvrager en penvoerder van dit project en verricht het beoogde onderzoek samen met TUD en in beperkte mate GH.
- Technische Universiteit Delft (TUD): De TUD houdt zich binnen dit project bezig met onderzoek op het gebied van detectie van falen en Fault Tolerant Control.
- Garrad Hassan & Partners Ltd. (GH): Binnen het project vervult de consultant GH een belangrijke rol op het gebied van projectsturing en reviewing.
- Nordex Energy GmbH (Nordex): Nordex, een Duitse windturbine fabrikant, was betrokken in dit project voor de ondersteuning van experimenten aan een N80 wind turbine op het ECN testveld in de Wieringermeer (EWTW). Nordex heeft zich teruggetrokken van het project; de geplande experimenten zijn verricht met een Mitsubishi windturbine.
- ALSTOM Wind (ALSTOM): ALSTOM is een Spaanse windturbine fabrikant, die vanwege de synergie tussen dit project en door ALSTOM zelf voorzien onderzoek, meewerkte aan systeemidentificatie experimenten aan een Eco100 windturbine in Spanje.
- Mitsubishi Heavy Industries, Ltd (MHI): MHI is een Japanse windturbine fabrikant die nadrukkelijk geïnteresseerd is in regelmethoden die turbinebelastingen verder kunnen verlagen. Hiertoe stelde MHI haar MHI-92 prototype turbine beschikbaar voor experimenten met OFC, EEC en OSC.

Beschrijving van de resultaten, knelpunten en perspectief voor toepassing

Resultaten

OFC (Deel II)

Binnen OFC zijn methoden ontwikkeld voor het ontwerp van terugkoppelregelingen waarin reductie van vermoeiingsbelastingen centraal staat (Hoofdstuk 1). "Individual pitch control" (IPC) rond veelvouden van het toerental (multi-mode IPC) is een veelbelovende optie gebleken waarmee de belastingen op zowel roterende (bladen en as) als niet-roterende (gondel, toren) onderdelen kunnen worden verlaagd. Daarvoor zijn algoritmen ontwikkeld voor IPC-1p, IPC-2p en hoger, via zogenaamde multi-blade transformaties. Tijdsdomein simulaties hebben uitgewezen dat een combinatie van IPC-1p, IPC-2p en IPC-3p te nemen, een vermoeiingsbelasting reductie op verschillende onderdelen tot wel 20-30% mogelijk in vollast condities. Het is wel gebleken dat daarvoor een aanzienlijke inspanning van de pitchactuatoren is vereist. Dit is vaak de beperkende factor voor de toepassing in het praktijk van hogere mode IPC (IPC-2p en hoger). Daarnaast is verder in Hoofdstuk 2 ook aangetoond dat nog verdere belastingreductie mogelijk is als het bovengenoemde terugkoppelalgoritme voor IPC-1p wordt gecombineerd met zogenaamde "feedforward IPC control", op basis van geschatte bladeffectieve windsnelheden.

Om het meeste uit de pitchactuatoren te halen, is in Hoofdstuk 3 een procedure beschreven voor het zo optimaal mogelijk hanteren van de hardware limieten op blad pitch positie, snelheid en versnelling. Daarbij wordt de beschikbare actuatorcapaciteit wordt getransformeerd naar multi-blade coördinatenen, en vervolgens verdeeld onder de verschillende IPC lussen, waarbij de snelheidsregeling met het collectief bladverstelalgoritme (CPC) altijd prioriteit heeft voor de IPC algoritmen. Op deze manier wordt het CPC algoritme in staat gesteld om alle daarvoor benodigde actutatorcapaciteiten (binnen bepaalde grenzen) te gebruiken om het toerental goed te regelen, terwijl het IPC de beschikking krijgt over de resterende actuator capaciteit om belastingen te reduceren.

Verder is er gekeken naar algoritmen voor compensatie van aerodynamisch onbalans, hetgeen een dermate verstorende werking kan hebben op de IPC dat met name torenbelastingen flink kunnen toenemen. Een quasi-statisch algoritme is ontwikkeld dat het effect van statisch aerodynamisch onbalans volledig kan compenseren onder de voorwaarden dat er offset-vrije bladwortelmoment metingen beschikbaar zijn. Omdat met de huidige sensoren niet wordt voldaan aan deze voorwaarde is er ook gekeken naar verschillende alternatieven die, in plaats van bladmetingen, toren top versnellingsmetingen gebruiken. Een bijkomend nadeel van deze alternatieven is dat hun werking kan worden verstoord door een eventueel aanwezige massaonbalans, het effect waarvan ook (net als dat van aerodynamisch onbalans) te zien is in de gemeten torentopversnelling. Daardoor wordt het erg lastig onderscheid te maken tussen aerodynamisch en massa onbalans, en als gevolg daarvan compenseren de alternatieve algoritmen ook (gedeeltelijk) voor de massa onbalans. Dit is ongewenst doordat de belastingen in theorie zouden kunnen toenemen. Gedetailleerde simulatieresultaten tonen echter aan dat de voordelen zwaarder wegen dan dit nadeel. Echter zijn deze resultaten strict confidentieel en zijn daarom niet vermeld in dit openbaar rapport.

Met betrekking tot stabiliteitsanalyse zijn de bestaande methoden voor lineaire systemen in de literatuur in de meeste gevallen al voldoende, omdat vaak gelineariseerde regelmodellen worden gebruikt bij het regelaar ontwerp. Een uitzondering hierop is IPC-2p, dat gepaard gaat met een niet-lineair, periodiek model. Voor de stabilitietsanalyse van IPC-2p is er een methode ontwikkeld in Hoofdstuk 4, gebaseerd op Floquet analyse voor periodieke systemen.

Ter behoeve van de simulaties met de verschillende regelalgoritmen van het SusCon-concept, en in het bijzonder IPC, is een model ontwikkeld waarbij wordt gewerkt met fictieve, zogenaamde blad-effectieve windsnelheden. Deze 3 signalen (bij een 3-bladige molen) zijn realistisch in de zin dat zij zodanig worden ontworpen dat het resulterende aerodynamische koppel op het rotor dezelfde spectrale eigenschappen heeft als het koppel dat resulteert als de rotor draait in een 3-

dimensionaal windveld. Een procedure voor de generatie van blad effectieve windsnelheiden is ontwikkeld in Hoofdstuk 5, wat de simulatie, en dus ook het hele regelaar ontwerpproces aanzienlijk versnelt. Echter, voor een betrouwbare verificatie van de prestatie van IPC algoritmen met betrekking tot belastingen is een veel gedetailleerdere modellering noodzakelijk. De huidige, op Blad Element Momentum (BEM) gebaseerde, modellen die standaard worden gebruikt in commerciële aeroelastische simulatietools zoals Bladed en Phatas, schieten tekort in de beschrijving van de enerzijds instationaire aerodynamica, en anderzijds de verschillende werkcondities van de bladen, welke typerend zijn voor de individuele bladverstelling bij IPC regelingen. Een zogenaamd "free vortex wake" model wordt geacht als beter geschikt voor belastinganalyse bij het gebruik van IPC controllers. In dit project zijn verbeteringen gemaakt aan het "free vortex wake" model welke de toepassing van het model voor een gedetailleerde analyse van IPC regelingen een stap dichterbij zetten. Dit model wordt verder doorontwikkeld in het vervolgproject "Improvement of advanced design tools" (zie Hoofdstuk "Perspectief voor toepassing" hieronder).

FTC (Deel III)

Fout-tolerant regelen, beschouwd in Deel III van dit rapport, heeft als doel om stilstand te voorkomen in gevallen van "milde" sensor- en actuator falen door middel van foutdetectie en reconfiguratie van de regelaar. In verband met IPC control kan het uitvallen van, bijvoorbeeld, een bladsensor worden gezien als een mild falen. Afhankelijk van de beschikbare instrumentatie kan daarbij worden gedacht aan het buiten werking stellen van de IPC regeling (als de bladsensoren niet redundant zijn uitgevoerd), of aan de vervanging van de foutieve meting met een correcte (als de bladsensoren dubbel zijn uitgevoerd). In het eerste geval is het voldoende om te detecteren dat een sensor faalt (fout detectie), maar het is niet strikt noodzakelijk om de sensor die gefaald heeft te kunnen aanwijzen (fout diagnose). In het laatste geval daarentegen verdient fout diagnose de voorkeur omdat men dan meerdere sensor falen kan "accommoderen" voordat onderhoud moet plaatsvinden. Dit maakt het mogelijk het onderhoud beter te plannen wat de O&M kosten m.b.t. IPC control flink kan reduceren.

In Hoofdstuk 6 wordt een algoritme beschreven voor de detectie en diagnose van falen in bladwortelmoment sensoren, en pitch en krui actuatoren. Het algoritme is gebaseerd op een geavanceerd observer, met de eigenschap dat het vrijwel ongevoelig is voor verstoringen van de wind, maar tegelijkertijd wel gevoelig is voor sensor en actuator falen. Door een realistisch wind model toe te voegen aan het windturbine model wordt het mogelijk om een zogenaamd Kalman filter te gebruiken voor de reconstructie van de toestand van dit "augmented model". Het residu van het Kalman filter, d.w.z. het verschil tussen de gemeten signalen en de schatting van het filter, heeft bij normaal bedrijf de eigenschappen van een witte ruis signaal. In geval van falen verandert de gemiddelde waarde van het residu dermate dat foutdetectie met een GLRT test binnen ca. 1 seconde geschiedt.

Een soortgelijke aanpak is gevolgd in Hoofdstuk 7 voor de detectie van kruimotor falen. Het mechanisme van reconfiguratie van de regeling is hier echter geheel anders: bij kruimotor falen wordt een speciaal ontwikkeld IPC regeling in werking gezet dat een kruimoment op de rotor opwekt. Het is aangetoond dat deze IPC kruiregeling zodanig kan worden ontworpen dat het ongeveer dezelfde dynamische eigenschappen vertoond als de normale kruiregeling. Het kruien van de windturbine met individuele bladverstelling gaat echter altijd gepaard met extra bladbelastingen welke onmisbaar zijn bij het opwekken van een kruimoment.

EEC (Deel IV)

Extreme windvlagen en windrichtingsveranderingen kunnen leiden tot grote belastingen op verschillende onderdelen van de windturbine, alsmede tot onnodig stilstand. Met als doel om de zekerheid van levering onder extreme bedrijfscondities te verhogen, is in Hoofdstuk 8 een algoritme ontwikkeld voor de detectie en het pareren van extreme aanstotingen. Het algoritme maakt gebruik van een schatter van de bladeffectieve windsnelheiden. Deze schattingen worden vervolgens gebruikt in een CUSUM test voor detectie van abrupte veranderingen in de gemiddelde waarde van deze signalen. Dit resulteert in een vlotte herkenning van aankomende windvlagen

en veranderingen in de windrichting, dat ertoe leidt dat er op tijd kan worden ingegrepen door de bladen snel naar vaanstand te verstellen. Gedetailleerde aeroelastische simulaties met de software tool TURBU tonen aan dat het EEC zodanig kan worden ontworpen dat het niet aanspringt tijdens normaal bedrijf, maar wel tijdig aanspringt bij harde vlagen met als gevolg dat veiligheidsshutdown door overtoeren van de rotor vaak kan worden vermeden. Dit onderzoek is verder uitgebreid naar een procedure waarmee een onderscheid kan worden gemaakt tussen de volgende zes windvlaagklassen: (1) rotor-coherente windsnelheidsvariatie, (2) plotselinge hoogte afhankelijke draaiing van de wind ("backing and veering wind"), (3) jetstroom, (4) windrichtingsvariatie, (5) plotselinge windschaduw voor een zijgedeelte van het rotorvlak van de windturbine ("partial wake condition"), en (6) door een plotselinge coherente verticale component in de windsnelheid (sloping wind). Voor deze werkwijze is een Nederlands octrooi verleend [79].

Verder is er in Hoofdstuk 9 gekeken naar modelgebaseerde alternatieven voor de signaal-gebaseerde CUSUM test, en met name naar de toepassing van de zogenaamde "Geleralized Likelihood Ratio test" (GLRT). Door gebruik te maken van een gelinearizeerd model van de windturbine en een lineair model van de "windverstoring" is deze benadering in staat om bepaalde windvlagen (zoals bijv. de bekende "Mexicaanse hoed") iets eerder te onderscheiden dan de CUSUM test. Dit algoritme staat echter nog in zijn kinderschoenen, en het is met name niet triviaal de GLRT methode zodanig uit te breiden dat het kan werken bij verschillende gemiddelde windsnelheden binnen het werkgebied. De eenvoud van de modelvrije CUSUM test daarentegen, en de mogelijkheid om deze relatief makkelijk uit te breiden naar het volledige windgebied (dit is inmiddels gedaan in het kader van het vervolg project FLOW-CDTup, zie Hoofdstuk "Perspectief voor toepassing"), levert grote praktische meerwaarde op ten opzichte van het GLRT.

OSC (Deel V)

OSC heeft te maken met het tot stilstand brengen van de windturbine bij serieus systeemfalen. Dit onderwerp wordt beschouwd in Deel V, waarbij de nadruk ligt op specifieke gevallen, namelijk op pitch actuator falen en het wegvallen van het elektrische koppel op de rotor (als gevolg van bijv. netuitval of as breuk). Het doel is om het shutdown proces regeltechnisch zodanig te begeleiden dat de belastingen zo laag mogelijk worden gehouden. Methoden met verschillende complexiteit zijn ontwikkeld en vergeleken, waaruit blijkt dat een geavanceerd regelalgoritme op basis van "Nonlinear Model Predictive Control" het beste resultaat oplevert, maar wel ten koste van een aanzienlijke toename van de benodigde rekenkracht. Daarentegen biedt een eenvoudige shutdown oplossing op basis van een standaard "het blad zo snel mogelijk verstellen naar vaanstand", uitgebreid met een notch filter op de toren eerste frequentie om ervoor te zorgen dat de eerste torenmode niet wordt aangestoten door de snelle pitch actie, een uitstekende afweging tussen rekencomplexiteit en belastingreductie.

De ontwikkelde OSC methoden zijn verder verbeterd en bijgesteld voor de toepassing op prototype windturbine van MHI (zie ook "Proof-of-principle experimenten" hieronder).

Experimentele modelvorming (Deel VI)

De experimentele modelvorming heeft betrekking op het verkrijgen van modellen op basis van meetdata. Voor het verkrijgen van bruikbare data zijn tijdens normaal bedrijf specifieke experimenten aan de windturbine nodig, waarbij de voor regelaar ontwerp en -analyse relevante dynamica wordt voorzichtig geëxciteerd met speciaal daarvoor ontworpen testsignalen. In Hoofdstuk 15 wordt beschreven hoe deze testsignalen zodanig kunnen worden ontworpen dat er geen eigen modes worden aangestoten ter vermijding van ongewenste resonanties en onacceptabele belastingen. Deze testsignalen worden vervolgens opgeteld bij de regelacties bladhoek en elektrisch koppel die in elke regelcyclus door de regelaar worden berekend en uitgestuurd. Verder zijn er een aantal methoden ontwikkeld voor modelidentificatie, waarbij de nadruk ligt op identificatie in gesloten lus doordat de windturbine regeling tijdens de experimenten niet mag worden uitgezet. Deze technieken zijn eerst in simulatiestudies gevalideerd, en later in Hoofdstuk 16 met echte metingen aan een Eco100 windturbine van de partner ALSTOM Wind. De verkregen modellen werden eerst gevalideerd met speciaal voor dat doel ontwikkelde in Hoofdstuk 15

validatiealgoritmen, en later op gedetailleerde aeroelastische modellen verkregen met Bladed. De resultaten tonen aan dat de ontwikkelde algoritmen voor systeemidentificatie als nauwkeurig genoeg voor regelaar ontwerp moeten worden beschouwd. De betrokken partner in de experimenten, ALSTOM Wind, was dermate tevreden met de resultaten dat hij zelf het initiatief nam om de resultaten op vier verschillende internationale conferenties te publiceren ([9, 10, 22, 23]).

Proof-of-principle experimenten

PoP experimenten zijn gedaan met de SusCon algoritmen OFC, EEC en OSC. De voorbereiding van deze experimenten en met name het bijstellen van de algoritmen, de uitvoering en de resultaten zijn strict vertrouwelijk en worden niet beschreven in dit openbaar rapport. Al deze PoP experimenten zijn gedaan aan een MHI prototype windturbine in twee verschillende meetcampagnes: eerst werd het IPC algoritme als onderdeel van OFC in april 2010 getest, en een jaar later werden experimenten gedaan met EEC en OSC. Deze laatste experimenten bevatten ook testen met de combinatie OFC-OSC-EEC dat het overgrote deel van het SusCon concept omvat. Het PoP met FTC is uitgevoerd aan de hand van meetdata verkregen tijdens de tweede meetcampagne (geen gerichte PoP experimenten met FTC konden worden uitgevoerd, zie "Knelpunten"). De resultaten van alle experimenten zijn zeer positief ontvangen door de projectpartner MHI, en laten zien dat een reductie van de vermoeiingsbelastingen op de bladen tot wel 17% kan worden gerealiseerd met OFC, terwijl de extreme belastingen in bepaalde gevallen tot wel 50% lager worden met EEC en OSC.

Knelpunten

Tijdens de loop van het project hebben de volgende knelpunten zich voorgedaan:

- De contractuele einddatum 31 december 2009 is in 2008 voor het eerst verschoven naar 31 december 2011 wegens een sterke personele onderbezetting in het eerste deel van het project en een aanmerkelijk langere benodigde doorlooptijd bij de industriële partners van de Proof-of-Principle experimenten.
- De industriële partner Nordex heeft op 17 november 2009 te kennen gegeven zich terug te trekken uit het consortium. Nordex is tot deze beslissing gekomen op grond van langdurige interne discussies en gedetailleerde presentaties, die op 28 mei 2009 door ECN bij de Nordex vestiging in Norderstedt (Hamburg) zijn gehouden, over inhoudelijke en uitvoeringstechnische aspecten van de experimenten met betrekking tot het integrale SusCon concept. De hoofdoorzaken waren personeelsgebrek en erg strakke time-to-market schema's voor hun nieuwe ontwikkelingen. Hierom werd het beschikbaar stellen van een voldoende bemande experimentele windturbine opstelling voor uitvoering van SusCon-concept PoP experimenten te bezwaarlijk voor de bedrijfsvoering. Snel daarop volgend is MHI verzocht om de SusCon-concept PoP experimenten uit te voeren. Tot groot genoegen bleek MHI blij verrast te zijn met dit verzoek, zodat de uitvoering van alle experimenten gewaarborgd bleef.
- Eind 2011 werd de einddatum van het project opnieuw verschoven naar 30 juni 2012, enerzijds door de langdurige afwezigheid wegens ziekte van de oorspronkelijke projectleider Tim van Engelen, en anderzijds doordat de PoP experimentenmet FTC bij MHI niet op tijd konden worden uitgevoerd. Omdat later ook bleek dat de uitvoering van de FTC PoP experimenten ook in de eerste helft van 2012 niet kon plaatsvinden doordat er grootschalige werkzaamheden waren gepland aan de gondel van de windturbine van MHI, werd in overleg met Agentschap NL begin 2012 besloten de PoP experimenten met FTC te doen aan de hand van simulaties met de software GH Bladed en de meetdata verkgregen tijdens de andere PoP experimenten.

Perspectief voor toepassing

De ontwikkelde methoden en daarop gebaseerde integrale benaderingswijze van regelen, SusCon, zullen na het project worden doorontwikkeld in onderlinge samenhang met de in gang te zetten productontwikkeling op het gebied van meet- en regeltechniek. De nadruk ligt hierbij op het ontwikkelen van algoritmen die opgenomen kunnen worden in de procescomputers van prototype windturbines. Het doel hiervan is om via beproevingen van veel langere duur dan in dit project het SusCon concept van haar kinderziektes te ontdoen en de markt er enthousiast voor te maken. Dit laatste vooral door het concept te kunnen presenteren als "proven technology". Met dit als doel, zijn al voor afloop van dit project twee vervolg projecten geïnitieerd binnen het "Far and Large Offshore Wind Innovation" programma (FLOW):

- "Control Design Tool Upgrade" (CDTup), nummer P201101-014-ECN: Dit project is de eerste fase van een grootschalige upgrade van het Control Design Tool (CDT) van ECN, een gereedschap voor het ontwerp van industriële windturbine regelingen. In deze eerste fase worden de OFC en de EEC algoritmen, zoals ontwikkeld in het SusCon project, doorontwikkeld en geïmplementeerd in het CDT.
- "Improvement of advanced design tools", nummer P201203-006-ECN: In dit vervolgproject, fase 2, worden de resterende SusCon algoritmen (namelijk OSC en FTC) verbeterd en toegevoegd aan het nieuwe tool, en wordt de complete regeling (incl. het gehele SusCon concept) uitvoerig getest op een 2-bladige prototype windturbine van de Nederlandse windturbine fabrikant 2-B Energy.

Daarbij wordt op het moment van schrijven van dit rapport gewerkt aan een derde gerelateerde FLOW voorstel met de windturbine fabrikant XEMC-Darwind als partner. Dit project heeft als doel het nieuwe tool additioneel te verifiëren op een 3-bladige windturbine. De introductie van het nieuwe regeltool op de markt wordt verwacht in het jaar 2013.

Daarna zal al in het ontwerp van nieuwe generaties windturbines rekening worden gehouden met de voordelen van SusCon, zodat deze voor lagere belastingen worden berekend. Eerst zal dit turbines van het gangbare formaat betreffen, daarna veel grotere en wel tot aan het voor offshore windconversie optimale vermogen van 10MW of zelfs meer.

Beschrijving van de bijdrage aan de doelstellingen van de regeling

Bijdrage aan een duurzame energiehuishouding

Het project draagt bij tot de hoofddoelstelling, het concurrerend maken van offshore windconversie met fossiele opwekking op land in 2020, door verhoging van de beschikbaarheid en verlaging, dan wel meer gelijkmatig maken, van de turbinebelastingen. Dit laatste maakt verdere opschaling mogelijk, waarbij moet worden gedacht aan windturbines met een vermogen van 10MW of zelfs meer. Een schaalgrootte van 10MW of meer is nodig om de kosten van offshore windconversie uiteindelijk terug te kunnen brengen tot het vereiste niveau. De nieuwe regelconcepten voor de individuele turbine staan hierin centraal en zullen in hoge mate bijdragen aan het mogelijk maken van efficiënte bouwtechnieken die deel uitmaken van de vereiste doorbraaktechnologie voor opschaling.

De ontwikkeling van fundamenteel andere bedrijfsvoeringconcepten voor individuele turbines en clusters daarvan zal de beschikbaarheid sterk doen toenemen en de problemen van de netinpassing doen afnemen. De "Extreme Event Control" methode verhoogt de zekerheid van energielevering sterk bij stormfronten. Door "Fault Tolerant Control" kunnen de windturbines, ondanks kleine gebreken, toch doordraaien waardoor minder stilstand optreedt en het onderhoud beter gepland kan worden.

Er wordt voorzien dat door SusCon de kosten van offshore windconversie met zo'n 16% zullen dalen. Hiervan neemt de verhoogde beschikbaarheid 11% voor haar rekening, de verlaagde belastingen 2.5%, en de betere planbaarheid van het onderhoud nog eens 2.5%. Dit komt neer op het vermijden van de inzet van primaire energie van ca. 8.2 PJ per jaar in 2020 voor wat betreft offshore windconversie in de Nederlandse situatie.

Versterking van de kennispositie van Nederland

Windconversie offshore is een speerpunt in het LT-EOS programma, met ontwerpkennis als onderzoeksterrein. Zowel wat betreft het speerpunt als op het onderzoeksterrein behoort ECN Windenergie tot de wereldtop van de onderzoeksinstituten, zoals blijkt uit haar rol in de European Academy of Wind Energy (EAWE), de rol als medecoördinator van het Integrated Project (IP) "Upwind" in het kader van het Europese 6th Framework Programme, en haar betrokkenheid bij de Europeese projecten STABCON en DOWNVIND.

Bij de TUD, afdeling Delft Center for Systems and Control (DCSC), onder leiding van Prof. Michel Verhaegen, is hoogwaardige specialistische kennis aanwezig op het gebied van Fault Tolerant Control en klassieke regeltheorie. De affiniteit met windenergie is hoog.

Dit project levert kennis op het gebied van bedrijfsvoeringmethoden voor offshore windconversie met een sterk vernieuwend karakter:

- voor het eerst worden regel-, bewakings-en beveiligingstaken zodanig geïntegreerd dat hiermee de beschikbaarheid van de windturbines substantieel wordt verhoogd;
- er worden baanbrekende regelmethoden ontwikkeld op het gebied van vermoeiingsbelastingreductie en het pareren van extreme condities zoals harde windvragen;
- er wordt voor het eerst gekeken naar het optimaal tot stilstand brengen van de turbine bij ernstig falen met minimale vervolgschade.

Dit is bijzonder gunstig voor de kennispositie van Nederland omdat dit soort kennis niet makkelijk operationeel is te maken zonder de expertise die opgebouwd is tijdens de uitvoering van het project. De versterkte kennispositie op dit gebied biedt kansen voor substantiële kennisexport gegeven het enorme potentieel van windconversie en de toepasbaarheid van de methoden op zowel offshore als on-shore windconversie.

Om de ontwikkelde kennis te beschermen zijn de volgende patentaanvragen ingediend:

- [79] van Engelen, T., L. Machielse and S. Kanev (2010): Method and system for wind gust detection in a wind turbine. Publication number NL C 2005400.
- [77] van Engelen, T. (pending): System and method for compensating rotor imbalance in a wind turbine. International publication number WO 2010/016764 Al.
- [42] Kanev, S., J. Schuurmans and T. van Engelen (pending): Apparatus and method for Individual Pitch control in Wind turbines. Publication number P6029490US.

Spin off binnen en buiten de sector

De product/marktcombinatie wordt gevormd door regelsystemen op offshore windturbines voor de elektriciteitsmarkt. De windturbinefabrikanten spelen hierin een sleutelrol. Omdat SusCon ook interessant zal blijken voor on-shore windconversie zal de markt een mondiale omvang aannemen, maar zal vooral worden geconcentreerd in Europa, Noord Amerika en Azië.

De ontwikkelde integrale benaderingswijze van regelen kan na het project leiden tot nieuwe productontwikkeling op het gebied van meet- en regel-equipment waarbij de nadruk ligt op de aanpassing van pitch-actuatoren om toepassing van multi-mode individual pitch control mogelijk te maken, maar ook op de verbetering en het betrouwbaarder maken van de belastingsensors benodigd voor IPC.

Overzicht van publicaties

In de lijst hieronder staan alle project-gerelateerde publicaties opgenomen, waarbij de nummering overeenkomt met die in de Bibliografie aan het end van dit rapport.

- [9] Carcangiu, C., I.F. Balaguer, S. Kanev and M. Rossetti (2011): Closed-Loop System Identification of Alstom 3MW Wind Turbine. Proceedings of IMAC XXIX. Jacksonville-FL, USA
- [10] Carcangiu, C., S. Kanev, M. Rossetti and I.F. Balaguer (2010): System Identification on Alstom ECO100 Wind Turbine. Proceedings of the POWER-GEN International Conference.
- [22] Font, I., S. Kanev and M. Rossetti (2010): System identification on the ECO 100 wind turbine. poster in the European Wind Energy Conference.
- [23] Font, I., S. Kanev, D. Tcherniak and M. Rossetti (2010): System identification methods on Alstom ECO 100 wind turbine. Proceedings of The Science of Making Torque from Wind Conference. FORTH, Heraklion, Crete, Greece.
- [38] Kanev, S. (2009): Dealing with actuator constraints in multi-mode blade load reduction control. Report ECN-Wind Memo-09-069, ECN Wind Energy.
- [39] Kanev, S. (2009): System identification from BLADED simulations with the Ecotècnia 100 wind turbine. Confidential report ECN-X-09-026, Energy Research Centre of the Netherlands (ECN).
- [40] Kanev, S. (2009): System identification from field measurements on Ecotècnia 100 wind turbine. Report ECN-X–09-089, Energy Research Center of the Netherlands.
- [41] Kanev, S. and T. van Engelen (2009): Exploring the Limits in Individual Pitch Control. Proceedings of the European Wind Energy Conference (EWEC). Marseille, France.
- [42] Kanev, S., J. Schuurmans and T. van Engelen (pending): Apparatus and method for Individual Pitch control in Wind turbines.
- [43] Kanev, S. and T. van Engelen (2008): Wind Turbine Extreme Gust Control. Report ECN-E-08-069, ECN Wind Energy.
- [44] Kanev, S. and T. van Engelen (2010): Wind Turbine Extreme Gust Control. Wind Energy, 13(1):18-35.
- [65] Selvam, K., S. Kanev, J.W. van Wingerden, T. van Engelen and M. Verhaegen (2009): Feedback-feedforward individual pitch control for wind turbine load reduction. International Journal of Robust and Nonlinear Control, 19(1):72-91.
- [75] van Engelen, T. (2006): Design model and load reduction assessment for multi-rotational mode individual pitch control (higher harmonics control). Proceedings of the European Wind Energy Conference. Athens, Greece.
- [76] van Engelen, T. (2007): Control design based on aero-hydro-servo-elastic linear models from TURBU (ECN). Proceeding of the European Wind Energy Conference. Milan, Italy.

- [77] van Engelen, T. (pending): System and method for compensating rotor imbalance in a wind turbine.
- [79] van Engelen, T., L. Machielse and S. Kanev (2010): Method and system for wind gust detection in a wind turbine.
- [81] van Engelen, T. and P. Schaak (2007): Oblique Inflow Model for Assessing Wind Turbine Controllers. Proceedings of the 2nd Conference on The Science of Making Torque From Wind. Lyngby, Denmark.
- [82] van Engelen, T., J. Schuurmans, S. Kanev, J. Dong, M. Verhaegen and Y. Hayashi (2011): Fault tolerant wind turbine production operation and shutdown (Sustainable Control). Proceedings of the EWEA Conference. Brussels, Belgium.
- [96] Wei, X. (2009): Fault Detection of Large Scale Off-shore Wind Turbine Systems. Report 09-044, Delft University of Technology.
- [97] Wei, X. and M. Verhaegen (2008): Fault Detection of Large Scale Wind Turbine Systems: A mixed H_infinity/H_ Index Observer Approach. Proceedings of the 16th Mediterranean Conference on Control and Automation. Ajaccio, France.
- [98] Wei, X. and M. Verhaegen (2008): Mixed H_infinity/H_index Fault Detection Observer Design for LPV systems. Proceedings of the 47th IEEE Conference on Decision and Control. Cancun, Mexico, pages 1073-1078.
- [99] Wei, X. and M. Verhaegen (2009): Mixed H_/H_infinity Dynamic Observer Design for Fault Detection. Proceedings of the European Control Conference. Budapest, Romania, pages 1913-1918.
- [100] Wei, X. and M. Verhaegen (2009): Robust Fault Detection Observer Design for LTI Systems Based on GKYP Lemma. Proceedings of the European Control Conference. Budapest, Romania, pages 1919-1924.
- [101] Wei, X. and M. Verhaegen (2009): Robust Fault Detection Observer for LTI Systems with Additive Uncertainties. Proceedings of the 7th IFAC Symposium on Fault Detection, Supervision and Safety of Technical Processes (SAFEPROCESS). Barcelona, Spain, pages 756-761.
- [102] Wei, X., M. Verhaegen and T. van Engelen (2008): Sensor Fault Diagnosis of Wind Turbines for Fault Tolerant Control. Proceedings of the 17th World congress of IFAC. Seoul, Korea, pages 3222-3227.
- [103] Wei, X., M. Verhaegen and T. van Engelen (2010): Sensor Fault Detection and Isolation for Wind Turbines Based on Subspace Identification and Kalman Filter Techniques. International Journal of Adaptive Control and Signal Processing, 24(8).

Projectgegevens

Projectnummer: EOSLT02013

Projecttitel: Sustainable Control. A new approach to operate wind turbines

Coordinator: ECN

Partners: TU-Delft, Mitsubishi Heavy Industry, ALSTOM Wind, Nordex, Gerrad Hassan

Doorlooptijd: 1 januari 2006 - 30 juni 2012

Contact: S. Kanev (ECN), email: kanev@ecn.nl

Het project is uitgevoerd met subsidie van het Ministerie van Economische Zaken, Landbouw en Innovatie, regeling EOS: Lange Termijn uitgevoerd door Agentschap NL.

Part I

Introduction

Nowadays, control has been well established as a driver for cost reduction of wind energy conversion. Usually, the associated control algorithms relate to production operation in stationary turbulent conditions without any deteriorated wind turbine behavior (regular conditions). Unfortunately, extreme environmental conditions as well as system failure are real-life phenomena. Especially offshore, the need arises to deal in an effective way with (short-term) extreme environmental conditions and with minor or more severe types of system failure.

For reasons of the environment and future generations, the Dutch government has aimed to start a transition in short-term to a more sustainable way for the generation of electricity way by utilizing (offshore) wind power. Offshore wind energy conversion will become economical if the costs of energy decreases and the risks for investments are acceptable.

For this, further up scaling of wind turbines towards 10MW is necessary, because of the expensive foundation and installation costs in case of offshore locations. Additionally, due to the low accessibility for offshore locations, it is needed to improve the turbine reliability to achieve a high availability. A higher availability will also result in less urgent maintenance (expensive) and gives improved guarantee of energy production.

As a consequence, it is aimed to achieve large and efficiently built offshore wind turbines in the future, which should be able to produce electrical energy during almost all circumstances and despite of failures. Aiming to contribute significantly to this goal, the long-term research project *Sustainable Control, a new approach to operate wind turbine* (SusCon) has been set up under grant EOSLT02013 of AgentschapNL (2006-2012).

The approach of Sustainable Control is strongly innovative with respect to ongoing research. Sustainable Control differs from the currently used in practice "isolated approach" in its integral approach of turbine operation (integrating feedback control and supervising control) and the use of advanced wind turbine control methods.

Within the scope of wind turbine management, the objective of this project is defined as finding control methods that contribute significantly to the solution of the following specific problems:

- unnecessary turbine standstill due to "isolated turbine control approach",
- high costs and upscale limitation due to high turbine loads and stability problems,
- production uncertainty and high loads during extreme (weather) conditions,
- serial damages during shut-down after serious failure detection.

It is aimed in the project to realize these objectives by developing an innovative approach to manage offshore wind turbines, called Sustainable Control. The Sustainable control concept includes the development and integration of the following cornerstones that relate to wind turbine control in four different types of operating conditions:

- Optimized Feedback Control (OFC): for load reduction by advanced control methods during normal operating conditions (Part II).
- Fault Tolerant Control (FTC), for avoiding unnecessary standstill in cases of minor system failures by fault detection and controller reconfiguration (Part III),
- Extreme Event Control (EEC), for avoiding excessive loads and unnecessary shut-down under extreme conditions (Part IV),

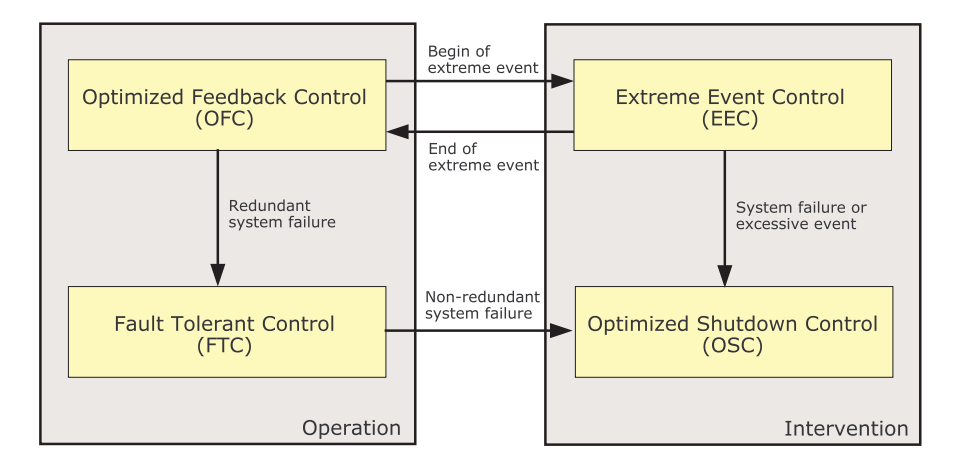


Figure 1 Schematic visualization of the Sustainable Control concept

• Optimal Shutdown Control (OSC), for avoiding excessive loads and serial damage after serious system failure or hyper-extreme conditions (Part V).

The integration of these four cornerstones will make it possible to achieve significant reduction of turbine costs and achieve further up-scaling of wind turbines.

Figure 1 shows a top-level visualization of the Sustainable Control concept. The development of each of the four cornerstone methods consists of:

- definition of suitable models for controller design and evaluation,
- controller synthesis based on the control objectives,
- evaluation and analysis of the results based on detailed aeroelastic models,
- proof-of-principle experiments.

Supportive to the development of these four major cornerstones are the following additional activities:

- development of methods for stability analysis of periodic systems (Section 4), required for performing closed-loop stability analysis of the higher-harmonics IPC loops developed in Section 1.4.
- procedure for generating time-domain realizations of blade-effective wind speed signals (Section 5), needed for performing fast simulations for intermediate testing of the control methods developed in Parts II-V,
- wind turbine model identification (Part VI), required for fine-tuning the control-oriented models using real-time measurement data,
- integration of the control methods into the Sustainable Control concept (Part VII),
- performing proof of principle experiments and detailed simulation tests for validating the developed control concepts (not reported here due to confidentiality).

The project activities are organized in work packages. Figure 2 depicts the dependencies between the work packages of the project, and provides reference to the part of this report where each work package is treated. The starting point of the research is the state-of-the-art knowledge and methods in the field of modeling, control, stability analysis and experiments. Work packages

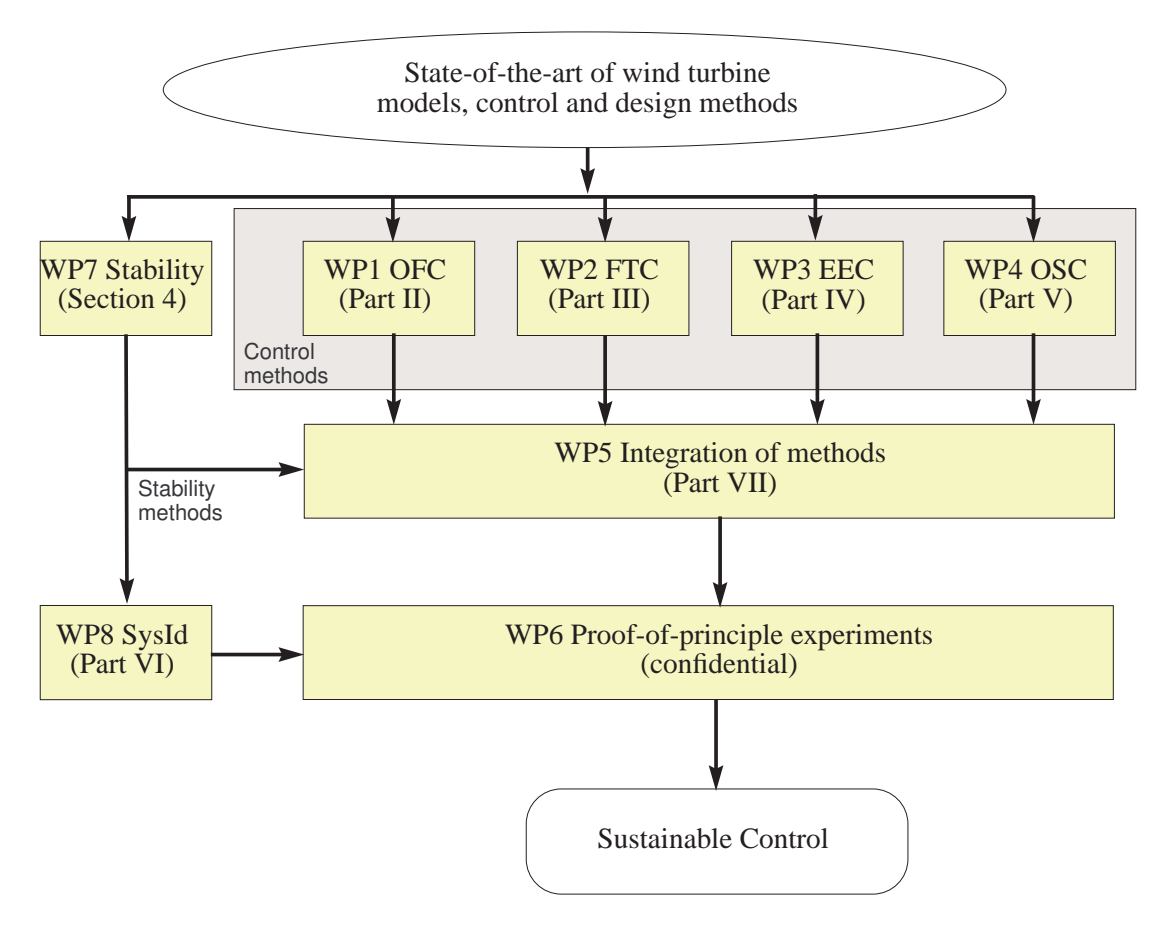


Figure 2 Overview of the work packages of the SusCon project

1-4 concern the developments of the control methods OFC, FTC, EEC and OSC, i.e. the four cornerstones of the SusCon concept. Work packages 7 and 8 are supportive for the stability analysis in WP1-5, and the proof-of-principle experiments in WP6.

Many of the results, presented in this report, have been published in journals, conferences, and in form of technical reports. Below, a list is provided giving an overview of the parts of this report that have appeared in one or another form in the literature.

- Section 1 "Multi-rotational mode individual pitch control" is published in: [75]
- Section 2 "Feedback-feedforward IPC" is published in: [65]
- Section 3 "Constraints handling in IPC" is published in: [42, 41, 38]
- Section 6 "GLRT for detecting blade moment sensor faults" is published in: [103, 96]
- Section 8 "Dealing with wind gusts in combination with wind direction changes" is published in: [44, 43]
- Section 9 "Fast wind gust detection with GLRT" is published in: [82]
- Part VI "Experimental methods" is published in [23, 10, 9, 22]
- Section VII "Integration of methods: Sustainable Control concept" is published in: [82]

A list of all project-related publications can be found in the Summary.

Part II

Optimized feedback control (OFC)

1 Multi-rotational mode individual pitch control

Summary

A model-based design approach for individual pitch control has been derived for 3 bladed HAWTs. Control loops were designed for a typical 3 MW variable speed wind turbine and the performance was evaluated in aero-elastic simulations. The individual pitch control reduces the loads from rotationally sampled turbulence, tower stagnation and wind shear. The involved pitching activity is centered around the rotational frequency (IPC-1p) and multiples of it (IPC-2p, IPC-3p; 'higher harmonics control'). The fatigue damage of the blades in full load is substantially reduced while one third or more is obtained from IPC-2p and IPC-3p; the fatigue damage reduction of the nacelle is almost completely obtained from IPC-2p. Very elementary feedback laws appear to satisfy when combined with modulation and demodulation schemes based on multi-blade coordinate transformations in the kp-frequencies (k = 1, 2, 3). This is clarified via the decomposition of the sampled turbulent wind field by the rotor blades in rotational modes. Integrated stability analysis has to be based on Floquet theory; the required model formulation is supplied.

1.1 Introduction

The loads on the rotor blades, drive-train and tower of horizontal axis wind turbines are caused for a significant part by the rotational sampling of turbulence, the tower shadow and the wind shear. These loads can be reduced via individual pitch control. The earlier publications [13] and [6] give an impression of the potential of this control concept, focused on load reduction around one time the rotational frequency (IPC-1p). The method for the design of the feedback loops for individual pitch control has been explained in [6].

However, a control design model and a model-based motivation for the choice of the structure of the feedback loops (feedback laws) as well as a model-based parametrization of these loops have not yet been published. Besides, a drawback of the limitation to IPC-1p is the still existing blade load components around multiples of the rotational speed (2p, 3p, ...). Perhaps even more important are the loads on the nacelle around the 3p-frequency in case of a three bladed wind turbine, which is the prevailing layout. So, compensation for the higher harmonic excitation from the wind is expected to be worthwhile.

This section presents a simple control design model that caters for the individual blade behavior (Section 1.2). The model is used for the design of feedback loops for IPC-1p (Section 1.3). It also appears to allow for the design of feedback loops for individual pitch control around the 2p-and 3p-frequency (IPC-2p, IPC-3p; Section 1.4). The model is only feasible for the design of a set of IPC-kp feedback loops after a multi-blade coordinate transformation in the concerning kp-frequency (k = 1, 2, 3). Two equal, elementary feedback laws can be applied for load reduction within the scope of such an kp-transformed model. This immediately becomes clear when a rotational mode decomposition of the sampled turbulent wind field by the rotor blades is added to the model equations.

The IPC-kp feedback laws are designed independently while they will operate simultaneously. The feedback laws, together with an kp modulation and demodulation scheme, set up the 'true' feedback loops for IPC-kp. Model analysis with the true feedback loops included proves the expectations: compensation for the kp harmonic excitation from the wind (Section 1.5). Timedomain simulations with this controlled model show the effect of IPC-kp control on the stationary blade and nacelle loads (Section 1.6).

Although the IPC-kp designs are performed independently, there will exist some interaction since the IPC-kp loops are simultaneously active and the required low-pass filters in the loops cannot be realized for ideal behavior. A model formulation for integrated stability analysis is derived; the

model contains periodic coefficients and requires application of the Floquet theory for stability assessment (Section 1.7).

The control design model does not include blade bending and unsteady aerodynamics. Besides the stability assessment procedure has not yet been established. Therefore, the adopted approach should be considered as the first step in the development of a model-based design method for IPC-kp rather than a fully validated method.

1.2 Control design model

The control design model pertains to a three bladed horizontal axis wind turbine (B=3). The main features of the model are:

- individually pitch-controlled rigid blades;
- main rotation and 1st drive-train torsion mode;
- 1st fore-aft and sideward tower bending mode;
- controllable generator torque.

A schematic layout of the wind turbine model is pictured below. The model also contains three

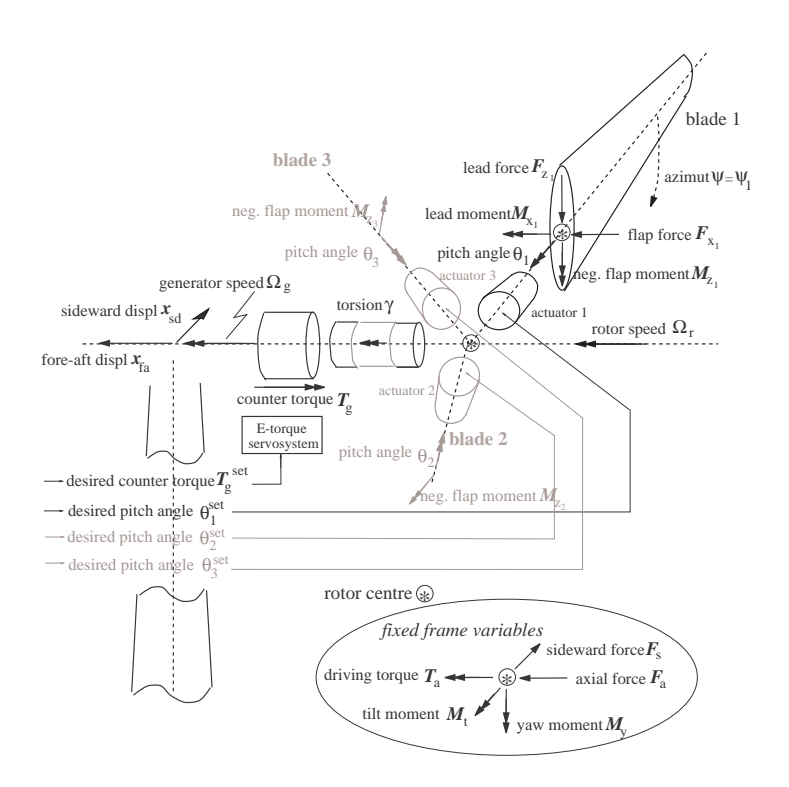


Figure 3 Schematic layout wind turbine model

so called *blade effective* wind input signals. When such a signal acts as a uniform wind speed on the rotor blade, it causes blade root loads that are similar to those arising from a rotating blade in a wind field. This concept allows for describing the wind influence on the blade root loads via a single input signal while yet taking into account the properties of the rotationally sampled wind field affected by wind shear and tower shadow (longitudinal turbulence only). A comprehensive description is in [80].

The next two subsections deal with the linearized aerodynamic conversion behavior for the individual rotor blades and the basic linear model equations.

1.2.1 Linearized aerodynamic conversion

The aerodynamic conversion is based on linearized BEM-theory; dynamic wake effects and unsteady aerodynamics are not taken into account. The BEM-based aerodynamic conversion characteristics are translated into multipliers that map a variation in the flapwise relative wind speed $v_{\rm fl_i}$ to variations in the flap- and leadwise blade root moments and forces (aerodynamic gains). Aerodynamic gains are also derived for the linearized influence of a variation in the pitch angle. The pitch angle variation θ_i and relative wind speed variation $v_{\rm fl_i}$ for the $i^{\rm th}$ blade thus cause variations in the aerodynamic loads on the blade root by (see fig. 3 for orientation):

$$\begin{split} \delta M_{z_i} &= h_{M_z} \, v_{\mathrm{fl}_i} + k_{M_z} \, \theta_i \quad \text{(neg. flapwise moment)} \\ \delta F_{x_i} &= h_{F_x} \, v_{\mathrm{fl}_i} + k_{F_x} \, \theta_i \quad \text{(pos. flapwise force)} \\ \delta M_{x_i} &= h_{M_x} \, v_{\mathrm{fl}_i} + k_{M_x} \, \theta_i \quad \text{(pos. leadwise moment)} \\ \delta F_{z_i} &= h_{F_z} \, v_{\mathrm{fl}_i} + k_{F_z} \, \theta_i \quad \text{(pos. leadwise force)} \end{split}$$

For variation $\delta T_{\rm a}$ in the driving torque, $\delta F_{\rm a}$ in the axial force, $\delta M_{\rm t}$ in the tilt moment and $\delta F_{\rm s}$ in the sideward force holds:

$$\delta T_{\mathbf{a}} = \sum_{i=1}^{B} \delta M_{x_{i}} \qquad ; \quad \delta F_{\mathbf{a}} = \sum_{i=1}^{B} \delta F_{x_{i}}$$

$$\delta M_{\mathbf{t}} = \sum_{i=1}^{B} \sin \psi_{i} \, \delta M_{z_{i}} \quad ; \quad \delta F_{\mathbf{s}} = -\sum_{i=1}^{B} \sin \psi_{i} \, \delta F_{z_{i}}$$

$$(2)$$

The flapwise relative wind speed variation v_{fl_i} for the i^{th} blade is the sum of the blade effective wind speed \tilde{u}_i and the upwind motion of the rotor blade. The latter is caused by fore-aft tower bending only since rigid blades are assumed. The upwind structural motion involves both the fore-aft translation \dot{x}_{fa} and tilt rotation $\dot{\phi}_{\mathrm{fa}}$ of the tower top; the latter has an azimuth dependent effect on the relative wind speed which varies over the rotor radius. The 3/4 blade radius location of the rotor blades $(\frac{3R_{\mathrm{b}}}{4})$ is assumed to be the effective location for taking into account $\dot{\phi}_{\mathrm{fa}}$ in the one-point-model-approach to blade loading. The flapwise relative wind speed v_{fl_i} is determined as:

$$v_{fl_i} = \tilde{u}_i - \dot{x}_{fa} + \sin(\psi_i) \frac{3}{2H} \frac{3R_b}{4} \dot{x}_{fa}$$
 (3)

The multiplier $\frac{3}{2H}$ is exactly the ratio between displacement and rotation if a prismatic beam of length H is subjected to a bending force load.

At azimuth angle $\psi = \int_{-\infty}^{t} \Omega_{\rm r}(\tau) d\tau$ equal to 0, the first blade is in the horizontal position while it is rotating downward. For the azimuth angles ψ_1 , ψ_2 and ψ_3 of the three blades holds:

$$\psi_1 = \psi$$
 ; $\psi_2 = \psi + \frac{2}{3}\pi$; $\psi_3 = \psi + \frac{4}{3}\pi$ (4)

The gains $h_{M_z} cdots k_{F_z}$ are derived from the power and thrust coefficient data in a chosen working point, characterized by wind speed, rotor speed and pitch angle. The derivation is constrained by the assumption of equal aerodynamic efficiency along the blade radius, which implies a *linear increasing* flapwise force per unit span $f_{\rm fl}(r)$ over the rotor radius and *constant* leadwise force per unit span $f_{\rm fl}(r)$.

1.2.2 Periodic linear model equations

The model equations that are required for controller design are the equations of motions and the output equations; the latter express the measurement variables that are input to the feedback loops

in state and input variables, the 'typical' variables in the equations of motion.

Equations of motion

The variables of the drive-train are the rotor speed $\Omega_{\rm r}$, generator speed $\Omega_{\rm g}$ and the shaft torsion γ ; all drive-train variables are scaled to the speed level of the rotor shaft. The drive-train is accelerated by the aerodynamic driving torque $T_{\rm a}$ and decelerated by the generator torque $T_{\rm g}$. With linear and angular fore-aft tower motion included in the relative wind speed on the rotor blades, the equations of motion for the rotor speed $\Omega_{\rm r}$ and shaft torsion γ (eom1, eom2) become:

$$J_{\rm r} \dot{\Omega}_{\rm r} \stackrel{\rm com1}{=} \delta T_{\rm a} - s_{\rm sh} \gamma - d_{\rm sh} \dot{\gamma}$$

$$\frac{J_{\rm r} J_{\rm g}}{J_{\rm r} + J_{\rm g}} \ddot{\gamma} \stackrel{\rm com2}{=} \frac{J_{\rm g}}{J_{\rm r} + J_{\rm g}} \delta T_{\rm a} - s_{\rm sh} \gamma - d_{\rm sh} \dot{\gamma} + \frac{J_{\rm r}}{J_{\rm r} + J_{\rm g}} \delta T_{\rm g}$$
(5)

with linearised torque variation δT_a by (equation 1 2, 3):

$$\delta T_{\rm a} = \sum_{i=1}^{B} \left[h_{M_x} \, \tilde{u}_i + k_{M_x} \, \theta_i \right] - B \, h_{M_x} \, \dot{x}_{\rm fa} \tag{6}$$

The drive-train parameters are the slow-shaft equivalent moments of inertia $J_{\rm r}$ and $J_{\rm g}$ of the rotor and generator and the stiffness and damper constant $s_{\rm sh}$ and $d_{\rm sh}$. The values are to be tuned such that torsion behavior agrees with the first collective lead mode; this yields a slightly underestimated moment of inertia $J_{\rm r}$ in the equation of motion for $\Omega_{\rm r}$, which is of minor importance since this hardly affects rotor speed regulation control.

The variables of the included tower model are the fore-aft and sideward tower top displacement $x_{\rm fa}$ and $x_{\rm sd}$. The fore-aft motion is driven by the thrust force $F_{\rm a}$ and aerodynamic tilt moment $M_{\rm t}$. A positive tilt moment causes upward tilting of the rotor center, so positive fore-aft translation. The sideward motion is driven by the generator torque $T_{\rm g}$ and the sideward aerodynamic force $F_{\rm s}$. The equations of motion for fore-aft and sideward tower bending are:

$$m_{\text{tw}} \ddot{x}_{\text{fa}} \stackrel{\text{eom3}}{=} \delta F_{\text{a}} + \frac{3}{2H} \delta M_{\text{t}} - s_{\text{tw}} x_{\text{fa}} - d_{\text{tw}} \dot{x}_{\text{fa}}$$

$$m_{\text{tw}} \ddot{x}_{\text{sd}} \stackrel{\text{eom4}}{=} \frac{3}{2H} \delta T_{\text{g}} + \delta F_{\text{s}} - s_{\text{tw}} x_{\text{sd}} - d_{\text{tw}} \dot{x}_{\text{sd}}$$
(7)

The multiplication factor $\frac{3}{2H}$ for the bending moment loads in the equations of motion exactly applies if a prismatic beam is involved.

For the linearised variation in the axial force, tilt moment and sideward force holds ((equation 1 2, 3; $\sum_{i=1}^{B} \sin^2 \psi_i = \frac{1}{2}B$):

$$\delta F_{a} = \sum_{i=1}^{B} \left[h_{F_{x}} \, \tilde{u}_{i} + k_{F_{x}} \, \theta_{i} \right] - B \, h_{F_{x}} \, \dot{x}_{fa} \quad .$$

$$\delta M_{t} = \sum_{i=1}^{B} \sin \psi_{i} \, \left[h_{M_{z}} \, \tilde{u}_{i} + k_{M_{z}} \, \theta_{i} \right] + \frac{3}{2} \, \frac{9Rb}{8H} \, h_{M_{z}} \, \dot{x}_{fa} \tag{8}$$

$$\delta F_{s} = \sum_{i=1}^{B} -\sin \psi_{i} \, \left[h_{F_{z}} \, \tilde{u}_{i} + k_{F_{z}} \, \theta_{i} \right] - \frac{3}{2} \, \frac{9Rb}{8H} \, h_{F_{z}} \, \dot{x}_{fa}$$

Equal values for the tower top equivalent mass $m_{\rm tw}$, damper constant $d_{\rm tw}$ and spring constant $s_{\rm tw}$ apply in the fore-aft and sideward equation of motion. These are based on structural data:

- horizontal tower displacement at unity force;
- damping rate of the 1st bending mode(s);
- average of the 1st fore-aft and sideward frequency.

Output equations

Next to the equations of motion, output equations apply when feedback control is considered. The

individual pitch control can be realized by feedback of the blade root bending moments, the shaft bending moments or the yaw and tilt moment on the nacelle. In order to describe the approach to multi-rotational mode individual pitch control as straightforward as possible, we choose the feedback of the blade root bending moment variations δM_{z_i} . It holds (oe1 means 1st output equation, etc.; use equation 1, 3):

$$\delta M_{z_1} \stackrel{\text{oel}}{=} -h_{M_z} \left(1 - \sin \psi_1 \, \frac{9R_b}{8H} \right) \dot{x}_{fa} + h_{M_z} \, \tilde{u}_1 + k_{M_z} \, \theta_1
\delta M_{z_2} \stackrel{\text{oel}}{=} -h_{M_z} \left(1 - \sin \psi_2 \, \frac{9R_b}{8H} \right) \dot{x}_{fa} + h_{M_z} \, \tilde{u}_2 + k_{M_z} \, \theta_2
\delta M_{z_3} \stackrel{\text{oes}}{=} -h_{M_z} \left(1 - \sin \psi_3 \, \frac{9R_b}{8H} \right) \dot{x}_{fa} + h_{M_z} \, \tilde{u}_3 + k_{M_z} \, \theta_3$$
(9)

Next to IPC, also control concepts apply for speed regulation, torsion damping and tower damping. The involved additional model output signals are the slow-shaft equivalent generator speed $\Omega_{\rm g}$ and the fore-aft and sideward tower speed $v_{\rm a}$ and $v_{\rm s}$:

$$\Omega_{\rm g} \stackrel{\text{oe4}}{=} \Omega_{\rm r} - \dot{\gamma}
v_{\rm a} \stackrel{\text{oe5}}{=} \dot{x}_{\rm fa}
v_{\rm s} \stackrel{\text{oe6}}{=} \dot{x}_{\rm sd}$$
(10)

Although it is more realistic to assume that the fore-aft and sideward tower *acceleration* will be measured instead of the speed, it is more straightforward to use the speed signals from a conceptual point of view on control.

In this study on individual pitch control, only a collective pitch feedback loop for speed regulation is added to the feedback loops for IPC-np. The damping loops for the tower and drive-train are not considered here. The generator torque is tuned to the filtered rotor speed in order to maintain rated power production on the average (cut-off frequency 0.1 Hz).

1.3 1P Individual pitch control

As already mentioned, the design of feedback loops in this section is focused on

- rotor speed regulation by collective pitch control;
- blade load reduction by individual pitch control.

In [6] is argued that the reduction of the (flapwise) blade loading around the 1p-frequency can be straightforward achieved by low-frequency control of the so-called 'dq-axis loads'. The blade flap loads become tilt- and yaw-oriented loads in a dq-axis representation, which is commonly used in electric machine theory. Because of the modulating effect of the rotating blade, the low-frequency contents of tilt- and yaw-loads correspond with the frequency contents around 1p of the blade flap loads. Appropriate low-frequent 'dq-axis pitch actions' reduce the 1p blade loads after having been transformed from the dq-axes to differential (1p-individual) pitch actions along the rotating blade axes.

If the dq-axis representation for an electric machine is extended with the 'DC-component' then this would correspond with adding the collective pitch actions to the 1p-individual actions. Actually, combined collective and 1p-individual pitch control can be derived from the same model when the *multi-blade coordinate transformation* as proposed by Coleman and Feingold [18] is effectuated on all model variables that are attached to the rotor blades ('rotating variables'); the feedback laws are then designed in the transformed model. It is common use to apply the 'Coleman transformation' in the aeroelastic stability analysis [32] of wind turbines and helicopters with polar symmetry (≥3 blades): the homogeneous part of the equations of motion is transformed into multi-blade coordinates, which makes the periodic coefficients to vanish. In that case

only the rotating *state* variables are transformed, while in our case also the rotating *input* and *output* variables are transformed. The latter yields a model formulation for control design which is completely time-invariant.

The following two subsections deal with the transformation of the control design model in multiblade coordinates, the linear time-invariant *1p-transformed model*, and with the design of the feedback laws for 1p-individual pitch control, combined with collective pitch control for speed regulation.

1.3.1 Linear time-invariant model

The equations of motion that depend on ψ from Section 1.2 do not include state variables attached to the blades or the rotor shaft except the rotational speed $\Omega_{\rm r}$ and shaft torsion γ . Since $\Omega_{\rm r}$ and γ have a co-axial orientation, not any state variable is to be transformed. The flapwise bending moments, pitch angles and blade effective wind speeds are the only variables to be transformed. When the corresponding variables on the three rotor blades are assumed to set up a coordinate vector, the Coleman transformation matrix \boldsymbol{P} maps the so called multi-blade coordinates in vector $\underline{p}_{\rm cm}$ to rotating coordinates in vector \underline{p} . It then holds ($\underline{\theta} = [\theta_1 \ \theta_2 \ \theta_3]', \underline{\theta}_{\rm cm} = [\theta_{\rm cm_1} \ \theta_{\rm cm_2} \ \theta_{\rm cm_3}]'$, etc.):

$$\underline{\theta} = P \, \underline{\theta}_{\rm cm} \,, \quad \underline{\tilde{u}} = P \, \underline{\tilde{u}}_{\rm cm} \,, \quad \delta \underline{M}_{z_{\rm cm}} = P^{-1} \, \delta \underline{M}_{z}$$
 (11)

with

$$\mathbf{P} = \begin{pmatrix} 1 \sin \psi_1 \cos \psi_1 \\ 1 \sin \psi_2 \cos \psi_2 \\ 1 \sin \psi_3 \cos \psi_3 \end{pmatrix}, \quad \mathbf{P}^{-1} = \begin{pmatrix} \frac{1}{3} & \frac{1}{3} & \frac{1}{3} \\ \frac{2}{3} \sin \psi_1 & \frac{2}{3} \sin \psi_2 & \frac{2}{3} \sin \psi_3 \\ \frac{2}{3} \cos \psi_1 & \frac{2}{3} \cos \psi_2 & \frac{2}{3} \cos \psi_3 \end{pmatrix} \tag{12}$$

It can be observed from figure 3 and the transformation with matrix P^{-1} that the $2^{\rm bd}$ and $3^{\rm rd}$ multi-blade flap moment coordinates $\delta M_{z_{\rm cm_2}}$ and $\delta M_{z_{\rm cm_3}}$ have a tilt- and yaw-orientation. The 1p-transformed model equations are obtained by carrying through the signal transformations by equation 11 in the periodic model of Section 1.2 (B=3; equation 5, 7):

$$J_{r} \dot{\Omega}_{r} \stackrel{\text{eom1}}{=} -s_{\text{sh}} \gamma - d_{\text{sh}} \dot{\gamma} - 3 h_{M_{x}} \dot{x}_{\text{fa}} \dots$$

$$+3k_{M_{x}} \theta_{\text{cm}_{1}} + 3h_{M_{x}} \tilde{u}_{\text{cm}_{1}}$$

$$\frac{J_{r} J_{g}}{J_{r} + J_{g}} \ddot{\gamma} \stackrel{\text{eom2}}{=} -s_{\text{sh}} \gamma - d_{\text{sh}} \dot{\gamma} - \frac{J_{g}}{J_{r} + J_{g}} 3 h_{M_{x}} \dot{x}_{\text{fa}} \dots$$

$$+ \frac{J_{g}}{J_{r} + J_{g}} 3k_{M_{x}} \theta_{\text{cm}_{1}} + \frac{J_{r}}{J_{r} + J_{g}} \delta T_{g} + \frac{J_{g}}{J_{r} + J_{g}} 3h_{M_{x}} \tilde{u}_{\text{cm}_{1}}$$

$$m_{\text{tw}} \ddot{x}_{\text{fa}} \stackrel{\text{eom3}}{=} -s_{\text{tw}} x_{\text{fa}} - (d_{\text{tw}} + 3h_{F_{x}} - \frac{81Rb}{32H^{2}} h_{M_{z}}) \dot{x}_{\text{fa}} \dots$$

$$+ 3k_{F_{x}} \theta_{\text{cm}_{1}} + \frac{9}{4H} k_{M_{z}} \theta_{\text{cm}_{2}} + 3h_{F_{x}} \tilde{u}_{\text{cm}_{1}} + \frac{9}{4H} h_{M_{z}} \tilde{u}_{\text{cm}_{2}}$$

$$m_{\text{tw}} \ddot{x}_{\text{sd}} \stackrel{\text{eom4}}{=} -s_{\text{tw}} x_{\text{sd}} - d_{\text{tw}} \dot{x}_{\text{sd}} - \frac{27Rb}{16H} h_{F_{z}} \dot{x}_{\text{fa}} \dots$$

$$-\frac{3}{2} k_{F_{x}} \theta_{\text{cm}_{2}} - \frac{3}{2} h_{F_{x}} \tilde{u}_{\text{cm}_{2}} + \frac{3}{2H} \delta T_{g}$$

$$(13)$$

and (equation 9; expressions for $v_{\rm fa}$ and $v_{\rm fa}$ omitted):

$$\delta M_{z_{\text{cm}_{1}}} \stackrel{\text{oel}}{=} -h_{M_{z}} \dot{x}_{\text{fa}} + k_{M_{z}} \theta_{\text{cm}_{1}} + h_{M_{z}} \tilde{u}_{\text{cm}_{1}}$$

$$\delta M_{z_{\text{cm}_{2}}} \stackrel{\text{oel}}{=} h_{M_{z}} \frac{9R_{\text{b}}}{8H} \dot{x}_{\text{fa}} + k_{M_{z}} \theta_{\text{cm}_{2}} + h_{M_{z}} \tilde{u}_{\text{cm}_{2}}$$

$$\delta M_{z_{\text{cm}_{3}}} \stackrel{\text{oel}}{=} k_{M_{z}} \theta_{\text{cm}_{3}} + h_{M_{z}} \tilde{u}_{\text{cm}_{3}}$$

$$\Omega_{\text{g}} \stackrel{\text{oel}}{=} \Omega_{\text{r}} - \dot{\gamma}$$
(14)

The equations of motion for $\Omega_{\rm r}$, γ and $x_{\rm fa}$ show that the 1st multi-blade pitch angle coordinate $\theta_{\rm cm_1}$ represents collective pitching; this can also be concluded from the transformation of $\theta_{\rm cm_1}$ with matrix \boldsymbol{P} to contributions to θ_1 , θ_2 and θ_3 . The output equations for $\delta M_{z_{\rm cm_2}}$ and $\delta M_{z_{\rm cm_3}}$ show that the 2nd and 3rd multi-blade pitch angle coordinates $\theta_{\rm cm_2}$ and $\theta_{\rm cm_3}$ have also a tilt and yaw orientation.

The use of this time-invariant 1p-transformed model is identical to the use of the periodic model of Section 1.2 if

• blade input variables are demodulated before they enter the 1p-transformed model:

$$\underline{\theta}_{\rm cm} = \boldsymbol{P}^{-1} \, \underline{\theta} \,, \quad \underline{\tilde{u}}_{\rm cm} = \boldsymbol{P}^{-1} \, \underline{\tilde{u}} \,,$$

• blade output variables are remodulated after they have left the 1p-transformed model:

$$\delta \underline{M}_z = \boldsymbol{P} \, \delta \underline{M}_{z_{cm}}$$

A general receipt for obtaining and handling a linear time invariant state space model for polar-symmetric wind turbines ($B \geq 3$)is as follows (see e.g. [78]; co-axial, down-wind pointing x-axis, vertically down-ward pointing z-axis at rotor azimuth ψ equal to 0; ψ equals azimuth ψ_1 of $1^{\rm st}$ blade):

• set up periodic linear model equations in state space format with input vector \underline{v} , state vector \underline{z} and output vector \underline{y} :

$$\begin{array}{rcl} \underline{\dot{z}} & = & \boldsymbol{A}(\bar{\Omega}t)\,\underline{z} + \boldsymbol{B}(\bar{\Omega}t)\,\underline{v} \\ y & = & \boldsymbol{C}(\bar{\Omega}t)\,\underline{z} + \boldsymbol{K}(\bar{\Omega}t)\,\underline{v} \end{array}$$

• compose matrices T_v , T_z and T_y with (i) multi-blade transformation matrix kernels P for all input, state and output variables attached to the rotor blade and (ii) shaft transformation matrix kernels R for all variables attached to the rotor shaft:

$$oldsymbol{P} = egin{pmatrix} 1 & \sin \psi_1 & \cos \psi_1 \\ 1 & \sin \psi_2 & \cos \psi_2 \\ 1 & \sin \psi_3 & \cos \psi_3 \end{pmatrix} \quad oldsymbol{R} = egin{pmatrix} 1 & 0 & 0 \\ 0 & \cos \psi_1 & \sin \psi_1 \\ 0 & -\sin \psi_1 & \cos \psi_1 \end{pmatrix}$$

• derive parameter matrices of the transformed model via matrix transformation with fixed azimuth angle $\bar{\psi}$:

$$egin{array}{lcl} oldsymbol{A_{
m cm}} &=& oldsymbol{T}_z^{-1}(ar{\psi}) \, oldsymbol{A}(ar{\psi}) \, oldsymbol{T}_z(ar{\psi}) - oldsymbol{T}_z^{-1}(ar{\psi}) oldsymbol{\dot{T}}_z(ar{\psi}) \ oldsymbol{B_{
m cm}} &=& oldsymbol{T}_z^{-1}(ar{\psi}) \, oldsymbol{C}(ar{\psi}) \, oldsymbol{T}_z(ar{\psi}) \ oldsymbol{K_{
m cm}} &=& oldsymbol{T}_y^{-1}(ar{\psi}) \, oldsymbol{K}(ar{\psi}) \, oldsymbol{T}_v(ar{\psi}) \end{array}$$

The matrices $A_{\rm cm}$ up to $K_{\rm cm}$ no longer depend on ψ and are to be derived from matrices with ψ -dependency for an instance $\bar{\psi}$ of ψ .

• use the transformed model with input demodulation and output remodulation in the actual rotor azimuth ψ :

$$\underline{\epsilon} = \mathbf{T}_{v}^{-1}(\psi) \underline{v}
\underline{\dot{q}} = \mathbf{A}_{cm} \underline{q} + \mathbf{B}_{cm} \underline{\epsilon}
\underline{\eta} = \mathbf{C}_{cm} \underline{q} + \mathbf{K}_{cm} \underline{\epsilon}
\underline{y} = \mathbf{T}_{y}(\psi) \underline{\eta}$$

1.3.2 Feedback laws for IPC-1p

The layout of the feedback loops for rotor speed regulation and blade load reduction around 1p is pictured below.

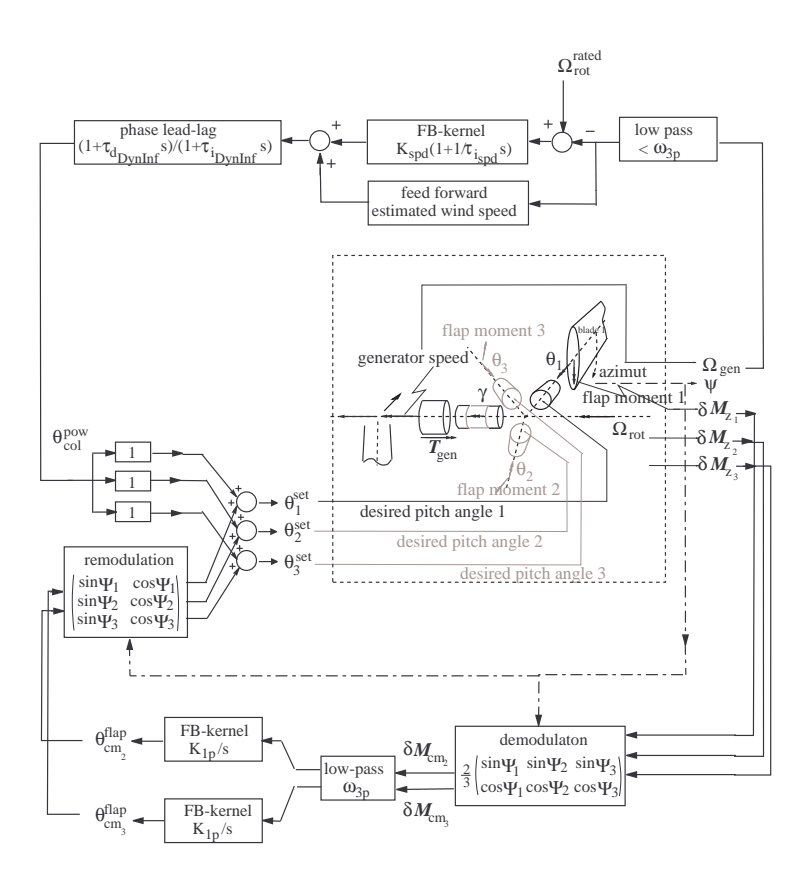


Figure 4 Layout of control loops for pitch control

The feedback loops map

- the low-pass filtered rotational speed Ω_g to the collective pitch angle setpoint θ_{col}^{pow} via a proportional/integral scheme (PI-compensator), enforced by 'feedforward' of the estimated wind speed while catering for dynamic inflow effects.
- the identically low-pass filtered tilt- and yaw-oriented multi-blade flap moment coordinates $\delta M_{z_{\rm cm_2}}$ and $\delta M_{z_{\rm cm_3}}$ to the tilt- and yaw-oriented multi-blade pitch angle coordinates $\theta_{\rm cm_2}$ and $\theta_{\rm cm_3}$ via equal integral gains (I-compensator).

The latter implies the following (1p-demodulating) creation scheme for the 'artificial measurement signals' $\delta M_{z_{\rm cm_2}}$ and $\delta M_{z_{\rm cm_3}}^{(1)}$ and $\delta M_{z_{\rm cm_3}}^{(1)}$ since they pertain to IPC-1p):

$$\begin{bmatrix}
\delta M_{z_{\text{cm}_2}}^{(1)} \\
\delta M_{z_{\text{cm}_3}}^{(1)}
\end{bmatrix} = \begin{bmatrix}
\frac{2}{3}\sin\psi_1 & \frac{2}{3}\sin\psi_2 & \frac{2}{3}\sin\psi_3 \\
\frac{2}{3}\cos\psi_1 & \frac{2}{3}\cos\psi_2 & \frac{2}{3}\cos\psi_3
\end{bmatrix} \begin{pmatrix}
\delta M_{z_1} \\
\delta M_{z_2} \\
\delta M_{z_3}
\end{pmatrix}$$
(15)

while pitch angle additions around the 1p frequency are obtained via a 1p-modulation scheme on

the 'artificial control signals' θ_{cm_2} and θ_{cm_3} (= $\theta_{cm_2}^{(1)}, \theta_{cm_3}^{(1)}$):

$$\begin{bmatrix} \theta_1^{(1)} \\ \theta_2^{(1)} \\ \theta_3^{(1)} \end{bmatrix} = \begin{pmatrix} \sin \psi_1 & \cos \psi_1 \\ \sin \psi_2 & \cos \psi_2 \\ \sin \psi_3 & \cos \psi_3 \end{pmatrix} \begin{bmatrix} \theta_{\rm cm_2}^{(1)} \\ \theta_{\rm cm_3}^{(1)} \end{bmatrix}$$
(16)

The model equations below are derived from the 1p-transformed model and are used for the parametrization of the three pitch feedback loops (delay τ_v models all dynamics of measuring, data processing and pitch actuation; use equation 13, 14; drive-train torsion and tower fore-aft motion excluded):

$$(J_{\rm r} + J_{\rm g}) \dot{\Omega}_{\rm g}(t) = 3 k_{M_x} \theta_{\rm cm_1}(t - \tau_{\rm v}) + 3 h_{M_x} \tilde{u}_{\rm cm_1}(t)$$

$$\delta M_{\rm cm_2}(t) = k_{M_z} \theta_{\rm cm_2}(t - \tau_{\rm v}) + h_{M_z} \tilde{u}_{\rm cm_2}(t)$$

$$\delta M_{\rm cm_3}(t) = k_{M_z} \theta_{\rm cm_3}(t - \tau_{\rm v}) + h_{M_z} \tilde{u}_{\rm cm_3}(t)$$
(17)

These equations are completely decoupled so that pure single-input/single-output (SISO) control theory can be applied. A short note on the neglected interaction is added in the paragraph below. As argued in the begin of Section 1.3, the 1p-load reduction objective is satisfied by zeroing the tilt- and yaw-oriented multi-blade flap moment coordinates $M_{\rm cm_2}$ and $M_{\rm cm_3}$. Thus, three so called SISO 'regulator problems' are to be solved.

The PI-compensator is commonly used as the basic feedback law for regulation of a system characterized by a delayed integrator, which applies in the speed regulation loop [74]. The cutoff frequency loop must lay below 3p in order to avoid the feedthrough of rotor-wide rotational sampling effects ($\tilde{u}_{\rm cm_1} = \tilde{u}_1 + \tilde{u}_2 + \tilde{u}_3$), which occur around (multiples of) the 3p-frequency. The lead-lag filter is derived for the compensation of dynamic inflow at collective pitching [84] . The estimated wind speed $\hat{V}_{\rm w}$ is fed forward to a pitch angle value that corresponds to rated power capture in $\hat{V}_{\rm w}$ [72] .

The load regulation loops actually behave as a delayed proportional system. In that case just an I-compensator satisfies for regulation and thus IPC-1p. In these loops it is also required to filter out the signal contents around and beyond 3p. This becomes clear when the multi-blade wind speed coordinates $\tilde{u}_{\rm cm_2}$ and $\tilde{u}_{\rm cm_3}$ are decomposed in rotational modes.

For homogeneous turbulence in the rotor plane, a *time-dependent* Fourier expansion of the wind speed \tilde{u}_i experienced in a rotating point on radius r exists [21]:

$$\tilde{u}_i(t) = \sum_{p=-\infty}^{\infty} e^{jp\psi_i} \hat{u}_p(t), \quad \hat{u}_p(t) = \frac{1}{2\pi} \int_0^{2\pi} e^{-jp\phi} u(t, r, \phi) d\phi$$
(18)

The Fourier coefficients $\hat{u}_p(t)$, the *rotational modes*, are time-dependent. A rotational mode is a harmonic basis function over the circle on radius r of the wind field. The time-dependency represents the evolution of the amplitude and the phase of such a rotational mode, which mainly occurs in frequencies below 0.1Hz^1 . For the multi-blade coordinates \tilde{u}_{cm_2} and \tilde{u}_{cm_3} then holds (use row 2 and 3 of P^{-1} by equation 12 and see expressions in Section 1.8 for k=1)

$$\tilde{u}_{\text{cm}_{2}}(t) = \sum_{m=-\infty}^{\infty} j e^{j3m\psi} (\hat{u}_{3m+1}(t) - \hat{u}_{3m-1}(t))$$

$$\tilde{u}_{\text{cm}_{3}}(t) = \sum_{m=-\infty}^{\infty} e^{j3m\psi} (\hat{u}_{3m+1}(t) + \hat{u}_{3m-1}(t))$$
(19)

¹In a linearized approach, tower shadow and wind shear can be considered as the mean-value part of the rotational modes

These expressions tell that the rotational mode pair $\{\hat{u}_1,\hat{u}_{-1}\}$ contributes straightforward to $\tilde{u}_{\rm cm_2}$ and $\tilde{u}_{\rm cm_3}$ while the mode pairs $\{\hat{u}_2,\hat{u}_4\}$ and $\{\hat{u}_{-2},\hat{u}_{-4}\}$ deliver contributions that are modulated with the 3p-frequency. Similarly, the pairs $\{\hat{u}_5,\hat{u}_7\}$ and $\{\hat{u}_{-5},\hat{u}_{-7}\}$ yield 6p-modulated contributions.

It is clear that the integral action in the feedback loops compensate for the low frequent variations in the modes $\{\hat{u}_1,\hat{u}_{-1}\}$ as well as for the mean-value parts associated with tower shadow and wind shear, and thus realizes IPC-1p. The pursued bandwidth of the feedback loop amounts to ca. 0.1 Hz. In Section 1.5 it is analytically proved that regulation of $\delta M_{z_{\rm cm_2,3}}^{(1)}$ eliminates all excitation by the wind of the blade root flap moment around the 1p-frequency. In order to eliminate the influence of higher harmonics in IPC-1p it is required to apply low pass filtering around and beyond 3p.

IPC-1p can thus be realized by solving a regulator problem. The receipt is:

- transform the three flapwise blade root moments δM_{z_i} into artificial '1p-demodulated' measurement signals $\delta M_{z_{\rm cm_2}}^{(1)}$ and $\delta M_{z_{\rm cm_3}}^{(1)}$ by equation 15;
- generate artificial control signals $\theta_{\rm cm_2}^{(1)}$ and $\theta_{\rm cm_3}^{(1)}$ via I-compensators for $\delta M_{z_{\rm cm_2}}^{(1)}$ and $\delta M_{z_{\rm cm_3}}^{(1)}$ with low pass filters around and beyond 3p;
- transform $\theta_{\rm cm_2}^{(1)}$ and $\theta_{\rm cm_3}^{(1)}$ into three '1p-modulated' pitch signals $\theta_i^{(1)}$ by equation 16.

Interaction between feedback loops

When $\Omega_{\rm g}$ and $M_{\rm cm_2}$ are fed back to $\theta_{\rm cm_1}$ and $\theta_{\rm cm_2}$ some interaction exists between the two loops via the fore-aft speed $\dot{x}_{\rm fa}$ because both $\theta_{\rm cm_1}$ and $\theta_{\rm cm_2}$ excite the tower fore-aft motion (see eom1, eom3 in equation 13 and oe1 in equation 14). The interaction can be quantified by expressing $\dot{x}_{\rm fa}$ in $\theta_{\rm cm_1}$ and $\theta_{\rm cm_2}$ and substituting the result in the above equations for $\Omega_{\rm g}$ and $M_{\rm cm_2}$, extended with the influence from $\dot{x}_{\rm fa}$. The effect on the closed loop behavior does not appear significant.

1.4 Higher harmonics control

In the previous section it was shown that artificial measurement signals, viz. the $2^{\rm nd}$ and $3^{\rm rd}$ multi-blade flap moment coordinates $\delta M_{z_{\rm cm_2}}$ and $\delta M_{z_{\rm cm_3}}$ enable the realization of IPC-1p by solving a regulation problem. The outputs of the regulator are artificial control signals, viz. the $2^{\rm nd}$ and $3^{\rm rd}$ multi-blade pitch angle coordinates $\theta_{\rm cm_2}$ and $\theta_{\rm cm_3}$. These artificial signals are linked to flap moment measurements and pitch angle additions around the 1p-frequency via the Coleman transformation (equation 11 and 12). The transformation shifts the higher harmonics of the wind to the 3p-frequency and higher. This allows for low pass filtering of $\delta M_{z_{\rm cm_2}}$ and $\delta M_{z_{\rm cm_3}}$ conveniently far away from the pursued pass-band of the feedback loops ($\sim 0.1 Hz$).

In the following two subsections it is proved that the same approach can be adopted for load reduction in the rotor blades around the 2p-frequency and the 3p-frequency (IPC-2p and IPC-3p).

1.4.1 Feedback loops for IPC-2p

We assumed that pitch angle additions for IPC-2p could also be obtained from low-frequent artificial control signals. These control signals were defined $\theta_{\rm cm_2}^{(2)}$ and $\theta_{\rm cm_3}^{(2)}$ and are as follows related to the pitch angle variations $\theta_1^{(2)}$, $\theta_2^{(2)}$ and $\theta_3^{(2)}$ for IPC-2p:

$$\begin{bmatrix} \theta_1^{(2)} \\ \theta_2^{(2)} \\ \theta_3^{(2)} \end{bmatrix} = \begin{pmatrix} \sin 2\psi_1 & \cos 2\psi_1 \\ \sin 2\psi_2 & \cos 2\psi_2 \\ \sin 2\psi_3 & \cos 2\psi_3 \end{pmatrix} \begin{bmatrix} \theta_{\rm cm_2}^{(2)} \\ \theta_{\rm cm_3}^{(2)} \end{bmatrix}$$
(20)

This 2p-modulation scheme was carried through in the periodic linear model of Section 1.2 and yielded the 2p-transformed model. It appeared that also these pitching actions do not affect

aerodynamic torque $T_{\rm a}$ and axial force $F_{\rm a}$ but do affect the tilt moment $M_{\rm t}$ and sideward force $F_{\rm s}$ around 3p.

This 2p-modulation scheme was carried through in the periodic linear model of Section 1.2 and yielded the 2p-transformed model. It appeared that these pitching actions affect neither the aerodynamic torque T_a nor the axial force F_a , tilt moment M_t and sideward force F_s since $\sum_{i=1}^B \sin 2\psi_i = 0$, $\sum_{i=1}^B \cos 2\psi_i = 0$, $\sum_{i=1}^B \sin \psi_i \cdot \sin 2\psi_i = 0$ and $\sum_{i=1}^B \sin \psi_i \cdot \cos 2\psi_i = -\frac{3}{2}\cos 3\psi$ (see equation 6 and 8). Thus, the proposed 2p pitch angle additions can be used for reduction of 3p tilt (and yaw) loading.

The $i^{\rm th}$ blade flap moment is affected as follows by $\theta_{\rm cm_2}^{(2)}$ and $\theta_{\rm cm_3}^{(2)}$ (see equation 9):

$$\delta M_{z_i} = -h_{M_z} \left(1 - \sin \psi_i \, \frac{9R_b}{8H} \right) \dot{x}_{fa} + h_{M_z} \, \tilde{u}_i + k_{M_z} \left(\sin 2\psi_i \, \theta_{cm_2}^{(2)} + \cos 2\psi_i \, \theta_{cm_2}^{(2)} \right)$$
(21)

Now define the artificial measurement signals $\delta M_{z_{\rm cm_2}}^{(2)}$ and $\delta M_{z_{\rm cm_3}}^{(2)}$ as:

$$\begin{bmatrix}
\delta M_{z_{\text{cm}_2}}^{(2)} \\
\delta M_{z_{\text{cm}_3}}^{(2)}
\end{bmatrix} = \begin{bmatrix}
\frac{2}{3}\sin 2\psi_1 & \frac{2}{3}\sin 2\psi_2 & \frac{2}{3}\sin 2\psi_3 \\
\frac{2}{3}\cos 2\psi_1 & \frac{2}{3}\cos 2\psi_2 & \frac{2}{3}\cos 2\psi_3
\end{bmatrix} \begin{pmatrix}
\delta M_{z_1} \\
\delta M_{z_2} \\
\delta M_{z_3}
\end{pmatrix}$$
(22)

Substitution of equation 21 in the right hand side of the creation scheme above mentioned yields:

$$\delta M_{z_{\text{cm}_2}}^{(2)} = k_{M_z} \theta_{\text{cm}_2}^{(2)} + h_{M_z} \frac{2}{3} \sum_{i=1}^{B} \sin 2\psi_i \, \tilde{u}_i$$

$$\delta M_{z_{\text{cm}_3}}^{(2)} = k_{M_z} \theta_{\text{cm}_3}^{(2)} + h_{M_z} \frac{2}{3} \sum_{i=1}^{B} \cos 2\psi_i \, \tilde{u}_i$$
(23)

These equations can be rewritten by use of the expressions for the modulated Fourier expansion of the rotationally sampled wind speed by equation 18 as listed in Section 1.8 (k = 2)

$$\delta M_{z_{\text{cm}_2}}^{(2)} \stackrel{\text{oe2}}{=} k_{M_z} \theta_{\text{cm}_2}^{(2)} + h_{M_z} \tilde{u}_{\text{cm}_2}^{(2)}
\delta M_{z_{\text{cm}_3}}^{(2)} \stackrel{\text{oe3}}{=} k_{M_z} \theta_{\text{cm}_3}^{(2)} + h_{M_z} \tilde{u}_{\text{cm}_3}^{(2)}$$
(24)

with

$$\tilde{u}_{\text{cm}_{2}}^{(2)}(t) = \sum_{m=-\infty}^{\infty} j e^{j3m\psi} (\hat{u}_{3m+2}(t) - \hat{u}_{3m-2}(t))
\tilde{u}_{\text{cm}_{3}}^{(2)}(t) = \sum_{m=-\infty}^{\infty} e^{j3m\psi} (\hat{u}_{3m+2}(t) + \hat{u}_{3m-2}(t))$$
(25)

The dependency on \dot{x}_{fa} vanishes because $\sum_{i=1}^{B} \sin 2\psi_i = 0$, $\sum_{i=1}^{B} \cos 2\psi_i = 0$, $\sum_{i=1}^{B} \sin \psi_i \sin 2\psi_i = 0$ and $\sum_{i=1}^{B} \sin \psi_i \cos 2\psi_i = 0$.

Equations 24 and 25 tell that the rotational mode pair $\{\hat{u}_2,\hat{u}_{-2}\}$ contributes straightforward to the artificial measurement signals $\delta M_{z_{\rm cm_2}}^{(2)}$ and $\delta M_{z_{\rm cm_3}}^{(2)}$ while the remaining mode pairs deliver contributions that are modulated with (multiples of) 3p.

These equations also tell that integral action in SISO feedback loops from $\delta M_{z_{\rm cm_2}}^{(2)}$ and $\delta M_{z_{\rm cm_3}}^{(2)}$ to the artificial control signals $\theta_{\rm cm_2}^{(2)}$ and $\theta_{\rm cm_3}^{(2)}$ will compensate for the mean and the low frequent variations of the mode-pair $\{\hat{u}_2,\hat{u}_{-2}\}$. In Section 1.5 it is analytically proved that regulation of $\delta M_{z_{\rm cm_2,3}}^{(2)}$ eliminates all excitation by the wind of the blade root flap moment around the 2p-frequency.

Low pass filtering is required around and beyond 3p in order to avoid unwanted controller excitation from mode-pairs $\{\hat{u}_{\pm 5}, \hat{u}_{\pm 1}\}$, $\{\hat{u}_{\pm 8}, \hat{u}_{\pm 4}\}$, etc.

As mentioned above, the system dynamics are not excited at all by the 2p-modulated pitch angle additions. IPC-2p can thus be realized by solving a regulator problem just as IPC-1p. The receipt is:

- transform the three flapwise blade root moments δM_{z_i} into artificial '2p-demodulated' measurement signals $\delta M_{z_{cm_2}}^{(2)}$ and $\delta M_{z_{cm_3}}^{(2)}$ by equation 22;
- generate artificial control signals $\theta_{\rm cm_2}^{(2)}$ and $\theta_{\rm cm_3}^{(2)}$ via I-compensators for $\delta M_{z_{\rm cm_2}}^{(2)}$ and $\delta M_{z_{\rm cm_3}}^{(2)}$ with low pass filters around and beyond 3p;
- transform $\theta_{\rm cm_2}^{(2)}$ and $\theta_{\rm cm_3}^{(2)}$ into three '2p-modulated' pitch signals $\theta_i^{(2)}$ by equation 20.

1.4.2 Feedback loops for IPC-3p

Just as for IPC-2p, we defined artificial control signals $\theta_{\rm cm_2}^{(3)}$ and $\theta_{\rm cm_3}^{(3)}$ for IPC-3p, but now with a 3p-modulation scheme:

$$\begin{bmatrix} \theta_1^{(3)} \\ \theta_2^{(3)} \\ \theta_3^{(3)} \end{bmatrix} = \begin{pmatrix} \sin 3\psi_1 & \cos 3\psi_1 \\ \sin 3\psi_2 & \cos 3\psi_2 \\ \sin 3\psi_3 & \cos 3\psi_3 \end{pmatrix} \begin{bmatrix} \theta_{\rm cm_2}^{(3)} \\ \theta_{\rm cm_3}^{(3)} \end{bmatrix}$$
(26)

This scheme was carried through in the periodic linear model of Section 1.2 and yielded the 3p-transformed model. The pitching actions now do affect the aerodynamic torque T_a and axial force F_a since for $B = 3 \sum_{i=1}^{B} \sin 3\psi_i = 3 \sin \psi_1$, $\sum_{i=1}^{B} \cos 3\psi_i = 3 \cos \psi_1$ (see equation and 7):

$$\delta T_{a} = -3 h_{M_{x}} \dot{x}_{fa} + \sum_{i=1}^{3} h_{M_{x}} \tilde{u}_{i} + 3 k_{M_{x}} \left(\sin 3\psi_{1} \theta_{cm_{2}}^{(3)} + \cos 3\psi_{1} \theta_{cm_{3}}^{(3)} \right)$$

$$\delta F_{a} = -3 h_{F_{x}} \dot{x}_{fa} + \sum_{i=1}^{3} h_{F_{x}} \tilde{u}_{i} + 3 k_{F_{x}} \left(\sin 3\psi_{1} \theta_{cm_{2}}^{(3)} + \cos 3\psi_{1} \theta_{cm_{3}}^{(3)} \right)$$

$$(27)$$

The pitching actions do *not* affect the tilt moment M_t and sideward force F_s since $\sum_{i=1}^B \sin \psi_i \cdot \sin 3\psi_i = 0$ and $\sum_{i=1}^B \sin \psi_i \cdot \cos 3\psi_i = 0$.

Thus, the system dynamics are excited by the proposed 3p pitch angle additions via the driving torque and the axial force. This excitation can be assumed to be caused by the 3p-modulated artificial control signals $\theta_{\rm cm_2}^{(3)}$ and $\theta_{\rm cm_3}^{(3)}$.

The i^{th} blade flap moment is affected as follows by $\theta_{\text{cm}_2}^{(3)}$ and $\theta_{\text{cm}_3}^{(3)}$ (see equation 9):

$$\delta M_{z_i} = -h_{M_z} \left(1 - \sin \psi_i \, \frac{9R_b}{8H} \right) \dot{x}_{fa} + h_{M_z} \, \tilde{u}_i + k_{M_z} \left(\sin 3\psi_i \, \theta_{cm_2}^{(3)} + \cos 3\psi_i \, \theta_{cm_3}^{(3)} \right)$$
(28)

Now define the artificial measurement signals $\delta M_{z_{\rm cm_2}}^{(3)}$ and $\delta M_{z_{\rm cm_3}}^{(3)}$ as:

$$\begin{bmatrix}
\delta M_{z_{\text{cm}_2}}^{(3)} \\
\delta M_{z_{\text{cm}_3}}^{(3)}
\end{bmatrix} = \begin{bmatrix}
\frac{2}{3}\sin 3\psi_1 & \frac{2}{3}\sin 3\psi_2 & \frac{2}{3}\sin 3\psi_3 \\
\frac{2}{3}\cos 3\psi_1 & \frac{2}{3}\cos 3\psi_2 & \frac{2}{3}\cos 3\psi_3
\end{bmatrix} \begin{pmatrix}
\delta M_{z_1} \\
\delta M_{z_2} \\
\delta M_{z_3}
\end{pmatrix}$$
(29)

Substitution of equation 28 in the right hand side of the creation scheme above mentioned yields

$$\delta M_{z_{\text{cm}_{2}}}^{(3)} = -2h_{M_{z}} \sin 3\psi \, \frac{9R_{\text{b}}}{8H} \, \dot{x}_{\text{fa}} + h_{M_{z}} \, \frac{2}{3} \sum_{i=1}^{3} \sin 3\psi_{i} \, \tilde{u}_{i} + \\ k_{M_{z}} \, \left(\frac{2}{3} \sum_{i=1}^{3} \sin 3\psi_{i} \sin 3\psi_{i} \, \theta_{\text{cm}_{2}}^{(3)} + \sin 3\psi_{i} \cos 3\psi_{i} \, \theta_{\text{cm}_{3}}^{(3)}\right) \\ \delta M_{z_{\text{cm}_{3}}}^{(3)} = -2h_{M_{z}} \sin 3\psi \, \frac{9R_{\text{b}}}{8H} \, \dot{x}_{\text{fa}} + h_{M_{z}} \, \frac{2}{3} \sum_{i=1}^{3} \cos 3\psi_{i} \, \tilde{u}_{i} + \\ k_{M_{z}} \, \left(\frac{2}{3} \sum_{i=1}^{3} \cos 3\psi_{i} \sin 3\psi_{i} \, \theta_{\text{cm}_{2}}^{(3)} + \cos 3\psi_{i} \cos 3\psi_{i} \, \theta_{\text{cm}_{3}}^{(3)}\right)$$

$$(30)$$

These equations can be rewritten as follows (see equation 18 and the expressions in Section 1.8 for k = 3):

$$\delta M_{z_{\text{cm}_2}}^{(3)} = -2h_{M_z} \sin 3\psi \, \frac{9R_b}{8H} \, \dot{x}_{\text{fa}} + h_{M_z} \, \tilde{u}_{\text{cm}_2}^{(3)} + \\ k_{M_z} \left(\, \theta_{\text{cm}_2}^{(3)} - \cos 6\psi \, \theta_{\text{cm}_2}^{(3)} + \sin 6\psi \, \theta_{\text{cm}_3}^{(3)} \right) \\ \delta M_{z_{\text{cm}_3}}^{(3)} = -2h_{M_z} \cos 3\psi \, \frac{9R_b}{8H} \, \dot{x}_{\text{fa}} + h_{M_z} \, \tilde{u}_{\text{cm}_3}^{(3)} + \\ k_{M_z} \left(\, \theta_{\text{cm}_3}^{(3)} + \cos 6\psi \, \theta_{\text{cm}_3}^{(3)} + \sin 6\psi \, \theta_{\text{cm}_2}^{(3)} \right)$$

$$(31)$$

with

$$\tilde{u}_{\text{cm}_{2}}^{(3)}(t) = \sum_{m=-\infty}^{\infty} j e^{j3m\psi} (\hat{u}_{3m+3}(t) - \hat{u}_{3m-3}(t))
\tilde{u}_{\text{cm}_{3}}^{(3)}(t) = \sum_{m=-\infty}^{\infty} e^{j3m\psi} (\hat{u}_{3m+3}(t) + \hat{u}_{3m-3}(t))$$
(32)

Equations 31 and 32 tell that the rotational mode pair $\{\hat{u}_3, \hat{u}_{-3}\}$ contributes straightforward to the artificial measurement signals $\delta M_{z_{\rm em_2}}^{(3)}$ and $\delta M_{z_{\rm em_3}}^{(3)}$ while the remaining mode pairs deliver contributions that are modulated with (multiples of) 3p.

These equations also tell that integral action in SISO feedback loops from $\delta M_{z_{\rm cm_2}}^{(3)}$ and $\delta M_{z_{\rm cm_3}}^{(3)}$ to the artificial control signals $\theta_{\rm cm_2}^{(3)}$ and $\theta_{\rm cm_3}^{(3)}$ will compensate for the mean and the low frequent variations of the mode-pair $\{\hat{u}_3, \hat{u}_{-3}\}$. In Section 1.5 it is analytically proved that regulation of $\delta M_{z_{\rm cm_{2,3}}}^{(3)}$ eliminates all excitation by the wind of the blade root flap moment around the 3pfrequency.

Low pass filtering is required around and beyond 3p in order to avoid undesired feedback that is caused by:

- mode-pairs $\{\hat{u}_{\pm 6}, \hat{u}_{\pm 0}\}$, $\{\hat{u}_{\pm 9}, \hat{u}_{\pm 12}\}$, etc.;
- 6p-modulated terms like $-k_{M_z}\cos 6\psi \, \theta_{\rm cm_2}^{(3)};$ 3p-modulated term $-2h_{M_z}\sin 3\psi \, \frac{9R_{\rm b}}{8H}\, \dot{x}_{\rm fa}.$

It has been mentioned above that the excitation of the system dynamics via the 3p pitching scheme by equation 26 is equivalent to excitation by the 3p-modulated artificial control signals $\theta_{\rm cm_2}^{(3)}$ and $\theta_{\rm cm_3}^{(3)}$. It is shown by time-domain simulation in Section 1.6 that this interaction with the speed regulation loop is favorable instead of undesired; this also holds for the tower fore-aft motion: reductions of the 3p-component of the flap moment, the lead moment and the axial force coincide.

Since part of the 3p-excitation is shifted around the 6p-frequency, IPC-3p can thus be realized by solving a regulator problem. The receipt is:

- transform the three flapwise blade root moments δM_{z_i} into artificial '3p-demodulated' measurement signals $\delta M_{z_{\rm cm_2}}^{(3)}$ and $\delta M_{z_{\rm cm_3}}^{(3)}$ by equation 29;
- generate artificial control signals $\theta_{\rm cm_2}^{(3)}$ and $\theta_{\rm cm_3}^{(3)}$ via I-compensators for $\delta M_{z_{\rm cm_2}}^{(3)}$ and $\delta M_{z_{\rm cm_3}}^{(3)}$ with low pass filters around and beyond 3p;

• transform $\theta_{\rm cm_2}^{(3)}$ and $\theta_{\rm cm_3}^{(3)}$ into three '2p-modulated' pitch signals $\theta_i^{(3)}$ by equation 26.

1.5 Closed-loop analysis

The IPC-np feedback laws are designed independently while they will operate simultaneously. The feedback laws, together with an np de- and re-modulation scheme, set up the 'true' feedback loops for IPC-np. In this section it is analytically proved that the true feedback loops compensate for the np harmonic excitation from the wind if well-functioning low pass filters are included.

The analytic proof for the proper working of the proposed feedback loops for IPC-np involves the following steps:

- inclusion of the feedback laws in the output equations for the artificial measurement signals ('np-transformed' output equations);
- expression of the artificial control signals in the rotational modes of the wind speed
- carrying through the expressions for the control signals in the output equations for the blade flap root moments

1.5.1 Feedback laws in output equations

The three sets of two identical feedback laws from the artificial measurement to control signals all have the same structure. They involve an integrating action and low pass filter around and beyond the 3p-frequency and are denoted as:

$$\theta_{\text{cm}_2}^{(k)}(t) = -L^{(k)}(t) * \delta M_{z_{\text{cm}_2}}^{(k)}(t)$$

$$\theta_{\text{cm}_3}^{(k)}(t) = -L^{(k)}(t) * \delta M_{z_{\text{cm}_3}}^{(k)}(t)$$
(33)

The asterisks '*' represents the convolution operation, which is a short hand notation of the general response expression for the linear system with impulse response $L^{(k)}(t)$. For $\theta_{\rm cm_2}^{(k)}(t)$ then holds:

$$\theta_{\rm cm_2}^{(k)}(t) = \int_{-\infty}^{t} L^{(k)}(t-\tau) \, \delta M_{z_{\rm cm_2}}^{(k)}(\tau) \, d\tau \tag{34}$$

The impulse response $L^{(k)}(t)$ is the inverse Laplace transform of the transfer function $L(s)^2$:

$$L^{(k)}(t) = \int_{-\infty}^{\infty} e^{st} L^{(k)}(s) ds$$
 (35)

The feedback laws, together with an np de- and re-modulation scheme, set up the 'true' feedback loops for IPC-np. In this section it is analytically proved that the true feedback loops do what they are intended to do, viz. to compensate for the np harmonic excitation from the wind if well-functioning low pass filters are included.

With the feedback laws included, equation 14 for the artificial measurements signals for IPC-1p becomes:

$$(1+k_{M_z}L^{(1)}(t))*\delta M_{z_{\rm cm_2}}^{(1)}(t) = h_{M_z} \frac{9R_{\rm b}}{8H} \dot{x}_{\rm fa}(t) + h_{M_z} \tilde{u}_{\rm cm_2}^{(1)}(t) (1+k_{M_z}L^{(1)}(t))*\delta M_{z_{\rm cm_3}}^{(1)}(t) = h_{M_z} \tilde{u}_{\rm cm_3}^{(1)}(t)$$
(36)

²The Laplace operator s can be interpreted as the product of the frequency ω [rad/s] and imaginary unit number η

and equation 24 for IPC-2p:

$$(1 + k_{M_z} L^{(2)}(t)) * \delta M_{z_{\text{cm}_2}}^{(2)}(t) = h_{M_z} \tilde{u}_{\text{cm}_2}^{(2)}(t)$$

$$(1 + k_{M_z} L^{(2)}(t)) * \delta M_{z_{\text{cm}_3}}^{(2)}(t) = h_{M_z} \tilde{u}_{\text{cm}_3}^{(2)}(t)$$
(37)

and equation 31 for IPC-3p:

$$(1 + k_{M_z}L^{(3)}(t)) * \delta M_{z_{\text{cm}_2}}^{(3)}(t) = -2h_{M_z}\sin 3\psi \frac{9R_b}{8H} \dot{x}_{\text{fa}}(t) + h_{M_z} \tilde{u}_{\text{cm}_2}^{(3)}(t) + k_{M_z} \cos 6\psi \left(L^{(3)}(t) * \delta M_{z_{\text{cm}_2}}^{(3)}(t)\right) - k_{M_z} \sin 6\psi \left(L^{(3)}(t) * \delta M_{z_{\text{cm}_3}}^{(3)}(t)\right)$$

$$(1 + k_{M_z}L^{(3)}(t)) * \delta M_{z_{\text{cm}_3}}^{(3)}(t) = -2h_{M_z}\cos 3\psi \frac{9R_b}{8H} \dot{x}_{\text{fa}}(t) + h_{M_z} \tilde{u}_{\text{cm}_3}^{(3)}(t) - k_{M_z} \cos 6\psi \left(L^{(3)}(t) * \delta M_{z_{\text{cm}_3}}^{(3)}(t)\right) - k_{M_z} \sin 6\psi \left(L^{(3)}(t) * \delta M_{z_{\text{cm}_2}}^{(3)}(t)\right)$$

$$(38)$$

The 'closed loop' equations for IPC-1p and IPC-2p can be transformed into explicit equations for $\delta M_{z_{\rm cm}(.)}^{(k)}(t)$ (k=1,2): then holds:

$$\delta M_{z_{\text{cm}_2}}^{(1)}(t) = h_{M_z} \hat{G}^{(1)}(t) * (\tilde{u}_{\text{cm}_2}^{(1)}(t) + \frac{9R_b}{8H} \dot{x}_{\text{fa}}(t))$$

$$\delta M_{z_{\text{cm}_3}}^{(1)}(t) = h_{M_z} \hat{G}^{(1)}(t) * \tilde{u}_{\text{cm}_3}^{(1)}(t)$$

$$\delta M_{z_{\text{cm}_2}}^{(2)}(t) = h_{M_z} \hat{G}^{(2)}(t) * \tilde{u}_{\text{cm}_2}^{(2)}(t)$$

$$\delta M_{z_{\text{cm}_3}}^{(2)}(t) = h_{M_z} \hat{G}^{(2)}(t) * \tilde{u}_{\text{cm}_3}^{(2)}(t)$$

$$(39)$$

with $\hat{G}^{(k)}(t)$ the inverse Laplace transform of the closed form of the so called 'loop gain' $k_{M_z}L^{(k)}(s)$:

$$\hat{G}^{(k)}(t) = \int_{s=-\infty}^{\infty} e^{st} \frac{1}{1 + k_{M_s} L^{(k)}(s)} ds$$
(40)

The closed loop equations for IPC-3p can be transformed in a similar way as described above. However, this still results in implicit equations. For $\delta M_{z_{\rm cm}_{(2)}}^{(3)}(t)$ then holds (similar for $\delta M_{z_{\rm cm}_{(3)}}^{(3)}(t)$):

$$\delta M_{z_{\text{cm}_{2}}}^{(3)}(t) = h_{M_{z}} \hat{G}^{(3)}(t) * \left(\tilde{u}_{\text{cm}_{2}}^{(3)}(t) - 2\sin 3\psi \frac{9R_{\text{b}}}{8H} \dot{x}_{\text{fa}}(t) \right)
+ \frac{k_{M_{z}}}{h_{M_{z}}} \left[\cos 6\psi \left(L^{(3)}(t) * \delta M_{z_{\text{cm}_{2}}}^{(3)}(t) \right) - \sin 6\psi \left(L^{(3)}(t) * \delta M_{z_{\text{cm}_{3}}}^{(3)}(t) \right) \right] \right)$$
(41)

The feedback law $L^{(3)}(t)$ contains a low pass filter around and beyond the 3p-frequency. Therefore, the contribution of the 6p-modulated terms $L^{(3)}(t)*\delta M_{z_{\mathrm{cm}_{(2,3)}}}$ to equation 41 in frequencies below 3p will be negligible.

1.5.2 Rotational modes in control signals

The feedback scheme listed below applies when the feedback law for the $3^{\rm rd}$ multi-blade coordinate in IPC-2p is effectuated (closed loop). are effectuated The scheme only includes the *artificial* process signals and is equal for the $2^{\rm nd}$ multi-blade coordinate in IPC-2p and $3^{\rm rd}$ multi-blade coordinate in IPC-1p; the $2^{\rm nd}$ multi-blade coordinate in IPC-1p inludes a contribution by

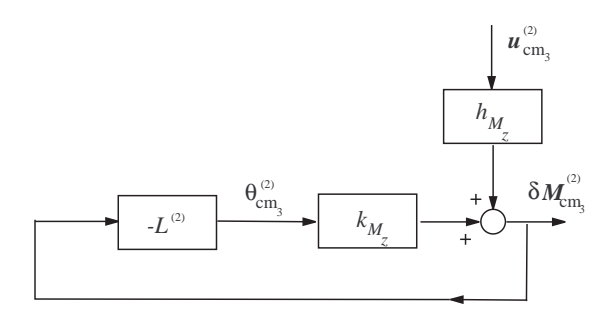


Figure 5 Feedback scheme 2nd multi-blade coordinate IPC-2p

the fore-aft tower motion.

The following closed loop expressions hold for the artificial control signals in IPC-1p and IPC-2p (substitute right hand side of equation 39 in equation 33; k = 1, 2):

$$\theta_{\rm cm_2}^{(1)}(t) = G^{(1)}(t) * (\tilde{u}_{\rm cm_2}^{(1)}(t) + \frac{9R_{\rm b}}{8H}\dot{x}_{\rm fa}(t))$$

$$\theta_{\rm cm_3}^{(1)}(t) = G^{(1)}(t) * \tilde{u}_{\rm cm_3}^{(1)}(t)$$

$$\theta_{\rm cm_2}^{(2)}(t) = G^{(2)}(t) * \tilde{u}_{\rm cm_2}^{(2)}(t)$$

$$\theta_{\rm cm_3}^{(2)}(t) = G^{(2)}(t) * \tilde{u}_{\rm cm_3}^{(2)}(t)$$

$$(42)$$

with $G^{(k)}(t)$ the inverse Laplace transform given by:

$$G^{(k)}(t) = \int_{s=-\infty}^{\infty} e^{st} \frac{-h_{M_z} L^{(k)}(s)}{1 + k_{M_z} L^{(k)}(s)} ds$$
(43)

As mentioned above, the 6p-modulated terms in equation 41 hardly contribute in frequencies below 3p. Because of the low pass filter in the feedback law $L^{(3)}(t)$ in equation 33 the following expressions approximately hold for the artificial control signals that belong to IPC-3p $(G^{(3)}(t))$ by equation 43 for k=3)

$$\theta_{\rm cm_2}^{(3)}(t) \sim G^{(3)}(t) * (\tilde{u}_{\rm cm_2}^{(3)}(t) - 2\frac{9R_b}{8H}\sin 3\psi \,\dot{x}_{\rm fa}(t))$$

$$\theta_{\rm cm_3}^{(3)}(t) \sim G^{(3)}(t) * (\tilde{u}_{\rm cm_3}^{(3)}(t) - 2\frac{9R_b}{8H}\cos 3\psi \,\dot{x}_{\rm fa}(t))$$
(44)

For the rotational mode decomposition of the kp-transformed wind speed signal holds (see Section 1.8)

$$\tilde{u}_{\text{cm}_{2}}^{(k)}(t) = \sum_{m=-\infty}^{\infty} j e^{j3m\psi} (\hat{u}_{3m+k}(t) - \hat{u}_{3m-k}(t))$$

$$\tilde{u}_{\text{cm}_{3}}^{(k)}(t) = \sum_{m=-\infty}^{\infty} e^{j3m\psi} (\hat{u}_{3m+k}(t) + \hat{u}_{3m-k}(t))$$
(45)

The properties of $G^{(k)}(t)$ can be derived from those of the feedback law $L^{(k)}(t)$ via equation 43. $L^{(k)}(t)$ represents an integrator and low pass filter around and beyond 3p, which can be written as the inverse Laplace transform of the product of integrator transfer function $K^{(k)}/s$ and low-pass filter transfer function $F_{3p}^{(k)}(s)$. For the transfer function $G^{(k)}(s)$ then holds (omit superscript $F_{3p}^{(k)}(s)$) then holds (omit superscript $F_{3p}^{(k)}(s)$).

replace s by $j\omega$):

$$G(\omega) = \frac{-h_{M_z} K F_{3p}(\omega)}{j\omega + k_{M_z} K F_{3p}(\omega)} = \begin{cases} \frac{-h_{M_z}}{k_{M_z}} & \text{if } \omega \ll k_{M_z} K \\ 0 & \text{if } \omega \ge \omega_{3p} - \epsilon \end{cases}$$
(46)

For appropriate choices of controller gain K and offset ϵ from the 3p-frequency, just the rotational modes \hat{u}_k and \hat{u}_{-k} appear in the artificial control signals for IPC-kp control:

$$G^{(k)}(t) * \tilde{u}_{\text{cm}_2}^{(k)}(t) \sim \jmath \frac{-h_{M_z}}{k_{M_z}} (\hat{u}_k(t) - \hat{u}_{-k}(t))$$

$$G^{(k)}(t) * \tilde{u}_{\text{cm}_3}^{(k)}(t) \sim \frac{-h_{M_z}}{k_{M_z}} (\hat{u}_k(t) + \hat{u}_{-k}(t))$$
(47)

1.5.3 Controlled blade root flap moments

The true pitch angle addition $\theta_i^{(1,2,3)}$ for the ith blade is as follows composed from the artifical control signals (see 1p-modulation scheme in Fig. 4 and 2p- and 3p-modulation schemes in equation 20 and 26):

$$\theta_i^{(1,2,3)}(t) = \sum_{k=1}^3 \sin k\psi_i \,\theta_{\text{cm}_2}^{(k)}(t) + \cos k\psi_i \,\theta_{\text{cm}_3}^{(k)}(t) \tag{48}$$

This expression can be rewritten as (carry through equation 47 in equation 42 and 44):

$$\theta_i^{(1,2,3)}(t) \sim \frac{-h_{M_z}}{k_{M_z}} \left(\sum_{k=1}^3 e^{jk\psi} \hat{u}_k(t) + e^{-jk\psi} \hat{u}_{-k}(t) \right) + f(\dot{x}_{fa})$$
 (49)

Now use this expression for $\theta_i^{(1,2,3)}(t)$, together with the rotational mode decomposition by equation 18 for the wind speed on the i^{th} blade, in equation 9 for the blade root flap moment M_{z_i} .

$$\delta M_{z_{i}} \sim -h_{M_{z}} (1 - \sin \psi_{i} \frac{9R_{b}}{8H}) \dot{x}_{fa} + h_{M_{z}} \sum_{p=-\infty}^{\infty} e^{\jmath p \psi_{i}} \hat{u}_{p}(t)
+k_{M_{z}} \frac{-h_{M_{z}}}{k_{M_{z}}} \left(\sum_{k=1}^{3} e^{\jmath k \psi} \hat{u}_{k}(t) + e^{-\jmath k \psi} \hat{u}_{-k}(t) \right) + k_{M_{z}} f(\dot{x}_{fa})
\sim -h_{M_{z}} \left(1 - \sin \psi_{i} \frac{9R_{b}}{8H} \right) \dot{x}_{fa} + k_{M_{z}} f(\dot{x}_{fa})
+h_{M_{z}} \left(\hat{u}_{0}(t) + \sum_{p=4}^{\infty} e^{\jmath p \psi_{i}} \hat{u}_{p}(t) + e^{-\jmath p \psi_{i}} \hat{u}_{-p}(t) \right)$$
(50)

This expression shows that the excitation of the blade root flap moment by the first three rotational modes is compensated completely with the adopted approach for multi-rotational mode individual pitch control.

1.6 Simulation results

Time-domain simulations with the controlled model show the effect of IPC-kp control on the stationary blade and nacelle loads. These simulations are driven by the earlier mentioned *blade effective* wind input signals in Section 1.2, which cater for longitudinal turbulence, wind shear and tower shadow.

The parameters of the model equations were determined for a mean wind speed of 16 m/s, mean rotor speed to 15 rpm and mean pitch angle to 10°. The power and thrust coefficient data of a

typical 3MW wind turbine were used. The rotor radius $R_{\rm b}$ amounted to 45 m, the tower height H to 70 m, the overall drive-train inertia $J_{\rm r}+J_{\rm g}$ to $12\cdot 10^6~{\rm kgm^2}$ and the $1^{\rm st}$ tower eigenfrequency to 0.35 Hz. Parasite dynamics are supposed to be caused by the pitch actuators, sensors and data processing equipment. These have been taken into account via an overall loop delay of 0.2 s.

Simulations were performed in which four cases were addressed:

- collective pitch only;
- collective pitch and IPC-1p;
- collective pitch and IPC-1p, IPC-2p;
- collective pitch and IPC-1p, IPC-2p, IPC-3p.

Each box always contains the results for collective pitch control only as a blue (dark) line. The results with any individual pitch control included are plotted as a green (light) line.

Figures 8-8 shows realizations and power spectra of the blade root flap moment and the tilt moment in the rotor center. The three boxes with realizations for a signal pertain to different levels of activity of individual pitch control; the upper box includes results for IPC-1p, the middle box for combined IPC-1p and IPC-2p, and the lower for combined IPC-1p, IPC-2 and IPC-3. The three boxes with auto power spectra for a signals represent these IPC-activity levels from left to right. Figures 9-11 provides these graphical results for the yaw moment in the rotor centre and the aerodynamic driving torque.

The graphs show the respective reduction of blade loads around 1p, 2p and 3p and of yaw and tilt loads in very low frequency and around 3p; the latter is caused by the reduction of blade flap loads around 2p. The driving torque loads are reduced around 3p, which is caused by the reduction of blade *lead* loads around 3p; it can be argued that full elimination of the flapwise load variations coincides with partial elimination of leadwise load variations.

Figures 12-14 shows the reduction in 1H equivalent fatigue damage for the blade root flap moment, tilt moment and yaw moment. These fatigure damage reduction estimations were derived via rainflow counting. Rainflow counts were made from 6 time-domain simulations of 800 s each. They were transformed into 1Hz equivalent fatique loads and translated into fatigue damage via the industrially accepted approach by Palmgren and Miner [57]. The achieved reduction in fatigue damage are shown for different values of the slope m; a low value of 3 or 4 is representative for steel, while a high value of 9 or 10 is representative for reinforced plastic materials. Fatigue damage reduction up to 20 to 30% in frequently occurring full load conditions seems realistic.

Figures 15-17 shows the 'cost' of multi-rotational mode individual pitch control. Here also, the three boxes per signal pertain to the three distighuised IPC activity levels, viz. IPC-1p (upper), IPC-1p and IPC-2p (middle), and IPC-1p, IPC-2 and IPC-3 (lower); the reference 'collective pitch' is represented in each box by a blue (dark) line. The required maximum pitch speed rises from ca. 2 °/s at collective pitch only, via $7^{o}/s$ and $10^{o}/s$ at IPC-1p and IPc-2 up to $12^{o}/s$ at IPC-3p. The respective pitch acceleration maxima are ca $3^{o}/s^{2}$, $18^{o}/s^{2}$, $27^{o}/s^{2}$ and $50^{o}/s^{2}$. The fore-aft tower motion is somewhat raised by IPC-1p, which remains active when IPC-2p and IPC-3p are added. This is caused by the presence of the $2^{\rm nd}$ multi-blade pitch angle coordinate $\theta_{\rm cm_2}$ in the equation of motion for the fore-aft speed $\dot{x}_{\rm fa}$ (see equation 13; pitch angle variations for IPC-1p are based on variations in $\theta_{\rm cm_2}$).

1.7 Model for stability analysis

In Section 1.3 it was proven that 1p individual pitch control (IPC-1p) can be approached as a linear time invariant control problem after transformation of the rotor variables into multiblade coordinates according to Coleman and Feingold [18]. The resulting '1p-transformed model' can be formulated generically in state space form, as was mentioned in the general receipt at the end of Section 1.3.

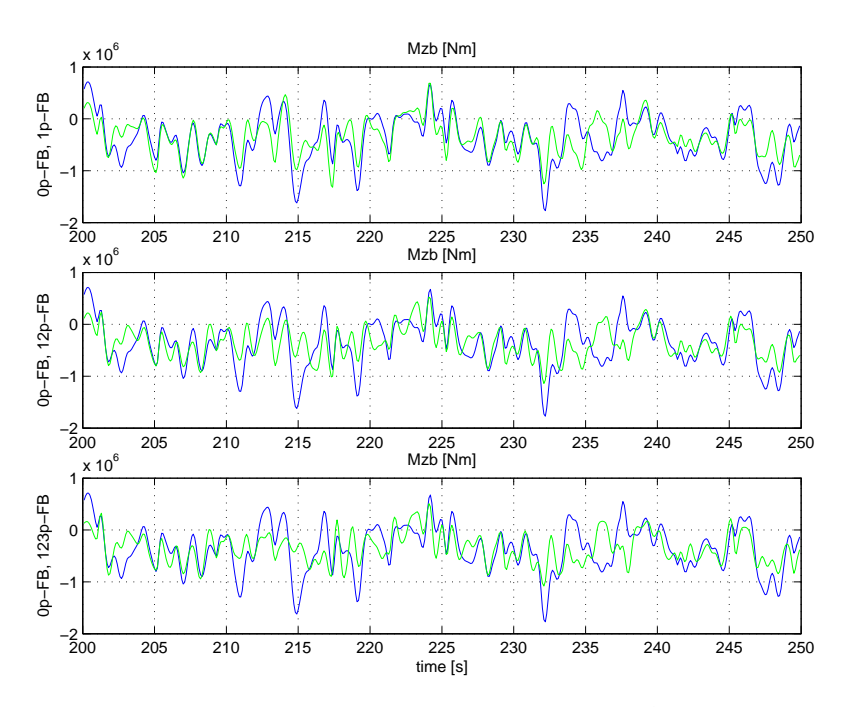


Figure 6 Time realizations the blade root flap moment (Mzb) at 16 m/s

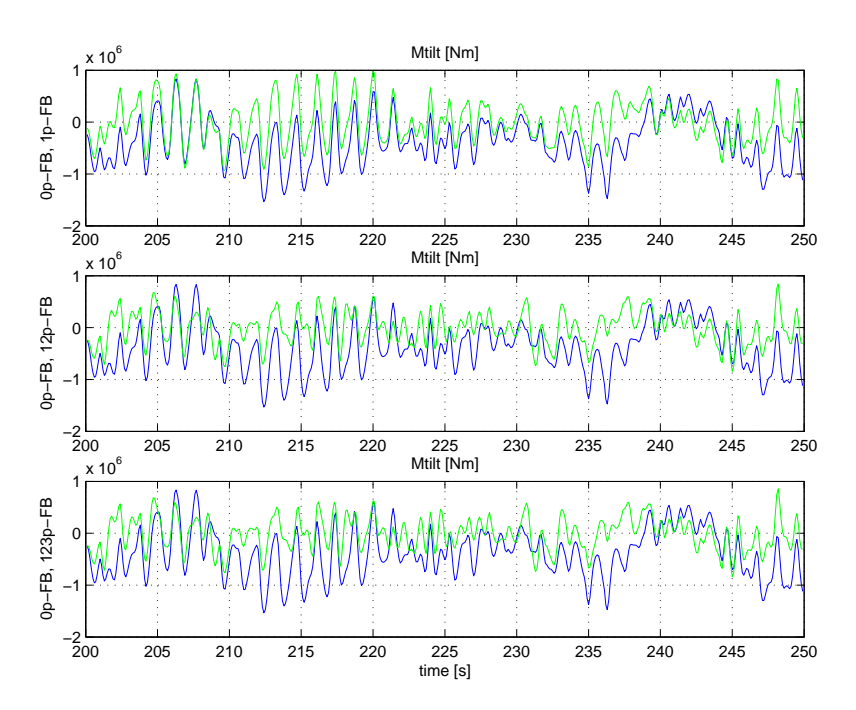


Figure 7 Time realizations of the tilt moment in the rotor center (Mtilt) at 16 m/s

In this section it is shown how the feedback loops for IPC-1p, IPC-2p and IPC-3p are linked to the 1p-transformed model. This yields a model formulation that can be used for stability analysis. When the model inputs and outputs are restricted to the pitch angles and blade root flap moments, the linear time invariant state space representation of the wind turbine model from Section 1.3

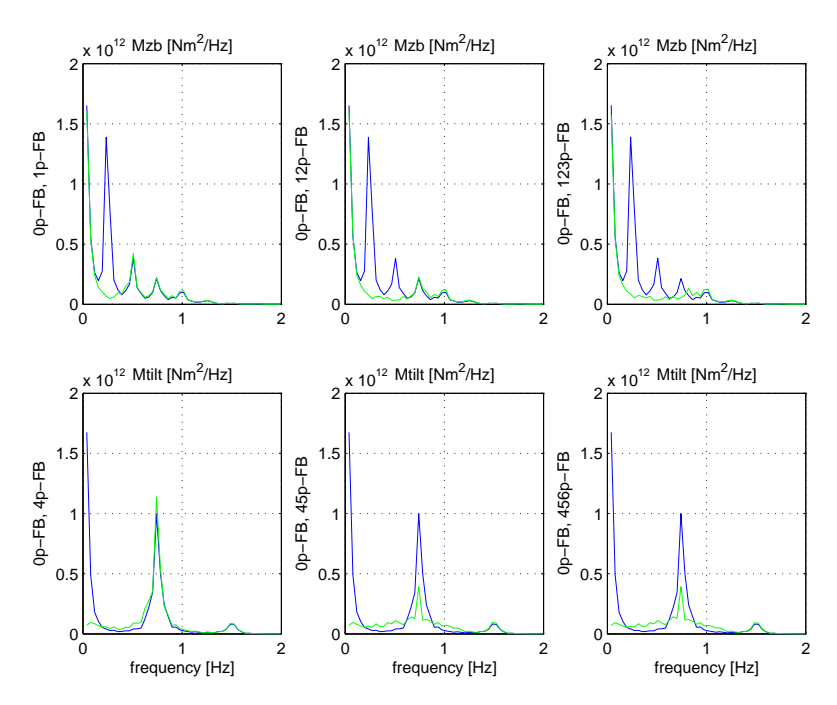


Figure 8 Power spectra for the blade root flap moment (Mzb) and the tilt moment in the rotor center (Mtilt) at 16 m/s

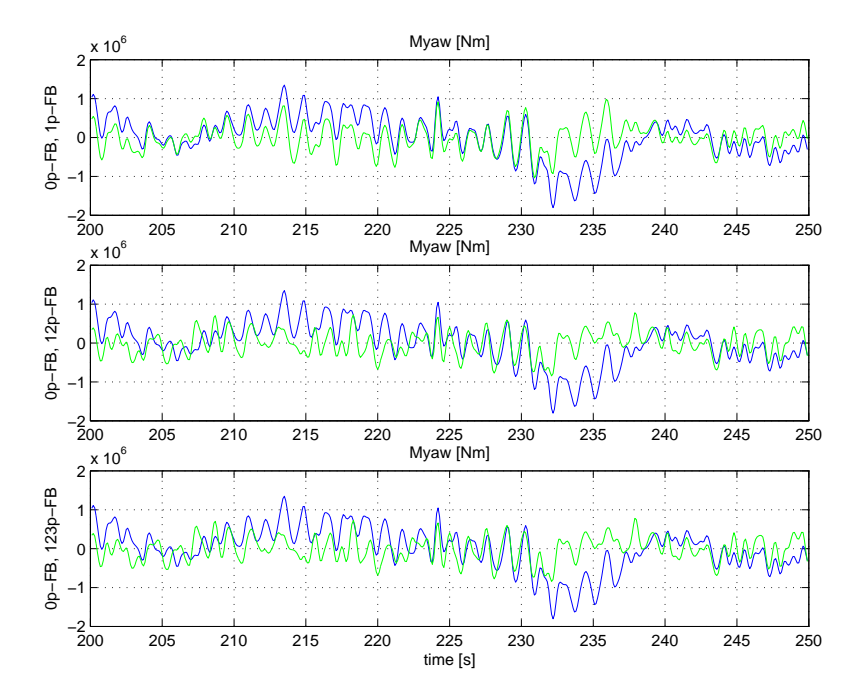


Figure 9 Time realizations for the yaw moment in the rotor center (Myaw) at 16 m/s

looks as follows:

$$\underline{\epsilon}_{t} = \mathbf{P}^{-1}(\psi) \underline{\theta}
\underline{\dot{q}}_{t} = \mathbf{A}_{t} \underline{q}_{t} + \mathbf{B}_{t} \underline{\epsilon}_{t}
\underline{\eta}_{t} = \mathbf{C}_{t} \underline{q}_{t} + \mathbf{K}_{t} \underline{\epsilon}_{t}
\delta \underline{M}_{z} = \mathbf{P}(\psi) \underline{\eta}_{t}$$
(51)

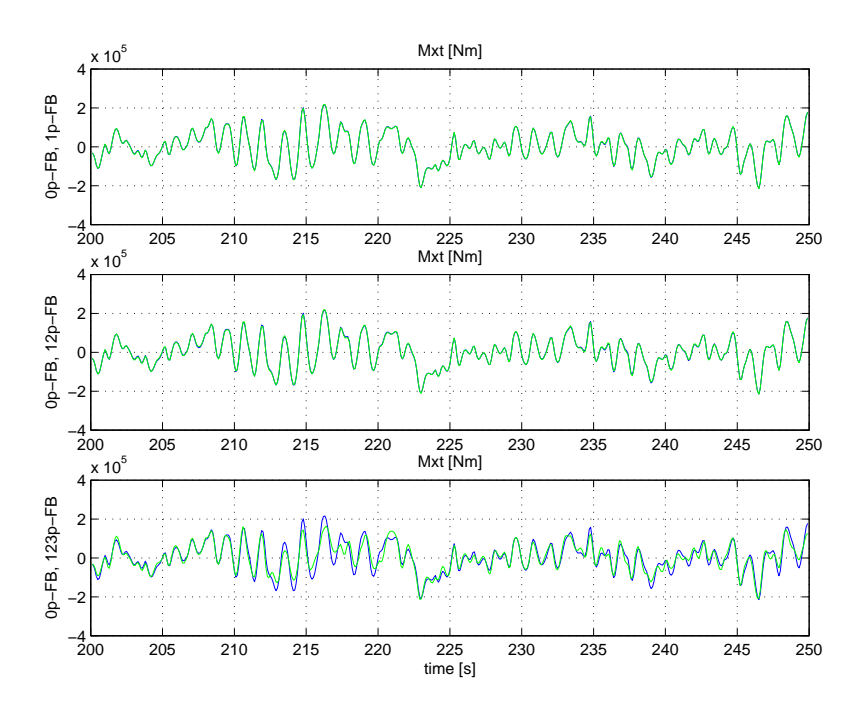


Figure 10 Time realizations for the driving torque (Mxt) at 16 m/s

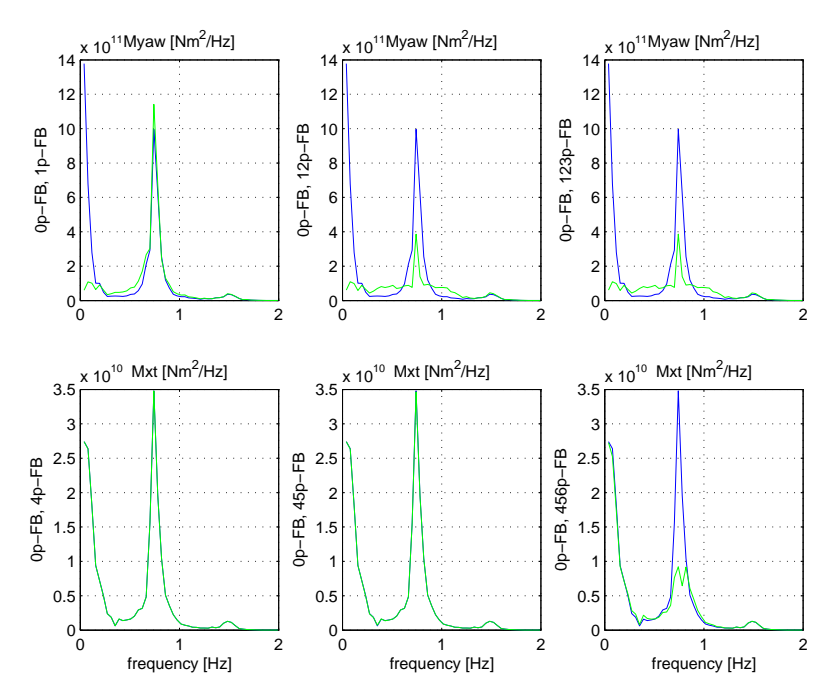


Figure 11 Power spectra for the yaw moment in the rotor center (Myaw) and the driving torque (Mxt) at 16 m/s

The state vector name $\underline{\dot{q}}_{\rm t}$ is used instead of $\underline{\dot{q}}$. The parameter matrices now have the subscript to (turbine) instead of cm. It should be noted that

- $B_{\rm t}$ contains only 3 columns of $B_{\rm cm}$;
- $C_{\rm t}$ contains only 3 rows of $C_{\rm cm}$;
- $K_{\rm t}$ contains only 3 rows and 3 columns of $K_{\rm cm}$.

A pair of feedback laws $\{L^{(k)}(t), L^{(k)}(t)\}$ for IPC-kp can be formulated as a state space model.

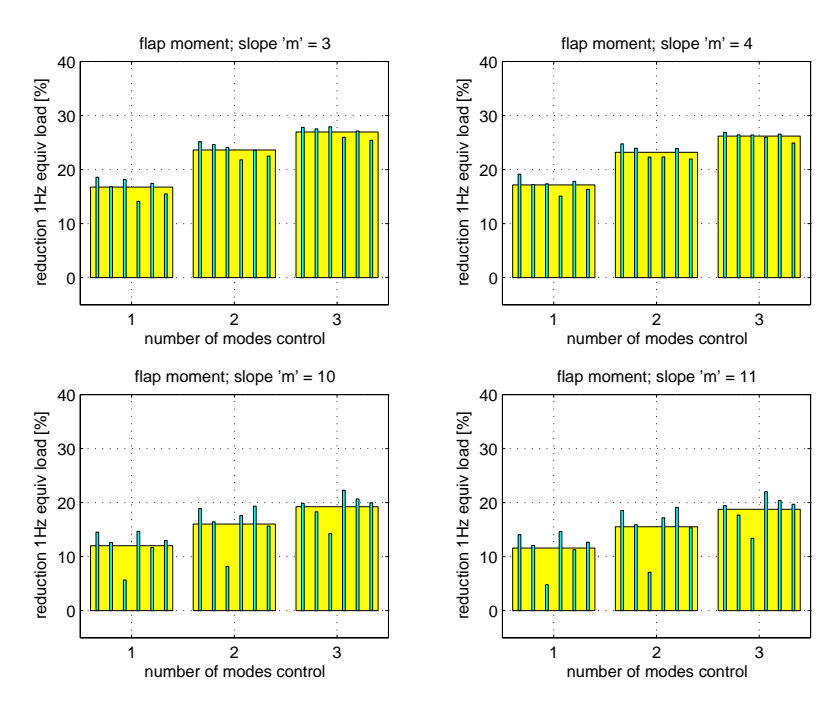


Figure 12 Relative fatigue damage reduction via 1Hz equivalent fatigue loading for blade root flap moment at 16 m/s

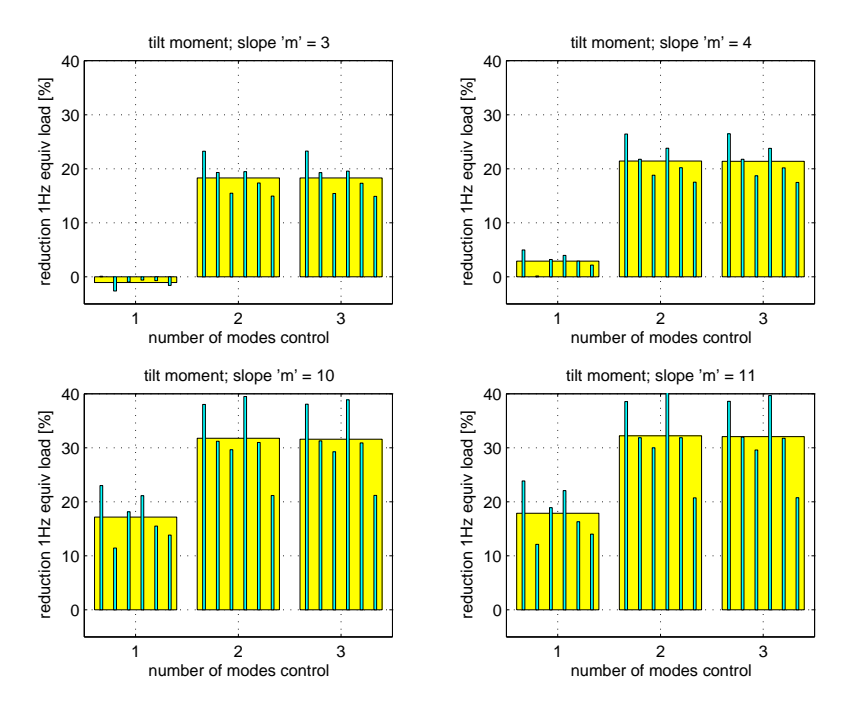


Figure 13 Relative fatigue damage reduction via 1Hz equivalent fatigue loading for tilt moment at 16 m/s

The involved parameter matrices have subscript f (feedback):

$$\underline{\dot{q}}_{f}^{(k)} = \boldsymbol{A}_{f}^{(k)} \, \underline{q}_{f}^{(k)} + \boldsymbol{B}_{f}^{(k)} \, \underline{\epsilon}_{f}^{(k)} \quad \text{with} \quad \underline{\epsilon}_{f}^{(k)} = \begin{bmatrix} \delta M_{z_{\text{cm}_{2}}}^{(k)} \\ \delta M_{z_{\text{cm}_{3}}}^{(k)} \end{bmatrix}
\underline{\eta}_{f}^{(k)} = \boldsymbol{C}_{f}^{(k)} \, \underline{q}_{f}^{(k)} \quad \text{with} \quad \underline{\eta}_{f}^{(k)} = \begin{bmatrix} \theta_{\text{cm}_{2}}^{(k)} \\ \theta_{\text{cm}_{3}}^{(k)} \end{bmatrix}$$
(52)

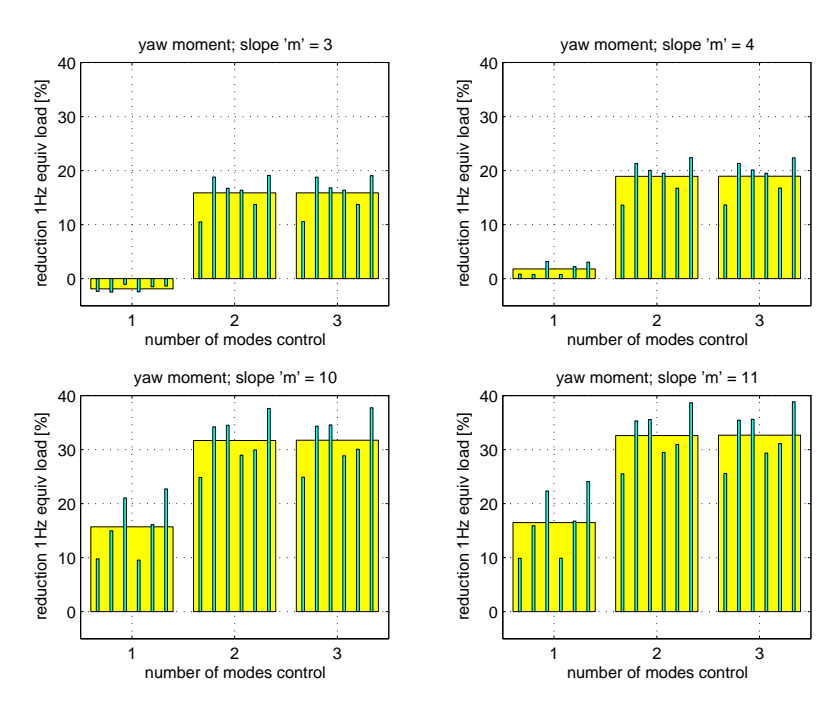


Figure 14 Relative fatigue damage reduction via 1Hz equivalent fatigue loading for yaw moment (Myaw) at 16 m/s

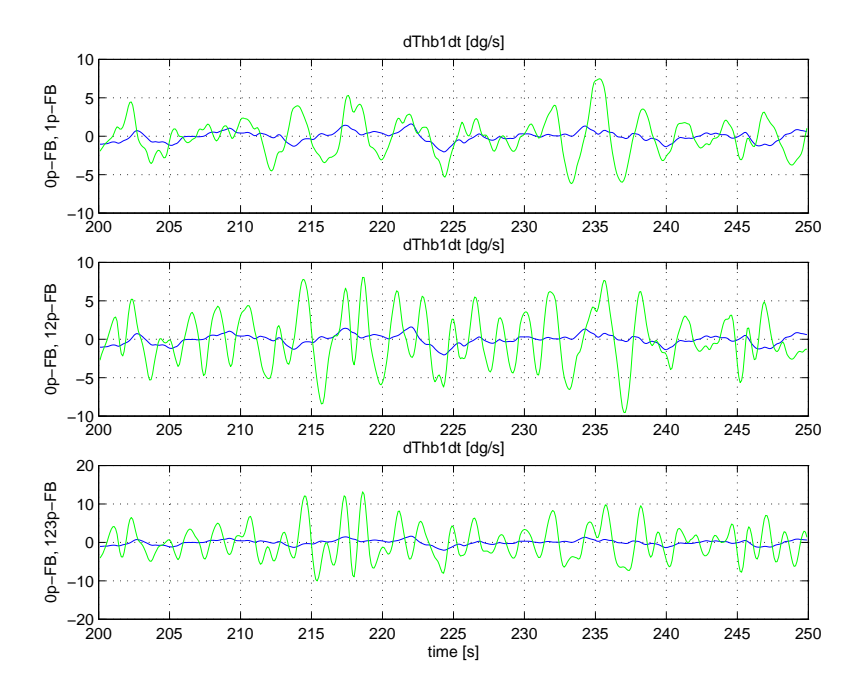


Figure 15 Realizations of pitch speed (dThb1dt) at 16 m/s

Since the feedback laws include integral action and low pass filtering there is no feedthrough from the input $\underline{\epsilon}_{\mathbf{f}}^{(k)}$ to the output $\eta_{\mathbf{f}}^{(k)}$.

Define the kp-demodulation matrix $\hat{D}^{(k)}$ and jp-remodulation matrix $\hat{M}^{(j)}$ in accordance with the modulation schemes for the artificial measurement and control signals in the IPC-loops as

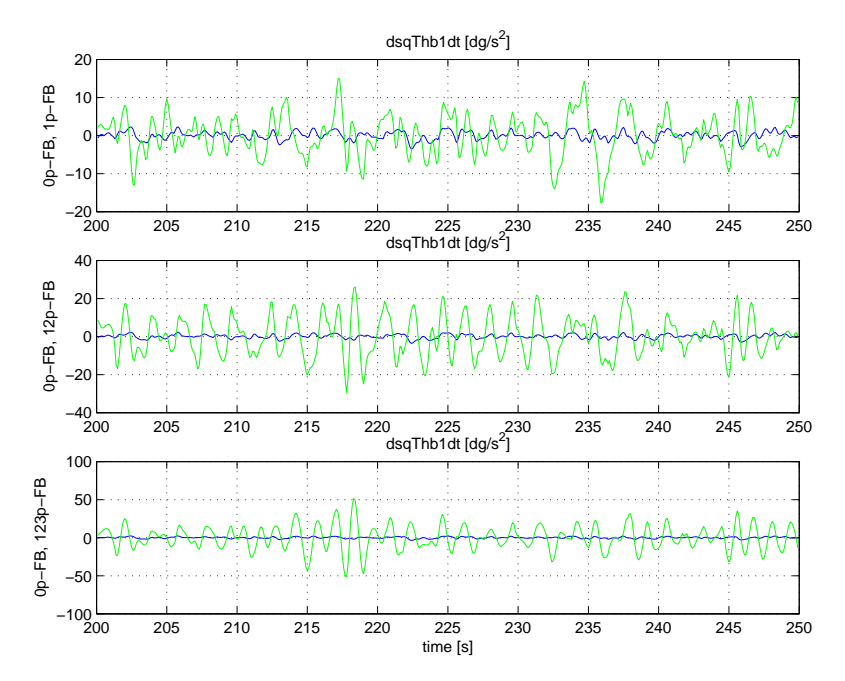


Figure 16 Realizations of pitch acceleration (dsqdThb1dt) at 16 m/s

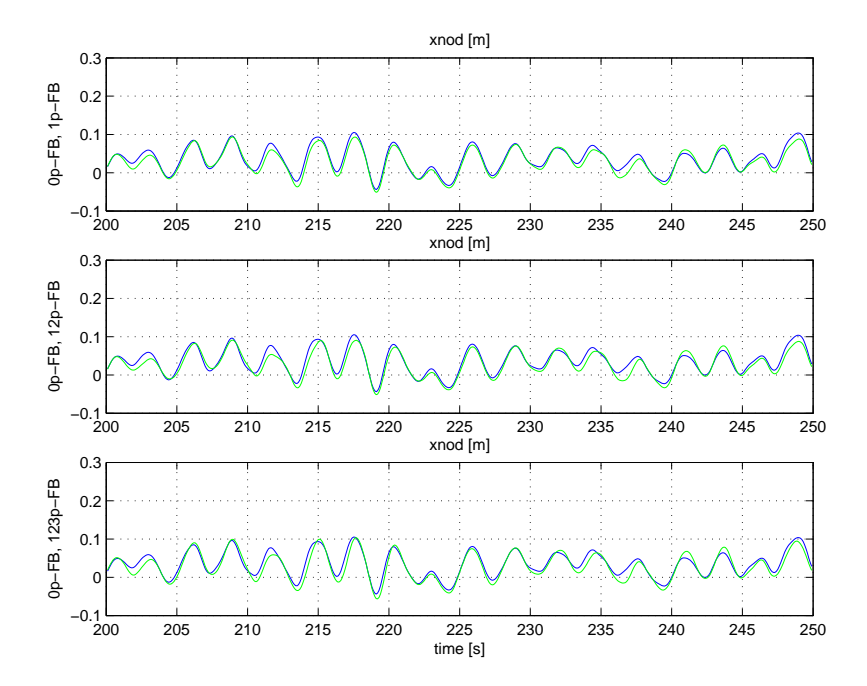


Figure 17 Realizations of fore-aft tower motion (xnod) at 16 m/s

dealt with in Sections 1.3-1.4:

$$\hat{\boldsymbol{D}}^{(k)} \stackrel{?}{=} \frac{2}{3} \begin{pmatrix} \sin k\psi_1 \sin k\psi_2 \sin k\psi_3 \\ \cos k\psi_1 \cos k\psi_2 \cos k\psi_3 \end{pmatrix}, \quad \hat{\boldsymbol{M}}^{(j)} \stackrel{?}{=} \begin{pmatrix} \sin j\psi_1 \cos j\psi_1 \\ \sin j\psi_2 \cos j\psi_2 \\ \sin j\psi_3 \cos j\psi_3 \end{pmatrix}$$
(53)

The link between the wind turbine model and the feedback laws is established via these matrices:

$$\underline{\epsilon}_{\mathbf{f}}^{(k)} = \hat{\boldsymbol{D}}^{(k)} \boldsymbol{P} \, \underline{\eta}_{\mathbf{t}} = \boldsymbol{D}^{(k)} \, \underline{\eta}_{\mathbf{t}} \quad \text{for } k = 1, 2, 3$$

$$\underline{\epsilon}_{\mathbf{t}} = \sum_{j=1}^{3} \boldsymbol{P}^{-1} \, \hat{\boldsymbol{M}}^{(j)} \, \underline{\eta}_{\mathbf{f}}^{(j)} = \sum_{j=1}^{3} \boldsymbol{M}^{(j)} \, \underline{\eta}_{\mathbf{f}}^{(j)}$$
(54)

with $(k = 1, 2, 3 \ j = 1, 2, 3;$ Kronecker δ_{mk} equals 1 if k = m else 0):

$$\mathbf{D}^{(k)} = \begin{pmatrix} 2\delta_{3k}\sin 3\psi & \delta_{1k} - \delta_{2k}\cos 3\psi & \delta_{2k}\sin 3\psi \\ 2\delta_{3k}\cos 3\psi & \delta_{2k}\sin 3\psi & \delta_{1k} + \delta_{2k}\cos 3\psi \end{pmatrix}$$

$$\mathbf{M}^{(j)} = \begin{pmatrix} \delta_{3j}\sin 3\psi & \delta_{3j}\cos 3\psi \\ \delta_{1j} - \delta_{2j}\cos 3\psi & \delta_{2j}\sin 3\psi \\ \delta_{2j}\sin 3\psi & \delta_{1j} + \delta_{2j}\cos 3\psi \end{pmatrix}$$
(55)

Substitution of the coupling conditions by equation 54 in the turbine and controller equations 51 and 52 yields the following coupled state equations (k = 1, 2, 3):

$$\underline{\dot{q}}_{t} = \boldsymbol{A}_{t} \, \underline{q}_{t} + \boldsymbol{B}_{t} \sum_{j=1}^{3} \boldsymbol{M}^{(j)} \, \boldsymbol{C}_{f}^{(j)} \, \underline{q}_{f}^{(j)}$$

$$\underline{\dot{q}}_{f}^{(k)} = \boldsymbol{A}_{f}^{(k)} \, \underline{q}_{f}^{(k)} + \boldsymbol{B}_{f}^{(k)} \, \boldsymbol{D}^{(k)} \cdot$$

$$(\boldsymbol{C}_{t} \, \underline{q}_{t} + \boldsymbol{K}_{t} \sum_{j=1}^{3} \boldsymbol{M}^{(j)} \, \boldsymbol{C}_{f}^{(j)} \, \underline{q}_{f}^{(j)})$$
(56)

These results were obtained by elimination of the output vectors $\underline{\eta}_{\mathrm{t}}$ and $\underline{\eta}_{\mathrm{f}}^{\scriptscriptstyle(j)}$ which in first instance appear in the right hand sides. The matrix products $\boldsymbol{D}^{(k)}\boldsymbol{K}_{\mathrm{t}}\,\boldsymbol{M}^{(j)}$ in the feedback state equations imply that the coupled system is periodic in 3p and 6p. When written as *one* matrix-vector equation the state equation becomes $(\underline{q}=[\underline{q}_{\mathrm{t}}'\ \underline{q}_{\mathrm{f}}^{\scriptscriptstyle(i)'}\ \underline{q}_{\mathrm{f}}^{\scriptscriptstyle(3)'}]')$:

$$\underline{\dot{q}} = \mathbf{A}_{d} \, \underline{q} + \cos 3\psi \mathbf{A}_{c} \, \underline{q} + \sin 3\psi \mathbf{A}_{s} \, \underline{q}
+ \cos 6\psi \mathbf{A}_{cc} \, \underline{q} + \sin 6\psi \mathbf{A}_{ss} \, \underline{q}$$
(57)

Manageable expressions for the coefficient matrices $A_{\rm d}$ etc. are obtained when the state space formulation by equation 56 is rewritten in modulated sub-matrices:

$$\underline{\dot{q}}_{t} = A_{t} \, \underline{q}_{t} + \sum_{j=1}^{3} (A_{tf_{d}}^{(j)} + \cos 3\psi A_{tf_{c}}^{(j)} + \sin 3\psi A_{tf_{s}}^{(j)}) \, \underline{q}_{f}^{(j)}
\underline{\dot{q}}_{f}^{(k)} = (A_{ft_{d}}^{(k)} + \cos 3\psi A_{ft_{c}}^{(k)} + \sin 3\psi A_{ft_{s}}^{(k)}) \underline{q}_{t} + A_{f}^{(k)} \, \underline{q}_{f}^{(k)}
+ \sum_{j=1}^{3} (A_{ff_{d}}^{(k,j)} + \cos 3\psi A_{ff_{c}}^{(k,j)} + \sin 3\psi A_{ff_{s}}^{(k,j)}
+ \cos 6\psi A_{ff}^{(k,j)} + \sin 6\psi A_{ff_{c}}^{(k,j)}) \, q_{f}^{(j)}$$
(58)

The expressions for the coefficient matrices $A_{
m d}$ etc. then become:

$$\mathbf{A}_{d} = \begin{pmatrix} \mathbf{A}_{t} & \mathbf{A}_{tf_{d}}^{(1)} & \mathbf{A}_{tf_{d}}^{(2)} & \mathbf{A}_{tf_{d}}^{(3)} \\ \mathbf{A}_{ft_{d}}^{(1)} & \mathbf{A}_{f}^{(1)} + \mathbf{A}_{ff_{d}}^{(1,1)} & \mathbf{A}_{ff_{d}}^{(1,2)} & \mathbf{A}_{ff_{d}}^{(1,3)} \\ \mathbf{A}_{ft_{d}}^{(2)} & \mathbf{A}_{ff_{d}}^{(2,1)} & \mathbf{A}_{f}^{(2)} + \mathbf{A}_{ff_{d}}^{(2,2)} & \mathbf{A}_{ff_{d}}^{(2,3)} \\ \mathbf{A}_{ft_{d}}^{(3)} & \mathbf{A}_{ff_{d}}^{(3,1)} & \mathbf{A}_{ff_{d}}^{(3,2)} & \mathbf{A}_{f}^{(3)} + \mathbf{A}_{ff_{d}}^{(3,3)} \end{pmatrix}$$

$$(59)$$

and (for x=c,s):

$$\boldsymbol{A}_{x} = \begin{pmatrix} \mathbf{0} & \boldsymbol{A}_{tf_{x}}^{(1)} & \boldsymbol{A}_{tf_{x}}^{(2)} & \boldsymbol{A}_{tf_{x}}^{(3)} \\ \boldsymbol{A}_{ft_{x}}^{(1)} & \boldsymbol{A}_{ff_{x}}^{(1,1)} & \boldsymbol{A}_{ff_{x}}^{(1,2)} & \boldsymbol{A}_{ff_{x}}^{(1,3)} \\ \boldsymbol{A}_{ft_{x}}^{(2)} & \boldsymbol{A}_{ff_{x}}^{(2,1)} & \boldsymbol{A}_{ff_{x}}^{(2,2)} & \boldsymbol{A}_{ff_{x}}^{(2,3)} \\ \boldsymbol{A}_{ft_{x}}^{(3)} & \boldsymbol{A}_{ff_{x}}^{(3,1)} & \boldsymbol{A}_{ff_{x}}^{(3,2)} & \boldsymbol{A}_{ff_{x}}^{(3,3)} \end{pmatrix}$$
(60)

and (for xx=cc,ss):

$$A_{xx} = \begin{pmatrix} 0 & 0 & 0 & 0 \\ 0 & A_{ff_{xx}}^{(1,1)} & A_{ff_{xx}}^{(1,2)} & A_{ff_{xx}}^{(1,3)} \\ 0 & A_{ff_{xx}}^{(2,1)} & A_{ff_{xx}}^{(2,2)} & A_{ff_{xx}}^{(2,3)} \\ 0 & A_{ff_{xx}}^{(3,1)} & A_{ff_{xx}}^{(3,2)} & A_{ff_{xx}}^{(3,3)} \end{pmatrix}$$

$$(61)$$

The matrices $D^{(k)}$ and $M^{(j)}$ are rewritten in order to ease the derivation of the above used submatrices (k, j = 1, 2, 3):

$$D^{(k)} = D_{d}^{(k)} + \cos 3\psi D_{c}^{(k)} + \sin 3\psi D_{s}^{(k)}$$

$$M^{(j)} = M_{d}^{(j)} + \cos 3\psi M_{c}^{(j)} + \sin 3\psi M_{s}^{(j)}$$
(62)

with

$$\mathbf{D}_{d}^{(k)} = \begin{pmatrix} 0 & \delta_{1k} & 0 \\ 0 & 0 & \delta_{1k} \end{pmatrix} ; \quad \mathbf{M}_{d}^{(j)} = \begin{pmatrix} 0 & 0 \\ \delta_{1j} & 0 \\ 0 & \delta_{1j} \end{pmatrix}
\mathbf{D}_{c}^{(k)} = \begin{pmatrix} 0 & -\delta_{2k} & 0 \\ 2\delta_{3k} & 0 & \delta_{2k} \end{pmatrix} ; \quad \mathbf{M}_{c}^{(j)} = \begin{pmatrix} 0 & \delta_{3j} \\ -\delta_{2j} & 0 \\ 0 & \delta_{2j} \end{pmatrix}
\mathbf{D}_{s}^{(k)} = \begin{pmatrix} 2\delta_{3k} & 0 & \delta_{2k} \\ 0 & \delta_{2k} & 0 \end{pmatrix} ; \quad \mathbf{M}_{s}^{(j)} = \begin{pmatrix} \delta_{3j} & 0 \\ 0 & \delta_{2j} \\ \delta_{2i} & 0 \end{pmatrix}$$
(63)

The expressions for the state transition submatrices are:

$$A_{tf_{x}}^{(j)} = B_{t} M_{x}^{(j)} C_{f}^{(j)} \quad \text{for } x = d, c, s$$

$$A_{ft_{x}}^{(k)} = B_{f}^{(k)} D_{x}^{(k)} C_{t} \quad \text{for } x = d, c, s$$

$$A_{ff_{d}}^{(k,j)} = B_{f}^{(k)} D_{d}^{(k)} K_{t} M_{d}^{(j)} C_{f}^{(j)} + \frac{1}{2} B_{f}^{(k)} (D_{c}^{(k)} K_{t} M_{c}^{(j)} + D_{s}^{(k)} K_{t} M_{s}^{(j)}) C_{f}^{(j)}$$

$$A_{ff_{s}}^{(k,j)} = B_{f}^{(k)} (D_{c}^{(k)} K_{t} M_{d}^{(j)} + D_{d}^{(k)} K_{t} M_{c}^{(j)}) C_{f}^{(j)}$$

$$A_{ff_{c}}^{(k,j)} = B_{f}^{(k)} (D_{s}^{(k)} K_{t} M_{d}^{(j)} + D_{d}^{(k)} K_{t} M_{s}^{(j)}) C_{f}^{(j)}$$

$$A_{ff_{cc}}^{(k,j)} = \frac{1}{2} B_{f}^{(k)} (D_{c}^{(k)} K_{t} M_{c}^{(j)} - D_{s}^{(k)} K_{t} M_{s}^{(j)}) C_{f}^{(j)}$$

$$A_{ff_{cc}}^{(k,j)} = \frac{1}{2} B_{f}^{(k)} (D_{s}^{(k)} K_{t} M_{c}^{(j)} + D_{s}^{(k)} K_{t} M_{c}^{(j)}) C_{f}^{(j)}$$

Inclusion of the IPC-1p loops yields an LTI closed loop model whereas the IPC-2p and IPC-3p loops cause '3p periodic coefficients' in the closed loop model. This model formulation is feasible for performing stability analysis based on Floquet theory [35].

1.8 Rotational mode expansions

Expressions are listed for multi-blade wind speed coordinates in the rotational modes $\{\hat{u}_p\}$ of the wind speed as experienced on corresponding blade locations of a 3-bladed rotor $(\tilde{u}_1, \tilde{u}_2 \text{ and } \tilde{u}_{3})$. The multi-blade wind speed coordinates $\tilde{u}_{cm_1}^{(k)}$, $\tilde{u}_{cm_2}^{(k)}$ and $\tilde{u}_{cm_3}^{(k)}$ are obtained via the following transformation:

$$\begin{bmatrix} \tilde{u}_{\text{cm}_{1}}^{(k)} \\ \tilde{u}_{\text{cm}_{2}}^{(k)} \\ \tilde{u}_{\text{cm}_{3}}^{(k)} \end{bmatrix} = \begin{pmatrix} \frac{1}{3} & \frac{1}{3} & \frac{1}{3} \\ \frac{2}{3} \sin k \psi_{1} \frac{2}{3} \sin k \psi_{2} \frac{2}{3} \sin k \psi_{3} \\ \frac{2}{3} \cos k \psi_{1} \frac{2}{3} \cos k \psi_{2} \frac{2}{3} \cos k \psi_{3} \end{pmatrix} \begin{bmatrix} \tilde{u}_{1} \\ \tilde{u}_{2} \\ \tilde{u}_{3} \end{bmatrix}$$
(65)

With rotor azimuth ψ equal to the azimuth ψ_1 of the first blade it holds:

$$\tilde{u}_{\text{cm}_1}^{(k)} = \frac{1}{3} \sum_{p=-\infty}^{\infty} \sum_{i=1}^{3} (\cos p\psi_i + j \sin p\psi_i) \,\hat{u}_p = \frac{1}{3} \sum_{p=-\infty}^{\infty} \sum_{i=1}^{3} e^{j(p)\psi_i} \,\hat{u}_p = \frac{1}{3} \sum_{m=-\infty}^{\infty} 3 e^{j3m\psi} \hat{u}_{3m}$$
 (66)

$$\tilde{u}_{\text{cm}_{2}}^{(k)} = \frac{2}{3} \sum_{p=-\infty}^{\infty} \sum_{i=1}^{3} (\cos p\psi_{i} + j \sin p\psi_{i}) \sin k\psi_{i} \,\hat{u}_{p}
= \frac{1}{3} \sum_{p=-\infty}^{\infty} \sum_{i=1}^{3} (\sin(p+k)\psi_{i} - \sin(p-k)\psi_{i} - j \cos(p+k)\psi_{i} + j \cos(p-k)\psi_{i}) \,\hat{u}_{p}
= \frac{1}{3} \sum_{p=-\infty}^{\infty} \sum_{i=1}^{3} -j e^{j(p+k)\psi_{i}} \,\hat{u}_{p} + j e^{j(p-k)\psi_{i}} \,\hat{u}_{p}
= \frac{1}{3} \sum_{p'=-\infty}^{\infty} \sum_{i=1}^{3} -j e^{jp'\psi_{i}} \,\hat{u}_{p'-k} + \frac{1}{3} \sum_{p''=-\infty}^{\infty} \sum_{i=1}^{3} j e^{jp''\psi_{i}} \,\hat{u}_{p''+k}
= \frac{1}{3} \sum_{p'=-\infty}^{\infty} 3 j e^{j3m\psi} (\hat{u}_{3m+k} - \hat{u}_{3m-k})$$
(67)

$$\tilde{u}_{\text{cm}_{3}}^{(k)} = \frac{2}{3} \sum_{p=-\infty}^{\infty} \sum_{i=1}^{3} (\cos p\psi_{i} + j \sin p\psi_{i}) \cos k\psi_{i} \,\hat{u}_{p}
= \frac{1}{3} \sum_{p=-\infty}^{\infty} \sum_{i=1}^{3} (\cos(p+k)\psi_{i} + \cos(p-k)\psi_{i} + j \sin(p+k)\psi_{i} + j \sin(p-k)\psi_{i}) \,\hat{u}_{p}
= \frac{1}{3} \sum_{p=-\infty}^{\infty} \sum_{i=1}^{3} e^{j(p+k)\psi_{i}} \,\hat{u}_{p} + e^{j(p-k)\psi_{i}} \,\hat{u}_{p}
= \frac{1}{3} \sum_{p'=-\infty}^{\infty} \sum_{i=1}^{3} e^{jp'\psi_{i}} \,\hat{u}_{p'-k} + \frac{1}{3} \sum_{p''=-\infty}^{\infty} \sum_{i=1}^{3} e^{jp''\psi_{i}} \,\hat{u}_{p''+k}
= \frac{1}{3} \sum_{p''=-\infty}^{\infty} 3 e^{j3m\psi} (\hat{u}_{3m+k} + \hat{u}_{3m-k})$$
(68)

1.9 Conclusion

A simple design model has been derived for the parametrization of feedback loops for individual pitch control around one time the rotational frequency (1p) for 3 bladed wind turbines. The model has been obtained via a multi-blade transformation in the azimuthh angles of the rotor blades. It allows for independent design of a feedback loop for rotor speed regulation and a pair of identical uncoupled feedback loops for reduction of blade loads around 1p which arise from tower shadow, wind shear and turbulence (IPC-1p). Basic scalar control theory can be applied in these three loops (phase and gain margins).

The adopted approach has been extended to reduction of blade loads in multiples of the rotational

frequency (IPC-2p, IPC-3p; multi-rotational mode individual pitch control). Now multi-blade transformations in two and three times the blade azimuthh angles apply. A similar design approach for the feedback loops appeared to be valid. Especially IPC-2p allows for implementation without any influence on the system dynamics and has a very beneficial effect on the tilt and yaw loading: the excitation around the 3p-frequency is significantly reduced.

The decomposition of the sampled wind field by the rotor blades in rotational modes plays a key role in the clarification of the working of the IPC.

Rainflow counting and power spectra were obtained from preliminary time-domain simulations. Fatigue damage reduction of up to 20 to 30% in both the blade loads and the nacelle loads seems realistic in frequently occurring full load conditions .

A general receipt has been given for the formulation of a linear model in which the feedback loops for IPC-1p, IPC-2p and IPC-3p are included. The point of departure is a linear time invariant (LTI) model formulation in multi-blade coordinates for a wind turbine with three or more blades. Inclusion of the IPC-1p loops yields an LTI closed loop model whereas the IPC-2p and IPC-3p loops cause '3p periodic coefficients' in the closed loop model. This model formulation is feasible for performing stability analysis based on Floquet theory.

It is recommended

- to include blade bending and unsteady aerodynamic behavior in the design approach;
- to set up a procedure for stability assessment based on Floquet theory and the proposed model formulation with feedback loops included.

2 Feedback-feedforward IPC

Summary

This section explores the possibilities for wind turbine fatigue load reduction by applying advanced control design methods to the IPC design. The investigated control approach has a twodegree-of-freedom structure, consisting of an optimal multivariable LQG controller and a feedforward disturbance rejection controller based on estimated wind speed signals. Similarly to the standard IPC-1p approach (Section 1.3), the control design problem is first made time-invariant by using the Coleman transformation to the non-rotating coordinates. In Coleman domain, the LQG control objective is minimization of the rotor tilt and yaw moments, while the feedforward controller tries to achieve an even further improvement by rejecting the influence of the lowfrequency components of the wind on the rotor moments. To this end, the tilt and yaw-oriented components of the blade effective wind speeds are approximated using stochastic random walk models, the states of which are then augmented with the turbine states and estimated using a Kalman filter. The effects of these (estimated) disturbances on the controlled outputs are then reduced using stable dynamic model inversion. The approach is tested and compared to the conventional IPC method in simulation studies with models of different complexity. The results demonstrate very good load reduction at not only low frequencies (1p blade fatigue load reduction), but also at the 3p frequency, giving rise to fatigue load reduction of the non-rotating turbine components.

2.1 Introduction

This section describes a new IPC design method inspired by the optimal multivariable control in Coleman domain [5, 37] on the one hand, and by the wind speed estimation methods, proposed in [56, 68, 47] on the other hand. In particular, the axial, tilt-oriented and yaw oriented components of the blade effective wind speed signals are modeled by stochastic random walk models, the states of which are then augmented with the states of the turbine to be estimated all together using a single Kalman filter. The wind signals estimates are subsequently used in a dynamic disturbance feedforward controller [28, §10.5.2]. The feedforward control action is added to the control action from an optimal feedback LQG controller. The resulting feedback-feedforward control structure is similar to the periodic disturbance accommodating control structure in [68], although the design approach proposed in this section is fundamentally different in the following three aspects. First, the complete control design is now performed on a linear time invariant system, as obtained by making use of the Coleman transform. This offers many possibilities for further improvements such as extension to LPV control for covering a wider range of operating points of the wind turbine, similarly to the work of Bianchi for collective pitch control [4]. Secondly, the disturbance attenuation in [68] is based on a simple (static) pseudo-inverse of the system B matrix, while the present approach focuses on a dynamic feedforward controller achieving minimization of the effect of the disturbance on the tilt and yaw moments. To this end, stable dynamic model inversion is used [25]. And third, the current method deals with blade effective wind speeds, which allows for more accurate approximation of the loads on the individual blades than when only rotor effective wind speed is considered, as in [68].

The method is tested in simulation on two models of different complexity. First, a simple rigid turbine model with just a few degrees of freedom is used that provides useful insights and serves as a good basis for analysis of the presented control strategy. Next, a detailed aero-elastic linear model, generated by the computer program Turbu [76], is used for more detailed study of the control strategy. The results are compared to the results obtained with a conventional PI-based IPC. It is demonstrated that the present method achieves a significant improvement over the conventional one in that it reduces the rotor tilt and yaw moments over a much larger frequency band,

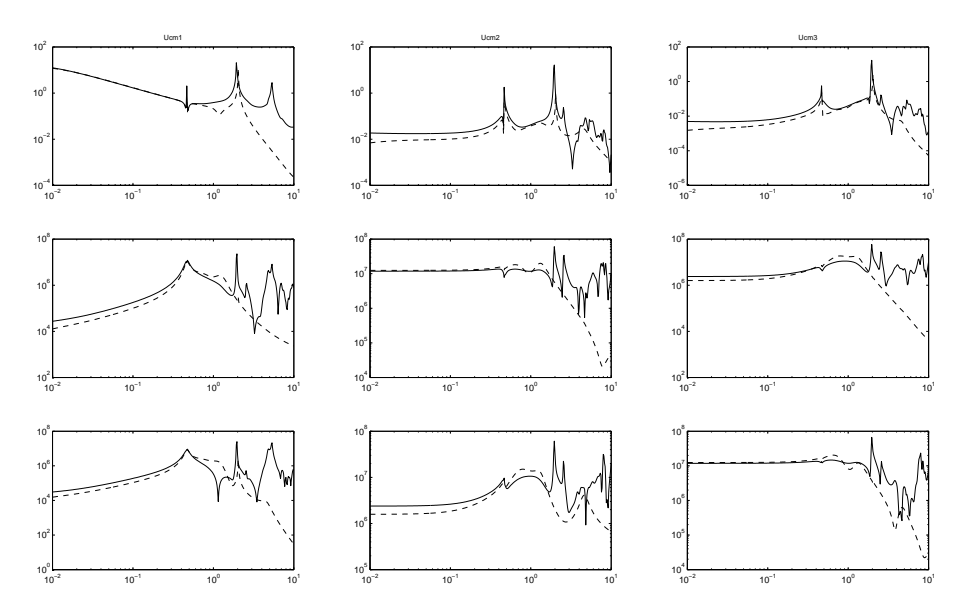


Figure 18 Frequency response from multi-blade pitch angles to rotor speed, tilt moment and yaw moment, both for the multibody (solid) and the lumped models (dashed)

including the fatigue-relevant 3p components.

2.2 Wind turbine model

The ECN computer code TURBU [76] generates elaborate linearised aero-elastic models of 3-bladed horizontal axis wind turbines. These models include considerable features that are necessary for control design and aero-elastic stability analysis, like bending and torsion deformation, (unsteady) aerodynamic and hydrodynamic conversions and wake dynamics. All model inputs for the drive-train and rotor blades are transformed into multi-blade coordinates before they enter the LTI model, and the model outputs from the drive-train and rotor blades are transformed back to rotating coordinates. A linear model is computed for a given aerodynamic equilibrium state. The latter is derived via the blade element momentum theory. The average deformation state is matched to the aerodynamic equilibrium. This is based on non-linear propagation of the deformation of the individual elements caused by the average loading. The average deformation per element is based on slender beam bending theory. A multibody approach is used to model the structural dynamics, as illustrated in [76]. The multibody wind turbine model has N elements per blade ($\{D_i, E_i, F_i\}$, $i = 1, 2, \ldots, N$) and M elements for the tower (S_i , $i = 1, 2, \ldots, M$), with each element having 5 degrees of freedom. There are 6 degrees of freedom in the rotor shaft R_r .

A typical TURBU model (with N=14 and M=15) has around 600 state variables, and therefore needs simplification when used for control design. For reducing the model order, TURBU provides model reduction based on elimination of high-frequency modes. This allows significant model order reduction without any loss of accuracy in the dynamic behavior of the lower frequency modes which are within the bandwidth of the controllers. This yields a model order of about 150. This reduced order model is here referred to as the *multibody model*. In addition to that, TURBU allows for modeling only a distinct number of degrees of freedom in the blade roots and tower bottom. The model obtained in this way is referred to as the *lumped model*. It has only 28 states and still models dynamic pitch servo actuation. Figure 18 shows the frequency responses from the multiblade pitch angle signals θ_i^{cm} , i=1,2,3, to the rotor speed Ω , tilt moment M_{tilt} and yaw moment M_{yaw} for both the full multibody (solid line) and reduced lumped (dashed line) models. Sufficient accuracy is observed at frequencies below 1 Hz.

From the frequency plots it is clear that at low frequencies (below about 0.3Hz) there is little

coupling between the channel $\theta_1^{cm} \to \Omega$ on the one hand, and the IPC channels $\theta_2^{cm} \to M_{tilt}$ and $\theta_3^{cm} \to M_{yaw}$ on the other hand. However, above this frequency there is a clear interaction between these loops. Therefore, when the collective controller is separately designed from the IPC it is very important that these loops are further "decoupled" using suitable filters. It is especially important that structural resonant frequencies that are well inside the bandwidth of the collective controller (e.g. the tower frequency at about 0.47 Hz) are filtered out from θ_1^{cm} so that it does not get influenced by the IPC control actions.

Similar conclusions can be made for the IPC loops, these are only decoupled from the collective loop at low frequencies, and if designed independently, filtering should be used to reduce high frequency effects from the collective pitch action. However, in this section a different approach is used for IPC design that does not need additional filter design. The starting point is the design of the collective pitch controller and the generator torque controller using conventional methods, including filters, as discussed above. These controllers are then interconnected with the turbine, so that the IPC design is performed on the closed-loop turbine system with the generator torque control and the collective pitch control in the loop. Then, a multivariable robust control design approach is used to synthesize one MIMO IPC loop that stabilizes the turbine and minimizes a suitably defined performance criterion based on the rotor moments. Of course, one could choose to include also the collective pitch and generator torque control loops into the MIMO controller; this is not done here as the present approach assumes that the speed and power loops are given, and it focuses on the inclusion of additional actuation via IPC for the purpose of fatigue load reduction. Notice that this MIMO approach also takes into account the coupling between the tilt and the yaw-oriented multi-blade coordinates, which coupling is clearly much stronger than the coupling with the collective pitch loop (see Figure 18). This coupling was absent in the simple model from the previous subsection.

2.3 Controller design

In this section the proposed IPC design approach is explained. Since it is compared in the next section to the conventional SISO approach to IPC, it is briefly described next.

2.3.1 Conventional SISO control approach

The conventional IPC is a scalar approach based on the assumption that the multi-blade coordinate transformation, described in Section 1.3.1, results in three independent time-invariant control loops: from collective pitch angle to rotor speed, from yaw-oriented pitch angle to yaw moment, and from tilt-oriented pitch angle to tilt angle. It is assumed that the generator speed is measured.

The speed regulation loop is usually based on a PI compensator that has as input the difference between the filtered generator speed and its rated value. The filter, used in the simulations, includes

- a low-pass filter (inverse Chebychev [type II], 4th order, 20dB reduction) with cut-off frequency of (3p-0.8) rad/s.
- notch filter (elliptic filter, 4th order, 30dB reduction) with stop-band $[0.8\omega_{tsd}, 1.05\omega_{tsd}]$, where ω_{tsd} is the first tower naying frequency.
- notch filter (elliptic filter, 2nd order, 30dB reduction) with stop-band $[0.8\omega_{cll}, 1.05\omega_{cll}]$, where ω_{cll} is the collective lead-lag frequency of the blades.

The PI compensator is designed to achieve a gain margin of 2 and a phase margin of 45 degrees. The torque controller is designed for achieving constant power production by keeping the generator torque equal to the rated power P_T divided by the rotor speed. After linearization around

the rated generator speed $\Omega_{g,r}$, the generator controller has the form of a P-compensator with gain $(-\frac{P_r}{n_{gb}\Omega_{g,r}^2})$, where n_{gb} is the gearbox ratio. It should be noted that this generator controller has a slightly destabilizing effect on the rotor speed as the generator torque decreases when the generator speed increases.

The load regulation loops aim at blade fatigue load reduction by reducing the 1p load component in the blade root bending moments. It is demonstrated in [75], that $(3m \pm 1)$ components, $m = 1, 2, \ldots$, in the load spectrum of the blade effective wind speed signals u_i , i = 1, 2, 3, contribute to the 3m components in the multi-blade wind coordinates u_i^{cm} . In other words, 1p loads on the blades are modulated into 0p loads on the tilt and yaw moments, meaning that the former can be reduced by reducing the static loads on the rotor moments. This can be achieved by means of a simple I-compensator. In order to prevent the influence of higher harmonics it is necessary to apply low pass filtering around and beyond 3p.

2.3.2 Feedback-Feedforward multivariable control approach to IPC

In this section the multivariable control approach to IPC, proposed in this section, will be introduced. It has a two-degree-of-freedom structure, containing an optimal feedback LQG controller from the rotor tilt and yaw moments to the multi-blade pitch angles θ_i^{cm} , and a feedforward disturbance rejection controller acting on the estimated multi-blade wind signals and producing additional multi-blade pitch angles.

As discussed above, this section assumes that the collective pitch controller $C_{col}(s)$ and generator torque controller $C_{gen}(s)$ (including the filters) are available and interconnected with the wind turbine to regulate the produced power by controlling the generator torque and the rotor speed, as explained in the previous subsection. Below it is assumed that the controllers $C_{col}(s)$ and $C_{gen}(s)$ are interconnected to the linear turbine model, be that the simple rigid model in Section 1.3.1, or the multibody TURBU model, (by substituting $\theta_1^{cm} = C_{col}(s)\Omega$ and $T_g = C_{gen}\Omega$ in the turbine model), after which discretization is performed, resulting in

$$x_{wt}(k+1) = A_{wt}x_{wt}(k) + B_{wt,\theta}\theta_{23}^{cm}(k) + B_{wt,u}u^{cm}(k),$$

$$y(k) = C_{wt}x_{wt}(k) + D_{wt,\theta}\theta_{23}^{cm}(k) + D_{wt,u}u^{cm}(k) + v(k),$$
(69)

where the state x_{wt} contains the state of the wind turbine model and the states of the torque and pitch controllers, $\theta_{23}^{cm} = [\theta_2^{cm}, \theta_3^{cm}]^T$ is the input, $u^{cm} = [u_1^{cm}, u_2^{cm}, u_3^{cm}]^T$ is the disturbance input, $y = [M_{tilt}, M_{yaw}]$ is the measured output, and $v \in \mathbb{R}^2$ is zero-mean white noise process with covariance matrix $Q_v = Q_v^T > 0$. Notice that the rotor tilt and yaw moments are assumed measured. In practice, conventional wire strain gauges can be used to measure the flapwise bending moments at the blade roots, which can be then converted into M_{tilt} and M_{yaw} using the Coleman transformation. While strain gauges are not very reliable devices as such for this application, due to the potential danger caused by lighting. The recent developments of optical strain gages are likely to overcome this disadvantage.

2.3.2.1 Design of optimal LQG controller

The optimal LQG controller consists of a linear quadratic regulator (LQR) and a Kalman filter. However, the conventional assumption in the Kalman filter design that the external input is a random white Gaussian process is clearly not satisfied for the model (69), as the multi-blade wind signals $u^{cm}(k)$ have no flat spectrum. To circumvent this problem, one can identify a stochastic linear model $M_{wind}(z)$ that has (approximately) the same spectrum as the wind signals $u^{cm}(k)$. This would allow modeling of u^{cm} as the output of a filtered white noise process, $u^{cm} = M_{wind}(z)w$. Substituting this into the turbine model (69), and augmenting the states x^{wt} with the filter model states, will yield a new model that has the white noise process w as external input,

so standard Kalman filter design can be performed. This approach, however, requires (a) that the spectrum of the multi-blade wind signals is given, and (b) that it is accurately represented by a linear model of low order (in order to keep the order of the final controller low). To avoid this approach, one might instead use a much simpler wind modeling, by noting that

- the energy of u^{cm} is concentrated at low frequencies (below 0.1 Hz), and
- the signal u^{cm} is stationary under mild assumptions, as proved in the following Lemma.

Lemma 1 (Stationarity of multi-blade wind speeds). *Under the assumption homogeneous turbulence, constant rotational speed and non-oblique oriented wind flow, the multi-blade components* u_i^{cm} , i = 1, 2, 3, of the blade effective wind speeds are stationary processes.

Proof.

For homogeneous turbulence and purely axial wind direction, the blade effective wind speed u_i on a fixed point on a rotating blade, can be expressed as a time-varying Fourier expansion

$$u_i(t, \psi_i) = \sum_{p=-\infty}^{\infty} e^{jp\psi_i(t)} \hat{u}_p(t), \ \hat{u}_p(t) = \frac{1}{2\pi} \int_0^{2\pi} e^{jp\phi} u(t, \phi) d\phi$$

where $\hat{u}_p(t)$ are time-dependent rotational modes. It has been shown in [75] that the following expression holds for the multi-blade coordinates of the blade effective wind speeds

$$\begin{bmatrix} u_1^{cm}(t) \\ u_2^{cm}(t) \\ u_3^{cm}(t) \end{bmatrix} = \sum_{m=-\infty}^{\infty} e^{j3m\psi} \begin{bmatrix} \hat{u}_{3m}(t) \\ j(\hat{u}_{3m+1}(t) - \hat{u}_{3m-1}(t)) \\ j(\hat{u}_{3m+1}(t) + \hat{u}_{3m-1}(t)). \end{bmatrix}$$

Then, with a^* denoting the conjugate of a, it can easily be shown that

$$\begin{bmatrix} u_1^{cm}(t+\tau) \\ u_2^{cm}(t+\tau) \\ u_3^{cm}(t+\tau) \end{bmatrix}^* = \sum_{n=-\infty}^{\infty} e^{-j3n\psi} \begin{bmatrix} \hat{u}_{3n}(t+\tau) \\ -j(\hat{u}_{3n+1}^*(t+\tau) - \hat{u}_{3n-1}^*(t+\tau)) \\ -j(\hat{u}_{3n+1}^*(t+\tau) + \hat{u}_{3n-1}^*(t+\tau)) \end{bmatrix}.$$

Therefore, for the variance of u_2^{cm} one has

$$E\{u_2^{cm}(t)(u_2^{cm}(t+\tau))^*\}$$

$$=E\left\{\sum_{m,n=-\infty}^{\infty}e^{j3(m-n)\psi}\left(\hat{u}_{3m+1}(t)-\hat{u}_{3m-1}(t)\right)\left(\hat{u}_{3n+1}^*(t+\tau)-\hat{u}_{3n-1}^*(t+\tau)\right)\right\}$$

$$=\sum_{m,n=-\infty}e^{j3(m-n)\psi}E\left\{\left(\hat{u}_{3m+1}(t)-\hat{u}_{3m-1}(t)\right)\left(\hat{u}_{3n+1}^*(t+\tau)-\hat{u}_{3n-1}^*(t+\tau)\right)\right\}$$

since under assumption of constant rotational speed one has that $\psi = \Omega t + \psi(0)$, so that $e^{j3(m-n)\psi}$ are purely deterministic signals. Furthermore, in [81] it is proved that, under the considered assumptions, the rotational modes are orthogonal and stationary, i.e.

$$E\left\{\hat{u}_p(t)\hat{u}_q^*(t+\tau)\right\} = \delta_{p,q}\sigma_{\hat{u}_p}(\tau),$$

where $\delta_{p,q}$ denotes the Kronecker delta function, and $\sigma_{\hat{u}_p}(\tau)$ is the covariance function of \hat{u}_p . Therefore, in the above expression for $E\{u_2^{cm}(t)(u_2^{cm}(t+\tau))^*\}$ all terms for $n\neq m$ drop, giving

$$E\{u_2^{cm}(t)(u_2^{cm}(t+\tau))^*\} = \sum_{m=-\infty}^{\infty} (\sigma_{\hat{u}_{3m-1}}(\tau) + \sigma_{\hat{u}_{3m+1}}(\tau)).$$

Clearly, the correlation function of $u_2^{cm}(t)$ is not a function of the time t. The same lines can be followed for the first and third multi-blade components $u_1^{cm}(t)$, and $u_3^{cm}(t)$ to arrive at the same conclusion. Therefore, $u_i^{cm}(t)$, i=1,2,3, are stationary processes.

This suggests that a random walk model could be sufficient to represent the relevant low frequency behavior of u^{cm}

$$u^{cm}(k+1) = u^{cm}(k) + w(k). (70)$$

Where, w is a random white Gaussian process with zero-mean and covariance matrix Q_w . Usually, the covariance matrix Q_w is viewed as a design parameter that provides a trade-off between tracking speed and smoothness of the estimates. For simplicity, it is often selected as a diagonal matrix. Faster tracking of the true signals can be obtained by appropriately increasing the elements of Q_w , which however results in less smooth (i.e. more noisy) estimates, and vice versa. A value of $0.1I_2$ is selected for the simulations in this section. The random walk model is particularly suitable, and often used, for the estimation of an unknown time-varying bias on the state and output equations [45], that has already proved to be an accurate and robust approach to rotor-effective wind speed estimation [56].

Interconnecting the random walk model (70) with the turbine model (69) results in

$$\begin{bmatrix} x_{wt}(k+1) \\ u^{cm}(k+1) \end{bmatrix} = \begin{bmatrix} A_{wt} & B_{wt,u} \\ 0 & I \end{bmatrix} \begin{bmatrix} x_{wt}(k) \\ u^{cm}(k) \end{bmatrix} + \begin{bmatrix} B_{wt,\theta} \\ 0 \end{bmatrix} \theta_{23}^{cm}(k) + \begin{bmatrix} 0 \\ I \end{bmatrix} w(k),$$

$$y(k) = \begin{bmatrix} C_{wt} & 0 \end{bmatrix} \begin{bmatrix} x_{wt}(k) \\ u^{cm}(k) \end{bmatrix} + \begin{bmatrix} D_{wt,\theta} \\ 0 \end{bmatrix} \theta_{23}^{cm}(k) + v(k).$$
(71)

A Kalman filter is used to estimate the state of this augmented system. The state estimate $\hat{x}_{wt}(k)$ will then be used by the LQR controller, discussed next, while the wind signal estimate $\hat{u}_{cm}(k)$ will be used by the feedforward controller, discussed later on.

The conditions, under which the system (71) is observable, are discussed in [56]. A sufficient condition for the observability is that the pair (A_{wt}, C_{wt}) is observable, and that the turbine system (69) has no poles and zeros at z=1, which holds for the models considered in this section. Notice, however, that the augmented system is *not* controllable, due to the fact that part of the states belong to the wind model. It is assumed that the remaining part of the augmented states (i.e. the pair (A_{wt}, B_{wt})) is controllable.

Given the Kalman filter turbine state estimate, $\hat{x}_{wt}(k)$, the LQR control action has the form $(K_{lqr}\hat{x}_{wt}(k))$, where the gain K_{lqr} is chosen to optimize the following standard quadratic criterion

$$J_{lqr} = \sum_{k=0}^{\infty} \begin{bmatrix} x_{wt}(k) \\ \theta_{cm} \end{bmatrix}^T \begin{bmatrix} Q \\ R \end{bmatrix} \begin{bmatrix} x_{wt}(k) \\ \theta_{cm} \end{bmatrix}.$$

2.3.2.2 Feedforward estimated wind disturbance rejection

An additional IPC action is added to the optimal LQG control action, discussed above. It uses a feedforward disturbance rejection control algorithm based on the estimated multi-blade wind speed signal $\hat{u}_{23}^{cm}(k)$. To this end, define the following transfer functions

$$G(z) = C_{wt}(zI - A_{wt})^{-1}B_{wt,\theta} + D_{wt,\theta},$$

$$H(z) = C_{wt}(zI - A_{wt})^{-1}B_{wt,u},$$
(72)

so that (with slight abuse of notation) it can be written $y(k) = G(z)\theta_{23}^{cm}(k) + H(z)u^{cm}(k) + v(k)$. Under the assumption of unbiasedness of the Kalman filter estimates, it follows that

$$y(k) = G(z)\theta_{23}^{cm}(k) + H(z)\hat{u}^{cm}(k) + \tilde{v}(k),$$

where $\tilde{v}(k)$ is a zero-mean random process. The feedforward controller $C_{ff}(z)$ should hence be designed in such a way, that the control action $\theta_{23}^{cm}(k) = C_{ff}G(z)\hat{u}_{23}^{cm}(k)$ minimizes the influence of $\hat{u}^{cm}(k)$ on y(k). The optimal controller will then be given by

$$C_{ff}(z) = -H(z)G^{-1}(z).$$

However, it can happen (as is the case with the numerical models, considered in this section) that the transfer function G(z) is non-minimum phase, resulting in an unstable optimal feedforward controller. To avoid that, the inverse of G(z) will be substituted by a stable inverse, as obtained using the stable dynamic model inversion (SDMI) method in [25].

The basic idea behind the SDMI method is, similar to the wind estimation method above, the use of a random walk model. To summarize the method, suppose that n(k) is some (unknown) signal and let q(k) = G(z)n(k). Then finding a stable inverse means computing a stable transfer function $G_{inv}(z)$ such that $\hat{n}(k) = G_{inv}(z)q(k) \approx n(k)$. To this end, the signal n(k) can be viewed as an unknown bias, that can be estimated using the same idea of random walk model in combination with a Kalman filter. Writing $n(k+1) = n(k) + \eta(k)$, with $E\{\eta_k\} = 0$ and $E\{\eta(k)\eta(k)^T\} = Q_{\eta}$, adding this to the state of G(z) and including (if necessary for numerical reasons) small additional process and/or measurement noise terms, results in an augmented model $G_{aug}(z)$, for which a Kalman filter can be designed. The Kalman filter transfer function from q(z) to $\hat{n}(k)$ represents the inverse of G(z). Hence, for the considered model (72), the SDMI method results in the following stable inverse of G(z)

$$G_{inv} = \begin{bmatrix} 0, & I \end{bmatrix} \begin{pmatrix} zI - \begin{bmatrix} A_{wt} & B_{wt,\theta} \\ 0 & I \end{bmatrix} + K[C_{wt}, & 0] \end{pmatrix}^{-1} K.$$

The feedforward controller then takes the form $C_{ff}(z) = -H(z)G_{inv}(z)$, so that the complete feedback-feedforward control action is formed as shown in Figure 19. This IPC loop, together with the basic power control loop, including the generator torque P-controller and the collective pitch PI-controller, is depicted in Figure 20. The figure shows both the conventional collective pitch control and generator torque control loops, acting on the rotor speed Ω , as well as the individual pitch control algorithm, acting on the measured flapwise blade root bending moments M_{zi} and computing additional actions to the collective pitch angles. Notice the required modulation and demodulation of the signals, discussed above.

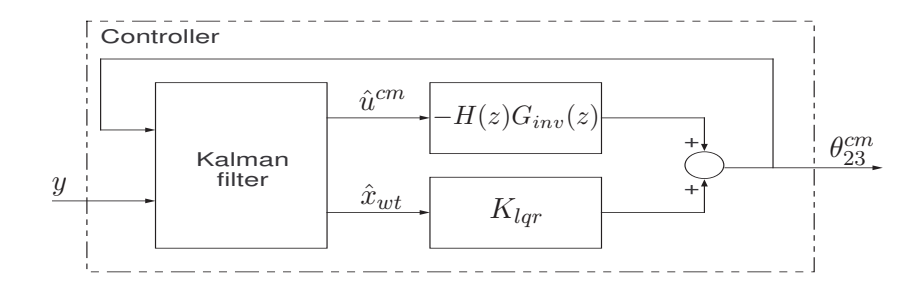


Figure 19 The feedback-feedforward IPC control scheme

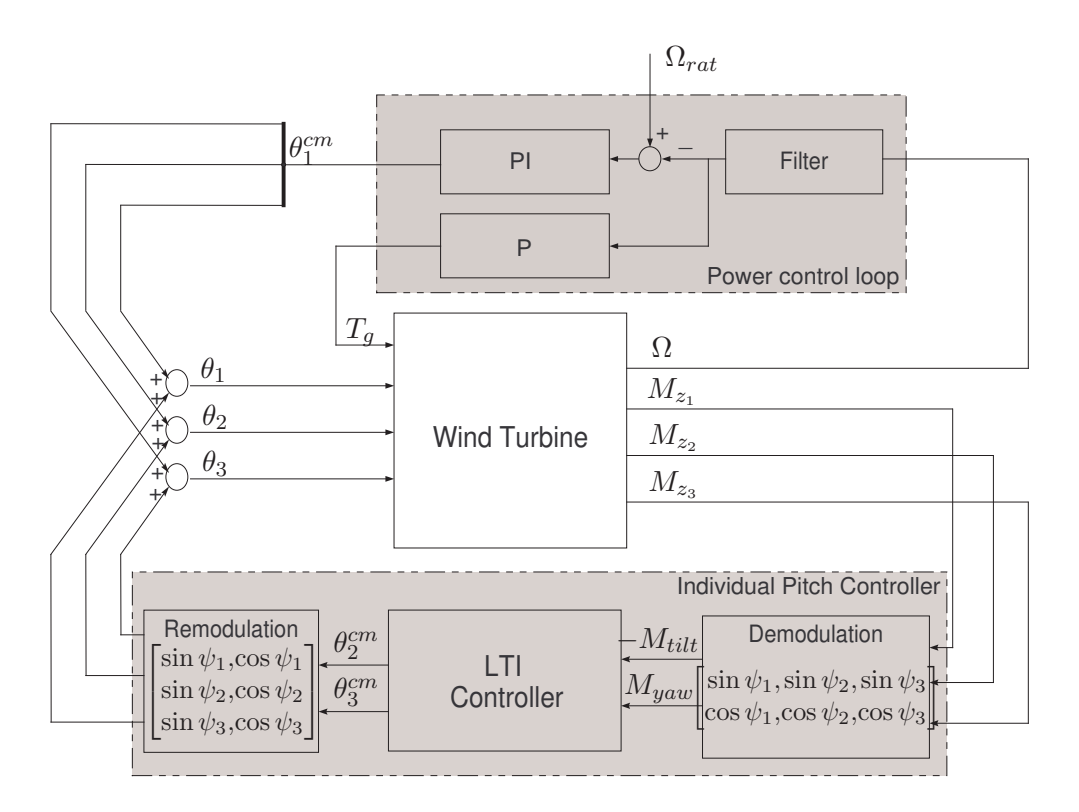


Figure 20 Layout of the complete control structure

2.4 Frequency domain analysis

This section presents results that demonstrate a significant improvement in the load reduction of the non-rotating turbine components, obtained with the presented feedback-feedforward IPC, as compared to the conventional PI-based IPC. The controllers are designed and compared on both the simple rigid model, developed in Section 1.3.1, and the detailed multibody TURBU model described in Section 2.2. The parameters of the simple model of Section 1.3.1 for a fictitious 2,5 MW wind turbine are listed in Table 1. This model, as well as the TURBU model, is derived for wind speed of 16 m/s, pitch angle of 10 degrees, and rotor speed of 1.806 rad/sec.

parameter	value	parameter	value
H	55.953 m	h_{M_x}	$8.3806 \times 10^4 \text{ N.s}$
R_b	40 m	h_{F_z}	$4.0683 \times 10^3 \text{ N.s/m}$
J	$11.2553 \times 10^6 \text{ kg.m}^2$	h_{M_z}	$-1.8948 \times 10^5 \text{ N.s}$
m_{tw}	$1.5657 \times 10^5 \text{ kg}$	k_{F_x}	$-6.1478 \times 10^3 \text{ N}$
s_{tw}	$1.235 \times 10^6 \text{ N/m}$	k_{M_x}	$-3.7711 \times 10^4 \text{ N.m}$
d_{tw}	$2.7995 \times 10^{3} \text{ N.s/m}$	k_{F_z}	$-1.8306 \times 10^3 \text{ N}$
h_{F_x}	$7.2019 \times 10^3 \text{ N.s/m}$	k_{M_z}	$1.6174 \times 10^{5} \text{ N.m}$

Table 1 Numerical values of the model parameters in the simple model of Section 1.3.1

The basic speed and power control loops are the same for both IPCs. These are designed as discussed in Section 2.3.1. The conventional IPC consists of two integrators, one for the tilt-oriented and one for the yaw-oriented channels. The new feedback-feedforward IPC controller is designed as discussed in Section 2.3.2. The parameters used in the design process are summarized in Table 2.

The comparison between the two control designs is performed in frequency domain. The frequency response plot for the simplified model is depicted in Figure 21. The figure shows the

parameter	Q_v	Q_w	Q	R	Q_{η}
value	0.01I	$0.1I_2$	I	0.8I	0.01

Table 2 Parameters used for the design of the feedback-feedforward IPC controller

transfer functions from the multi-blade wind signals u_{23}^{cm} to the rotor tilt and yaw moment M_{tilt} (left plot) and M_{yaw} (right plot). The solid lines in the plots represent the case of no IPC, the dash-dotted lines correspond to the conventional IPC method, while the dashed lines are for the new feedback-feedforward method. Only the diagonal channels of the transfer function from u^{cm} to y are given, since the off-diagonal ones are zero (even with the new MIMO controller, which preserves the intrinsic diagonal structure of the simple model). It can be clearly seen from the figure that the conventional IPC approach (dashed line) has good load reduction only at very low frequencies, while at 1p and higher frequencies in the fixed reference frame there is no reduction, and even a slight increase. The low frequency reduction is due to the integrator structure of this control method, making the method suitable for blade load reduction (as 0p reduction in M_{tilt} and M_{yaw} corresponds to 1p reduction in the flap-wise blade root bending moments), but cannot achieve fatigue-relevant load reduction on the non-rotating components of the wind turbine. On the other hand, by trading off low-frequency load reduction, the proposed feedback-feedforward method achieves reduction over a much wider frequency range, including the 3p frequency which is very relevant for fatigue on the non-rotating components, such as the nacelle, yaw bearing and tower [7]. Improved reduction at low frequencies can be obtained by including integral action in the controller.

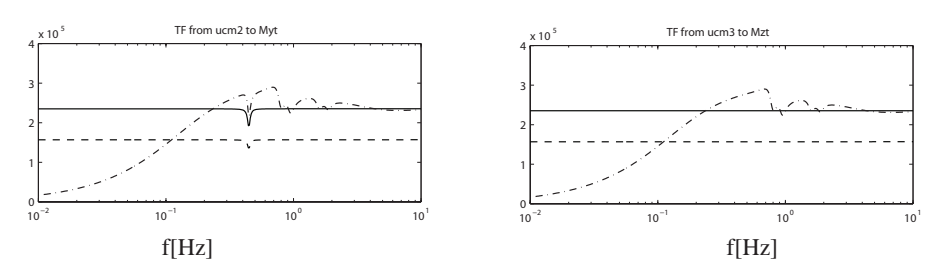


Figure 21 Frequency response plot of tilt moment M_{tilt} (left) and yaw moment M_{yaw} (right) due to the multi-blade wind inputs u_2^{cm} and u_3^{cm} , respectively, for the simple rigid turbine model with no IPC (solid), conventional IPC (dash-dotted) and new feedback-feedforward IPC (dashed).

Similar conclusions can be made based on the results with the TURBU model, as depicted in Figure 22. Now there is coupling between tilt and yaw-oriented moment, so the off-diagonal channels are also plotted. Notice that, although the IPC controller design has been performed based on the reduced lumped TURBU model, the results in the figure represent the closed-loop system with the detailed multibody TURBU model. Note also that the advanced feedback-feedforward controller achieves improved load reduction over a much wider frequency band than the conventional IPC method, which only leads to improvement at very low frequencies, whereas it actually results in load amplification at frequencies of 1p (here 0.3Hz) and higher in the fixed reference frame (observe the high peak on the top-left plot in Figure 22, which is at about 1p). The performance of the present method at low frequencies can easily be improved by including integral action in the controller. Finally, it needs to be mentioned that the improved high-frequency reduction inevitably requires pitch control activity at these frequencies, which might in practice be undesirable. This can be circumvented by introducing additional penalty on the control signal at high frequencies in the optimal control optimization.

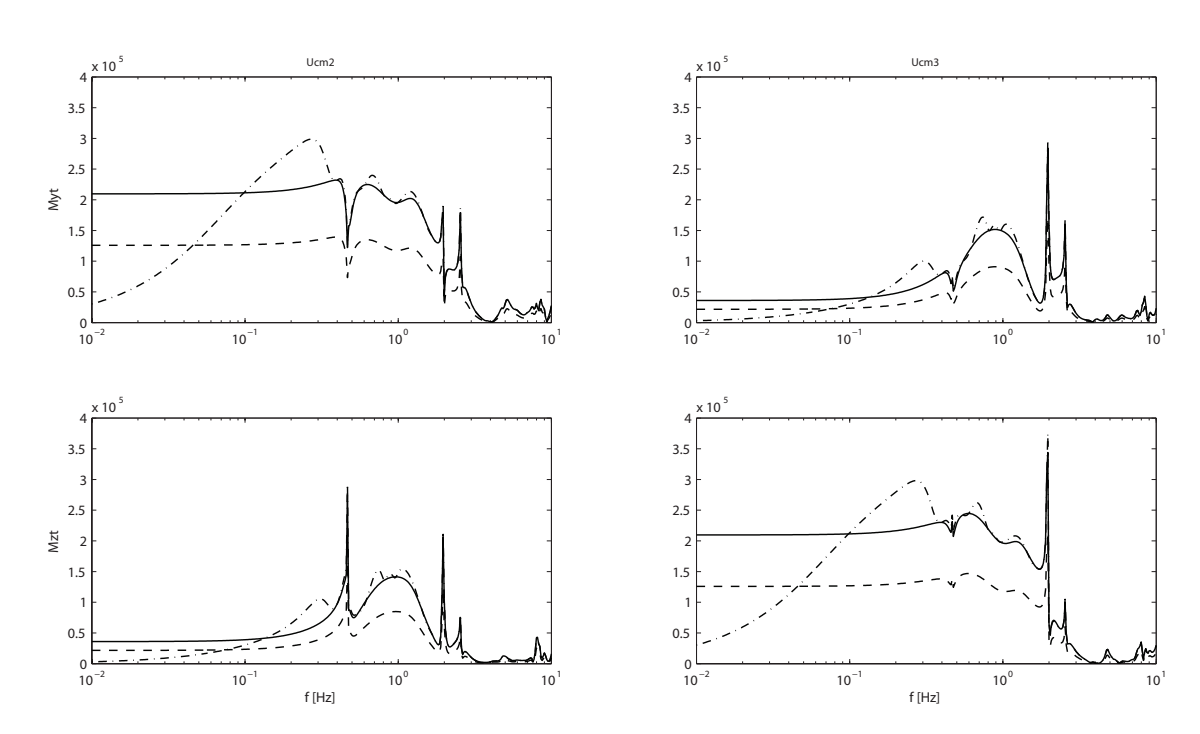


Figure 22 Frequency response plot of tilt moment M_{tilt} (first row) and yaw moment M_{yaw} (second row) due to the multi-blade wind inputs u_2^{cm} (left column) and u_3^{cm} (right column) for the TURBU model with no IPC (solid), conventional IPC (dash-dotted) and new feedback-feedforward IPC (dashed).

3 Constraints handling in IPC

Summary

Bringing modern IPC algorithms into practice necessitates the consideration of the actuator limitations, expressed as position, velocity and acceleration constraints on the blade pitch signals. Due to the intrinsic integral type of the IPC algorithms, anti-windup schemes must be implemented to avoid instability. In this section, such an anti-windup IPC scheme is developed. To this end, the original pitch actuator limits are transformed into constraints on the IPC tilt and yaw-oriented pitch signals. This is performed in such a way that the IPC for blade load reduction uses only the actuation freedom that is not used up by the CPC algorithm, achieving proper operation under the given blade pitch actuator limits.

3.1 Introduction

The pitch actuators in wind turbines have limits, and it is crucial that these limits are properly taken care of in the control algorithm. This is especially important for controllers with integral terms, as is the case with the discussed IPC algorithms above, as otherwise the well-known windup effect can occur, resulting in degraded performance or even instability. In this section, it is shown how anti-windup can be achieved for the IPC algorithm. Implementation of anti-windup scheme for the CPC algorithm is just as important, but less involved and is not reported here.

Since the IPC algorithm is defined in the non-rotating reference frame, the original blade pitch angle, speed and acceleration limits need to be translated to multi-blade coordinates before an anti-windup scheme can be applied. Moreover, in order to make sure that the IPC algorithm does not tamper with the CPC, it should only use the actuation freedom that is not used up by the CPC. In this way, proper simultaneous operation of all control algorithms is achieved, with priority to CPC.

The following positions, speeds and accelerations hard limits are considered for the blade actuators, i = 1, 2, 3,

$$\theta_{min} \leq \theta_i \leq \theta_{max},
\dot{\theta}_{min} \leq \dot{\theta}_i \leq \dot{\theta}_{max},
\ddot{\theta}_{min} \leq \ddot{\theta}_i \leq \ddot{\theta}_{max},$$
(73)

where the minimum and maximum values are assumed given. Part of this total actuation freedom is attributed to the basic CPC algorithm and the rotor balancing IPC (Section ??), and it is assumed that the following limits are met at all time

$$\theta_{min} \leq \theta_{min}^{col} \leq \theta_{col} \leq \theta_{max}^{col} \leq \theta_{max},
\dot{\theta}_{min} < \theta_{min}^{col} \leq \dot{\theta}_{col} \leq \dot{\theta}_{max}^{col} < \dot{\theta}_{max},
\ddot{\theta}_{min} < \ddot{\theta}_{min}^{col} \leq \ddot{\theta}_{col} \leq \ddot{\theta}_{max}^{col} < \ddot{\theta}_{max}.$$
(74)

Notice that the speed and acceleration constraints for the CPC action are chosen strictly inside the actuator limits, hence always leaving some freedom for the IPC controller. For the pitch angle it is not always possible to select $\theta_{min} < \theta_{min}^{col}$ strictly, as would be the case when the lower pitch angle bound θ_{min} coincides with the working position at below-rated conditions.

3.1.1 Multi-blade pitch limits

Without loss of generality, we assume for simplicity of the derivations below that IPC control is limited to 1p load reduction on blades (i.e. no higher harmonics IPC control). The results below can easily be extended to IPC-2p and higher. Defining $\psi_i \doteq \psi_k + \frac{2\pi(i-1)}{3}$ as the azimuth angle of

blade i, remember from Section 1 that the pitch setting angle of blade i has the following form, containing contributions from the collective pitch controller for power/rotor speed regulation and the IPC-1p controller for load reduction

$$\theta_i = \theta_{col} + \sin(\psi_i)\theta_{cm,2} + \cos(\psi_i)\theta_{cm,3}, i = 1, 2, 3.$$

Clearly, the IPC actions $\theta_{cm,2}$ and $\theta_{cm,3}$ have effect on all three blade angles, speeds and accelerations. Still, they should not lead to the original actuator limits (73) getting exceeded. To achieve this, limits on the IPC actions $\theta_{cm,2}$ and $\theta_{cm,3}$ will be derived for which (73) remain valid. It is desirable that these limits do not (explicitly) depend on the rotor azimuth ψ_k . To this end, the remaining freedom in the actuators after the CPC controller will be distributed among the two IPC controls. Define

$$\begin{array}{lcl} \theta^{rest} & \doteq & \max\{0, \min\{\theta_{max} - \theta_{col}, \theta_{col} - \theta_{min}\}\}, \\ \dot{\theta}^{rest} & \doteq & \max\{0, \min\{\dot{\theta}_{max} - \dot{\theta}_{col}, \dot{\theta}_{col} - \dot{\theta}_{min}\}\}, \\ \ddot{\theta}^{rest} & \doteq & \max\{0, \min\{\ddot{\theta}_{max} - \ddot{\theta}_{col}, \ddot{\theta}_{col} - \ddot{\theta}_{min}\}\}, \end{array}$$

where the current collective pitch speed $\dot{\theta}_{col}$ and acceleration $\ddot{\theta}_{col}$ should be substituted by their finite difference approximations.

Denoting

$$J(\psi, \theta_{cm,2}, \theta_{cm,3}) \doteq \sin(\psi)\theta_{cm,2} + \cos(\psi)\theta_{cm,3}$$

the purpose of this section is to derive limits on the IPC angles $\theta_{cm,2}$ and $\theta_{cm,3}$, as well as on their speeds and accelerations, such that for any ψ the following inequalities are satisfied

$$\begin{vmatrix}
J(\psi, \theta_{cm,2}, \theta_{cm,3}) \\
\dot{J}(\psi, \theta_{cm,2}, \theta_{cm,3}) \\
\ddot{J}(\psi, \theta_{cm,2}, \theta_{cm,3})
\end{vmatrix} \le \begin{bmatrix} \theta^{rest} \\ \dot{\theta}^{rest} \\ \ddot{\theta}^{rest} \end{bmatrix}.$$
(75)

To keep the problem tractable, we distribute the available freedom between the two IPC controls. In doing this, however, we do not use a constant factor, but rather look at the "activity" of the two signals. If, for instance, there is large rotor yaw misalignment, this will give raise to a large rotor tilt moment, so that $\theta_{cm,2}$ will need to get larger to compensate this, while at the same time the yaw-oriented component $\theta_{cm,3}$ might be negligible. Hence, we will distribute θ^{rest} (and, of course, $\dot{\theta}^{rest}$ and $\ddot{\theta}^{rest}$) by looking at the values of $\theta^{unlim}_{cm,2}$ and $\theta^{unlim}_{cm,3}$, required by the IPC controller before applying any limits on them, so that the signal that is larger in absolute value gets more freedom than the "less active" signal. This idea is used in the following to derive the limits on the IPC signals $\theta_{cm,j}$, $\dot{\theta}_{cm,j}$, $\dot{\theta}_{cm,j}$, $\dot{\theta}_{cm,j}$, $\dot{\eta}_{cm,j}$,

3.1.1.1 Position limit: $J(\psi, \theta_{cm,2}, \theta_{cm,3}) \leq \theta^{rest}$

To begin with, consider the first constraint in (75), and suppose that $\alpha_2 > 0$ and $\alpha_3 > 0$ are two given scalars, such that

$$|\theta_{cm,j}| \le \alpha_j \theta^{rest}, \ j = \{2, 3\}. \tag{76}$$

Then it holds that,

$$[\max_{\psi} J(\psi, \theta_{cm,2}, \theta_{cm,3}) \equiv \sqrt{(\theta_{cm,2}^2 + \theta_{cm,3}^2)}]$$

$$\leq \theta^{rest} \sqrt{\alpha_2^2 + \alpha_3^2}.$$

Since we need to make sure that $J(\psi, \theta_{cm,2}, \theta_{cm,3}) \leq \theta^{rest}$ for all ψ , the scalars α_2 and α_3 should be such that $\alpha_2^2 + \alpha_3^2 = 1$. Moreover, from the discussion above, we would like that the ratio

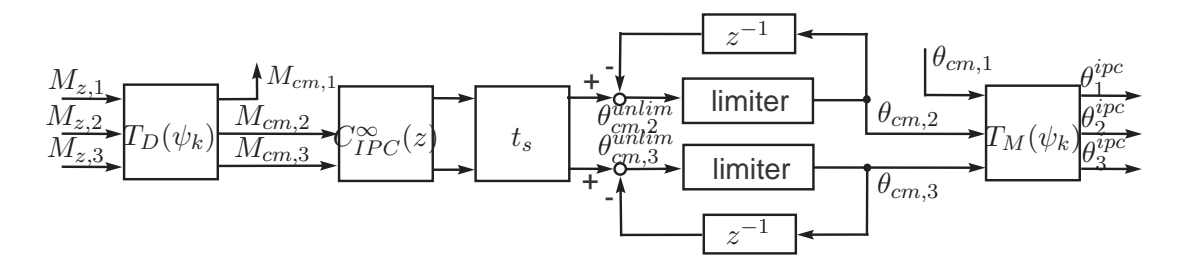


Figure 23 IPC anti-windup scheme

between the limits for $\theta_{cm,2}$ and $\theta_{cm,3}$ is proportional to the ratio between $|\theta_{cm,2}^{unlim}|$ and $|\theta_{cm,3}^{unlim}|$ (i.e. the ratio between the IPC controller outputs before applying any limits). This implies that

$$\frac{\alpha_2}{\alpha_3} = \frac{|\theta_{cm,2}^{unlim}|}{|\theta_{cm,3}^{unlim}|}.$$

Solving this equality together with $\alpha_2^2 + \alpha_3^2 = 1$ gives

$$\alpha_j \doteq \frac{\left|\theta_{cm,j}^{unlim}\right|}{\sqrt{(\theta_{cm,2}^{unlim})^2 + (\theta_{cm,3}^{unlim})^2}}, \ j = \{2,3\},\tag{77}$$

which, with (76), ensures the first inequality in (75).

3.1.1.2 Speed limit: $\dot{J}(\psi, \theta_{cm.2}, \theta_{cm.3}) \leq \dot{\theta}^{rest}$

Consider the speed constraint in (75), written as

$$\dot{J}(\psi, \theta_{cm,2}, \theta_{cm,3}) = \dot{J}_2(\psi, \theta_{cm,2}) + \dot{J}_3(\psi, \theta_{cm,3}),
\dot{J}_2(\psi, \theta_{cm,2}) = \Omega \cos(\psi) \theta_{cm,2} + \sin(\psi) \dot{\theta}_{cm,2},
\dot{J}_3(\psi, \theta_{cm,3}) = -\Omega \sin(\psi) \theta_{cm,3} + \cos(\psi) \dot{\theta}_{cm,3}.$$

In this case, similarly to what we did above for the position limit, we distribute $\dot{\theta}^{rest}$ between $\dot{J}_2(\psi, \theta_{cm,2})$ and $\dot{J}_3(\psi, \theta_{cm,3})$ by using β_2 and β_3 , such that

$$|\dot{J}_j(\psi, \theta_{cm,j})| \le \beta_j \dot{\theta}^{rest}, \ j = \{2, 3\},\tag{78}$$

implying

$$\max_{\psi} \dot{J}(\psi, \theta_{cm,2}, \theta_{cm,3}) = (\beta_2 + \beta_3) \dot{\theta}^{rest},$$

so $\beta_2 + \beta_3 = 1$ must hold. This, together with

$$\frac{\beta_2}{\beta_3} = \frac{|\theta_{cm,2}^{unlim}|}{|\theta_{cm,3}^{unlim}|},$$

gives

$$\beta_{j} \doteq \frac{\left|\theta_{cm,j}^{unlim}\right|}{\left|\theta_{cm,2}^{unlim}\right| + \left|\theta_{cm,3}^{unlim}\right|}, \ j = \{2, 3\}.$$

$$(79)$$

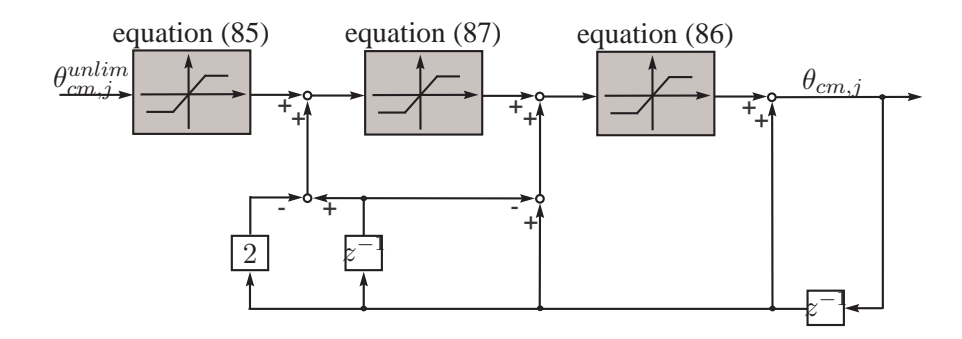


Figure 24 IPC pitch limiter realization

It remains to rewrite (78) in terms of $\theta_{cm,j}$ and $\dot{\theta}_{cm,j}$. Here, there is another degree of freedom in the choice of distributing $\beta_j \dot{\theta}^{rest}$ over the position $\theta_{cm,j}$ and speed $\dot{\theta}_{cm,j}$. For that purpose, we choose factors $\gamma_{pos} > 0$ and $\gamma_{spd} > 0$ such that for some $\dot{\theta}_j^{rest} > 0$ (derived below) we require that

$$|\theta_{cm,j}| \le \gamma_{pos} \dot{\theta}_{j}^{rest}, |\dot{\theta}_{cm,j}| \le \gamma_{spd} \dot{\theta}_{j}^{rest}.$$
(80)

To derive an expression for $\dot{\theta}_i^{rest}$, note that

$$\max_{\psi} \dot{J}_{j}(\psi, \theta_{cm,j}) = \sqrt{(\Omega \theta_{cm,j})^{2} + \dot{\theta}_{cm,j}^{2}} \\ \leq \dot{\theta}_{j}^{rest} \sqrt{\gamma_{pos}^{2} \Omega^{2} + \gamma_{spd}^{2}}.$$

Hence, inequality (78) will be satisfied for

$$\dot{\theta}_{j}^{rest} = \frac{\beta_{j}\dot{\theta}^{rest}}{\sqrt{\gamma_{pos}^{2}\Omega^{2} + \gamma_{spd}^{2}}},\tag{81}$$

with β_i defined in (79).

3.1.1.3 Acceleration limit: $\ddot{J}(\psi, \theta_{cm,2}, \theta_{cm,3}) \leq \ddot{\theta}^{rest}$

For the acceleration limit in (75), we can write

$$\begin{split} \ddot{J}(\psi,\theta_{cm,2},\theta_{cm,3}) &= \ddot{J}_{2}(\psi,\theta_{cm,2}) + \ddot{J}_{3}(\psi,\theta_{cm,3}), \\ \ddot{J}_{2}(\psi,\theta_{cm,2}) &\doteq (\ddot{\theta}_{cm,2} - \Omega^{2}\theta_{cm,2})\sin(\psi) \\ &+ (2\Omega\dot{\theta}_{cm,2} + \dot{\Omega}\theta_{cm,2})\cos(\psi), \\ \ddot{J}_{3}(\psi,\theta_{cm,3}) &\doteq (\ddot{\theta}_{cm,3} - \Omega^{2}\theta_{cm,3})\cos(\psi) \\ &- (2\Omega\dot{\theta}_{cm,3} + \dot{\Omega}\theta_{cm,3})\sin(\psi). \end{split}$$

Similarly to the speed limit case, we distribute $\ddot{\theta}^{rest}$ between $\ddot{J}_2(\psi, \theta_{cm,2})$ and $\ddot{J}_3(\psi, \theta_{cm,3})$ by using the same scalars β_2 and β_3 as in (79)

$$|\ddot{J}_j(\psi, \theta_{cm,j})| \le \beta_j \ddot{\theta}^{rest}, \ j = \{2, 3\}, \tag{82}$$

since then we get $\max_{\psi} \ddot{J}(\psi, \theta_{cm,2}, \theta_{cm,3}) = \ddot{\theta}^{rest}$, as required in (75). Now we have even more freedom than in the speed limit case above, since we have to distribute $\beta_j \ddot{\theta}^{rest}$ between

three components: the position $\theta_{cm,j}$, the speed $\dot{\theta}_{cm,j}$ and the acceleration $\ddot{\theta}_{cm,j}$. To do this, we choose, in addition to the already chosen factors γ_{pos} and γ_{spd} , a third factor $\gamma_{acc} > 0$, and we impose the following constraints for some $\ddot{\theta}_{i}^{rest} > 0$ that is yet to be derived

$$|\theta_{cm,j}| \leq \gamma_{pos} \ddot{\theta}_{j}^{rest}, |\dot{\theta}_{cm,j}| \leq \gamma_{spd} \dot{\theta}_{j}^{rest}, |\ddot{\theta}_{cm,j}| \leq \gamma_{acc} \ddot{\theta}_{j}^{rest}.$$
(83)

Under these constraints we have

$$\max_{\psi} \ddot{J}_{j}(\psi, \theta_{cm,j})$$

$$= \sqrt{(\ddot{\theta}_{cm,j} - \Omega^{2}\theta_{cm,j})^{2} + (2\Omega\dot{\theta}_{cm,j} + \dot{\Omega}\theta_{cm,j})^{2}}$$

$$\leq \ddot{\theta}_{j}^{rest} \sqrt{(\gamma_{acc} + \Omega^{2}\gamma_{pos})^{2} + (2\Omega\gamma_{spd} + \dot{\Omega}\gamma_{pos})^{2}}$$

Inequality (82) will then be satisfied under constraints (83) with

$$\ddot{\theta}_{j}^{rest} = \frac{\beta_{j}\ddot{\theta}^{rest}}{\sqrt{(\gamma_{acc} + \Omega^{2}\gamma_{pos})^{2} + (2\Omega\gamma_{spd} + \dot{\Omega}\gamma_{pos})^{2}}}$$
(84)

and β_i defined in (79).

3.1.2 Anti-windup scheme

To summarize, the final limits on the IPC actions in multi-blades coordinates are obtained by combining (76),(80),(83) together with the scalings (77),(79),(81),(84). In order to describe how the anti-windup scheme should finally be implemented into the wind turbine controller, we assume below that the IPC controller is discretized with sampling period of t_s seconds, and will approximate the speeds and accelerations with finite differences. At time instant k, the following constraints should then be active

$$|\theta_{cm,j}(k)| \le \min\left\{\alpha_j \theta^{rest}, \gamma_{pos} \dot{\theta}_j^{rest}, \gamma_{pos} \ddot{\theta}_j^{rest}\right\}$$
(85)

$$|\theta_{cm,j}(k) - \theta_{cm,j}(k-1)|$$

$$\leq \min \left\{ t_s \gamma_{spd} \dot{\theta}_j^{rest}, t_s \gamma_{spd} \ddot{\theta}_j^{rest} \right\}$$
(86)

$$|\theta_{cm,j}(k) - 2\theta_{cm,j}(k-1) + \theta_{cm,j}(k-2)|$$

$$\leq t_s^2 \gamma_{acc} \ddot{\theta}_j^{rest}$$
(87)

Notice, that a typical IPC controller consists of two (usually) independent channels, each containing an integrator and a filter (see Section 1). Hence, an IPC controller, discretized with sampling period t_s , has the same general representation

$$C_{IPC}(z) = \begin{bmatrix} \frac{t_s}{1-z^{-1}} & \\ & \frac{t_s}{1-z^{-1}} \end{bmatrix} C_{IPC}^{\infty}(z).$$

As discussed in [28], in order to achieve an anti-windup mechanism one needs to make sure that the integrator states are driven by the actual (constrained) inputs $\theta_{cm,2}$ and $\theta_{cm,3}$. This can be achieved easily by implementing the integrators by using one sample delay feedback around the limiters, as shown in Figure 23. The two limiters, having the same structure, but realizing the bounds in (85)-(87) for $j = \{2, 3\}$, are shown in Figure 24.

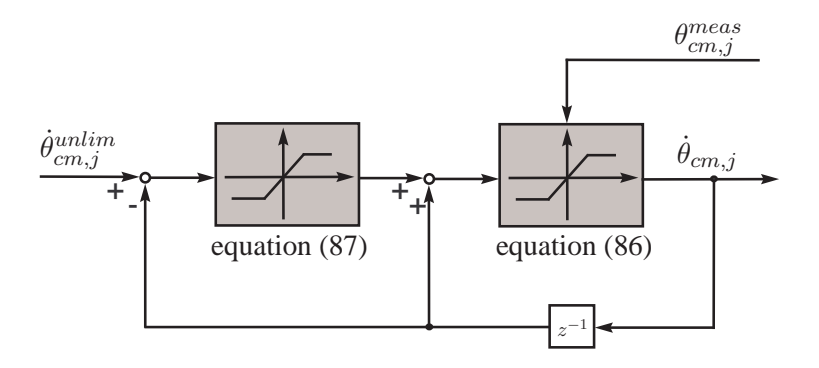


Figure 25 Limiter realization under speed control

3.1.3 Limits under blade speed control

Above, the discussion was focused on the blade pitch $angles\ \theta_i$ being the control signals. In practice, however, it is sometimes the case that the pitch $speeds\ \dot{\theta}_i$ are the control variables, which leads to controller structures that contain no integrators. Indeed, an I-compensator for IPC will take the form of a P-compensator when the pitch speed is used. For P and PD controllers, windup is not an issue, so the anti-windup scheme, presented in section 3.1.2, will not be an issue. In this case, the limiter block can be positioned simply after the controller. However, the limiter will have a different structure than the one in Figure 24. The reason for this is that the controller does not output a position signal. In order to incorporate position constraints, actual blade angle measurements $\theta_i^{meas}(k)$ are necessary, which we again transform to multiblade coordinates $\theta_{cm,j}^{meas}$ using the Coleman demodulation matrix \mathbf{P}^{-1} , defined in (12). The corresponding limiter scheme is depicted on Figure 25.

3.2 Nonlinear simulation study

In this section, the methods, discussed above are demonstrated via realistic nonlinear wind turbine simulations. The simulation model is briefly described in the next subsection, after which the results of different simulations are presented, aiming to illustrate the influence of IPC on the blade loads as well as the effect of the proposed IPC anti-windup scheme.

3.2.1 Simulation model

The nonlinear wind turbine simulation model, used for generating the results in this section, consists of the following components:

- 156-th order linearized structural dynamics model (SDM), obtained using the software Turbu [76]. A multi-body approach has been used to obtain this detailed SDM. The multi-body model has 14 elements per blade and 15 elements for the tower, with each element having 5 degrees of freedom. There are 6 degrees of freedom in the rotor shaft, and 12 for the pitch-servo actuation system. A linearization is computed for an aerodynamic equilibrium state at a mean wind speed of 15 m/s, rotor speed of approx. 17, 7 rpm and blade pitch angle of 7, 24 deg.
- nonlinear aerodynamic conversion module (ADM), based on blade element momentum (BEM) theory, including dynamic wake effects, the effects of oblique inflow on the axial induction speed, and angle of attack correction due to rotor coning. The ADM computes

parameter	θ_{min}	θ_{max}	$ \dot{ heta}_{min} $	$\dot{\theta}_{max}$	$\ddot{ heta}_{min}$	$\ddot{\theta}_{max}$	θ_{min}^{col}	θ_{max}^{col}	$\dot{ heta}_{min}^{col}$	$\dot{ heta}_{max}^{col}$	$\ddot{\theta}_{min}^{col}$	$ \ddot{ heta}_{max}^{col} $	$ \gamma_{pos} $	γ_{spd}	γ_{acc}
value	0	85	-8	8	-15	15	0	85	-4	4	-5	5	4	1	8
dimension	0	0	o/s	$^{o}/s$	$ ^o/s^2$	$ ^{o}/s^{2} $	0	0	$^{o}/s$	$^{o}/s$	$ ^o/s^2 $	$ ^o/s^2 $	-	-	-

Table 3 Numerical values of the algorithm parameters

forces and torques per blade elements, which are used to load the SDM. See [43] for details on the ADM.

- basic CPC controller, regulating the filtered generator speed at its rated level (when operating at above-rated conditions). It consisting of a PI-controller in series with low-pass filter at the 3p blade frequency, notch filter at the first tower sidewards frequency, and notch filter at the first collective lead-lag frequency. An anti-windup scheme is implemented for this CPC controller to guarantee that constraints (74) are satisfied.
- nonlinear generator torque controller based on static optimal-λ QN-curve at below rated conditions and *constant power* production above-rated, operating on the filtered generator speed signal (same three filters used as in pitch controller).
- IPC: the advanced \mathcal{H}_{∞} controller does not perform significantly better than the conventional I-compensator, the later is used in the simulations reported here. The gain scheduling is done based on support points corresponding to mean wind speeds, equally spaced over intervals of 1 m/s.
- realistic blade effective wind speed signals are generated based on the helix approximation concept, as proposed in [43, App. C], including both deterministic terms for wind shear, tower shadow, tilt and yaw misalignment, wind gust, and a stochastic term for blade-effective turbulence. The mean wind speed, used in the simulations, is 20 m/s, reaching the rotor at oblique inflow angle of 10 degrees.

To evaluate the performance of the proposed advanced IPC scheme for 1p blade load reduction, three simulations have been performed:

- Case 1: without IPC control.
- Case 2: with IPC for blade load reduction, no pitch limits,
- Case 3: with IPC for blade load reduction, pitch limits included.

The resulting blade 1 flapwise root bending moment spectrum for the three cases are plotted in Figure 26. Clearly, a significant reduction of blade loads is achieved around the 1p frequency, both without and with pitch limits (anti-windup), although the later case gives slightly less reduction, as expected. Figure 27 shows the pitch angle, speed and acceleration under Case 3, together with their limits, given in Table 3.

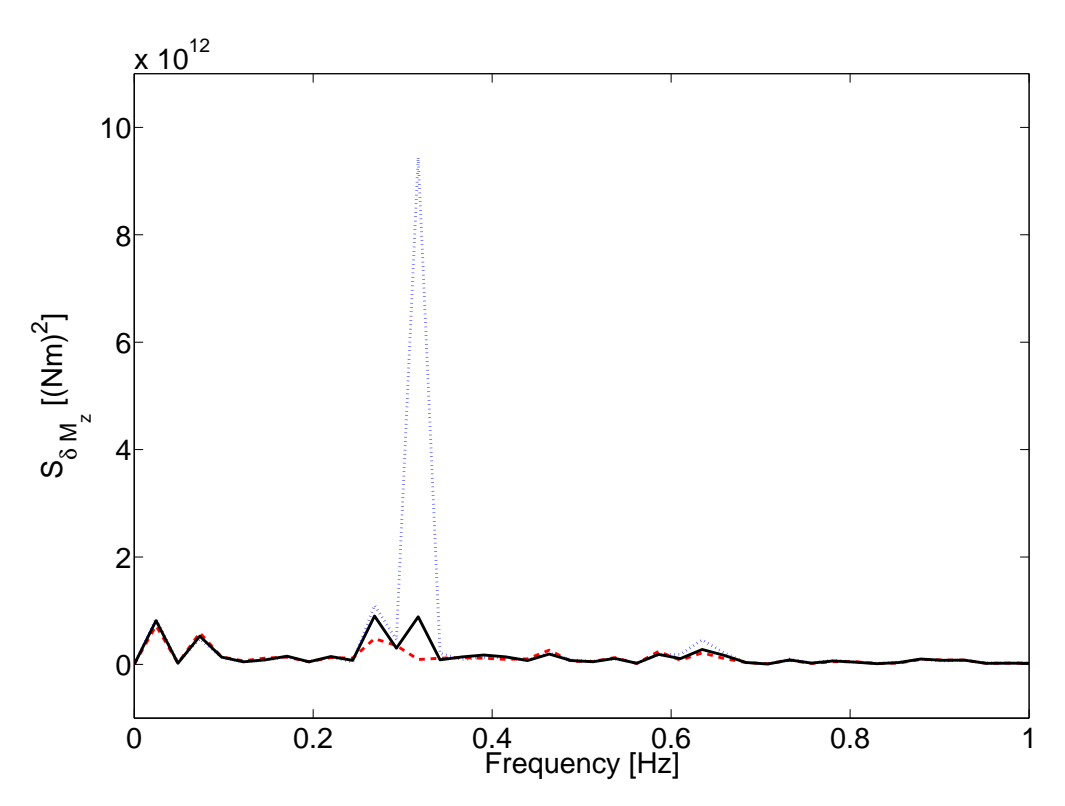


Figure 26 Blade 1 flapwise moment spectrum for Case 1 (dotted), Case 2 (dashed), Case 3 (solid)

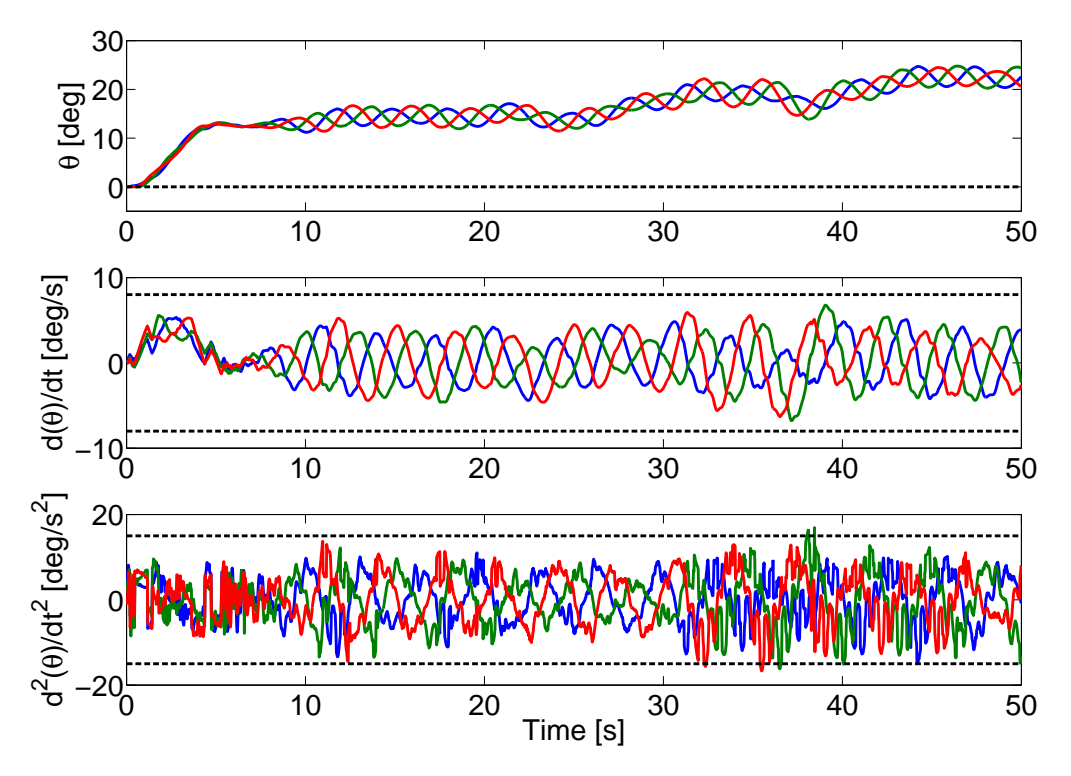


Figure 27 Pitch angle, speed and acceleration reference anti-windup IPC for blade load reduction

4 Stability analysis using Floquet theory

Summary

In Section 1 it is shown how modulation/demodulation matrices can utilized to target specific load reductions at frequencies that are a multiple of the rotational frequency of the rotor (the 2p, 3p, and higher loads). The IPC-1p control, aiming 1p blade load reduction, results in a linear time-invariant (LTI) model in fixed-frame coordinates, the stability of which can be analyzed using standard methods. However, 2p modulation, and higher, no longer results in LTI models, but in linear models with periodic coefficients. The stability of such periodic models can be examined using Floquet theory.

4.1 Floquet stability analysis

This appendix describes how the stability of controller with time-varying constants should be analysed. This analysis will be of particular use for windturbines with controllers that target specific np modes.

The analysis is based on Floquet-Lyapunov stability theory as described in [35].

4.1.1 Time-invariant vs periodic systems

Most control engineers will be familiar with a statespace descriptions of a Linear Time Invariant (LTI) system:

$$\dot{\mathbf{x}} = \mathbf{A}\mathbf{x} + \mathbf{B}\mathbf{u} \tag{88}$$

This system is stable of the real part of all the eigenvalues of A is negative (i.e. all the eigenvalues are in the left-hand part of the complex plane.

We know that for a wind turbine, there are at least some variables that depend on the position of the rotor. Considering that the position of the wind turbine is part of the state vector \mathbf{x} :

$$\dot{\mathbf{x}} = \mathbf{A}(\mathbf{x})\mathbf{x} + \mathbf{B}\mathbf{u} \tag{89}$$

To be able to actually work a system like this, we need to linearize this matrix around a operating point \mathbf{x}_0 . Substituting $\mathbf{x} = \mathbf{x}_0 + \Delta \mathbf{x}$:

$$(\mathbf{x}_0 + \Delta \mathbf{x}) = \mathbf{A}(\mathbf{x}_0 + \Delta \mathbf{x})(\mathbf{x}_0 + \Delta \mathbf{x}) + \mathbf{B}\mathbf{u}$$
(90)

$$\Delta \dot{\mathbf{x}} = \mathbf{A}(\mathbf{x}_0) \Delta \mathbf{x} + \mathbf{B} \mathbf{u} \tag{91}$$

A constant rotor speed should results in changes that depend (in first order approximation) on that speed to become periodic, so the above equation can also be written as:

$$\Delta \dot{\mathbf{x}} = \mathbf{A}(t)\Delta \mathbf{x} + \mathbf{B}\mathbf{u} \tag{92}$$

or even:

$$\Delta \dot{\mathbf{x}} = \mathbf{P}(t)\mathbf{A}_c \Delta \mathbf{x} + \mathbf{B}\mathbf{u} \tag{93}$$

To illustrate the problem, a simple model is used as an example.

Example 4.1 (A simple example system). Assuming a simple model: a system of two coupled mass-spring-damper (MSD) systems. The equation of motion of one MSD, excluding external

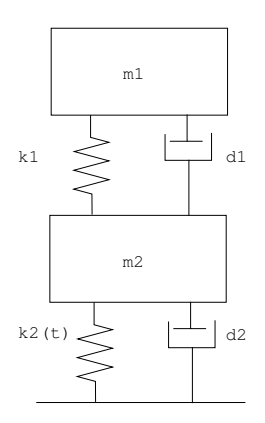


Figure 28 Two coupled mass-spring dampers

forces is:

$$\dot{\mathbf{x}} = \begin{bmatrix} 0 & 1 \\ -k_1/m_1 & -d_1/m_1 \end{bmatrix} \mathbf{x} \tag{94}$$

Which can also be written as:

$$\dot{\mathbf{x}} = \begin{bmatrix} 0 & 1 \\ -\omega_1^2 & -\zeta_1 \omega_1 \end{bmatrix} \mathbf{x} \tag{95}$$

Coupled the system becomes:

$$\dot{\mathbf{x}} = \begin{bmatrix} 0 & 1 & 0 & 0 \\ -\omega_1^2 & -2\zeta_1\omega_1 & \omega_1^2 & 2\zeta_1\omega_1 \\ 0 & 0 & 0 & 1 \\ k_1/m_2 & d_1/m_2 & -\omega_2^2 - k_1/m_2 & -2\zeta_2\omega_1 - d_1/m_2 \end{bmatrix} \mathbf{x}$$
(96)

Now, we will assume that one of the stiffnesses is time-varying, in a very simple sinusoid way:

$$\dot{\mathbf{x}} = \begin{bmatrix} 0 & 1 & 0 & 0 \\ -\omega_1^2 & -2\zeta_1\omega_1 & \omega_1^2 & 2\zeta_1\omega_1 \\ 0 & 0 & 0 & 1 \\ k_1/m_2 & d_1/m_2 & -(1+a\sin(t/b))\omega_2^2 - k_1/m_2 & -2\zeta_2\omega_1 - d_1/m_2 \end{bmatrix} \mathbf{x}$$
(97)

Note that this the time-variation does not have to be sinusoid, it can be any (finite) periodic variation.

Now we have a simple example model, we will continue with the theory.

4.1.2 Applying Floquet theory

Floquet theory is concerned with a linear, but time-varying dynamic system, described by:

$$\dot{\mathbf{x}} = \mathbf{A}(t)\mathbf{x} + \mathbf{B}(t)\mathbf{u} \tag{98}$$

The theory is based around the special case where $\mathbf{A}(t+T) = \mathbf{A}(T)$, i.e. $\mathbf{A}(t)$ varies periodically. The general solution of the above equation must be of the form:

$$\mathbf{x}(t) = \mathbf{\Phi}(t, t_0)\mathbf{x}(t_0) \tag{99}$$

This is because the system is linear and the solution at a time, t, must thus be a linear combination of the inputs at time, t_0 . The matrix $\Phi(t, t_0)$ is called the state transition matrix.

The Floquet theorem states that the state transition matrix of a system with a periodic variable must be of the form:

$$\mathbf{\Phi}(t, t_0) = \mathbf{P}(t)e^{\beta t} \tag{100}$$

where β is a constant matrix and $\mathbf{P}(t)$ is a periodic function. That means that P(t) = P(t+T). Combining the fact that $\mathbf{P}(t)$ is periodic and equations (100) and (99) results in:

$$\mathbf{x}(0) = \mathbf{\Phi}(0,0)\mathbf{x}(0)$$

$$= \mathbf{P}(0)e^{\beta 0}\mathbf{x}(0)$$

$$= \mathbf{P}(0)\mathbf{x}(0)$$
(101)

for any $\mathbf{x}(0)$, thus:

$$\mathbf{P}(0) = \mathbf{P}(T) = I \tag{102}$$

This covenient equality will be used later on.

Now substituting equation (100) back into the original differential equation, equation (98), gives us:

$$\dot{\mathbf{P}} = \mathbf{A}\mathbf{P} - \mathbf{P}\boldsymbol{\beta} \tag{103}$$

This looks like we just hit a dead end, because this is still a differential equation with periodicly varying coefficients. Indeed, this equation can only be solved directly in special cases.

Lets have another look at equation (100). The transition matrix describes how the system behaves from an initial input. We see that the response at time t + T is $e^{\beta T}$ times the response at time t. This means that stability of the system is defined by this matrix β . But we just saw that is very hard to find this matrix.

Lucky for us, we don't need to find β to show that the system is stable. We only need to show that the real part of its eigenvalues is equal to or smaller than zero (depending on what stability criterion you use).

To do this, we need numerical approximations to make the stability analysis work. In particular, we need to calculate $e^{\beta T}$ by numerically³ integrating $\dot{\mathbf{x}}_a = \mathbf{A}\mathbf{x}_a$ from 0 to T, with $\mathbf{x}_a(t_0) = I$: ⁴

$$\alpha = e^{\beta T} = \int_0^T \dot{\mathbf{x}}_a \, \mathrm{d}t = \int_0^T \mathbf{A} \mathbf{x}_a \, \mathrm{d}t$$
 (104)

A simple numerical way to calculate α is to set all the initial states of the system to zero and then sequentially set the next initial state to 1 and simulate the system over one period T and add the values of the states at the end of the period to one big matrix:

- Simulate equation (98) from an initial state $\mathbf{x}_{01} = [1 \quad 0 \quad 0 \quad \dots]^T$ during one period T, record the endstates \mathbf{x}_{T1}
- then simulate from an intitial state $\mathbf{x}_{02} = [0 \ 1 \ 0 \ \dots]^T$ during one period T and record \mathbf{x}_{T2} , etc ...
- Now assemble α :

$$\alpha = \begin{bmatrix} \mathbf{x}_{T1} & \mathbf{x}_{T2} & \mathbf{x}_{T3} & \dots \end{bmatrix} \tag{105}$$

 $^{^3}$ That we need to do this numerically is obvious, otherwise we would already have the solution and thus β

⁴Note that $\mathbf{x}_a(t_0)$ is a matrix rather than a vector. The response of the system at time T to any initial state $\mathbf{x}(t_0)$ can now be calculated by simply multiplying $\boldsymbol{\alpha}$ by $\mathbf{x}(t_0)$. It is a linear system after all

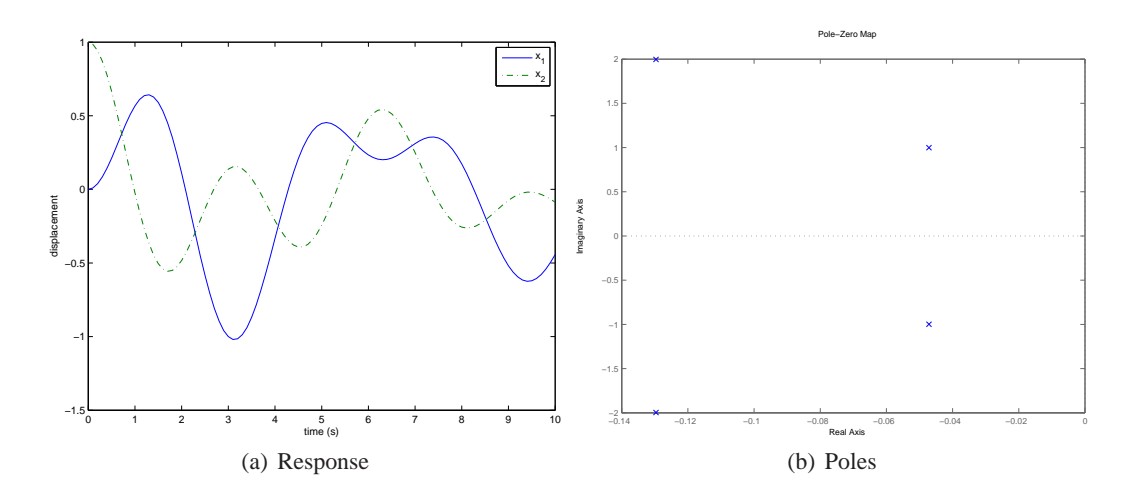


Figure 29 Example system reponse, no time variance

The matrix thus obtained satisfies equation (104).

Note that, because of equations (100) and (102) the solution of the system at times a multiple of the period T can thus be written as:

$$\mathbf{x}(nT) = \boldsymbol{\alpha}^n \mathbf{x}_0 \tag{106}$$

This shows a seeming similarity to discrete-time state-space systems.

One can relate the roots λ of β to the roots θ of α according to:

$$\lambda = 1/T \ln \theta \tag{107}$$

If these roots are in the left-half of the complex plane, the system will be stable. However, these eigenvalues are 'mirrored' in the frequency domain to reappear at frequencies $\frac{2(n-1)\pi}{T}$ with $n=1,2,3,\ldots$ above/below the original frequency. The poles can also move along those mirror frequencies, as continuous poles would do along the real axis.

Example 4.2 (Variation in amplitude). To see how time-dependence can influence the response of a system, we will simulate the response of the simple example system of example 4.1, starting each time with the displacement of the second mass set to 1.

Figure 29(a) shows the response for the case where the amplitude of the periodic variable is 0. The response seems damped and stable. The poleplot confirms this.

Now lets have a look for when the periodic variable is not 0. Figures 30(a) to 30(c) show the response for 3 different amplitudes of the periodic variable. The last one is clearly unstable, but with the other two it is more difficult to see. Figure 30(d) shows the poles of the system for different amplitudes of the periodic variable, as calculated with the Floquet theory. The three poles in the right-half-plane occur for gains of 1.6, 1.8 and 2.0. So despite the fact that figure 30(b) seems to be stable, Floquet predicts that the system is, in fact, unstable.

If we continue the simulation with the gains 1.4 and 1.8 we can see that they are, respectively, stable and unstable (figure 31(a) and 31(b))

One important thing to note is the fact the poles of the system calculated with Floquet do not match the poles of the LTI system even when the amplitude is zero. The poles and corresponding modeshapes calculated with Floquet behave differently than those of continuous or disctrete LTI systems.

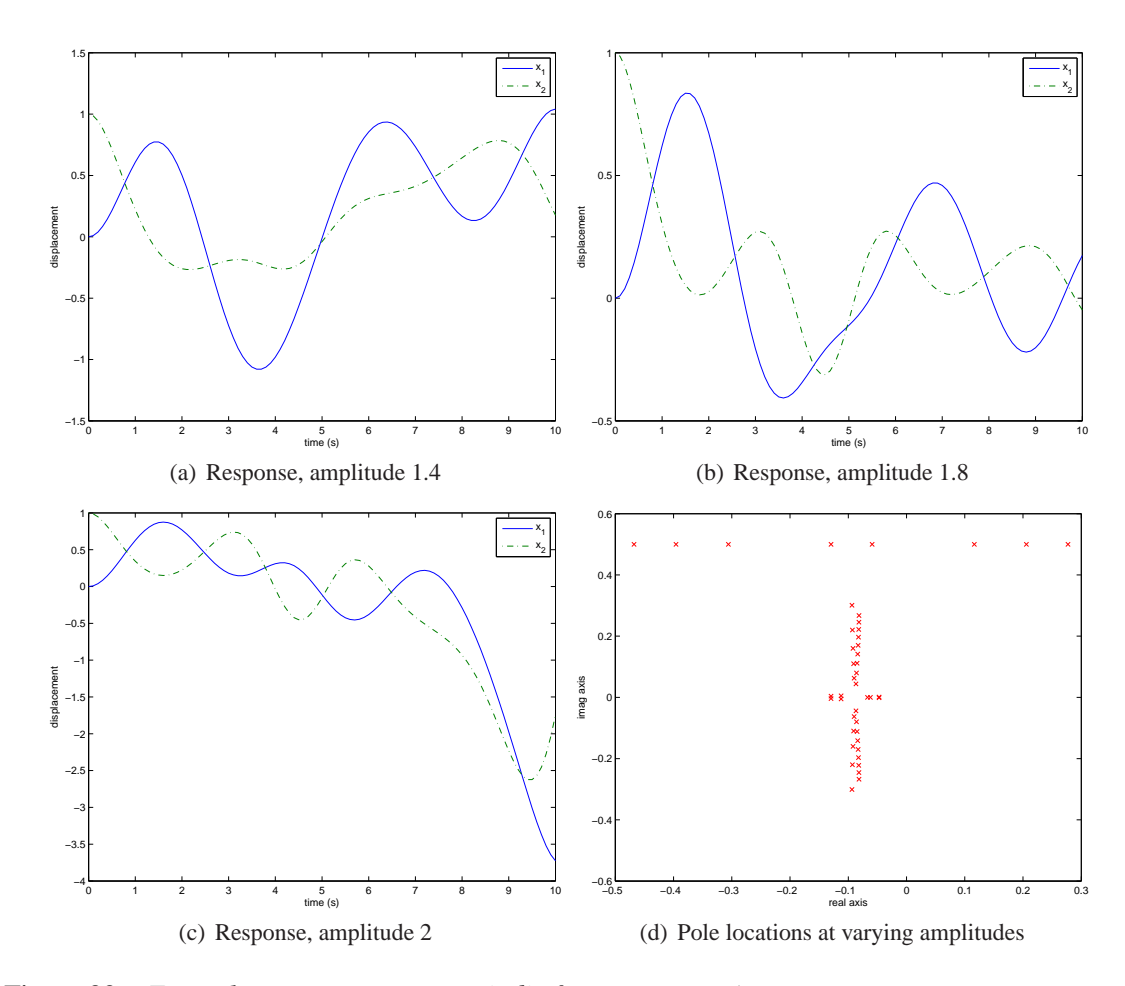


Figure 30 Example system reponse, periodic frequency $\omega = 1$

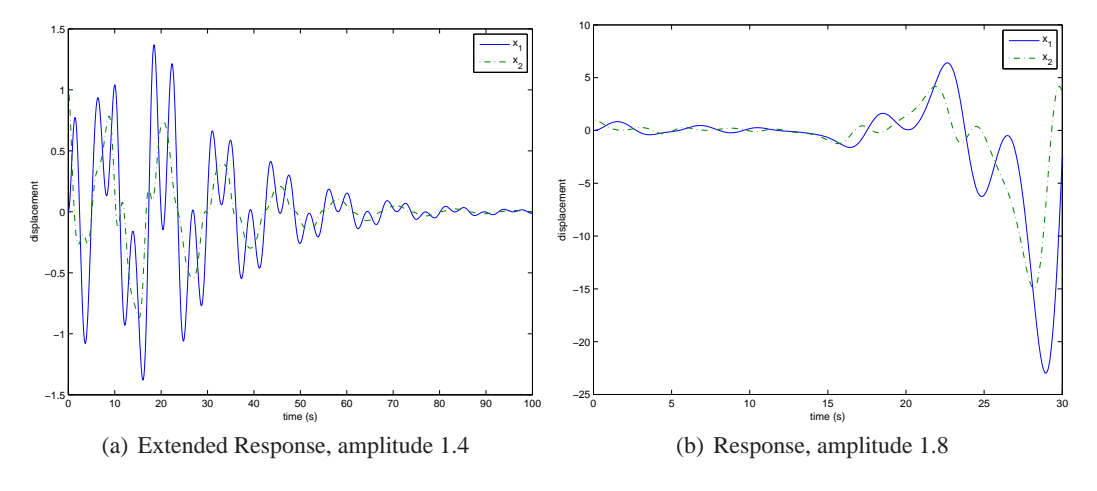


Figure 31 Example system reponse, periodic frequency $\omega = 1$

In comparison to a continuous time system, the poles in the plot in figure 31(a) move in a very unusual way whenthe amplitude of the periodic variable is increased. We can see that the pole plot becomes asymetric around the real axis and that the poles can move in the direction of the real axis once they reach a frequency $\omega/2\pi$. Once a pole reaches this frequency, it can quickly become unstable.

The Floquet system also behaves unlike discrete time-systems with which equation (106) implied

similarity. In discrete time-system, the poles indicate whether the system expands or contracts from time-step to the next, depending on whether the absolute value of the pole is larger or smaller than one. Poles that have a magnitude close to one are usually the biggest threat to stability. If one plotted the values θ rather than the values of λ , the poles on or near the real axis are most likely to become a problem, regardless of what their initial absolute value was. One could well see little movement of the poles, until, near instability, a pole will move quickly along the real axis to outside the unit-circle, i.e. almost jump, from 0 to instability.

Thus Floquet modeshapes should not be thought of in the same way as the modeshapes calculated for a structure.

In a structure oscillating in a modeshape at its corresponding eigenfrequency, the motions of the structure occur at the same frequency and remain in same phase.

For a Floquet modeshape, the 'modeshape' is rather a configuration of initial states, that after a period T happens to be a (complex) scaled version of itself, i.e.:

$$\mathbf{x}(t+T) = \alpha \mathbf{x}(t) = c\mathbf{x}(t) \tag{108}$$

The motions of the system in between these two points in time can not be calculated from α , but would need to be calculated from both P(t) (the periodic matrix) and α .

The above would also imply that the phase of the motions of the system is very important to the calculation of the modes. Thus one can also predict that the system is likely to be sensitive to changes in the frequency of the periodic variable.

Example 4.3 (Frequency variations). We have seen what impact amplitude variations have on the stability of a system with a periodic system. Now would also be a good time to have a look at how the stability of the system is influenced by changes in the frequency of the periodic variable.

Figure 32 shows how the poles move as function of gain for varying frequencies. It shows that stability can be heavily influenced by the period of the periodic variable. Depending on the frequency the system can become unstable at an amplitude between 1.0 and 1.2 or between 1.8 and 2.0.

4.1.3 Modal analysis with Floquet

The previous section have showed that using simulation, we can calculate if a system is stable or not. However, the eigenvectors calculated with Floquet are not directly insightful as they only show which combination of states achieve a scaled value after one period T. It would be useful to know how the system behaves withing a period T, so it can be established what gives rise to this instability. This means we want to calculate P(t).

To calculate what happens within a period, some further number crunching is needed. First, a small recap of what we already know, regarding P(t):

• The solution of a linear system with a time varying constant that varies with a period T, is given by:

$$\Phi(t, t_0) = \mathbf{P}(t)e^{\beta t}$$

where $\mathbf{P}(t)$ is a periodical, time varying matrix and the matrix $\boldsymbol{\beta}$ is time-invariant. Furthermore:

$$\mathbf{P}(0) = \mathbf{P}(T) = I$$

• The eigenvalues of the matrix β can be found by calculating the response of the system from a series of different initial states over a period T and they dictate the stability of the system. The eigenvectors of β do not imply that states move in phase during the period T,

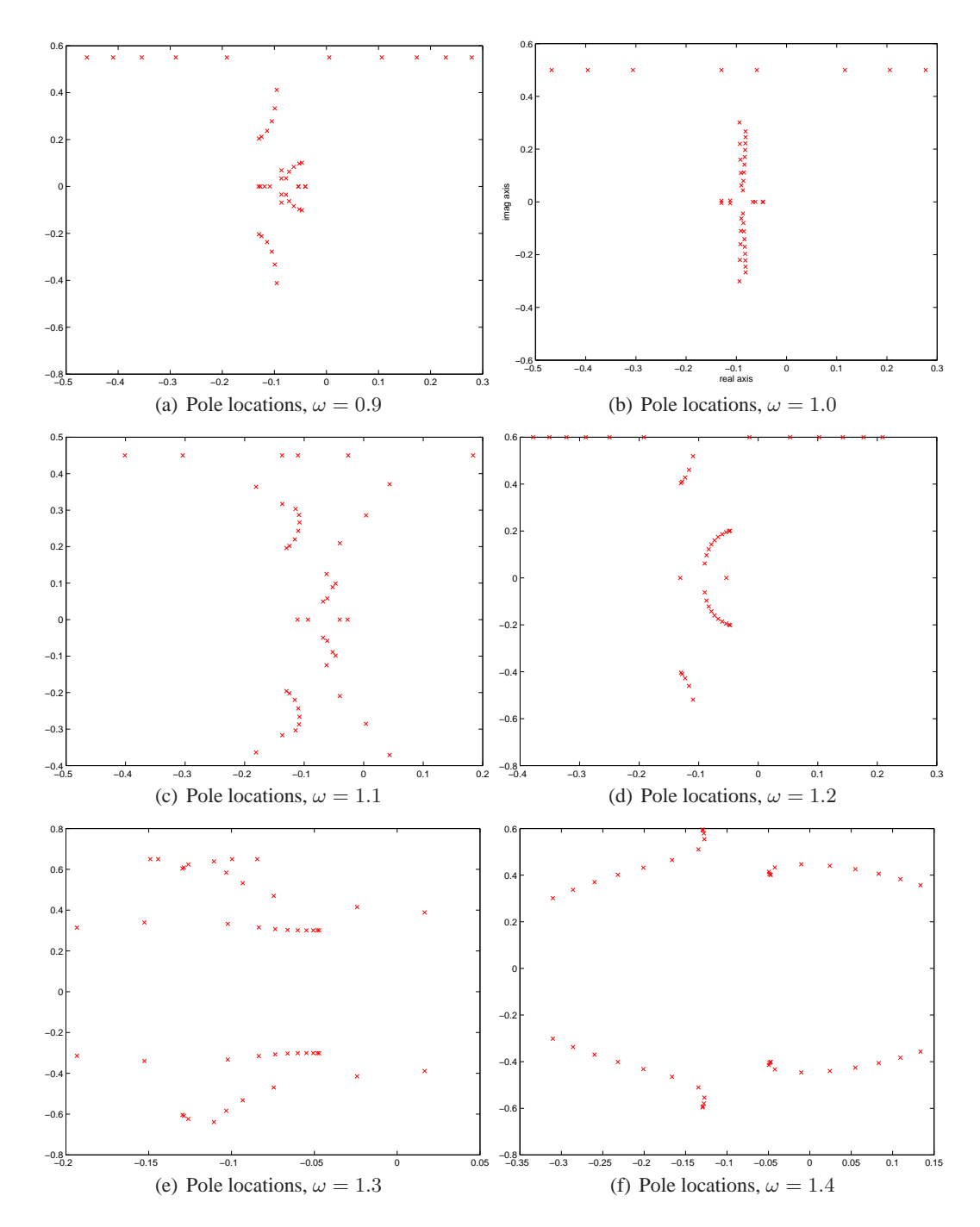


Figure 32 Example system, floquet poles for varying gains and varying frequencies

but only that they have an equal phase and magnitude relative to each other, at the end of a period \mathcal{T} .

To see how the response behaves within a single period, we need to calculate the matrix P(t). To do this we need:

• The (3D) matrix $\Phi(t, t_0)$, calculated by simulation between t = 0 and T (of which the matrix α is the value at T. The size of this matrix is $N_s \times N_s \times N_t$, where N_s is the number of states in the system, and N_t the number of points in time where we wish to calculate $\mathbf{P}(t)$.

• The matrix α

First we calculate the matrix β from α using equation (104):

$$\beta = 1/T \ln \alpha \tag{109}$$

Then we can calculate P(t) using equation (100):

$$\mathbf{P}(t) = \mathbf{\Phi}(t, t_0) \left[e^{\beta t} \right]^{-1} \tag{110}$$

For this to work, the inverse of $e^{\beta t}$ must exist. The 'eigen' motion of the kth mode calculated from the matrix α during one period at its eigenfrequency (see equation (107)), can then be calculated as:

$$\mathbf{x}_k(t) = \mathbf{P}(t)\mathbf{X}_{\alpha k} \tag{111}$$

where $\mathbf{X}_{\alpha k}$ is the kth eigenvector of the matrix α .

Though this works for systems with only a few degrees of freedom, it is not an appropriate way to handle large scale systems as it requires a significant computational effort and may suffer from numerical issues.

[35] suggests calculating the motions of the system associated with an eigenvalue as:

$$\mathbf{x}_k(t) = e^{-\lambda_k t} \mathbf{\Phi}(t) \mathbf{X}_{\alpha k} \tag{112}$$

This is a much simpler and more numerically stable way of calculating the motions of the mode-shapes.

Both equation (111) and (112) result in the same values, confirming that these methods are equal.

Example 4.4 (Floquet modal time analysis). For the simple example system, we can show that we can actually calculate the motion with equation (111) or (112). Figure 33(a) shows how the values of the elements of $\mathbf{P}(t)$ vary during one period. As required by equation (102), the calculated $\mathbf{P}(t)$ is indeed equal to the unit matrix at t=0 and t=T.

Figure 33(b) shows the response of the states during one period at the eigenfrequency of one of the four modes of the system. As can be seen, the Floquet mode is made up of motions of states, that can fluctuate at a different frequency than either the periodic variable or the frequency of the Floquet mode.

4.2 Floquet stability analysis of 1p+2p controller

The 1p + 2p controller design is applied to a 6MW reference windturbine design. The time-dependent variables are the caused by the 1p and 2p coleman transformations. To obtain a clear periodic variable, these coleman transforms are calculated using an azimuth that is based on the mean rotor speed and time only. The difference between the actual azimuth and the mean azimuth due to rotor speed variations can not, as far as the author is aware, be taken into account using Floquet theory,

The controller is analysed using Floquet theory. It is stable with this model as can be seen from the fact that all the poles are in the left half-plane in figure 34. The controller has a gain margin of a factor 6 on the 2p modulated part of the controller. The main component of this unstable mode is the first tower fore-aft mode.

Because of the way Floquet theory has to be applied, it is difficult to analyse how the system responds to changes in phase or delay. It is also difficult to predict whether or not the system

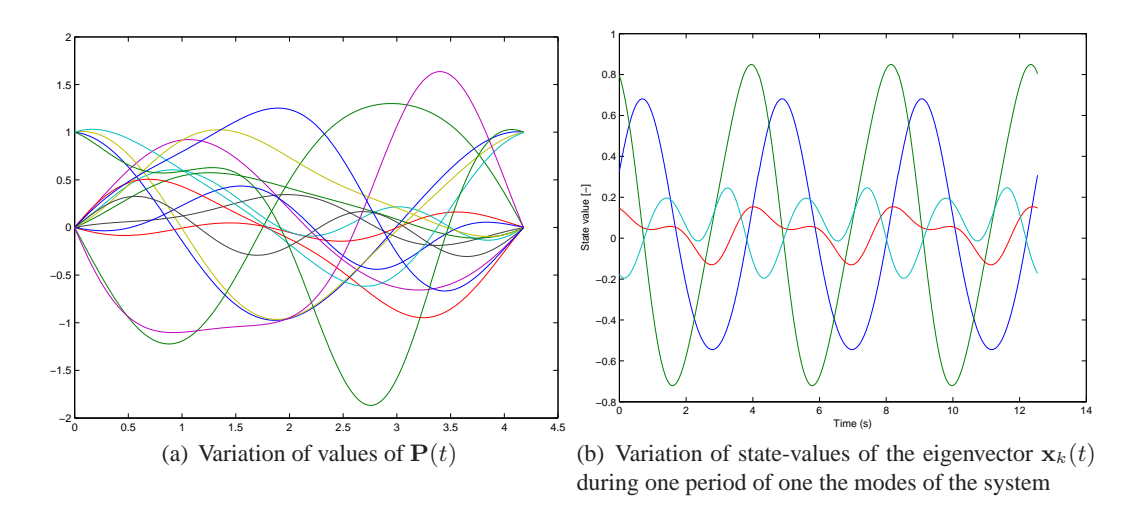


Figure 33 Example system and modal reponse, periodic frequency $\omega = 1.5$

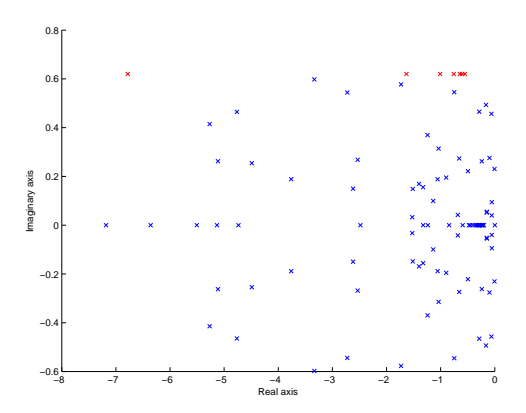


Figure 34 Poles calculated with Floquet analysis

remains stable if one uses the actual rotor azimuth for the Coleman transforms, rather than the approximate, mean rotor azimuth calculated with the mean rotor speed. These are also reasons for a fairly conservative gain margin.

5 Modeling external wind conditions in relation to IPC

Summary

For the development of IPC control algorithms, a simplified wind turbine model is derived in Section 1.2.2. The model includes degrees of freedom for modeling the first modes of the drive-train and tower in fore-aft and side-to-side directions. The aerodynamic modeling relates the three blade pitch setting angles and three fictive *the blade effective wind speeds* to the moments and forces acting on the blade and on the rotor. Therefore, for proper simulation and analysis of the IPC control algorithms it is necessary to be able to generate blade-effective winds to feed the model with. This section presents an algorithm for generation of realistic blade-effective wind speeds.

5.1 Introduction

A compact real-time simulation setting is obtained in Section 1.2.2 wherein three fictive, the so-called blade effective wind speed signals are used instead of a complete three-dimensional (3D) wind field. The three wind speed signals are designed in this section in such a way that they cause "realistic" blade root loads; in other words, the loads are similar to those that arise when a rotating rotor blade samples a 3D homogeneous turbulent wind field for longitudinal turbulence only. Deterministic effects, such as wind shear and tower shadow, can also be included to the blade effective wind speeds.

A point on a rotating blade experiences the wind velocity along a spiral-shaped trajectory (helix) in the "wind cylinder". Thus, a rotating point experiences the intersection of a helix with the rotor plane; in the figure, the rotating blades "move forward" along the x-axis at increasing rotor azimuth angle ψ .

Since the three blades have an azimuth separation of 120° , each blade tip samples along a specific helix. The derived blade effective turbulence signal effectively represents a weighted average of helix realizations over radial coordinate r for a blade. Actually, the *three* blade effective turbulence signals are obtained as a realization-set for a 3×3 power spectrum matrix.

At a constant rotational speed, the time separation between these helices is equal to the revolution time $(\frac{2\pi}{\Omega})$ divided by the number of blades (3). Consequently, the same non-moving location in

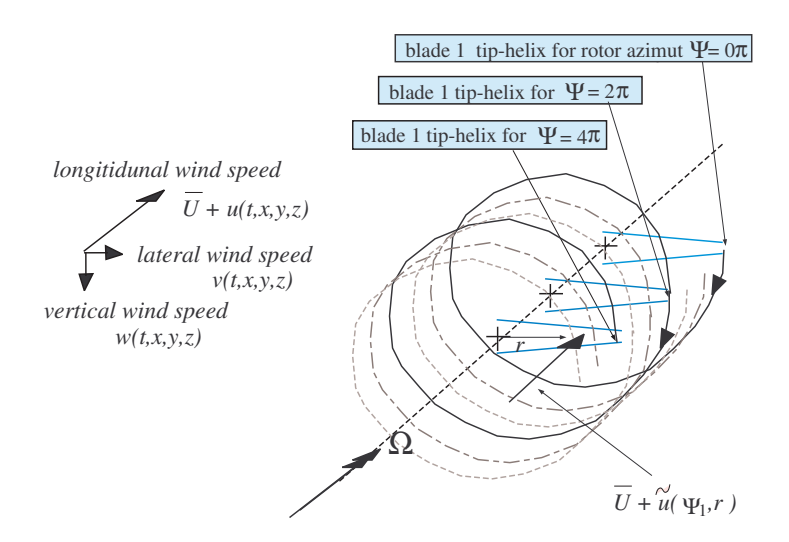


Figure 35 The sampling of helices in the wind field by one blade tip

the wind cylinder is "sampled" every $\frac{2\pi}{3\Omega}$ seconds. The latter is of importance when oblique inflow is considered in the context of a limited number of additional helix realizations.

5.2 Definition of blade-effective wind speeds

This section describes the idea behind the notion of blade-effective wind speeds, and paves the way for creating an algorithm for generation of such wind signals (which is the purpose of the next sections). The aim is summarized as follows.

Objective

The aim is to generate the three helices containing the blade-effective wind speeds in such a way that by using them into the simplified model in Section 1.2.2 results in blade root inplane moments that have approximately the same spectral properties as the those that would result from a conventional 3D wind field.

As an alternative, the blade flapping moments can be used in the approximation, instead of the aerodynamic torque T_a .

To this end, consider first the following nonlinear static expression for the aerodynamic power based on the power coefficient C_P

$$P = \frac{1}{2}\rho\pi R^2 C_P(\lambda^{(i)}, \theta^{(i)}) (u_{ax})^3$$

where u_{ax} is the undisturbed rotor-uniform longitudinal wind speed. Since $P = T_a \Omega$, the following expression for the aerodynamic torque on the rotor holds

$$T_a = \frac{1}{2\Omega} \rho \pi R^2 C_P(\lambda^{(i)}, \theta^{(i)}) (u_{ax})^3.$$

Assuming now that each blade has its own wind speed, above expression can be generalized to aerodynamic torque per blade as

$$T_a^{(i)} = \frac{1}{6\Omega} \rho \left(\pi R^2 \right) C_P^{(i)}(\lambda^{(i)}, \theta^{(i)}) (u_{ax}^{(i)})^3, \ i = 1, 2, 3, \tag{113}$$

or per blade element, by assuming that each blade i is divided into a number of elements (sections) $e=1,2,\ldots,N$ of equal width ΔR

$$T_a^{e,i} = \frac{1}{6\Omega} \rho \left(2\pi R_e \Delta R\right) C_P^{e,i}(\lambda^{e,i}, \theta^{(i)}) (u_{ax}^{e,i})^3, \ i = 1, 2, 3, \ e = 1, 2, \dots, N,$$
 (114)

where R_e is the radial position of section e, and $u_{ax}^{e,i}$ is the wind experienced by element e of blade i. In above expressions, $C_P^{(i)}$ and $C_P^{e,i}$ are the aerodynamic power coefficients per blade and per blade element, respectively. For simplicity, however, it is assumed that all blades, and all blade elements, have the same aerodynamic efficiency.

Assumption 5.1 (Uniform aerodynamic efficiency). The blade elements have equal aerodynamic efficiency, i.e. $C_P^{e,i} = C_P^{(i)} = C_P$.

By defining the parameter $K = \frac{1}{3\Omega}\rho\pi\Delta R$, and representing the wind as a sum of mean wind speed \bar{U} and turbulence $u^{(i)}$ (or $u_{e,i}$), the expressions in equations (113) and (114) can be rewritten

as follows

$$T_a^{(i)} = K \sum_{e=1}^{N} R_e C_P(\bar{U} + u^{(i)}) (\bar{U} + u^{(i)})^3$$
$$\sum_{e=1}^{N} T_a^{e,i} = K \sum_{e=1}^{N} R_e . C_P(\bar{U} + u_{e,i}) . (\bar{U} + u_{e,i})^3$$

In an attempt to equate the two expressions above, the goal would be to construct blade-effective wind turbulence $u^{(i)}$ such that

$$\sum_{e=1}^{N} R_e C_P(\bar{U} + u^{(i)}) (\bar{U} + u^{(i)})^3 \approx \sum_{e=1}^{N} R_e C_P(\bar{U} + u_{e,i}) \cdot (\bar{U} + u_{e,i})^3$$
(115)

Since a typical blade design achieves a power coefficient C_P that is relatively flat around its optimum, small wind variations due to turbulence have little effect on C_P , so that the following holds

$$C_P(\bar{U} + u^{(i)}) \approx C_P(\bar{U} + u_{e,i}),$$

and, therefore, expression (115) becomes

$$\sum_{e=1}^{N} R_e(\bar{U} + u^{(i)})^3 \approx \sum_{e=1}^{N} R_e(\bar{U} + u_{e,i})^3.$$
 (116)

The objective was defined as deriving $u^{(i)}$ such that the spectral properties of $T_a^{(i)}$ and $\sum_{e=1}^N T_a^{e,i}$ are approximately the same. However, for simplifying the derivation process we will further concentrate at obtaining a "linearized stochastic equivalence" by first linearizing both sides of (116) around $u^{(i)} = u_{e,i} = 0$, leading to the following expression (wherein now equality sign is used as this forms a basis for the derivation process in the sequel)

$$u^{(i)} \sum_{e=1}^{N} R_e \text{ stochastic sense } \sum_{e=1}^{N} R_e u_{e,i}$$

Notice that this equation implies that the blade effective wind speeds $u^{(i)}$ will be a weighted average of the blade-element effective wind speeds $u_{e,i}$, with the weighting factor increasing linearly with the radial position of the element. Indeed, this conclusion is not unexpected considering the fact that, under the assumption of equal aerodynamic efficiency, for rotor uniform wind the leadwise (tangential) blade element forces are equal over the blade length, and hence the corresponding contributions to the aerodynamic torque increases linearly with the radial position.

Performing Fourier transform on the equation above gives

$$U^{(i)}(j\omega) \sum_{e=1}^{N} R_e \overset{\text{stochastic sense}}{=} \sum_{e=1}^{N} R_e U_{e,i}(j\omega)$$

and for two different blades, i_1 and i_2 , and two different blade elements, e_1 and e_2 , it holds that

$$\underbrace{U^{(i_1)}(j\omega)\left(U^{(i_2)}(j\omega)\right)^*}_{S_{u^{(i_1)},u^{(i_2)}}} \left(\sum_{e=1}^N R_e\right)^2 = \sum_{e_1=1}^N \sum_{e_2=1}^N R_{e_1} R_{e_2} \underbrace{U_{e_1,i_2}(j\omega)\left(U_{e_2,i_2}(j\omega)\right)^*}_{S_{u_{e_1,i_1},u_{e_2,i_2}}}$$

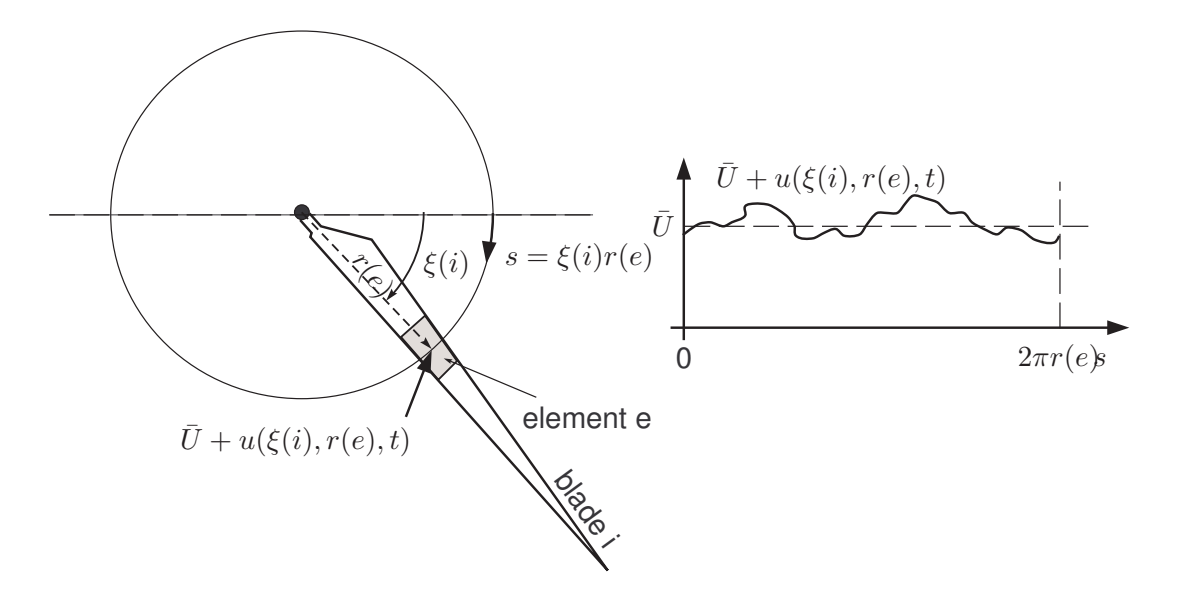


Figure 36 Turbulent wind experienced by a rotating blade element.

This implies the following expression for the cross power spectral density (CPSD) between two blade effective wind speeds $u^{(i_1)}$ and $u^{(i_2)}$

$$S_{u^{(i_1)},u^{(i_2)}} = \frac{1}{\left(\sum_{e=1}^{N} R_e\right)^2} \sum_{e_1=1}^{N} \sum_{e_2=1}^{N} R_{e_1} R_{e_2} S_{u_{e_1,i_1},u_{e_2,i_2}}.$$
(117)

Notice that the term $S_{u_{e_1,i_1},u_{e_2,i_2}}$, representing the cross power spectral density between the winds speeds u_{e_1,i_1} and u_{e_2,i_2} , includes rotational wind field sampling effects due to the rotor rotation, and still needs to be expressed in terms of the given turbulence model for the fixed wind field. This is the purpose of the next section.

It should be pointed out again that this equation was derived by aiming to equate the aerodynamic torques on the rotor resulting from three blade effecting wind speeds on the one side, and a 3D wind field on the other side. If one, instead, wishes to approximate the blade root flapping moments, then it can be shown in a similar fashion that equation (117) then gets the form

$$S_{u^{(i_1)},u^{(i_2)}} = \frac{1}{\left(\sum_{e=1}^N R_e^2\right)^2} \sum_{e_1=1}^N \sum_{e_2=1}^N R_{e_1}^2 R_{e_2}^2 S_{u_{e_1,i_1},u_{e_2,i_2}}.$$

5.3 CPSD between two blade elements

In this section, an expression is derived for the CPSD $S_{u_{e_1,i_1},u_{e_2,i_2}}$ in equation (117) will be derived. For convenience, we will denote the wind speed at element e of blade i as

$$u(\xi(i), r(e), t) = u_{e,i}(t),$$

wherein $\xi(i) = \Omega t + \frac{i-1}{3} 2\pi$ is the azimuth angle of blade i, and $r(e) = R_e$ is the distance from the rotor center to blade element e (see Figure 36).

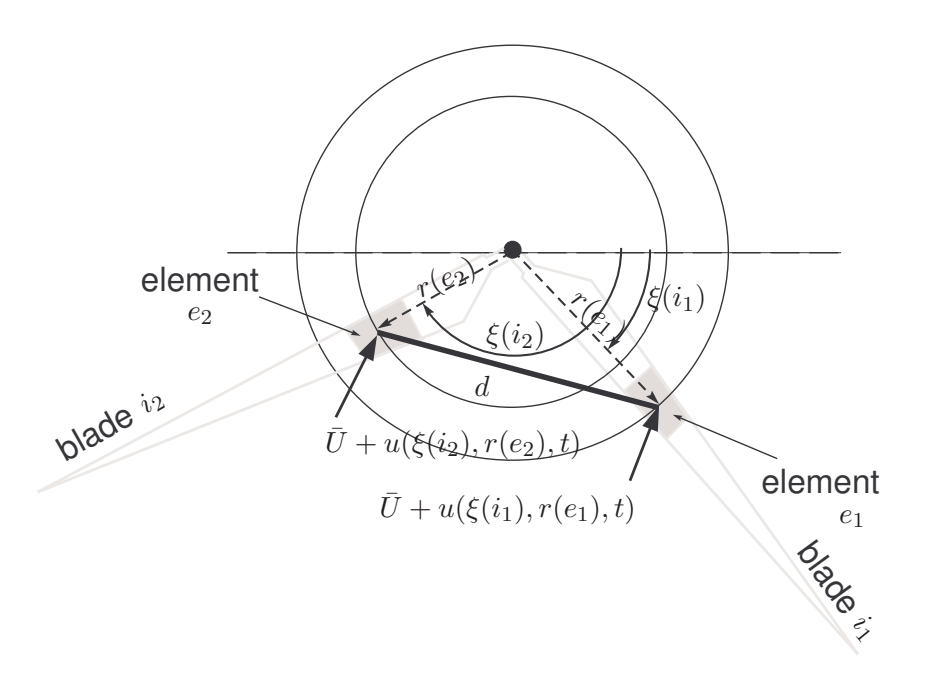


Figure 37 Definition of distance d between points (r_1, ξ_1) and (r_2, ξ_2)

To begin with, define $S_{uu}(\omega)$ as the (auto) power spectral density (APSD) of a fixed (non-rotating) point in space, $\gamma(\omega, d(\xi_1, \xi_2, r_1, r_2))$ is the coherence function,

$$d(\xi_1, \xi_2, r_1, r_2) = r_1^2 + r_2^2 - 2r_1r_2\cos(\xi_2 - \xi_1).$$

is the distance between element e_1 on blade i_1 and element e_2 on blade i_2 (see Figure 37), and ω is the frequency. Next, the following assumption is made (which holds with the standard turbulence model used in the norm IEC61400-1).

Assumption 5.2 (Homogeneous stationary turbulence). The turbulence in the wind field is homogeneous and stationary, i.e. the spectral properties are independent on the position in space and on time. More specifically,

$$\begin{array}{rcl} S_{u(\xi,r)u(\xi,r)}(\omega) & = & S_{uu}(\omega) \\ S_{u(\xi_2,r_2)u(\xi_1,r_1)}(\omega) & = & S_{uu}(\omega)\gamma(\omega,d(\xi_1,\xi_2,r_1,r_2)) \end{array}$$

are all independent on ξ , r and t.

The homogeneity of the wind field allows an azimuth expansion of the wind speed felt by a blade element. Consider Figure 36 again. If we "freeze" the wind field (i.e. for a fixed time t) and look along the path followed by the point $(\xi(i), r(e))$ (to be shortly denoted as (ξ, r) in the sequel) as time evolves, then the function $u(\xi, r, t)$ will be periodic in the azimuth ξ . Therefore, a Fourier series expansion of $u(\xi, r, t)$ has the form

$$u(\xi, r, t) = \sum_{p=-\infty}^{\infty} e^{jp\xi} . \hat{u}_p(r, t)$$
$$\hat{u}_p(r, t) = \frac{1}{2\pi} \int_0^{2\pi} e^{-jp\xi} . u(\xi, r, t) d\xi$$

wherein $\hat{u}_p(r,t)$ are the Fourier coefficients, also called in the sequel the rotational modes. This

Fourier series expansion is used in the sequel for the derivation of an expression for the CPSD $S_{u_{e_1,i_1},u_{e_2,i_2}}$ between the wind speeds on two elements on two blades, to be used in equation (117) for the formation of the CPSD $S_{u^{(i_1)},u^{(i_2)}}$ between two blade effective wind speeds.

For the rotational modes at two radial positions r_1 and r_2 it then holds that

$$\hat{u}_q(r_2, t+\tau) = \frac{1}{2\pi} \int_0^{2\pi} e^{-jq\xi_2} u(\xi_2, r_2, t+\tau) d\xi_2$$

$$\hat{u}_p(r_1, t) = \frac{1}{2\pi} \int_0^{2\pi} e^{-jp\xi_1} u(\xi_1, r_1, t) d\xi_1$$

and, therefore, for the cross-correlation function between $u_p(r_1,t)$ and $u_q(r_2,t)$ the following expression follows

$$C(\hat{u}_q(r_2, t+\tau), \hat{u}_p(r_1, t)) = E[\hat{u}_q(r_2, t+\tau)\hat{u}_p^*(r_1, t)]$$

$$= \frac{1}{4\pi^2} \int_0^{2\pi} \int_0^{2\pi} e^{-jq\xi_2} e^{+jp\xi_1} E[u(\xi_2, r_2, t+\tau)u^*(\xi_1, r_1, t)] d\xi_1 d\xi_2.$$

Due to the assumed stationarity of the turbulence $u(\xi, r, t)$ (Assumption 5.2),

$$E[u(\xi_2, r_2, t + \tau)u^*(\xi_1, r_1, t)] = E[u(\xi_2, r_2, \tau)u^*(\xi_1, r_1, 0)] = C(u(\xi_2, r_2), u(\xi_1, r_1), \tau),$$

and hence

$$C(\hat{u}_q(r_2, t + \tau), \hat{u}_p(r_1, t)) = \frac{1}{4\pi^2} \int_0^{2\pi} \int_0^{2\pi} e^{-jq\xi_2} e^{+jp\xi_1} C(u(\xi_2, r_2), u(\xi_1, r_1), \tau) d\xi_1 d\xi_2$$

$$= C(\hat{u}_q(r_2), \hat{u}_p(r_1), \tau)$$

Therefore, the cross-correlation function of the rotation modes is independent on time t, implying that the *rotational modes are stationary*. To show that the rotational modes are also orthogonal, notice first that homogeneity of $u(\xi, r, t)$ (Assumption 5.2) implies

$$C(u(\xi_2, r_2), u(\xi_1, r_1), \tau) = C(u(\xi_2 - \xi_1, r_2), u(0, r_1), \tau)$$

so that

$$\begin{split} &C[\hat{u}_q(r_2),\hat{u}_p(r_1),\tau] = \\ &= \frac{1}{4\pi^2} \int_0^{2\pi} \int_0^{2\pi} e^{-jq\xi_2} e^{+jp\xi_1} C[u(\xi_2-\xi_1,r_2),u(0,r_1),\tau] d\xi_1 d\xi_2 \\ &= \frac{1}{4\pi^2} \int_0^{2\pi} e^{-j(q-p)\xi_2} \left(\int_0^{2\pi} e^{-jp(\xi_2-\xi_1)} C[u(\xi_2-\xi_1,r_2),u(0,r_1),\tau] d\xi_1 \right) d\xi_2 \\ &= \frac{1}{4\pi^2} \int_0^{2\pi} e^{-j(q-p)\xi_2} \left(\int_{\xi_2-2\pi}^{\xi_2} \underbrace{e^{-jp(\xi_2-\xi_1)} C[u(\xi_2-\xi_1,r_2),u(0,r_1),\tau]}_{\text{periodical}} d(\xi_2-\xi_1) \right) d\xi_2 \end{split}$$

Due to to periodicity of the integrand:

$$\begin{split} &C[\hat{u}_q(r_2),\hat{u}_p(r_1),\tau] = \\ &= \frac{1}{4\pi^2} \int_0^{2\pi} e^{-j(q-p)\xi_2} \left(\int_0^{2\pi} e^{-jp(\xi_2-\xi_1)} C[u(\xi_2-\xi_1,r_2),u(0,r_1),\tau] d(\xi_2-\xi_1) \right) d\xi_2 \\ &= \left(\frac{1}{4\pi^2} \int_0^{2\pi} e^{-j(q-p)\xi_2} d\xi_2 \right) \left(\int_0^{2\pi} e^{-jp(\xi_2-\xi_1)} C[u(\xi_2-\xi_1,r_2),u(0,r_1),\tau] d(\xi_2-\xi_1) \right) \end{split}$$

The first integral in $C[\hat{u}_q(r_2), \hat{u}_p(r_1), \tau]$

$$\int_0^{2\pi} e^{-j(q-p)\xi_2} d\xi_2 = 2\pi . \delta_{pq}, \ \delta_{pq} \left\{ \begin{array}{l} 1, & p=q \\ 0, & p \neq q \end{array} \right.$$

so that

$$\begin{split} &C[\hat{u}_q(r_2),\hat{u}_p(r_1),\tau] = \\ &= \delta_{pq} \frac{1}{2\pi} \int_0^{2\pi} e^{-jp(\xi_2 - \xi_1)} C[u(\xi_2 - \xi_1,r_2),u(0,r_1),\tau] d(\xi_2 - \xi_1) \end{split}$$

Therefore, the rotational modes are orthogonal.

For the CPSD between two rotational modes it then holds that

$$\begin{split} S_{\hat{u}_q(r_2),\hat{u}_p(r_1)}(\omega) \\ &= \int_{-\infty}^{\infty} e^{-j\omega\tau} C[\hat{u}_q(r_2),\hat{u}_p(r_1),\tau]d\tau \\ &= \delta_{pq} \frac{1}{2\pi} \int_{0}^{2\pi} e^{-jp(\xi_2-\xi_1)} \left(\int_{-\infty}^{\infty} e^{-j\omega\tau} C[u(\xi_2-\xi_1,r_2),u(0,r_1),\tau]d\tau \right) d(\xi_2-\xi_1) \\ &= \delta_{pq} \frac{1}{2\pi} \int_{0}^{2\pi} e^{-jp(\xi_2-\xi_1)} S_{u(\xi_2-\xi_1,r_2),u(0,r_1)}(\omega) d(\xi_2-\xi_1) \end{split}$$

From Assumption 5.2 it follows that

$$S_{\hat{u}_q(r_2),\hat{u}_p(r_1)}(\omega) = \delta_{pq} \frac{1}{2\pi} \int_0^{2\pi} e^{-jp\xi} S_{uu}(\omega) \gamma(d,\omega) d\xi.$$
 (118)

Now that we have derived an expression for the CPSD between two rotational modes in terms of the APSD of a fixed point S_{uu} and the coherence function γ , lets step back and write the Fourier expansion of the wind turbulence felt by element e of blade i

$$u_{i,e} = \sum_{p=-\infty}^{\infty} e^{jp\xi(i)}.\hat{u}_p(r(e),t) = \sum_{p=-\infty}^{\infty} e^{jp(\Omega t + \frac{i-1}{3}2\pi)}.\hat{u}_p(r_e,t).$$

The CPSD between two elements, e_1 and e_2 , of two blades i_1 and i_2 is then given by

$$S_{u_{i_2,e_2},u_{i_1,e_1}}(\omega) = \int_{-\infty}^{\infty} e^{-j\omega\tau} C[u_{i_2,e_2}, u_{i_1,e_1}, \tau] d\tau$$
(119)

Due to orthogonality of rotational modes \hat{u}_p it holds that

$$C[u_{i_{2},e_{2}},u_{i_{1},e_{1}},\tau] = \sum_{p=-\infty}^{\infty} e^{jp(\Omega\tau + \frac{i_{2}-i_{1}}{3}2\pi)} E[\hat{u}_{p}(r_{2},\tau)\hat{u}_{p}^{*}(r_{1},0)]$$
$$= \sum_{p=-\infty}^{\infty} e^{jp(\Omega\tau + \frac{i_{2}-i_{1}}{3}2\pi)} C[\hat{u}_{p}(r_{2}),\hat{u}_{p}(r_{1}),\tau]$$

Substitution of this expression into equation (119) yields

$$S_{u_{i_{2},e_{2}},u_{i_{1},e_{1}}}(\omega) = \sum_{p=-\infty}^{\infty} e^{jp^{\frac{i_{2}-i_{1}}{3}}2\pi} \int_{-\infty}^{\infty} e^{-j(\omega-p\Omega)\tau} C[\hat{u}_{p}(r_{2}),\hat{u}_{p}(r_{1}),\tau]d\tau$$

$$= \sum_{p=-\infty}^{\infty} e^{jp^{\frac{i_{2}-i_{1}}{3}}2\pi} S_{\hat{u}_{p}(r_{2}),\hat{u}_{p}(r_{1})}(\omega-p\Omega). \tag{120}$$

Hence, the CPSD between the wind at two elements on two blades is equal to an infinite sum of shifted spectra of the rotational modes.

Substitution of equation (118) into equation (120), and the result into equation (117) yields the following final expression for the CPSD between two blade-effective wind speeds, expressed in terms of the APSD of a fixed point S_{uu} and the coherence function γ

$$S_{u^{(i_1)},u^{(i_2)}} = \frac{\sum_{e_1=1}^{N} \sum_{e_2=1}^{N} R_{e_1} R_{e_2}}{\left(\sum_{e=1}^{N} R_e\right)^2} \sum_{p=-\infty}^{\infty} e^{jp^{\frac{i_2-i_1}{3}} 2\pi} \frac{1}{2\pi} S_{uu}(\omega - p\Omega) \int_{0}^{2\pi} e^{-jp\xi} \gamma(d,\omega - p\Omega) d\xi.$$

$$(121)$$

For the APSD of a blade-effective wind speed, d = 0, $\gamma = 1$ and $i_1 = i_2$, so that the expression (121) significantly simplifies

$$S_{u^{(i)},u^{(i)}} = \frac{\sum_{e_1=1}^{N} \sum_{e_2=1}^{N} R_{e_1} R_{e_2}}{\left(\sum_{e=1}^{N} R_{e}\right)^2} \sum_{p=-\infty}^{\infty} S_{uu}(\omega - p\Omega)$$

Notice the sum of shifted spectra in this expression. As a result, the spectrum of a blade-effective wind speed exhibits peaks at frequencies equal to multiples of the rotational frequency of the rotor.

5.4 Realization algorithm for blade-effective wind speed signals

A realisation algorithm as proposed by Shinozuka [66] is applied. Such a realisation algorithm is also included in the ECN 3D-wind field simulation program SWIFT [105]. Here, the generation process is only outlined.

Consider the 3×3 spectral matrix

$$S_{bl} = \begin{bmatrix} S_{u^{(1)},u^{(1)}} & S_{u^{(1)},u^{(2)}} & S_{u^{(1)},u^{(3)}} \\ S_{u^{(2)},u^{(1)}} & S_{u^{(2)},u^{(2)}} & S_{u^{(2)},u^{(3)}} \\ S_{u^{(3)},u^{(1)}} & S_{u^{(3)},u^{(2)}} & S_{u^{(3)},u^{(3)}} \end{bmatrix}$$
(122)

with elements obtained from equation (121). Then the following procedure can be used to generate time realizations of three blade effective wind speed signals.

1 Define the APSD of a fixed point in space S_{uu} and the coherence function γ (e.g. according to the specification IEC61400-1),

- 2 Construct the spectral matrix S_{bl} in equation (122),
- 3 Evaluate the S_{bl} for a set of frequencies, and attribute a random phase angle to each,
- 4 Apply inverse Fourier transform to obtain time realizations of the blade effective wind speeds.

5.5 Modeling oblique inflow

In the sections above, the generation of blade-effective wind speeds has been considered in case of constant rotor speed, constant wind speed and non-oblique stream. This results in a set of three helices, one per blade. In case of oblique inflow (and/or varying rotational speed of the rotor), a number of intermediate helices can be used for interpolation purposes, as depicted on Figure 38 where the rotor is yawed at 40 degrees. As a result, the wind speed for a give blade is formed by interpolating between its corresponding blade-related helix and its nearest neighboring (intermediate) helix.

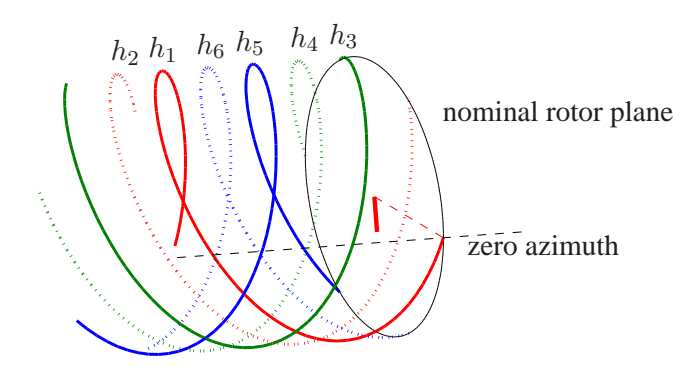


Figure 38 Interpolation based on six helices is used to approximate the blade effective wind speed in case of oblique wind flow

5.5.1 Preliminaries

The the derivation of the obligue inflow approximation algorithm below, some additional notation needs to be introduced first. The orientations of the rotor fixed frame axes, in the case of non-oblique inflow, is such that the x axis is perpendicular to the rotor plane and is positive downwind, the z axis points downwards and the y-axis points to the right as seen from a point on the negative x-axis (upwind). In case of oblique inflow (or, equivalently, tilted and yawed rotor), the rotor fixed reference frame $(0, x_r, y_r, z_r)$ is rotated with respect to the nominal (non-oblique) rotor fixed reference frame (0, x, y, z) as visualized on Figure 40. The rotor yaw angle ϕ_{yw} is defined as the angle between the y-axis and y_r -axis, measured from y to y_r in anti-clockwise direction as seen from a point on the positive z-axis. The rotor tilt angle, ϕ_{tlt} , on the other hand, is the angle between the z-axis and the z_r -axis in clockwise direction as seen from the positive y_r -axis. The turbulent wind flow is assumed to have only a longitudinal component. It is further assumed that a turbulence realization on six helixes is given, denoted as $h_i(\psi_i^{hx})$ for helix $i=1,2,\ldots,6$, where ψ_i^{hx} is the helix azimuth angle. The helixes are computed under the assumption of constant rotor speed $\bar{\Omega}$ and wind speed \bar{U} , so that under the Taylor's frozen wave hypothesis the helix azimuth angle explicitly defines a fixed point in time and space. The helixes are numbered anti-clockwise,

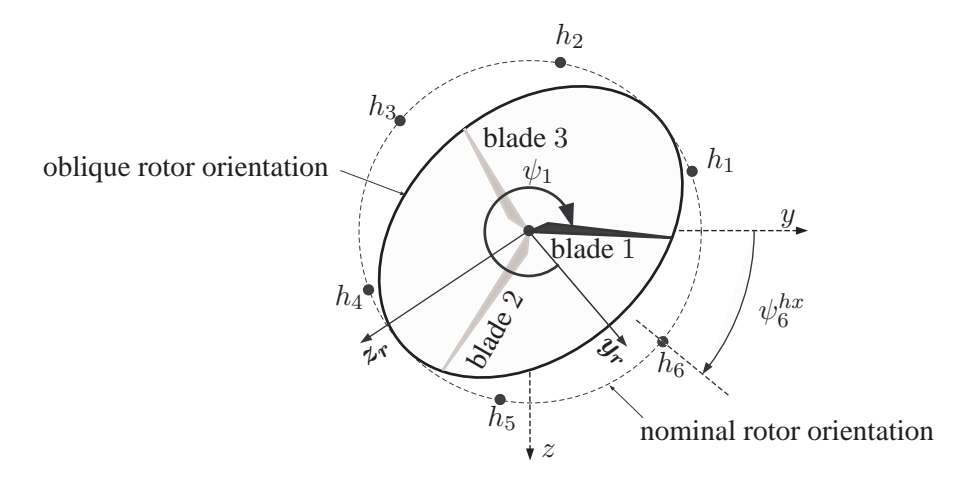


Figure 39 Visualization of tilted and yawed rotor, blade numbering, and helix numbering.

while the rotor blades - clockwise (see Figure 39). The azimuthal angles are measured clockwise starting from the positive y_r -axis. The helixes are azimuthally equally spaced over the rotor plane. Table 4 summarizes some of the notation used. The helix azimuth angle $\psi_i^{hx}(t)$ at a given time

notation	description
$\psi_i(t)$	azimuth of blade i
$\psi(t) \equiv \psi_1(t)$	rotor azimuth
$\psi_i^{hx}(t)$	azimuth of helix i
U(t)	wind speed
$ar{U}$	wind speed used in helix realization
$\Omega(t)$	rotor speed
$\bar{\Omega}$	rotor speed used in helix realization
$\phi_{tlt}(t)$	rotor tilt angle
$\phi_{yw}(t)$	rotor yaw angle

Table 4 Definitions of symbols.

instant t is defined as the azimuthal position of the intersection point of helix h_i with the nominal (non-oblique) rotor plane, and is hence independent on the rotor orientation (see angle ψ_6^{hx} on Figure 39). An algorithm for generating such helices for 3 blades was presented in the previous section, although it can easily be extended to helices for 6 blades as required in this section.

Finally, for a vector $v \in \mathbb{R}^n$, the notation v_i is used to denote the *i*-th element of v.

5.5.2 The interpolation algorithm

Given the rotor speed $\Omega(t)$ and the initial rotor position $\psi(0) = \psi_1(0)$, the azimuth angles of the rotor and the blades at time instant t are given by

$$\psi(t) = \psi_1(0) + \int_0^\infty \Omega(t)dt,$$

$$\psi_b(t) \doteq \psi(t) + \frac{2\pi(b-1)}{3}, \ b = 1, 2, 3.$$
(123)

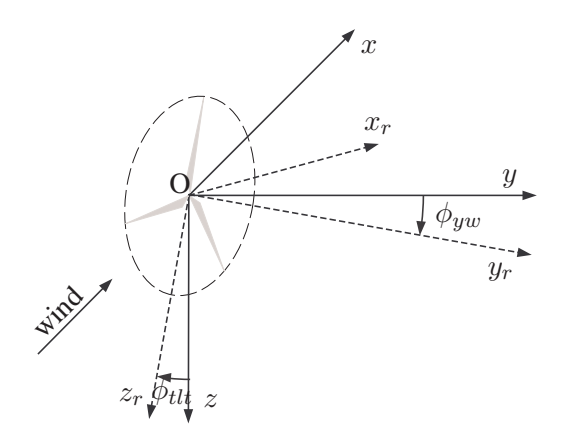


Figure 40 Nominal (0, x, y, z) and oblique $(0, x_r, y_r, z_r)$ reference frames, tilt and yaw angle definition and orientation.

The helix azimuth positions at time t, on the other hand, depend on the wind speed U(t) and the initial azimuth angle of the first helix $\psi_1^{hx}(0)$:

$$\psi_1^{hx}(t) = \psi_1^{hx}(0) + \frac{\bar{\Omega}}{\bar{U}} \int_0^\infty U(t)dt,
\psi_i^{hx}(t) \doteq \psi_1^{hx}(t) - \frac{\pi(i-1)}{3}, \ i = 1, 2 \dots, 6.$$
(124)

Assuming rigid rotor for simplicity of the presentation, for a given blade, say b, a point lying at distance $\frac{2R}{3}$ from the blade root⁵ has the following coordinates in $(0, x_r, y_r, z_r)$ at time t

$$p_{r,b}(t) = \begin{bmatrix} 0 \\ \cos(\psi_b(t)) \\ \sin(\psi_b(t)) \end{bmatrix} \frac{2R}{3}, \ b = 1, 2, 3.$$
 (125)

where R is the rotor radius. The coordinates of the same point in the non-oblique coordinate system (0, x, y, z) can be computed using the following transformation matrices

$$P_{tlt}(\phi) \doteq \begin{bmatrix} \cos(\phi) & 0 & \sin(\phi) \\ 0 & 1 & 0 \\ -\sin(\phi) & 0 & \cos(\phi) \end{bmatrix},$$

$$P_{yw}(\phi) \doteq \begin{bmatrix} \cos(\phi) & \sin(\phi) & 0 \\ -\sin(\phi) & \cos(\phi) & 0 \\ 0 & 0 & 1 \end{bmatrix}$$

that represent rotations around the z-axis (yaw) and around the y-axis (tilt) in the defined directions. Therefore, the coordinates of the $\frac{2R}{3}$ point on blade b in reference frame (0, x, y, z) are given by

$$p_b(t) = \begin{bmatrix} x_b(t) \\ y_b(t) \\ z_b(t) \end{bmatrix} = P_{tlt} (-\phi_{tlt}(t)) P_{yw} (-\phi_{yw}(t)) p_{r,b}(t), \ b = 1, 2, 3.$$
 (126)

⁵This point is assumed to be the effective location for taking into account the blade position relative to the helixes.

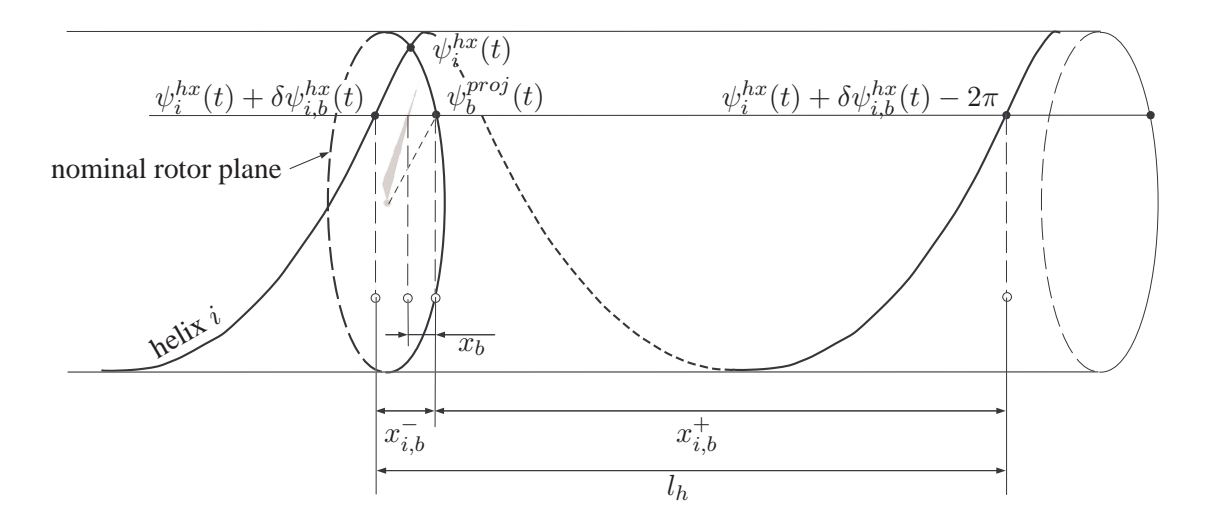


Figure 41 Visualization of the defined azimuth angles and lengths.

Hence, the projected blade onto the nominal rotor plane has azimuth (modulus 2π)

$$\psi_{b}^{proj}(t) = \begin{cases}
\pi - \arcsin\left(\frac{|z_{b}(t)|}{\sqrt{y_{b}^{2}(t) + z_{b}^{2}(t)}}\right), & \text{if } y_{b}(t), < 0 \text{ and } z_{b}(t) > 0 \\
\pi + \arcsin\left(\frac{|z_{b}(t)|}{\sqrt{y_{b}^{2}(t) + z_{b}^{2}(t)}}\right), & \text{if } y_{b}(t) < 0 \text{ and } z_{b}(t) < 0 \\
2\pi - \arcsin\left(\frac{|z_{b}(t)|}{\sqrt{y_{b}^{2}(t) + z_{b}^{2}(t)}}\right), & \text{if } y_{b}(t) > 0 \text{ and } z_{b}(t) < 0 \\
\arcsin\left(\frac{|z_{b}(t)|}{\sqrt{y_{b}^{2}(t) + z_{b}^{2}(t)}}\right), & \text{if } y_{b}(t) > 0 \text{ and } z_{b}(t) > 0
\end{cases} \tag{127}$$

For helix i, the difference between the helix azimuth $\psi_i^{hx}(t)$ and the projected azimuth of blade b is then

$$\delta \psi_{i,b}^{hx}(t) = (\psi_b^{proj}(t) - \psi_i^{hx}(t)) \mod (2\pi).$$
 (128)

Figure 41 depicts the helix tube on which the six helixes lie, as well as the nominal rotor plane, and some azimuth angles and lengths, needed in the sequel. At time instant t, the $\frac{2R}{3}$ point on blade b lines on the azimuth line through $\psi_b^{proj}(t)$, which line intersects with helix i at infinitely many points, but the closest two to the nominal rotor plane correspond to helix i azimuth angles $(\psi_i^{hx}(t) + \delta\psi_{i,b}^{hx}(t))$ and $(\psi_i^{hx}(t) + \delta\psi_{i,b}^{hx}(t) - 2\pi)$. In reference frame (0, x, y, z), these two points have cetrain x-coordinates $x_{i,b}^-(t)$ and $x_{i,b}^+(t)$. Given that the helix is generated under the assumption of constant wind speed and rotor speed, the helix length is given by

$$l_h = \bar{U}\frac{2\pi}{\bar{\Omega}},\tag{129}$$

so that

$$x_{i,b}^{-}(t) = \frac{-\delta \psi_{i,b}^{hx}(t)}{2\pi} l_h,$$

$$x_{i,b}^{+}(t) = l_h + x_{i,b}^{-}(t).$$
(130)

Given the current x-position of the $\frac{2R}{3}$ point of blade b at time instant t, $x_b(t)$, the next thing to do is to determine the closest two helixes, so as to subsequently interpolate between them. To this

end, define the matrices

$$X^{(b)}(t) \doteq \begin{bmatrix} x_{1,b}^{-}(t) \\ \vdots \\ x_{6,b}^{-}(t) \\ x_{1,b}^{+}(t) \\ \vdots \\ x_{6,b}^{+}(t) \end{bmatrix}, H^{(b)}(t) \doteq \begin{bmatrix} h_{1}(\psi_{1}^{hx}(t) + \delta\psi_{1,b}^{hx}(t)) \\ \vdots \\ h_{6}(\psi_{6}^{hx}(t) + \delta\psi_{6,b}^{hx}(t)) \\ h_{1}(\psi_{1}^{hx}(t) + \delta\psi_{1,b}^{hx}(t) - 2\pi) \\ \vdots \\ h_{6}(\psi_{6}^{hx}(t) + \delta\psi_{6,b}^{hx}(t) - 2\pi) \end{bmatrix}.$$
(131)

Then the closest helix in downwind direction is $H_{i_{\epsilon}^{(n)}}^{(b)}(t)$ with

$$i_b^{dn} = \arg\min_i \left\{ X_i^{(b)}(t) - x_b(t) : X_i^{(b)}(t) \ge x_b(t) \right\}, \ b = 1, 2, 3.$$
 (132)

Similarly, upwind the closest helix is $H_{i_u^{up}}^{(b)}(t)$ with

$$i_b^{up} = \arg\min_i \left\{ x_b(t) - X_i^{(b)}(t) : X_i^{(b)}(t) \le x_b(t) \right\}, \ b = 1, 2, 3.$$
 (133)

Notice that the indexes i_b^{dn} and i_b^{up} are also time depended, although not explicitly denoted.

Then a linear interpolation is performed based on the distances between the blade point and the closest helixes. This is done by defining the interpolation weighting factor

$$\alpha_b(t) = \frac{6\left(X_{i_b^{dn}}^{(b)}(t) - x_b(t)\right)}{l_b} \in [0, 1], \ b = 1, 2, 3, \tag{134}$$

so that the following convex combination between the two selected helixes can be used

$$\tilde{u}_b(t) = (1 - \alpha_b(t))H_{i_b^{(b)}}^{(b)}(t) + \alpha_b(t)H_{i_b^{(b)}}^{(b)}(t), \ b = 1, 2, 3.$$

In the above expression for $\tilde{u}_b(t)$, a convex combination is taken between two stochastic signals, namely $H_{i_b^{dn}}^{(b)}(t)$ and $H_{i_b^{up}}^{(b)}(t)$. Assuming stationary homogeneous turbulence field with spectrum at (any) fixed point in space $S_u(w)$, and denoting $\tilde{u}(t)$ as the turbulence at (any) fixed point in space at time t, the following two expressions hold for the first two moments of $u_b(t)$

$$E\{\tilde{u}_b(t)\} = E\{\tilde{u}(t)\} = 0,$$

$$E\{\tilde{u}_b^2(t)\} = ((1 - \alpha_b(t))^2 + \alpha_b^2(t))\underbrace{E\{\tilde{u}^2(t)\}}_{\sigma} + 2\alpha_b(t)(1 - \alpha_b(t))\underbrace{E\{H_{i_b^{dn}}^{(b)}(t)H_{i_b^{up}}^{(b)}(t)\}}_{c(d,0)},$$

where σ denotes the variance of a fixed point in space, while $c(d,\tau)$ is the covariance function between two fixes points in space at a distance $d=\left(X_{i_b^{dn}}^{(b)}(t)-X_{i_b^{up}}^{(b)}(t)\right)$. Hence, the variance of $\tilde{u}_b(t)$ is not equal to the turbulence variance σ . In order to make the two variances the same, an additional covariance correction factor, $\rho_b(t)$, will be used, so that $E\{(\rho_b(t)\tilde{u}_b(t))^2\}=\sigma$.

Then denoting $\gamma(d,\omega)$ as the coherence function between any two points in space at a distance d

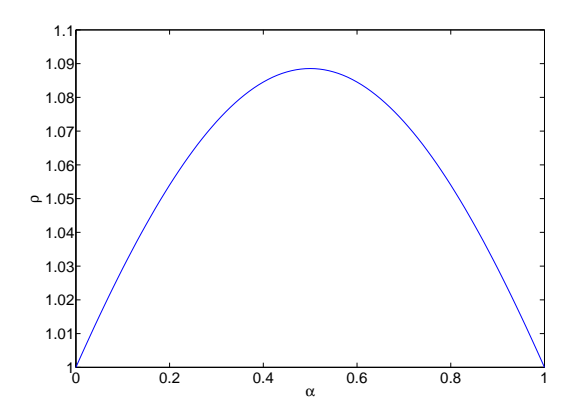


Figure 42 Plot of the covariance correction factor ρ as a function of the interpolation weighting factor α .

one has

$$\sigma = \int_{-\infty}^{\infty} S_u(\omega) d\omega,$$

$$c(d,0) = \int_{-\infty}^{\infty} \gamma(d,\omega) S_u(\omega) d\omega.$$
(135)

Then, since the distance, $\left(X_{i_b^{dn}}^{(b)}(t)-X_{i_b^{up}}^{(b)}(t)\right)$, between the (neighboring) helixes $H_{i_b^{dn}}^{(b)}(t)$ and $H_{i_i^{up}}^{(b)}(t)$ is exactly $\frac{1}{6}l_h$, it can easily be verified that

$$\rho_b(t) = \frac{1}{\sqrt{(1 - \alpha_b(t))^2 + \alpha_b^2(t) + 2\alpha_b(t)(1 - \alpha_b(t))\frac{c(\frac{l_h}{6}, 0)}{\sigma}}}, \ b = 1, 2, 3.$$
 (136)

achieves $E\{(\rho_b(t)\tilde{u}_b(t))^2\} = \sigma$. The parameter ρ as a function of the interpolation factor α is depicted on Figure 42 for the following specific choices for the spectrum $S_u(\omega)$ and coherence $\gamma(d,\omega)$

$$S_u(\omega) = \frac{\sigma_w^2 2L_1/\bar{U}}{\left(1+6L_1\omega/(2\pi\bar{U})\right)^{5/3}}$$
 (Kaimal spectrum), $\gamma(d,\omega) = e^{-8.8d\sqrt{(\omega/(2\pi\bar{U}))^2+(0.12\Lambda/3.5)^2}},$

with $\bar{U}=15$ m/s, $\sigma_w=\frac{I_{15}(15+a\bar{U})}{a+1}$, $I_{15}=0.17$, a=3, $L_1=170.1$ m, and $\Lambda=21$ m. Hence, adding the rotor-wide wind speed U(t) to the *corrected* expression for the turbulence $(\rho_b(t)\tilde{u}_b(t))$, the final expression for the blade-effective wind speed takes the form

$$u_b(t) = U(t) + \rho_b(t) \left((1 - \alpha_b(t)) H_{i_b^{(b)}}^{(b)}(t) + \alpha_b(t) H_{i_b^{(b)}}^{(b)}(t) \right), \ b = 1, 2, 3.$$
 (137)

5.5.3 Numerical implementation

The complete algorithm for approximation of blade effective wind speeds under oblique wind inflow conditions consists of evaluation of the expressions in equations (123)-(137) at each time instant t and for each blade b. In practice, the rotor speed and the azimuth angle of the rotor is measured, so (123) need not be numerically evaluated.

In a numerical implementation the same steps can be followed at discrete time instants (kt_s) ,

 $k = 0, 1, \dots$, after making the following small modifications:

Equation (124) Assuming that the wind speed does not change between any two time instants, i.e. $U(kt_s + \tau) = U(kt_s)$ for $\tau \in [0, t_s)$, the expression for the azimuth of the first helix takes the form

$$\psi_1^{hx}(kt_s) = \psi_1^{hx}(0) + \frac{\bar{\Omega}}{\bar{U}} \sum_{l=0}^{k-1} U(lt_s)t_s.$$

A better option would to use more advanced numerical integration methods to compute $\psi_1^{hx}(kt_s)$.

Equation (131) In a numerical implementation the helixes are only given at discrete azimuth angles, so that it is in general not possible to evaluate $H^{(b)}(t)$ at the desired azimuth angles. One way to circumvent this problem is to evaluate $H^{(b)}(t)$ instead at the closest azimuth angles at which the helixes are given. Assuming that helix i is defined at azimuth angles $(\psi_i^{hx}(0) + k\delta\psi^{hx})$, $k = 0, 1, \ldots$, and define the following projection

$$\begin{split} \Pi_i(x) & \stackrel{:}{=} & \psi_i^{hx}(0) + \left(\arg\min_k \left| \psi_i^{hx}(0) + k\delta\psi^{hx} - x \right| \right) \delta\psi^{hx} \\ & \stackrel{(124)}{=} & \psi_1^{hx}(0) - \frac{\pi(i-1)}{3} + \left(\arg\min_k \left| \psi_1^{hx}(0) - \frac{\pi(i-1)}{3} + k\delta\psi^{hx} - x \right| \right) \delta\psi^{hx} \\ & = & \psi_1^{hx}(0) - \frac{\pi(i-1)}{3} + \mathrm{round}\left(\frac{x - \psi_1^{hx}(0) + \frac{\pi(i-1)}{3}}{\delta\psi^{hx}}\right) \delta\psi^{hx} \end{split}$$

that maps x onto the set of azimuth angles at which helix i is defined. In this way, the expression for $H^{(b)}(t)$ in (131) should simply be replaced by

$$H^{(b)}(t) = \begin{bmatrix} h_1 \left(\Pi_1(\psi_1^{hx}(t) + \delta \psi_{1,b}^{hx}(t)) \right) \\ \vdots \\ h_6 \left(\Pi_6(\psi_6^{hx}(t) + \delta \psi_{6,b}^{hx}(t)) \right) \\ h_1 \left(\Pi_1(\psi_1^{hx}(t) + \delta \psi_{1,b}^{hx}(t) - 2\pi) \right) \\ \vdots \\ h_6 \left(\Pi_6(\psi_6^{hx}(t) + \delta \psi_{6,b}^{hx}(t) - 2\pi) \right) \end{bmatrix}.$$

5.5.4 Numerical example

The algorithm is numerically tested with the data given in Table 5. The helixes are generated based on the assumption of Kaimal fixed point turbulence spectrum, and under an extreme wind condition, occurring at t=5 s, and comprising of a rising wind gust of 15 m/s in combination of a yaw angle of 30 degrees. The wind gust and the yaw angle are given on Figure 43 as functions of time. On each plot in Figure 44 there are four lines. The three dashed lines on all three plots are the same and correspond to the three blade related helixes (helixes 1,5 and 3); these coincide with the blade effective wind speeds in the case of non-oblique inflow and constant rotor and wind speeds. The other three helixes are not plotted. The solid lines on the plots represent the blade effective wind speeds as computed by the proposed algorithm, one per plot.

symbol	value	description
$ar{U}$	15 m/s	mean wind speed
U(t)	see Figure 43 (left)	wind gust
$\bar{\Omega}$	1.85 rad/s	mean rotor speed
$\Omega(t)$	Ω	rotor speed
$\psi(0)$	354.7 deg	initial rotor azimuth
$\psi_1^{hx}(0)$	-5.3 deg	initial azimuth helix 1
t_s	0.02 s	sampling time
$\delta \psi^{hx}$	5.3 deg	helix azimuth sampling angle
$\phi_{yw}(t)$	see Figure 43 (right)	rotor yaw angle
$\phi_{tlt}(t)$	-5.1271 deg	rotor tilt angle
$c(l_h/6,0)/\sigma$	0.6879	parameter in equation (136)

Table 5 Data used in the numerical example

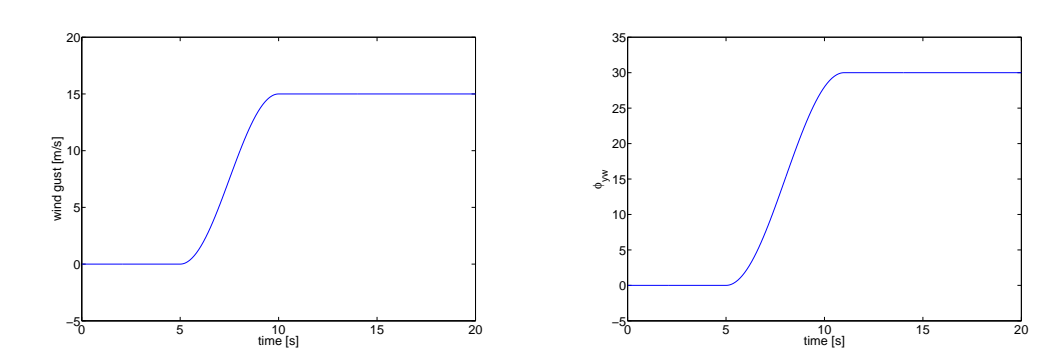


Figure 43 Wind gust U(t) (left) and yaw angle $\phi_{yw}(t)$ (right).

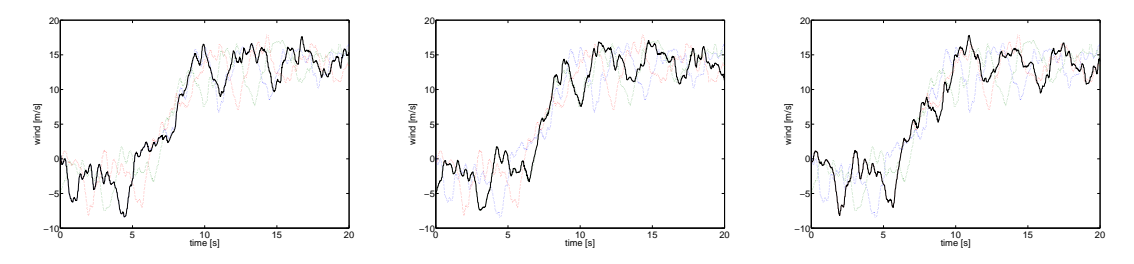


Figure 44 Helixes 1,3 and 5 (dashed lines) and the blade effective wind speeds (solid) of blades 1 (left), 2 (middle) and 3 (right).

Part III

Fault-tolerant control (FTC)

6 GLRT for detecting blade moment sensor faults

Summary

This section develops a method for the identification of faults in the blade root bending moment sensors fault in horizontal axis 3 bladed wind turbines. The underlying problem is crucial to the successful application of IPC control algorithms (as developed in Sections 1-2), which plays a key role for reducing the blade loads of large offshore wind turbines. In this section, a wind turbine model in non-rotating coordinates is constructed based on closed-loop identification. This linear time-invariant model includes the dynamics of the wind process. The fault detection is performed using the residuals generated by dual Kalman filters. The method deals with different types of fault models, including additive and multiplicative fault modeling. For additive faults, the mean value change detection of the residuals and the generalized likelihood ratio test are used. Multiplicative faults are handled by using the variance change detection of the residuals. Fault diagnosis is possible in case of dual sensor redundancy. The proposed approach is validated in simulations.

6.1 Introduction

Even though the availability of onshore wind energy can be as high as 98%, offshore it is much lower and gets sometimes as low as 60% due to long downtime of the wind turbines. This is often caused by the failures of wind turbines components. Therefore, much effort is needed in order to enhance the reliability of the wind turbines. Fault detection and diagnosis is expected to lead to a significant improvement of the availability of wind energy offshore.

In the wind energy field, the fault detection of components has already received significant attention. In [63], a survey on failures of wind turbine systems in Sweden, Finland and Germany is done, where the data are from the maintenance records in the last two decades. In [11, 12] and the references therein, the rotor condition monitoring and some other topics for improving the reliability and safety of offshore wind energy converters are presented, where the main techniques for fault detection are based on spectral analysis of the measurements. Some available techniques on wind turbine system monitoring are reported in [89]. Model based fault detection for wind turbine systems has also received some attention recently [90]. In [19], the pitch actuator delay and pitch actuator gain faults are considered based on the Kalman Filter technique and multiple model estimation technique respectively.

The focus of this section lies on the detection of blade root moment sensor faults. These sensors are typically used for the reduction of blade loads by IPC, as developed in Sections 1-2 (see also [83]). Strain gauge sensors are commonly used in the wind turbine field. However, its lifetime is normally not very long compared with that of other sensors. There are several reasons which cause higher failure rates. The strain in the blades is rather high, which has effect on the gauges themselves as well as on the bonding. The harsh environment factors, such as lightning, salty spray, moisture and corrosion, have direct effects on the bond and wiring. In addition, the sensors may be easily damaged during maintenance in general. On average, a sensor has one failure per year, which implies three failures for a 3 bladed wind turbine. This is undesired since the sensor failures would lead to wrong behavior of the individual pitch control system; the latter is crucial for reduced blade loads that prolong the wind turbine lifetime. Therefore, fault detection of blade moment sensors is extremely important.

This section presents a composite approach to blade moment sensor fault detection and isolation for a 3 bladed horizontal axis wind turbines. The approach includes detection techniques for both additive and multiplicative faults. These techniques utilize the residues of Kalman filters, wherein the residual (i.e. the difference between a sensor output and its filter estimate) is used for

fault detection. The residual has the property of being white noise with constant intensity under normal, fault-free operation, while these properties change under faults. In this way, any observed significant deviation of the statistical properties of the residual can be used for the detection of a sensor failure.

Additive faults are detected from mean value changes of residual, for example based on the so-called generalized likelihood ratio test (GLRT). In each time step, this test yields the upper limit for a likelihood ratio, viz. the ratio between the probabilities of two suppositions on a set of sensors: 'an additive fault has occurred within that sensor set' versus 'the complete sensor set is healthy'. A low value of the ratio's upper limit then implies NO additive fault.

Multiplicative faults are detected from the mean value change and the variance change of the residues via the so-called energy detector.

6.2 Problem Statement

In this section, the simple linearized model, developed in Section 1.3.1, us used. For convenience, this model is written in state-space form as follows

$$\dot{x} = A_{cm}x + B_{cm1}d_{cm} + B_{cm2}u_{cm}
y_{cm} = C_{cm}x + D_{cm1}d_{cm} + D_{cm2}u_{cm}$$
(138)

Here the index cm is used to express that the variables are in the Coleman domain. The system states, inputs, disturbances and outputs are defined as

$$x = \left(\Omega_r \quad x_{fa} \quad \dot{x}_{fa} \quad x_{sd} \quad \dot{x}_{sd} \quad \gamma \quad \dot{\gamma} \right)^T \tag{139}$$

$$d_{cm} = \begin{pmatrix} v_{cm1} & v_{cm2} & v_{cm3} \end{pmatrix}^T \tag{140}$$

$$u_{cm} = \begin{pmatrix} \theta_{cm1} & \theta_{cm2} & \theta_{cm3} \end{pmatrix}^{T}$$

$$u_{cm} = \begin{pmatrix} \theta_{cm1} & \theta_{cm2} & \theta_{cm3} & \delta T_g \end{pmatrix}^{T}$$

$$(141)$$

$$y_{cm} = \begin{pmatrix} \Omega_g & \dot{x}_{fa} & \dot{x}_{sd} & \delta M_{zcm1} & \delta M_{zcm2} & \delta M_{zcm3} \end{pmatrix}^T$$
 (142)

The control structure of the underlying wind turbine system is shown in Figure 45, where C_T , C_θ and C_{ind} are the generator torque controller, the collective pitch controller and the individual pitch controller respectively. V_w is the wind speed which is the energy source of the wind turbine system. Due to its stochastic property, it is also a disturbance source of the control system.

The sensors of the blade root moments M_{zi} , i=1,2,3 provide the feedback signals to the individual pitch controller for load reduction. If the sensors send incorrect signals to the controller, the loads are probably *enlarged* instead of reduced. So, it is extremely important to detect a sensor fault as soon as possible.

In the subsection on the wind turbine model, it appeared that the wind speed signals are unknown disturbances in the state *and* output equation.

The classical fault detection methods such as the unknown inputs observer in [14] cannot be directly applied since the disturbance term in the output equation cannot be nulled successfully. Application of the parity space approach to fault detection for deterministic systems may be successful. However, it does not work so well for most of the stochastic systems [30]. The handling of the wind speed disturbance appears a major difficulty.

Although the Coleman transformation yields a time invariant system description in fixed-frame coordinates (138), the *original* system, defined in rotating coordinates, remains time varying. Since one single sensor fault is defined in rotating coordinates, it will result in faults in all three sensors in fixed coordinates (138) due to the Coleman transformation (11). Nevertheless, it is preferable to develop the fault detection approach for the fixed-frame model (138), due to its

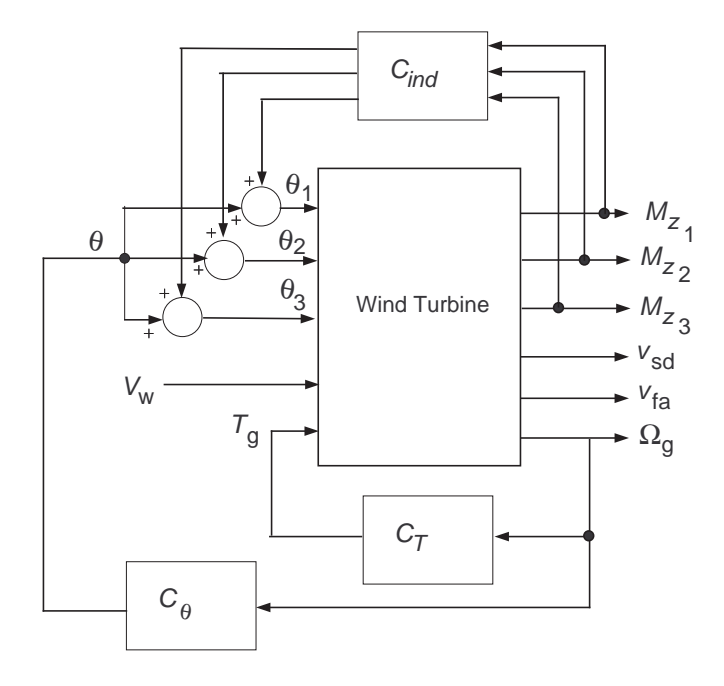


Figure 45 The control structure of wind turbine systems

linearity and time-invariance.

The point of departure for the method development is dual sensor redundancy. It is assumed that two identical blade moment sensors are installed at each blade root for the purpose of reliability and fault tolerance. The dual sensors are divided into two sets. Initially, one set supplies feedback signals to the individual pitch controller while the other set contains the redundant sensors.

The problem considered in this section is the fault detection and isolation issue of the blade root moment sensors for a 3 bladed wind turbine with dual sensors installed, driven by non-white wind speed disturbances; the wind turbine can be modeled by linear periodic equations which can be transformed to linear time invariant equations with modulation requirements on the input and output signals.

6.3 Wind Turbine Modeling via Closed-loop Subspace Identification

The introduction told that the examined methods of fault diagnosis are based on residues from online operating Kalman filters. In order to parameterize a Kalman filter, the dynamic wind turbine behavior must be modeled as a linear time-invariant model that is driven by white noise. A wind turbine is driven by the wind, which varies both slowly and fast. The slow, uniform variations in the wind field allow for considering the operation of a wind turbine in a working point during a certain time, say ten minutes. This enables to linearize the highly non-linear aerodynamic behavior, which is the starting point of the model description in the previous section.

As already mentioned in the previous section, the effect on the wind turbine of fast variations in the wind field, known as turbulence, cannot be assumed to be caused by a limited number of white noise sources. However, this effect can be reasonably well approximated by letting work three partially correlated stochastic signals on the rotor as pure stationary "blade effective wind speeds".

The previous section also showed that a linear model of a wind turbine in a working point is still

time varying. A modulated coupling exists between small deformations in the rotor blades and the tower; the model coefficients depend on the azimuth position of the rotor (instantaneous value of the "rotation angle"). It was shown that a linear time invariant model (LTI) can be derived via azimuth dependent mappings of corresponding variables on the three rotor blades, the Coleman transformation [80]. This yields a model in so called 'fixed-frame coordinates'; coordinates with a meaning of perpendicular *to*, or vertical or horizontal *in* the wind plane. The price of it is azimuth dependent preprocessing of model inputs and post-processing of model outputs.

The transformation of the blade effective wind speeds to fixed-frame coordinates, and thus to inputs of the LTI-model, appears not to introduce *cyclo*-stationarity for a 3 bladed rotor. The fixed-frame wind speed coordinates are still *pure* stationary processes, which is a consequence of the polar symmetry of the turbine rotor (see Lemma 1 on page 71). Thus it is valid to assume an *extended* LTI-model with independent white noise sources as input signals for the wind turbine behavior in turbulence. Such a white-noise driven *extended* model can be successfully derived with an adequate closed-loop system identification technique from records of the three blade root flap moments. The structure of a thus obtained model, the *innovation form*, is such that its parameter matrices can be uniquely and simply mapped to the desired Kalman filter for the generation of residues. Be aware that the Kalman filter is driven by (control) input signals and sensor output signals that are both processed with the azimuth angle. Actually, two identical Kalman filters work parallel: one is driven by a primary sensor set *A*, the other by a secondary, redundant sensor set *B*.

So, we chose to derive an extended model via system identification with blade root moments as output signals; the "extension part" of this model filters, the white noise input signals in such a way that the "wind turbine part" responds in fixed-frame coordinates as if it experienced transformed turbulence, as experienced by three rotating rotor blades, in fixed-frame coordinates.

Another approach to the derivation of such an extended model could be based on factorization of the spectrum matrix of the fixed-frame coordinates of the blade effective wind speeds. This will yield an innovation model with the fixed-frame wind speeds as output signals; see [1] for details on spectral factorisation. This 'wind model' must then be combined with an analyticly derived wind turbine model like the simple one in the previous section or a full dynamic model, which can be obtained with a computer program like Turbu[76].

There are some fault detection approaches for handling systems subjected to unknown inputs [14]. Closed loop subspace identification appeared a suitable technique for the derivation of an extended system model driven by white noise ('innovation model') with active controller. The extended model includes the behavior of the wind and of the open loop wind turbine. The applied technique is also successful if the open loop system is unstable, which is the case for a wind turbine.

The controlled wind turbine system can be represented by the structure shown in Figure 46, where v represents the wind speed and it is approximated by the output of a linear system driven by white noise e. Since we only consider the fault detection issue of the three blade root moments in this section, the other outputs $\{\Omega_r, \dot{x}_{fa}, \dot{x}_{sd}\}$ are not included in the model afterwards. The extended model for the wind turbine behaviour, which has an innovation model structure as argued before, has the following state space parameterisation:

$$x_{k+1} = \overline{A} x_k + \overline{B} u_k^{cm} + K e_k (143)$$

$$y_k^{cm} = \overline{C} x_k + \overline{D} u_k^{cm} + e_k \tag{144}$$

The identification issue now is to determine the system matrix set $\{\overline{A}, \overline{B}, \overline{C}, \overline{D}, K\}$. The gain K can be directly utilized as the steady Kalman filter gain. Detailed explanations on this model are in [91].

Subspace identification has attracted much attention in the last decades. Some pioneered work

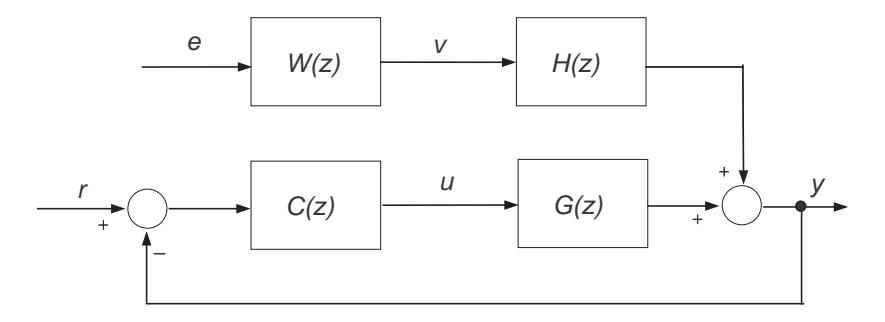


Figure 46 The wind turbine feedback system

can be found in [85, 86, 93, 92]. Recent years the closed loop subspace identification technique also makes a great progress [86, 33, 51, 61, 16, 15]. In all these methods, it is shown in [16, 15] that the methods based on [33, 16, 15] have some potential advantages which is suitable for unstable systems and high order systems. The method adopted in this section is the one described in [33, 16, 15].

The identified model on blade root moment records from simulation data has an order of 20; the wind turbine has 7 states while the other states set up the wind model. Validation results show that the identified model has satisfied precision. The variance account for (VAF) values are over 84%, where VAF is defined as

$$VAF = max\{1 - \frac{var(y_k - \hat{y}_k)}{var(y_k)}, 1\} \times 100\%$$
 (145)

where \hat{y}_k denotes the estimated output signal and var denotes the variance of a stationary signal.

6.4 Fault Detection and Isolation

Next to fault detection, which has already been discussed in the introduction, also fault isolation is a non-trivial issue in the examined sensor failure case. Since the fault detection is performed with the LTI model in fixed-frame coordinates, it is clear that *one* sensor fault results in deviations of the *three* fixed-frame coordinates that relate to the blade moments (3 *virtual sensor* faults). A sensor fault can nevertheless be isolated by combination of two detection procedures, which are based on the difference in the

- mean value and variance between the members of a sensor signal pair on each blade;
- Kalman filter residue behavior between the sensor sets A and B.

These two procedures respectively tell on which blade a sensor fault occurred and to which sensor set the faulty sensor belongs.

6.4.1 Fault Modeling

The faults considered in this section are the additive fault, multiplicative fault, sensor output stuck on a fixed value and slow drifting fault:

- Additive fault $M_{zi}^f = M_{zi} + \Delta M_{zi}$, which is mainly used for describing the sensor bias.
- Multiplicative fault $M_{zi}^f = \delta M_{zi}$, where $0 \le \delta \le \infty$, which is mainly for sensor gain change.

- Output stuck $M_{zi}^f = C_o$, where C_o is a constant, which describes sensor output stuck into a constant value.
- Slow drifting $M_{zi}^f = M_{zi} + \alpha t$, which is used for the slow varying sensor bias.

where $i = 1, 2, 3, \alpha$ is a small variation rate and t is the time.

With the inverse Coleman transformation (see Section 1.3.1), one sensor fault results in the variation of all the virtual moments M_{cm1} , M_{cm2} , M_{cm3} in Coleman domain as follows (i = 1, 2, 3):

Additive fault

$$\begin{pmatrix} M_{cm1}^f \\ M_{cm2}^f \\ M_{cm3}^f \end{pmatrix} = \begin{pmatrix} M_{cm1} + \frac{1}{3}\Delta M_{zi} \\ M_{cm2} + \frac{2}{3}\sin(\psi_i)\Delta M_{zi} \\ M_{cm3} + \frac{2}{3}\cos(\psi_i)\Delta M_{zi} \end{pmatrix}$$

Multiplicative fault

$$\begin{pmatrix} M_{cm1}^f \\ M_{cm2}^f \\ M_{cm3}^f \end{pmatrix} = \begin{pmatrix} M_{cm1} + \frac{1}{3}(\delta - 1)M_{zi} \\ M_{cm2} + \frac{2}{3}\sin(\psi_i)(\delta - 1)M_{zi} \\ M_{cm3} + \frac{2}{3}\cos(\psi_i)(\delta - 1)M_{zi} \end{pmatrix}$$

Output stuck

$$\begin{pmatrix} M_{cm1}^f \\ M_{cm2}^f \\ M_{cm3}^f \end{pmatrix} = \begin{pmatrix} M_{cm1} + \frac{1}{3}(C_o - M_{zi}) \\ M_{cm2} + \frac{2}{3}\sin(\psi_i)(C_o - M_{zi}) \\ M_{cm3} + \frac{2}{3}\cos(\psi_i)(C_o - M_{zi}) \end{pmatrix}$$

Slow drifting

$$\begin{pmatrix} M_{cm1}^f \\ M_{cm2}^f \\ M_{cm3}^f \end{pmatrix} = \begin{pmatrix} M_{cm1} + \frac{1}{3}\alpha t \\ M_{cm2} + \frac{2}{3}\sin(\psi_i)\alpha t \\ M_{cm3} + \frac{2}{3}\cos(\psi_i)\alpha t \end{pmatrix}$$

Note that e.g. in the additive fault the constant sensor bias ΔM_{zi} results in three virtual sensor faults in the Coleman domain: one constant and two time varying biases.

6.4.2 Residue Generation by Kalman Filters

The residue generator that is used for sensor fault detection is shown in Figure 47. For each of two sensor sets, the output signal vector prediction \hat{y}_k on time point k is obtained via a Kalman filter from output signal measurements up to k-1 and input signal values up to k. The residues $r_{A,k}$ and $r_{B,k}$ for the two sensor sets are obtained as the differences $y_{A,k} - \hat{y}_{A,k}$ and $y_{B,k} - \hat{y}_{B,k}$ between the measured and predicted output signal vectors.

The *actual* Kalman filters are represented by blocks KF_A and KF_B in Figure 47 and work in the Coleman domain. This implies that the filter inputs are obtained from the true input and output signals via the inverse of the Coleman transformation matrix (P^{-1} defined in equation 12). Similarly, the filter outputs are mapped to output signal predictions for the determination of the residues via the Coleman transformation matrix itself (P defined in equation 12). As explained in the previous subsection, the sensfor faults f_A and f_B can be additive or multiplicative while a single non-zero element in f_A or f_B will affect all three elements of the actual Kalman filter input $y_A^{\rm cm}$ or $y_B^{\rm cm}$.

In the previous subsection, it was mentioned that a white-noise driven *extended* model has been derived, which includes the wind and the open loop wind turbine behavior. Further, the obtained

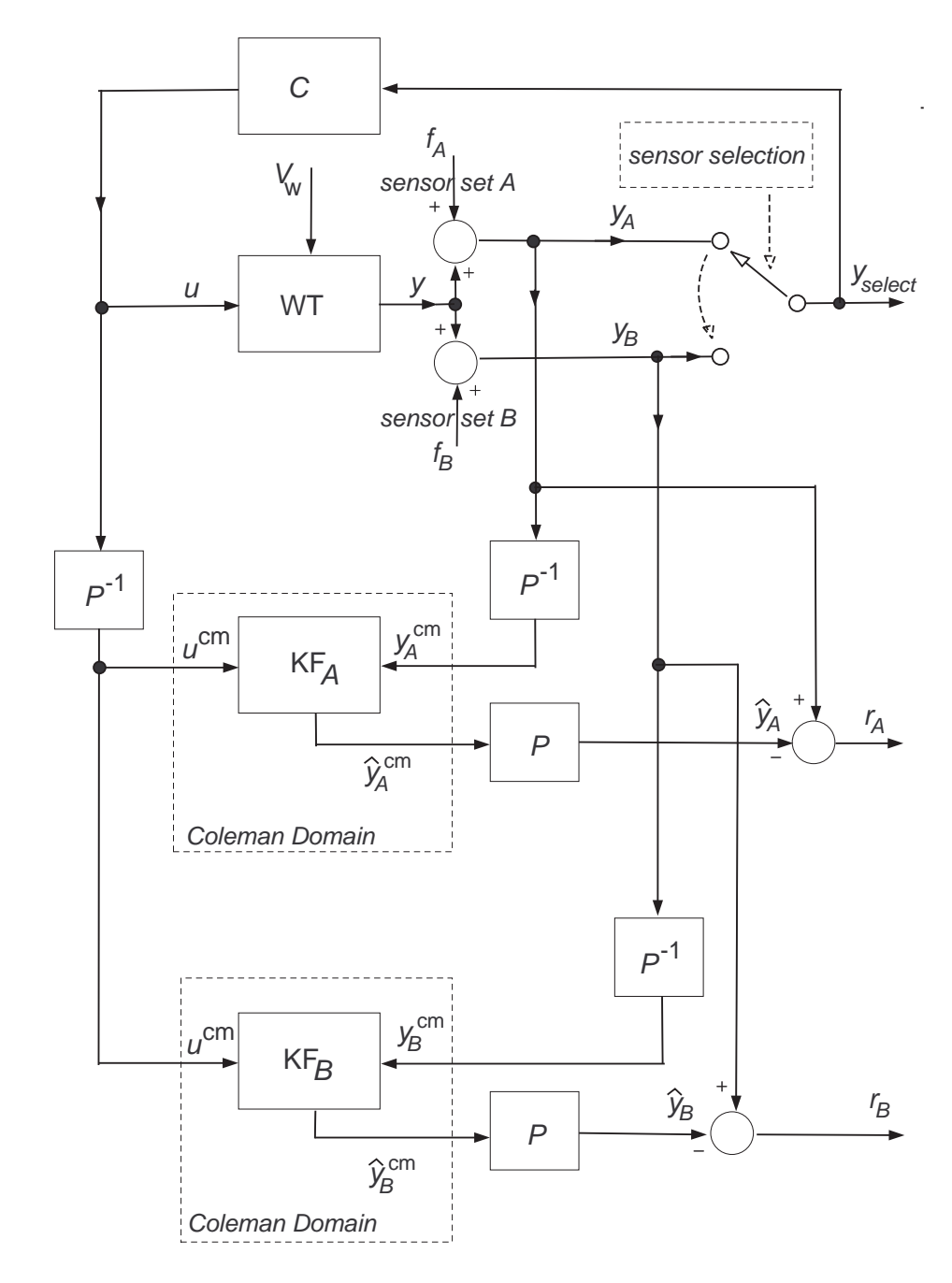


Figure 47 Dual Kalman filter fault detection scheme

state equation 143 and output equation 144 of the model are driven by the same white noise vector process e_k (innovation form). The latter feature, which is specific for the innovation form, allows for expressing *all* noise input signals as a function of state and output signals:

$$e_k = y_k^{\text{cm}} - \overline{C} x_k - \overline{D} u_k^{\text{cm}}$$
(146)

By use of relationship $y_k = P_k \cdot y_k^{\rm cm}$ the model equations 143 and 144 can then be rearranged as

(consider update of x_{k-1} instead of x_k):

$$x_{k} = (\overline{A} - K\overline{C}) x_{k-1} + (\overline{B} - K\overline{D}) u_{k-1}^{cm} + K P_{k-1}^{-1} y_{k-1}$$
(147)

$$y_k = P_k \overline{C} x_k + P_k \overline{D} u_k^{cm} + P_k e_k$$
 (148)

The matrix $(\overline{A} - K\overline{C})$ has eigenvalues in the unit disc [91, 55].

Since e_k has no relationship with passed value e_{k-1} , e_{k-2} , ..., it is intuitively clear that the best output prediction \widehat{y}_k based on output measurements up to k-1 is obtained with the following algorithm:

$$y_{k-1}^{cm} = P_{k-1}^{-1} y_{k-1} (149)$$

$$\hat{x}_{k} = \tilde{A} \hat{x}_{k-1} + \tilde{B} u_{k-1}^{cm} + K y_{k-1}^{cm}$$
 (150)

$$\widehat{y}_k^{cm} = \widetilde{C} \, \widehat{x}_k + \widetilde{D} \, u_k^{cm} \tag{151}$$

$$\widehat{y}_k = P_k \, \widehat{y}_k^{cm} \tag{152}$$

The equations 150 and 151 establish the Kalman filter for the innovation model by equation (143) and 144, where $\widetilde{A} = \overline{A} - K\overline{C}$, $\widetilde{B} = \overline{B} - K\overline{D}$, $\widetilde{C} = \overline{C}$ and $\widetilde{D} = \overline{D}$.

In case of a perfectly modeled system by equation (143) and 144, the difference between the measured and predicted output value in the Coleman domain is given by.

$$y_k^{\rm cm} - \widehat{y}_k^{\rm cm} = \widetilde{C} \,\varepsilon_k + \,e_k \tag{153}$$

where $\varepsilon_k = x_k - \widehat{x}_k$, $\varepsilon_k \sim (0, \sigma_{\varepsilon})$ and e_k is a three-element white noise sequence with mean value $E\{e_k\} = 0$ and 3×3 diagonal covariance matrix $\operatorname{cov}(e_k) = \sigma^2 I$.

We defined the residue as the difference between output measurement and prediction in the 'real domain'. If no sensor failure has occurred before or on time point k, the residue is identified by r_k and is expressed by:

$$r_k = y_k - \widehat{y}_k = P_k(\widetilde{C}(x_k - \widehat{x}_k) + e_k) = P_k\widetilde{C}\varepsilon_k + P_k e_k \tag{154}$$

The 'state estimation error' ε_k will go to zero because $\widetilde{A}=\overline{A}-K\overline{C}$ has eigenvalues within the unit circle. The residual r_k then becomes the modulated white noise process P_k e_k ; Since the three elements of r_k are linear combinations of those of e_k only, so they do NOT depend on e_{k+m} for $m\neq 0$, it is clear the the vector process r_k is also white noise. The covariance matrix of r_k is derived by elaborating the expectation $\mathrm{E}[P_k\ e_k\ e_k'\ P_k']$, with P_k being the Coleman modulation matrix, and $\mathrm{E}[e_k\ e_k']$ equal to σ^2I . It then appears that $\mathrm{cov}(r_k)$ is time-independent but the elements of r_k do depend upon each other. The covariance matrix $\mathrm{cov}(r_k)$ is further referred to as R_k and is expressed by:

$$R_k \stackrel{\Delta}{=} \operatorname{cov}(r_k) = \sigma^2 P_k \ I \ P'_k = \sigma^2 \begin{pmatrix} 2 & \frac{1}{2} & \frac{1}{2} \\ \frac{1}{2} & 2 & \frac{1}{2} \\ \frac{1}{2} & \frac{1}{2} & 2 \end{pmatrix}$$
 (155)

Since the elements of e_k have a Gaussian distribution, the residue vector r_k consists of three correlated Gaussian distributed processes with zero-mean and with equal variances $2\sigma^2$ and covariances $\frac{1}{2}\sigma^2$ as given by equation (155).

In case of a sensor fault, the residues are equal to the difference between the faulty measurements

 y_k^f and the 'sensor fault affected' output predictions \widehat{y}_k^f :

$$r_k^f = y_k^f - \widehat{y}_k^f \tag{156}$$

where output y_k^f equals in case of any sensor failure

$$y_k^f = y_k + \sum_{i=1}^3 f_k^i \tag{157}$$

and output predictions \widehat{y}_k^f follow from the Kalman filter driven by u_k and y_k^f :

$$\widehat{x}_{k+1}^f = \widetilde{A}\widehat{x}_k^f + \widetilde{B} u_k^{cm} + KP_k^{-1}y_k^f$$
(158)

$$\widehat{y}_k^f = P_k \widetilde{C} \widehat{x}_k^f + P_k \widetilde{D} u_k^{cm} \tag{159}$$

With state estimate \hat{x}_k^f split up into \hat{x}_k and $\Delta \hat{x}_k^f$, the residue by equation (156) can be expressed as (combine equation (154), 157 and 159):

$$r_k^f = y_k + \sum_{i=1}^3 f_k^i - P_k \widetilde{C} \, \widehat{x}_k - P_k \widetilde{D} \, u_k^{cm} - P_k \widetilde{C} \, \Delta \widehat{x}_k^f$$

$$= r_k + \Delta r_k^f$$
(160)

with

$$\Delta r_k^f = \sum_{i=1}^3 f_k^i - P_k \widetilde{C} \ \Delta \widehat{x}_k^f, \tag{161}$$

while separate Kalman filter state equations are derived from equation (159) for the update of \widehat{x}_k and $\Delta \widehat{x}_k^f$ (allowed because of linearity; use equation (157) for filter input separation):

$$\widehat{x}_{k+1} = \widetilde{A} \widehat{x}_k + \widetilde{B} u_k^{cm} + K P_k^{-1} y_k$$
(162)

$$\Delta \widehat{x}_{k+1}^f = \widetilde{A} \Delta \widehat{x}_k^f + K P_k^{-1} \sum_{i=1}^3 f_k^i$$
 (163)

Since after some time r_k equals the innovation e_k , it does not contribute to the mean value \overline{r}_k^f of the residue. Thus, Δr_k^f is the only contributor to the mean \overline{r}_k^f so that the non-stochastic $\{f_k^i\}$ are fully responsible for the evolution of \overline{r}_k^f via equation (163) and 161.

6.4.3 Additive fault detection based on mean value observation

The fault detection algorithm according to [30], the so called *CUSUM LS Filter*, is utilized for the mean value change detection of signal ζ_k .

$$\begin{split} \widehat{\vartheta} &= \frac{1}{t - t_0} \sum_{k = t_0 + 1}^t \zeta_k \\ \varepsilon_{k,i} &= \zeta_k - \widehat{\vartheta} \\ s_k^1 &= \varepsilon_k \\ s_k^2 &= -\varepsilon_k \\ g_k^1 &= \max(g_{k-1}^1 + s_k^1 - \mu, 0) \\ g_k^2 &= \max(g_{k-1}^2 + s_k^2 - \mu, 0) \end{split}$$

Alarm if $g_k^1 > h$ or $g_k^2 > h$. After alarm, reset $g_k^1 = 0$, $g_k^2 = 0$. Parameter μ and h need to be designed. μ is used to prevent positive drifting of the mean value and it can be chosen as one half of the expected change magnitude. The robustness and decreased false alarm rate can be achieved by requiring several $g_k^1 > h$ or $g_k^2 > h$ [30].

This method strongly appeals to the intuitive way of fault detection and appears suitable for any additive fault. However, it normally takes a long time to send an alarm after the fault has occurred and it is hard to estimate the time instance of the occurrence of the fault.

6.4.4 Additive abrupt jump fault detection based on Generalized Likelihood Ratio Test (GLRT)

In case of an additive abrupt jump fault, the changing statistic properties of the residues can be used for fault detection. A generalized likelihood ratio test (GLRT) in accordance with [104, 30, 29, 88, 55], is suited for this class of faults. The GLRT method will here be reviewed for the purpose of informing experts in the field of wind energy while fit to the wind turbine system for additive abrupt jump fault detection. A good overview of the strong and weak points of the GLRT is given in [55].

The GLRT yields in each time point k the upper limit of the probability ratio 'YES/NO occurrence of additive fault in a sensor set' anywhere in the interval [k-L,k] (L to be chosen). The determination of this ratio-maximum requires knowledge on the evolution of the mean value \overline{r}_k^f of the residue vector process. Of course, $\{f_k^i\}$ in equation (163) and 161, which is responsible for the evolution of \overline{r}_k^f , can not be isolated from the measurement y_k^f ; otherwise the measurement errors would be known! However, if we assume a potential stepwise error in the measurement, the error f_k^i in the measurement on blade i is defined by its starting point τ^i and size ν^i ; it can be expressed as:

$$f_k^i = V^i \cdot s_{k-\tau^i} \cdot \nu^i \tag{164}$$

with V^i the unit vector e_1 , e_2 or e_3 for i=1,2,3 respectively and $s_{k-\tau^i}$ the unit step function that starts in the (unknown) time point τ^i . Since the amplitude ν^i is constant and the equations $\{163,161\}$ for residue affection by sensor faults are linear, it is allowed to:

- consider the evolution of the sensor fault influences in normalized form;
- deal with the faults from different sensors in separate equation sets.

As a consequence, the equations 163, 161} for $\Delta r_{\rm k}^f$ can be replaced by the following set (i=1)

1, 2, 3):

$$\Delta \widehat{\xi}_{k+1}^{f^i} = \widetilde{A} \Delta \widehat{\xi}_k^{f^i} - K P_k^{-1} V^i s_{k-\tau^i}$$

$$\tag{165}$$

$$g_{k-\tau^{i}}^{i} = V^{i} s_{k-\tau^{i}} + P_{k} \widetilde{C} \Delta \widehat{\xi}_{k}^{f^{i}}$$

$$\Delta r_{k}^{f_{i}} = \nu_{i} g_{k-\tau^{i}}^{i}$$

$$(166)$$

$$\Delta r_k^{f_i} = \nu_i g_{k-\tau^i}^i \tag{167}$$

while

$$\Delta r_k^f = \sum_{i=1}^3 \Delta r_k^{f_i} \tag{168}$$

The intermediate variable $g^i_{k-\tau^i}$ represents the mean residue value from the normalized additive sensor fault V^i $s_{k-\tau^i}$. When we focus on the GLRT it will become clear that the 'scaled mean residues' $\{g_{k-\tau^i}^i\}$ enable to compute the searched ratio-maximum of probability density functions. Therefor, each $g_{k-\tau^i}^i$ has to be evaluated for a range of starting points τ^i with the failure signature equations 165 and 166.

Assume residue realization $\{\rho_j\}$ on time points $\{j|j=k-L,\ldots,k\}$ and let $P(\{\rho_j-\frac{1}{2}\Delta<$ $\varrho_j < \rho_j + \frac{1}{2}\Delta\}$) be the probability that the residues $\{\varrho_j\}$ get values in a δ -environment around this realization ($\Delta = (\delta \ \delta \ \delta)'$). This probability follows straightforward from the probability density functions $\{p(\rho_i)\}$ because the residue vectors are independent stochastic processes. For small δ then holds for the considered probability (short form $P(\{|\varrho_j - \rho_j| < \frac{1}{2}\Delta\})$):

$$P(\{|\varrho_j - \rho_j| < \frac{1}{2}\Delta\}) = p(\rho_{k-L}) \cdot \delta^3 \cdot p(\rho_{k-L+1}) \cdot \delta^3 \cdot \dots \cdot p(\rho_k) \cdot \delta^3 = \prod_{j=k-L}^k p(\rho_j) \cdot \delta^3$$
 (169)

If no sensor failure has occurred before or on time point j the residue ϱ_j becomes equal to the Coleman transformation of the innovation e_j after some initialization time $(r_j$ by equation (154)). The residue r_i consists of three zero-mean correlated Gaussian processes with variances $2\sigma^2$ and covariances $\frac{1}{2}\sigma^2$ as by matrix R_k in equation (155). Identify the supposition 'no sensor failure' as H_0 and let the belonging distribution function of the residue be $p(\varrho_j|H_0)$. It then holds:

$$p(\varrho_j|H_0) = \frac{1}{\sqrt{(2\pi \det[R_j])^3}} \cdot e^{\left[-\frac{1}{2} \varrho_j' R_j^{-1} \varrho_j\right]}$$
(170)

If a failure has occurred on the i^{th} sensor before or on time point j the residue ϱ_j equals $r_j + \Delta r_j^{f_i}$ with r_j the zero-mean Gaussian vector process with covariance matrix R_j and $\Delta r_j^{f_i}$ the evolving mean value of r_i in accordance with equation (165), 166 and 167. Identify the supposition 'failure on $i^{\rm th}$ sensor on time point τ^i with amplitude ν^i ' as $H^i_1(\tau^i,\nu^i)$ and let the belonging distribution function of the residue be $p(\varrho_i|H_1^i(\tau^i,\nu^i))$. It then holds:

$$p(\varrho_{j}|H_{1}^{i}(\tau^{i},\nu^{i})) = \frac{1}{\sqrt{(2\pi \det[R_{j}])^{3}}} \cdot e^{\left[-\frac{1}{2} \left(\varrho_{j} - \nu^{i} g_{j-\tau^{i}}^{i}\right)' R_{j}^{-1} \left(\varrho_{j} - \nu^{i} g_{j-\tau^{i}}^{i}\right)\right]}$$
(171)

The probability that the residues get values in a δ -environment around the realization $\{\rho_j\}$ can now be calculated under the suppositions $H_1^i(\tau^i,\nu^i)$ and H_0 . In other words we can compute the chance that the residue lies in a δ -environment around $\{\rho_i\}$ in case of a failure on the i^{th} sensor on time point τ^i with amplitude ν^i and in case of no sensor failure. Actually, we are interested in the ratio between these chances. For τ^i anywhere in the closed interval [k-L,k], this likelihood

ratio Λ_k^i is expressed as:

$$\Lambda_{k}^{i} \stackrel{\triangle}{=} \frac{P(\{|\varrho_{j} - \rho_{j}| < \frac{1}{2}\Delta\} | H_{1}^{(\tau^{i}, \nu^{i})})}{P(\{|\varrho_{j} - \rho_{j}| < \frac{1}{2}\Delta\} | H_{0})} \bigg|_{j=k-L,\dots,k} =$$

$$\prod_{j=k-L}^{\tau^{i-1}} \frac{e^{\left[-\frac{1}{2} \rho'_{j} R_{j}^{-1} \rho_{j}\right]}}{\sqrt{(2\pi \det[R_{j}])^{3}}} \cdot \delta^{3} \cdot \prod_{j=\tau^{i}}^{k} \frac{e^{\left[-\frac{1}{2} (\rho_{j} - \nu^{i} g_{j-\tau^{i}}^{i})' R_{j}^{-1} (\rho_{j} - \nu^{i} g_{j-\tau^{i}}^{i})\right]}}{\sqrt{(2\pi \det[R_{j}])^{3}}} \cdot \delta^{3}$$

$$\prod_{j=k-L}^{k} \frac{e^{\left[-\frac{1}{2} \rho'_{j} R_{j}^{-1} \rho_{j}\right]}}{\sqrt{(2\pi \det[R_{j}])^{3}}} \cdot \delta^{3}$$
(172)

It is clear that the factors in the numerator and denominator cancel for $j=k-L...\tau^i-1$. So the likelihood ratio Λ_k^i on time point k, which is used for testing if a failure on the $i^{\rm th}$ sensor has occurred in the interval [k-L,k], depends on τ^i and ν^i . Since the same covariance matrix R_j and the same multiplier δ^3 are in the numerator and denominator, only the exp-functions are retained as factors. It is allowed to replace the product of exp-functions by one exp-function with summed exponents:

$$\Lambda_k^i(\tau^i, \nu^i) = \frac{e^{\sum_{j=\tau^i}^k \left[-\frac{1}{2} \left(\rho_j - \nu^i g_{j-\tau^i}^i \right)' R_j^{-1} \left(\rho_j - \nu^i g_{j-\tau^i}^i \right) \right]}}{e^{\sum_{j=\tau^i}^k \left[-\frac{1}{2} \rho_j' R_j^{-1} \rho_j \right]}}$$
(173)

If $\Lambda_k^i >> 1$ then a fault in the $i^{\rm th}$ sensor is very likely, or at least a fault in the sensor set for which Λ_k^i is computed is very likely. However, three items prohibit straightforward detection of a sensor fault with constant amplitude:

- what is a reliable threshold value for sensor fault detection? (>> arbitrary)?
- if a sensor fault has occurred, when did it happen (τ^i unknown)?
- if a sensor fault has occurred, what is its amplitude (ν^i unknown)?

Although the starting point τ^i and amplitude ν^i are unknown, it is yet possible to base the fault detection on the likelihood ratio Λ^i_k . Actually, the threshold test is performed with the potential maximum value of Λ^i_k . It appears possible to compute ν^i such that Λ^i_k is maximal for a certain τ^i in [k-L,k]:

- compute the evolving normalized residue mean $\{g_{j-\tau^i}^i\}$ for $j=\tau^i\dots k$ from the failure signature equations 165 and 166 (replace k by j with initialization $\Delta \widehat{\xi}_{\tau^i}^{f^i}=0$);
- derive ν_{\max}^i from the residue realization $\{\rho_j\}$ and its evolving mean $\{g_{j-\tau^i}^i\}$ such that the exponent $\sum_{j=\tau^i}^k \left[-\frac{1}{2} \left(\rho_j \nu_{\max}^i g_{j-\tau^i}^i\right)' R_j^{-1} \left(\rho_j \nu_{\max}^i g_{j-\tau^i}^i\right)\right]$ in equation (173) is maximal

The potential maximum of Λ_k^i is typed as the *Generalized Likelihood Ratio* \mathcal{L}_k^i (GLR) and the associated threshold test as the *Generalized Likelihood Ratio Test* (GLRT).

The quadratic form of the exponent in the numerator of equation (173) allows for straightforward

determination of ν_{\max}^i from the first derivative:

$$\frac{\mathrm{d}\sum_{j=\tau^{i}}^{k} \left[-\frac{1}{2} \left(\rho_{j} - \nu^{i} g_{j-\tau^{i}}^{i}\right)' R_{j}^{-1} \left(\rho_{j} - \nu^{i} g_{j-\tau^{i}}^{i}\right)\right]}{\mathrm{d}\nu^{i}} = \sum_{j=\tau^{i}}^{k} \left[-\nu^{i} g_{j-\tau^{i}}^{i}' R_{j}^{-1} g_{j-\tau^{i}}^{i} + \frac{1}{2} \left(g_{j-\tau^{i}}^{i}' R_{j}^{-1} \rho_{j} + \rho_{j}' R_{j}^{-1} g_{j-\tau^{i}}^{i}\right)\right] \tag{174}$$

Because of the equal variances $2\sigma^2$ and equal covariances $\frac{1}{2}\sigma^2$ in matrix R_j , the zero-making of the first derivative can be expressed as:

$$-\nu^{i} \sum_{j=\tau^{i}}^{k} g_{j-\tau^{i}}^{i} R_{j}^{-1} g_{j-\tau^{i}}^{i} + \sum_{j=\tau^{i}}^{k} g_{j-\tau^{i}}^{i} R_{j}^{-1} \rho_{j} = 0$$
 (175)

The amplitude $\nu^i = \nu^i_{\max}(\tau^i)$, determined by:

$$\nu_{\max}^{i}(\tau^{i}) = \frac{\sum_{j=\tau^{i}}^{k} g_{j-\tau^{i}}^{i} R_{j}^{-1} \rho_{j}}{\sum_{j=\tau^{i}}^{k} g_{j-\tau^{i}}^{i} R_{j}^{-1} g_{j-\tau^{i}}^{i}},$$
(176)

will yield the maximum value of $\Lambda^i_k(\tau^i,\nu^i)$ for $\nu^i\epsilon R$ because the second derivative of the exponent of the numerator equals $\sum_{j=\tau^i}^k [-g^i_{j-\tau^i}{'}R^{-1}_j g^i_{j-\tau^i}]$, which is always negative.

Thus the GLR or ratio-maximum \mathcal{L}_k^i is determined each time point k by (i) evaluation of Λ_k^i via equation (173) for $\tau^i = k - L \dots k$ with amplitude $\nu_i^{\max}(\tau^i)$ by equation (176), and (ii) taking the maximum of $\Lambda_k^i(\tau^i, \nu_{\max}^i(\tau^i))$ over τ^i in [k - L, k]:

$$\mathcal{L}_k^i = \max_{\tau^i \in [k-L,k]} \Lambda_k^i(\tau^i, \nu_{\max}^i(\tau^i))$$
(177)

The GLRT still requires choices for the 'window length' L and the threshold value for fault detection; the GLR \mathcal{L}_k^i represents the upper limit for the ratio between the probabilities of the suppositions H_1^i and H_0 : 'an additive fault has occurred in the sensor set, most likely sensor i^{th} ' versus 'the complete sensor set is okay'; a value of the ratio's upper limit below a chosen threshold value then implies NO additive fault. Threshold selection is a trade off between the false alarm rate and the detection time.

Since a single sensor fault f^i affects all three elements of the Kalman filter input $y^{\rm cm}$, it will also affect all elements of the output prediction $\widehat{y}^{\rm cm}$ in the Coleman domain. Further, although the 'true' output predictions \widehat{y} are obtained via the 'modulation matrix' P from $\widehat{y}^{\rm cm}$, the sensor fault f^i will yet affect all elements of \widehat{y} . Thus, all three elements of the 'disturbed' residue vector r^f will differ from the 'undisturbed' r. This implicates that the GLRT, when performed for all assumed sensor faults, that is to say for the (alternate) suppositions H^i_1 for i=1,2,3, may yield high values in all three cases. So, the GLRT does not tell which sensor in the fault-identified sensor set is fault. However, when we in addition monitor the mean value change, the faulty sensor can yet be selected from the faulty set. This is fixed by direct comparison of the outputs of the sensor pairs: the output difference from the faulty pair will show a sharp increase of its mean value.

ECN-E-12-028 125

Multiplicative fault detection based on residue variance observation

Detection The multiplicative sensor fault can be described as

$$y_k^f = \Delta_i y_k \tag{178}$$

$$= \Delta_i(P_k\widetilde{C} \ x_k + P_k\widetilde{D} \ u_k^{cm}) + P_k \ e_k \tag{179}$$

where Δ_i is a unit diagonal matrix except that one element is δ_i and $0 < \delta_i < +\infty$. The expression for the residue then becomes:

$$r_k^f = P_k \widetilde{C} \varepsilon_k^f + (\Delta_i - I) P_k \widetilde{C} x_k + (\Delta_i - I) P_k \widetilde{D} u_k + P_k e_k$$
 (180)

Just in the case of additive faults, the residue can be split up in the value r_k by equation (154) that would occur without sensor fault and a contribution from the sensor fault:

$$r_k^f = r_k + \eta_k + (\Delta_i - I)P_k\widetilde{C} x_k + (\Delta_i - I)P_k\widetilde{D} u_k,$$

with η_k resulting from the sensor fault $(\Delta_i - I)y_k$ that is fed into the Kalman filter:

$$\widehat{\xi}_{k+1} = \widetilde{\xi}\widehat{x}_k + KP_k^{-1}(\Delta_i - I)y_k$$

$$\eta_k^{cm} = \widetilde{C}\widehat{\xi}_k$$
(181)

$$\eta_k^{cm} = \widehat{C}\widehat{\xi}_k \tag{182}$$

$$\eta_k = P_k \widetilde{C} \widehat{\xi}_k \tag{183}$$

The deterministic part from $(\Delta_i - I)P_k\widetilde{D} u_k$ does not contribute to the residue variance. However, η_k and $(\Delta_i - I)P_k\widetilde{C} x_k$ definitely make the residue variance change.

The change of the residue variance can be easily observed with the so called *energy detector* according to [46]. The energy detector monitors the sum of the squared residue in a sliding window. An alarm is generated if

$$V(r_i) = \sum_{i=k-N+1}^{k} r_i^2 > h$$

where N is the window size and h is the threshold. This method also appeals to the intuitive way of fault detection.

Since all three elements of the residue are affected by any multiplicative sensor fault, it is not trivial to isolate the faulty sensor. Fortunately, this can be done by the comparison of the outputs of the sensor pairs, just as mentioned above in the case of the additive sensor fault.

Sensor Fault Isolation Logic and Recombination

As shown in Figure 48, there are two sets of sensors, identified by S^A and S^B , which send signals to the corresponding Kalman filters KF_A and KF_B. The individual sensors are $S_1^A, S_1^B, \cdots, S_3^A, S_3^B$ For the two sensors at each blade, the differences $\gamma_i = S_i^A - S_i^B$, i = 1, 2, 3 of their output are monitored all the time. Due to measured noise, γ_i is not equal to zero even when the sensors are not faulty. However, we can monitor the mean value change or variance change of these differences in order to detect in which sensor pair a fault has occurred. Of course, this kind of examination of sensor pairs only works in case of only one sensor fault. In the meanwhile, the sensor set in which a fault has occurred can be detected from the changes of the residues $r_{A,k}$ or $r_{B,k}$ of the two parallel Kalman filters by the CUSUM, GLRT and Energy detector presented be-

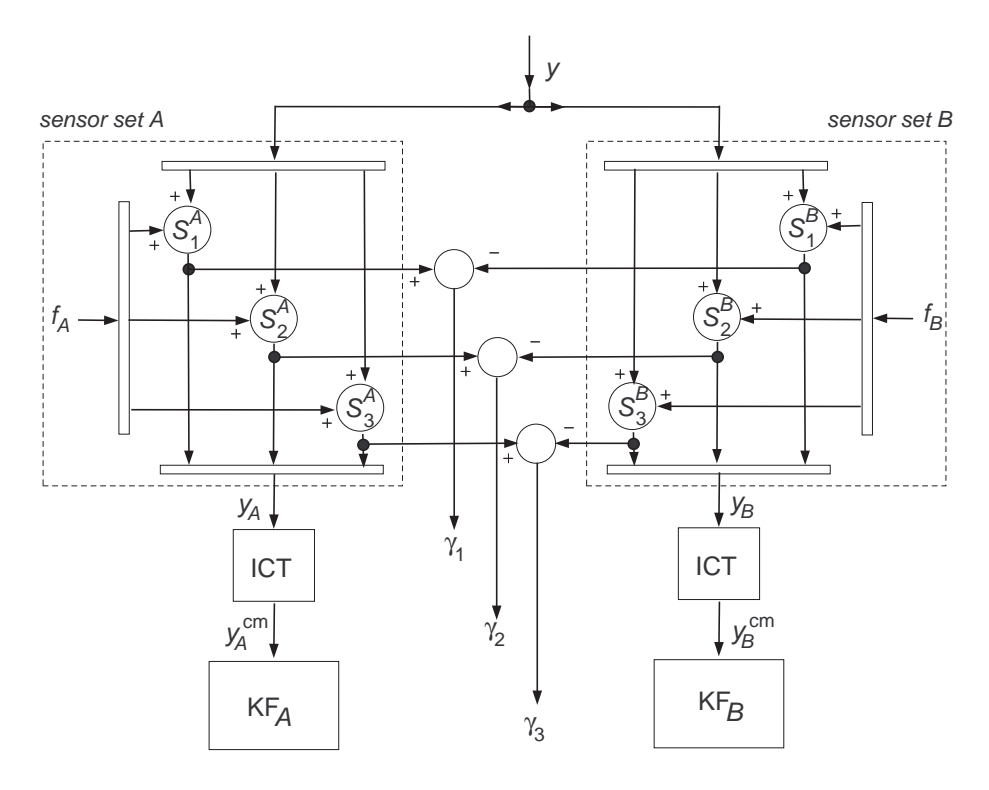


Figure 48 Dual sensor redundancy and dual Kalman filters for fault isolation

fore. For instance, if γ_2 and $r_{A,k}$ have changed, while $r_{B,k}$, γ_1 and γ_3 have not, we can conclude a fault in sensor S_2^A has occurred. If both the residues $r_{A,k}$ or $r_{B,k}$ have changed while the comparison outputs $\gamma_i, i=1,2,3$ have not, the faults are from other parts of the system rather than from the sensors, under the assumption that faults can occur in only one sensor set in a time instance or short time interval. For example, our approach is insensitive to model errors and uncertainties. Althoug the model may be perfect for the wind turbine in its 'design state', a model error will arise when the behavior of a component changes, e.g. by icing, contamination and deterioration.

6.4.7 Fault detection from difference outputs based on GLRT (concepts)

The GLRT could possibly also be applied to the difference output γ_i of sensor pairs In case of dual sensor redundancy, the GLRT would then just tell that a sensor fault has occured close to a certain time-instance. However, the sensor set cannot be identified. When three sensor sets are installed $(S^A, S^B \text{ and } S^C)$, three configurations of difference outputs exist: γ_i^{AB} , γ_i^{AC} and γ_i^{BC} . In case of a sensor fault in a specific set, the GLRT on *one* configuration will not give an alarm; this very configuration identifies the two sound sensor sets.

We expect that the GLRT on the difference outputs is very well suited for fault detection in case of output stuck and multiplicative faults. In both cases the difference outputs often show a *relatively* very significant abrupt jump when the fault appears. The relative size of the jump is often much smaller when the sensor sets are individually considered.

The way of determining the likelihood ratio-maximum (GLR) for suppositions on the residues of the difference outputs must be substantially reviewed: the variance matrix of the residue vector hugely changes when a sensor fault appears. In addition, it is not allowed to use the failure signature equations for the normalized residue affection in case of output stuck and multiplicative faults. Normalized residue affection plays a key role in the determination of the GLR: it enables simple computation of the fault amplitude that maximizes the likelihood ratio. However, we

ECN-E-12-028 127

believe that the concept of normalized residue affection still can be applied as an approximation because of the expected relatively strong abrupt jumps and the limited time window 'k-L,k' for evaluation of the GLR.

6.5 Simulation Results

In this section, we will show some simulation results for several fault scenarios. The simulation is done with a linearized wind turbine model. The wind speed signals for the blades are generated by a lookup table, which caters for the rotational sampling of the wind turbulence by the rotor blades, for the wind shear and for the tower shadow.

Fig 49 to 51 are the simulation results in case of an additive abrupt jump fault in sensor S_2^A (the first sensor at the second blade). Figure 49 shows the comparison output γ_2 of the sensor pair $\{S_2^A, S_2^B\}$ and the mean value change detection output from the CUSUM LS filter. The detector begins to alarm repeatedly after 188s, which identifies a fault in sensor S_2^A or S_2^B . Figure 50 shows the mean value change of the residue of Kalman filter KF_A . The residue of Kalman filter KF_B did not change; the trivial results are not included in a picture. The three subplots in Figure 51 show the likelihood ratio-maximum for the GLRT under the three alternate suppositions of an additive fault in sensor S_1^A , S_2^A amd S_3^A (H_1^1, H_1^2 and H_1^3 versus H_0). It can be seen that under all these three alternate suppositions, the likelihood ratio-maximum has a large peak after the abrupt jump fault in the only sensor S_2^A has occurred. Thus, the faulty sensor in a set can be only *detected* by the GLRT, but it can not be *isolated* out of the sensor set in which it has been detected. The likelihood ratio-maxima for the GLRT on the residues of Kalman filter KF_B were also determined. Since no fault has occurred in sensor set B, the results are trivial (no peaks) and are not pictured.

Figure 52 shows the comparison output γ_2 of the sensors at the second blade when a slow drifting fault starts in S_2^A or S_2^B . The lower subplot shows the estimate of the mean value from the CUSUM LS filter. It can be seen that the alarm frequency is increasing after the slow drifting fault appears. The mean value change of the residue of Kalman filter KF_A is shown in Fig.53. The GLR are shown in Fig.54 for the three alternate suppositions of an *abrupt jump* fault $(H_1^i, i = 1, 2, 3)$. These GLR's show some peaks after the slow drifting fault appears on time point 100s but do *not* estimate the time instance of the fault at all. Nevertheless, we can still conclude from the sensor pair output difference and the GLRT on the residues of KF_A that sensor S_2^A has a slow drifting fault.

The simulation results in case of a sensor output stuck are shown in Fig. 55 and Fig. 56. The CUSUM LS filter has an irregular output. The figures show that the mean value of γ_2 and that of the residue of Kalman filter KF_A have changed. Finally, a multiplicative fault in sensor S_2^A is considered. The fault is a gain change to 1.5 times of its normal value that appears from 300s. Figure 57 and Figure 58 show the detection results of energy detector, which are based on the variance of the sensor pair output difference γ_2 and the residues of Kalman filter KF_A respectively. The sum of the squared output difference γ_2 in a finite window (N points) undergoes a large change quite soon after the appearance of the fault on 300s. The variance of the residues of KF_A also change significantly after 300s; this does not occur with the residues of KF_A (not pictured). It is not difficult to draw a conclusion that the sensor S_2^A has a fault.

6.6 Conclusion

This section presents a method for sensor fault diagnosis (detection and isolation) applied to large scale wind turbine systems. The diagnosis of sensor faults, focused on the flapwise blade root bending moments, is very important for successful reduction of blade loads by controlling the aerodynamic conversion of the rotor blades individually. In a working point, the model of a wind

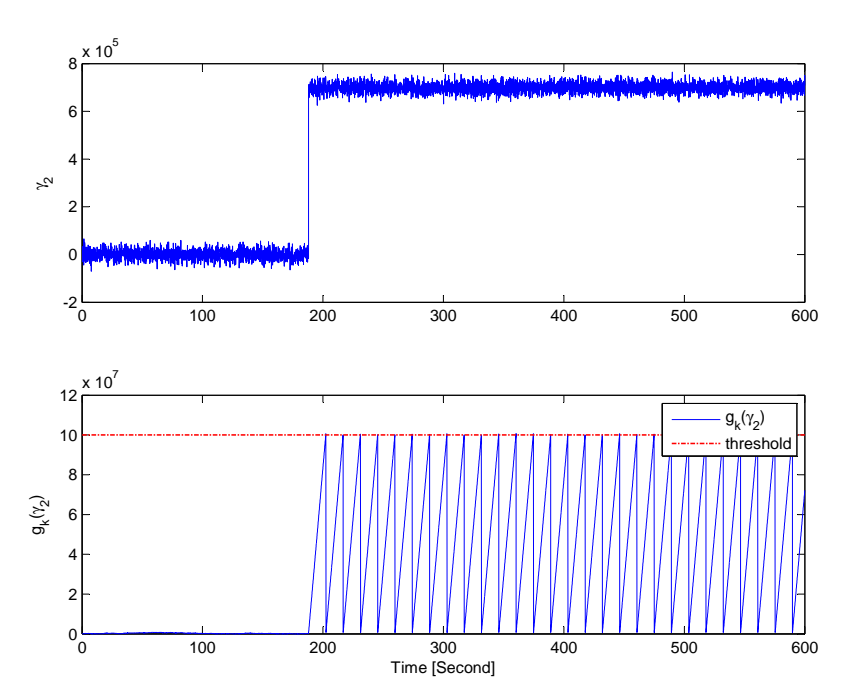


Figure 49 Upper subplot shows the comparison output γ_2 of the sensors at the second blade. The lower subplot shows the mean value change detection estimate from the CUSUM LS filter, where the dashed line is the threshold.

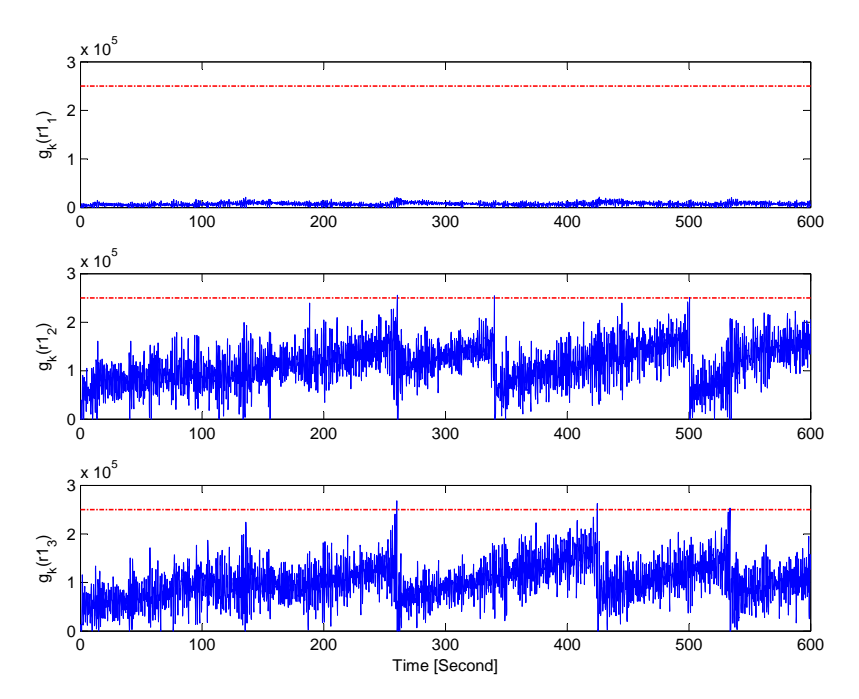


Figure 50 Mean value change detection results of the three residues of Kalman filter KF_B from the CUSUM LS filter, where the dashed line is the threshold.

turbine is still time varying and it is subjected to unknown inputs; the latter cannot be considered as white noise. With the aid of the Coleman transformation and a closed loop subspace identification technique, a linear time invariant model description can be obtained, which is subjected to white noise disturbance. A modified Kalman filter is derived for residue generation.

To the end of sensor fault diagnosis, a mean value method and a generalized likelihood ratio test (GLRT) are derived for additive fault detection. A variance change method has been fit

ECN-E-12-028 129

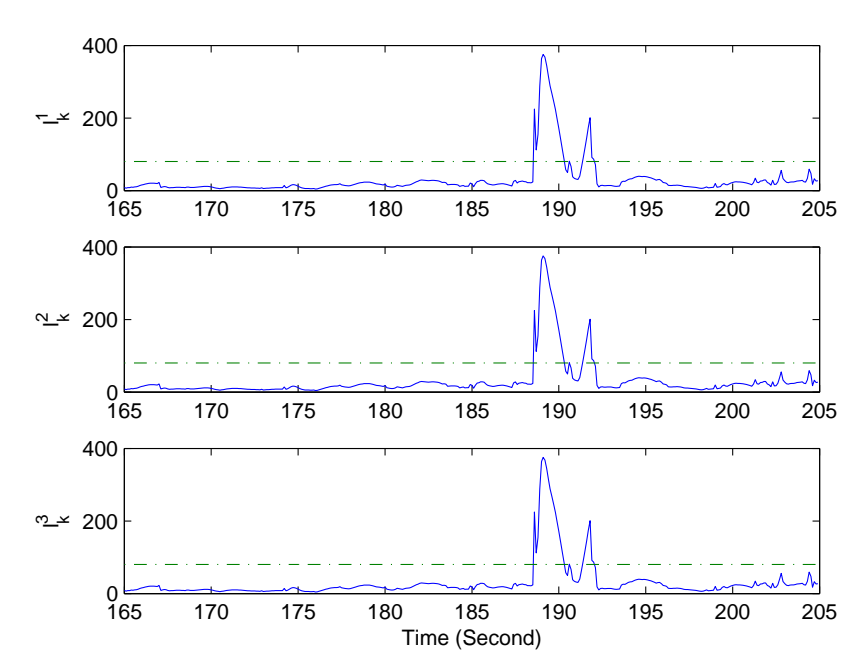


Figure 51 The top subplot contains the likelihood ratio-maximum (GLR) under the alternate supposition of an abrupt jump fault in sensor S_1^A (H_1^1 ; the middle one contains the GLR under alternate supposition H_1^2 (jump in S_2^A); the bottom one under H_1^3 . The dash-dotted lines represent the detection threshold

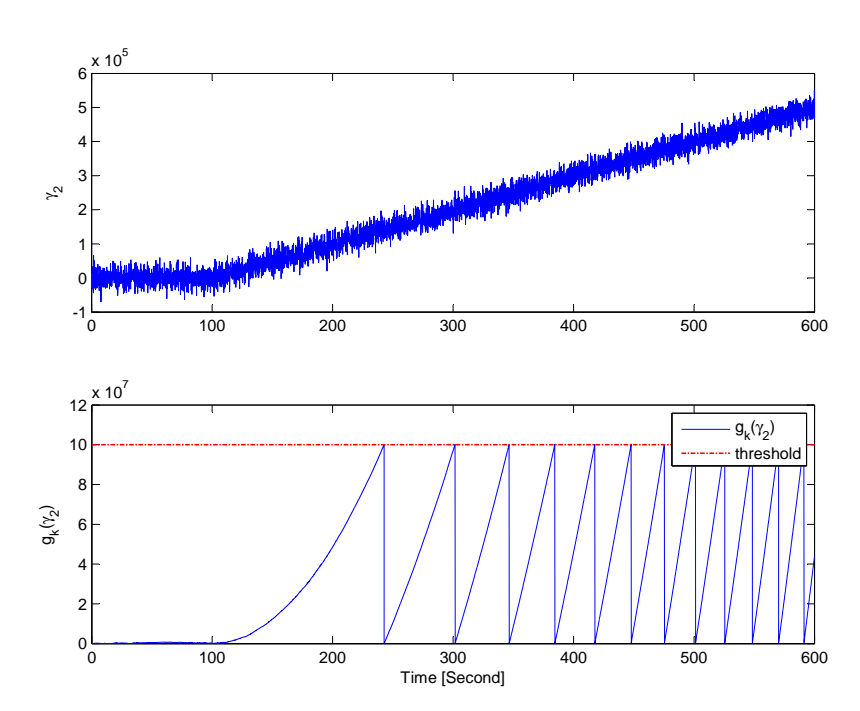


Figure 52 Upper subplot shows the comparison output γ_2 of the sensors at the second blade while sensor S_2^A has slow drifting fault since 100s. The lower subplot shows the mean value change detection estimate from the CUSUM LS filter, where the dashed line is the threshold.

to the detection of multiplicative faults. The fault isolation is proceeded with the aid of the dual redundancy sensors (sensor pairs on each blade) where two Kalman filters are utilized. Simulation results show that the proposed methods are suitable for both sensor fault detection and sensor fault isolation.

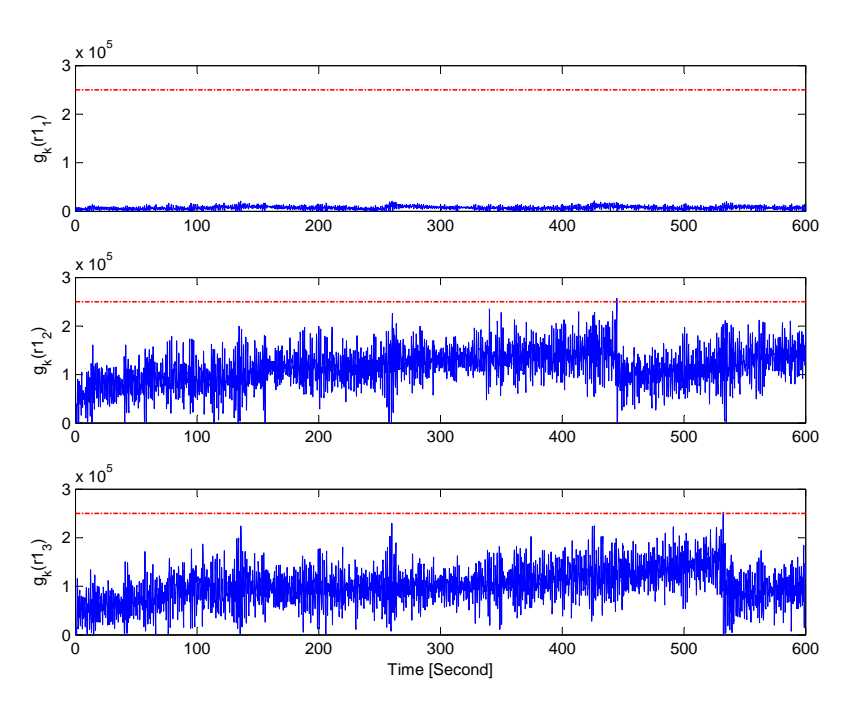


Figure 53 Mean value change detection results of the three innovation outputs of Kalman filter 1 from the CUSUM LS filter while sensor S_2^A has slow drifting fault since 100s.

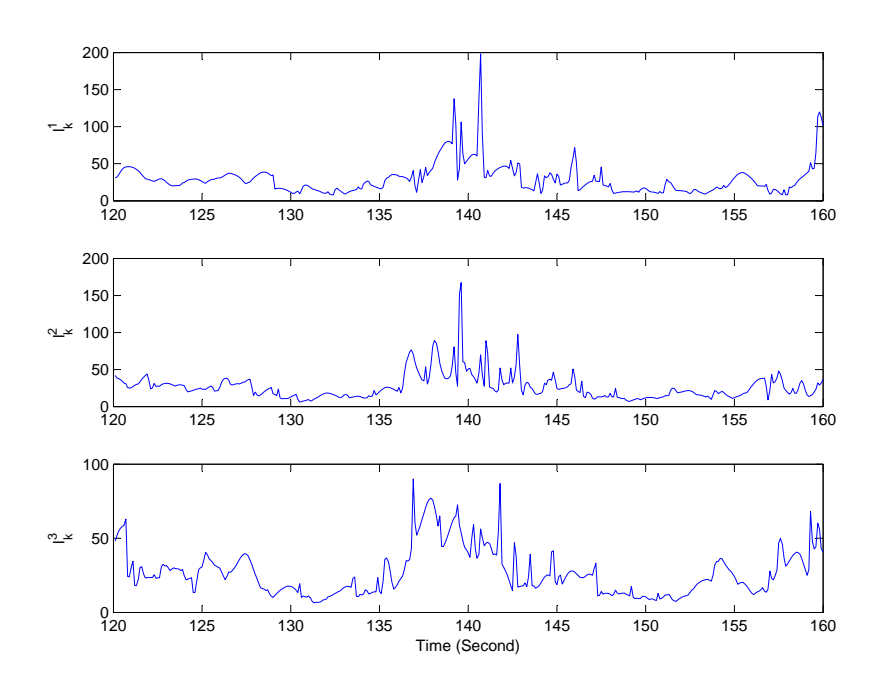


Figure 54 The top subplot is the GLRT result while assuming sensor S_1^A has slow drifting change. The middle one is the GLRT output while assuming S_2^A has slow drifting change. The bottom subplot is the result while assuming that S_3^A has fault.

The sensor fault diagnosis method based on mean value observations appears suitable for the abrupt jump additive fault, the slow drifting additive fault and the output stuck additive fault. However, it cannot provide the time instance on which the fault appears. In contrast, the proposed GLRT gives a good estimate of this time instance in case of abrupt jump fault and this kind of fault is very fast detected. Although the GLRT can also be used for the *detection* of slow drifting faults, the time-instance of appearance cannot be accurately estimated; the test measure is not

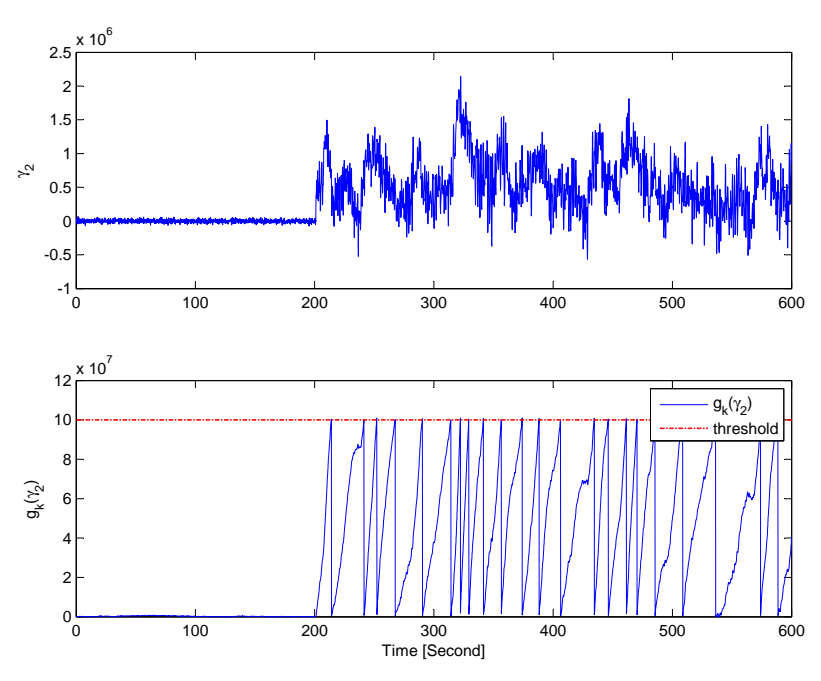


Figure 55 Upper subplot shows the comparison output γ_2 of the sensors at the second blade while sensor S_2^A is stuck at a constant output since 200s. The lower subplot shows the mean value change detection estimate from the CUSUM LS filter, where the dashed line is the threshold.

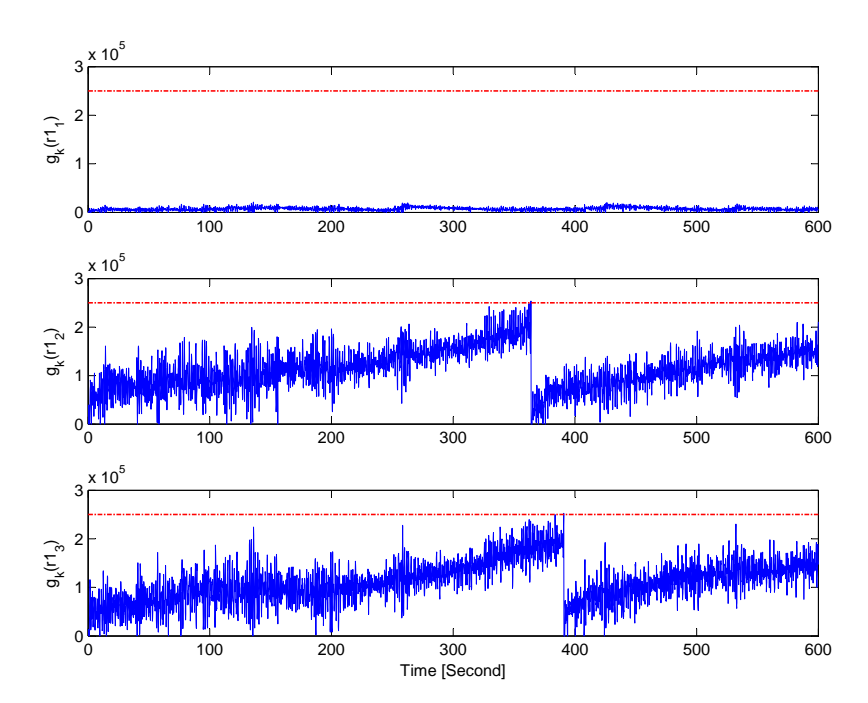


Figure 56 Mean value change detection results of the three residues of Kalman filter KF_A from the CUSUM LS filter while sensor S_2^A is stuck at a constant output since 200s, where the dashed line is the threshold.

sensitive to small slow variations, so the GLRT only responds after a while. Output stuck faults can be fairly well detected with the proposed GLRT while it is expected that a modified GLRT enables much better detection of these faults. As so far, only the proposed variance change method appeared suited for the detection of multiplicative faults.

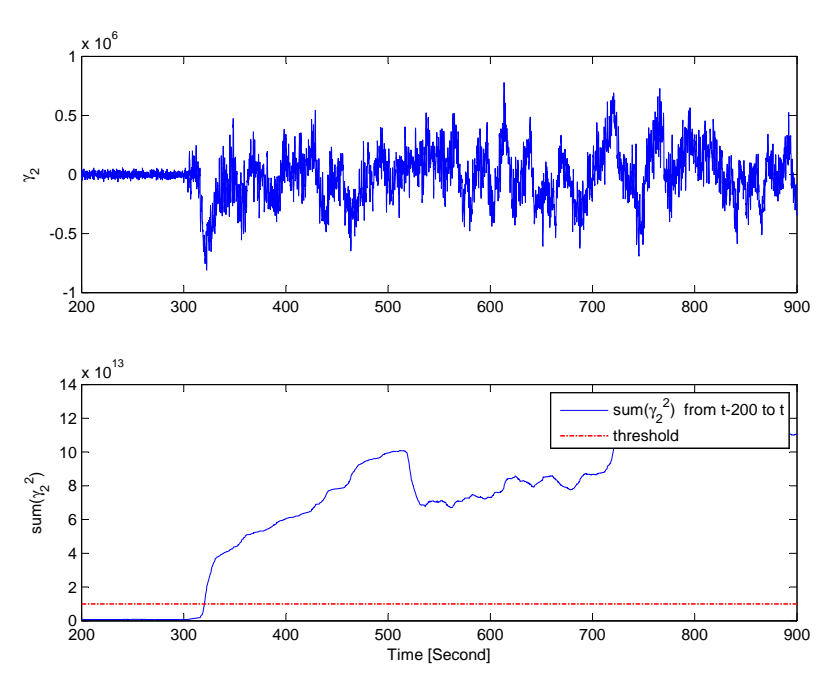


Figure 57 Upper subplot shows the comparison output γ_2 of the sensors at the second blades while sensor S_2^A has a 1.5 times of its normal gain since 300s. The lower subplot shows the variance change detection estimate from energy detector, where the dashed line is the threshold.

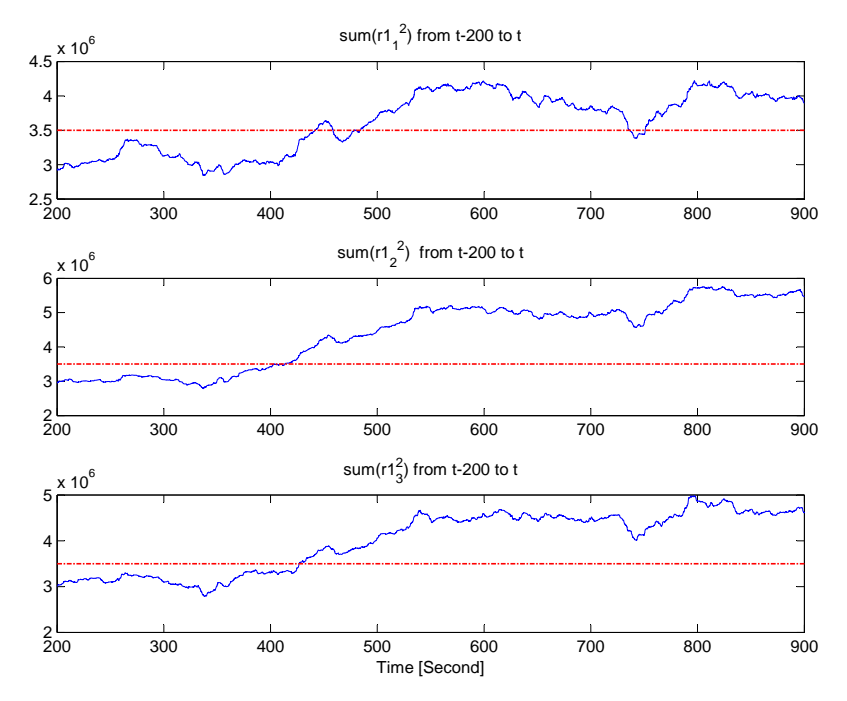


Figure 58 Variance change detection results of the three innovation outputs of Kalman filter KF_A from the energy detector while the gain of sensor S_2^A is changed to its 1.5 times since 300s, where the dashed line is the threshold.

The method presented in this section is limited to one working point. Extending the current result to a large working region or the full region of the wind turbine system is our future work. We foresee to examine alternate designs of the GLRT, like configurations focused on output stuck and multiplicative errors. Furthermore, the modeling error will also be considered into our future

analysis. Some techniques for sensor fault diagnosis in [17, 34] are very useful for our future investigation.

7 Accommodation of yaw motor failures using IPC control

7.1 Summary

The objective of this section is the design of an integrated fault tolerant control (FTC) scheme against the yaw motor failure. To this end, first a yaw motor fault detection scheme is developed. Once the motor failure is detected, the blade pitch angles are controlled individually (IPC) in such a way as to create a yawing moment of the rotor. Advanced algorithms are used for the design of the fault detection scheme and the IPC yaw controller. To this end, first $\mathcal{H}_-/\mathcal{H}_\infty$ index observer approach in finite frequency domain is used in designing the fault detection observer. Next, an \mathcal{H}_∞ pitch controller is designed and integrated with the the fault detection observer. The performance of the integrated FTC solution is verified in TURBU simulations.

7.2 Introduction

In the previous Section 6, methods are developed for the detection and diagnosis of faults in the blade root bending moment sensors. The objective of the present section is to design an integrated fault tolerant control (FTC) scheme that handles yaw motor failures. To this end, a wind turbine model constructed with the software TURBU [76], is used (see Figure 59). Here, the IPC is used to replace the yaw motor, once its failure is detected. The main focus is on the development of a an integrated fault detection and FTC scheme.

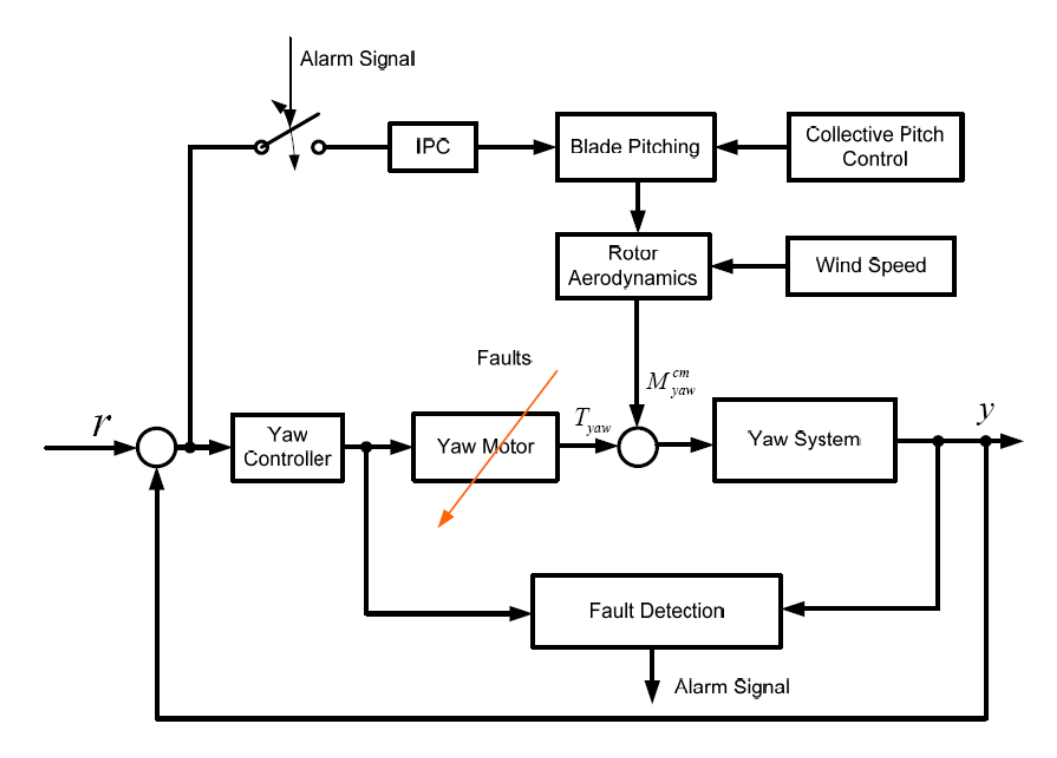


Figure 59 FTC scheme of yaw motor failure in the TURBU model

In the rest of the section, first the TURBU model is described in Section 7.3. It is chosen to design the fault detection observer based on the mixed $\mathcal{H}_-/\mathcal{H}_\infty$ index observer approach in finite frequency domain as proposed in [96]. The detailed observer design and results are presented in Section 7.4. In section 7.5, an \mathcal{H}_∞ controller is developed and integrated with the fault detection observer. The performance of the entire fault tolerant control system is then verified in simulation. Section 7.6 gives some concluding remarks.

ECN-E-12-028 135

7.3 TURBU wind turbine model

TURBU wind turbine model [76] generates a complete linearized aerohydro-elastic model with control, wave and wind inputs for 3-bladed wind turbines.

Specifically, TURBU models the following substructures or components: support structure, drive train, rotor blades, and wake. These individual physical models are then linearized under equilibrium conditions, defined by the equilibrium driving variables, the mean induction speeds in the rotor annuli, and the mean values of linear (set as zero) and angular degrees of freedom (DOFs). These individual models are lumped into one single state-space model description, as schematically illustrated in Figure 60.

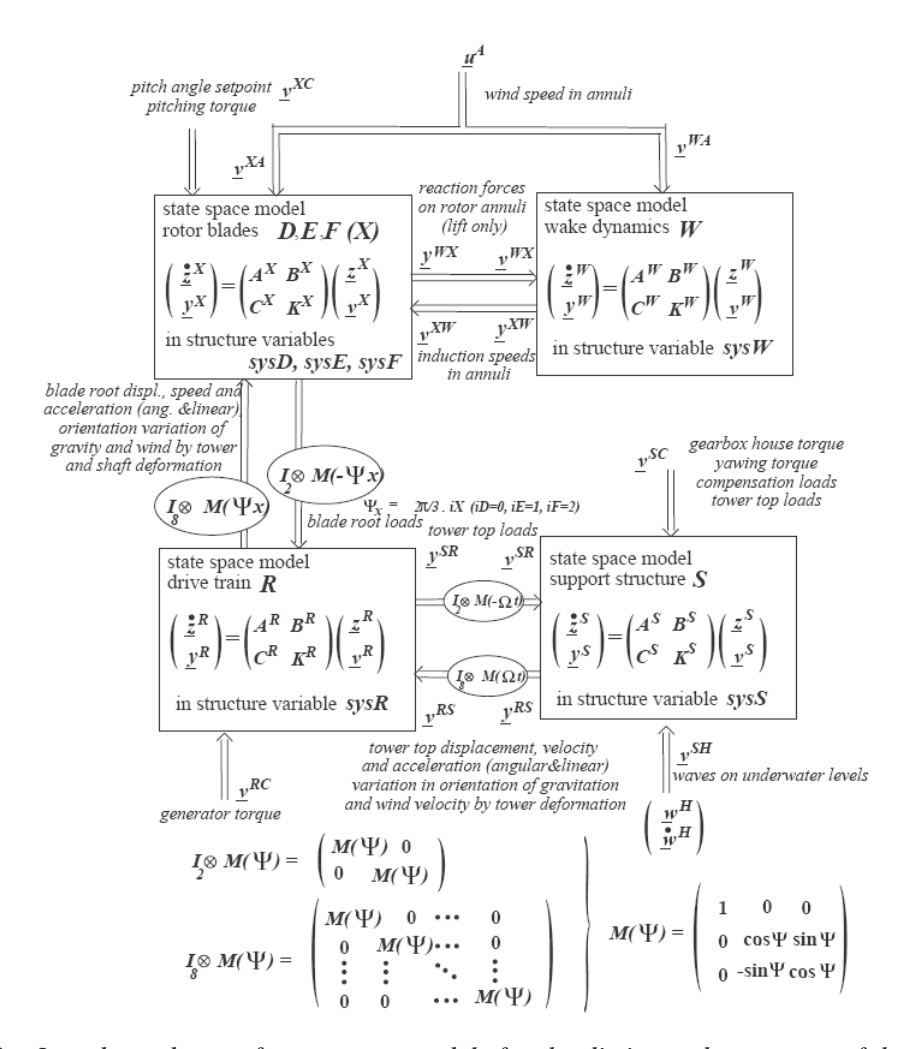


Figure 60 Interdependency of state space models for the distinct substructures of the wind turbine [76].

The matrices in the lumped state-space model depend on the rotor azimuth angle, and are hence periodically varying. As described in Section 1.3.1, Coleman transformation can be used to transform the variables to fixed-frame coordinates, which results in an LTI model. ECN's TURBU program generates a reduced-order continuous-time state-space model of this LTI form with 80

states, 8 inputs, and 10 outputs. This model can be represented as,

$$\epsilon = T_{v_{cm}}^{-1}(\bar{\psi}) \cdot v, \tag{184}$$

$$\dot{x}_{cm} = A_{cm} x_{cm} + B_{cm} \epsilon, \tag{185}$$

$$y_{cm} = C_{cm}x_{cm} + K_{cm}\epsilon, (186)$$

$$y = T_{y_{cm}}(\bar{\psi}) \cdot y_{cm}. \tag{187}$$

Here, v,y represent the I/Os in the fixed coordinates; $\bar{\psi}$ is the rotor Azimuth angle; and $T_{v_{cm}}$ and $T_{v_{cm}}^{-1}$ are respectively the Coleman and inversion Coleman transformation.

Due to the model order reduction, the states have no physical meaning. On the other hand, Table 6 shows the physical entities of the I/Os in the Coleman domain; i.e. ϵ , y_{cm} .

Table 6 I/O description of the TURBU model.

No.	Inputs ϵ	Outputs y_{cm}
1	axial wind	collective pitch angle
2	tilt-oriented wind	tilt pitch angle
3	yaw-oriented wind	yaw pitch angle
4	collective pitch angle	mean flap moment
5	tilt pitch angle	tilt flap moment
6	yaw pitch angle	yaw flap moment
7	yaw torque	rotor speed
8	generator torque	yaw orientation
9		tower nodding speed
10		tower naying speed

7.4 Detecting yaw motor failure by robust detection observer

In this project, we design the fault detection observer based on the mixed $\mathcal{H}_-/\mathcal{H}_\infty$ index observer approach in finite frequency domain as proposed in [96]. Since the technical details of this approach have been presented in section 6 of [96], we shall not repeat them here, but show the details of how to apply this approach in designing the robust detection observer for the yaw motor failure in the TURBU model.

7.4.1 Modeling yaw motor failure as an additive fault

Recall the TURBU model in the Coleman domain:

$$\begin{array}{lll} \dot{x}_{cm} & = & A_{cm}x_{cm} + B_{cm}\epsilon, \\ y_{cm} & = & C_{cm}x_{cm} + K_{cm}\epsilon. \end{array}$$

Here,
$$x_{cm} \in \mathbb{R}^{80}$$
, $\epsilon \in \mathbb{R}^{8}$, $y_{cm} \in \mathbb{R}^{10}$.

From the I/O descriptions in Table 6, we know that the first three inputs are wind signals, ϵ_1 , ϵ_2 , ϵ_3 , which are not measurable. We hence have to treat them as unknown disturbances. The seventh input channel, ϵ_7 , is the yaw torque, and is hence the signal that can be changed due to a yaw motor failure. Therefore, we can define the control and disturbance signals as:

$$u_{cm} = \begin{bmatrix} \epsilon_4 & \epsilon_5 & \epsilon_6 & \epsilon_7 & \epsilon_8 \end{bmatrix}^T, d_{cm} = \begin{bmatrix} \epsilon_1 & \epsilon_2 & \epsilon_3 \end{bmatrix}^T;$$

and correspondingly the control, disturbance, and fault input matrices as

Here, $B_{cm,i}$, $i=1,\dots,8$ represents the i-th column of the matrix B_{cm} . The control, disturbance, and fault feedthrough matrices, $D_{cm,u}$, $D_{cm,d}$, $D_{cm,f}$, can be defined in the same way.

We can now rewrite the TURBU model in a more convenient fashion for fault detection observer design; i.e.

$$\dot{x}_{cm} = A_{cm}x_{cm} + B_{cm,u}u_{cm} + B_{cm,d}d_{cm} + B_{cm,f}f_{cm}, \tag{188}$$

$$y_{cm} = C_{cm}x_{cm} + D_{cm,u}u_{cm} + D_{cm,d}d_{cm} + D_{cm,f}f_{cm}.$$
 (189)

In the case that the yaw motor fails, it cannot provide the yawing torque to the TURBU model; i.e. $u_{cm,4}=0$. This is equivalent to $u_{cm,4}=\epsilon_7$ and $f_{cm}=-\epsilon_7$ in the above model with additive faults.

7.4.2 Optimal observer design method

Fault detection relies on comparing the difference between the measured outputs y_{cm} and the estimated ones from a model, denoted by \hat{y}_{cm} . This difference is called residual, i.e. $r=y_{cm}-\hat{y}_{cm}$. The output estimates, \hat{y}_{cm} , can be computed via an observer; i.e.

$$\dot{\hat{x}}_{cm} = A_{cm}\hat{x}_{cm} + B_{cm,u}u_{cm} + L_o(y_{cm} - \hat{y}_{cm}), \tag{190}$$

$$\hat{y}_{cm} = C_{cm}\hat{x}_{cm} + D_{cm.u}u_{cm}, \qquad (191)$$

$$r = y_{cm} - \hat{y}_{cm}. \tag{192}$$

Denote $e = x_{cm} - \hat{x}_{cm}$. The error dynamics can be written as

$$\dot{e} = (A_{cm} - L_o C_{cm})e + (B_{cm,d} - L_o D_{cm,d})d_{cm} + (B_{cm,f} - L_o D_{cm,f})f_{cm},
r = C_{cm}e + D_{cm,d}d_{cm} + D_{cm,f}f_{cm},$$

The transfer function from d_{cm} , f_{cm} to r is therefore

$$\begin{array}{rcl} r & = & N_d(s)d_{cm} + N_d(s)d_{cm}, \\ N_d(s) & = & C_{cm}[sI - (A_{cm} - L_oC_{cm})]^{-1}(B_{cm,d} - L_oD_{cm,d}) + D_{cm,d}, \\ N_f(s) & = & C_{cm}[sI - (A_{cm} - L_oC_{cm})]^{-1}(B_{cm,f} - L_oD_{cm,f}) + D_{cm,f}. \end{array}$$

Note that in the observer, only the measurable I/Os are processed. Neither wind nor fault signals is used, because they are unknown. The objectives of the observer (190,191,192) are hence to

- stabilize the error dynamics, or *stability*;
- minimize the effect of the unknown disturbance d_{cm} to the residual r, or *robustness*;
- and maximize the effect of the unknown fault f_{cm} to the residual r, or *sensitivity*.

The design, which takes all the three objectives into account is called mixed $\mathcal{H}_{-}/\mathcal{H}_{\infty}$ index observer approach [95]. Here, the \mathcal{H}_{∞} index deals with the robustness; while the \mathcal{H}_{-} index treats the sensitivity.

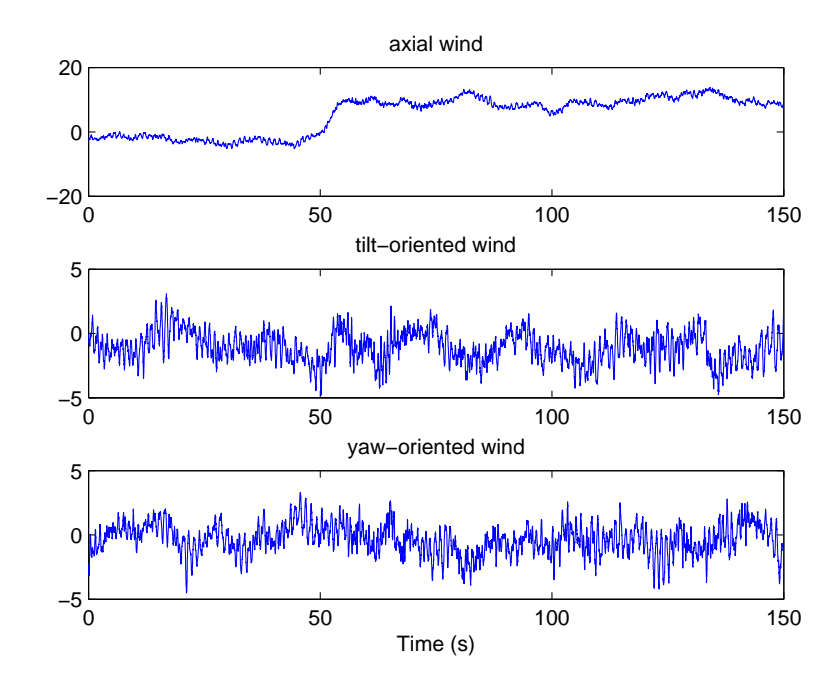


Figure 61 Wind signals.

In this specific wind turbine application, we are only interested in finite specific frequency bands. The wind signals along three directions and their spectrums are respectively plotted in Figures 61 and 62. Obviously, the wind signals have dominating power at low frequencies. We therefore

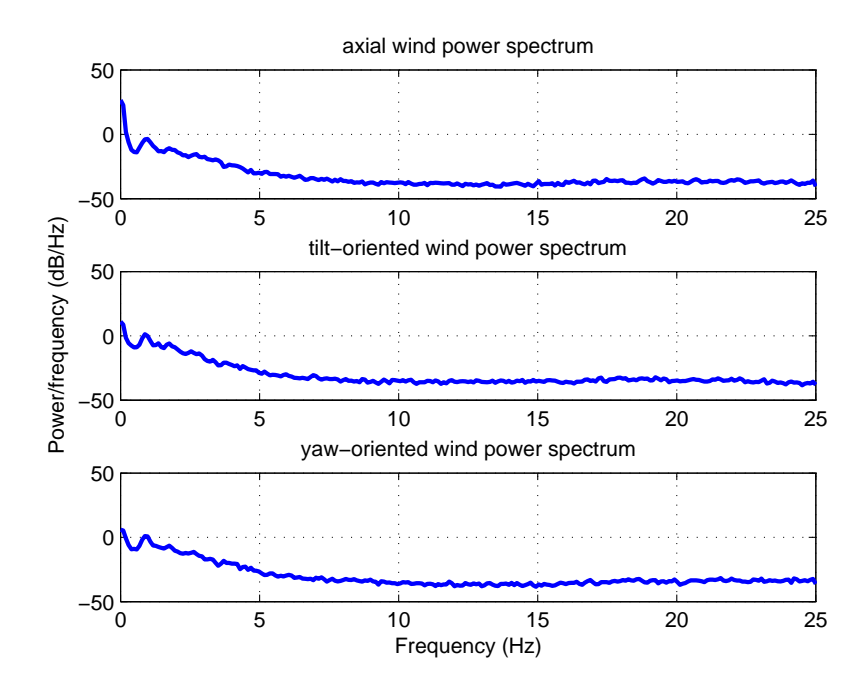


Figure 62 Power spectrums of the wind signals.

consider the robustness of the observer against the wind disturbance especially in the frequency range of [0,2]Hz, or $[0,4\pi]$ rad/s. On the other hand, the yaw motor failure can be described by $f_{cm}=-\epsilon_7$, which is as slow as 0.4deg/s, or 0.007rad/s, due to the limitation in the yawing

motion. The mixed $\mathcal{H}_-/\mathcal{H}_\infty$ approach in finite frequency domain as proposed in [96] is hence a suitable tool to solve this problem. This approach respectively requires solving three groups of linear matrix inequalities (LMIs), listed in the following subsections.

7.4.2.1 Stability conditions

Given arbitrary real scalar q, p, satisfying pq < 0. Find X, Y, such that

$$P_0 \succ 0, \tag{193}$$

$$\begin{bmatrix} 0 & P_0 \\ P_0 & 0 \end{bmatrix} \quad \prec \quad He\left(\begin{bmatrix} -X \\ A_{cm}^T X - C_{cm}^T Y \end{bmatrix} \begin{bmatrix} -qI & pI \end{bmatrix}\right), \tag{194}$$

Here, $He(M)=M+M^*$, for a square matrix M. The superscript "*" denotes conjugate transpose.

7.4.2.2 Robustness conditions

Denote the frequency range of the disturbance signals as $[\omega_{dl}, \omega_{dh}]$. Specifically, in this wind turbine application, $\omega_{dl}=0$ and $\omega_{dh}=4\pi$. Define $\omega_{dc}=(\omega_{dl}+\omega_{dh})/2$. Choose $\gamma>0$. Let X,Y satisfy (194). Let the following matrices be defined, with the new decision variables Q_1,P_1,V_1 .

$$T = \begin{bmatrix} I & 0 & 0 & 0 \\ 0 & 0 & I & 0 \\ 0 & I & 0 & 0 \\ 0 & 0 & 0 & I \end{bmatrix}, \Pi_1 = \begin{bmatrix} I & 0 \\ 0 & -\gamma^2 I \end{bmatrix}, \Xi_1 = \begin{bmatrix} -Q_1 & P_1 + j\omega_{dc}Q_1 \\ P_1 - j\omega_{dc}Q_1 & -\omega_{dl}\omega_{dh}Q_1 \end{bmatrix},$$

$$R_1 = \begin{bmatrix} 0 & 0 & I & 0 \end{bmatrix}, \Psi_1 = T \begin{bmatrix} \Xi_1 & 0 \\ 0 & \Pi_1 \end{bmatrix} T^T.$$

Find Q_1, P_1, V_1 , such that

$$Q_1 \succ 0, \tag{195}$$

$$\Psi_{1} \prec He \begin{pmatrix} \begin{bmatrix} -I & 0 & 0 \\ 0 & -I & 0 \\ A_{cm}^{T} & C_{cm}^{T} & -C_{cm}^{T} \\ B_{cm,d}^{T} & D_{cm,d}^{T} & -D_{cm,d}^{T} \end{bmatrix} \begin{bmatrix} XR_{1} \\ V_{1} \\ YR_{1} \end{bmatrix} ,$$
 (196)

$$0 \succ \begin{bmatrix} -I & 0 & 0 \\ 0 & -I & 0 \\ A_{cm}^{T} & C_{cm}^{T} & -C_{cm}^{T} \\ B_{cm,d}^{T} & D_{cm,d}^{T} & -D_{cm,d}^{T} \end{bmatrix}^{\perp} \Psi_{1} \begin{bmatrix} -I & 0 & 0 \\ 0 & -I & 0 \\ A_{cm}^{T} & C_{cm}^{T} & -C_{cm}^{T} \\ B_{cm,d}^{T} & D_{cm,d}^{T} & -D_{cm,d}^{T} \end{bmatrix}^{\perp,T}$$
(197)

Here, the superscript " \perp " denotes orthogonal complement. Then the maximum singular value of $N_d(s)$ in the frequency range $[\omega_{dl}, \omega_{dh}]$ is upper bounded by γ .

7.4.2.3 Sensitivity conditions

Denote the frequency range of the fault signal as $[\omega_{fl}, \omega_{fh}]$. Specifically, in this wind turbine application, $\omega_{fl} = 0$ and $\omega_{dh} = 0.007$. Define $\omega_{fc} = (\omega_{fl} + \omega_{fh})/2$. Choose $\beta > 0$. Let X, Y

satisfy (194). Let the following matrices be defined, with the new decision variables Q_2, P_2, V_2 .

$$\Pi_2 = \begin{bmatrix} -I & 0 \\ 0 & \beta^2 I \end{bmatrix}, \Xi_2 = \begin{bmatrix} -Q_2 & P_2 + j\omega_{fc}Q_2 \\ P_2 - j\omega_{fc}Q_2 & -\omega_{fl}\omega_{fh}Q_2 \end{bmatrix},$$

$$R_2 = \begin{bmatrix} I & 0 & I & -B_{cm,f} \end{bmatrix}, \Psi_2 = T \begin{bmatrix} \Xi_2 & 0 \\ 0 & \Pi_2 \end{bmatrix} T^T.$$

Find Q_2, P_2, V_2 , such that

$$Q_2 \succ 0, \tag{198}$$

$$\Psi_{2} \prec He \begin{pmatrix} \begin{bmatrix} -I & 0 & 0 \\ 0 & -I & 0 \\ A_{cm}^{T} & C_{cm}^{T} & -C_{cm}^{T} \\ B_{cm,f}^{T} & D_{cm,f}^{T} & -D_{cm,f}^{T} \end{bmatrix} \begin{bmatrix} XR_{2} \\ V_{2} \\ YR_{2} \end{bmatrix},$$
(199)

$$0 \succ \begin{bmatrix} -I & 0 & 0 \\ 0 & -I & 0 \\ A_{cm}^T & C_{cm}^T & -C_{cm}^T \\ B_{cm,f}^T & D_{cm,f}^T & -D_{cm,f}^T \end{bmatrix}^{\perp} \Psi_2 \begin{bmatrix} -I & 0 & 0 \\ 0 & -I & 0 \\ A_{cm}^T & C_{cm}^T & -C_{cm}^T \\ B_{cm,f}^T & D_{cm,f}^T & -D_{cm,f}^T \end{bmatrix}^{\perp,T} . \tag{200}$$

Then the minimum singular value of $N_f(s)$ in the frequency range $[\omega_{fl}, \omega_{fh}]$ is lower bounded by β .

7.4.2.4 Summary of the design method

Algorithm 7.1 (Observer design by the mixed $\mathcal{H}_-/\mathcal{H}_\infty$ index approach in finite frequency domain).

- 1 Choose the bounds, $\gamma, \beta > 0$, the frequency ranges, $[\omega_{dl}, \omega_{dh}]$ and $[\omega_{fl}, \omega_{fh}]$, and the scalars p, q.
- 2 Find X, Y, Q₁, P₁, V₁, Q₂, P₂, V₂, such that the LMIs (193, 194, 195, 196, 197, 198, 199, 200) hold.
- 3 Compute the observer gain by

$$L_o = (Y \cdot X^{-1})^T.$$

The observer such designed stabilizes the error dynamics of the observer, and guarantees the performance of the observer, in terms of its robustness to the wind disturbances and its sensitivity to the fault signal. This design problem can be solved by the standard SDP toolboxes, like YALMIP [52].

7.4.3 Implementation of the design method

Recall that $x_{cm} \in \mathbb{R}^{80}$. The order of the model is too large for the optimal design algorithm 7.1 to be computed on a normal PC. A model order reduction is hence essential. To this end, we follow the standard procedures of a balanced realization, and an elimination of those balanced model states corresponding to relatively small Hankel singular values. The criteria of the model reduction is to enforce the DC gain of the reduced model to match that of the original system.

In this particular wind turbine application, we found that the order of the reduced state-space model has to be smaller than 9, in order for the optimal design algorithm to be computable on a normal PC. In fact, with a ninth order reduced model, it took 1.8 hours to solve the LMIs (193, 194, 195, 196, 197). On the other hand, by plotting the magnitude responses of the transfer functions of the original system, we found that the bandwidth of the system is as low as 1rad/sec; and the transfer functions behave like first-order systems. These motivated us to reduce the order of the original TURBU model to 2, which was further reduced to 1 by a minimal realization.

With this first-order model, we then implemented Algorithm 7.1, with following parameters:

$$\gamma = 10^{-3}, \beta = 10^{-2}, \omega_{dl} = 0, \omega_{dh} = 4\pi, \omega_{fl} = 0, \omega_{fh} = 0.007, p = 1, q = -2.$$

Unfortunately, Algorithm 7.1 did not end up with a feasible solution. We also tried to tune the parameters listed above, but still could not get a feasible solution. This motivated us to get rid of some of the LMI constraints listed in Algorithm 7.1.

Indeed, what we can discard are the LMIs for the sensitivity performance. This is because the fault that we are dealing with is the yaw motor failure. This is a very severe fault, rather than a tiny change in the yawing torque that has to be detected by an observer, which is highly sensitive to it. After deleting the sensitivity LMIs, a feasible solution was found for the set of LMIs (193, 194, 195, 196, 197); i.e. with only the stability and robustness constraints. The observer gain L_o was found to be

$$[10.0315, -83.4437, 1230.1, 0.0002, -0.00035, 0.0059, 142.8778, -813.15, -226.6369, 3.7882].$$

The continuous-time observer (190,191,192) then has to be discretized at the sampling frequency of 50Hz, which is the sampling frequency used by the controllers in the TURBU model.

7.4.4 Simulation results

In this section, we show the fault detection results using the optimal observer designed in the previous section, which is robust against wind disturbances.

We used the *MatLab* file "sim_ttb_tbu_incl_YAW.m" from ECN in simulating the TURBU model, together with the wind data contained in "wind.mat". Three "abnormal" events were considered in the simulations:

- a big step change in the axial wind from 50 seconds on, see Figure 61;
- a wind gust in the time interval [50, 60] seconds, see Figure 61;
- yaw motor failure from 80 seconds on, see Figure 63.

The wind orientation and rotor orientation during the simulation are shown in Figure 64. Obviously, without the yawing torque, the rotors could not follow the wind orientation, which then reduced the power production of the turbine. This is obviously what we have to handel by the controller reconfiguration later on.

The fault detection result is shown in Figure 65. The 2 norm of the residual vectors at each sampling instant was computed. The detection threshold was chosen as 2.5×10^{18} . The detection delay was 1.44 seconds. Two observations were made from the result.

• The residual is robust to the step change in the axial wind. To further elaborate on this, we designed an observer, only stabilizing the error dynamics, instead of guaranteeing the

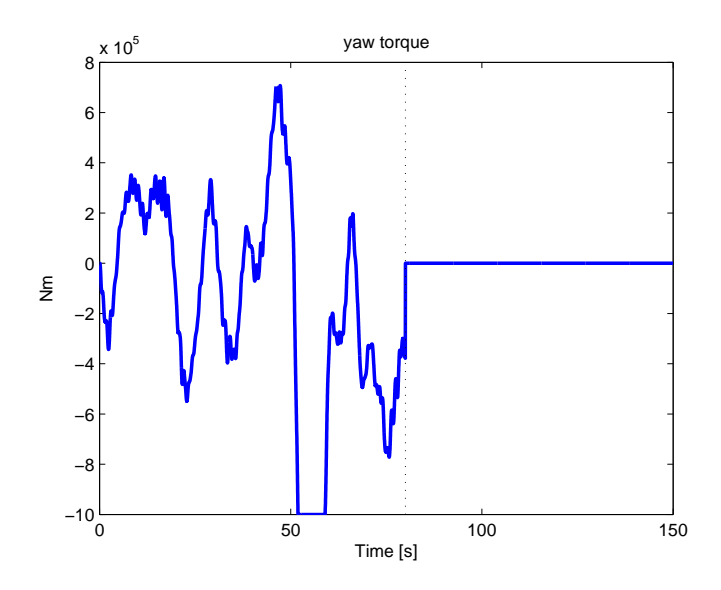


Figure 63 Yaw motor torque with a failure from 80 seconds.

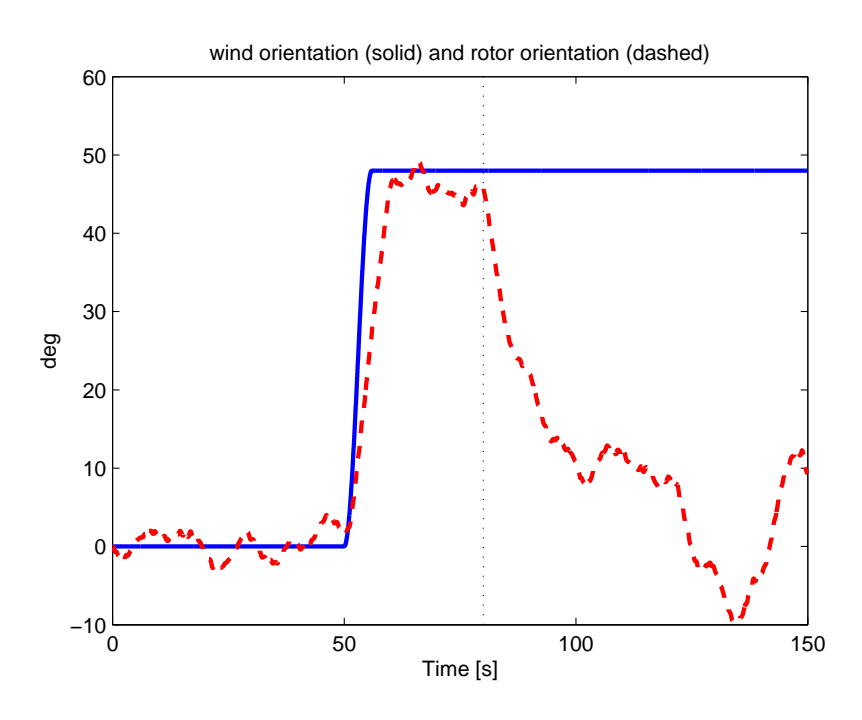


Figure 64 Wind and rotor orientation with the yaw motor failure from 80 seconds.

robust performance. The detection result is shown in Figure 66. Clearly, without the robustness, the yaw motor failure is masked beneath the wind disturbances, and cannot be detected.

• The yaw motor failure results in an increase in the residual energy, much bigger than the wind gust did.

We finally did a further verification of the robustness of the designed observer to the wind disturbances. We doubled the two outputs from the *MatLab* funciton "genwindgust.m", and simulated the TURBU model and the observer all over again. The result is shown in Figure 67. Obviously, the doubling of the wind gust strength did not invalidate the robust performance of the observer.

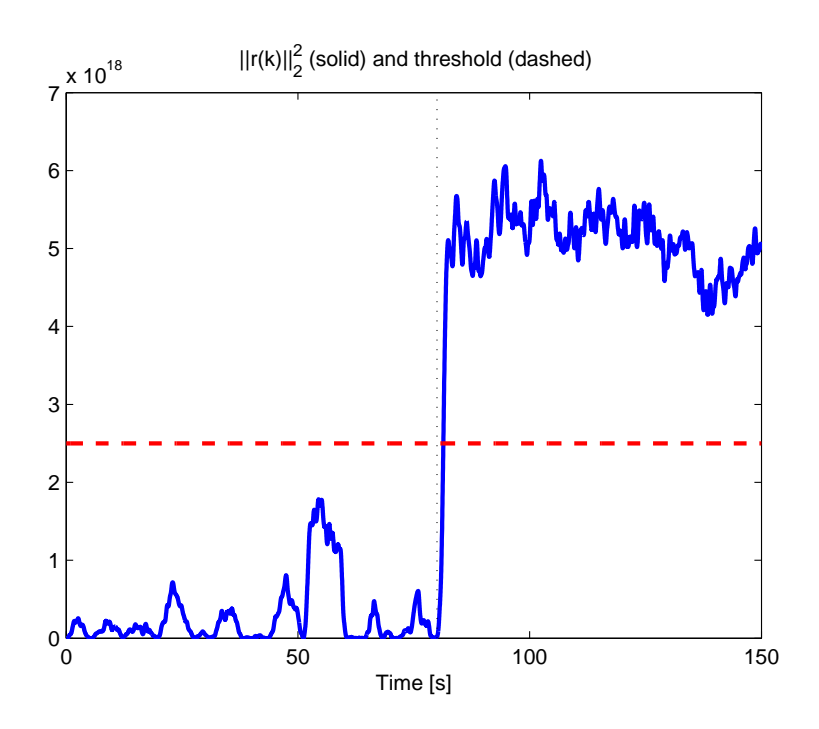


Figure 65 Detecting the yaw motor failure with a robust observer.

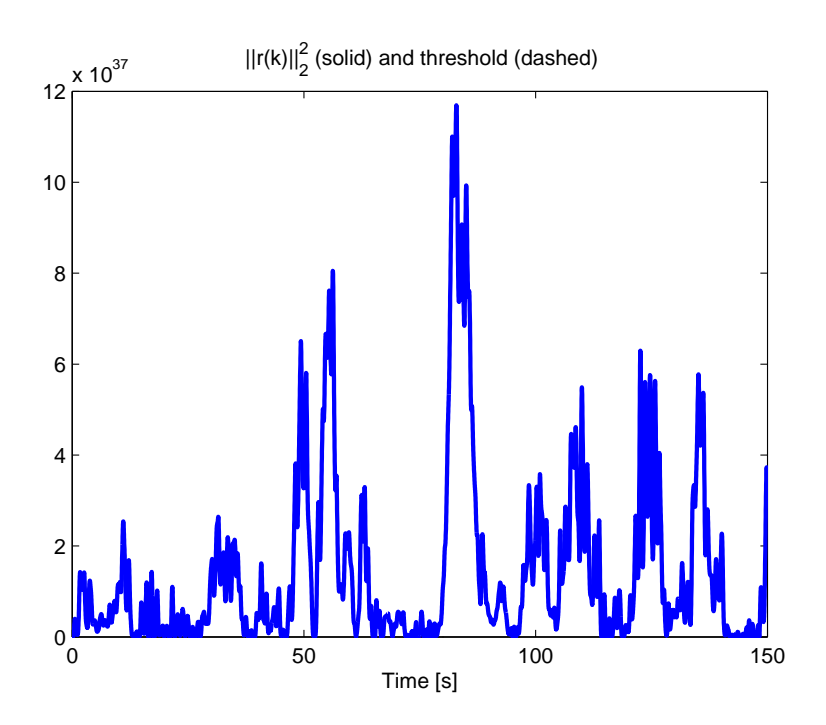


Figure 66 Detecting the yaw motor failure with a stable-only observer.

It is also worth mentioning that the large magnitudes of the residual energy are due to the reduction of the TURBU model from 80-th order to first order, since the model reduction is inevitable in using Alg. 7.1.

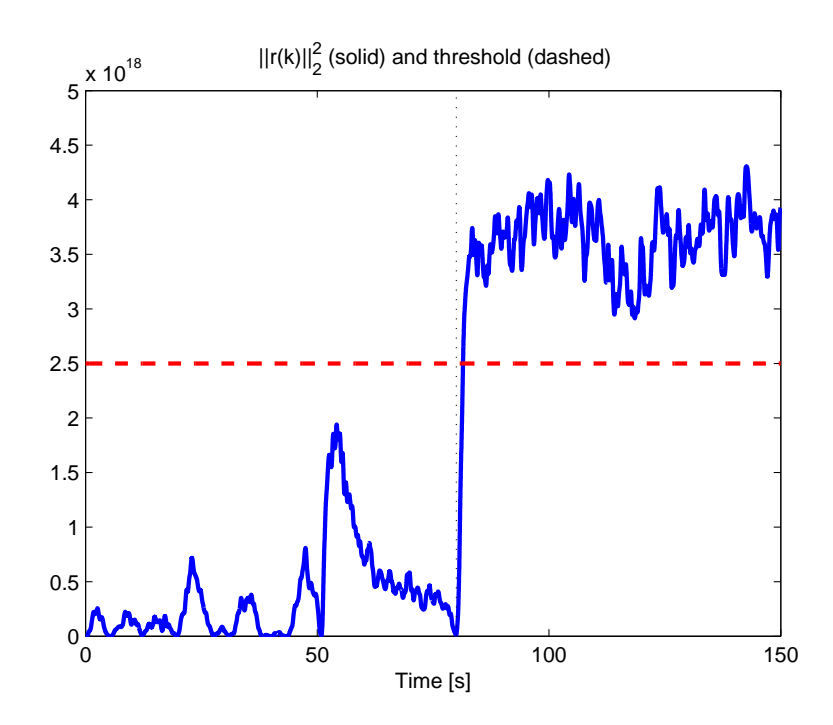


Figure 67 Detecting the yaw motor failure with a robust observer in the presence of doubled wind gust.

7.5 Control reconfiguration via IPCs

7.5.1 Control objectives

The consequence of the yawing motor failure has been illustrated in Figure 64. Obviously, the rotor cannot be directed to the wind orientation, when no yawing actuation is available in the plant. This then significantly reduces the power production, and may even damage the turbine.

The main objective is therefore to use the "redundant" actuators in the turbine to compensate for the loss of the yawing motor. As introduced in section 7.2, we intend to use the individual pitch controllers (IPCs) to fulfill this task. This is possible, because the input "yaw pitch angle" has a significant influence on the output "yaw orientation", whose transfer function is shown in Figure 68. Here, the transfer function is derived from the TURBU model in the Coleman domain as given in (184, 185, 186, 187), and has an order of 80. The first control objective is to track the wind orientation by designing the control signal of the "yaw pitch angle".

On the other hand, from Figure 61, the "yaw-oriented wind" is the disturbance to the yawing dynamics, and has to be taken into account in the controller design. The transfer function is shown in Figure 68. The second control objective is hence to reject the effect of the unknown "yaw-oriented wind".

Besides, the actuator limitations have to be taken into account. Since ECN is still in the process of patenting its constrained IPC controller, it is not the scope of the current SusCon project to verify it in the FTC design.

Taking into account the above objectives, we chose to use \mathcal{H}_{∞} control design to improve the tracking and disturbance rejection performance.

7.5.2 Control design

The \mathcal{H}_{∞} control design considers the closed-loop plant with a structure illustrated in Fig. 70.

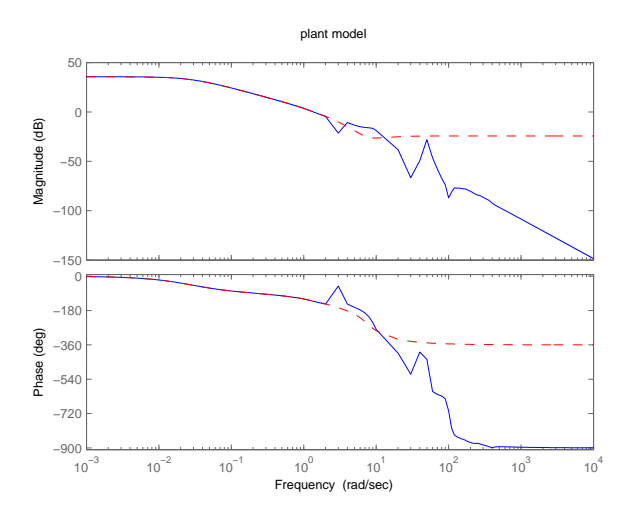


Figure 68 Transfer function from yaw pitch angle to yaw orientation. Solid: the original 80th-order model. Dashed: 2nd-order reduced model.

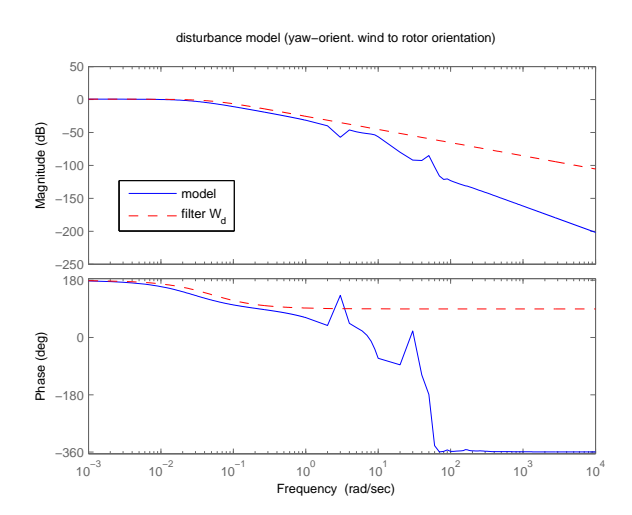


Figure 69 Transfer function from yaw-oriented wind to yaw orientation. Solid: the original 80th-order model. Dashed: upper-bounding 1st-order filter with matched DC gain, W_d .

Here, W_r, W_u, W_e, W_d are weighting filters. The \mathcal{H}_{∞} controller $K_c(s)$ can be designed by solving the following problem.

$$\min_{K_c(s)} \|H(s)\|_{\infty},$$

where the "interconnection matrix" is defined by

$$\left[\begin{array}{c} Z_e(s) \\ Z_u(s) \end{array}\right] = H(s) \cdot \left[\begin{array}{c} D(s) \\ R(s) \end{array}\right].$$

Here, Z, D, R respectively represent the Lapalace transform of the time-domain signals z, d, r. This problem can be solved by an LMI approach [24].

Unfortunately, the original 80th-order model induces heavy computational burden for an \mathcal{H}_{∞} control design. We shall also first reduce the model order. Similar to the observer design, we

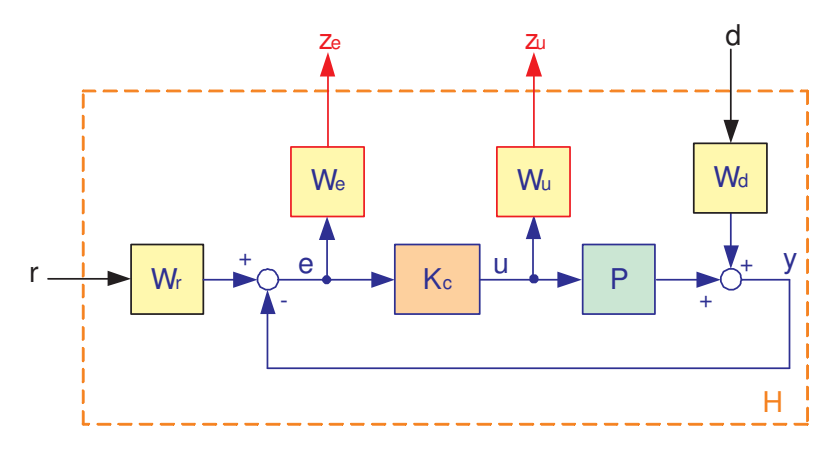


Figure 70 Interconnection structure for \mathcal{H}_{∞} control design.

reduced the plant model to the following 2nd-order description,

$$\frac{Y_{cm,8}(s)}{\mathcal{E}_6(s)} = \frac{0.06101s^2 - 0.4258s + 3.768}{s^2 + 2.245s + 0.06244}.$$
 (201)

For the disturbance model, we simply used an upper-bounding 1st-order filter, i.e. W_d , with matched DC gain of the following form,

$$W_d(s) = \frac{-0.05387}{s + 0.05}. (202)$$

The other weighting filters were chosen as

$$W_u = 0.5, W_r(s) = \frac{0.1}{s + 0.1}, W_e(s) = \frac{5s + 0.05}{s^2 + 5s + 0.01}.$$

Here, W_e was chosen to yield good tracking performance and also to reduce the speed of the closed-loop response due to the yawing motion limitation, whose bode plot is illustrated in Fig. 71.

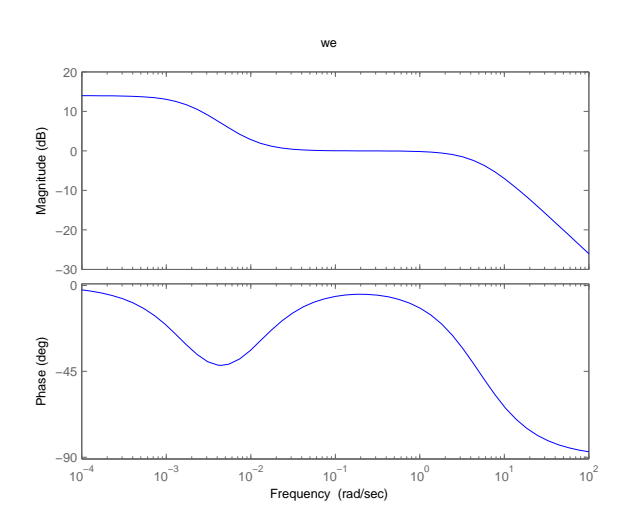


Figure 71 Bode plot of the weighting filter, W_e .

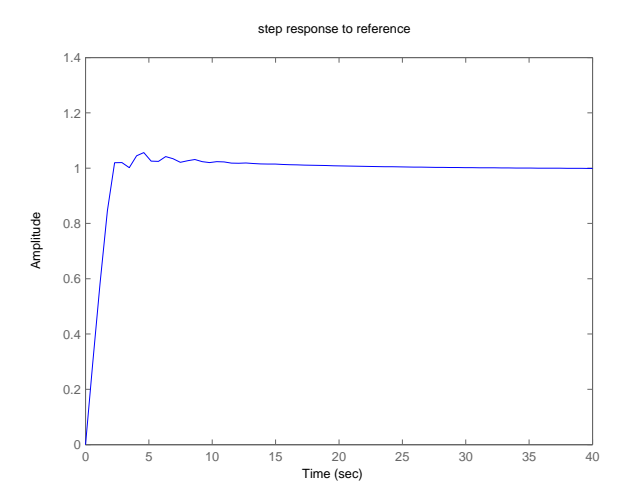


Figure 72 Step response of the closed-loop plant.

The designed \mathcal{H}_{∞} controller turned out to be

$$K_c(s) = \frac{27.55s^5 + 510.1s^4 + 1151s^3 + 251.7s^2 + 18.52s + 0.4351}{s^6 + 44.99s^5 + 505.6s^4 + 1978s^3 + 316.5s^2 + 12.79s + 0.08032}.$$
 (203)

The unit step response of the closed-loop plant is shown in Fig. 72.

7.5.3 Simulation results

We now show the integrated FTC results using both the optimal observer designed in section 7.4 and the \mathcal{H}_{∞} IPC controller designed in this section.

We used the same *MatLab* file "sim_ttb_tbu_incl_YAW.m" in simulating the TURBU model, together with the wind data contained in "wind.mat", as in section 7.4. The yaw motor failure was injected into the simulation from 80 seconds on, see Figure 63. The motor failure was detected at 81.44 seconds, when the IPC controller (203) was switched on. The resulted rotor orientation was illustrated in Figure 73. Obviously, the IPC controller (203) re-directed the turbine toward the wind orientation, after the yaw motor failed. The control signal, yaw pitch angle, is shown in Figure 74, which had acceptable amplitude.

7.6 Conclusions

In this report, we have studied the TURBU model with yawing motion, designed a robust fault detection observer against yaw motor failure, tuned a robust IPC controller as a remedy of the motor failure, and developed an integrated FTC scheme for the TURBU model.

The designed observer has a good performance, in terms of its robustness to wind gust and step changes in the axial wind. The integrated FTC scheme is effective in reconfiguring the yawing system of the wind turbine.

On the other hand, through the experience in implementing the model-based optimal observer design on the TURBU model, we found two difficulties in implementing model-based methods:

- For a large-scale system, a model itself is very difficult to build (c.f. [76]).
- Even if a very accurate mode is available, it may not be directly utilized in observer (and

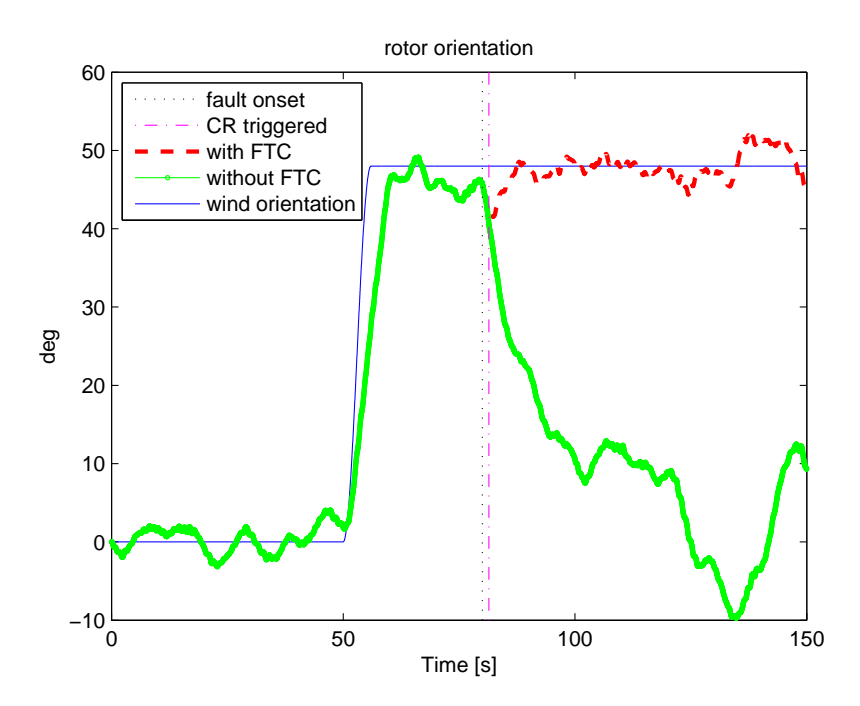


Figure 73 Performance of the integrated FTC scheme. CR: controller reconfiguration.

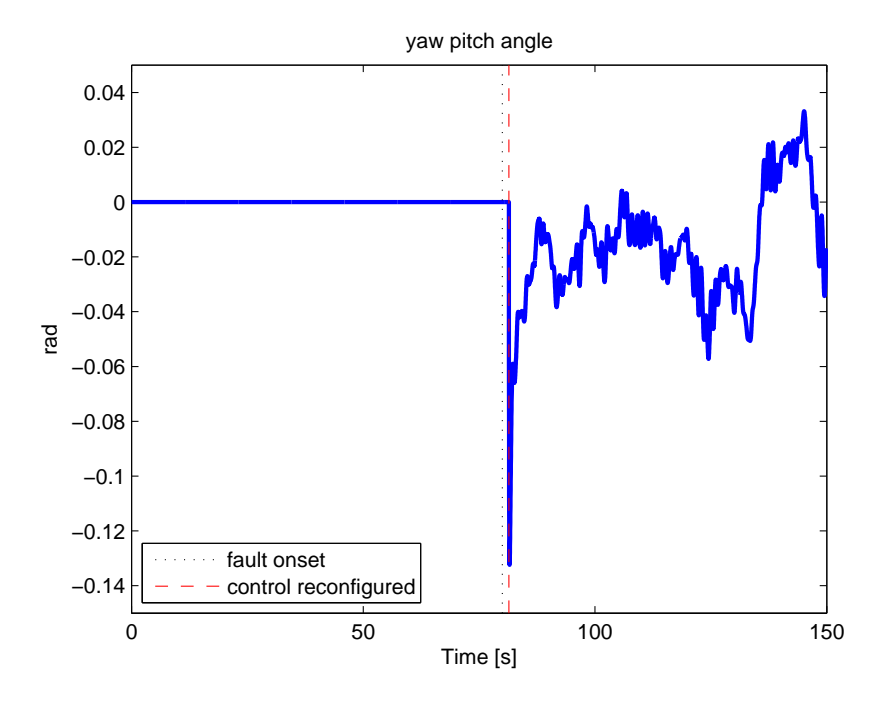


Figure 74 Amplitude of the control input, i.e. the yaw pitch angle.

controller) design, because its order may be too large for the optimization problem to be computable. When model reduction is necessary, model-plant mismatch is then inevitable.

The difficulties in model-based designs have motivated data-driven designs in the recent fundamental development of the fault detection literature; e.g. [20, 60]. This then provides a new future direction for data-driven FTC of wind turbines.

Part IV

Extreme Event Control (EEC)

8 Dealing with wind gusts in combination with wind direction changes

Summary

This section focuses on the problem of extreme wind gust and direction change recognition (EG&DR) and control (EEC). An extreme wind gust with direction change can lead to large loads on the turbine (causing fatigue) and unnecessary turbine shut-downs by the supervisory system due to rotor overspeed. The proposed EG&DR algorithm is based on a nonlinear observer (extended Kalman filter) that estimates the oblique wind inflow angle and the blade effective wind speed signals, which are then used by a detection algorithm (CUSUM test) to recognize extreme events. The nonlinear observer requires that blade root bending moments measurements (in-plane and out-of-plane) are available. Once an extreme event is detected, an EEC algorithm is activated that (i) tries to prevent the rotor speed from exceeding the overspeed limit by fast collective blade pitching, and (ii) reduces 1p blade loads by means of individual pitch control algorithm, designed in an \mathcal{H}_{∞} optimal control setting. The method is demonstrated on a complex nonlinear test turbine model. For the EEC method, a Dutch patent is granted [79] and a world patent is pending.

8.1 Introduction

Extreme wind conditions, such as wind gusts and/or wind direction changes, can lead to very large turbine loads causing fatigue, automatic shut-downs or even damage to some turbine components. Such effects could be circumvented by means of timely recognition of the extreme event (extreme event recognition), followed by a promptly and proper control system reaction (extreme event control). In this section, the extreme wind gust and direction change recognition (EG&DR) is performed by means of estimating the oblique inflow angle (yaw misalignment) together with blade-effective wind speed signals from measurements on the flapwise (out-of-plane) and leadwise (in-plane) bending moments in the blade roots. These estimates are used to recognize extreme events (wind gusts and/or wind direction changes), which activates an extreme event control (EEC) algorithm. The EEC has on the one hand the purpose of preventing rotor overspeed (which can trigger complete turbine shutdown by the supervisory system) by collectively pitching the blades toward feather, and on the other hand to reduce 1p (once per revolution) blade loads by individually pitching the blades.

The problem of rotor-effective wind speed estimation has been addressed in the literature on several occasions, where the usual approach is to estimate the aerodynamic torque on the rotor $T_a(u)$, which is subsequently inverted to obtain the rotor-uniform wind speed u. The estimation of T_a is done either by neglecting the rotor dynamics and using the static power-wind curve [69, 54], or by considering a simple first-order model of the rotor dynamics (i.e. neglecting shaft torsion) [72, 48, 64]. Recently, somewhat more advanced models have been used, including first shaft torsion mode to the rotor dynamics [59]. In estimating the aerodynamic torque, the majority of these methods rely on the computation of the time-derivative of the rotor speed measurement, and are as such very sensitive to measurement noise as well as to unmodelled higher order dynamics such as tower sidewards motion and collective blade lead-lag motion. To avoid this, appropriate filtering of the rotor speed is necessary, which inevitably introduces time delay and, hence, sacrifices the performance of the wind estimator. More advanced methods have, though, also been studied, including extended Kalman filter [54], linear Kalman filter in combination with T_a tracking control loop [59], or augmented-state nonlinear filters [64]. Still, all these publications have several things in common: they all assume one single rotor-effective wind speed signal, no yaw misalignment, a rigid rotor and tower, and use equilibrium-wake aerodynamics based on static power-wind curves.

To the best of the authors' knowledge there has been no publication on simultaneous estimation

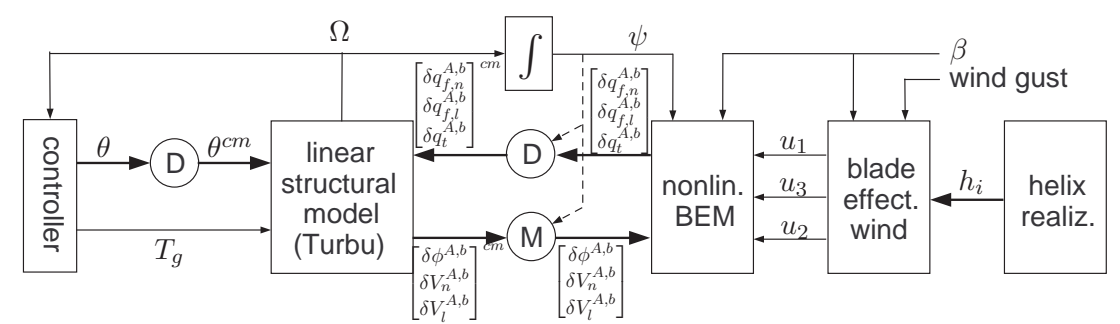


Figure 75 Turbine simulation scheme

of *blade*-effective wind speeds and yaw misalignment angle, which is in the basis of the EG&DR algorithm developed in this section. More specifically, an augmented state extended Kalman filter (EKF) is utilized, based on a nonlinear wind turbine model. This model consists of a linear structural dynamics module (SDM) on which aerodynamic forces and torques are acting as computed by a nonlinear aerodynamic conversion module (ADM), driven by realistic blade-effective wind speed signals. Compared to the model used in the Kalman filter, a model of an even higher complexity is used for simulation and analysis, the main components of which are given in block-schematic form in Figure 75 (in which the physical meaning of the signals is described later on). These components are:

- 40-th order linearized structural dynamics model (SDM), obtained using the software TURBU [76], with degrees of freedom in tower foundation, blade flanges and drive train, and including pitch actuator dynamics,
- nonlinear aerodynamic conversion module (ADM) based on blade element momentum (BEM) theory, including
 - dynamic wake effects as modeled by the ECN Differential Equation Model [67],
 - Glauert's azimuth-dependent correction term for the axial induction speed in case of oblique inflow [73],
 - correction on the angle of attack due to rotor coning, as implemented in the nonlinear aero-elastic wind turbine simulation tool PHATAS [49],
- linear blade pitch controller regulating the filtered generator speed at its rated level (when operating at above-rated conditions), and consisting of a PI-controller in series with low-pass filter at the 3P blade frequency, notch filter at the first tower sideward frequency, and notch filter at the first collective lead-lag frequency,
- nonlinear generator torque controller based on static optimal-λ QN-curve at below rated conditions and *constant power* production above-rated, operating on the filtered generator speed signal (same three filters used as in pitch controller),
- additional azimuth-dependent nonlinearities arising from the Coleman transformations between the fixed reference frame (in which the input/output signals of the SDM are defined) and the rotating reference frame (in which the signals of the ADM are defined), see blocks M (modulation) and D (demodulation) in Figure 75,
- realistic blade effective wind speed signals are generated based on the helix approximation concept, as proposed in [43, App. C], including both a deterministic term for modeling wind shear, tower shadow, tilt and yaw misalignment, wind gust, and a stochastic term that models blade-effective turbulence.

The EKF uses a simplified model in which the structural dynamics model is reduced to order 20, and the ADM model excludes dynamic wake effects, as well as the effects of the structural dynamics onto the aerodynamics, i.e. the effects of the vibration and deformation of the blades and the tower onto the apparent wind speeds are neglected (the leadwise speeds of the blade elements resulting from the rotation of the rotor is, of course, not neglected, only the variations around these speeds).

Based on the blade-effective wind speeds and oblique inflow angle, estimated by the EKF, an extreme event detection mechanism is used, consisting of a cumulative sum (CUSUM) test that detects (significant) changes in the mean value of the estimated signals. Once the extreme event flag is raised by the CUSUM test, an EEC algorithm is activated that consists of two components. The first one is a rotor overspeed prevention algorithm that immediately starts pitching the blades to feather with the maximally allowed pitch speed, and at the same time sets the reference generator torque equal to its rated value. This action has the purpose to prevent rotor overspeed in order to avoid a possibly unnecessary turbine shutdown by the supervisory system. The conventional power control is switched on again when either the (filtered) rotor speed begins decreasing, or the pitch angles have reached a suitably defined reference value, which is a function of the axial component of the (estimated) wind speed. The last one is computed off-line under the assumption of rated rotor speed and rated generator torque. The process of switching the conventional control algorithm back on is performed in a bumpless manner by means of proper controller state re-initialization. The second component of the EEC consists of an individual pitch control (IPC) algorithm aiming at the reduction of 1p blade loads, which are rather large under oblique inflow conditions. A modern optimal- \mathcal{H}_{∞} control methodology is used for the design of the IPC. This loads reduction control should be only activated after the rotor overspeed prevention system is deactivated, as their simultaneous activity would require blade pitch speeds exceeding the maximal allowable speed. In fact, the IPC could, principally, be let working even when there is no extreme event, although the resulting continuous cyclic blade pitching might be undesirable. In the implementation in this section, the IPC is only active whenever the estimated oblique inflow angle is larger (in absolute value) than 10° .

The section is organized as follows. The next subsection explains the notation used throughout this section, as well as the physical meaning of the used variables. Subsection 8.3 describes the structure and the main components of the turbine simulation model. The algorithm for detection of extreme events is developed in Subsection 8.4, while extreme event control is the topic of Subsection 8.5. The complete EG&DR-EEC method is tested in simulations in Section 8.6.

8.2 Notation and Symbols

For a scalar or vector variable v, \bar{v} denotes its equilibrium or mean value, while $\delta v = v - \bar{v}$ is called the (current) variation around the equilibrium value. An superscript cm, as in v^{cm} , means that the variable is defined in multi-blade coordinates as obtained by performing a Coleman demodulation (see Section 8.4.1) of the signal v (v being defined in the rotating reference frame). Subscripts/subscripts b and A, as in $U_n^{A,b}$, denote the number of the blade (b=1,2,3) and the number of the blade element ($A=1,2,\ldots,N_{ann}$) for which the variable is defined. For simplicity of notation it is assumed in the ADM that the number of blade elements is equal to the number of annuli, and that the length of the A-th blade element is equal to the breadth of annulus A. The operation $A\otimes B$ denotes the Kronecker product between A and B, while Vec(()A) stacks the columns of the matrix A below each other into one vector. The operator \oplus represents the direct sum of matrices, i.e. $A\oplus B = \text{blockdiag}(A,B)$. The n-by-n identity matrix is denoted as I_n , and $\delta_{b,i}$ is the Kronecker delta function.

The following symbols (with SI dimensions) are used in the text:

 c_A cord length of blade element A,

 C_L, C_D, C_M lift, drag, and pitch-wise torque coefficients, M_r^b, M_z^b lead-wise (in-plane) and flap-wise (out-of-plane) blade b root bending moment, $(=[M_x^1,M_x^2,M_x^3,M_z^1,M_z^2,M_z^3]^T)$ vector of blade root bending moments, M_k state covariance matrix in the extended Kalman filter, $q_t^{\tilde{A},b}$ aerodynamic pitch-wise moment (nose-down positive) of element A of blade b, $q_{f,n}^{A,b}, q_{f,l}^{A,b}$ Raerodynamic forces in normal and leadwise direction of element A of blade b, rotor radius, distance from hub center to center of blade element A, T_g T_s, T_s^{ctr} generator torque reference (output of controller), sample time turbine model, sample time of controller mean undisturbed wind speed in the longitudinal wind field direction, $\bar{U}_{ax}, \bar{U}_{yw}, \bar{U}_{tlt}$ axial, yaw-oriented and tilt-oriented components of U $\bar{U}_i^A, \bar{V}_i^A \\ \delta U_i^A$ equilibrium axial and tangential induction wind speeds, dynamic term on the axial induction wind speed, $\delta U_{i,corr}^{A,b} \\ U_{i}^{A_{2/3}}$ Glauert's correction term to U_i^A for oblique inflow, axial induction wind speed of annulus at 2/3Rblade b effective wind speed, $\bar{V}_n^A, \bar{V}_l^A \\ \delta V_n^{A,b}, \delta V_l^{A,b}$ equilibrium normal and lead-wise effective wind speed at blade element A, normal and lead-wise effective wind speed variation at element A of blade b, x, x^a state of the (reduced) SDM model, augmented state $\alpha^{A,b}$ angle of attack of element A of blade b, β additional (to $\bar{\phi}_{uw}$) yaw misalignment angle for modeling wind direction change, θ_b pitch angle reference for blade b (output of controller), air density, $\phi^{A,b}$ pitch angle of element A of blade b, $\bar{\phi}_{yw}, \bar{\phi}_{tlt}$ equilibrium yaw and tilt angles of the wind speed \bar{U} (see Figure 76), $\psi^{\tilde{b}},\;\psi$ azimuth angle of blade b, rotor azimuth $\delta\psi$ azimuth offset angle due to oblique inflow orientation, Ω, Ω^f rotor speed, filtered rotor speed,

8.3 Turbine Simulation Model

The turbine simulation model represents a typical 3-bladed horizontal axis wind turbine (HAWT). The model consists of an integration of several blocks, as sketched on Figure 75. These blocks are explained in more detail in the following subsections.

8.3.1 Structural dynamics system (SDM)

The SDM block consists of a linearized model, obtained with the software Turbu [76]. The model assumes rigid blades and tower, but contains degrees of freedom in the blade flanges, in the tower foundation, in the rotor shaft, and includes the pitch actuator dynamics. Although the blades are considered rigid, there are $N_{ann}=14$ blade elements per blade, allowing for a better representation of the aerodynamic forces, as computed from the ADM block, described in Section 8.3.3. The model (see Figure 75) has:

- 40 states: positions and speeds in 3 directions for the three blade flange elements and the tower bottom element, rotational position and speed for the two drive-train elements, and 4 states per blade for modeling the servo-pitch actuators at the three blades (all states defined in multi-blade coordinates, see Section 8.4.1),
- 130 inputs: 3 reference blade pitch angles θ^{cm} , one reference generator torque T_g , $3N_{ann}$

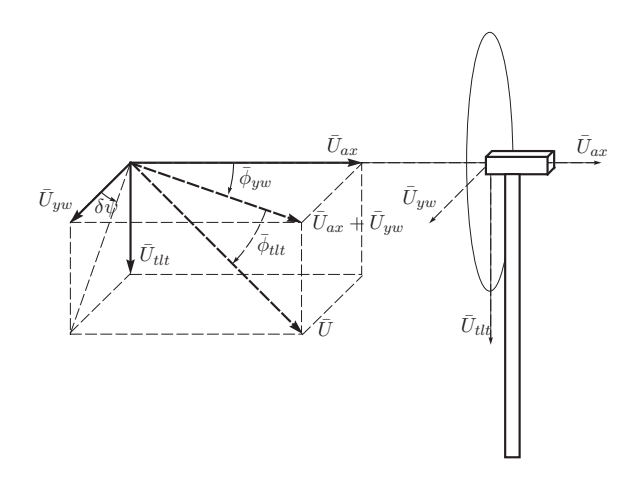


Figure 76 Definitions of tilt \bar{U}_{tlt} , yaw \bar{U}_{yw} and axial \bar{U}_{ax} oriented components of the equilibrium wind vector \bar{U} , and yaw $\bar{\phi}_{yw}$ and tilt $\bar{\phi}_{tlt}$ angles.

blade element torques q_t^{cm} , $3N_{ann}$ normal forces $q_{f,n}^{cm}$ and $3N_{ann}$ leadwise forces $q_{f,l}^{cm}$, all in multi-blade coordinates, and

• 133 outputs: rotor speed Ω , 3 blade root out-of-plane bending moments M_z^{cm} , 3 blade root in-plane bending moments M_x^{cm} , $3N_{ann}$ blade element pitch angles $(\delta\phi^{A,b})^{cm}$, $3N_{ann}$ normal velocities $(\delta V_n^{A,b})^{cm}$ and $3N_{ann}$ leadwise velocities $(\delta V_l^{A,b})^{cm}$, also in multi-blade coordinates.

The inputs θ^{cm} and T_g are controlled inputs, the outputs Ω , M_z^{cm} , and M_x^{cm} are assumed measured, and the remaining inputs and outputs are used for interconnecting the SDM with the ADM.

8.3.2 Wind generation

The generated blade effective wind speeds u_b have two components: a deterministic component which is the same for all blades and is used to represent wind gusts, wind shear and tower shadow, and a stochastic turbulence component, which is computed on the basis of the helix interpolation algorithm, described in [43, App. C]. These blade-effective wind speeds are computed in such a way that the resulting flapwise blade root bending moments approximate (in terms of spectrum) those arising from a three-dimensional wind field turbulence. The blade effective wind speed signals are defined in longitudinal wind field direction (i.e. parallel to the undisturbed wind vector \bar{U}). In addition to that, an oblique inflow angle β is generated by the wind generation module, which represents yawed flow.

8.3.3 Aerodynamic module (ADM)

Due to page limitation, only a summary of the ADM algorithm is given here. For details, see [43].

Algorithm 8.1 (ADM).

Equilibrium values and parameters from Turbu: \bar{U}_{ax} , \bar{U}_{yw} , \bar{U}_{tlt} , \bar{U}_i^A , \bar{V}_i^A , \bar{V}_i^A , \bar{V}_l^A , $\bar{\phi}^{A,b}$, $\bar{q}_{f,n}^{A,b}$, $\bar{q}_{f,n}^{A,b}$, $\bar{q}_t^{A,b}$, $\bar{q}_t^{A,b}$, r_A , c_A , R, ρ , $C_L(\alpha)$, $C_D(\alpha)$, $C_M(\alpha)$.

From SDM and wind module: ψ , $\delta\phi^{A,b}$, $\delta V_n^{A,b}$, $\delta V_l^{A,b}$, β , u_b

From ADM at previous time instant: δU_i^A

Step 1 Compute the undisturbed wind speeds in axial, yaw and tilt orientation, including turbulence and wind gusts contained in the blade-effective wind speed variations u_b :

$$\begin{bmatrix} U_{ax}^{\beta,gust} \\ U_{yw}^{\beta,gust} \\ U_{tlt}^{\beta,gust} \end{bmatrix} = \begin{bmatrix} \cos(\bar{\phi}_{tlt})\cos(\bar{\phi}_{yw} + \beta) \\ \cos(\bar{\phi}_{tlt})\sin(\bar{\phi}_{yw} + \beta) \\ \sin\bar{\phi}_{tlt} \end{bmatrix} \left(\bar{U} + \frac{1}{3} \sum_{b=1}^{3} u_b \right)$$
(204)

Step 2 Compute Glauert's correction $\delta U_{i,corr}^{A,b}$ to the axial induction speed

$$\delta U_{i,corr}^{A,b} = \frac{15\pi}{64R} r_A \tan \left(\arctan \left(\frac{\sqrt{\left(U_{yw}^{\beta,gust} \right)^2 + \left(U_{tlt}^{\beta,gust} \right)^2}}{U_{ax}^{\beta,gust} - U_i^{A_{2/3}}} \right) / 2 \right) \cos(\psi^b - \delta \psi) U_i^{A_{2/3}}$$

Step 3 Compute setting angles of blade elements $\phi^{A,b}$, including angle of attack correction due to rotor coning.

Step 4 Compute normal $U_n^{A,b}$ and leadwise $U_l^{A,b}$ effective wind speeds and angle of attacks:

$$\begin{bmatrix}
\delta u_{ax}^{b} \\
\delta u_{yw}^{b} \\
\delta u_{tlt}^{b}
\end{bmatrix} = \begin{bmatrix}
\cos(\bar{\phi}_{tlt})\cos(\bar{\phi}_{yw} + \beta) \\
\cos(\bar{\phi}_{tlt})\sin(\bar{\phi}_{yw} + \beta)
\end{bmatrix} \begin{pmatrix} u_{b} - \frac{1}{3}\sum_{b=1}^{3} u_{b} \end{pmatrix} \\
U_{n}^{A,b} = U_{ax}^{\beta,gust} - \bar{U}_{i}^{A} - \bar{V}_{n}^{A} + \delta u_{ax}^{b} - \delta U_{i}^{A} + \delta U_{i,corr}^{A,b} - \delta V_{n}^{A,b}, \\
U_{l}^{A,b} = \delta V_{l}^{A,b} - \bar{V}_{l}^{A} - \bar{V}_{i}^{A} + \sin(\psi^{b}) \left(U_{yw}^{\beta,gust} + \delta u_{yw}^{b} \right) - \cos(\psi^{b}) \left(U_{tlt}^{\beta,gust} + \delta u_{tlt}^{b} \right), \\
\alpha^{A,b} = \arctan\left(\frac{U_{n}^{A,b}}{U_{l}^{A,b}} \right) - \phi^{A,b}.$$
(205)

Step 5 Compute normal and lead-wise forces and pitch-wise torques per blade element

$$\delta q_{f,n}^{A,b} = \frac{1}{2} \rho c_A \left(C_L(\alpha^{A,b}) U_l^{A,b} + C_D(\alpha^{A,b}) U_n^{A,b} \right) \sqrt{\left(U_n^{A,b} \right)^2 + \left(U_l^{A,b} \right)^2} - \bar{q}_{f,n}^{A,b},
\delta q_{f,l}^{A,b} = \frac{1}{2} \rho c_A \left(C_L(\alpha^{A,b}) U_n^{A,b} - C_D(\alpha^{A,b}) U_l^{A,b} \right) \sqrt{\left(U_n^{A,b} \right)^2 + \left(U_l^{A,b} \right)^2} - \bar{q}_{f,l}^{A,b},
\delta q_t^{A,b} = -\frac{1}{2} \rho c_A^2 C_M(\alpha^{A,b}) \left(\left(U_n^{A,b} \right)^2 + \left(U_l^{A,b} \right)^2 \right) - \bar{q}_t^{A,b}.$$
(206)

Step 6 Update dynamic term on axial induction speed, to be used in next time instant, δU_i^A , using the ECN Differential Equation Model.

8.3.4 Conventional controller

The conventional controller is typical and contains two loops [71]: pitch control for generator speed regulation (active above rated only) and generator torque control for power regulation (according to optimal- λ QN-curve below rated, and constant power above rated). Both loops act on the rotor speed filtered with a series of low-pass filter at the 3P frequency (4th order inverse Chebyshev type II filter with cutoff frequency of (3P-0.8) rad/s and 20 dB reduction), bandstop filter around the first tower sidewards frequency f_{sd} (2nd order elliptic filter with stop-band $[0.85f_{sd}, 1.15f_{sd}]$ rad/s, 30 dB reduction and 1 dB ripple), and a band-stop filter at the first collective lead-lag frequency f_{ll} (4th order elliptic filter with stop-band $[0.8f_{ll}, 1.05f_{ll}]$ rad/s, 30 dB reduction and 1 dB ripple). The pitch controller is a PI compensator designed to achieve a gain

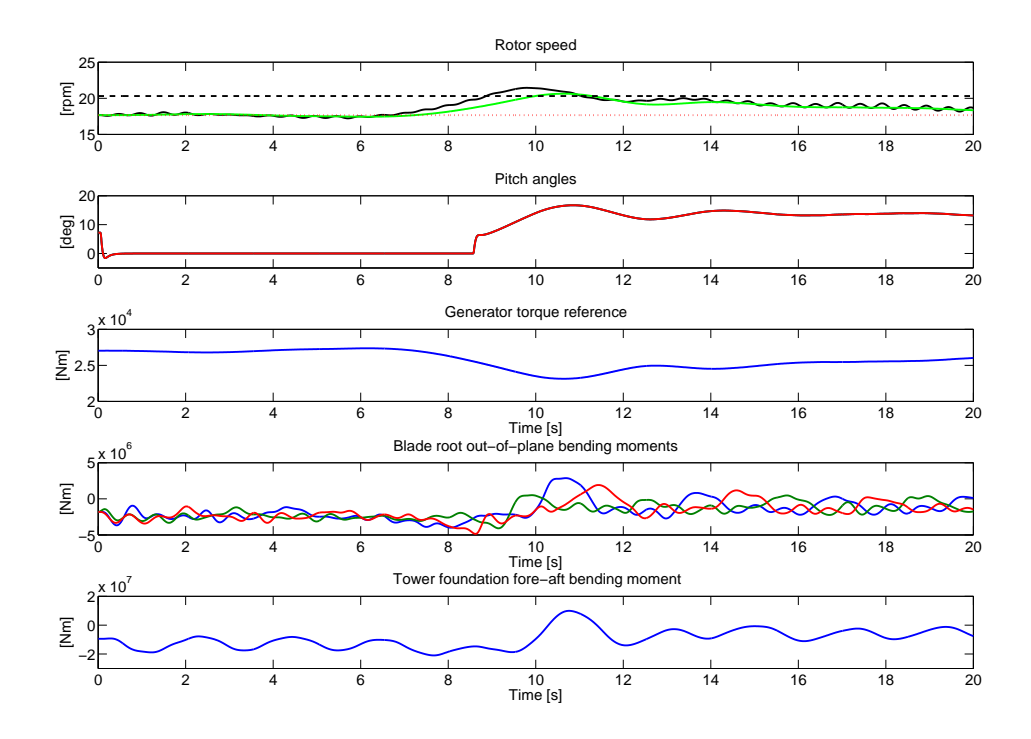


Figure 77 Turbine simulation under extreme rising gust and direction change at $t=5\,$ sec, without EEC

margin of 2 and a phase margin of 45 degrees.

8.3.5 Problem Formulation

In this section, an extreme rising wind gust with simultaneous wind direction change is simulated. These have been chosen as specified in IEC 61400-1 as "extreme coherent gust with direction change (ECD)": 15 m/s rising wind gust (on top of the mean wind $\bar{U}=15$ m/s and the additional blade-effective turbulence) in conjunction with a direction change of $720/U = 48^{\circ}$. A simulation of the complete turbine model with the described extreme event occurring 5 sec after the beginning of the simulation, is shown in Figure 77. On the top subplot of the figure the rotor speed Ω_k (the fluctuating [black] curve), together with its filtered version Ω_k^f (the smoother [green] curve) are given. The rated speed $\bar{\Omega}$, being approximately 17.7 rpm is given by the bottom dotted line, while the overspeed limit, which should not be exceeded as this would trigger the supervisory system to start an emergency stop of the turbine, is given by the top dashed line. The overspeed limit is set to 15 % above the rated value (20.3 rpm). The supervisory system is not modeled in the simulation, so the turbine is not stopped after the rotor speed exceeds the overspeed limit around t = 9 sec. The second subplot in Figure 77 gives the collective pitch angle of the rotor blades. In the beginning of the simulation the controller works at below-rated operation region, and switches to above rated when the filtered rotor speed exceeds 18.7 rpm (= $\Omega + 1$ rpm). The third subplot (middle) shows the generator torque. The constant-power control strategy above rated is easily recognizable by the inverse proportionality of the generator torque to the filtered rotor speed. The fourth subplot gives the three flap-wise blade root bending moments. The 1p loads, resulting from the oblique inflow, are clearly seen in the second half of the simulation. Finally, the last (fifth) subplot in Figure 77 shows the tower base fore-aft bending moment.

The purpose of the section is to develop algorithm for extreme event control that

- is capable of preventing rotor overspeed, when possible, and
- achieves 1p blade root bending moment reduction.

To this end, the extreme event should be detected at an early stage, which is the focus of the next section.

8.4 Extreme Event Recognition

The recognition of extreme events, proposed here, is based on the estimation of the wind parameters u_b and β by means of a nonlinear estimator (EKF), which estimates are then used in a CUSUM test for detecting changes in their mean values as resulting from extreme wind gusts and/or extreme wind direction changes. This section describes these components in detail.

8.4.1 Simplified model

The algorithm for EG&DR utilizes an EKF for the estimation of a so-called *augmented state* x^a , consisting of the turbine structural model state x and the unknown inputs (i.e. the three blade effective wind speed signals u_b and the oblique inflow angle β). In order to somewhat reduce the computational complexity of the EKF, it is based on a more simplified model than the one used for turbine simulation, described in Section 8.3. This simplified model also consists of an interconnection of an SDM and ADM blocks, although their complexity is somewhat simplified as described below:

- (ADM) The aerodynamics neglects the effects of the movement of the blades and tower onto the torques and forces acting on the blade elements (with the exception of the leadwise blade element velocity due to rotor rotation, which is, of course, not neglected). This boils down to setting $\delta V_l^{A,b} = \frac{\bar{V}_l^{A,b}}{\bar{\Omega}} (\Omega \bar{\Omega})$ and $\delta V_n^{A,b} = 0$ in Section 8.3.3. Furthermore, the blade element pitch angle variations are assumed to be constant over the blade, i.e. $\delta \phi^{A,b} = \delta \phi^b$, and are assumed measured at the blade roots. The third simplification is that equilibrium wake is considered, being equivalent to setting $\delta U_i^A = 0$ (and skipping Step 6 in the algorithm of Section 8.3.3). The variations of the axial induction wind speed around the equilibrium value will then be (approximately) incorporated into the blade effective wind speed estimates as if there was equivalent longitudinal wind speed variation.
- (SDM) The order of the structural model which is used for simulating the wind turbine (being 40), is reduced to 20 using the model reduction by balanced truncation technique. In this way, the 20 least controllable and observable states in the SDM model are removed. This model reduction is performed on the SDM model with all 130 inputs inputs, but only the 10 measured outputs (i.e. Ω , $\delta \phi^b$, M_z^{cm} and M_z^{cm}).
- (T_s) The model reduction, mentioned above, is performed after resampling the SDM model to $T_s^{ctr}=0.02~{\rm sec}$ (the sampling time SDM for turbine simulation is $T_s=0.005~{\rm sec}$).

Define the Coleman transformation $T_M(\cdot)$ (modulation) and inverse Coleman transformation $T_D(\cdot)$ (demodulation)

$$T_D(\psi) \doteq \frac{1}{3} \begin{bmatrix} 1 & 1 & 1 \\ 2\sin(\psi_1) & 2\sin(\psi_2) & 2\sin(\psi_3) \\ 2\cos(\psi_1) & 2\cos(\psi_2) & 2\cos(\psi_3) \end{bmatrix}, T_M(\psi) \doteq \begin{bmatrix} 1 & \sin(\psi_1) & \cos(\psi_1) \\ 1 & \sin(\psi_2) & \cos(\psi_2) \\ 1 & \sin(\psi_3) & \cos(\psi_3) \end{bmatrix} = T_D^{-1}(\psi).$$

The map T_D is used to transform variables, defined in the rotating reference frame, to the non-rotating reference frame (e.g. $M_z^{cm} = T_D(\psi)M_z$), while T_M is used for the inverse operation.

Using this notation, the simplified model can be compactly described in the following state-space form

Aerodynamics:	$\delta d_k = f_{ADM}(\delta \Omega_k, \delta \phi_k, u_k, \beta_k)$	
Structural dynamics:	Coleman (de)modulation:	
$x_{k+1} = Ax_k + B\delta v_k^{cm} + B_d \delta d_k^{cm}$	$\delta M_k = (I_2 \otimes T_M(\psi_k)) \delta M_k^{cm}$	(207)
$\delta M_k^{cm} = Cx_k + D\delta v_k^{cm} + D_d \delta d_k^{cm}$	$\delta\phi_k = T_M(\psi_k)\delta\phi_k^{cm}$	(207)
$\delta\Omega_k = C_{\Omega} x_k + D_{\Omega} \delta v_k^{cm}$	$\delta d_k^{cm} = (I_{3N_{ann}} \otimes T_D(\psi_k))\delta d_k$	
$\delta\phi_k^{cm} = C_\phi x_k + D_\Omega \delta v_k^{cm}$	$\delta v_k^{cm} = (T_D(\psi_k) \oplus 1)\delta v_k$	

where $x_k \in \mathbb{R}^n$ contains the (reduced) SDM model state, $\delta M_k^T = [\delta M_z^1, \delta M_z^2, \delta M_z^3, \delta M_x^1, \delta M_x^2, \delta M_x^3]_k$ is a vector of in-plane and out-of-plane blade root bending moments, $\delta v_k^T = [\delta \theta^T, \delta T_g]_k \in \mathbb{R}^4$ contains the control signals (being the reference blade pitch angles and generator torque), $u_k^T = [u_1, u_2, u_3]_k$ represents the blade-effective wind speeds, $\delta \phi_k^T = [\delta \phi^1, \delta \phi^2, \delta \phi^3]_k$ contains the blade pitch angles, and

$$\delta d_k = \text{vec} \left(\begin{bmatrix} \delta q_n^{1,1} & \dots & \delta q_n^{N_{ann},1} & \delta q_l^{1,1} & \dots & \delta q_l^{N_{ann},1} & \delta q_t^{1,1} & \dots & \delta q_t^{N_{ann},1} \\ \delta q_n^{1,2} & \dots & \delta q_n^{N_{ann},2} & \delta q_l^{1,2} & \dots & \delta q_l^{N_{ann},2} & \delta q_t^{1,2} & \dots & \delta q_t^{N_{ann},2} \\ \delta q_n^{1,3} & \dots & \delta q_n^{N_{ann},3} & \delta q_l^{1,2} & \dots & \delta q_l^{N_{ann},3} & \delta q_t^{1,3} & \dots & \delta q_t^{N_{ann},3} \end{bmatrix}_k \right)$$

$$(208)$$

is a long vector consisting of all blade element normal and lead-wise force variations and pitchwise torque variations. The function $f_{ADM}(\delta\Omega_k, \delta\phi_k, u_k, \beta_k)$ represents the ADM output equations (206), rewritten in terms of the variables $\{\Omega_k, \delta\phi_k, u_k, \beta_k\}$ under the simplifying assumptions for the ADM, described in the beginning of this section.

The following nonlinear model then relates the inputs to the measured outputs

$$x_{k+1} = Ax_k + B(T_D(\psi_k) \oplus 1)\delta v_k + B_d(I \otimes T_D(\psi_k))f_{ADM}(\delta\Omega_k, \delta\phi_k, u_k, \beta_k)$$

$$\delta M_k = (I \otimes T_M(\psi_k))(Cx_k + D(T_D(\psi_k) \oplus 1)\delta v_k + D_d(I \otimes T_D(\psi_k))f_{ADM}(\delta\Omega_k, \delta\phi_k, u_k, \beta_k))$$

$$\delta \Omega_k = C_\Omega x_k + D_\Omega(T_D(\psi_k) \oplus 1)\delta v_k,$$

$$\delta \phi_k = T_M(\psi_k)(C_\phi x_k + D_\phi(T_D(\psi_k) \oplus 1)\delta v_k)$$
(209)

where the rotor azimuth ψ_k is viewed as known time-varying parameter since ψ_k is needed in $f_{ADM}(\delta\Omega_k,\delta\phi_k,u_k,\beta_k)$ but depends only on the rotor speed Ω up to time instant (k-1), but not on Ω_k (and, hence, is not a function of the current state).

The goal is to construct a filter that uses the blade root bending moment measurements M_k to estimate the state x_k together with the unknown inputs u_k and β_k .

8.4.2 Augmented-state extended Kalman filter

For the purpose of EG&DR, the unknown inputs u_k and β_k in model (209) need to be estimated. One way to do this is model them as the response of a given stochastic model to a random white noise process, to append this model to the turbine dynamics model and then use a Kalman filter to estimate both the state of the turbine and the state of the stochastic model from which u_k and β_k are computed. Although blade-effective wind turbulence models do exist [81], their parametrization is in practice not an easy task. A much more practical approach is the so-called augmented-state Kalman filter technique, which is often used in the literature for the estimation of (time-varying) unknown input signals (disturbances), see e.g. [45] and the references therein. The basic idea behind this approach is to model the unknown input using a random walk model

$$\begin{bmatrix} u_{k+1} \\ \beta_{k+1} \end{bmatrix} = \begin{bmatrix} u_k \\ \beta_k \end{bmatrix} + r_k,$$
 (210)

where r_k is a zero-mean white Gaussian process with covariance matrix R_r . Usually, the covariance matrix R_r of the noise term r_k is viewed as design parameter that provides a trade-off between tracking speed and smoothness of the estimates. For simplicity, it is often selected as diagonal matrix. Faster tracking of the true signals can be obtained by appropriately increasing the elements of R_r , which however results in less smooth (i.e. more noisy) estimates, and vice versa.

Basically, the model (210) represents an integrated white noise variable, so that the output will have its energy concentrated in the lower frequency band, and hence using such model is mostly suitable for modeling constant or slowly varying signals. The blade effective wind speeds and the wind orientation angle are naturally low frequency signals, making such kind of modeling sufficient. Given the random walk model (210), the state x of the system (209) is augmented with the unknown inputs, resulting in the following augmented-state model

$$\underbrace{\begin{bmatrix} x_{k+1} \\ u_{k+1} \\ \beta_{k+1} \end{bmatrix}}_{x_{k+1}} = \underbrace{\begin{bmatrix} Ax_k + B_d(I \otimes T_D(\psi_k)) f_{ADM}(\delta\Omega_k, \delta\phi_k, u_k, \beta_k) \\ u_k \\ \beta_k \end{bmatrix}}_{x_{k+1}} + \underbrace{\begin{bmatrix} B(T_D(\psi_k) \oplus 1) \\ 0 \\ 0 \end{bmatrix}}_{x_{k+1}} \delta v_k + \underbrace{\begin{bmatrix} 0 \\ I_4 \end{bmatrix}}_{x_k} r_k,$$

$$\delta M_k = \underbrace{(I \otimes T_M(\psi_k)) (Cx_k + D_d(I \otimes T_D(\psi_k)) f_{ADM}(\delta\Omega_k, \delta\phi_k, u_k, \beta_k))}_{\hat{D}_k(\psi_k)} + \underbrace{(I \otimes T_M(\psi_k)) D(T_D(\psi_k) \oplus 1)}_{\hat{D}_k(\psi_k)} \delta v_k,$$

that, using the equations for $\delta\Omega_k$ and $\delta\phi_k$ in (209), can compactly be written in the form

$$x_{k+1}^{a} = f(x_{k}^{a}, \psi_{k}) + \tilde{B}_{k}(\psi_{k})\delta v_{k} + Er_{k},$$

$$\delta M_{k} = g(x_{k}^{a}, \psi_{k}) + \tilde{D}_{k}(\psi_{k})\delta v_{k} + e_{k}.$$
(211)

The signal e_k , which is included in (211), is a zero mean white Gaussian processes with covariance matrix R_e , which can be used to represent measurement noise. Of course, additional measurements can be added to the blade root bending moments in (211) such as the rotor speed and blade pitch setting angles, as in equation (209). However, this does not noticeably improve the quality of the estimation and hence the measurements $\delta\Omega_k$ and $\delta\phi_k$ will only be used to parameterize the nonlinear function $f_{ADM}(\delta\Omega_k, \delta\phi_k, u_k, \beta_k)$.

An extended Kalman filter [8] can now be applied to the nonlinear state-space model (211) to estimate the augmented state x_k^a , containing the blade effective wind speeds u_k and the oblique inflow angle β_k . The EKF can be summarized as follows

Algorithm 8.2 (Extended Kalman Filter).

Initialization
$$\hat{x}_0^a = E\{x_0^a\}, P_0 = E\{(x_0^a - \hat{x}_0^a)(x_0^a - \hat{x}_0^a)^T\}.$$

Step 1 Compute
$$A_{k-1} = \partial f(x^a, \psi_k)/\partial x^a|_{x^a = \hat{x}_{k-1}^a}$$

Step 2 Time update
$$\begin{vmatrix} \hat{x}_{k|k-1}^{a} &=& f(\hat{x}_{k-1}^{a}, \psi_{k}) + \tilde{B}_{k} \delta v_{k-1} \\ P_{k|k-1} &=& A_{k-1} P_{k-1} A_{k-1}^{T} + E R_{r} E^{T} \end{vmatrix}$$

Step 3 Compute
$$C_k = \partial g(x^a, \psi_k)/\partial x^a|_{x^a = \hat{x}_{k|k-1}^a}$$

Step 4 Measurement update:
$$\begin{vmatrix} K_k & = & P_{k|k-1}C_k^T \left(C_k P_{k|k-1}C_k^T + R_e \right)^{-1} \\ \hat{x}_k^a & = & \hat{x}_{k|k-1}^a + K_k (\delta M_k - g(x_{k|k-1}^a, \psi_k) - \tilde{D}_k \delta v_k) \\ P_k & = & (I - K_k C_k) P_{k|k-1} \end{vmatrix}$$

Remark 8.1. The EKF requires the partial derivatives of the nonlinear functions with respect to the state variables. These can be analytically computed [43, App. A]. Of course, they can also be computed numerically; however, this results in a significant increase of the computational burden, as well as in numerical inaccuracies. Another, still computationally involved, but derivative-free alternative to the EKF is the unscented Kalman filter [94, 36]. The author's experience, however, is that for the model described here it often runs into numerical problems due to the output covariance matrix becoming numerically singular.

8.4.3 CUSUM test for Extreme Event Detection

The EKF, discussed above, estimates the turbine structural model state x, together with the blade effective wind speed signals u and the oblique inflow angle β , contained in the augmented state x^a . Under normal conditions, u and β will be stochastic signals with zero mean value, while under extreme conditions their mean values will undergo a change. In order that appropriate extreme event control actions are triggered timely, it is necessary to be able to detect such mean value changes promptly (with small detection delay and no missed alarms), yet accurately (no false alarms). An algorithm that directly looks at the current values of the estimates \hat{u}_k and $\hat{\beta}_k$ would be fast but too sensitive to noise and inaccuracies in the estimates, and would trigger many false alarms:

To circumvent this, a one-sided CUSUM test [2] is used here that offers a good speed/accuracy trade-off. This algorithm, in combination with the EKF, detects an extreme wind gust at a very early stage, before any significant increase of the (filtered) rotor speed. This makes it possible to react timely by pitching the blades, keeping the rotor speed within allowable limits. The algorithm can be summarized as follows

Algorithm 8.3 (CUSUM test).

Initialization Choose integers k_u (moving window length), ν (insensitivity parameter), h (threshold) and set $\hat{u}_0^f = \hat{u}_0$ (vector with initial wind speed estimates), $\epsilon_0 = 0$.

$$\mathbf{Update} \ \, \textit{Compute} \left| \begin{array}{l} \hat{u}_k^f = \frac{(k_u - 1)\hat{u}_{k-1}^f + \hat{u}_k}{k_u} \\ \\ \epsilon_k = \max\left(0, \epsilon_{k-1} + \hat{u}_k - \hat{u}_k^f - \nu\right). \end{array} \right.$$

Detection If
$$(\|\epsilon_k\|_1 > h)$$
, set $f_{ee,k} = 1$, else set $f_{ee,k} = 0$.

The signal $\epsilon_k \in \mathbb{R}^3$, computed by the CUSUM test, remains small under normal circumstances. The first equation in the update step represents a moving average filter used to estimate the mean value of the three blade effective wind speed signals. If the wind speed estimate \hat{u}_k starts increasing, ϵ_k will also increase until \hat{u}_k converges, at which point $(\hat{u}_k - \hat{u}_k^f) < \nu$ and ϵ_k will start decreasing to zero again. In this way, an easy detection mechanism would be to put a threshold h on the sum of the elements of the vector ϵ_k , so that an extreme event flag is raised $(f_{ee,k} = 1)$ whenever $\|\epsilon_k\|_1 > h$, where $\|\cdot\|_1$ denotes the vector 1-norm. Once $f_{ee,k}$ gets one, the EEC algorithm, described later on, will be activated, aiming at preventing rotor overspeed and reducing blade loads. This is the subject of the next section. It should be pointed out at this stage that the extreme event flag $f_{ee,k}$ can be pulled-down by either the CUSUM test algorithm above (i.e. when $\|\epsilon_k\|_1 \le h$), or by the EEC algorithm itself (when it decides that no further pitching of the blades is necessary, see Algorithm 8.4). In the later case the extreme event might not have finished when the flag is pulled-down, but the EEC algorithm reckons no (further) action needed.

8.5 Extreme Event Control

This section develops an algorithm for EEC that consists of two parts, (i) collective feedforward pitch control for preventing rotor overspeed, and (ii) individual pitch control for blade load reduction. These two control loops are described in more detail in the following subsections.

8.5.1 Rotor Overspeed Prevention

As already shown in the simulation on Figure 77, the conventional PI pitch controller is uncapable to keep the rotor speed within its limits under extreme wind gusts. The reason for that is that (a) it reacts on the filtered rotor speed Ω_k^f which is delayed by about 1 sec with respect to the true speed Ω_k , and (b) it does not respond quick enough. In order to react as fast as possible for preventing rotor overspeed, once an extreme event flag is raised by the CUSUM algorithm in Section 8.4.3, the EEC starts pitching the blades to feather with the maximally allowable pitch speed under extreme conditions $\dot{\theta}_{mx,ext}$. This results in fast reduction of the rotor speed, but has as a side effect a very large tower base fore-aft moment due to the large reduction of the rotor thrust force. In order to limit the tower base moment, after some time Δt_{eec} (about 1 sec) the pitching speed is reduced to the maximum pitch speed under normal conditions, $\dot{\theta}_{mx}$.

The conventional generator torque control at above-rated conditions was designed to achieve constant power, equal to the rated power (see Section 8.3.4). This implies a negative generator torque sensitivity to rotor speed variation, i.e. $\partial T_g/\partial\Omega < 0$. This has a destabilizing effect on the rotor speed, which is stabilized by the pitch control algorithm. However, due to the very slow dynamics of the pitch actuators, this results in higher oscillations of the rotor speed around its reference (rated) value. At extreme conditions, this destabilizing effect is removed by using a constant generator torque curve equal to the rated value \bar{T}_g . This results, of course, in an increase of the generated power of up to 10-15%. Whenever this is not acceptable for the power electronics, the original constant-power generator torque curve should be used.

The EEC for rotor overspeed prevention is switched off once the extreme event flag $f_{ee,k}$ is pulled down to zero by CUSUM algorithm in Section 8.4.3, or whenever the pitch angle θ_k gets "close" to a reference pitch angle $\theta_{ref,ext}$, dependent on the estimated axial wind speed $\hat{U}_{ax,k}^{\beta,gust}$

$$\hat{U}_{ax,k}^{\beta,gust} = \cos(\bar{\phi}_{tlt})\cos(\bar{\phi}_{yw} + \hat{\beta}_k) \left(\bar{U} + \frac{1}{3}\sum_{b=1}^{3} \hat{u}_{b,k}\right).$$
(212)

More specifically, $\theta_{ref,ext}(\hat{U}_{ax,k}^{\beta,gust})$ is defined as the collective pitch angle that, for axial wind speed $\hat{U}_{ax,k}^{\beta,gust}$, rated rotor speed $\bar{\Omega}$ and rated generator torque \bar{T}_g , achieves azimuth-averaged static aerodynamic torque $\bar{T}_a = \bar{T}_g$. For a given $U_{ax}^{\beta,gust}$, $\theta_{ref,ext}$ is computed by solving the following nonlinear optimization problem

$$\theta_{ref,ext}(U_{ax}^{\beta,gust}) = \arg\min_{\theta} \|\bar{T}_a(\bar{\Omega}, \theta, U_{ax}^{\beta,gust}) - \bar{T}_g\|_2.$$

The function $\theta_{ref,ext}(U_{ax}^{\beta,gust})$ is numerically computed off-line and stored for different values of $U_{ax}^{\beta,gust}$. Simple linear interpolation is then performed on-line.

To avoid unnecessary on/off switchings of the EEC due to fluctuations in $\theta_{ref,ext}(\hat{U}_{ax}^{\beta,gust})$, hysteresis is introduced: the EEC will switch on only when the extreme event flag gets raised (i.e. $f_{ee,k}=1$ and $f_{ee,k-1}=0$) and the current collective pitch angle is at least $\Delta\theta_{ee}^{on}$ (e.g. 5^o) below the reference pitch angle. The extreme event flag gets pulled down to zero ($f_{ee,k}=0$), implying EEC switch-off, by either the CUSUM test in Algorithm 8.3 (meaning that the extreme event has ended), or when the difference between the reference pitch angle $\theta_{ref,ext}(\hat{U}_{ax}^{\beta,gust})$ and the true

current collective pitch angle drops below $\Delta\theta_{ee}^{off}$ (e.g. 4^o), meaning that no further EEC action is needed. The rotor speed limitation algorithm is can be summarized as follows.

Algorithm 8.4 (Collective EEC).

Initialization Select $\Delta \theta_{ee}^{on}$, $\Delta \theta_{ee}^{off} < \Delta \theta_{ee}^{on}$, $t_{eec} = 0$.

Step 1 Use the current EKF estimates \hat{u}_k and $\hat{\beta}_k$ to compute $\hat{U}_{ax,k}^{\beta,gust}$ using (212).

Step 2 Run CUSUM test in Algorithm 8.3. If $f_{ee,k} = 0$ then set $t_{eec} = 0$ and go to Step 5.

Step 3 Compute
$$\Delta \theta_{ee,k} = \theta_{ref,ext}(\hat{U}_{ax,k}^{\beta,gust}) - \frac{1}{3} \sum_{b=1}^{3} \phi_{k}^{b}$$
.

Step 4 If $(f_{ee,k-1}=1 \text{ and } \Delta\theta_{ee,k} \geq \Delta\theta_{ee}^{off})$ or $(f_{ee,k-1}=0 \text{ and } \Delta\theta_{ee,k} \geq \Delta\theta_{ee}^{on})$ then

else

$$\begin{aligned}
t_{eec} &= 0, \\
f_{ee,k} &= 0.
\end{aligned}$$

Step 5 If $f_{ee,k-1} = 1$ and $f_{ee,k} = 0$ then

reinitialize conventional pitch control switch on conventional control.

Notice that the conventional pitch and generator torque controllers are switched off when the EEC becomes active. The selected EEC strategy causes no transient effects after the transition from conventional control to EEC. The inverse transition (back to conventional PI control), however, should be performed with much care since this can result in a very large transient. To prevent this, the conventional controllers are properly reinitialized before being switched on. This can be achieved by considering an interval of N time steps back, [k-N,k-1], and choosing the state of the conventional controller at time (k-N) in such a way that, if the conventional controller was active in the interval [k-N,k-1], it would have produced a control signal that matches the true control signal observed in this interval. This is described in more detail in [43, App. B].

8.5.2 Blade load reduction

As mentioned in the beginning of Section 8.5, besides rotor overspeed prevention, an important issue under extreme wind gusts with direction change is the reduction of blade loads. A yawed wind inflow results in large 1p blade load variations (see Figure 77), and a 0p (i.e. static) rotor tilt moment, that can be reduced by means of individual blade pitch control. This is the purpose of this section.

For IPC control design purposes, the nonlinear model (207) is linearized at a given operating point, resulting in the following linear model in Coleman domain

$$\mathcal{T}: \left\{ \begin{array}{ll} x_{k+1} &=& \tilde{A}x_k + \tilde{B}\theta_k^{ty} + \tilde{B}_u u_k^{ty}, \\ M_k^{ty} &=& \tilde{C}x_k + \tilde{D}\theta_k^{ty} + \tilde{D}_u u_k^{ty}, \end{array} \right.$$

where the signals u_k^{ty} , θ_k^{ty} and M_k^{ty} contain the tilt and yaw oriented components of the multi-

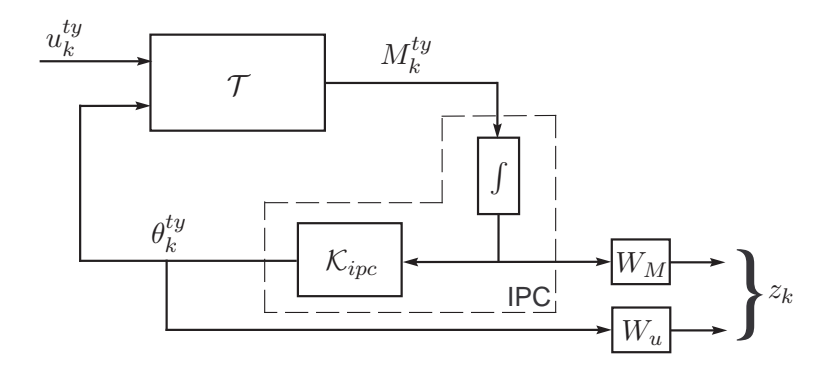


Figure 78 Block scheme for IPC design.

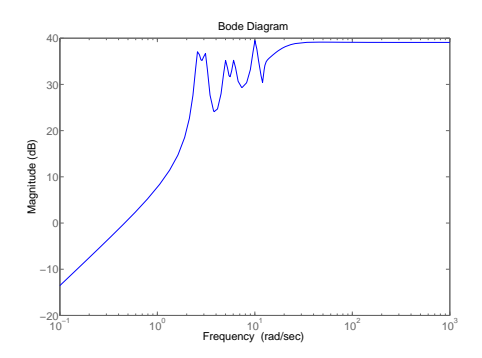
blade blade effective wind speed vector u_k^{cm} , blade pitch angles θ_k^{cm} and flapwise blade root bending moments M_z^{cm} , respectively⁶. The considered extreme event in this report (gust with direction change) can be modeled by a nonzero constant tilt-oriented (i.e. first) component in u_k^{ty} . The collective pitch control loop has only a negligible influence on the rotor tilt and yaw moments and has been left out for simplicity. Similarly, the controls θ_k^{ty} also barely affect the rotor speed dynamics and need not be taken into consideration in the conventional rotor speed control design.

The goal here is to design a stabilizing controller that uses the rotor moments M_k^{ty} as inputs and computes the control actions θ_k^{ty} so as to minimize the low frequency components of the rotor moments' signals. In the rotating reference frame this corresponds to the suppression of 1p load components in the blades. In order to achieve zero steady state rotor moments, an integral action will be included in the controller. Furthermore, the control action should not be too active at certain frequencies, excited by the external wind disturbance, such as the 3p frequency f_{3P} , and eventually the 6p frequency f_{6P} and the first tower frequency f_{tow} . In addition to that, no high frequency control activity is desired.

To achieve all these performance specifications, an \mathcal{H}_{∞} -optimal controller with integral action will be designed, optimizing the transfer from the external inputs u_k^{ty} to some suitable chosen weighted versions of the rotor moments and control action. More specifically, Figure 78 provides an block-schematic view of the IPC design model. In order to include integral action into the controller, the output of the system \mathcal{T} is appended with integrators (one integrator per output), which integrated model is used for an optimal \mathcal{H}_{∞} controller design \mathcal{K}_{ipc} . Once designed, the final controller is constructed by moving the integrators, used in the design model, to the inputs of the computed controller (see the area inside the dashed curve on Figure 78).

Of course, an optimal controller designed based on the linearized turbine model \mathcal{T} will only remain optimal at the working point at which the model is linearized. As the working point continually changes, it is important that once the controller has been designed, its stability and performance are evaluated at different working points. To achieve improved robustness properties to unmodelled dynamics, an \mathcal{H}_{∞} controller is designed. It should be pointed out that it is relatively simple to achieve better performance throughout the whole operation range of the turbine by means of gain-scheduling. To this end, an approach similar to the conventional way of including gain-scheduling collective pitch control algorithms [71] can be used, i.e. the gain of the IPC controller can be scheduled as a function of the pitch angle in such a way that the DC

⁶Note that the tilt and yaw components (u_k^{ty}) of the *multi-blade* wind signals should not be mistaken with the tilt and yaw oriented components of the wind velocity vector relative to the rotor plane (see Figure 76). The former are obtained as a result of the Coleman transformation of the three axial blade effective wind speeds and are such that the yaw-oriented (tilt-oriented) component of u_k^{ty} affects (mainly) the yaw (tilt) rotor moment. On the other hand, the yaw-oriented (tilt-oriented) component of the wind velocity vector mainly affects the tilt (yaw) rotor moment, respectively.



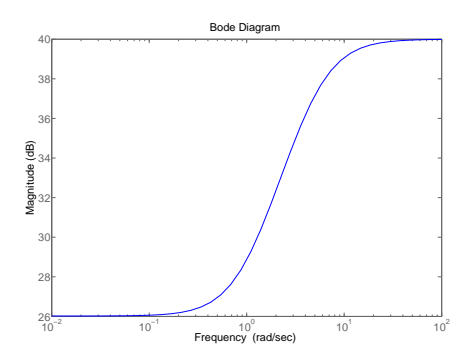


Figure 79 Bode magnitude plots of the weighting functions W_u (left) and W_M (right)

gain of the resulting open-loop transfer function remains constant. In practice, gain-scheduling of the IPC controller is usually not necessary due to the limited open-loop gain change over the operating region (it changes typically by a factor 2 over the full load region).

In order to comply with these frequency domain design specifications, the controller \mathcal{K}_{ipc} is designed by minimizing the \mathcal{H}_{∞} norm of the closed-loop transfer from the external inputs u_k^{ty} to the weighted integrated rotor moments and weighted control signals, as shown in Figure 78 (see the generalized output signal z_k). To this end, two weighting functions, W_M and W_u , can be selected with Bode magnitude plots as shown on Figure 79. For producing the left subplot on Figure 79, the weighting function for the control signals has been chosen as

$$W_u(z) = 10(F_{hp}(z) + F_{3p}(z)F_{6p}(z)F_{tow}(z) - 2)I_2,$$
(213)

where $F_{hp}(z)$ is a second order inverse Chebyshev high-pass filters (frequency $f_{hp}=4P$, reduction 20 dB, ripple 1dB), and $F_{3p}(z)$, $F_{6p}(z)$ and $F_{tow}(z)$ are second order inverse Chebyshev bandpass filters with the same reduction and ripple and bandpass intervals of $[0.9,1.1]f_{3P}$, $[0.9,1.1]f_{6P}$ and $[0.9,1.1]f_{tow}$, respectively. All filters have been scaled to achieve unity DC-gain, so that W_u computed via (213) has a DC gain of zero. The so-selected weighting function W_u punishes control activity at frequencies f_{tow} , f_{3P} , f_{6P} and higher. The weighting function W_M , on the other hand, puts a frequency domain weighting on the integrated rotor moments. As there is integral action in the controller anyway, the lower frequencies need not to be weighted additionally. Instead, W_M could be used to eventually put some weighting on certain frequencies within the desired controller bandwidth which are otherwise not sufficiently actuated by the integral type control action. The weighting function W_M used for producing the right subplot in Figure 79 is a lead-lag filter with lead frequency of 1 rad/sec, lag frequency of 5 rad/sec and DC-gain of 20. Notice that W_M acts on the integrated rotor moments. Translating this to the original the rotor moments M^{ty} , this results in some additional weighting of the frequency band [1,5] rad/sec.

The augmented plant with the integrators and the weighting filters has then the following form

$$\mathcal{T}^{a}(z): \left\{ z_{k} = \begin{bmatrix} \begin{bmatrix} 0 & W_{u}(q^{-1}) \\ \frac{T_{s}^{ctr}}{1-q^{-1}} W_{M}(q^{-1}) \mathcal{T}(q^{-1}) \\ \mathcal{T}(q^{-1}) \end{bmatrix} \begin{bmatrix} u_{k}^{ty} \\ \theta_{k}^{ty} \end{bmatrix}. \right.$$

The \mathcal{H}_{∞} optimal controller for $\mathcal{T}^a(z)$ is computed via the following optimization problem

$$\mathcal{K}_{ipc} = \arg\min_{K} \|\mathcal{F}(\mathcal{T}^{a}(z), K(z))\|_{\infty},$$

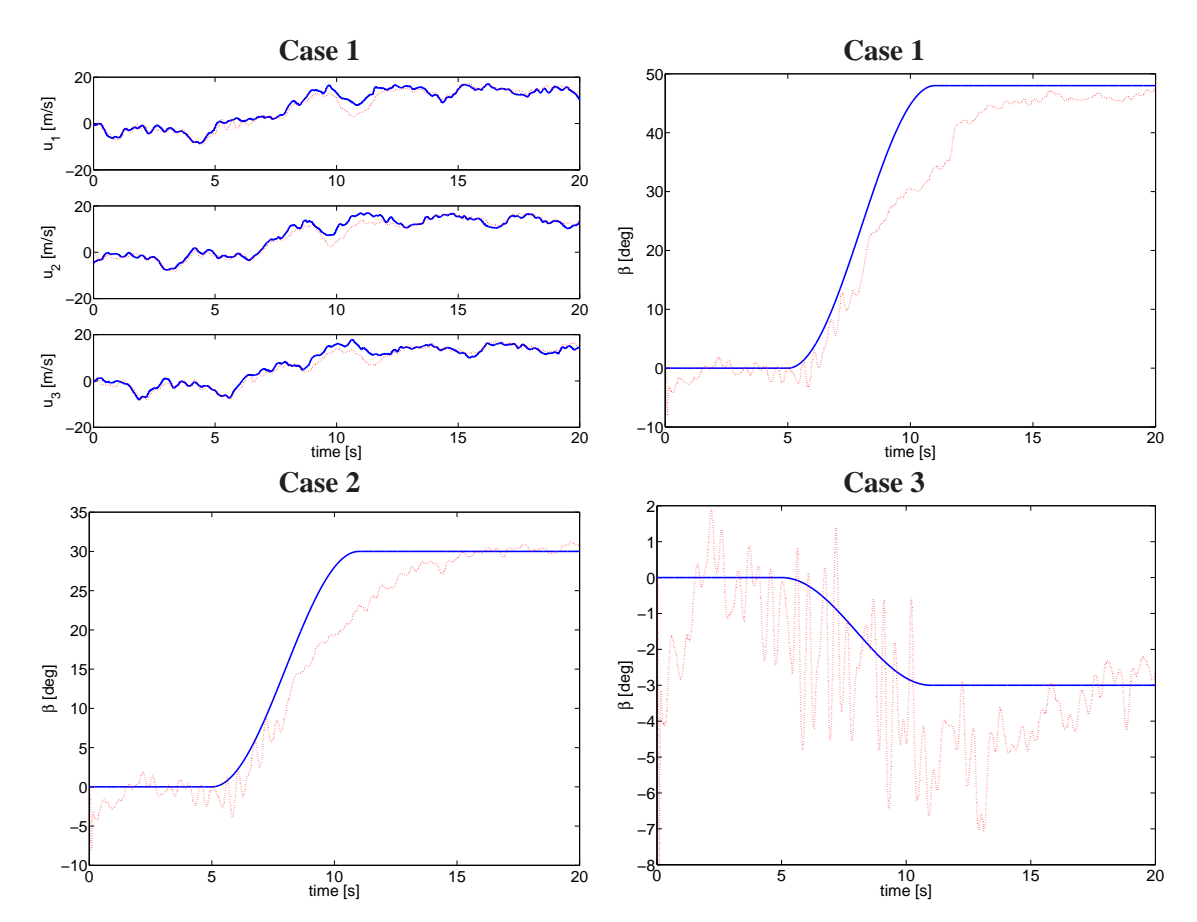


Figure 80 Simulated (solid blue) and estimated (dotted red) blade effective wind speeds u_b (top, left) for case 1, and oblique inflow angle β (right) for case 1 (top, right), case 2 (bottom, left) and case 3 (bottom, right)

where $\mathcal{F}(\mathcal{T}^a(z), K(z))$ denotes the closed-loop system, $\|\cdot\|_{\infty}$ denote the \mathcal{H}_{∞} system norm, and wherein the optimization is defined over all controllers K(z) that have the same number of states as the augmented model $\mathcal{T}^a(z)$. For more details on modern robust control design, the reader is referred to [106]. The controller \mathcal{K}_{ipc} , designed in this way, will be a MIMO (2-by-2) transfer function, mapping the *integrated* rotor tilt and yaw moments to the tilt and yaw oriented blade pitch angles. Moving the integrators back to the controller results in the final IPC

$$\mathcal{K}_{ipc}^i = \mathcal{K}_{ipc} egin{bmatrix} rac{T_s^{ctr}}{z-1} & & \ & rac{T_s^{ctr}}{z-1} \end{bmatrix}.$$

8.6 Simulation

The performance of the complete algorithm, including extreme event recognition and control, is demonstrated on simulation data, obtained with the nonlinear test turbine model described in Section 8.3. The model represents a 3-bladed HAWT with rated power of 2.5MW, rotor radius of R=40 m, and rated rotor speed of $\bar{\Omega}=1.85$ rad/sec. In the BEM module, the blades are represented by $N_{ann}=15$ elements. The structural model is linearized around an equilibrium point corresponding to rated rotor speed, mean longitudinal wind speed of $\bar{U}=15$ m/s (with $\bar{\phi}_{tlt}=-5.138^o$ [mainly due to tilted rotor] and $\bar{\phi}_{yw}=0.01^o$) and blade pitch angles of $\bar{\phi}^b=7.24^o$. The values selected for the tuning parameters of the EG&DR and EEC schemes are given

Alg.	Variable	Value	Description	
EKF	n	20	state dimension	
	\hat{x}_0^a	0	initial state estimate	
	P_0	$\begin{bmatrix} 10^{-4}I_{n+3} & & \\ & 10^{-5} \end{bmatrix}$	initial state covariance matrix	
	R_r	$\begin{bmatrix} 10^{-2}I_2 & & & \\ & 10^{-4} \end{bmatrix}$	process noise covariance matrix	
	R_e	$\begin{bmatrix} 10^3 I_3 & \\ & 10^2 I_3 \end{bmatrix}$	measurement noise covariance matrix	
Cusum	k_u	25	moving window length	
	ν	1	insensitivity parameter	
	h	100	threshold	
EEC	$\dot{\theta}_{mx,ext}$	$10^{o}/s$	max pitch speed under extreme event	
	$\dot{ heta}_{mx}$	$4^o/s$	max pitch speed under normal conditions	
	$\Delta heta_{ee}^{on}$	$5^{o'}$	EEC activation zone	
	$\Delta heta_{ee}^{off}$	4^o	EEC deactivation zone	
	$F_{3p}(z)$	$\frac{z^4 - 3.973z^3 + 5.948z^2 - 3.977z + 1.002}{z^4 - 3.953z^3 + 5.883z^2 - 3.908z + 0.9774}$	3p band pass filter	
	$F_{6p}(z)$	1	6p band pass filter	
	$F_{tow}(z)$	1	tower frequency band pass filter	
	$F_{hp}(z)$	$\frac{10z^2 - 19.48z + 9.57}{z^2 - 1.554z + 0.6415}$	control signal weighting filter	
	$F_M(z)$	$\frac{100z - 98.1}{z - 0.9048}$	integrated rotor moments lead-lag filter	

Table 8 Parameters used in the described algorithms.

case	1	2	3
V_{gust} [m/s]	15	15	3
β_{gust}^{s} [deg]	48	30	-3

Table 9 Simulated wind gust cases

in Table 8. In order to evaluate the performance of the proposed algorithm under different wind gust conditions, three different cases are simulated, as summarized in Table 9. The first case corresponds to the extreme direction change (EDC) as specified in the norm IEC 61400-1. The EDC consists of a rising $V_{qust} = 15$ m/s wind gust with a simultaneous wind direction change of $\beta_{gust} = 720/U$ degrees. The effects of this on the turbine loads have been described in Section 8.3.5. The second case corresponds to the same rising wind gust ($V_{gust} = 15 \text{ m/s}$) but a different, smaller wind direction change angle ($\beta_{qust} = 30$ degrees). This results in even larger 1p loads on the blades as compared to the first case due to the much larger axial component of the wind velocity vector, i.e. $\cos(\beta_{gust})(U+V_{gust})$. Hence, the second case has the purpose to test the capabilities of the proposed algorithm to even more serious wind gust conditions, than specified in the IEC norm. The third case, on the other hand, has the purpose to test whether the algorithm is not overly sensitive, and is not responding to minor events, which is not desirable as the conventional controller should be able to handle them. For that purpose, the third case comprises a 3 m/s wind gust in combination with a -3 degrees direction change. This last case should not trigger the EEC algorithm. Different simulations are run. The turbine dynamics is simulated at a sample rate of 200 Hz, while the controllers (CPC and IPC) work at 50 Hz. In the time series, presented in the figures below, only the first 20 seconds are plotted. The (extreme) events occur 5 sec from the beginning of each simulation. For the power spectra plots later on, the time series from the 10th sec to the end of the simulations are used, so that only the data after the event occurrence (and after the transients have died out) is taken. The first two cases are simulated two times, once with the EEC algorithm turned off (i.e. conventional controller active all the time), and once with the EEC algorithm turned on. This makes it possible to investigate to what extend the proposed EEC algorithm improves on the rotor speed control

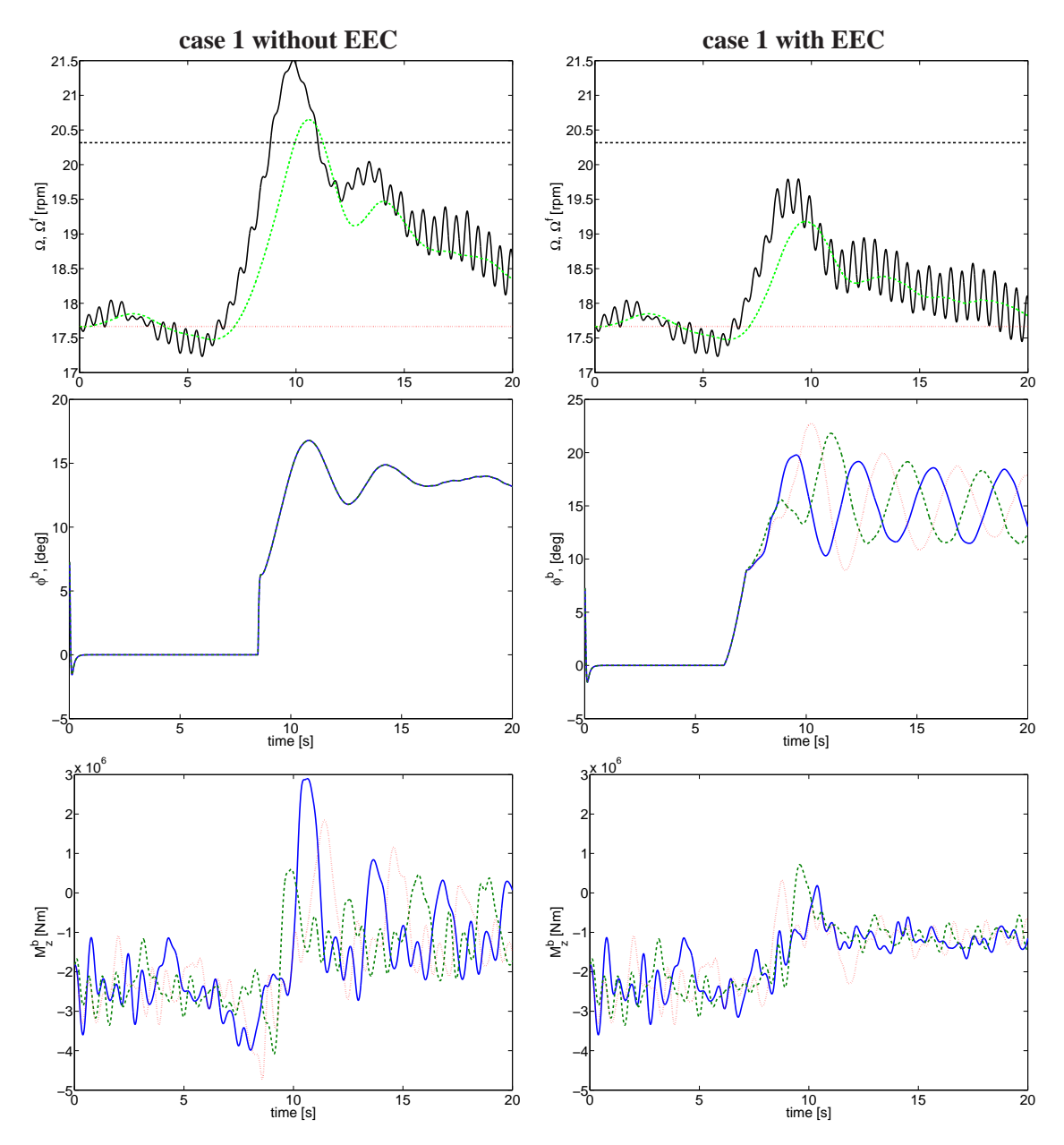


Figure 81 Turbine simulation under case 1 (extreme 15 m/s rising gust and 48 deg direction change at t = 5 sec) without EEC (left) and with EEC (right)

and load reduction under extreme gust conditions. The third case is simulated only once, since even when the EEC algorithm is turned on, it doesn't get activated by the EG&DR scheme as the event is not recognized as major.

Evaluation of the EG&DR

The performance of the EG&DR scheme is determined by the accuracy of the estimates of the EKF. To evaluate that, we will compare the simulated blade effective wind speeds u_b and the simulated wind direction change angle β to their estimates, computed by the EKF.

Figure 80 shows the performance of the EKF scheme under the three simulated scenarios. The top left subplot represents the three simulated blade effective wind speeds (solid blue curves) and their estimates (dotted red curves) by the EKF for case 1 only. The excellent accuracy of the wind estimates remains unchanged under cases 2 and 3, though these are not reported here for the sake of brevity. The remaining three subplots in Figure 80 depict the simulated oblique inflow angle

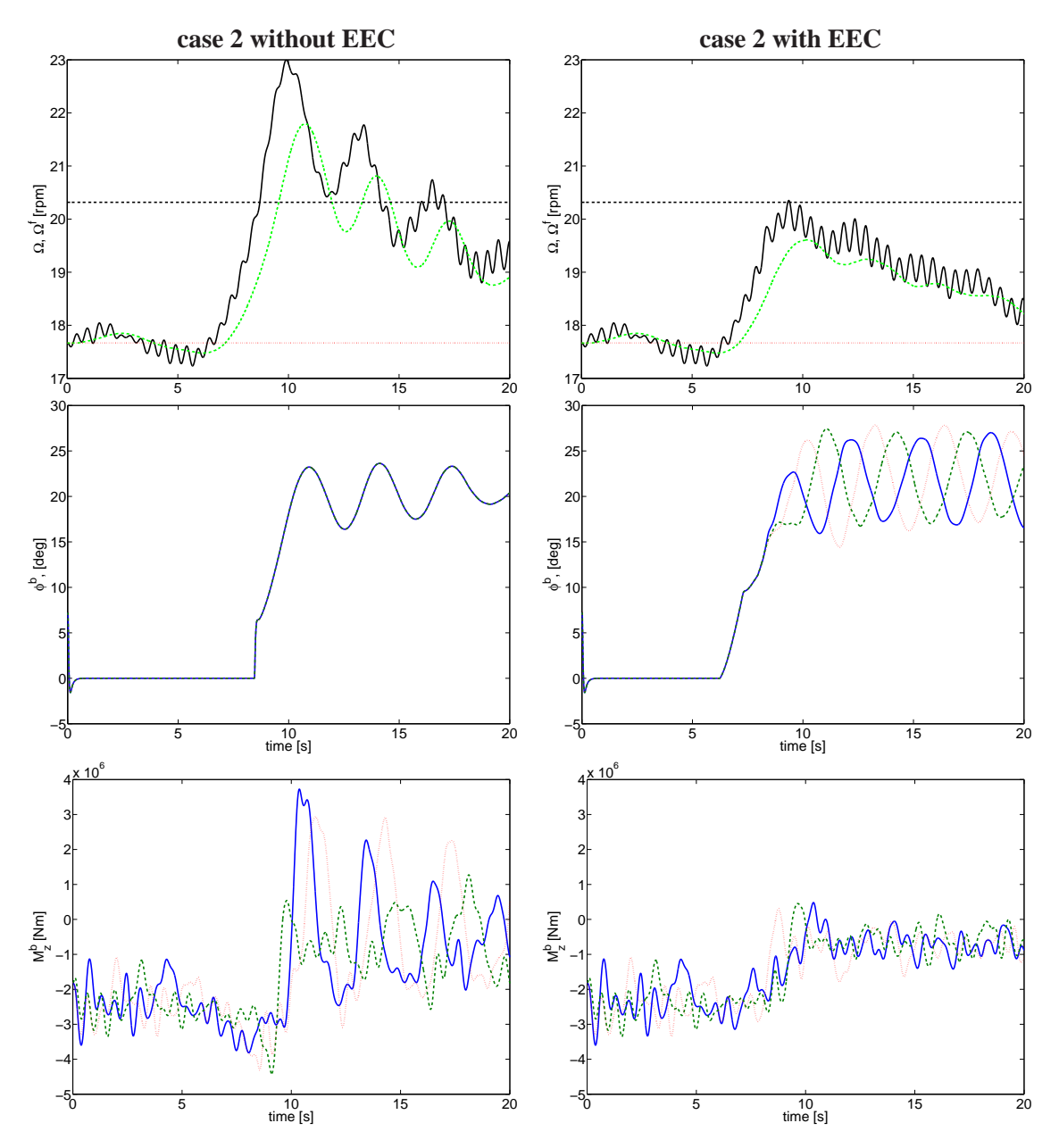


Figure 82 Turbine simulation under case 2 (extreme 15 m/s rising gust and 30 deg direction change at t = 5 sec) without EEC (left) and with EEC (right)

 β (solid blue curves) together with its EKF estimates (dotted red curves) for the three different cases. Clearly, these estimates are sufficiently accurate for the detection of wind direction changes since the estimates do not differ more than about ± 3 degrees from the simulated values.

Evaluation of the EEC

As discussed in Section 8.3.5, the purpose of the EEC algorithm is to prevent rotor overspeed (that can trigger unnecessary emergency shutdown of the turbine) and to reduce large blade 1p loads under extreme wind gust conditions. On the other hand, the EEC algorithm should remain inactive under mild gust conditions. To demonstrate its performance, the rotor speed Ω , the blade pitch angles ϕ^b and the blade root out-of-plane bending moments M_z^b are next investigated under the above-mentioned three load cases. Figure 81 pertains to load case 1, where the subplots on the left hand side correspond to the case without EEC, while the subplots on the right – to the case with EEC. Clearly, when the EEC algorithm is not present, this load case leads to the rotor

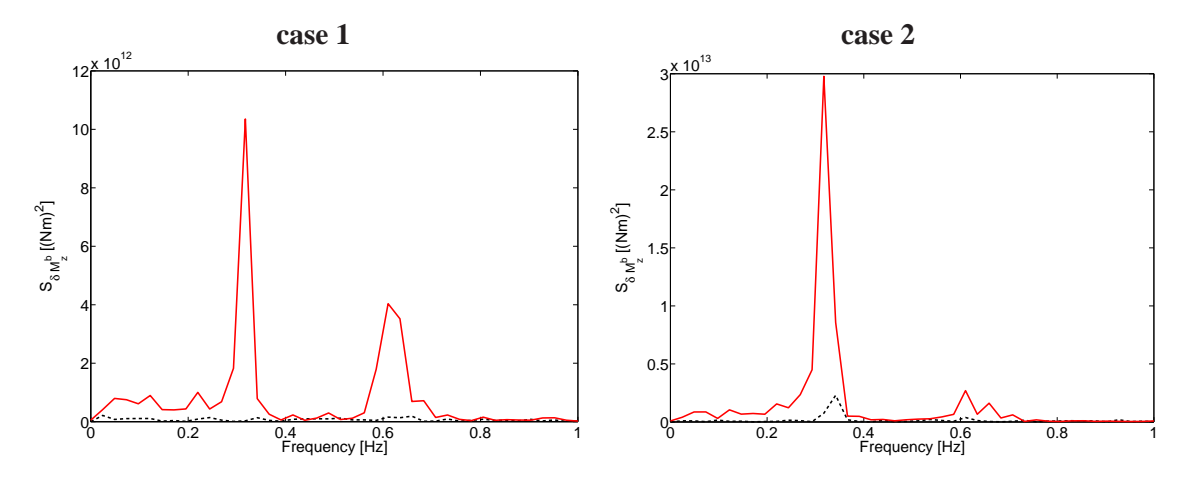


Figure 83 PSD of blade root flapwise bending moments M_z^b for case 1 (left) and case 2 (right), without EEC (solid curves) and with EEC (dashed curves)

speed Ω getting much above its limit. This is due to the conventional controller remaining in partial load regime until the *filtered* rotor speed Ω^f (dashed green line) exceeds the rated speed $\bar{\Omega}$ by 1rpm, at which point the true speed Ω is already too large. The EEC algorithm, on the other hand, detects the gust at an early stage (at time 6.125 seconds) and starts pitching the blades to feathering position, preventing rotor overspeed (see top and middle right-hand side subplots). Moreover, once the estimated oblique inflow angle exceeds 10 degrees (the red dashed curve on top-right subplot in Figure 80), the IPC control is activated achieving substantial blade load reduction, as observed by comparing the bottom subplots on Figure 81 during the second half of the simulation (where the IPC is active). The achieved blade load reduction can be also appreciated by observing the left subplot on Figure 83 that depicts the spectra of the blade root out-of-plane bending moment variations δM_z^b in the cases without (solid red curve) and with (dashed black curve) EEC. The simulation results under case 2 are depicted in Figure 82. Again, the subplots on the left hand side correspond to the case without EEC, while the subplots on the right – to the case with EEC. As already mentioned, this load case is even more serious than the first one. This can indeed be seen by observing that the rotor speed (top left subplot in Figure 82) rises to as much as 23 rpm (i.e. more than 30% above the rated value). Similarly, the 1p blade loads also have a much higher amplitude as compared to case 1. With EEC, again, the rotor speed remains within its limits (top right subplot in Figure 82), while the IPC action, initiated after the oblique inflow angle exceeds 10 degrees, achieves significant 1p blade load damping, as can be seen from the bottom right subplot in Figure 82, as well as from the power spectra in the right-hand side subplot of Figure 83.

Finally, case 3 is simulated only once, i.e. with the EEC algorithm on, although it does not get activated by the EG&DR scheme since the simulated event does not get recognized as a major one by the CUSUM test. As a result, the conventional controller remains active through the whole simulation. The rotor speed Ω , the blade pitch angles ϕ^b , and the blade root out-of-plane bending moments M_z^b are given in Figure 84. It can be observed, indeed, that no EEC is necessary in this case as the rotor speed remains well within its limits, and the blade root bending moments M_z^b after the event occurrence remain comparable to those before the gust.

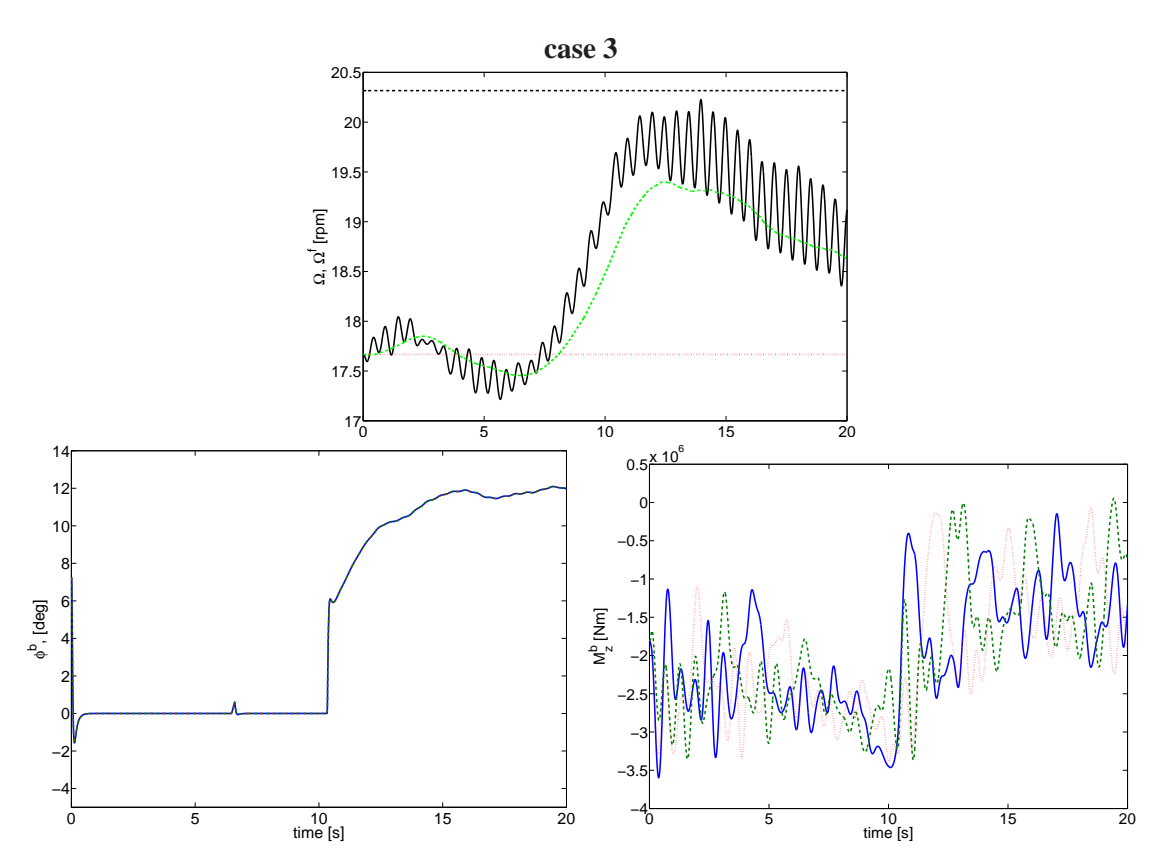


Figure 84 Turbine simulation under case 3 (3 m/s rising gust and -3 deg direction change at t=5 sec). Due to the mild gust condition, the EEC does not get activated.

9 Fast wind gust detection with GLRT

Sumamry

Extreme conditions are detected from wind speed estimates or residues of a Kalman filter. The Kalman filter is derived from an augmented turbine model with 'wind dynamics', similar to that for fault detection in the previous section. ECN developed detection algorithms that are based on the cumulated sum of the wind speed estimates or on generalized maximum likelihood ratio tests (GLRTs) for the residues.

Likelihood ratio tests can be performed for the residues of the Kalman filter. These tests allow for the identification of abnormal behavior that relates to gusts.

9.1 Brief method description

In this section, an alternative method to the CUSUM test, presented in Section 8.4.3, is described using the GLRT. A detailed description of the method can be found in the patent [79]; here only a brief summary is provided.

Contrary to the model-free (signal-based) CUSUM method, the GLRT method relies on a discrete-time linearized model of the wind turbine of the form

$$x(n+1) = A x(n) + B u(n) + B_{d} d(n)$$

$$y_{\text{valid}}(n) = C x(n) + D u(n) + D_{d} d(n)$$
(214)

wherein u is the control signal vector containing the generator torque and three blade pitch angle setpoints in fixed coordinates, x is the state of the wind turbine, y is the vector of measurements on the wind turbine, and d is the disturbance signal dominated by wind speed variations. This model can be constructed, e.g., by discretizing the model described in Section 1.3.1.

The wind speed variations that dominate the disturbance signal \underline{d} can be modeled as blade (root) effective wind speed signals; one or two per blade. If only axial wind speed variations are taken into account, then only one wind speed signal per blade applies. A power spectrum matrix formulation for these blade effective wind speed signals is given in equation 122 on page 122. The existence of such a power spectrum matrix allows for the deriavation of a linear state space model (wind model) that generates the wind speeds in d from completely uncorrelated Gaussian distributed noise e (white noise):

$$x_{\rm w}(n+1) = A_{\rm w} x_{\rm w}(n) + B_{\rm w} e(n)$$

 $d(n) = C_{\rm w} x_{\rm w}(n) + e(n)$ (215)

It is clear that we can add this wind model to the above wind turbine model formulation by equation 214. This yields a so called augmented model. For this model, a Kalman filter can be constructed which now directly relates to (three) Gaussian white noise sources e.

Now, assume that an extreme wind speed or wind direction change occurs. The evolution of the residue r in addition to its "gust-free value" e can then be approximated by the outputs of the turbine state space model by equation 214 that is driven by an assumed related gust evolution with amplitude $A_{\rm g}$. Of course, we measure the overall values of the residues.

The white, Gaussian character of e now allows to derive expressions for the joint probability density functions of the residue in case of the occurrence of the assumed gust and in the gust-free case; the attribute 'joint' pertains to the simultaneous consideration of the time points in a fixed-length window of which the end point moves with the current time instance n. The ratio of these joint

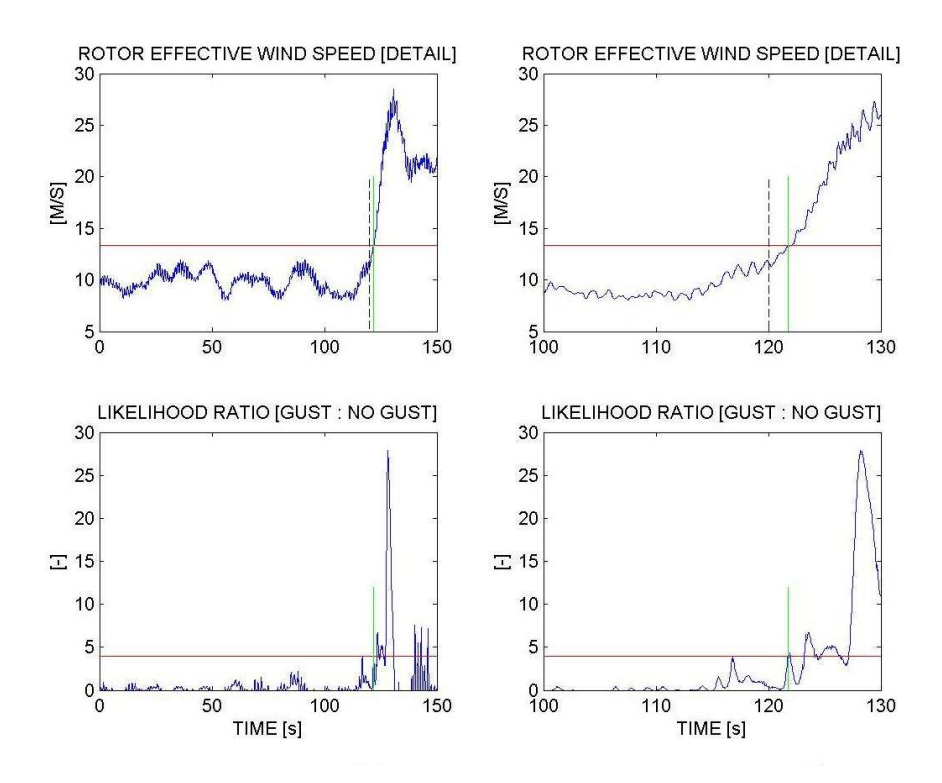


Figure 85 Gust detection by likelihood ratio test

probability expressions can be analytically maximized over the gust amplitude $A_{\rm g}$. The resulting Geralized Maximum Likelihood Ratio (GLR) will grow very rapidly during the occurrence of a gust of which the normalized evolution is fed through in the probability density function ratio.

It is known that rotor uniform wind speed changes affect the thrust force and driving rotor torque while uniform wind direction changes affect the tilting rotor torque and horizontal force. So it is clear that residue analysis for different measurement signals is needed for different rotor coherent wind condition changes (gust classes). Six wind classes are distinguished in [79]. Next to the uniform gust and change of wind direction, these include the fast change of a backing and veering wind, of a jet stream, of a partial wake condition, and of a sloping wind.

The total involved measurement signals are the thrust force and driving torque, the yawing rotor torque and vertical force, and the tilting torque and horizontal force. Alternatively, load measurements can be done in a rotating frame, as long as a non-singular relationship exists with the six rotor loads. Of course, it can be decided to detect gust from less classes. In that case the according rotor loads can be left out the detection algorithm. Note that the wind (disturbance) generating model as per equation 215 is to match to the considered load signals.

For a certain gust class, it is of course allowed to perform a GLRT for more than one assumed evolution of the related normalized gust (gust class evolution prototype [GCP]). GCPs for a uniform gust can be a '1 minus cosine' evolution and a "Mexican hat"; details are in [79].

Figure 85 gives an example of GLRT based detection of a uniform gust that starts at time instance 120 s. The left hand boxes show the enveloping time frame whereas the right hand boxes show details around the start of the gust. The solid horizontal line in the lower plots identifies the detection threshold; the solid vertical line the time instance of detection. The upper right plot tells that detection occurs after a 'fast moving average' wind speed increase of ca. 1.5 to 2 m/s. The nearly exceedance of the detection threshold at 118 s proves the probability of 'over detection'. An other choice for the length of the moving window may release this ambiguity at the cost of a slightly later gust detection.

Effectively, an involved GLRT agrees with a threshold test for the ratio between the auto-correlation of the residues and its cross-correlations with assumed normalized extreme event evolution. These correlations are determined over a relatively short moving time window.

Part V

Optimal shutdown control (OSC)

Summary

This section considers the design of an Optimal Shutdown Controller (OSC). It has the purpose to bring the wind turbine to a stop under serious system failures in such a way that the loads are kept as low as possible in order to reduce the chance of (further) damage. Serious failures and occasions that require a shutdown, and which are considered in this section, include failure of one pitch actuator and a sudden drop to zero of electric torque (as a result of, e.g., loss of electric grid, or rotor axis fracture). For control (design) a relatively simple (nonlinear) wind turbine was developed, based on physics. The performance of shutdown control is quantified using a cost function that weighed generator speed deviations from idle speed, tower foot moment deviations from 0, and rotor axis bending moment deviations from zero. The shutdown control problem are analyzed, which showed that with conventional shutdown, the tower fore-aft oscillations were caused mainly by exciting the tower eigenfrequencies by the pitch actuators. Furthermore, the rotor bending moments can be reduced by pitching more slowly. Based on the analysis, three novel shutdown control methods are proposed:

- 1 a simple variation on the conventional procedure, namely, by filtering the (open-loop) control signals first (and choosing the filter such that the tower is not excited),
- 2 a closed-loop shutdown control method where the rotor speed reference slowly drops to 0, and where conventional pitch control is used,
- 3 a closed-loop shutdown control method using Nonlinear Model Predictive Control (NMPC).

The latter method directly uses the performance objective and the control-oriented model to calculate control actions.

The shutdown control methods are compared with conventional method in simulations on a detailed aeroelastic model of a hypothetical wind turbine (referred to as TTURB). The results showed that the first method achieves a considerable reduction in tower fore-aft movements, even though a simple first order low pass filter was used. Still, NMPC realizes the best results in reducing tower foot oscillations, rotor bending and avoiding rotor overspeed.





Figure 86 Snapshots of a movie of a wind turbine 'run-away'. As a result, the blades were torn away from the wind turbine.

10 Introduction

This section focuses on the design of OSC algorithm capable of stopping the wind turbine after a serious system failure in such a way, that the extreme loads are as low as possible. In this way, (the accumulation of) damage can be prevented during operation. Ultimate loads, especially at the tower bottom, can also be reduced by OSC, which can be used during the design process for optimizing the design and saving on material costs.

Serious failures and occasions that require a shutdown, and which are considered in this section, include:

- failure of one pitch actuator
- sudden drop to zero of electric torque (loss of electric grid, or rotor axis fracture)

Pictures below (see figure 86) show what can happen if a turbine is not or cannot shutdown correctly after a serious failure. In this case, the rotor speed ran away, leading to a complete destruction of the wind turbine.

The basic reason to shut down the wind turbine, after one of the above mentioned cases, is to avoid (further) damage to the wind turbine: the loads on the wind turbine are smallest when the rotor speed is zero (or sufficiently low). The conventional shutdown procedure, with a variable pitch regulated wind turbine, is (at the time of writing this section) to pitch the blades to vane position at a fixed speed. Essentially, this is an open-loop control method. The question is if there exist better control methods that would lead to smaller peak loads during a shutdown. Such a control method can lead to better (lighter) wind turbines. To clarify this: wind turbines are designed to survive various load cases, among which severe failures. Experience by ECN wind turbine specialists has shown that the stresses and strains occurring during a shutdown can be design leading; hence, a shutdown procedure that induces smaller stresses and strains can result in less material use.

To be more specific, we introduce the following definitions.

Definition of a shutdown

A shutdown is defined as an operation where the rotor speed is reduced to idle speed or lower.

Optimal Shutdown

A shutdown is optimal if (subsequent) damage is minimized during shutdown. Subsequent damage, in this section, refers to

- structural damage to the tower due to excessive peaks in the fore-aft tower root moment
- structural damage to the blades and/or generator due to generator over speed
- structural damage to the rotor shaft, main bearing, or the yaw bearing due to excessive peaks in the rotor shaft bending moment

The main question posed in this section is:

Is it possible to develop Shutdown Control algorithms that shut down a wind turbine in such a way, that the rotor speed does not exceed a given maximum value, and that peaks in the rotor axis bending moment and tower foot fore-aft moment are minimized?

To answer this question, the following subquestions need to be answered:

- 1 how can the wind turbine dynamics be modeled during the serious failure conditions leading to a shutdown, and during the shutdown, such that the model is suited for control (design) purposes?
- 2 how can the performance of a shutdown controller be quantified?
- 3 what shutdown control methods can be found/developed to achieve the desired goal of an Optimal Shutdown?
- 4 how do the developed shutdown control methods compare with the conventional shutdown method (where the blades pitch to vane with a fixed speed)?

11 Control-oriented model for OSC design

This section presents a control-oriented model of a wind turbine that is suitable for (nonlinear) control (design) purposes. Since we are considering control during a shutdown, the model should be 'valid' for shutdown conditions. As specified in chapter 1, these conditions include the case where at least one blade has a different pitch angle.

11.1 Modeling structural dynamics and aerodynamics

For control design, a model that is as simple as possible, yet is sufficiently accurate, is desirable. The wind turbine model presented below consists of a simple linear model for the structural dynamics (described below), and a Blade Element Model for the aerodynamics (described in Section 8.3.3).

The structural dynamics of the wind turbine have been based on [4], and are modeled by

```
J_{r}\dot{\omega}_{r} = T_{a} - K_{d}\theta - C_{d}\dot{\theta}
J_{g}\dot{\omega}_{g} = -T_{g} + K_{d}\theta + C_{d}\dot{\theta}
\dot{\theta} = \omega_{r} - \omega_{g}
m_{tw}\dot{v}_{fa} = K_{b}(x_{1} + x_{2} + x_{3}) + C_{b}(v_{1} + v_{2} + v_{3}) + k_{t}M_{t} - s_{tw}x_{fa} - d_{tw}v_{fa}
m_{i}(\dot{v}_{b} + \dot{v}_{fa}) = F_{b} - K_{b}x_{b} - C_{b}v_{b} \qquad b = 1, 2, 3
\dot{x}_{fa} = v_{fa}
\dot{x}_{b} = v_{b} \qquad b = 1, 2, 3
\dot{\psi}_{1} = \omega_{r}
\dot{\beta}_{b} = -1/\tau(\beta_{b} + u_{b}) \qquad b = 1, 2, 3
M_{t} = \sum_{b=0}^{B} \sin(\psi_{b})M_{f,b}
M_{f,b} = (\frac{2}{3}R)(K_{b}x_{i} + C_{b}v_{i})
(216)
```

with

```
\omega_r = rotation speed of rotor (rad/s)
```

 θ = torsion angle between rotor shaft and generator shaft (rad)

 ω_q = rotation speed of generator (rad/s)

b =blade number

 x_{fa} = fore-aft position of tower top (m)

 v_{fa} = fore-aft velocity of tower top (m/s)

 x_b = position of blade tip b in axial direction, relative to tower top position (m)

 v_b = velocity of blade tip in axial direction (m/s)

 m_b = effective mass of (one) rotor blade (kg)

 J_r = inertia of rotor (kg m^2)

 J_g = slow shaft equivalent inertia of generator (kg m^2)

 F_b = aerodynamic force on blade b in fore-aft direction

 $k_t = \text{tilt gain } (m^{-1})$

 T_a = aerodynamic torque by the blades (Nm)

 M_t = tilt moment exerted by the blades (Nm)

 N_q = transmission ratio (-)

 K_d = stiffness of transmission (Nm/rad)

 B_d = damping of the transmission (Nm/rad/s)

 β_b = pitch angle of blade b (rad)

 ψ_b the azimuth of the b-th blade

 $M_{f,b}$ the blade root moment in a blade, in flap-wise direction

with R the blade length (m)

Outputs of the model

The control oriented model should relate the controlled outputs to the states and inputs of the model. The controlled outputs are:

- Generator speed (ω_q)
- Rotor axis bending moment (M_{rb})
- Tower foot moment in fore-aft direction (M_{tw})
- Torsion angle between generator and rotor shaft (θ)

The generator speed and torsion angle are states of the structural model. The rotor axis bending moment, fixed to the rotor axis, is the vector sum of all flap-wise blade moments. This moment has two components (in y and z direction):

$$M_{rb} = \sqrt{M_{rby}^2 + M_{rbz}^2}$$

$$M_{rby} = M_{f3} \cos\left(\frac{2}{3}\pi - \frac{1}{2}\pi\right) + M_{f2} \cos\left(\frac{4}{3}\pi - \frac{1}{2}\pi\right)$$

$$= M_{f3} \cos\left(\frac{1}{6}\pi - \right) + M_{f2} \cos\left(\frac{5}{6}\pi\right) \approx 0.86M_{f3} - 0.86M_{f2}$$

$$M_{rbz} = M_{f1} + M_{f2} \cos\left(\frac{4}{3}\pi\right) + M_{f3} \cos\left(\frac{2}{3}\pi\right)$$

$$= M_{f1} - 0.5M_{f2} - 0.5M_{f3}$$
(217)

The tower foot moment is calculated from:

$$M_{tw} = \left(\frac{2}{3}H\right)\left(s_{tw}x_{fa} + d_{tw}v_{fa}\right) \tag{218}$$

with H being the height.

Measured outputs

It is assumed that the following outputs can be measured (and used in feedback control, if applicable):

- Generator speed ω_q
- Blade root moments of each blade $(M_{f,i})$
- Tower foot moment (M_{tw})
- Pitch angle of each blade (β)

11.2 Blade effective wind model

The blade effective wind speed $V_{w,b}$ acting on blade b is modeled as the sum of integrated white noise (V_m) and a wind speed variation $(V_{p,b})$ that is periodic (deterministic):

$$V_{w,b} = V_m + V_{n,b} (219)$$

with

$$\frac{dV_m}{dt} = w_1 \tag{220}$$

with w_1 being white noise process.

The periodic component $(V_{p,b})$ models wind speed variations due to wind shear, rotational sampling, and tower shadow. One possibility is to model the periodic wind speed variations acting on

blade b by:

$$V_{p,b} = A_p cos(\psi_b) \qquad b = 1, 2, 3$$

$$\frac{dA_p}{dt} = k_2 w_2$$
(221)

However, in this section the periodic components of the wind are ignored to simplify matters.

Fatigue modeling 11.3

This section briefly considers the modeling of fatigue, although the model has not been used directly in this study on shutdown: if shutdowns occur frequently, fatigue can be important and during normal operation, fatigue is of dominant importance.

Summary of control-oriented fatigue model 11.3.1

Fatigue is usually computed by a rain-flow analysis in combination with an SN curve (load S versus the maximum number of cycles N, above which fatigue damage can be expected). In this method, the loads are "transformed" by rainflow analysis to an equivalent load at one frequency, after which the life time/fatigue is inferred from an SN curve. For control purposes, this method is not suitable. A, for control purposes suitable, fatigue model was presented in [53]:

$$d = \dot{D} = -\frac{1}{b\sigma_f} \left(\frac{|\sigma|}{\sigma_f} \right)^{-(1+b)/b} |\dot{\sigma}|$$

where d is the damage rate (s^{-1}, D) is a damage number between 0 and 1 (0 indicating "no damage", and 1 - failure), and b and σ_f material constants from the SN curve. The derivation is summarized in Section 11.3.2 below.

Based on this model, the fatigue damage rate at for instance the tower foot, due to fore-aft movements, can be modelled by:

$$d_{fa} = -\frac{1}{b\sigma_f} \left(\frac{|\sigma_{fa}|}{\sigma_f} \right)^{-(1+b)/b} |\dot{\sigma}_{fa}| \tag{222}$$

with $\sigma_{fa}=K_{fa}x_{fa}$ and $\dot{\sigma}_{fa}=K_{fa}v_{fa}$. Clearly, the fatigue damage rate is smaller, if x_{fa} , or v_{fa} is smaller.

Derivation of the control-oriented fatigue model

For wind turbine design, fatigue damage is usually calculated using Palmgren-Miner's damage

$$D = \sum_{i=1}^{N} \frac{n_i}{N_i}$$

 $D = \sum_{i=1}^{N} \frac{n_i}{N_i}$ wherein D is quantifies the damage (with D=1 meaning total failure), n_i is the number of cycles with stress range σ_i , N_i is the number of cycles to failure at stress level σ_i , and N_i can be related to σ_i by the SN curve, i.e. $N_i = \frac{K}{\sigma_i^k}$, N is the total number of cycles, σ_i is the stress range of cycle(s) i, and K and k are material constants of the SN curve (for steel, typical values are $K = 6.2510^{32}$ and k = 4, while for glass/epoxy $S_{min}/S_{max} = 0.1$, $K = 10^{19}$, k = 6 [58]).

The Palmgren Miner rule requires the stress history to be divided into stress cycles with fixed stress ranges. Rainflow counting is often used to convert arbitrary signals in equivalent stress cycles. Roughly speaking, rainflow counting identifies local maxima M_i in the stress history, then finds the maximum of the local minima (left (m_j^-) and right m_j^+) surrounding M_j , and calculates the equivalent rainflow cycle as: $s_j = M_j - \max(m_j^-, m_i^+)$.

However, this fatigue quantification method is not suitable for on-line estimation of the fatigue damage.

In [3] fatigue damage is estimated from spectral properties of the stress signal. In this work, the stress signal, which is assumed to be Gaussian distributed, is approximated by a narrow banded approximation with the same variance as the original process. The damage rate of this approximation forms an upper bound on the damage rate of the original process, and is given by:

$$E[\dot{d}] = \frac{1}{2\pi} \sqrt{\frac{\lambda_4}{\lambda_2}} \frac{1}{K} (2\sqrt{2\lambda_0}\Gamma(1 + \frac{k}{2}))$$

with λ_i being the *i*-th spectral moment of the signal x (note that it can be shown that $\lambda_0 = \sigma_x^2$, $\lambda_2 = \sigma_x^2$, $\lambda_2 = \sigma_x^2$). This expression can be extended with a correction factor to account for the signal not being narrow banded. In [31] this fatigue model is used in (linear) control design calculations for a wind turbine. This fatigue model is specifically suitable for that purpose, but it is not directly applicable for on-line estimation of the fatigue rate. For that, the spectral moments would have to be estimated on-line.

In [53] and [62] a control oriented fatigue model is presented. There, under the assumptions of

- · zero means stress
- Plamgren's Miner damage rule

the number of cycles until failure (N_f) is given by:

$$N_f = 0.5 \left(\frac{\sigma_a}{\sigma_f}\right)^{1/b}$$

with d_{cyc} being the damage per cycle (with 0: no damage, 1: failure), σ_a the amplitude of the stress variation, σ_f and b are material constants (e.g. $\sigma_f = 1.19*10^8$ Pa, b = -0.25, and for steel). Note that this model is similar to the above described SN curve with b = -1/k and $\sigma_f = (2*K)^{1/k}$.

Define the damage per cycle as (d_{cyc}) as $d_{cyc} = 1/N_f$. Then

$$d_{cyc} = 2\left(\frac{\sigma_a}{\sigma_f}\right)^{-1/b}$$

Define the damage rate δ as $\int_0^{\sigma_a} \delta d\sigma = d_{cyc}$, then

$$\frac{d\delta}{d\sigma} = -\frac{2}{b\sigma_f} \left(\frac{|\sigma|}{\sigma_f}\right)^{-(1+b)/b}$$

The damage rate, as a function time, is given by

$$\dot{D} = \begin{cases} \frac{d\delta}{d\sigma} \dot{\sigma} & \text{if } \sigma > 0, \text{if } \dot{\sigma} > 0 \\ 0 & \text{otherwise} \end{cases}$$

This model is even accurate (though somewhat conservative) for nonzero mean stress levels, not exceeding 92% of σ_f . To avoid the discontinuity in this damage model, the damage rate model is simplified to

 $\dot{D} = 0.5 \left| \frac{d\delta}{d\sigma} \right| \left| \dot{\sigma} \right|.$

11.4 Control-oriented model parameters for TTURB

The control oriented model described above has been parameterized for the hypothetical wind turbine TTURB, which consists of a linear model for the structural dynamics (40-th order), created by TURBU, that is coupled (via a Coleman transformation) to the nonlinear BEM model of

Parameter	Meaning	Value	Unit
J_r	Rotor Intertia	$8.16 \cdot 10^6$	$kg \cdot m^2$
J_a	Slow shaft generator intertia	$1.125 \cdot 10^6$	$kg \cdot m^2$
$\left egin{array}{c} J_g \ N_g \end{array} \right $	Transmission ratio	50	_
K_d	Stifness of transmission	$2.37 \cdot 10^4$	Nm/rad
C_d	Damping of transmission	$1.42 \cdot 10^8$	Nm/(rad/s)
m_{tw}	Equivalent mass at hub heigt	$300 \cdot 10^3$	kg
$ s_{tw} $	Stifness of tower	$1.72 \cdot 10^6$	Nm/m
d_{tw}	Damping of tower	110	Nm/(m/s)
m_i	Blade mass	9800	kg
K_b	Blade stifness	$7.9 \cdot 10^5$	Nm/m
C_b	Blade damping	7056	Nm/(m/s)
k_t	Gain for tilt moment	0	
/tau	Time constant of pitch actuator	0.08	s
r_1	Distance of centre of blade element 1 to rotor axis	11.48	$\mid m \mid$
r_2	Distance of centre of blade element 2 to rotor axis	31.8	$\mid m \mid$
R	Blade length	40	$\mid m \mid$
$\mid H \mid$	Hub height	60	$\mid m \mid$

Table 10 Wind turbine model parameters

the aerodynamics with 14 blade elements described in Section 8.3.3. In this section, the TTURB is considered as the "reference" model, using which the simulations are performed.

The parameters of the Control Oriented model have been fit to the TTURB wind turbine, and are shown in Table 10. Note that k_t is assumed 0. This assumption allowed to avoid using the Coleman transformation and therefore, simplified matters, while the model accuracy was hardly effected.

Figure 87 shows a comparison between the control-oriented model and the detailed TTURB model. Both models were fed with the same inputs (wind speed, pitch setpoint and electric torque). Blade 1 is not pitching, while blades 2 and 3 pitch at maximum speed until the pitch angle (β) is 0.09 rad. At t = 10 s, the electric torque (T_g) is increased. The wind speed was not varied.

Clearly, the control-oriented model agrees roughly with the ECN model, but there are significant differences. Its fore-aft moment agrees reasonably well, although the variations around the eigenfrequency of 3 rad/s are smaller with the control-oriented model than the ECN model. The rotor axis bending moments agree roughly with the ECN model, but the oscillations of the Control Oriented model are still different, in spite of the flexible blade model included in the control-oriented model. Similarly, the drive train oscillations of the control-oriented model are smaller than those of the ECN model.

The results of this comparison suggest that the control Oriented model can be used for control (design) purposes, but its inaccuracies must be taken into account. Furthermore, the results suggest that the blade dynamics may as well be removed from the model, since those are not captured correctly. This would simplify the model, reduce the amount of parameters that need to be known/estimated, and save computation time. It should be noted that this single comparison is not sufficient to conclude about the suitability of the Control Oriented model. The best test of suitability is performed when using the Control Oriented model for its purpose, and checking whether its serves it well. This will be done in chapter 4.

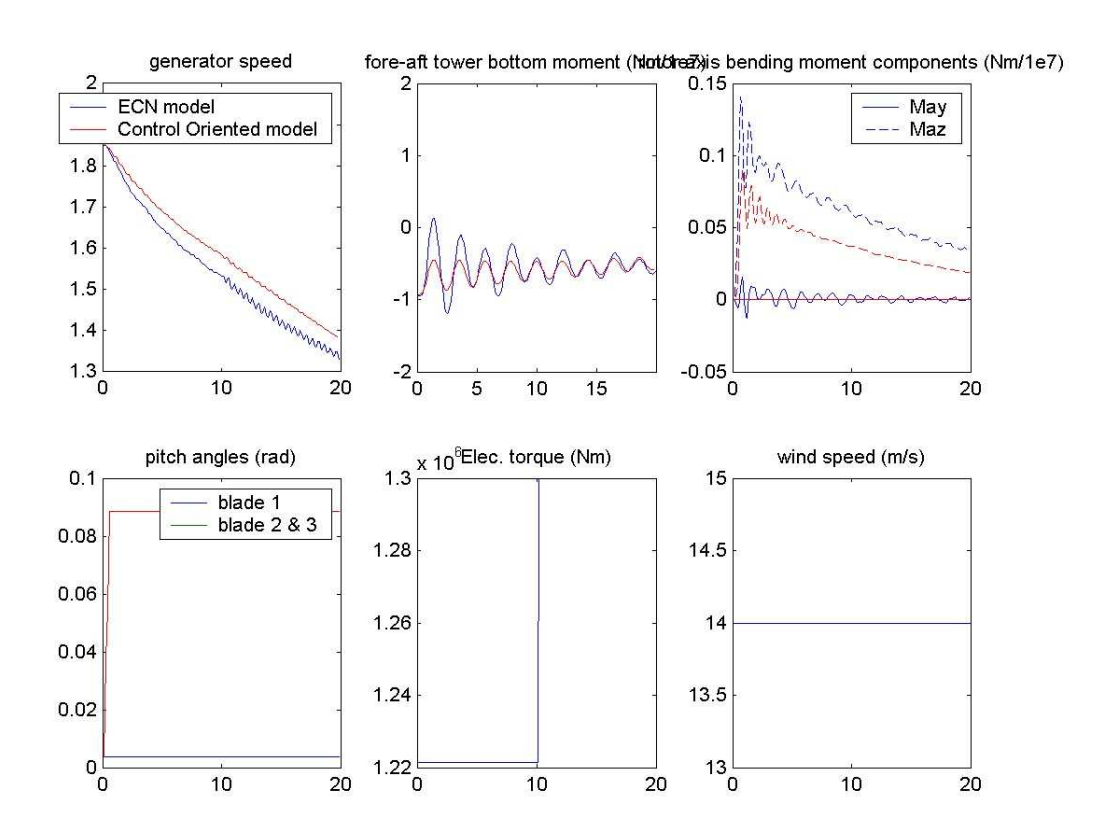


Figure 87 Simulated responses of the Control Oriented model and the ECN full model.

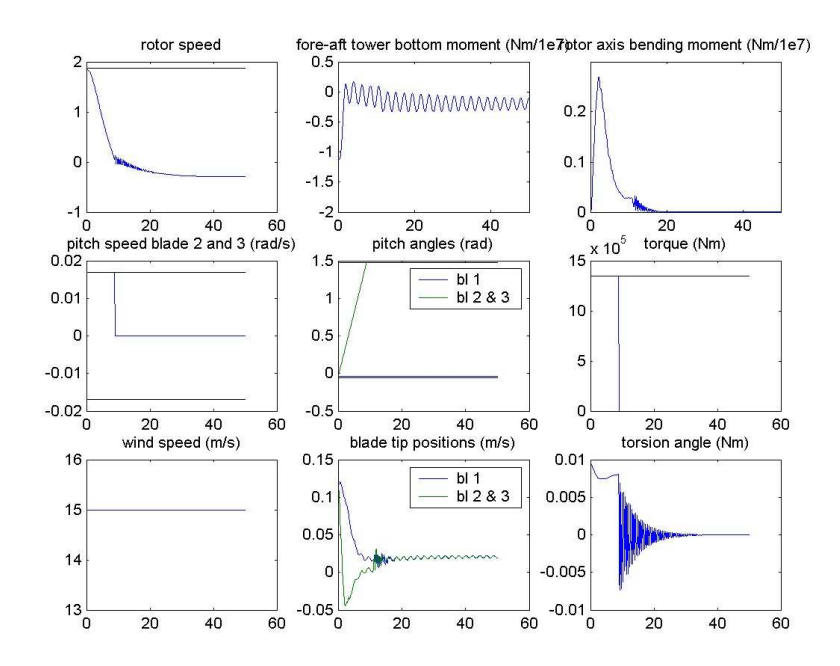


Figure 88 Simulation of a shutdown with a constant pitch speed of 0.17 rad/s, while pitch actuator 1 is inactive (blade 1 is stuck)

12 Shutdown control

This section presents shutdown control methods. Section 12.1 analyses the shutdown control problem. Section 12.2 presents a simple improvement on the conventional open-loop shutdown control method. Section 12.2 proposes a closed-loop shutdown control method using classical control. Section 12.4 presents an closed-loop shutdown using Nonlinear Model Predictive Control (NMPC).

12.1 Shutdown analysis

Wind turbines must have at least 3 independent brake systems for IEC certification. In case of three bladed wind turbines, three independent actuated pitch actuators can serve as the required 3 independent brake systems. We assume the conventional shutdown procedure is as follows:

- all (remaining) blades pitch to vane position at a fixed speed (Sopt),
- if possible (e.g. if there is no grid loss), the electric torque setpoint is set to its maximum value, so as to slow down the rotor

Figure 88 shows a Conventional shutdown after pitch actuator 1 failed at t= 0, during constant wind speed of 15 m/s (and no wind shear, tower shadow, etc.), simulated on the control oriented model presented in chapter 2.

Figure 89 shows a shutdown after grid loss at t=0 (i.e. $T_g=0$, during constant wind speed of 15 m/s (and no wind shear, tower shadow, etc.), simulated on the control oriented model presented in chapter 2.

Clearly, the tower oscillates considerably in both shutdown occasions, and dampens only slowly, since the aerodynamic damping of the fore-aft movement is reduced to a minimum as soon as the blades have pitched to vane.

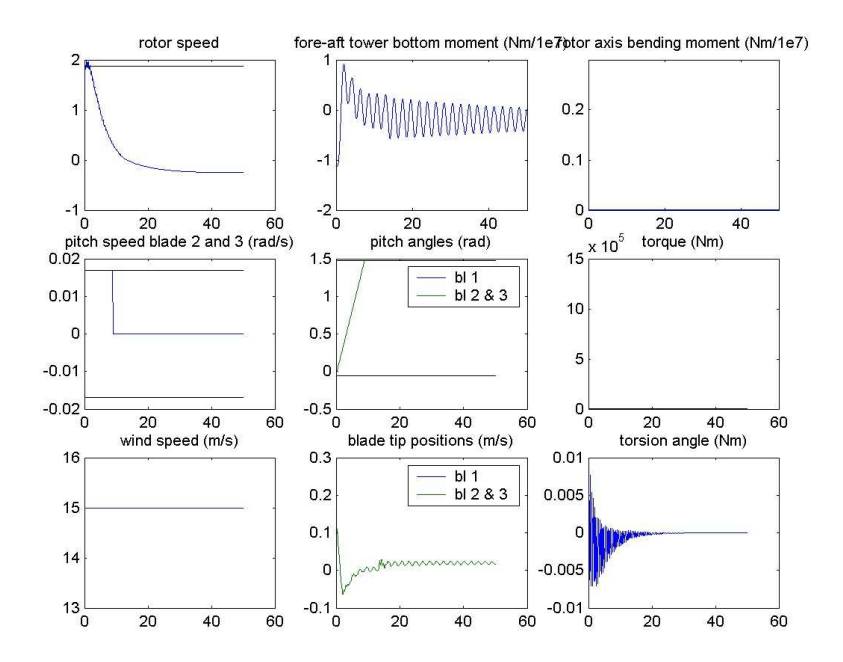


Figure 89 Simulation of a shutdown with a constant pitch speed of 0.17 rad/s, the electric torque $T_q = 0$.

In case one blade is stuck during shutdown, the rotor axis bending moment peaks considerably for an obvious reason. In case of grid loss, the possible danger of overspeed is avoided by pitching at maximum speed to vane.

The challenge is now to reduce, during shutdown, the peak moments in the rotor and tower foot to a minimum, while avoiding rotor overspeed.

12.1.1 Optimal shutdown

Given a model of the wind turbine, and known wind speed conditions, it is possible to optimize the control inputs so as to achieve an optimal shutdown. Such an exercise gives insight into 'how does an optimal shutdown ideally look like'?

The cost function, to be minimized in the optimization, is chosen as:

$$J(k) = \sum_{k=0}^{\infty} c_{ra} (M_{Ay}(k)^2 + M_{Az}(k)^2) + c_{tw} (M_{tw}(k))^2 + c_{rs} (\omega_g(k) - \omega_e)^2$$
 (223)

where c_{ra} is the cost factor for rotor bending, c_{tw} is the cost factor for tower bending, and ω_e is the cut-in rotor speed (rad/s). Hence, this cost function penalizes the (weighed) sum of rotor bending moment, tower fore-aft moment and generator speed deviations from idle speed. The weigh factors influence the importance of the three objectives.

The following constraints must be satisfied at all times

$$u_{min} < u_i < u_{max}$$

$$|\Delta u_i(k)| < s_{max}$$

$$T_g < T_{max}$$
(224)

with $u_{min} = -0.06$ rad, $u_{max} = 1.48$ rad, limits on the pitch angle setpoint (rad/s), $s_{max} = 0.17$ rad/s, limit on pitch (setpoint) speed (rad/s), $T_{max} = 1.35 \cdot 10^6$ Nm. Furthermore, the rotor speed

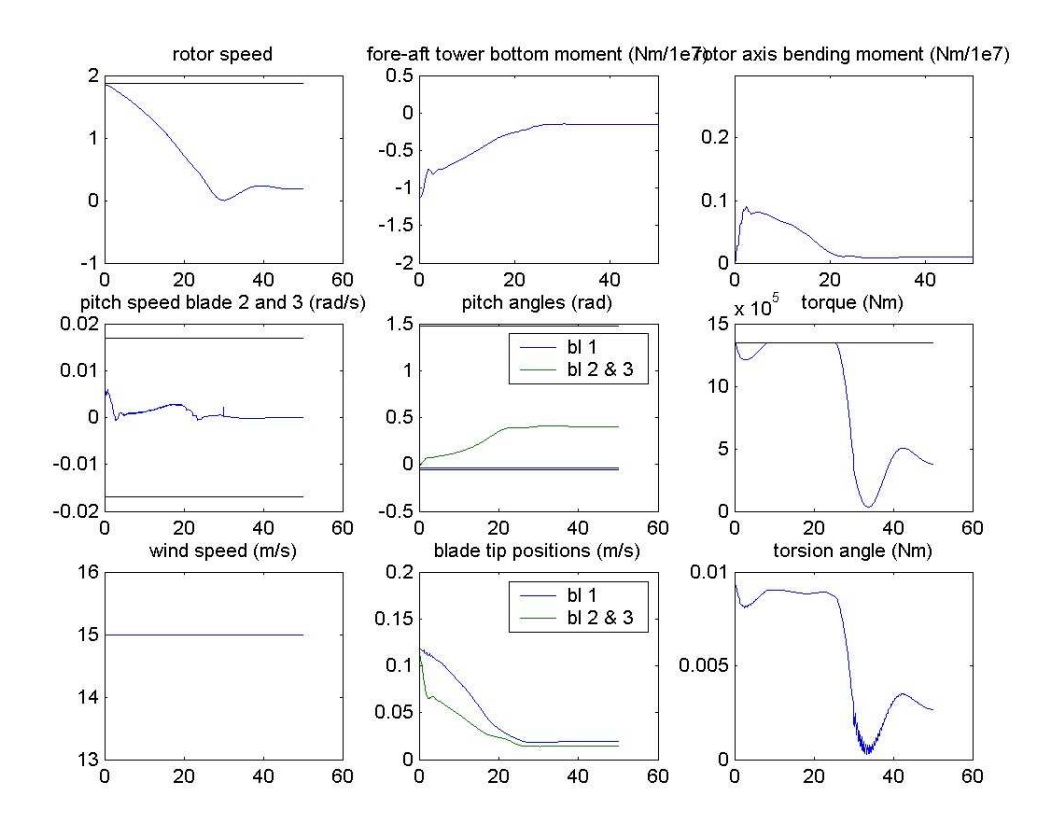


Figure 90 Result of optimised shutdown with one pitch actuator stuck at t = 0

should not exceed the maximum value of ω_{max} which we set at 1.9 rad/s.

Optimal shutdown after failure of a pitch actuator

To get insight into how an optimal shutdown looks like in case of a pitch actuator failure, the cost function (223), subject to the constraints (224), and the Control Oriented model, presented in chapter 2, has been minimized with respect to the pitch setpoints of the two active blades $(u_2(k))$ and the Electric Torque $T_q(k)$ at the discrete times k=0,1,2,...,N.

We used NMPC (which will be presented in section 3.3) to find a (possibly suboptimal) solution to the optimization problem, although any other nonlinear optimization method could have been used for this optimization problem as well. In case a pitch actuator fails, the main issue is to minimize the rotor bending peak moment. Therefore, the weigh coefficients in J were chosen as $c_{ra}=1$, $c_{tw}=0.01$, $c_{rs}=0.1$. Figure 90 shows the result. Clearly, the rotor bending moment has decreased considerably, compared to the simple conventional shutdown procedure at a fixed pitch speed of 0.17 rad/s: the peak rotor bending moment has been reduced by roughly 60 %. Furthermore, tower fore-aft oscillations do not occur at all. Appearently, they are damped actively.

Optimal shutdown after grid loss

Similarly as before, an optimal shutdown was calculated for the case the electric torque suddenly drops to 0 at t=0. As before, initial conditions were chosen such that the wind turbine was in a steady state at k=t=0. During shutdown, the pitch setpoints for blade 1, 2 and 3 were assumed to be the same $(u_1(k)=u_2(k)=u_3(k))$. The optimisation problem was to find the pitch setpoints of the blades $(u_1(k))$ at the discrete times k=0,1,2,...,N that optimized J (equation 223), subject to the constraints 224, and the additional constraint $T_q(k)=0$.

In case of electric grid loss, the main issues are to minimize rotor overspeed, and tower fore-aft bending. Therefore, the weigh coefficients in J were chosen as $c_{ra} = 0.1$, $c_{tw} = 1$, $c_{rs} = 1$.

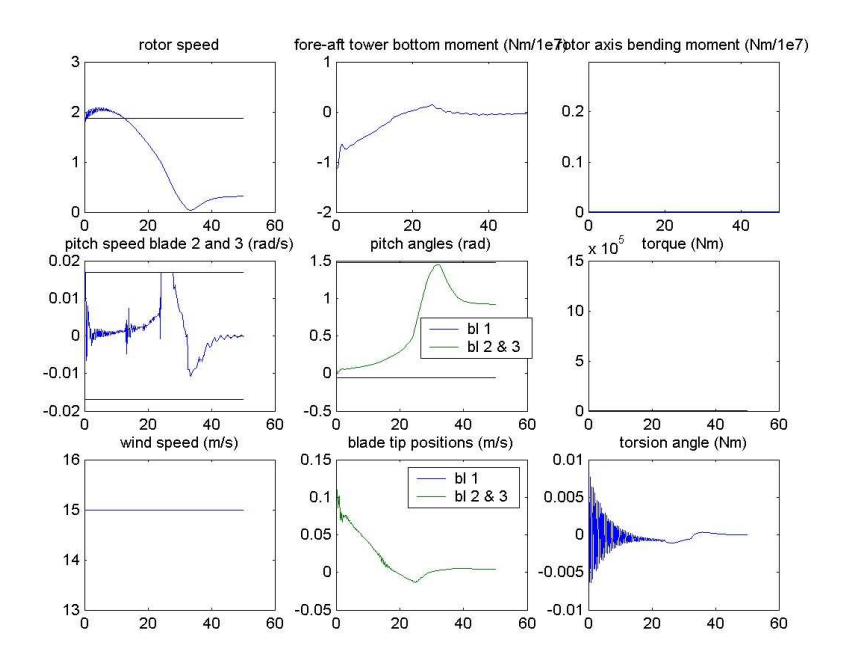


Figure 91 Result of optimized shutdown when the electric torque (T_g) suddenly drops to 0 at t=0

Figure 91 shows the result. Clearly, the tower foot moment oscillations have decreased considerably, compared to the conventional shutdown procedure at a fixed pitch speed of 0.17 rad/s.

Discussion

The conventional shutdown methods result in large oscillations of the tower fore-aft movement, and large rotor bending moments in case one pitch actuator fails. The optimized results showed that in case one pitch actuator fails, it is optimal to pitch slowly to vane. This is logical, since the asymmetric loading on the blades (that causes the rotor bending) is minimal as long as the difference between the pitch angles is minimal. A danger of pitching slowly (using an open loop control adjustment of the pitch angle) is that in case of wind speed increase the rotor speed may exceed the maximum or even run away.

In case of an electric grid loss, the pitch speed must increase sufficiently to avoid rotor overspeed. In the conventional procedure, the pitch speed is immediately set to its maximum, by which it excites the tower fore-aft movement. In the optimized shutdown, tower oscillations are completely damped.

12.2 Improvement on the Conventional Shutdown Control method

The previous section indicates that a conventional shutdown in case of grid loss or pitch actuator failure can result in large oscillatory bending moments on the tower foot if the blades pitch at maximum speed to vane. These oscillations are primarily induced by the pitch control actions, that excite the wind turbine at the eigenfrequencies. Therefore, they can be reduced considerably with a simple measure: instead of stepping the pitch speed to its maximum value, filter the pitch (speed) reference first by a low pass filter with a cutoff below the tower fore-aft eigenfrequency. Alternatively, a more advanced filter with notches at the tower eigenfrequencies can be selected, or an input shaping technique.

For the wind turbine TTURB considered in this section, the lowest tower eigenfrequency is around 3 rad/s. We therefore choose a first order low pass filter with cutoff at 1 rad/s. Similarly, the electric torque can be filtered by a low pass filter (or a filter with notches) to avoid rotor

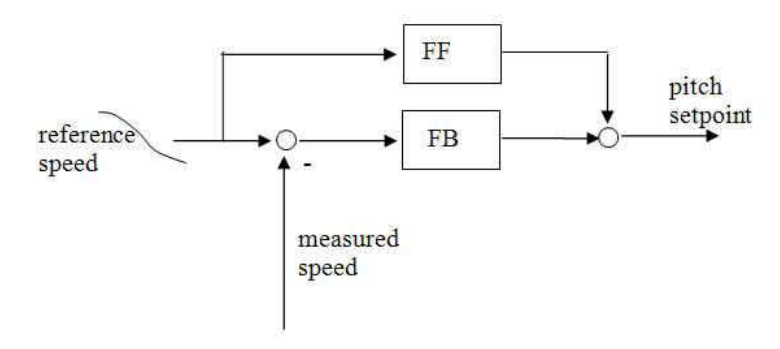


Figure 92 Closed Loop Controller for Shutdown

shaft oscillations.

The rotor axis bending moment can be reduced by pitching at a lower speed. However, the lower the pitch speed, the more risk at generator overspeed. To reduce that risk, a closed loop method is proposed in the next section.

12.3 Closed Loop Shutdown with classical control

As shown in section (12.1), a low pitch speed and a slow reduction of rotor speed is optimal in case of a constant wind speed and one pitch actuator stuck. However, if the wind speed increases, the pitch speed needs to be increased to avoid rotor overspeed (and an increasing rotor axis bending moment). This problem can be avoided by applying a closed-loop shutdown strategy, where the generator reference speed decreases slowly with time. Figure 92 shows a block-scheme of the proposed control scheme for shutdown (either due to grid loss or pitch actuator failure). It is proposed to apply a pre-defined generator speed profile with a slow decent. In principle, the existing wind turbine rotor speed control system can be used, while it is useful to add feedforward on the (generator speed) reference change.

12.4 Optimal Shutdown with Nonlinear Model Predictive Control (NMPC)

When applying NMPC for shutdown, the following algorithm is applied:

- 1 based on the measured outputs of the wind turbine, estimate the state of the CO-model
- 2 optimize u(k) en $T_g(k)$ for $k = 0, 1, 2, ..., n_p$ to minimize (an approximation of) the cost function defined by (223), subject to the constraints defined in (224).
- 3 apply of the optimized control signal only u(0) and $T_q(0)$
- 4 return to step 1

For step 1 an extended Kalman filter was applied. The approximation of the cost function 223, as mentioned in step 2, was chosen as:

$$J_{NMPC}(k) = \sum_{k=0}^{n_p} c_{ra} (M_{Ay}(k)^2 + M_{Az}(k)^2) + c_{tw} (M_{tw}(k))^2 + c_{rs} (\omega_g(k) - \omega_e)^2 + x(n_p + 1)^T P_e x(n_p + 1)$$

with $x(n_p + 1)^T P_e x(n_p + 1)$ being the optimal LQ solution of minimizing J_{NMPC} , with initial condition $x(k + n_p + 1)$, subject to a linear model that was obtained by linearizing the control-oriented model around x_e . Note that the approximation J_{NMPC} allows to prove stability.

The steady state x_e was computed by iterating the pitch angle until both the generator speed was close to $0.2~{\rm rad/s}$, and the aerodynamic torque was sufficiently close to zero.

13 Simulation results

In this section, 3 shutdown control strategies are tested on the wind turbine model TTURB:

- Conventional shutdown (where pitch actuators pitch to vane as fast as possible)
- the Improvement on Conventional shutdown (by filtering the open loop control signal to avoid excitation); this method will be referred to as "Filtered Control"
- NMPC

Section 13.1 presents the simulation results in case of normal wind speed variations. Section 13.3 presents the results in case a gust occurs at the same time of a failure (grid loss or pitch actuator stuck).

13.1 Normal wind speed variations

In all simulations the three blade effective wind speeds are as shown in Figure 93

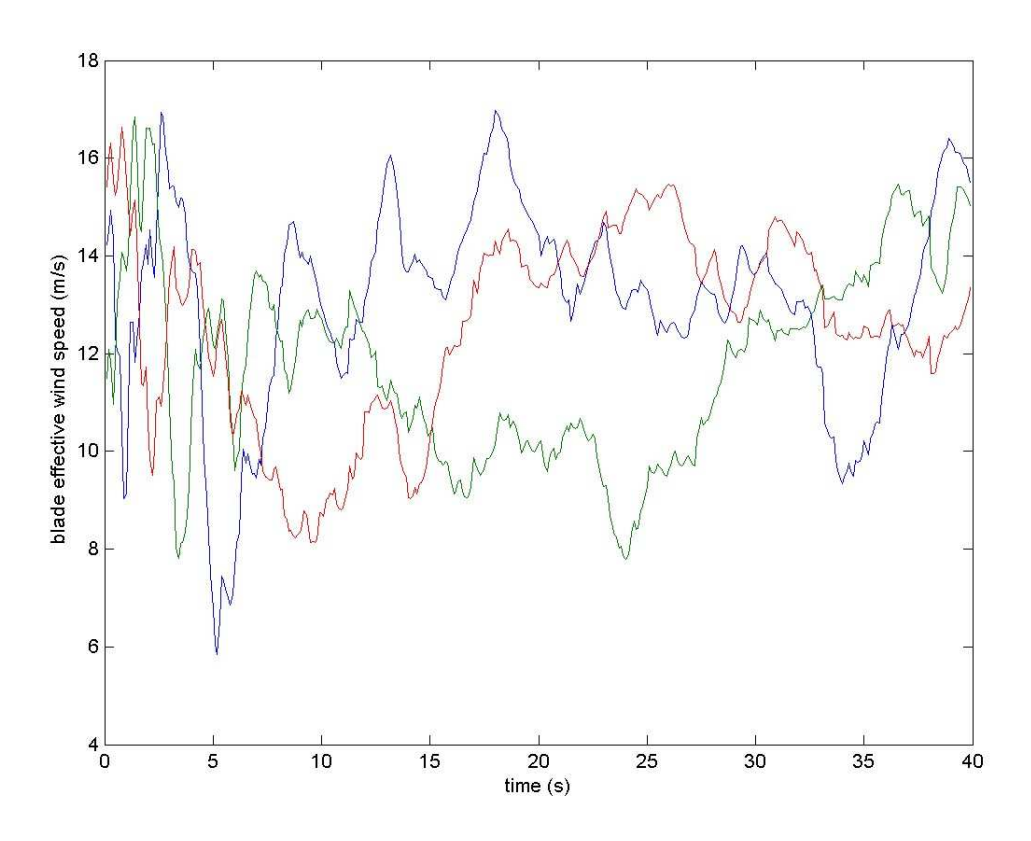


Figure 93 Blade effective windspeed

13.1.1 Grid loss

In case of grid loss, the electric torque suddenly drops to 0 at t=0, i.e. $T_g=0$. Figure 94 shows the simulations results for the three shutdown methods in case of grid loss. Clearly, the method "Filtered Control" where the pitch angle setpoint is filtered by a low pass filter, reduces the tower foot oscillations considerably. With NMPC the tower foot deviations from zero are smallest.

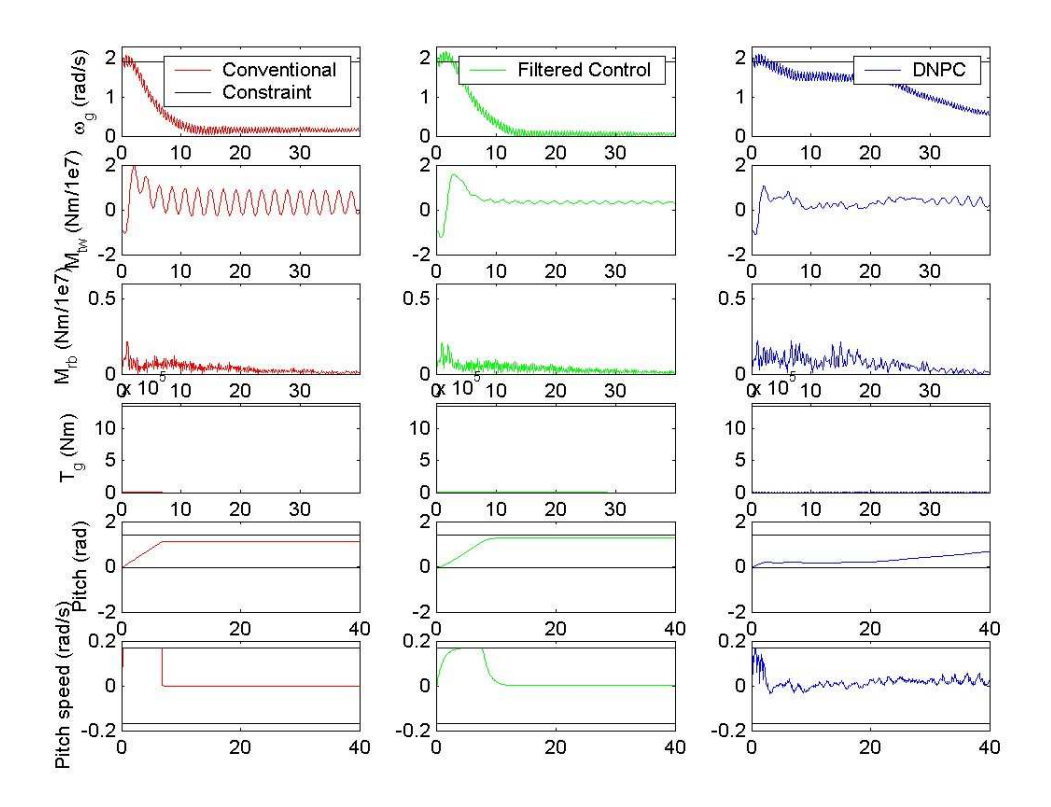


Figure 94 Shutdown (for three different control methods), after grid loss

13.2 Pitch actuator stuck

Figure 95 shows the shutdown simulations in case pitch 1 of blade 1 is stuck. Again, the method "Filtered Control" reduces the tower foot oscillations, but does not reduce the rotor axis bending moment. With NMPC, the tower foot oscillations are reduced, and in addition, the rotor axis peak moment is reduced by more than 40%.

13.3 Shutdown during a strong gust

So far, the wind speed in the simulations was assumed to vary around 14 m/s (see Figure 93). This section considers the case where the wind speed increases during shutdown, as shown in Figure 96. The wind speed increases at the same time a failure occurs.

Figure 97 shows the simulation results for the three control methods when the pitch actuator of blade 1 fails (and the pitch angle of blade 1 remains constant). Figure 98 shows the simulation results during grid loss. The Conventional control method does not lead to overspeed, but the filtered Control method does lead to some overspeed, in the case of grid loss. Again, the tower oscillations are reduced, compared to the conventional control method. With NMPC, the generator speed is only slightly exceeding the constraint, set at 1.9 rad/s. To achieve this, NMPC pitches at maximum speed until the generator speed is below its maximum again. After that, it actively reduces tower foot oscillations, resulting in the lowest tower foot moment fluctuations of all control methods. This simulation illustrates that NMPC is also capable of dealing with output constraints, in this case a generator speed constraint.

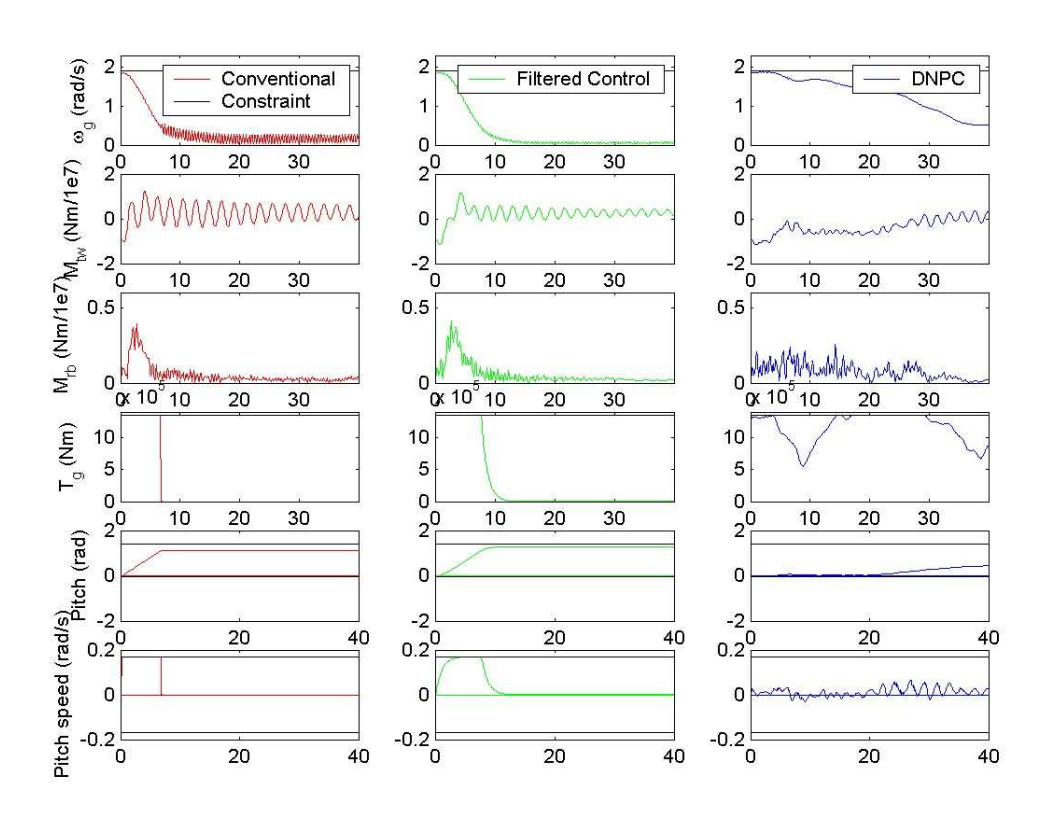


Figure 95 Shutdown (for three different methods), with blade 1 stuck

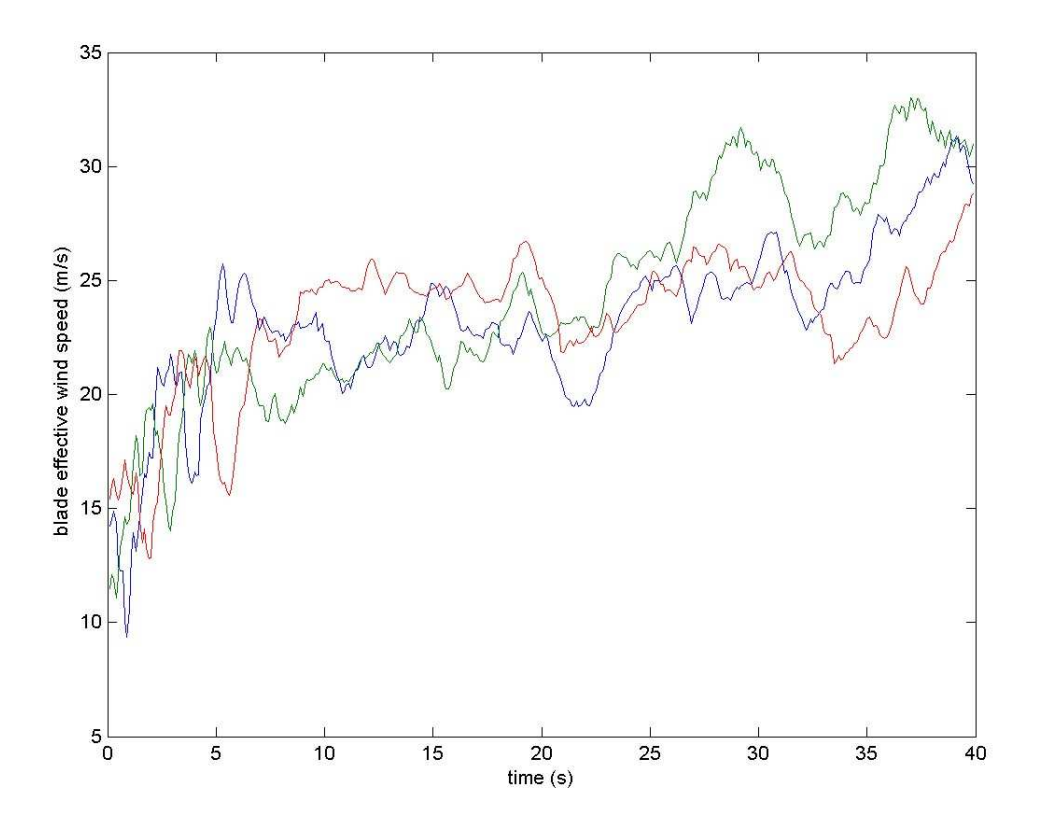


Figure 96 Blade effective windspeed

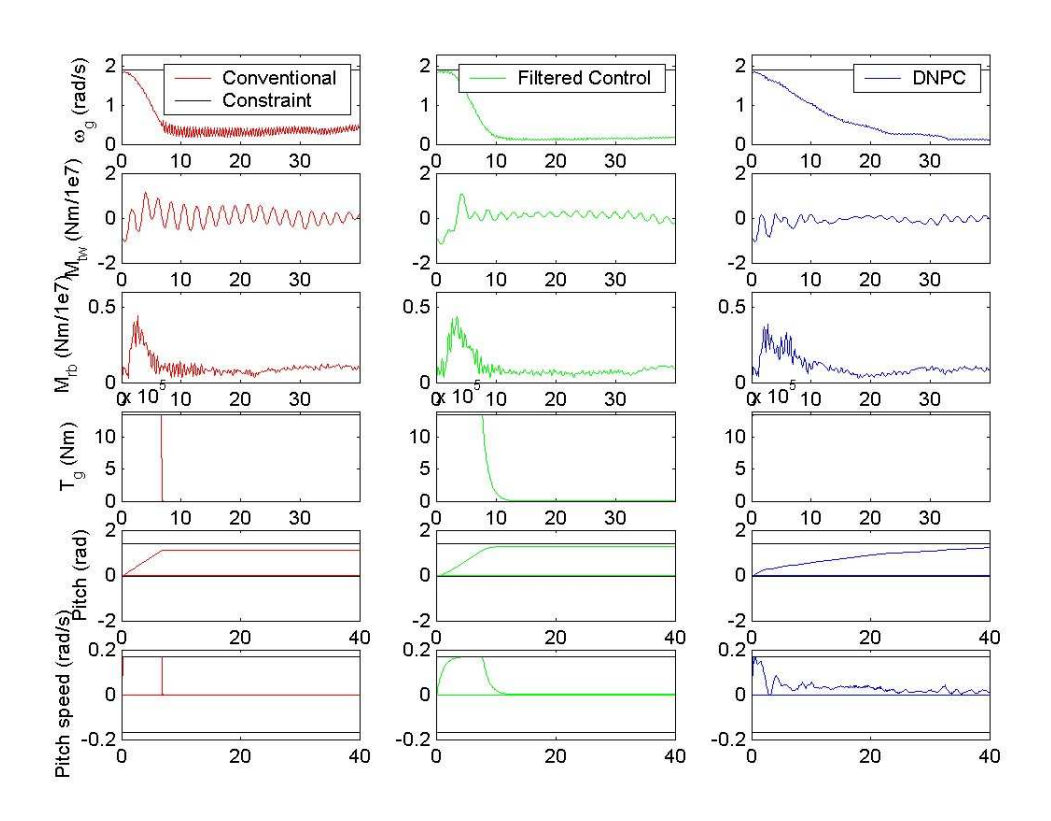


Figure 97 Shutdown (for three different methods), after blade 1 got stuck and during a strong gust

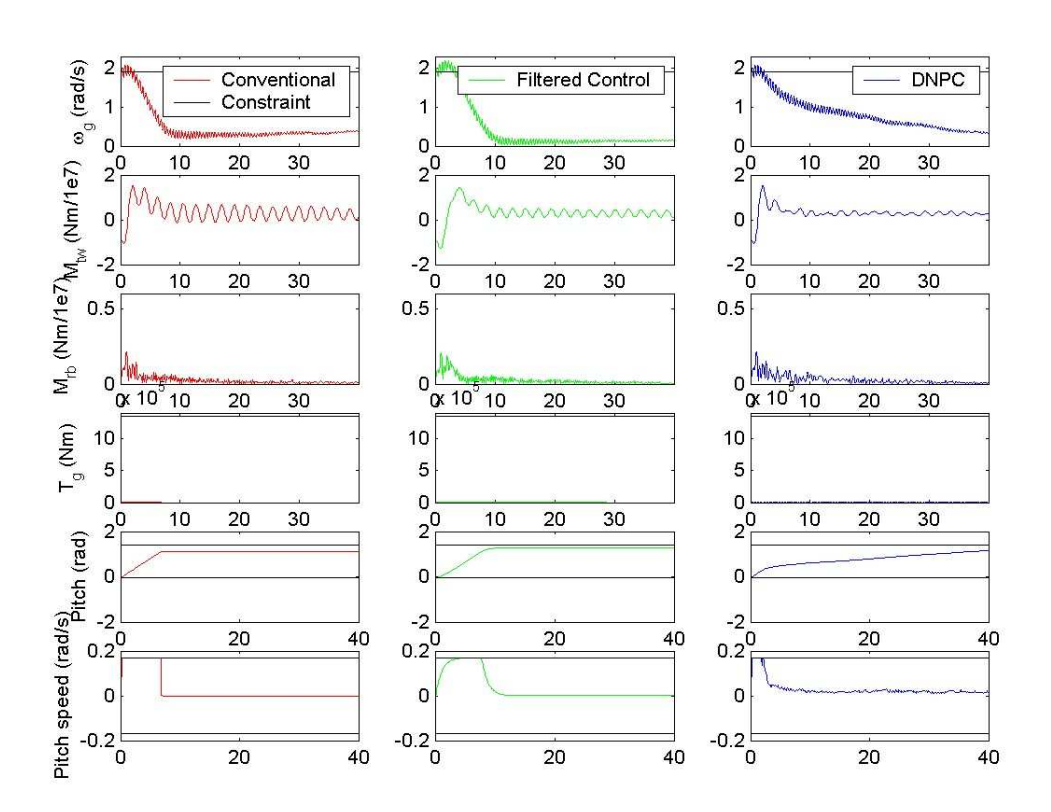


Figure 98 Shutdown (for three different methods), after grid loss and during a strong gust

14 Conclusions

This section investigate the possibility to develop Shutdown Control algorithms that shut down a wind turbine after a serious failure in such a way, that the rotor speed remains below a given maximum value, and that peaks in the rotor axis bending moment and tower foot fore-aft moment are minimized. Two failure types were considered: grid loss and one blade stuck.

For control (design) a relatively simple wind turbine was developed (referred to as the Control Oriented model), consisting of a linear model of the structural dynamics, and a nonlinear BEM model for the aerodynamics. The structural model consisted of one flexible mode in fore-aft direction, one flexible mode for each blade in fore-aft direction, and one mode in the drive-train. The BEM model consisted of only two elements, and oblige inflow effects, as well as wake dynamics, were ignored.

The performance of shutdown control was quantified using a cost function that weighed generator speed deviations from idle speed, tower foot moment deviations from zero, and rotor axis bending moment deviations from zero.

Three novel shutdown control methods were proposed:

- 1 a simple variation on the conventional procedure, namely, by filtering the (open-loop) control signals first (and choosing the filter such, that the eigenmodes are not excited);
- 2 a closed-loop shutdown control method where the rotor speed reference slowly drops to 0, and where conventional pitch control is used;
- 3 a closed-loop shutdown control method using NMPC

The shutdown control methods (except for the 2nd) were compared with conventional method in simulations on the ECN model of TTURB. The results showed that method 1 showed a considerable reduction in tower fore-aft movements, even though a simple first order low pass filter was used. However, reducing the rotor bending moment is more complicated. To achieve the best result (in reducing the rotor bending moment), a closed-loop method should be used, since this moment can only be reduced by slow pitching. If, however, the wind speed increases, the pitch speed must be increased (to avoid overspeed, and increased rotor bending). NMPC was able to realise the best results in reducing tower foot oscillations, rotor bending and avoiding rotor overspeed.

The results of this section suggest that shutdown can indeed be improved considerably, starting with very simple means.

Part VI

Experimental methods

15 Wind turbine model identification: method development

Summary

This section is focused on wind turbine model identification based on closed-loop measurements in above-rated conditions with the purpose of obtaining accurate and compact models suitable for control design. Both collective and individual settings are considered. In the collective setting, the goal is the identification of the transfer function $T_{\Omega\theta}^{+trq}$ from the collective blade pitch angle to the rotor speed, as necessary for the design of the collective pitch controller in the rotor speed regulation loop. This transfer function needs to be identified in the presence of the torque controller. In the individual setting, in addition to the transfer function $T_{\Omega\theta}^{+trq}$, the transfers from the tilt-wise and yaw-wise pitch angles to the tilt-wise and yaw-wise blade bending moments (in the so-called Coleman domain) need to be estimated.

A number of closed-loop identification methods have been summarized and applied to the collective identification setting. Among these are the direct, indirect, instrumental variable, joint input-output, two-stage, tailor-made instrumental variable and the closed-loop N4SID method. The CL-N4SID method is chosen as the most suitable method as it (a) provides the most accurate identification results, and (b) is directly applicable to MIMO problems in which some input-output channels participate in the feedback loop, while others not. This method is subsequently used in the MIMO identification setup corresponding to the individual pitch setting.

The presented results have been obtained on the basis of simulation data from a simplified linearized model of a wind turbine under realistic blade effective wind speed conditions. In section 16, the methods are applied on experimental data and the results are discussed.

15.1 Introduction

Control design of wind turbines is conventionally based on physical modeling of the turbine behavior with imprecise and uncertain turbine parameters. This results in suboptimal controllers that, when interconnected with the real-life turbine, might have unsatisfactory performance. A significant performance improvement could be expected when the controllers are designed on accurate, yet simple, mathematical models that describe the most significant dynamics of the turbine by *fitting the model parameters to the field input/output measurements*. Such system identification approach to turbine modeling for control design would require the following approach:

- 1 initial (conventional) controller design based on (uncertain) turbine physical parameters,
- 2 controller implementation and collecting field measurements,
- 3 turbine model identification,
- 4 model validation on a "fresh" data batch, i.e. data not used for the identification,
- 5 final controller design based on identified and validated model.

To avoid confusion, in the sequel all transfer function will be expressed in discrete-time. The sampling time is assumed $T_s=0.1\,\mathrm{s}$, which is considered sufficient to capture the control-relevant turbine dynamics.

Open vs. closed-loop

It is important to notice that the data from field measurements at above-rated wind conditions will usually be collected with the pitch controller $C_{\theta}(z)$ in the loop, and will therefore represent closed-loop measurements, as shown in Figure 99. One might prefer, whenever possible, to perform the measurements in open-loop with the pitch controller turned off in order to make

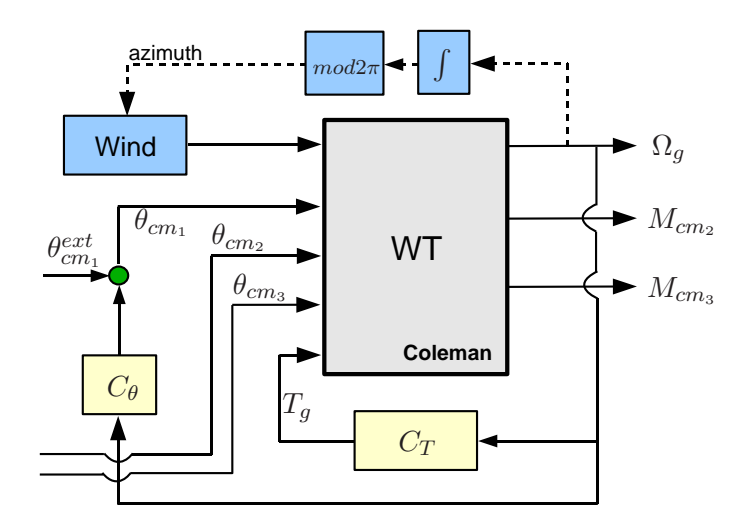


Figure 99 System identification setup in Coleman domain

the use of conventional open-loop identification techniques possible. However, one should make sure that the loop with only the torque controller $C_T(z)$ remains stable. This is not the case with the usual constant-power torque control approach, where the torque controller on itself has a destabilizing effect on the turbine generator speed in full load conditions due to the decreasing generator torque T_g with the increase of the generator speed Ω_g . Although it is possible to adapt the torque control algorithm so that the generator speed is stabilized, this may not be desirable as it can result in overloading of the generator. For that reason, only the closed-loop approach with the pitch controller kept in the loop, which is preferable in practice, will be considered here. In any case, whether one choses for the open-loop or the closed-loop approach, an additional persistently excited signal will have to be added to the collective pitch angle (see $\theta_{cm_1}^{ext}$ on Figure 99).

Linearity

Another important issue is the availability of a well developed field of system identification for linear time-invariant (LTI) systems. The wind turbine system is, of course, highly nonlinear with respect to the wind speed V, the blade pitch angles θ_{cm_i} and rotor speed Ω . Still, for control design, it is common practice to linearize the turbine model around a given working point in order to make use of the very well developed control design theory for LTI systems. In the identification process, the same approach will be pursued by assuming that the wind turbine is operating in the vicinity of some working point $\{V^*, \theta^*_{cm_1}, \Omega^*\}$.

Another source of nonlinearity is the azimuth dependence of the out of plane blade root bending moments M_{flp_i} , i=1,2,3. This is important for individual pitch control design that aims at reduction of the frequency contents of M_{flp_i} at multiples (kp) of the rotor frequency p. This periodicity, caused by the azimuth dependence, can however easily be removed by means of a coordinate change, i.e. by projecting the moments M_{flp_i} defined on the rotating blade reference frame (x,y_1,z_1) to the non-rotating hub reference frame (x,y,z), see Figure 100. This projection, called Coleman demodulation, is given by

$$\begin{bmatrix} M_{cm_1} \\ M_{cm_2} \\ M_{cm_3} \end{bmatrix} = \frac{1}{3} \underbrace{\begin{bmatrix} 1 & 1 & 1 \\ 2sin(\psi) & 2sin(\psi + \frac{2}{3}\pi) & 2sin(\psi + \frac{4}{3}\pi) \\ 2cos(\psi) & 2cos(\psi + \frac{2}{3}\pi) & 2cos(\psi + \frac{4}{3}\pi) \end{bmatrix}}_{P-1} \underbrace{\begin{bmatrix} M_{flp_1} \\ M_{flp_2} \\ M_{flp_3} \end{bmatrix}}_{P-1},$$

where ψ is the azimuth angle. The demodulated bending moments M_{cm_2} and M_{cm_3} , scaled by factors of $-\frac{2}{3}$ and $+\frac{2}{3}$, respectively, are good approximations of the tilt-wise and yaw-wise

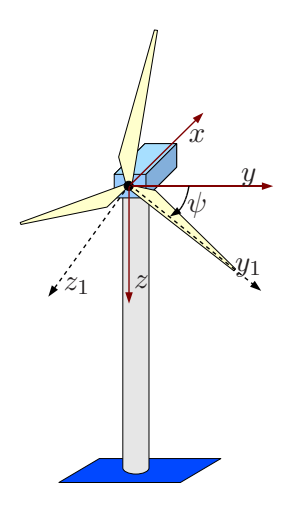


Figure 100 Rotating and fixed reference frame conventions

bending moments at the hub center [80]. The moment M_{cm_1} has no physical meaning, and will be left out in the sequel. A similar demodulation of the three individual blade pitch angles θ_i , i = 1, 2, 3, using the same Coleman transformation matrix, gives

$$\begin{bmatrix} \theta_{cm_1} \\ \theta_{cm_2} \\ \theta_{cm_3} \end{bmatrix} = P^{-1} \begin{bmatrix} \theta_1 \\ \theta_2 \\ \theta_3 \end{bmatrix},$$

where now θ_{cm_1} represents the collective pitching, while θ_{cm_3} and θ_{cm_3} can be though of as tilt-wise and yaw-wise components, and are used for individual pitch control. The transfer from pitch actions in the fixed coordinate system θ_{cm_i} to the Coleman demodulated blade root bending moments M_{cm_j} is no longer dependent on the azimuth angle. However, notice that the Coleman transformed signals M_{cm_j} are not directly measured, but need to be computed from the measured out-of-plane blade root bending moments M_{flp_i} . Similarly, the tilt-wise and yaw-wise pitch angles need also be computed from the blade pitch angles θ_i .

Channels to identify

To simplify the discussion, we introduce the following notation. The wind turbine in "Coleman domain" is represented by the transfer matrix

$$T(z) \triangleq \begin{bmatrix} T_{\Omega\theta_{1}} & T_{\Omega\theta_{2}} & T_{\Omega\theta_{3}} & T_{\Omega T_{g}} \\ T_{M_{2}\theta_{1}} & T_{M_{2}\theta_{2}} & T_{M_{2}\theta_{3}} & T_{M_{2}T_{g}} \\ T_{M_{3}\theta_{1}} & T_{M_{3}\theta_{2}} & T_{M_{3}\theta_{3}} & T_{M_{3}T_{g}} \end{bmatrix} (z)$$

from the inputs $\{\theta_{cm_1}, \theta_{cm_2}, \theta_{cm_3}, T_g\}$ to the outputs $\{\Omega_g, M_{cm_2}, M_{cm_3}\}$. By closing the loop with the torque controller, $T_g = C_T(z)\Omega_g$, one gets

$$T^{+trq}(z) \triangleq \begin{bmatrix} T_{\Omega\theta_{1}}^{+trq} & T_{\Omega\theta_{2}}^{+trq} & T_{\Omega\theta_{3}}^{+trq} \\ T_{M_{2}\theta_{1}}^{+trq} & T_{M_{2}\theta_{2}}^{+trq} & T_{M_{2}\theta_{3}}^{+trq} \\ T_{M_{3}\theta_{1}}^{+trq} & T_{M_{3}\theta_{2}}^{+trq} & T_{M_{3}\theta_{3}}^{+trq} \end{bmatrix} (z)$$
(225)

with

$$\begin{split} T_{\Omega\theta_{j}}^{+trq} &= (1 - T_{\Omega T_{g}}C_{T})^{-1}T_{\Omega\theta_{j}}, \ j = 1, 2, 3. \\ T_{M_{i}\theta_{j}}^{+trq} &= T_{M_{i}\theta_{j}} + T_{M_{i}T_{g}}C_{T}(1 - T_{\Omega T_{g}}C_{T})^{-1}T_{\Omega\theta_{j}}, \ i = 2, 3, \ j = 1, 2, 3. \end{split}$$

When the (collective) pitch controller C_{θ} is also interconnected, resulting in $\theta_{cm_1} = C_{\theta}\Omega_g + \theta_{cm_1}^{ext}$, the complete closed-loop mapping $\{\theta_{cm_1}^{ext}, \theta_{cm_2}, \theta_{cm_3}\}$ to $\{\Omega_g, M_{cm_2}, M_{cm_3}\}$ has the following transfer matrix

$$T^{cl}(z) \triangleq \begin{bmatrix} T^{cl}_{\Omega\theta_1} & T^{cl}_{\Omega\theta_2} & T^{cl}_{\Omega\theta_3} \\ T^{cl}_{M_2\theta_1} & T^{cl}_{M_2\theta_2} & T^{cl}_{M_2\theta_3} \\ T^{cl}_{M_3\theta_1} & T^{cl}_{M_3\theta_2} & T^{cl}_{M_3\theta_3} \end{bmatrix} (z)$$

with

$$T_{\Omega\theta_{j}}^{cl} = (1 - T_{\Omega\theta_{1}}^{+trq} C_{\theta})^{-1} T_{\Omega\theta_{j}}^{+trq}, \ j = 1, 2, 3.$$

$$T_{M_{i}\theta_{j}}^{cl} = T_{M_{i}\theta_{j}}^{+trq} + T_{M_{2}\theta_{1}} C_{\theta} (1 - T_{\Omega\theta_{1}}^{+trq} C_{\theta})^{-1} T_{\Omega\theta_{j}}^{+trq}, \ i = 2, 3, \ j = 1, 2, 3.$$
(226)

There are several channels that need to be identified for control design, and others, that are of less importance. First of all, whenever the generator torque controller $C_T(z)$ will be simply based on the QN-curve for constant power production above rated, its design would require no knowledge of the turbine dynamics. The pitch controller $C_{\theta}(z)$, on the other hand, has the purpose to regulate the rotor speed at rated level, so the transfer $T_{\Omega\theta_1}^{+trq}$ from the collective pitch angle θ_{cm_1} to the generator speed Ω_g is necessary for its design, and should hence be identified as accurately as possible. Note that this channel needs to be identified with the torque controller in the loop, since the pitch controller is to be designed by accounting the presence of $C_T(z)$. The identification of $T_{\Omega\theta_1}^{+trq}$ is discussed in Section 15.2.

For individual pitch control design the channels $T_{M_i\theta_j}^{+trq}$, i,j=2,3, are also needed, and should also be identified. The individual pitch identification problem is treated in Section 15.3. The are basically two possibilities:

- 1 open-loop setting: identify the closed-loop transfers $T^{cl}_{M_i\theta_j}$, i,j=2,3, from the tilt and yaw-oriented pitch components θ_{cm_2} and θ_{cm_3} to the tilt and yaw-wise moments M_{cm_2} and M_{cm_3} in the presence of the pitch controller $C_{\theta}(z)$. This can be achieved by using open-loop identification technique on the data $\{\theta_{cm_2},\theta_{cm_3},M_{cm_2},M_{cm_3}\}$ collected in closed-loop. This should only be done when there are reasons to believe that there is little interaction between these channels and the speed regulation channel $\theta_{cm_1} \mapsto \Omega$, i.e. when the dependence of $T^{cl}_{M_i\theta_j}$, i,j=2,3, on the pitch controller $C_{\theta}(z)$ can be neglected. Otherwise the so-identified models might be inaccurate after re-optimization of the pitch speed controller $C_{\theta}(z)$. The open-loop setting is discussed in Section 15.3.1.
- 2 closed-loop setting: identify the *open-loop* transfers $T_{M_i\theta_j}^{+trq}$, i,j=2,3, by means of closed-loop identification techniques. This step could eventually be combined with the closed-loop identification of the speed regulation channel $T_{\Omega\theta_1}^{+trq}$ as discussed above. This closed-loop setting is treated in Section 15.3.2.

Before continuing with the identification methods, a simplified linearized model of a wind turbine is presented in Section 15.1, that has the purpose to provide the necessary data for the identification, and is also used for the purpose of model validation. In practice, no such model will be available for validation purposes, so the validation will also need to be done on the basis of input-output measurements. However, it should be pointed out that the conventional time-domain identification is here not directly applicable due to the unstable open-loop system. For that reason, a better suited alternative would be to perform the validation in the frequency domain, by using nonparametric estimation methods, such as the spectral analysis discussed in Section 15.2.1.

Simplified linearized wind turbine model

For verification of the presented methods, ideintification data is obtained using the simplified linearized wind turbine model described in Section 1.3.1. The model is based on linearized blade element momentum theory, and contains the first bending mode of the tower in nodding and

naying directions, the first shaft torsion mode, and the main rotation of a 3-bladed horizontal axis wind turbine. The blades are assumed rigid; dynamic wake effects and unsteady aerodynamics are neglected. The model has inputs: the three blade pitch positions, three blade effective wind speeds and the generator torque. The simulations are performed with realistic blade effective wind speeds, accounting for kp effects on the blades, due to rotational wind field sampling, tower shadow and wind shear. A representative blade effective wind speed is depicted on Figure 101. The Bode plots of the pitch and torque controllers used in the simulation, including the filters, are

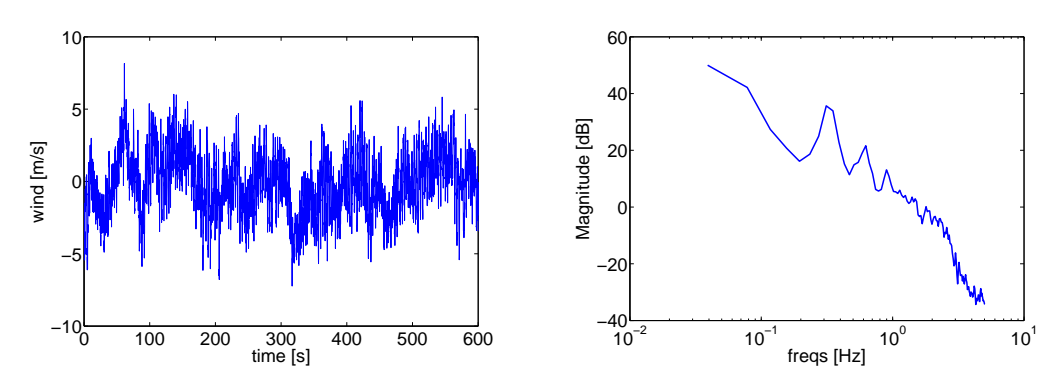


Figure 101 Blade effective wind speed: time series (left) and spectrum (right)

given on Figure 102.

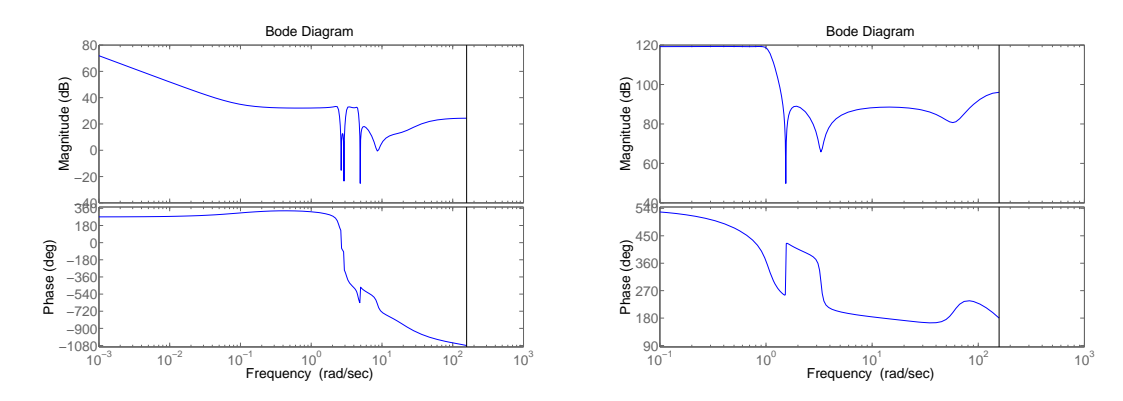


Figure 102 Bode plots of the pitch (left) and torque (right) controllers

Wind turbine model identification

Below, several method for closed-loop identification are briefly summarized and applied to the identification of wind turbine models from closed-loop data⁷. To begin with, only the channel $T_{\Omega\theta_1}^{+trq}$ will be considered, which can be used for the design of *collective pitch* control for speed regulation. Subsequently, the identification of other channels of the transfer matrix $T^{+trq}(z)$ (see equation (225)) will be discussed, which can be used for *individual pitch control* design.

15.2 Collective pitch identification

This section outlines different methods for the identification of a turbine model $T_{\Omega\theta_1}^{+trq}(z)$ from closed-loop data. The identification setup is depicted on Figure 103, where the rotor speed Ω_q is

⁷ An exception is the open-loop setting for individual pitch identification, discussed in Section 15.3.1.

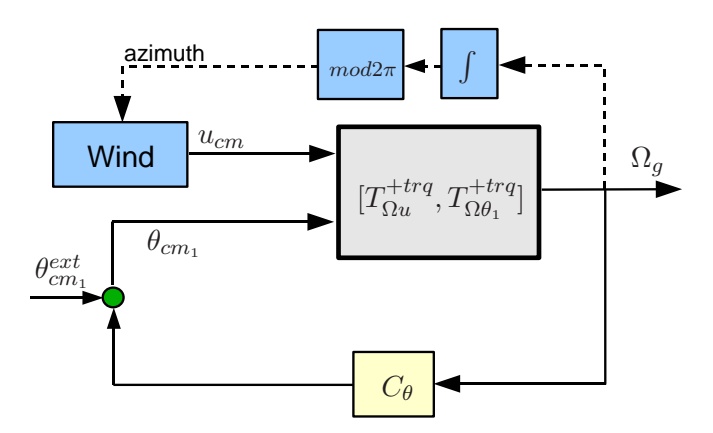


Figure 103 System identification setup for collective pitch control design

formed as

$$\Omega_g(k) = T_{\Omega\theta_1}^{+trq}(q)\theta_{cm_1}(k) + \underbrace{T_{\Omega u}^{+trq}(q)u_{cm}(k)}_{v(k)}.$$

The method that produces the best results will be further on applied in Section 15.3 to the problem of identification of all three input and output channels of the transfer matrix $T^{+trq}(z)$, which can be used for individual pitch control design.

Notice that the channel to be identified includes the torque controller $C_T(z)$, compare to Figure 99. It is also important to point out, that the to-be-identified system is *open-loop unstable*, as already discussed in Section 15.1. This is an important fact as some closed-loop identification techniques require open-loop stability (e.g. the Two-Stage Method), which makes them not directly applicable here. Another consequence of the instability of $T_{\Omega\theta_1}^{+trq}(z)$ is that it significantly complicates the validation of the identified models based on conventional time-domain criteria. One may argue that the validation can take place after closing the loop with the pitch controller; however, the pitch controller does not always stabilize the *identified* model \hat{T}^{+trq} , which prevents time-domain validation even in closed-loop. This necessitates the validation of the models in the frequency domain.

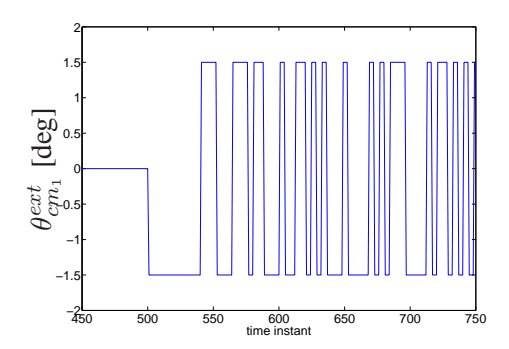
All simulation results, provided in this section (i.e. related to collective pitch), are carried out using the same simulation data, obtained with an external excitation signal $\theta_{cm_1}^{ext}$ based on a *pseudo random binary signal* (PRBS) $s_{prbs}(k)$ with length $(2^{13}-1)$ samples. The external signal is computed as follows:

$$\theta^{ext}_{cm_1}(k) = \left\{ \begin{array}{ll} 0, & k \leq 500 \text{ samples}, \\ \frac{3}{2}.s_{prbs}(\left\lceil \frac{k-500}{4} \right\rceil), & k > 500 \text{ samples}, \end{array} \right.$$

where the operation $\lceil a \rceil$ denotes the smallest integer larger than or equal to a. Notice that the final excitation used, $\theta_{cm_1}^{ext}$, is formed by keeping each value of the PRBS s_{prbs} constant during four samples, and that the excitation is switched on after 500 samples. The time series zoomed in the interval $450 \le k \le 750$ samples, as well as the power spectral density of $\theta_{cm_1}^{ext}$, are given on Figure 104.

15.2.1 Nonparametric model identification using spectral analysis

To begin with, the identification of nonparametric models is briefly discussed. To this end, we will restrain ourselves to frequency response functions only. Time domain nonparametric models (e.g. step or impulse responses) would anyway be unappropriate due to the open-loop instability



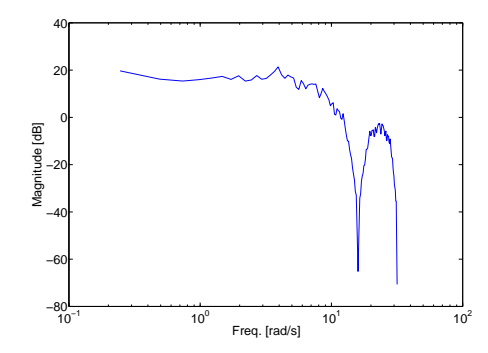


Figure 104 The external excitation signal $\theta_{cm_1}^{ext}$ used in the simulation of Section 15.2: time series (left) and power spectral density (right)

of the system. Although nonparametric models might seem unappropriate for control design, they can be used for the purpose of model validation.

One of the most popular methods for obtaining transfer function estimates is based on *spectral analysis* (SA). To explain the method, consider first the open-loop situation⁸

$$\Omega_q(k) = T_{\Omega\theta_1}^{cl}(q)\theta_{cm_1}^{ext}(k) + v(k), \tag{227}$$

where q is the forward shift operator (qu(k)=u(k+1)), and where the signals $\theta_{cm_1}^{ext}(k)$ and the wind-related signal v(k) are assumed to be uncorrelated, i.e. $E(\theta_{cm_1}^{ext}(k)v(k))=0$. The signal v(k) is a generalized wind signal that is related to (i.e., is a filtered version of) the Coleman domain wind signals u_{cm_1} and u_{cm_2} . Then the auto $(\Phi_{\theta_{cm_1}^{ext}})$ and cross $(\Phi_{\Omega\theta_{cm_1}^{ext}})$ spectral densities are related as follows

$$\Phi_{\Omega\theta_{cm_1}^{ext}}(\omega) = T_{\Omega\theta_1}^{cl}(e^{j\omega})\Phi_{\theta_{cm_1}^{ext}}(\omega).$$

Given finite-time data sequence $\{\theta_{cm_1}^{ext}(k)\Omega_g(k)\}$, $k=1,2,\ldots,N$, these spectra can be approximated as

$$\hat{\Phi}_{\Omega\theta_{cm_1}^{ext}}(\omega) = \frac{1}{N} \mathcal{F}\{\Omega\} \mathcal{F}\{\theta_{cm_1}^{ext}\}^*, \ \hat{\Phi}_{\theta_{cm_1}^{ext}}(\omega) = \frac{1}{N} |\mathcal{F}\{\theta_{cm_1}^{ext}\}|^2,$$

 $\mathcal{F}\{\cdot\}$ denoting the discrete Fourier transform. Hence, an estimate of the transfer function is given by

$$\hat{T}^{cl}_{\Omega\theta_1}(e^{j\omega}) = \frac{\hat{\Phi}_{\Omega\theta^{ext}_{cm_1}}(\omega)}{\hat{\Phi}_{\theta^{ext}_{cm_1}}(\omega)}.$$

Since in the limit case $N \to \infty$ the spectral estimates become equal to the real spectra, it follows that in the considered open-loop situation (227) the transfer function estimated is asymptotically unbiased

$$\lim_{N \to \infty} \hat{T}_{\Omega\theta_1}^{cl}(e^{j\omega}) = T_{\Omega\theta_1}^{cl}(e^{j\omega}).$$

The application of this approach to closed-loop data $\{\Omega_g(k), \theta_{cm_1}(k)\}$, obtained from the system

$$\begin{cases} \Omega_g(k) = T_{\Omega\theta_1}^{+trq}(q)\theta_{cm_1}(k) + v(k), \\ \theta_{cm_1}(k) = C_{\theta}(q)\Omega_g(k) + \theta_{cm_1}^{ext}(k). \end{cases}$$

leads in general to biased estimates. To see this, denote the sensitivity function as S(q) = (1 -

⁸The term "open-loop" might seem a bit misleading here since the closed-loop transfer function $T^{cl}_{\Omega\theta_1}(q)$ appears in equation (227). Nevertheless, we refer to it as open-loop as there is no feedback from $\Omega_g(k)$ to $\theta^{ext}_{cm_1}(k)$.

 $T_{\Omega\theta_1}^{+trq}(q)C_{\theta}(q))^{-1}$, and observe that

$$\Omega_g(k) = S(q) \left(T_{\Omega\theta_1}^{+trq}(q) \theta_{cm_1}^{ext}(k) + v(k) \right),$$

$$\theta_{cm_1}(k) = S(q) \left(C_{\theta}(q) v(k) + \theta_{cm_1}^{ext}(k) \right).$$

Then, still under the assumption that $\theta_{cm_1}^{ext}(k)$ and v(k) are uncorrelated, one gets

$$\begin{split} \hat{T}^{+trq}_{\Omega\theta_1}(e^{j\omega}) &= \frac{\hat{\Phi}_{\Omega\theta_{cm_1}}(\omega)}{\hat{\Phi}_{\theta_{cm_1}}(\omega)} &= \frac{\mathcal{F}\{\Omega_g\}\mathcal{F}^*\{\theta_{cm_1}\}}{|\mathcal{F}\{\theta_{cm_1}\}|^2} \\ &= \frac{|S(e^{j\omega})|^2 \left(T^{+trq}_{\Omega\theta_1}(e^{j\omega})\hat{\Phi}_{\theta^{ext}_{cm_1}}(\omega) + C^*_{\theta}(e^{j\omega})\hat{\Phi}_{v}(\omega)\right)}{|S(e^{j\omega})|^2 \left(\hat{\Phi}_{\theta^{ext}_{cm_1}}(\omega) + |C_{\theta}(e^{j\omega})|^2\hat{\Phi}_{v}(\omega)\right)} \end{split}$$

Clearly, in the absence of the disturbance v(k), i.e when $\Phi_v(\omega)=0$, this method gives an unbiased estimate $(\hat{T}_{\Omega\theta_1}^{+trq}(e^{j\omega})=T_{\Omega\theta_1}^{+trq}(e^{j\omega}))$ in the limit $N\to\infty$). However, this case, corresponding to the absence of turbulence in the wind, is of no practical relevance here. On the other hand, when there is no external excitation $(\Phi_{\theta_{cm_1}^{ext}}(\omega)=0)$, the above expression simplifies to $\hat{T}_{\Omega\theta_1}^{+trq}(e^{j\omega})=1/C_{\theta}(q)$, i.e. the inverse of the controller is identified. When both external excitation and disturbance are present, the result will be in between these two cases, giving a biased estimate.

A much better alternative is to estimate the transfer function from the following relation

$$\hat{T}_{\Omega\theta_1}^{+trq}(e^{j\omega}) = \frac{\hat{\Phi}_{\Omega\theta_{cm_1}^{ext}}(\omega)}{\hat{\Phi}_{\theta_{cm_1}\theta_{cm_1}^{ext}}(\omega)} = \frac{|S(e^{j\omega})|^2 T_{\Omega\theta_1}^{+trq}(e^{j\omega}) \hat{\Phi}_{\theta_{cm_1}^{ext}}(\omega)}{|S(e^{j\omega})|^2 \hat{\Phi}_{\theta_{cm_1}^{ext}}(\omega)} = T_{\Omega\theta_1}^{+trq}(q), \tag{228}$$

which is clearly unbiased whenever $E(v(k)\theta_{cm_1}^{ext}(k)) = 0$.

The application of this method to simulation data obtained from the linearized model, described in Section 15.1, gives the results, depicted on Figure 105, where the bode plots of the real $\hat{T}_{\Omega\theta_1}^{+trq}(e^{j\omega})$ (black solid) and the estimated $T_{\Omega\theta_1}^{+trq}(e^{j\omega})$ (red dashed) transfer functions are given. The results show that the SA estimate is sufficiently accurate.

15.2.2 Parametric model identification

In what follows, several methods for the identification of *parametric* models based on closed-loop data will be discussed and tested on the linearized model, described in Section 15.1.

15.2.2.1 Direct ARX identification

In the direct identification approach a common open-loop identification method is applied to the data, collected while the process is operating in closed-loop. The identification is hence performed on a batch of input-output data $\{\Omega_g(k), \theta_{cm_1}(k)\}$ by completely disregarding the feedback. To summarize this, we will consider the identification of *linear regression models*, although other identification structures could be used as well.

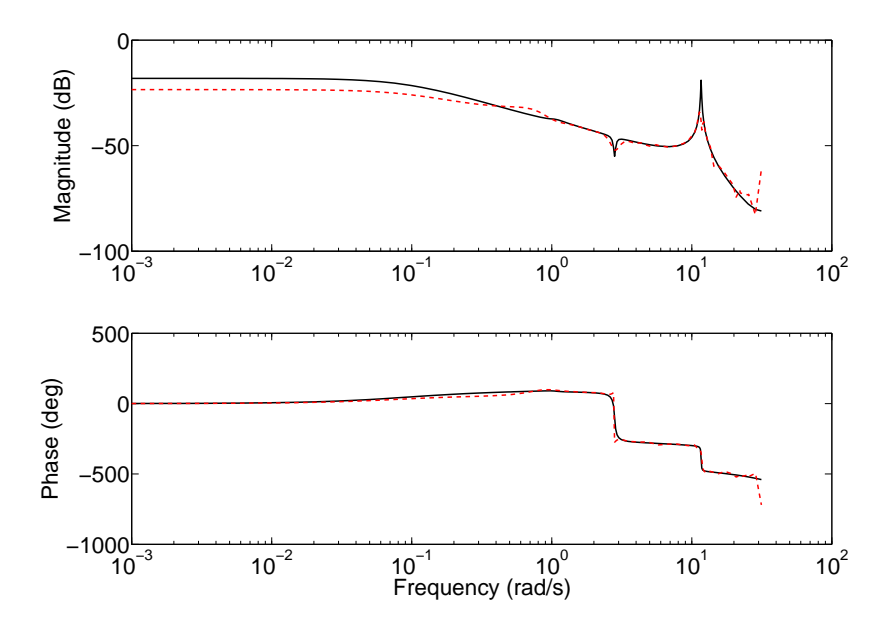


Figure 105 Bode plots of the transfer function $T_{\Omega\theta_1}^{+trq}(e^{j\omega})$ and its spectral analysis estimate based on equation (228)

The starting point in the identification of linear regression models is an ARX model structure⁹

$$\Omega_g(k) = \frac{B(q^{-1}, p)}{A(q^{-1}, p)} \theta_{cm_1}(k) + \frac{1}{A(q^{-1}, p)} v(k), \tag{229}$$

where the polynomials $A(q^{-1}, p)$ and $B(q^{-1}, p)$ are given by

$$A(q^{-1}, p) = 1 + a_1 q^{-1} + a_2 q^{-2} + \dots + a_{n_a} q^{-n_a},$$

$$B(q^{-1}, p) = b_0 + b_1 q^{-1} + b_2 q^{-2} + \dots + b_{n_b} q^{-n_b},$$

with $p = \begin{bmatrix} a_1 & \dots & a_{n_a} & b_0 & b_1 & \dots & b_{n_b} \end{bmatrix}^T$ being the unknown parameter vector. By defining the regression vector

$$\varphi^T(k) = \begin{bmatrix} -\Omega_g(k-1) & \dots & -\Omega_g(k-n_a) & \theta_{cm_1}(k) & \dots & \theta_{cm_1}(k-n_b) \end{bmatrix},$$

equation (229) can be rewritten in the more convenient for identification regression form

$$\Omega_g(k) = \varphi^T(k)p + v(k). \tag{230}$$

Suppose a set of input/output data of length N is collected, i.e. $\{\Omega_g(k), \theta_{cm_1}(k)\}_{k=1}^N$. The idea is then to compute the optimal parameter vector p that minimizes the following prediction error cost function

$$V(p) = \frac{1}{N} \sum_{k=1}^{N} \left(\Omega_g(k) - \varphi^T(k) p \right)^2, \tag{231}$$

⁹Actually, FIR models also fall into this category, but we will not treat them separately as they can be viewed as a special case of the ARX model with $A(q^{-1}, p) = 1$.

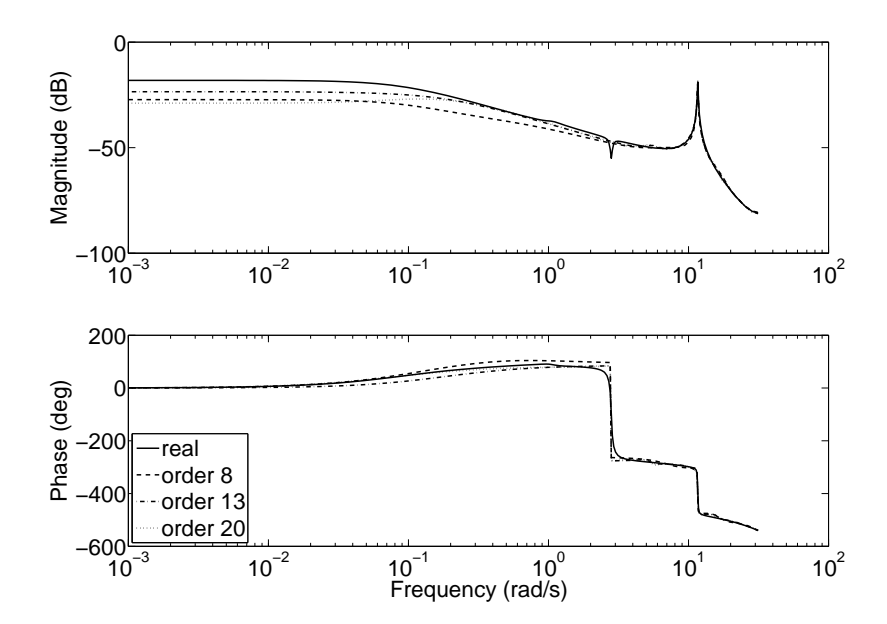


Figure 106 Bode plots of the transfer function $T_{\Omega\theta_1}^{+trq}(e^{j\omega})$ and its estimate based on direct ARX identification

that is.

$$\hat{p} = \arg\min_{p} V(p) = \left(\frac{1}{N} \sum_{k=1}^{N} \varphi(k) \varphi(k)^{T}\right)^{-1} \left(\frac{1}{N} \sum_{k=1}^{N} \varphi(k) \Omega_{g}(k)\right). \tag{232}$$

It can be shown [70] that this method produces a consistent estimate provided that

- the true system has ARX structure, i.e. can be written in the form (229),
- the input signal $\theta_{cm_1}(k)$ is persistently exciting (which would be the case when the external input $\theta_{cm_1}^{ext}(k)$ is sufficiently exciting), and
- the disturbance v(k) is uncorrelated with $\Omega_g(k-1-\tau)$ and $\theta_{cm_1}^{ext}(k-\tau)$, $\tau \in \mathbb{N}_+$. To be more precise, it should hold that $E\left(\varphi(k)v(k)\right)=0$. This would hold if v(k) is a white noise process.

However, if the disturbance signal v(k) is non-white, as is the case with the wind, then the ARX estimate will be biased.

The results of the application of this approach to the linearized example here is depicted on Figure 106. Three ARX models of different order have been identified, one with $n_a=n_b=8$ (dashed curve), another with $n_a=n_b=13$ (dash-dotted curve), and the third one with $n_a=n_b=20$ (dotted curve). The true transfer function is represented by the solid curve on the figure. In real-life experiments when this transfer function is unknown, it should be substituted with its SA estimate, i.e. the dashed curve in Figure 105. It can be seen from the figure that the most accurate model is of order 13, and that increasing the model order further does not improve the accuracy. The phase is approximated accurately, while the magnitude is most accurately modeled in the frequency range above approximately 0.2 rad/s. The zero is not accurately estimated by any of the models.

Similar results are obtained with other model structures, such as ARMAX and Box-Jenkins models. The disadvantage of such more extended models is that the corresponding prediction error optimization criterion is no longer a quadratic optimization problem in the parameter vector p,

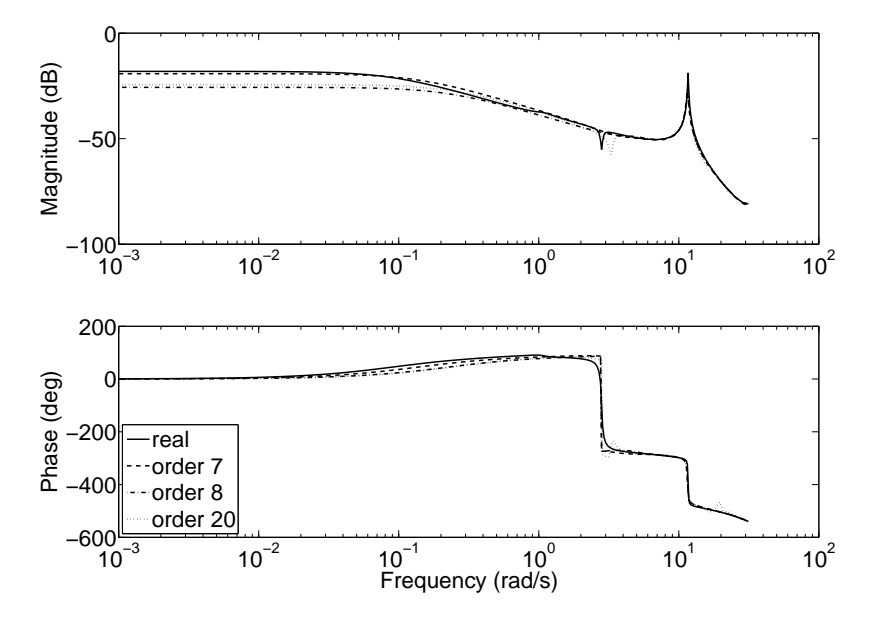


Figure 107 Bode plots of the transfer function $T_{\Omega\theta_1}^{+trq}(e^{j\omega})$ and its IV estimate

but becomes a nonlinear optimization problem, with the consequence that only locally optimal solutions for p can be computed using numerical iterative procedures.

15.2.2.2 Instrumental variable method

Similarly to the direct ARX identification, the instrumental variable (IV) method is also based on the ARX model structure written in regression form, as in equation (230). In the IV method, however, instead of obtaining the parameter vector by means of a minimization of the quadratic cost function (231), the estimate is constructed by correlation with a suitably defined auxiliary signal $\zeta(k)$, referred to as the *instrumental variable*. For a reason that will become obvious in what follows, the IV should be selected in such a way, that the following expression holds

$$\frac{1}{N} \sum_{k=1}^{N} \zeta(k) \left(\Omega_g(k) - \varphi^T(k) p \right) = 0,$$

with optimal solution given by

$$\hat{p} = \left(\frac{1}{N} \sum_{k=1}^{N} \zeta(k) \varphi(k)^{T}\right)^{-1} \left(\frac{1}{N} \sum_{k=1}^{N} \zeta(k) \Omega_{g}(k)\right), \tag{233}$$

provided that the matrix to be inverted is nonsingular. Note that this estimate becomes equal to the ARX least-squares estimate in equation (232) when the IV is selected as $\zeta(k) = \varphi(k)$.

Under the assumption that (230) holds, (233) takes the form

$$\hat{p} = p + \left(\frac{1}{N} \sum_{k=1}^{N} \zeta(k) \varphi^{T}(k)\right)^{-1} \left(\frac{1}{N} \sum_{k=1}^{N} \zeta(k) v(k)\right),$$

meaning that the IV estimator provides a consistent parameter estimate, i.e. $\lim_{N\to\infty} \hat{p} = p$,

under the conditions that (a) the matrix $E(\zeta(k)\varphi^T(k))$ is nonsingular, and (b) $E(\zeta(k)v(k))=0$. Both conditions are satisfied by taking

$$\zeta^T(k) = \begin{bmatrix} \theta_{cm_1}^{ext}(k) & \theta_{cm_1}^{ext}(k-1) & \dots & \theta_{cm_1}^{ext}(k-n_a-n_b) \end{bmatrix},$$

under the assumption that $\theta_{cm_1}^{ext}$ is uncorrelated with the signal v.

Figure 107 visualizes the results, obtained with this identification method on the simulation data with the linearized wind turbine model, described in Section 15.1. The figure shows the Bode plots of the true model (solid curve), and three identified models of different orders: $n_a = n_b = 7$ (dashed curve), $n_a = n_b = 8$ (dash-dotted curve), and $n_a = n_b = 20$ (dotted curve). Similarly to the direct ARX method, the IV estimates approximate the phase accurately. Regarding the amplitude estimation, the 7th order model is the most accurate one. In real-life experiments the transfer function if the true system is unknown, so the black curve in Figure 107 should be interchanged with the estimate, obtained from measured data using SA analysis, i.e. the dashed line on Figure 105.

15.2.2.3 Indirect identification

The idea, used in the indirect identification, is to first identify the closed-loop transfer function $T^{cl}_{\Omega\theta_1}(z)$ by applying standard open-loop identification technique on the data $\{\Omega_g(k), \theta^{ext}_{cm_1}(k)\}$, and then compute the system transfer $T^{+trq}_{\Omega\theta_1}(z)$ using the knowledge of the pitch controller $C_{\theta}(z)$. Clearly, given $C_{\theta}(z)$ and an estimate $\hat{T}^{cl}_{\Omega\theta_1}(z)$, an estimate of the system dynamics can be computed from (226) as

$$\hat{T}_{\Omega\theta_1}^{+trq}(z) = \hat{T}_{\Omega\theta_1}^{cl}(z) \left(1 + C_{\theta}(z) \hat{T}_{\Omega\theta_1}^{cl}(z) \right)^{-1}.$$

The disadvantage of this method is that the model order of $\hat{T}_{\Omega\theta_1}^{+trq}(z)$ will be equal to that of the identified closed-loop system plus the order of the pitch controller.

In the first step of the indirect method, the open-loop identification can be performed with any existing method. For the simulation data used in this section, three open-loop identification methods have been used to fit the model parameters to the data $\{\Omega_g(k), \theta_{cm_1}^{ext}(k)\}$:

- prediction error identification based on an ARX model structure. This is similar to the approach in Section 15.2.2.1 with the difference that it is now applied to data $\{\Omega_g, \theta_{cm_1}^{ext}\}$ instead. Theoretically, this estimate should be biased due to the non-whiteness of the disturbance process v(k), as discussed above.
- IV method is used to compute the parameters of an ARX model structure, with "optimal" choice of the instrumental variable as implemented in the function IV4 from the SYSTEM IDENTIFICATION TOOLBOX of MATLAB [50].
- The N4SID subspace identification method is used to estimate the parameters of a state-space model. This method is also implemented in the SYSTEM IDENTIFICATION TOOLBOX of MATLAB.

All three models have the same model order, 20. Other methods (MOESP [93]), model structures (ARMAX [70, 50]), and orders (in the range 7-30) have also been tested, but do not lead to significant improvement of the results, reported in Figure 108. The Bode plots on the right-hand side of the figure depict the identified closed-loop models $\hat{T}^{cl}_{\Omega\theta_1}$. As it can be seen from the figure, all methods are able to estimate an accurate model in the frequency range above 0.1 rad/s. Below that frequency the models are inaccurate. Due to that, the computed open-loop models $\hat{T}^{+trq}_{\Omega\theta_1}(e^{j\omega})$ are also quite inaccurate. By increasing the length of the data one could improve the accuracy at the lower frequencies.

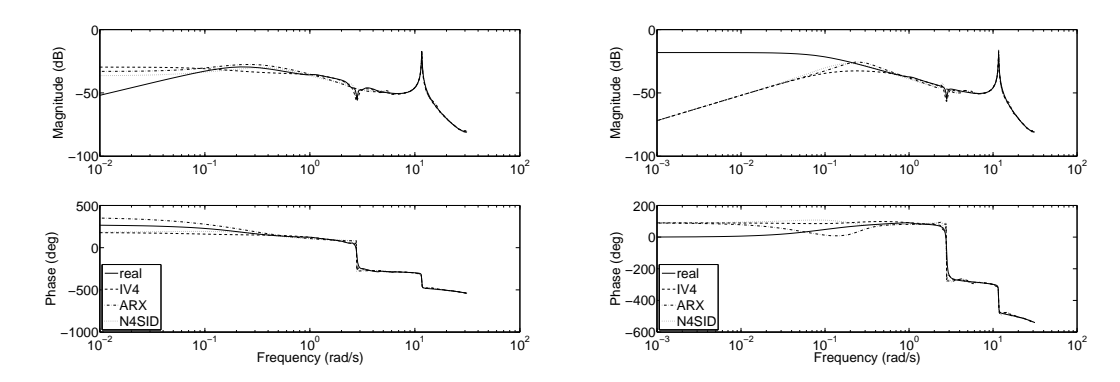


Figure 108 Bode plots of the transfer functions $T^{cl}_{\Omega\theta_1}(e^{j\omega})$ (left) and $T^{+trq}_{\Omega\theta_1}(e^{j\omega})$ (right). Both true (solid), and estimated transfer functions are given, using the methods IV (dashed), ARX (dash-dotted) and N4SID (dotted)

15.2.2.4 Joint input-output identification

The idea behind this approach is to use open-loop identification techniques to identify the transfers from $\theta_{cm_1}^{ext}(k)$ to both $\omega_g(k)$ and $\theta_{cm_1}(k)$ simultaneously. Although any open-loop identification method can be used here, we will employ subspace identification, as in [92], referred to as CL-MOESP here.

Using the relations in equation (226) one can write

$$\begin{bmatrix}
\Omega_{g}(k) \\
\theta_{cm_{1}}(k)
\end{bmatrix} = \begin{pmatrix}
1 - T_{\Omega\theta_{1}}^{+trq}(q)C_{\theta}(q)
\end{pmatrix}^{-1} \begin{bmatrix}
T_{\Omega\theta_{1}}^{+trq}(q) & 1 \\
1 & C_{\theta}(q)
\end{bmatrix} \begin{bmatrix}
\theta_{cm_{1}}^{ext}(k) \\
v(k)
\end{bmatrix} \\
= \begin{bmatrix}
T_{1}(q) \\
T_{2}(q)
\end{bmatrix} \theta_{cm_{1}}^{ext}(k) + T_{2} \begin{bmatrix}
1 \\
C_{\theta}(q)
\end{bmatrix} v(k),$$
(234)

and suppose, that estimates $\hat{T}_1(q)$ and $\hat{T}_2(q)$ of the transfer functions $T_1(q)$ and $T_2(q)$ have been identified. Then,

$$\hat{T}_{\Omega\theta_1}^{+trq}(q) = \frac{\hat{T}_1(q)}{\hat{T}_2(q)}.$$
(235)

Notice that, just as the indirect identification method, the accuracy of the identified model $\hat{T}_{\Omega\theta_1}^{+trq}(q)$ is influenced by the accuracy of the estimated closed-loop transfer function $T_1(q) = T_{\Omega\theta_1}^{cl}(q)$. In addition to that, any inaccuracies in the estimation of the second channel, $T_2(q)$, would additionally contribute to the final error in $\hat{T}_{\Omega\theta_1}^{+trq}(q)$, which makes the method even more sensitive to model imperfections than the indirect identification method. The results, obtained with the joint input-output method are presented in Figure 109, where the Bode plot of the true transfer function $T_{\Omega\theta_1}^{+trq}(q)$ (black solid), and its estimate using the CL-MOESP joint input-output method (red dotted).

15.2.2.5 Two-stage method

Another method for closed-loop system identification is the two-stage method. As its name implies, the method consists of two steps, that are executed consequently. In the first step, the transfer function from the external input $\theta_{cm_1}^{ext}$ to the turbine input θ_{cm_1} , i.e. the transfer function $T_2(q)$ in equation (234), is identified. Then, the following auxiliary signal is computed based on the identified model $\hat{T}_2(q)$

 $\theta_{cm_1}^{aux}(k) = \hat{T}_2(q)\theta_{cm_1}^{ext}(k)$

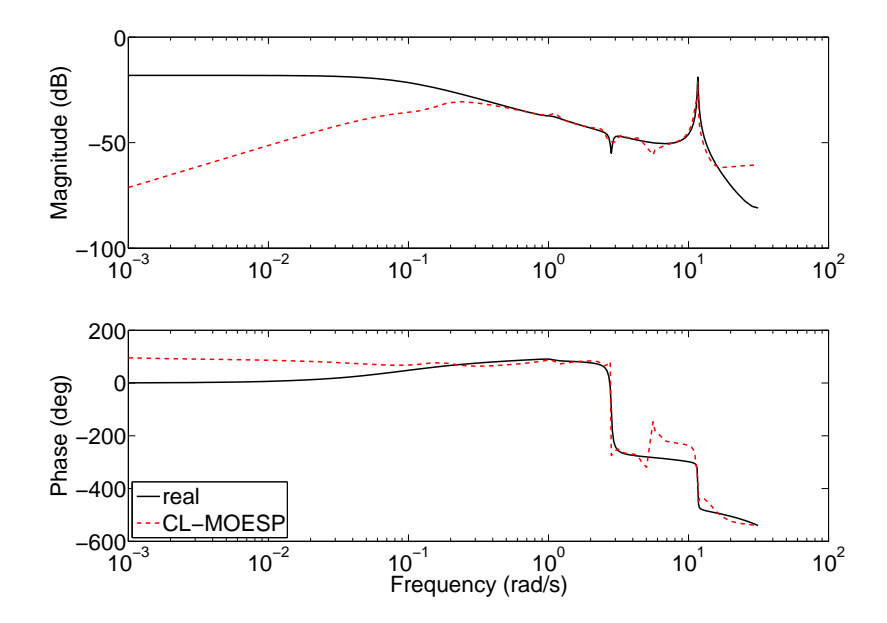


Figure 109 Bode plots of the transfer functions $T_{\Omega\theta_1}^{+trq}(e^{j\omega})$ (black solid), and its estimate using the CL-MOESP joint input-output (red dotted)

which, unlike the true input signal $\theta_{cm_1}(k)$, is uncorrelated with the disturbance v(k). Thus, in the second step of the method the input signal $\theta_{cm_1}(k)$ is substituted with $\theta_{cm_1}^{aux}(k)$, resulting in

$$\Omega_g(k) = T_{\Omega\theta_1}^{+trq}(q)\theta_{cm_1}^{aux}(k) + T_2(q)v(k) + T_{\Omega\theta_1}^{+trq}(q)(T_2(q) - \hat{T}_2(q))\theta_{cm_1}^{ext}(k)
= T_{\Omega\theta_1}^{+trq}(q)\theta_{cm_1}^{aux}(k) + W(q)\tilde{v}(k),$$

from which a model of the transfer $T^{+trq}_{\Omega\theta_1}(q)$ is identified using again open-loop methods based on the data $\{\Omega_g(k), \theta^{aux}_{cm_1}(k)\}$.

Similarly to the two-stage method, the choice of an identification method for the open-loop problem in the two steps is free. This method, applied to the present problem, was uncapable of producing a reasonably accurate model of $T_{\Omega\theta_1}^{+trq}(q)$, and the results are hence not reported here.

15.2.2.6 Tailor-made instrumental variable method

The advantage of the Tailor-made IV method is that it provides an unbiased estimate of the transfer function $T_{\Omega\theta_1}^{+trq}$, while at the same time it pertains the simple linear regression type of algorithms [26, 27]. The main idea is to parameterize the closed-loop model $T_{\Omega\theta_1}^{cl}$ with the open-loop model parameters, which parameters are then estimated using linear regression algorithms applied on the closed-loop data.

To summarize the method, let

$$C_{\theta}(q) \triangleq \frac{n_{c}(q^{-1})}{d_{c}(q^{-1})},$$

$$T_{\Omega\theta_{1}}^{+trq}(q) \triangleq \frac{n_{p}(q^{-1})}{d_{p}(q^{-1})} \triangleq \frac{b_{0} + b_{1}q^{-1} + b_{2}q^{-2} + \dots + b_{n}q^{-n}}{1 + a_{1}q^{-1} + a_{2}q^{-2} + \dots + a_{n}q^{-n}}.$$

From equation (234) it follows that

$$\Omega_g(k) = \frac{T_{\Omega\theta_1}^{+trq}(q)}{1 - T_{\Omega\theta_1}^{+trq}(q)C_{\theta}(q)} \theta_{cm_1}^{ext}(k) + \frac{1}{1 - T_{\Omega\theta_1}^{+trq}(q)C_{\theta}(q)} v(k),$$

or, equivalently,

$$\left(d_p(q^{-1}) d_c(q^{-1}) - n_p(q^{-1}) n_c(q^{-1}) \right) \Omega_g(k) = n_p(q^{-1}) d_c(q^{-1}) \theta_{cm_1}^{ext}(k) + d_p(q^{-1}) d_c(q^{-1}) v(k).$$
(236)

Note also, that

$$\theta_{cm_1}(k) = \theta_{cm_1}^{ext}(k) + C_{\theta}(q)\Omega_g(k) \implies d_c(q^{-1})\theta_{cm_1}^{ext}(k) = d_c(q^{-1})\theta_{cm_1}(k) - n_c(q^{-1})\Omega_g(k).$$

Substitution of the last equation into (236) gives

$$d_p(q^{-1})d_c(q^{-1})\Omega_g(k) = n_p(q^{-1})d_c(q^{-1})\theta_{cm_1}(k) + \bar{v}(k),$$

where $\bar{v}(k) \triangleq d_p(q^{-1})d_c(q^{-1})v(k)$. Next, by defining

$$\bar{\Omega}_{g}(k) \triangleq d_{c}(q^{-1})\Omega_{g}(k),
\bar{\theta}_{cm_{1}}(k) \triangleq d_{c}(q^{-1})\theta_{cm_{1}}(k),
p \triangleq \begin{bmatrix} a_{1} \dots a_{n} & b_{0} & b_{1} \dots b_{n} \end{bmatrix}^{T},
\bar{\varphi}(k) \triangleq \begin{bmatrix} -\bar{\Omega}_{g}(k-1) \dots -\bar{\Omega}_{g}(k-n) & \bar{\theta}_{cm_{1}}(k) & \bar{\theta}_{cm_{1}}(k-1) \dots & \bar{\theta}_{cm_{1}}(k-n) \end{bmatrix}^{T},$$

one finally obtains the following linear regression equation

$$\bar{\Omega}_q(k) = \bar{\varphi}^T(k)p + \bar{v}(k).$$

Using the IV method with instrumental variable

$$\bar{\zeta}(k) = \begin{bmatrix} \theta_{cm_1}^{ext}(k) & \dots & \theta_{cm_1}^{ext}(k-2n) \end{bmatrix}^T,$$

the following IV estimate of the parameter vector p will be asymptotically unbiased

$$\hat{p} = \left(\frac{1}{N} \sum_{k=1}^{N} \bar{\zeta}(k) \bar{\varphi}(k)^{T}\right)^{-1} \left(\frac{1}{N} \sum_{k=1}^{N} \bar{\zeta}(k) \bar{\Omega}_{g}(k)\right), \tag{237}$$

provided that $\theta_{cm_1}^{ext}(k)$ is persistently exciting and uncorrelated with v(k).

The method is applied to the simplified wind turbine model, described in Section 15.1. The results are depicted on Figure 110 for three different model orders, ten (dashed curve), eleven (dash-dotted curve), and twelve (dotted curve). The nominal Bode plot is represented by the solid curve on the figure. As it can be observed from the figure, the best model has order 10. The amplitude is well approximated above 0.2 rad/s, while the phase is reasonably well-modeled throughout the whole frequency range. For other model orders, though, the phase might be less accurately modeled.

15.2.2.7 Closed-loop N4SID method

The closed-loop N4SID (CL-N4SID) method [87] is a generalization of the open-loop subspace identification method N4SID [86]. The method has the following useful features:

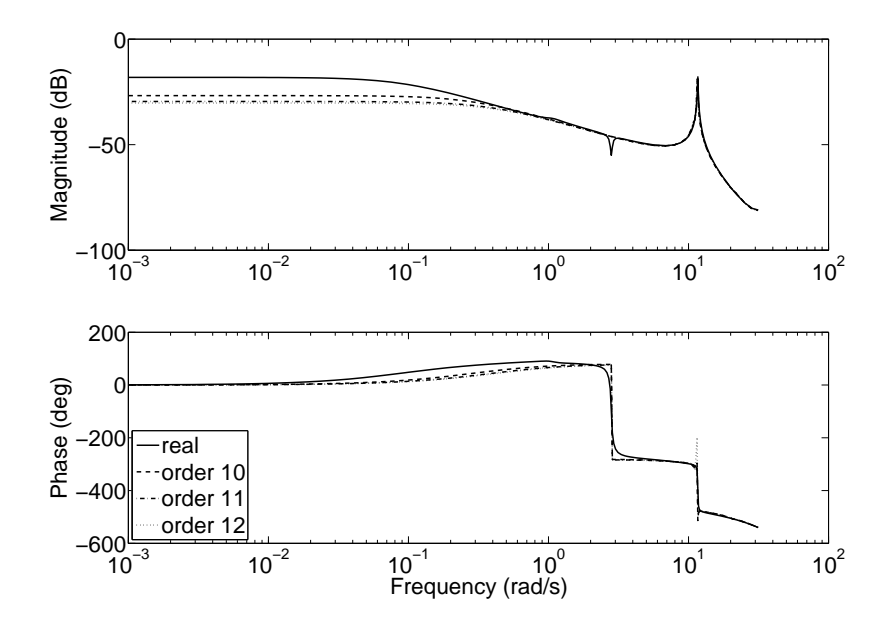


Figure 110 Bode plots of the transfer functions $T_{\Omega\theta_1}^{+trq}(e^{j\omega})$ (solid), and its 10th (dashed), 11th (dash-dotted) and 12th (dotted)) order estimate using the Tailor-made IV method

- 1 provides asymptotically unbiased estimates,
- 2 deals with MIMO systems,
- 3 deals with unstable open-loop systems,
- 4 simplifies to conventional open-loop N4SID algorithm when no controller is present.

The third feature is extremely important since the open-loop transfer $T_{\Omega\theta_1}^{+trq}(z)$ is unstable in the case of constant-power torque control, as explained in Section 15.1. The last feature will also prove to be very useful when the closed-loop identification for individual pitch control design is treated in the next section, where some of the input-output channels are interconnected with feedback $(\theta_{cm_1} \to \Omega_q)$, while other are not $(\theta_{cm_i} \to M_{cm_i}, i=2,3)$.

Below, the CL-N4SID will be outlined briefly. Since this method will later on also be used for the MIMO identification case in Figure 99, a general notation will be used in this section, wherein the inputs, outputs and the controller will not be explicitly specified. This is depicted on Figure 111. The SISO case of collective pitch, discussed in this section, corresponds to taking

$$u \equiv \theta_{cm_1}, \ y \equiv \Omega_g, \ r \equiv \theta_{cm_1}^{ext}, \ \text{and} \ K = C_{\theta}.$$

The starting point of the CL-N4SID method is the following state-space model of the open-loop system

$$T: \left\{ \begin{array}{rcl} x(k+1) & = & Ax(k) + Bu(k) + \xi(k), \\ y(k) & = & Cx(k) + Du(k) + \nu(k), \end{array} \right.$$

where $u(k) \in \mathbb{R}^m$ is the input signal, $y(k) \in \mathbb{R}^p$ is the output signal, $x(k) \in \mathbb{R}^n$ is the state of the system, and $\xi(k) \in \mathbb{R}^n$ and $\nu(k) \in \mathbb{R}^p$ are unobserved, zero mean, white noise vector processes.

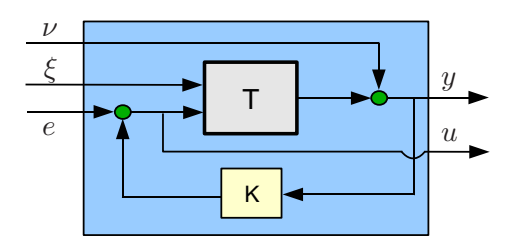


Figure 111 General closed-loop system identification setting

The controller, on the other hand, is governed by the equations

$$K: \begin{cases} x_c(k+1) &= A_c x_c(k) + B_c y(k), \\ u_c(k) &= C_c x_c(k) + D_c y(k), \\ u(k) &= u_c(k) + e(k). \end{cases}$$

The state-dimension of the controller is immaterial ¹⁰.

Further, let

$$E\left\{\begin{bmatrix} \xi(k) \\ \nu(k) \end{bmatrix} \begin{bmatrix} \xi(l) \\ \nu(l) \end{bmatrix}^T \right\} = \begin{bmatrix} Q & S \\ S^T & R \end{bmatrix} \delta(k-l) \ge 0,$$

where $\delta(k)$ is the Dirac delta function, and where for a matrix M the expression M > 0 ($M \ge 0$) means that M is positive (semi-)definite.

Since the derivation of the method is rather involved, only an algorithmic summary, with some add-ons for numerical efficiency and automatic model order selection, will be provided here. For more details, the reader is referred to [87]. Before summarizing the complete algorithm, the following additional notation needs to be defined:

$$\mathcal{H}_{i,j,r}(v) \triangleq \begin{bmatrix} v_{i} & v_{i+1} & \dots & v_{i+r-1} \\ v_{i+1} & v_{i+2} & \dots & v_{i+r} \\ \vdots & \vdots & \ddots & \vdots \\ v_{j} & v_{j+1} & \dots & v_{j+r-1} \end{bmatrix} \\ \mathcal{T}_{i}(A,B,C,D) \triangleq \begin{bmatrix} D & 0 & \dots & 0 \\ CB & D & \dots & 0 \\ CAB & CB & \dots & 0 \\ \vdots & \vdots & \ddots & \vdots \\ CA^{i-2}B & CA^{i-3}B & \dots & D \end{bmatrix}$$

	CL-N4SID Algorithm
Given:	Data $\{y_k, u_k\}, k = 0, 1, \dots, (N-1),$
	controller matrices (A_c, B_c, C_c, D_c) , and
	integer i (larger than expected system order).
Step 1.	Let $j = N - (2i - 1)$ and define the matrices

¹⁰In fact, it is not necessary that the state-space matrices of the controller are given; it suffices for the CL-N4SID algorithm that just the first several Markov parameters are known.

Step 2. Compute

$$\mathcal{O}_{i} = Y_{i|2i-1} \begin{bmatrix} U_{0|i-1} \\ Y_{0|i-1} \\ M_{i|2i-1} \end{bmatrix}^{\dagger} \begin{bmatrix} U_{0|i-1} \\ Y_{0|i-1} \\ 0 \end{bmatrix}, \quad \mathcal{Z}_{i} = Y_{i|2i-1} \begin{bmatrix} U_{0|i-1} \\ Y_{0|i-1} \\ M_{i|2i-1} \end{bmatrix}^{\dagger} \begin{bmatrix} U_{0|i-1} \\ Y_{0|i-1} \\ M_{i|2i-1} \end{bmatrix},$$

$$\mathcal{Z}_{i+1} = Y_{i+1|2i-1} \begin{bmatrix} U_{0|i-1} \\ Y_{0|i-1} \\ M_{i+1|2i-1} \end{bmatrix}^{\dagger} \begin{bmatrix} U_{0|i-1} \\ Y_{0|i-1} \\ M_{i+1|2i-1} \end{bmatrix}$$

Step 3. Compute an SVD of O_i

$$\mathcal{O}_1 = U \left[\begin{array}{ccc} \sigma_1 & & \\ & \ddots & \\ & & \sigma_{ip} \end{array} \right] V^T,$$

where U and U are unitary matrices, and $\sigma_l \geq \sigma_{l+1} \geq 0$, $\forall l = 1, \dots, ip-1$.

Step 4. Determine the model order by either using the following ad-hoc algorithm

$$\begin{vmatrix} d = \log_{10} \left(\left[\sigma_1 & \dots & \sigma_{ip} \right] \right), \\ \varepsilon_l = \frac{1}{l} (d_l - d_{l+1}), \ l = 1, 2, \dots, ip - 1, \\ n = \max \left\{ l : \ l \in \{1, 2, \dots, ip - 1\}, \ \varepsilon_l > \frac{1}{ip - 1} \sum_{t=1}^{ip - 1} \varepsilon_t \right\}$$

or let the user choose it using the plot of d.

Further, partition U and $M_{i|2i-\underline{1}}$ as follows

$$U = \begin{bmatrix} U_1 & U_2 \end{bmatrix} = \begin{bmatrix} U_1 & U_{2,0}^T \\ \vdots & \vdots \\ U_{2,i-1}^T \end{bmatrix}, M_{i|2i-1} = \begin{bmatrix} M_0 \\ \vdots \\ M_{i-1} \end{bmatrix}$$

with $U_1 \in \mathbb{R}^{ip \times n}$, $U_{2,l} \in \mathbb{R}^{(ip-n) \times p}$, $M_l \in \mathbb{R}^{m \times j}$, $l = 0, 2, \dots, i-1$.

Step 5. Let $G = U_1 \operatorname{diag} \left(\left[\sqrt{\sigma_1} \quad \dots \quad \sqrt{\sigma_n} \right] \right)$, and compute $K_l \in \mathbb{R}^{p \times m}$, $l = 0, \dots, i-1$ from the following least-squares optimization problem

Step 6. Define the matrix

$$\mathcal{K} = \begin{bmatrix} K_0 & 0 & \dots & 0 \\ K_1 & K_0 & \dots & 0 \\ \vdots & \vdots & \ddots & \vdots \\ K_{i-1} & K_{i-2} & \dots & K_0 \end{bmatrix},$$

and determine the states

$$\hat{X}_{i} = G^{\dagger}(\mathcal{Z}_{i} - \mathcal{K}M_{i|2i-1}),
\hat{X}_{i+1} = ([I_{p(i-1)}, 0]G)^{\dagger} \left(\mathcal{Z}_{i+1} - [I_{p(i-1)}, 0]\mathcal{K} \begin{bmatrix} I_{m(i-1)} \\ 0 \end{bmatrix} M_{i+1|2i-1} \right).$$

Step 7. Compute the matrices

$$\begin{array}{rcl} M_{i|i} & = & U_{i|i} + D_c Y_{i|i} \\ \begin{bmatrix} S_{11} & S_{12} \\ S_{21} & S_{22} \end{bmatrix} & = & \begin{bmatrix} \hat{X}_{i+1} \\ Y_{i|i} \end{bmatrix} \begin{bmatrix} \hat{X}_{i} \\ M_{i|i} \end{bmatrix}^{\dagger} \\ T & = & \begin{bmatrix} \hat{X}_{i+1} \\ Y_{i|i} \end{bmatrix} - \begin{bmatrix} S_{11} & S_{12} \\ S_{21} & S_{22} \end{bmatrix} \begin{bmatrix} \hat{X}_{i} \\ M_{i|i} \end{bmatrix} \end{array}$$

Step 8. Compute the system matrices
$$\hat{B} = S_{12}(I_m - D_c S_{22})^{-1}$$

$$\hat{D} = S_{22}(I_m - D_c S_{22})^{-1}$$

$$\hat{A} = S_{11} + BD_c S_{21}$$

$$\hat{C} = (I_p + \hat{D}D_c)S_{21}$$
 Step 9. Determine the covariance matrices
$$\begin{bmatrix} \hat{Q} & \hat{S} \\ \hat{S}^T & \hat{R} \end{bmatrix} = \frac{1}{j} \begin{bmatrix} I_n & \hat{B}D_c \\ 0 & I_p + \hat{D}D_c \end{bmatrix} TT^T \begin{bmatrix} I_n & \hat{B}D_c \\ 0 & I_p + \hat{D}D_c \end{bmatrix}^T .$$

Remark 15.1 (Numerically efficient implementation). The CL-N4SID algorithm, as summarized in [87], is computationally very involved even for problems with moderate number N of inputoutput data of about a few thousand data points. The reason for that is that the matrices, defined in Step 1 of the algorithm all have j columns, and for $i \ll N$, j is a very large number $(j \approx N)$. Performing SVD decompositions, and other matrix operations, on such large matrices is computationally very involved and not practical. Indeed, the V matrix of an SVD decomposition of the matrix O_i will be a $(j \times j)$ matrix; to even store such a matrix would require in MatLab $(8j^2)$ Bytes of RAM (meaning 200 MB for j = 5000), let alone performing computations with it. Fortunately, the algorithm can be efficiently implemented by avoiding such large-scale computations.

Step 3. The computation of an SVD of \mathcal{O}_i is computationally extremely involved due to the large number of columns of \mathcal{O}_i , resulting in very large matrix V. However, the matrix V is subsequently not used in the algorithm, and thus need not to be computed, if possible. Fortunately, this is possible, and the remaining elements of the SVD can efficiently be calculated as follows. First, use the "Q-less" QR decomposition to compute a lower-triangular matrix $R_1 \in \mathbb{R}^{ip \times ip}$ for which there exists a unitary matrix Q_1 such that

$$\begin{bmatrix} R_1 & 0 \end{bmatrix} Q_1^T = \mathcal{O}_i. \tag{238}$$

The unitary matrix $Q_1 \in \mathbb{R}^{j \times j}$ is not needed, and should not be computed. Next, perform an SVD on the matrix R_1 to get

$$R_1 = \tilde{U} \operatorname{diag} \left(egin{bmatrix} ilde{\sigma}_1 & \dots & ilde{\sigma}_{ip} \end{bmatrix}
ight) ilde{V}^T,$$

where the \tilde{V} matrix is now just an (ip)-by-(ip) matrix. It can easily be proved that \tilde{U} and the singular values $\tilde{\sigma}_l$ of R_1 are also elements of the SVD of \mathcal{O}_i in Step 3 of the algorithm. To see that, notice that equation (238) implies $\mathcal{O}_i\mathcal{O}_i^T=R_1R_1^T$, so that it follows that an SVD of $\mathcal{O}_i\mathcal{O}_i^T$ can be written as

$$\mathcal{O}_i \mathcal{O}_i^T = ilde{U} extit{diag} \left(egin{bmatrix} ilde{\sigma}_1^2 & \dots & ilde{\sigma}_{ip}^2 \end{bmatrix}
ight) ilde{U}^T.$$

Hence, $\tilde{\sigma}_l$ are the singular values of \mathcal{O}_i and the matrix \tilde{U} contains the corresponding left singular vectors. Notice that $\tilde{\sigma}_l \equiv \sigma_l$, and that for distinct and positive singular values also $\tilde{U} \equiv U$.

Step 5. The optimization in Step 5 of the CL-N4SID algorithm is also computationally rather involved, so its efficient implementation is very important. The least-squares problem in Step 5 is derived from the following matrix equation in [87]

$$U_2^T \mathcal{Z}_i = \sum_{t=0}^{i-1} \begin{bmatrix} U_{2,t} & \dots & U_{2,i-1} \end{bmatrix} \begin{bmatrix} K_0 \\ \vdots \\ K_{i-1-t} \end{bmatrix} M_t,$$
 (239)

which needs to be solved with respect to the matrices K_l , l = 0, 1, ..., i - 1. Indeed, vectorizing this matrix equation, and solving the resulting system of linear equations in least-squares sense is equivalent to the solution of the optimization problem in Step 5. This would be a system of

j(pi-n) equations and (pmi) unknowns. The huge number of equations can be brought down to im(pi-n), which is a substantial reduction of the computational burden when $im \ll j$. To this end, use the QR factorization to compute a lower-triangular matrix $\tilde{M}_{i|2i-1} \in \mathbb{R}^{im \times im}$ and (unstructured) matrices $\tilde{Y}_{i|2i-1}$, $\tilde{U}_{0|i-1}$ and $\tilde{Y}_{0|i-1}$ for which there exists a unitary matrix Q_2^T such that the following equation holds

$$\begin{bmatrix} \tilde{M}_{i|2i-1} & 0 \\ \tilde{Y}_{i|2i-1} & \star \\ \tilde{U}_{0|i-1} & \star \\ \tilde{Y}_{0|i-1} & \star \end{bmatrix} Q_2^T = \begin{bmatrix} M_{i|2i-1} \\ Y_{i|2i-1} \\ U_{0|i-1} \\ Y_{0|i-1} \end{bmatrix}, \tag{240}$$

where the symbols \star denote matrices that are of no importance in the sequel.

Notice that also here the matrix Q_2 is not needed and should not be computed. Furthermore, notice that in the right-hand side matrix of equation (240) only the first (im) rows, i.e. the matrix $M_{i|2i-1}$, need to be made lower-diagonal, i.e. the QR factorization is only computed for $M_{i|2i-1}$, but transformation matrix is also applied to the remaining matrices. Hence, the following matrix can be computed without the knowledge of Q_2

$$\mathcal{Z}_{i}Q_{2} = Y_{i|2i-1} \begin{bmatrix} U_{0|i-1} \\ Y_{0|i-1} \\ M_{i|2i-1} \end{bmatrix}^{\dagger} \begin{bmatrix} U_{0|i-1} \\ Y_{0|i-1} \\ M_{i|2i-1} \end{bmatrix} Q_{2} = Y_{i|2i-1} \begin{bmatrix} U_{0|i-1} \\ Y_{0|i-1} \\ M_{i|2i-1} \end{bmatrix}^{\dagger} \begin{bmatrix} \tilde{U}_{0|i-1} \\ \tilde{Y}_{0|i-1} \\ \tilde{M}_{i|2i-1} \end{bmatrix}^{\star} \star \\ \vdots$$

Therefore, by defining

$$\tilde{\mathcal{Z}}_{i} \triangleq Y_{i|2i-1} \begin{bmatrix} U_{0|i-1} \\ Y_{0|i-1} \\ M_{i|2i-1} \end{bmatrix}^{\dagger} \begin{bmatrix} \tilde{U}_{0|i-1} \\ \tilde{Y}_{0|i-1} \\ \tilde{M}_{i|2i-1} \end{bmatrix}, \quad \tilde{M}_{i|2i-1} = \begin{bmatrix} \tilde{M}_{0} \\ \vdots \\ \tilde{M}_{i-1} \end{bmatrix},$$

post-multiplication of equation (239) by the matrix Q_2 gives

$$U_2^T \begin{bmatrix} \tilde{\mathcal{Z}}_i & \star \end{bmatrix} = \sum_{t=0}^{i-1} \begin{bmatrix} U_{2,t} & \dots & U_{2,i-1} \end{bmatrix} \begin{bmatrix} K_0 \\ \vdots \\ K_{i-1-t} \end{bmatrix} \begin{bmatrix} \tilde{M}_t & 0 \end{bmatrix},$$

Hence, for the least-squares problem that corresponds to (239) can be written

$$\mathcal{K} = \arg\min_{\mathcal{K}} \left\| U_{2}^{T} \mathcal{Z}_{i} - \sum_{t=0}^{i-1} \left[U_{2,t} \quad \dots \quad U_{2,i-1} \right] \begin{bmatrix} K_{0} \\ \vdots \\ K_{i-1-t} \end{bmatrix} M_{t} \right\|_{F}$$

$$= \arg\min_{\mathcal{K}} \left\| U_{2}^{T} \left[\tilde{\mathcal{Z}}_{i} \quad \star \right] - \sum_{t=0}^{i-1} \left[U_{2,t} \quad \dots \quad U_{2,i-1} \right] \begin{bmatrix} K_{0} \\ \vdots \\ K_{i-1-t} \end{bmatrix} \begin{bmatrix} \tilde{M}_{t} & 0 \end{bmatrix} \right\|_{F}$$

$$= \arg\min_{\mathcal{K}} \left\| V_{2}^{T} \tilde{\mathcal{Z}}_{i} - \sum_{t=0}^{i-1} \left[U_{2,t} \quad \dots \quad U_{2,i-1} \right] \begin{bmatrix} K_{0} \\ \vdots \\ K_{i-1-t} \end{bmatrix} \tilde{M}_{t} \right\|_{F}$$

$$= \arg\min_{\mathcal{K}} \left\| \operatorname{vec} \left(U_{2}^{T} \tilde{\mathcal{Z}}_{i} \right) - \sum_{t=0}^{i-1} \left(\tilde{M}_{t}^{T} \otimes \left[U_{2,t} \quad \dots \quad U_{2,i-1} \right] \right) \operatorname{vec} \left(\begin{bmatrix} K_{0} \\ \vdots \\ K_{i-1-t} \end{bmatrix} \right) \right\|_{2}$$

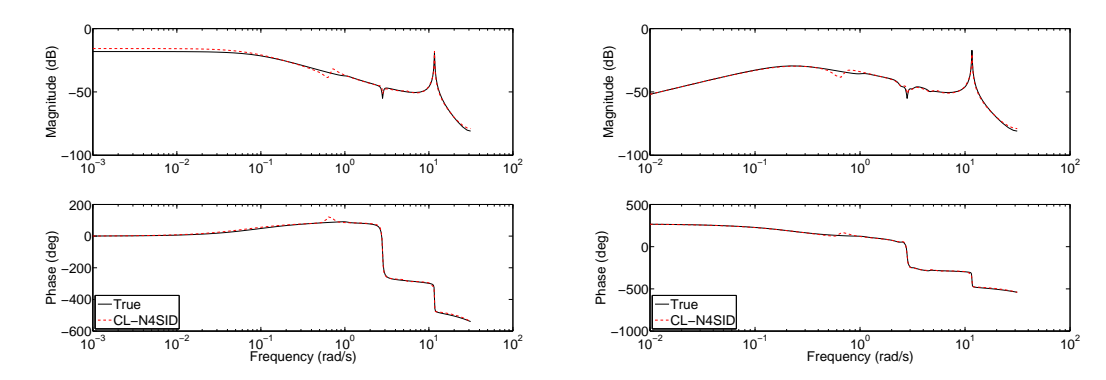


Figure 112 Bode plots of the transfer functions $T_{\Omega\theta_1}^{+trq}(e^{j\omega})$ (left) and $T_{\Omega\theta_1}^{cl}(e^{j\omega})$ (right). Both true (black solid), and estimated (red dashed) transfer functions are given.

where in deriving the last expression the properties $\operatorname{Vec}(ABC) = (C^T \otimes A)\operatorname{Vec}(B)$ and $\|A\|_F = \|\operatorname{Vec}(A)\|_2$ were used. Clearly, the solution of the optimization problem, defined in Step 5 of the CL-N4SID algorithm, coincides with the solution of the optimization problem, defined in the last equation of the expression above, where the vector inside the norm has just $\operatorname{im}(pi-n)$ elements, which is usually much less than the j(pi-n) elements that the vector inside the norm in Step 5 of the algorithm has.

With the implementation improvements, as suggested in Remark 15.1, the computational speed of the CL-N4SID algorithm is significantly improved.

The CL-N4SID algorithm was tested on the data obtained with the linearized wind turbine model, described in Section 15.1. The results are depicted on Figure 112, where the left-hand side represents the Bode plots of the open-loop transfer $T_{\Omega\theta_1}^{+trq}$, and the right-hand side – the closed-loop transfer $T_{\Omega\theta_1}^{cl}$. The black solid lines in the figure correspond to the true transfer function, while the red dashed lines – to the identified ones. The model order was chosen automatically, as suggested at Step 4 of CL-N4SID algorithm, which resulted in model order 13. Notice that, unlike most of the other methods, the CL-N4SID also accurately identifies the zero point around 3 rad/s.

15.2.2.8 Combined open and closed-loop identification using CL-N4SID

One of the main advantages of the CL-N4SID algorithm is that it is a generalization of the open-loop N4SID method in the sense that when in Figure 111 the controller K is absent, the open-loop solution can be obtained with the closed-loop CL-N4SID algorithm with the controller matrices set to zero (i.e. $A_c = B_c = C_c = D_c = 0$). This feature allows to easily apply the method to MIMO data, in which some inputs and outputs are used by the controller, while others not. This is the case when, in addition to the rotor dynamics, one wishes to identify the tower fore-aft dynamics as well. For instance, suppose that the tower top fore-aft speed is measured, then the CL-N4SID can simply by applied to this problem by setting in the algorithm (and in Figure 111)

$$u \equiv \theta_{cm_1}, \; y \equiv \begin{bmatrix} \Omega_g \\ \dot{x}_{nod} \end{bmatrix}, \; e \equiv \theta_{cm_1}^{ext}, \; \text{and} \; K = [C_{\theta}, 0],$$

i.e. the part of the MIMO controller that corresponds to the output \dot{x}_{nod} is simply set to zero. In the MIMO case, however, one should also bear in mind that when some of the input-output signals are significantly larger than the others, the channels corresponding to the later might be less accurately estimated. To prevent that it is sometimes advisable to scale some of the signals

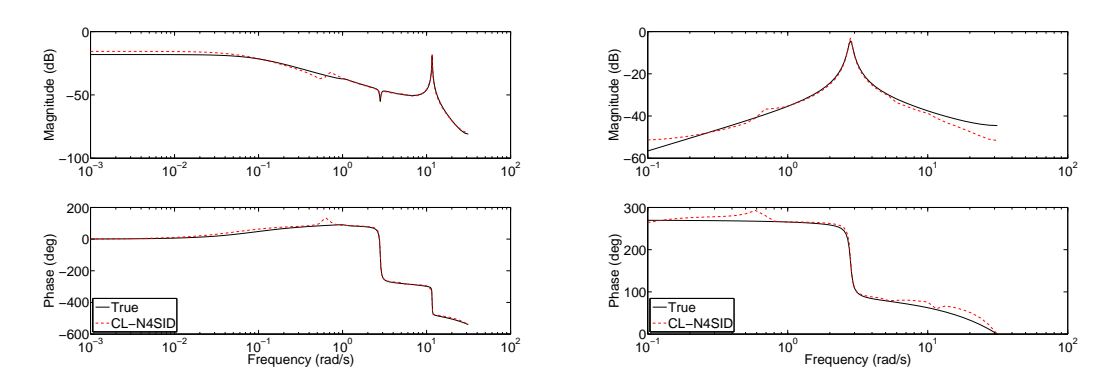


Figure 113 Bode plots of the transfer functions $T_{\Omega\theta_1}^{+trq}(e^{j\omega})$ (left) and $T_{\dot{x}_{nod}\theta_1}^{cl}(e^{j\omega})$ (right). Both true (black solid), and estimated (red dashed) transfer functions are given.

so that approximately equal weight is put to all channels in the identification. This scaling should be performed with care when the channels to be scaled appear in the feedback. The result of this MIMO closed-loop identification problem is demonstrated on Figure 113, where the transfer functions $T_{\Omega\theta_1}^{+trq}$ and $T_{\dot{x}_{nod}\theta_1}^{+trq}$ are identified. To this end, the "measured" signal \dot{x}_{nod} is first downscaled by a factor of 100, before it is used on the identification; at the end, the identified channel $\hat{T}_{\dot{x}_{nod}\theta_1}^{+trq}$ is up-scaled by a factor of 100. Clearly, both channels are rather accurately identified.

15.3 Individual pitch identification

For individual pitch control design not only the channel $T_{\Omega\theta_1}^{+trq}$ is needed, but also the channels from the tilt and yaw oriented pitch actions, θ_{cm_2} and θ_{cm_3} , to the tilt and yaw-wise bending moments, M_{cm_2} and M_{cm_3} . As already discussed in Section 15.1, there are basically two possibilities for identification of these channels: via open-loop identification, and via closed-loop identification. In the first case the goal is the identification of the transfer functions $T_{M_i\theta_j}^{cl}$, i,j=2,3, i.e. with the pitch controller C_{θ} included. This has the disadvantage that the identified models will be functions of the pitch controller C_{θ} , so that any subsequent changes in the pitch controller would require a new identification of $T_{M_i\theta_j}^{cl}$, i=2,3, j=2,3. The second option, i.e. identification in closed-loop, aims at estimating $T_{M_i\theta_j}^{+trq}$, i,j=2,3, which does not suffer from the above drawback, but requires a more involved identification due to the closed-loop setting and the necessity to identify the speed regulation channel $T_{\Omega\theta_1}^{+trq}$ at the same time. These approaches are treated in the following subsections. In both cases, the CL-N4SID algorithm will be used.

15.3.1 Individual pitch identification in open-loop setting

In the open-loop setting, depicted on Figure 114, the tilt-wise θ_{cm_2} and yaw-wise θ_{cm_3} pitch signals are both free to choose, which allows us to select them as uncorrelated random signals – a necessary condition for computing unbiased estimates. Indeed, notice that

$$\begin{array}{lcl} M_{cm_2}(k) & = & T_{M_2\theta_2}^{cl}(q)\theta_{cm_2}(k) + T_{M_2\theta_3}^{cl}(q)\theta_{cm_3}(k) + T_{M_2u}^{cl}(q)u_{cm}(k) \\ M_{cm_3}(k) & = & T_{M_3\theta_2}^{cl}(q)\theta_{cm_2}(k) + T_{M_3\theta_3}^{cl}(q)\theta_{cm_3}(k) + T_{M_3u}^{cl}(q)u_{cm}(k), \end{array}$$

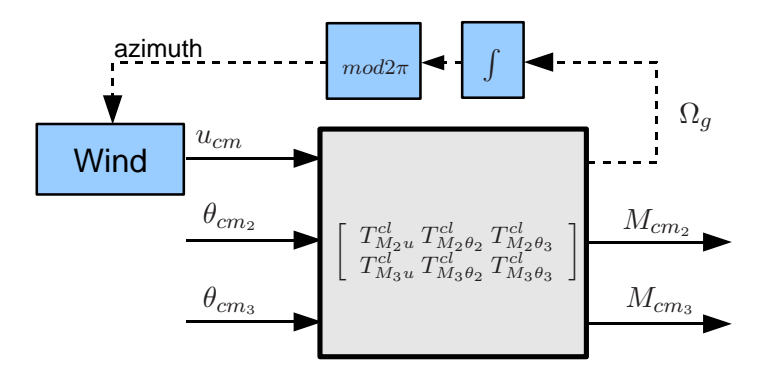


Figure 114 Open-loop setting for individual pitch system identification

from which it can be written that

$$\begin{array}{lcl} \Phi_{M_{cm_2}\theta_{cm_2}}(\omega) & = & T_{M_2\theta_2}^{cl}(e^{j\omega})\Phi_{\theta_{cm_2}}(\omega) + T_{M_2\theta_3}^{cl}(e^{j\omega})\Phi_{\theta_{cm_3}\theta_{cm_2}}(\omega) + T_{M_2u}^{cl}(e^{j\omega})\Phi_{u\theta_{cm_2}}(\omega), \\ \Phi_{M_{cm_3}\theta_{cm_2}}(\omega) & = & T_{M_3\theta_2}^{cl}(e^{j\omega})\Phi_{\theta_{cm_2}}(\omega) + T_{M_3\theta_3}^{cl}(e^{j\omega})\Phi_{\theta_{cm_3}\theta_{cm_2}}(\omega) + T_{M_3u}^{cl}(e^{j\omega})\Phi_{u\theta_{cm_2}}(\omega), \\ \Phi_{M_{cm_2}\theta_{cm_3}}(\omega) & = & T_{M_2\theta_2}^{cl}(e^{j\omega})\Phi_{\theta_{cm_2}\theta_{cm_3}}(\omega) + T_{M_2\theta_3}^{cl}(e^{j\omega})\Phi_{\theta_{cm_3}}(\omega) + T_{M_2u}^{cl}(e^{j\omega})\Phi_{u\theta_{cm_3}}(\omega), \\ \Phi_{M_{cm_3}\theta_{cm_3}}(\omega) & = & T_{M_3\theta_2}^{cl}(e^{j\omega})\Phi_{\theta_{cm_2}\theta_{cm_3}}(\omega) + T_{M_3\theta_3}^{cl}(e^{j\omega})\Phi_{\theta_{cm_3}}(\omega) + T_{M_3u}^{cl}(e^{j\omega})\Phi_{u\theta_{cm_3}}(\omega). \end{array}$$

Hence, under the assumption that the signals θ_{cm_2} , θ_{cm_3} and u are uncorrelated, a consistent estimate will be obtained using the spectral analysis method, i.e.

$$\lim_{N \to \infty} \begin{bmatrix} \frac{\hat{\Phi}_{M_{cm_2}\theta_{cm_2}}(\omega)}{\hat{\Phi}_{\theta_{cm_2}}(\omega)} & \frac{\hat{\Phi}_{M_{cm_2}\theta_{cm_3}}(\omega)}{\hat{\Phi}_{\theta_{cm_3}}(\omega)} \\ \frac{\hat{\Phi}_{M_{cm_3}\theta_{cm_2}}(\omega)}{\hat{\Phi}_{\theta_{cm_2}}(\omega)} & \frac{\hat{\Phi}_{M_{cm_3}\theta_{cm_3}}(\omega)}{\hat{\Phi}_{\theta_{cm_3}}(\omega)} \end{bmatrix} = \begin{bmatrix} T_{M_2\theta_2}^{cl}(e^{j\omega}) & T_{M_2\theta_3}^{cl}(e^{j\omega}) \\ T_{M_3\theta_2}^{cl}(e^{j\omega}) & T_{M_3\theta_3}^{cl}(e^{j\omega}) \end{bmatrix}$$

Similarly to Section 15.2, PRBS signals are used here for excitation

$$\begin{array}{ll} \theta_{cm_2}(k) & = & \left\{ \begin{array}{l} 0, & k \leq 500 \text{ samples}, \\ \frac{3}{2}.s_{prbs}^{(2)}(\lceil \frac{k-500}{4} \rceil), & k > 500 \text{ samples}, \\ \theta_{cm_3}(k) & = & \left\{ \begin{array}{l} 0, & k \leq 500 \text{ samples}, \\ \frac{3}{2}.s_{prbs}^{(3)}(\lceil \frac{k-500}{4} \rceil), & k > 500 \text{ samples}, \\ \end{array} \right. \end{array}$$

where $s_{prbs}^{(2)}$ and $s_{prbs}^{(3)}$ are independent pseudo random binary signals of length $(2^{13}-1)$ samples, uncorrelated with the wind-related signal u.

For collecting data, a simulation is performed with these θ_{cm_2} and θ_{cm_3} . The remaining simulation parameters (turbine parameters, controllers, filters, blade effective wind signals) are the same as in the collective pitch identification case. To get an idea of the pitch activity, the pitch angle of one of the blades is shown in Figure 115.

The CL-N4SID algorithms is next applied to this open-loopidentification problem by setting (see Figure 111)

$$u \equiv \begin{bmatrix} \theta_{cm_2} \\ \theta_{cm_3} \end{bmatrix}, \; y \equiv \begin{bmatrix} M_{cm_2} \\ M_{cm_3} \end{bmatrix}, \text{ and } K = [0,0].$$

The result of the identification is depicted on Figure 116. It can be observed from the figure that the diagonal channels, $T_{M_2\theta_2}^{cl}$ and $T_{M_3\theta_3}^{cl}$, are rather accurately estimated, although the phases become less accurate at frequencies above 5 rad/s. The off-diagonal cross-terms are less accurate (notice that these are completely absent in the true model, where the channels $\theta_{cm_2} \to M_{cm_2}$ and $\theta_{cm_3} \to M_{cm_3}$ are completely decoupled). The reason for the presence of these off-diagonal chan-

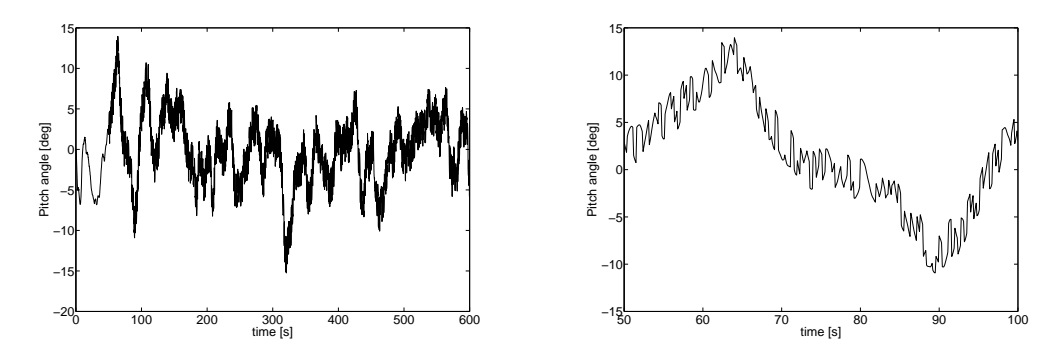


Figure 115 Pitch activity of first blade through the whole simulation (left) and a zoom on the interval [50, 100] s (right)

nels in the identified model is that for finite data length $N<\infty$, the cross spectra $\hat{\Phi}_{\theta_{cm_2}\theta_{cm_3}}(\omega)$, $\hat{\Phi}_{u\theta_{cm_2}}(\omega)$ and $\hat{\Phi}_{u\theta_{cm_3}}(\omega)$ are not zero, resulting in nonzero $\hat{\Phi}_{M_{cm_2}\theta_{cm_3}}(\omega)$ and $\hat{\Phi}_{M_{cm_3}\theta_{cm_2}}(\omega)$. One way of reducing this effect is to increase the data length, which however increases the

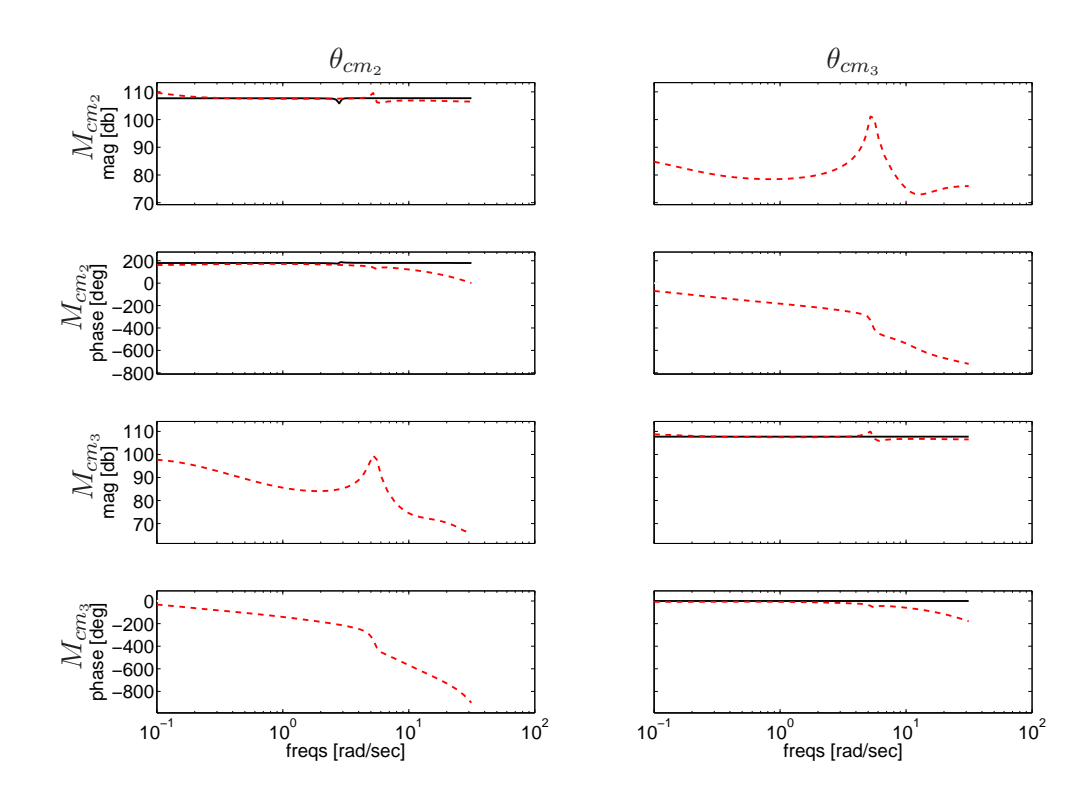


Figure 116 Bode plots of the identified transfer functions $T_{M_i\theta_j}^{cl}$, i, j = 2, 3. Both the true (black solid curves) and the identified (red dashed curves) models are shown.

computational burden. Another possibility is to increase the energy of the excitation signals θ_{cm_2} and θ_{cm_3} , which will result in a decrease of the influence on the wind-related disturbance signal u_{cm} as compared to the pitch excitation. This, however, requires more pitch activity which might also be restrictive in practice. To demonstrate the improvement as a result of "more" pitch excitation, another simulation is run with this time twice larger pitch excitation signals. To this end, the same signals are used θ_{cm_2} and θ_{cm_3} as in the first simulation, but scaled by a factor of two. The resulting pitch angle of the first blade is shown in Figure 117 (compare to Figure

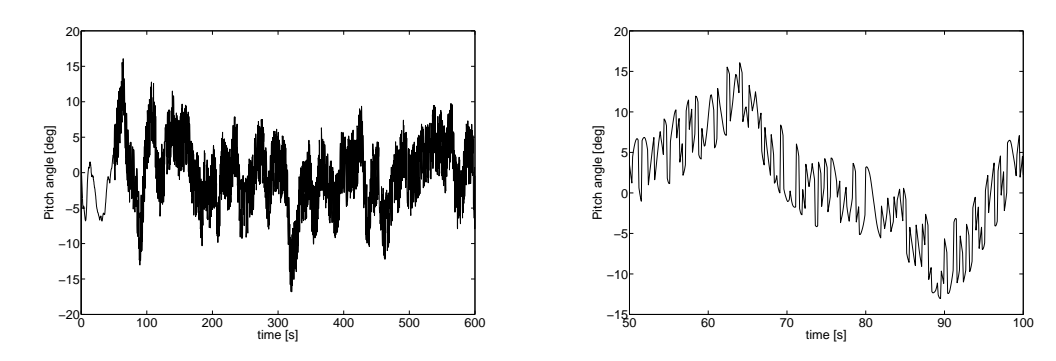


Figure 117 Pitch activity of first blade through the whole simulation (left) and a zoom on the interval [50, 100] s (right)

115). Again, the CL-N4SID algorithm is subsequently applied to the data to identify the transfers $T_{M_i\theta_j}^{cl}$, i,j=2,3. The results are given in Figure 118. When compared with Figure 116, it can be observed that the magnitude plots of the off-diagonal transfer functions $T_{M_2\theta_3}^{cl}$ and $T_{M_3\theta_2}^{cl}$ are indeed somewhat smaller. An evaluation of the \mathcal{H}_2 norms of $T_{M_2\theta_3}^{cl}$ and $T_{M_3\theta_2}^{cl}$ (which is related to the area below the magnitude plots) reveals that these are reduced by approximately a factor of two.

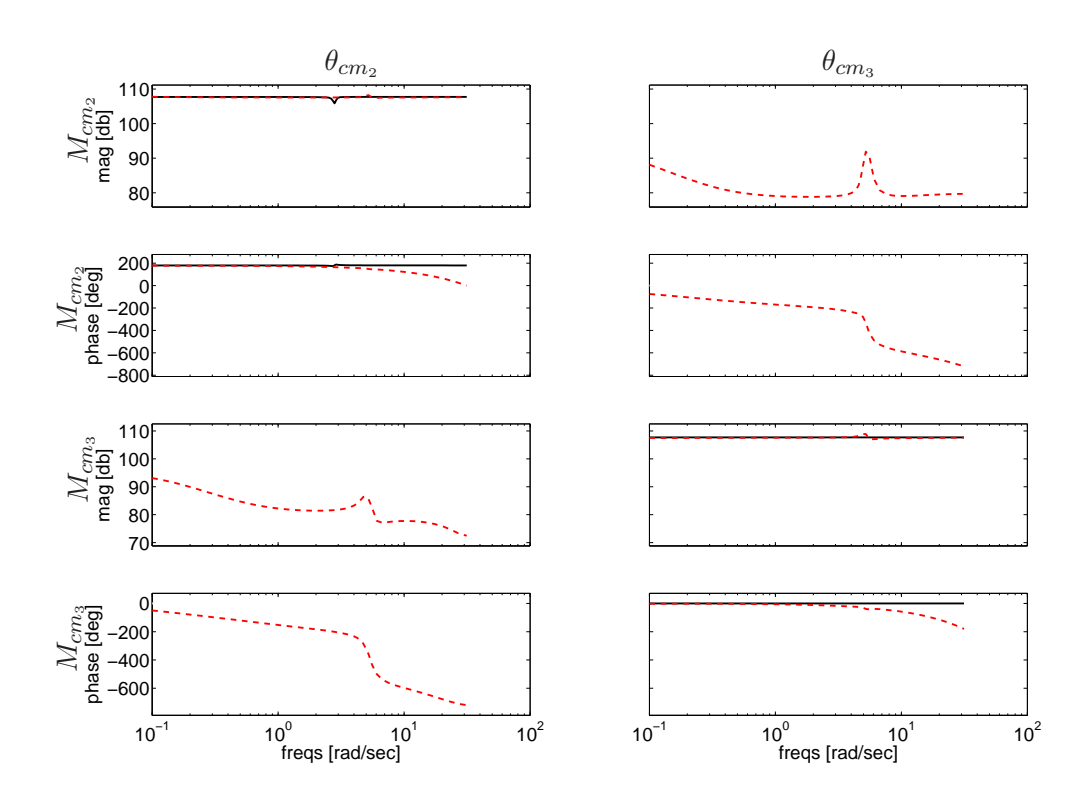


Figure 118 Bode plots of the identified transfer functions $T_{M_i\theta_j}^{cl}$, i,j=2,3, when twice more excitation is used. Both the true (black solid curves) and the identified (red dashed curves) models are shown.

Of course, one might also choose to estimate the channels $T^{cl}_{M_2\theta_2}$ and $T^{cl}_{M_3\theta_3}$ separately by means of two SISO identifications, one with the data $\{u=\theta_{cm_2},y=M_{cm_2}\}$ and another with $\{u=\theta_{cm_3},y=M_{cm_3}\}$. In this way one disregards the coupling of the tilt and yaw-wise dynamics.

Although in the simulation model, used in this section, there is no coupling anyway, this is not the case in practice. As can be observed by comparison of Figure 119 with the diagonal plots on Figure 116, separate identification of the tilt and yaw channels also results in some, though minor, improvement of the identified channels $T_{M_3\theta_3}^{cl}$ and $T_{M_3\theta_3}^{cl}$.

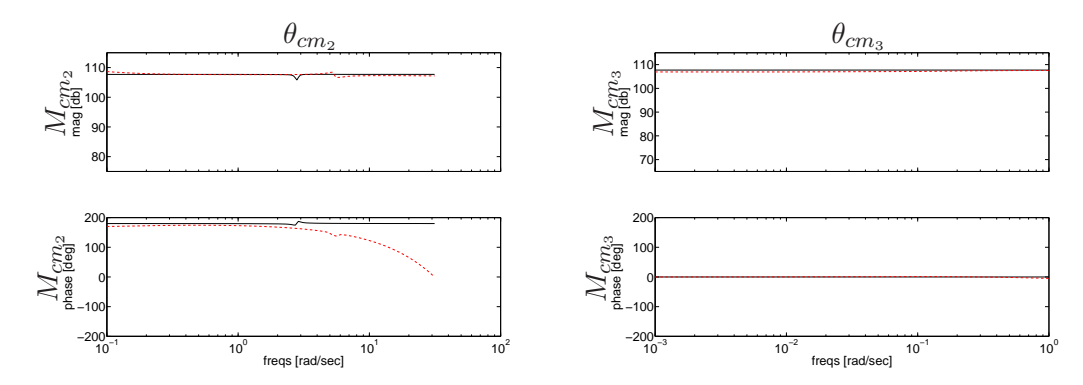


Figure 119 Bode plots of the separately identified transfer functions $T^{cl}_{M_2\theta_2}$ and $T^{cl}_{M_3\theta_3}$. Both the true (black solid curves) and the identified (red dashed curves) models are shown.

15.3.2 Individual pitch identification in closed-loop setting

In this subsection, the most involved problem is discussed, i.e. the problem of identification of the whole transfer matrix T^{+trq} , defined in equation (225). The identification setup is depicted on Figure 120, which is clearly a closed-loop identification problem. In this case, the dynamics of the (linearized) system is governed by the following equation

$$\begin{bmatrix} \Omega_g \\ M_{cm_2} \\ M_{cm_3} \end{bmatrix} = \begin{bmatrix} T_{\Omega\theta_1}^{+trq} & T_{\Omega\theta_2}^{+trq} & T_{\Omega\theta_3}^{+trq} \\ T_{M_2\theta_1}^{+trq} & T_{M_2\theta_2}^{+trq} & T_{M_2\theta_3}^{+trq} \\ T_{M_3\theta_1}^{+trq} & T_{M_3\theta_2}^{+trq} & T_{M_3\theta_3}^{+trq} \end{bmatrix} \begin{bmatrix} \theta_{cm_1} \\ \theta_{cm_2} \\ \theta_{cm_3} \end{bmatrix} + \begin{bmatrix} T_{\Omega u_1}^{+trq} & T_{\Omega u_2}^{+trq} & T_{\Omega u_3}^{+trq} \\ T_{M_2u_1}^{+trq} & T_{M_2u_2}^{+trq} & T_{M_2u_3}^{+trq} \\ T_{M_3u_1}^{+trq} & T_{M_3u_2}^{+trq} & T_{M_3u_3}^{+trq} \end{bmatrix} \begin{bmatrix} u_{cm_1} \\ u_{cm_2} \\ u_{cm_3} \end{bmatrix}.$$

Hence, the simplest way to address this MIMO problem is to put it into the general framework of the CL-N4SID algorithm with

$$u \equiv \begin{bmatrix} \theta_{cm_1} \\ \theta_{cm_2} \\ \theta_{cm_3} \end{bmatrix}, \ y \equiv \begin{bmatrix} \Omega_g \\ M_{cm_2} \\ M_{cm_3} \end{bmatrix}, \ \text{and} \ K = \begin{bmatrix} C_\theta \\ & 0 \\ & & 0 \end{bmatrix},$$

which would only require sufficient excitation of the three input signals θ_{cm_i} , i=1,2,3. Although such an approach indeed produces reasonable estimates of the diagonal terms of the transfer matrix $T^{+trq}(z)$, the cross-couplings between the speed regulation, tilt-wise and yaw-wise loops are much more difficult to estimate. To see that, consider for instance the generator speed which in the present simulation model is only affected by θ_{cm_1} , θ_{cm_2} , u_{cm_1} and u_{cm_2} . Figure 121 (left) shows the magnitude plots of the transfer functions $T_{\Omega\theta_1}^{+trq}$ (black solid curve), $T_{\Omega\theta_2}^{+trq}$ (red dashed curve), $T_{\Omega v_1}^{+trq}$ (blue dotted curve). Clearly, the transfer from the tilt-wise pitch θ_{cm_2} to the generator speed Ω_g is almost negligible as compared to the transfers from the collective pitch θ_{cm_1} and the collective effective wind speed u_{cm_1} to Ω_g , while at the same time the spectrum of θ_{cm_2} is comparable (and even smaller at low frequencies) to the spectra of θ_{cm_1} and u_{cm_1} . Hence, especially the lower frequency contents of θ_{cm_2} have a negligible effect on the generator speed, which makes this transfer function extremely difficult to identify. Notice that at the (lightly damped) eigenfrequencies $T_{\Omega\theta_2}^{+trq}$ the difference is much smaller, which should facilitate

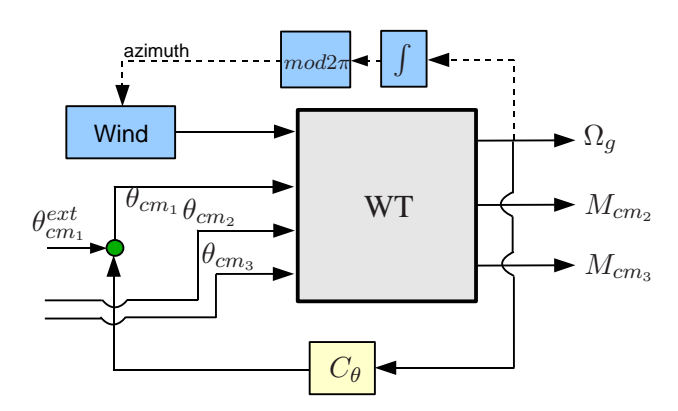


Figure 120 Closed-loop setting for individual pitch system identification

the identification (at those frequencies) as later on will be confirmed by the results.

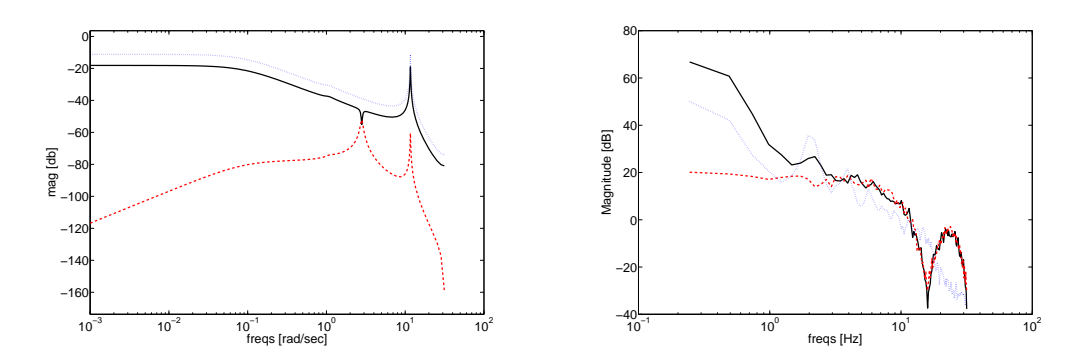
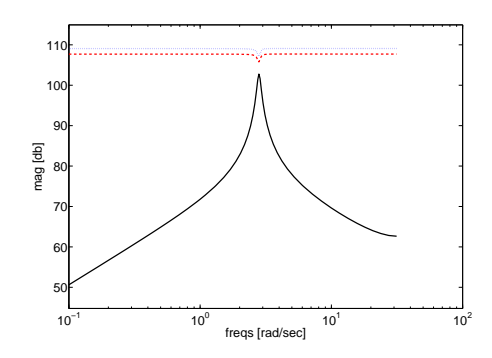


Figure 121 (left) magnitude plots of the transfer functions $T_{\Omega\theta_1}^{+trq}$ (black solid), $T_{\Omega\theta_2}^{+trq}$ (red dashed), $T_{\Omega v_1}^{+trq}$ (blue dotted); (right) spectra $\Phi_{\theta_{cm_1}}$ (black solid), $\Phi_{\theta_{cm_2}}$ (red dashed), $\Phi_{u_{cm_1}}$ (blue dotted).

Similar conclusions can be drawn regarding the cross-coupling of the tilt-wise moment M_{cm_2} with the inputs θ_{cm_1} and u_{cm_2} , for instance. As becomes obvious from Figure 122, $T_{M_2\theta_1}^{+trq}$ is negligible with respect to $T_{M_2v_2}^{+trq}$, which makes it very difficult to identify. One way to overcome this bad identifiability is to significantly increase the energy of the pitch signals θ_{cm_1} and θ_{cm_2} , which is clearly not a practical approach as it would require very large excursions of the pitch angles. Another possibility is to measure additional signals, e.g. the velocity of the fore-aft tower vibrations \dot{x}_{nod} . This output is much more sensitive to variations in the pitch signals (see Figure 123), which makes the identification of the transfer functions from the (measured) inputs to this output easier. Then, by assuming that the tilt and yaw-wise moments M_{cm_2} and M_{cm_3} are a linear combination of the signals \dot{x}_{nod} , θ_{cm_2} and θ_{cm_3} (and, of course, the wind signals u_{cm_2} and u_{cm_3}), as is the case with the model presented in Section 15.1, one can write

$$\begin{array}{lcl} M_{cm_2}(k) & = & c_{11}\dot{x}_{nod}(k) + c_{12}\theta_{cm_2}(k) + c_{13}\theta_{cm_3}(k) + d_1u_{cm_2}(k), \\ M_{cm_3}(k) & = & c_{21}\dot{x}_{nod}(k) + c_{22}\theta_{cm_2}(k) + c_{23}\theta_{cm_3}(k) + d_2u_{cm_3}(k). \end{array}$$

which allows a very simple estimation of the unknown parameters c_{ij} whenever the above equations are assumed to be static (the dynamic case will also be considered below). In the static case the above equations can be written for all data points k = 1, 2, ..., N, and the resulting system



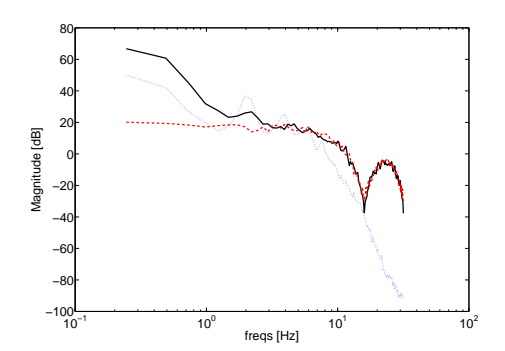


Figure 122 (left) magnitude plots of the transfer functions $T_{M_2\theta_1}^{+trq}$ (black solid), $T_{M_2\theta_2}^{+trq}$ (red dashed), $T_{M_2v_2}^{+trq}$ (blue dotted); (right) spectra $\Phi_{\theta_{cm_1}}$ (black solid), $\Phi_{\theta_{cm_2}}$ (red dashed), $\Phi_{u_{cm_2}}$ (blue dotted).

of linear equations can be solved in a least squares sense as follows

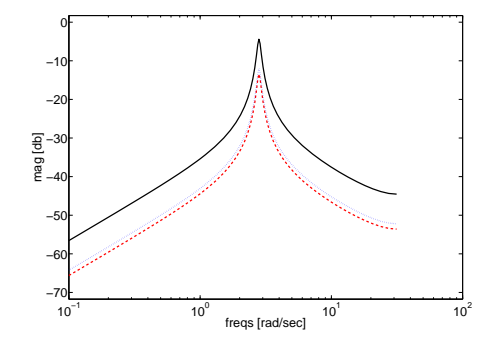
$$\begin{bmatrix} \hat{c}_{11} & \hat{c}_{12} & \hat{c}_{13} \\ \hat{c}_{21} & \hat{c}_{22} & \hat{c}_{23} \end{bmatrix}^{T} = \begin{bmatrix} \dot{x}_{nod}(1) & \theta_{cm_{2}}(1) & \theta_{cm_{3}}(1) \\ \dot{x}_{nod}(2) & \theta_{cm_{2}}(2) & \theta_{cm_{3}}(2) \\ \vdots & \vdots & \vdots \\ \dot{x}_{nod}(N) & \theta_{cm_{2}}(N) & \theta_{cm_{3}}(N) \end{bmatrix}^{\dagger} \begin{bmatrix} M_{cm_{2}}(1) & M_{cm_{3}}(1) \\ M_{cm_{2}}(2) & M_{cm_{3}}(2) \\ \vdots & \vdots \\ M_{cm_{2}}(N) & M_{cm_{3}}(N) \end{bmatrix}, (241)$$

where the symbol † denotes pseudo-inverse.

Suppose then that the following channels are first identified

$$\begin{bmatrix} \Omega_g \\ \dot{x}_{nod} \end{bmatrix} = \begin{bmatrix} \hat{T}^{+trq}_{\Omega\theta_1} & \hat{T}^{+trq}_{\Omega\theta_2} & \hat{T}^{+trq}_{\Omega\theta_3} \\ \hat{T}^{+trq}_{\dot{x}_{nod}\theta_1} & \hat{T}^{+trq}_{\dot{x}_{nod}\theta_2} & \hat{T}^{+trq}_{\dot{x}_{nod}\theta_3} \end{bmatrix} \begin{bmatrix} \theta_{cm_1} \\ \theta_{cm_2} \\ \theta_{cm_3} \end{bmatrix} + \begin{bmatrix} \star & \star \\ \star & \star \end{bmatrix} \begin{bmatrix} u_{cm_2} \\ u_{cm_3} \end{bmatrix}$$

by using CL-N4SID algorithm with the data $u = [\theta_{cm_1}, \theta_{cm_2}, \theta_{cm_3}], y = [\Omega_g, \dot{x}_{nod}],$ and $K = C_\theta \oplus 0_{2 \times 1}$.



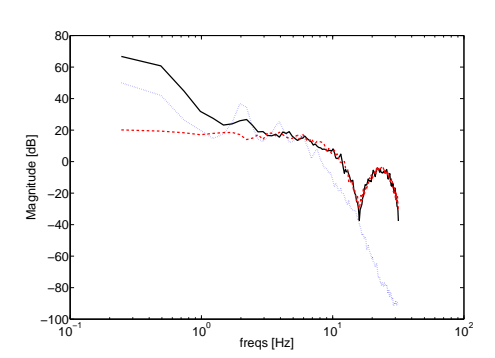


Figure 123 (left) magnitude plots of the transfer functions $T^{+trq}_{\dot{x}_{nod}\theta_1}$ (black solid), $T^{+trq}_{\dot{x}_{nod}\theta_2}$ (red dashed), $T^{+trq}_{\dot{x}_{nod}v_2}$ (blue dotted); (right) spectra $\Phi_{\theta_{cm_1}}$ (black solid), $\Phi_{\theta_{cm_2}}$ (red dashed), $\Phi_{u_{cm_2}}$ (blue dotted).

Then,

$$\hat{T}^{+trq} = \begin{bmatrix} 1 & 0 & 0 & 0 \\ & \hat{c}_{11} & \hat{c}_{12} & \hat{c}_{13} \\ & \hat{c}_{21} & \hat{c}_{22} & \hat{c}_{23} \end{bmatrix} \begin{bmatrix} \hat{T}^{+trq}_{\Omega\theta_1} & \hat{T}^{+trq}_{\Omega\theta_2} & \hat{T}^{+trq}_{\Omega\theta_3} \\ \hat{T}^{+trq}_{\dot{x}_{nod}\theta_1} & \hat{T}^{+trq}_{\dot{x}_{nod}\theta_2} & \hat{T}^{+trq}_{\dot{x}_{nod}\theta_3} \\ 0 & 1 & 0 \\ 0 & 0 & 1 \end{bmatrix}.$$
(242)

Notice that the parameters c_{ij} do not need to be static, but can also be transfer functions in which case, instead of using equation (241), the CL-N4SID algorithm can be used on the data $u = [\dot{x}_{nod}, \theta_{cm_2}, \theta_{cm_3}], y = [M_{cm_2}, M_{cm_3}],$ and $K = 0_{3 \times 2}$.

Therefore, the transfer functions in the tilt-wise moment equation can be estimated by using the following procedure:

Given: measurements $\{\theta_{cm_1}, \theta_{cm_2}, \theta_{cm_3}, \Omega_g, \dot{x}_{nod}, M_{cm_2}, M_{cm_3}\}$ pitch controller C_{θ} Step 1. Run the CL-N4SID algorithm on the data $u = \begin{bmatrix} \theta_{cm_1} \\ \theta_{cm_2} \\ \theta_{cm_3} \end{bmatrix}, \ y = \begin{bmatrix} \Omega_g \\ \dot{x}_{nod} \end{bmatrix}, \ K = \begin{bmatrix} C_{\theta} \\ 0_{2\times 1} \end{bmatrix}, \text{ obtaining the transfer functions}$ $T_{\Omega\theta_i}^{+trq} \text{ and } T_{\dot{x}_{nod}\theta_i}^{+trq}, \ i = 1, 2.$ Step 2. Compute the parameters c_{ij} either as static using equation (241), or as transfer functions using the CL-N4SID algorithm with $u = \begin{bmatrix} \dot{x}_{nod} \\ \theta_{cm_2} \\ \theta_{cm_3} \end{bmatrix}, \ y = \begin{bmatrix} M_{cm_2} \\ M_{cm_3} \end{bmatrix}, \ K = 0_{3\times 2}.$ Step 3. Compute the transfer matrix \hat{T}^{+trq} from equation (242).

Running this algorithm on simulation data, obtained with the linearized model, described in Section 15.1, and using three independent PRBS signals for $\theta_{cm_1}^{ext}$, θ_{cm_2} and θ_{cm_3} , again bounded between (-1.5) and (1.5) degrees as before. The results from the first step are presented in Figure 124. Notice that all transfers, but $T_{\Omega\theta_2}^{+trq}$, are rather accurately estimated. $T_{\Omega\theta_2}^{+trq}$ remains unidentifiable for the reason explained above. Notice though that, as reasoned earlier in this subsection, the two (lightly damped) eigenfrequencies of $T_{\Omega\theta_2}^{+trq}$ are indeed estimated accurately.

In Step 2 of the algorithm one can either choose for the static, or the dynamic approach for estimating the c_{ij} 's. Using the static approach in Step 2, the result of Step 3 is plotted in Figures 125 and 126. The identified transfer functions in Figure 126 suggest negligible coupling between the tilt and yaw-wise moments.

When the dynamic approach is used in Step 2 for estimating the c_{ij} 's, the result of Step 3 is plotted in Figures 127 and 128. Comparison of Figure 128 to the open-loop results on Figure 116 one sees that there is very little difference between the open-loop and closed-loop behavior.

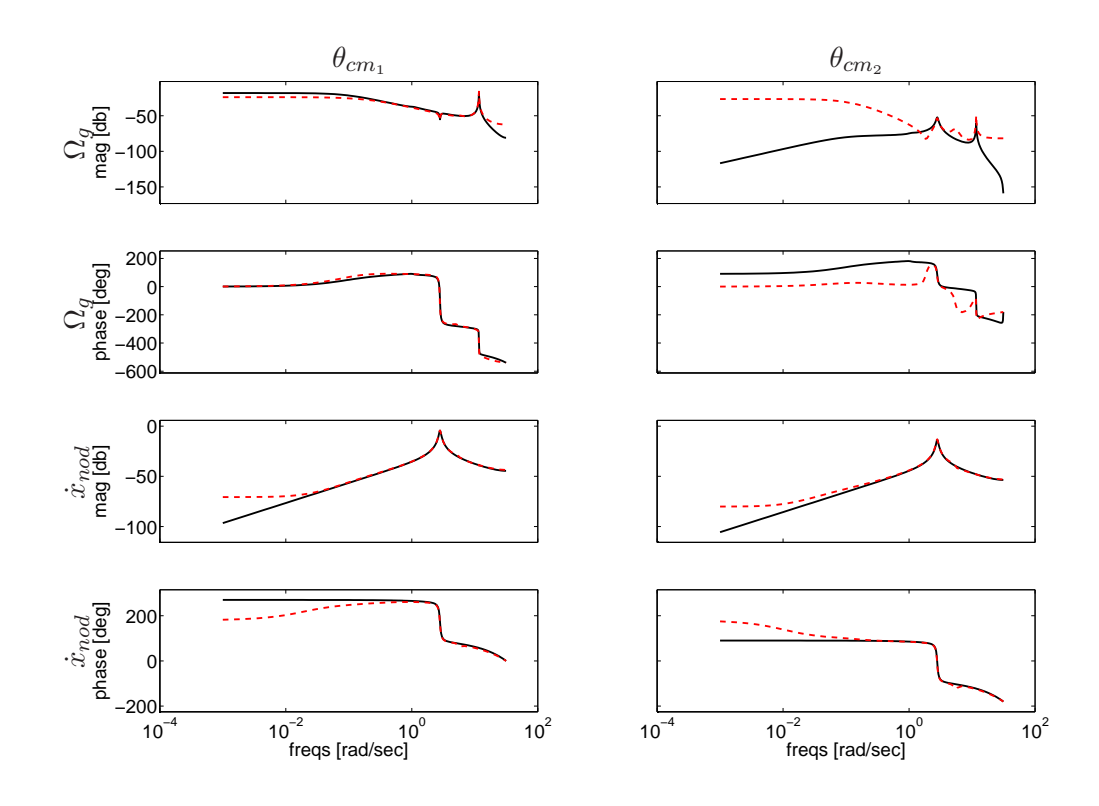


Figure 124 Bode plots of the transfer functions $T_{\Omega\theta_1}^{+trq}$ (top left), $T_{\Omega\theta_2}^{+trq}$ (top right), $T_{\dot{x}_{nod}\theta_1}^{+trq}$ (bottom left) and $T_{\dot{x}_{nod}\theta_2}^{+trq}$ (bottom right). Both real (black solid curves) and estimated (red dashed curves) transfers are plotted.

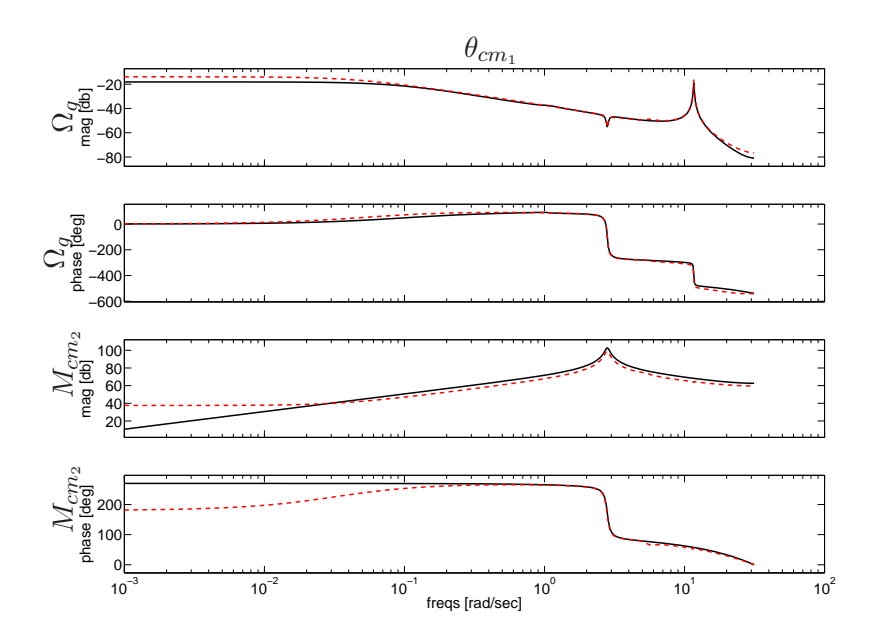


Figure 125 Bode plots of the transfer functions $T_{\Omega\theta_1}^{+trq}$ (top), $T_{M_2\theta_1}^{+trq}$ (bottom), based on static assumption of the transfer $[\dot{x}_{nod},\theta_{cm_2},\theta_{cm_3}] \rightarrow [M_{cm_2},M_{cm_3}]$. Both real (black solid curves) and estimated (red dashed curves) transfers are plotted.

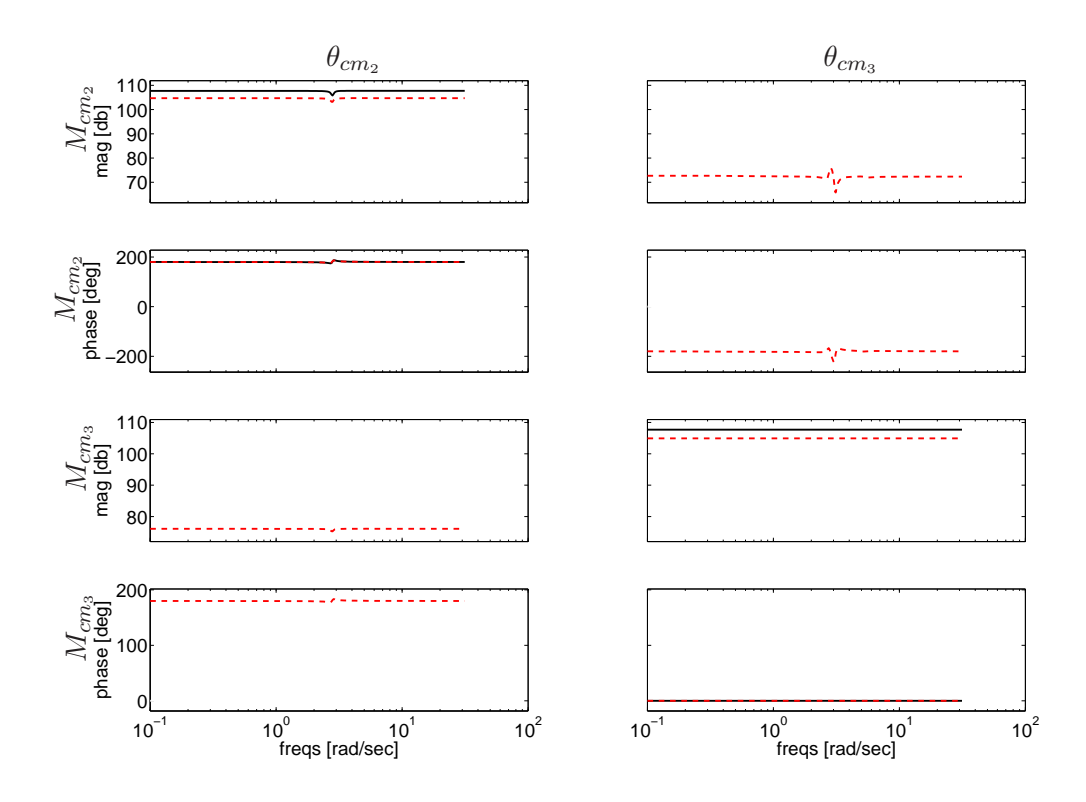


Figure 126 Bode plots of the transfer functions $T_{M_2\theta_2}^{+trq}$ (top left), $T_{M_2\theta_3}^{+trq}$ (top right), $T_{M_3\theta_2}^{+trq}$ (bottom left), $T_{M_3\theta_3}^{+trq}$ (bottom right), based on static assumption of the transfer $[\dot{x}_{nod},\theta_{cm_2},\theta_{cm_3}] \rightarrow [M_{cm_2},M_{cm_3}]$. Both real (black solid curves) and estimated (red dashed curves) transfers are plotted.

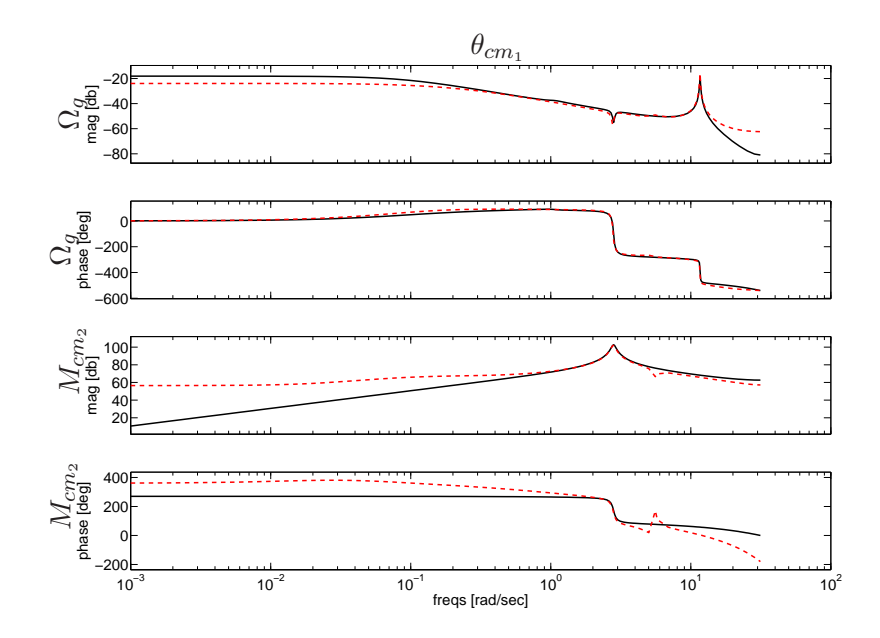


Figure 127 Bode plots of the transfer functions $T_{\Omega\theta_1}^{+trq}$ (top), $T_{M_2\theta_1}^{+trq}$ (bottom), based on dynamic transfer $[\dot{x}_{nod}, \theta_{cm_2}, \theta_{cm_3}] \rightarrow [M_{cm_2}, M_{cm_3}]$. Both real (black solid curves) and estimated (red dashed curves) transfers are plotted.

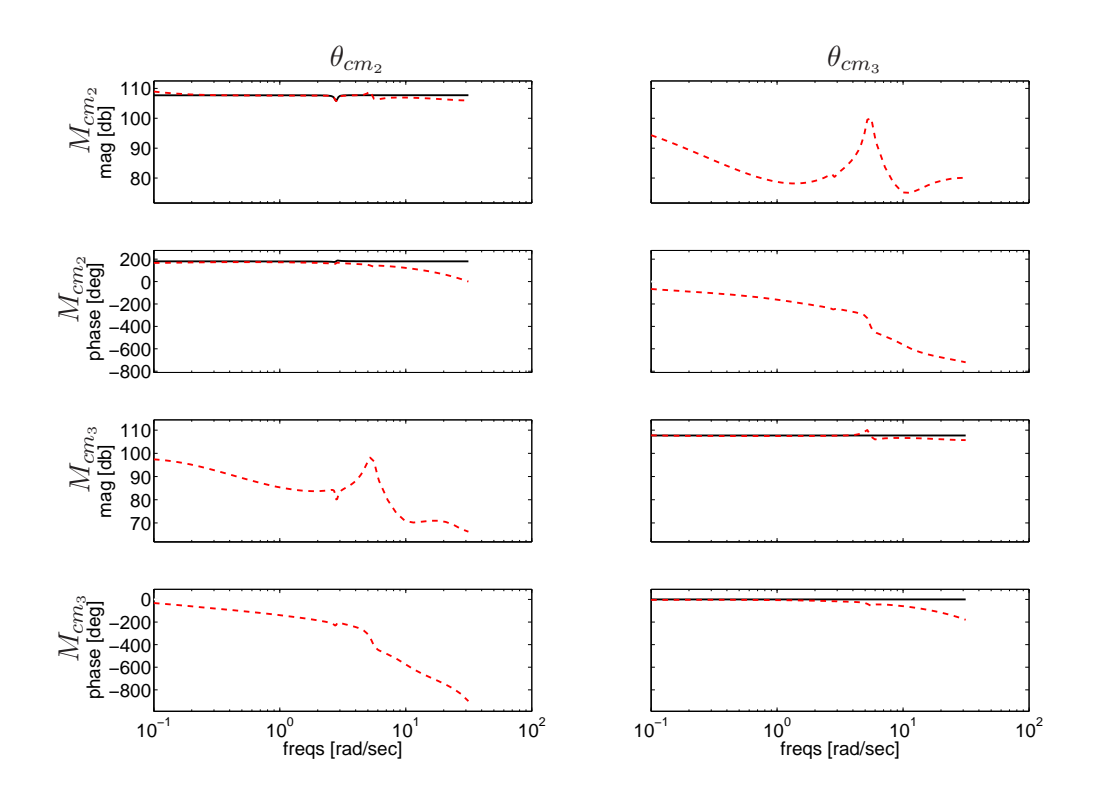


Figure 128 Bode plots of the transfer functions $T_{M_2\theta_2}^{+trq}$ (top left), $T_{M_2\theta_3}^{+trq}$ (top right), $T_{M_3\theta_2}^{+trq}$ (bottom left), $T_{M_3\theta_3}^{+trq}$ (bottom right), based on dynamic transfer $[\dot{x}_{nod}, \theta_{cm_2}, \theta_{cm_3}] \rightarrow [M_{cm_2}, M_{cm_3}]$. Both real (black solid curves) and estimated (red dashed curves) transfers are plotted.

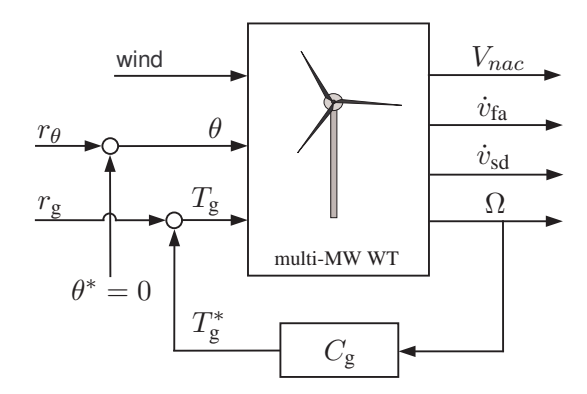


Figure 129 Measurement setup for system identification

16 Experimental results

Summary

This section summarizes the results from applying closed-loop identification methods, developed in Section 15, on field data. The data is collected by performing experiments on an ALSTOM Wind Eco100 prototype wind turbine. The measurement campaign is performed at below rated wind speeds between 3 and 8 m/s (at nacelle) by adding pseudo-random binary excitation to both the control signals pitch angle reference and generator torque reference. The excitation signals have been carefully designed to avoid the induction of undesired extra loads on the tower and rotor. Identification methods are applied for estimating the eigenfrequency and damping rate of the first fore-aft and sidewards tower modes and the first drive train mode. Due to the lack of information about the controller and the exact excitation used (only the excited pitch angle and generator torque are given), the following three closed-loop identification methods have been used: Direct, SSARX and PARSIM methods. Model validation results indicate excellent model accuracy.

16.1 The measurement campaign

16.1.1 The raw data

This section presents the results from applying closed-loop system identification on measurement data from a ALSTOM Wind Eco100 wind turbine. The purpose of the identification is to estimate the frequency and damping of the first tower fore-aft and side-to-side, and the first drive-train modes. To this end, the control inputs pitch angle reference and generator torque reference have been simultaneously excited with special, mutually uncorrelated, filtered pseudo-random binary test signals. The input/output signals, that have been measured, are summarized in Table 13 (see also Figure 129).

Notice that the excitation signals r_{θ} and r_{g} are not given. Also, no controller knowledge is used in the identification. The nacelle wind speed, V_{nac} , is not used in the identification.

Four measurement time series (Test1, Test2, Test3 and Test4) are available, each taken during partial load operation. In partial load the pitch controller is not active, the target pitch angle θ^* being equal zero (see Figure 129).

Signal name	Description	dim
Generator_speed	Generator speed Ω	rpm
Nacelle_x_acceleration	Tower top fore-aft acceleration $\dot{v}_{\rm fa}$	m/s ²
Nacelle_y_acceleration	Tower top sidewards acceleration $\dot{v}_{\rm sd}$	m/s ²
Blade_{1,2,3}_pitch_angle_ref	Excited blade pitch angle demand θ	deg
Generator_Torque_ref	Excited generator torque demand $T_{\rm g}$	Nm
Cup_anemometer_wind_speed	Wind speed at nacelle, V_{nac}	[m/s]

Table 13 Measured signals

Test case	begin time	end time	data length	$mean(V_{nac})$	purpose
Test1	70 s	1459 s	1389 s	4.5115 m/s	ident. @ 4.5 m/s
Test2	27 s	1157 s	1130 s	4.7783 m/s	valid. @ 4.5 m/s
Test3	95 s	1756 s	1651 s	6.1169 m/s	ident. @ 6.3 m/s
Test4	105 s	1088 s	983 s	6.5285 m/s	valid. @ 6.3 m/s

Table 14 Data concatenation for the four test cases

16.1.2 Data pre-processing

Due to the fact that each of these four measurement cases contain some irrelevant data from identification point of view (i.e. data without excitation on the inputs, data during turbine startup or shutdown), they have been concatenated as summarized in Table 14. Besides the concatenated data length, the Table also gives the mean nacelle wind speed and the purpose for which the test cases will be used, i.e. identification or validation. As can be seen from the table, the first two test cases (Test1 and Test2) correspond to mean nacelle wind speeds of about 4.5 m/s, so one test case (Test1) can be used for model identification and the other one (Test2) – for validation. Same holds for test cases Test3 and Test4, which correspond to a mean nacelle wind speed of about 6.3 m/s, so that Test3 will be used for identification at 6.3 m/s, while Test4 will serve as validation data at 6.3 m/s.

Another point that requires special attention is that the sampling rate is different per signal (Table 13), but is also time varying. For that reason, all signals have been first upsampled to 100 Hz by applying linear interpolation on the data. Subsequently, the data is downsampled for identification purposes, as explained later on.

For the estimation of the tower modes, the outputs tower top fore-aft $\dot{v}_{\rm fa}$ and sidewards $\dot{v}_{\rm sd}$ accelerations can be used. However, experience shows that working with the tower top velocities instead usually improves the quality of the identified models around the first tower modes. For that reason, the acceleration signals are integrated to velocities $v_{\rm nod}$ and $v_{\rm nay}$, which are used in the identification.

16.2 Identification and validation methods

16.2.1 Closed-loop identification methods

The following single-input-single-output models are identified:

- the open-loop transfer function from generator torque demand $T_{\rm g}$ to generator speed Ω , from which the first drive-train frequency and damping are extracted.
- the open-loop transfer function from the pitch angle demand θ to the tower top fore-aft velocity $v_{\rm nod}$, from which the first tower fore-aft mode is estimated.

• the open-loop transfer function from the generator torque demand $T_{\rm g}$ to the tower top sidewards velocity $v_{\rm nay}$, from which the first tower sidewards mode is identified.

As mentioned above, the velocities v_{nod} and v_{nay} are used in the identification, obtained by integration of the measured accelerations.

Due to the lack of information about the controller and the exact excitation signals used (only the excited pitch angle demand θ and generator torque demand $T_{\rm g}$ are given), the following three closed-loop identification methods, applicable to this situation, have been used:

- · Direct method,
- · SSARX method,
- PARSIM method.

For description of the methods, refer to Section 15.

16.2.2 Extraction of modal parameters

Given the identified models, the corresponding tower and drive-train frequency and damping are computed as follows. First, model reduction is performed (using the method of balanced truncation) to reduce the model order such that there is only one mode in a specified interval of interest where the frequency is expected to lie (this interval is chosen as [0.25,0.40] Hz for the tower, and [0.7,1] Hz for the drive train). The frequency and damping of this mode of the reduced system are then selected.

16.2.3 Model validation methods

The models, identified with these methods, are validated using the following validation criteria:

- VAF (variance-accounted-for): a model validation index often used with subspace identification methods. Given the measured output y and the output, predicted by the identified model \hat{y} , the VAF criterion is defied as VAF $(y,\hat{y}) = 1 \sigma_{\epsilon}/\sigma_{y}$, where σ_{y} is the variance of the signal y, and σ_{ϵ} the variance of the prediction error $\epsilon = y \hat{y}$. It is expressed in %. A VAF above the 95% is usually labelled as a very accurate model.
- PEC (prediction error cost): this is the value of the cost function that is used for minimization by the prediction error methods (such as the Direct method). It is defied as $PEC(\epsilon) = \frac{1}{N} \sum_{k=1}^{N} \frac{1}{2} \|\epsilon(k)\|_2^2$. The smaller the value, the better the model accuracy.
- R_{ϵ}^{ix} (auto-correlation index): when a consistent model estimate is made (including the disturbance model), the prediction error ϵ should be a white process so that its auto-correlation function $R_{\epsilon}(\tau)$ should be small for $\tau \neq 0$, where τ denotes the discrete time step. For a given confidence level α (e.g. $\alpha = 99\%$), a bound $R_{\epsilon}^{bnd}(\alpha)$ can be derived such that for an accurate model the inequality $|R_{\epsilon}(\tau)| \leq R_{\epsilon}^{bnd}(\alpha)$ should hold for all $\tau \geq 1$. The index R_{ϵ}^{ix} is then computed as the square sum of the distance between each value of the correlation function $|R_{\epsilon}(\tau)|$ and the bound $R_{\epsilon}^{bound}(\alpha)$, where only the values outside the bound are used.
- $R_{\epsilon u}^{\mathrm{ix}}$ (cross-correlation index): in the closed-loop situation the prediction error will be correlated with future values of the input, but should be uncorrelated with past inputs when the model is consistent. The cross-correlation function $R_{\epsilon u}(\tau)$ should then be limited in absolute value for $\tau \geq 1$. The index $R_{\epsilon u}^{\mathrm{ix}}$ is computed similarly to $R_{\epsilon}^{\mathrm{ix}}$.

Due to the lack knowledge of the excitation signals used, frequency domain validation using closed-loop spectral analysis is not possible here.

Besides these validation criteria, the identified models are compared to linearized models obtained with the software BLADED. Both Bode plots and modal parameters (eigenfrequency and damping ratio) are compared. However, due to the fact that BLADED models are only available at *undisturbed mean wind speeds* of 3, 5, 7, ..., 25 m/s, and the measured data is collected at *nacelle mean wind speeds* of about 4.5 and 6.3 m/s, it is decided to use in this comparison the BLADED models at undisturbed wind speed of 5 and 7 m/s. Notice also that, for evaluation of the accuracy of the identified models, comparison to BLADED should only be used with care because discrepancy between BLADED and identified models could just as well result from inaccurate BLADED modeling.

16.3 Tower first fore-aft mode identification

In order to estimate the tower first fore-aft frequency and damping, the transfer function from the blade pitch angle demand θ to the tower top fore-aft velocity $v_{\rm nod}$ is identified. To this end, as explained above already, the measured acceleration $\dot{v}_{\rm fa}$ is integrated to get the speed $v_{\rm nod}$. The methods Direct, SSARX and PARSIM are applied to the data $\{v_{\rm nod},\theta\}$ from test sets Test1 and Test3, as explained in Section 16.1.2. The validation results, based on sets Test2 and Test4, are summarized in Table 15. As can be seen from the table, the validation results indicate that all models have comparable, high accuracy. It should be pointed out here that the sample rate of the data has an effect on the validation results. The results, presented in this subsection are obtained by down-sampling the identification data to 4 Hz. Choosing higher or lower sample rate worsens the validation results a bit.

wind [m/s]				VAF	_
4.5			1.2×10^{-2}		
4.5	SSARX	2.744	1.344×10^{-2}	97.26	3.706×10^{-5}
4.5	PARSIM	2.517	6.346×10^{-2}	95.99	4.487×10^{-5}
6.3	Direct	0.7638	3.59×10^{-2}		
6.3	SSARX				
6.3	PARSIM	0.8528	4.164×10^{-2}	97.18	4.841×10^{-5}

Table 15 Validation results for identified models of the tower first fore-aft mode

The eigenfrequencies and logarithmic decrements, computed from the identified models, are compared in Table 16 to those obtained from the BLADED models linearized at 5 and 7 m/s.

wind [m/s]	Method	Normalized freq. [Hz]	Log. decr. [%]
5	BLADED	0.3133	27.45
4.5	Direct	0.3195	36.8
4.5	SSARX	0.3202	27.41
4.5	PARSIM	0.3204	21.38
7	BLADED	0.3161	33.49
6.3	Direct	0.3228	35.05
6.3	SSARX	0.3222	36.85
6.3	PARSIM	0.3278	29.55

Table 16 Frequency and logarithmic decrement of the tower first fore-aft mode computed from linearized BLADED model and identified models with methods Direct, SSARX and PARSIM

Figures 130-131 compare the Bode plots of the identified models with those of the BLADED models. Figure 130 represents the models identified at 4.5 m/s nacelle wind speed, while Figure

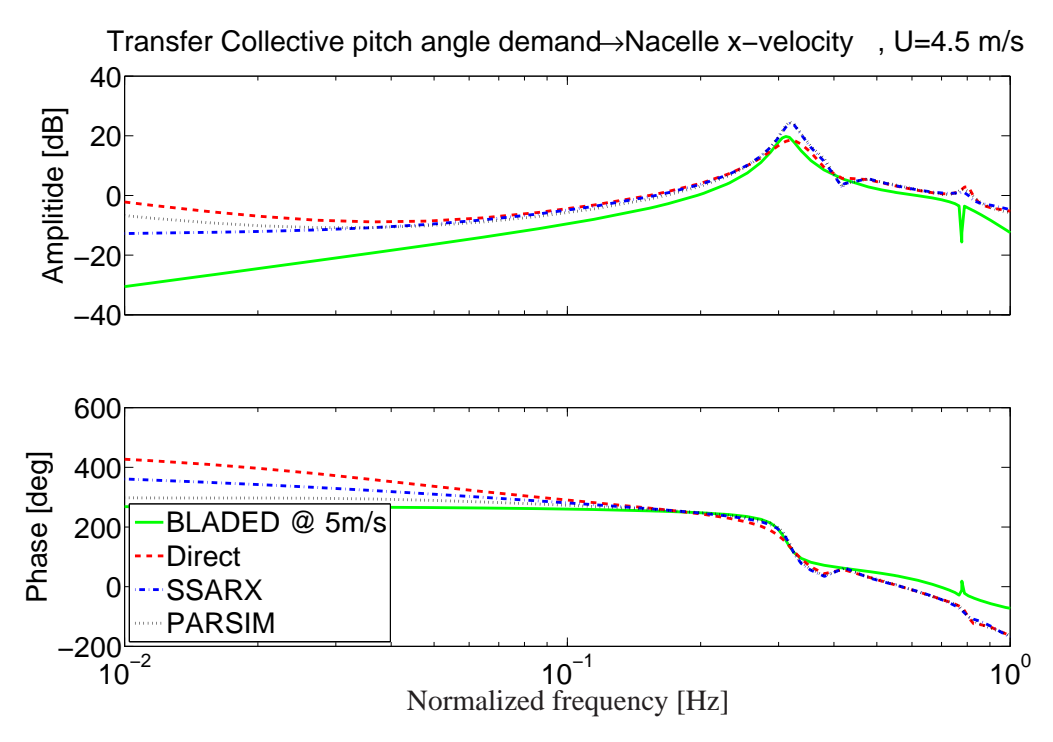


Figure 130 Bode plot of the identified tower fore-aft models from 4.5 m/s nacelle wind speed, compared to BLADED model at 5 m/s undisturbed mean wind speed

131 is related to the data at 6.3 m/s nacelle wind speed. It can be observed from the figures that the identified models are very well comparable to the BLADED models around the first tower frequency (in the intervals 0.1-1Hz).

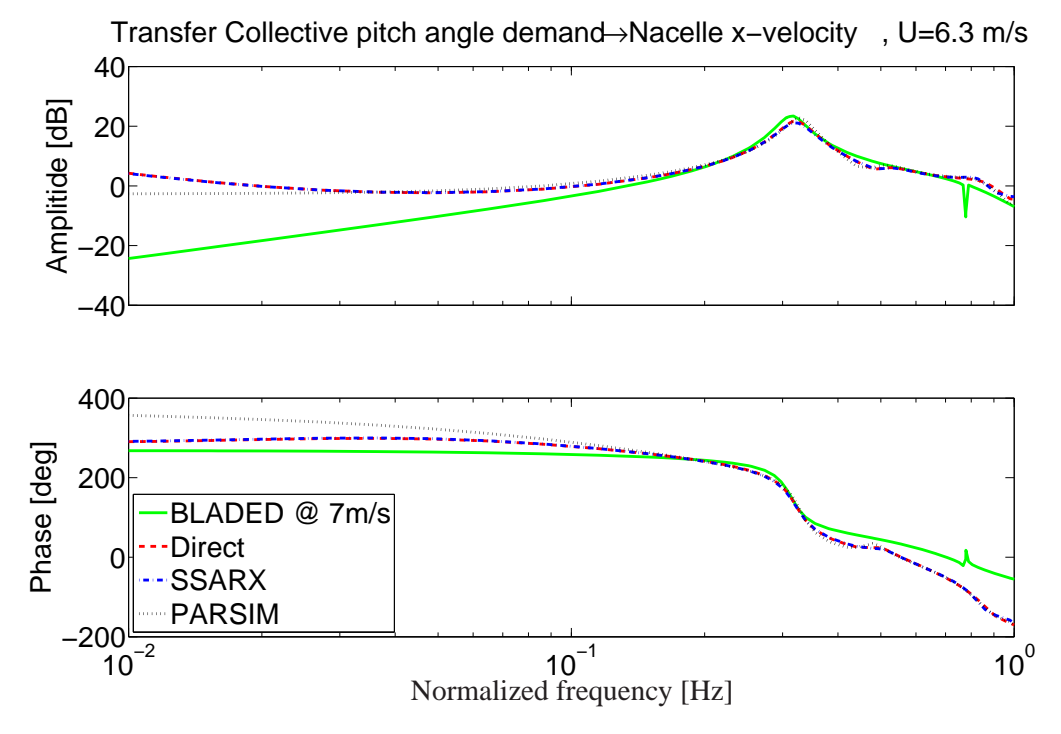


Figure 131 Bode plot of the identified tower fore-aft models from 6.3 m/s nacelle wind speed, compared to BLADED model at 7 m/s undisturbed mean wind speed

16.4 Tower first side-to-side mode identification

For estimating the tower first sidewards frequency and damping, the transfer function from the generator torque demand $T_{\rm g}$ to the tower top sidewards velocity $v_{\rm nay}$ is identified. Again, the measured acceleration $\dot{v}_{\rm sd}$ is integrated to get the speed $v_{\rm nay}$, and the methods Direct, SSARX and PARSIM are applied to the data $\{v_{\rm nay}, T_{\rm g}\}$ from test sets Test1 and Test3, resampled to 2 Hz. The validation results are given in Table 17. Similarly to the tower fore-aft mode identification results, presented in the previous subsection, the validation results indicate here also very high model accuracy.

The results, presented in this subsection are obtained by resampling the identification data to 2 Hz. Unlike the tower fore-aft case, the validation results here seem to be less sensitive to the sample rate of the identification data.

wind [m/s]	Method	$R_{\epsilon}^{\mathrm{ix}}$	$R_{\epsilon u}^{ m ix}$	VAF	PEC
4.5	Direct	1.118	8.9×10^{-3}	99.99	4.487×10^{-5}
4.5	SSARX	1.174	0	99.99	4.506×10^{-5}
4.5	PARSIM	1.467	0.136	99.99	5.03×10^{-5}
6.3	Direct	0.8991	0	99.99	5.514×10^{-5}
6.3	SSARX	0.8085	0	99.99	5.399×10^{-5}
6.3	PARSIM	0.9674	0.1165	99.99	6.557×10^{-5}

Table 17 Validation results for identified models of the tower first sidewards mode

As can be observed from Table 18, there is a very good correspondence between the eigenfrequencies and logarithmic decrements, computed from the identified models, and those obtained from the BLADED models. To a certain extend, this is confirmed in the frequency domain as seen from the Bode plots in Figures 132-133, although there is a good overlap only around the first tower sidewards frequency. The first drive-train frequency, on the other hand, is not present in the identified models. A possible reason for this is that this frequency not clearly present in the tower sidewards motion due to, for instance, an active drive-train damping mechanism in the controller.

wind [m/s]	Method	Normalized freq. [Hz]	Log. decr. [%]
5	BLADED	0.3115	5.426
4.5	Direct	0.3151	3.037
4.5	SSARX	0.3156	2.549
4.5	PARSIM	0.3147	4.763
7	BLADED	0.3115	5.556
6.3	Direct	0.3148	5.883
6.3	SSARX	0.3143	2.17
6.3	PARSIM	0.3153	3.861

Table 18 Frequency and logarithmic decrement of the tower first sidewards mode computed from linearized BLADED model and identified models with methods Direct, SSARX and PARSIM

16.5 First drive-train mode identification

The first drive-train frequency and damping are estimated from the identified transfer function from the generator torque demand $T_{\rm g}$ to the generator speed Ω . For this purpose, the methods Direct, SSARX and PARSIM are applied to the data $\{\Omega, \theta, T_{\rm g}\}$. Notice that although the channel $\theta \to \Omega$ is not necessary for estimation of the first drive-train mode, it is also identified together with the transfer function from $T_{\rm g}$ to Ω since the input θ also affects the generator speed Ω and is also excited. For identification, the test sets Test1 and Test3 are used, where the data is

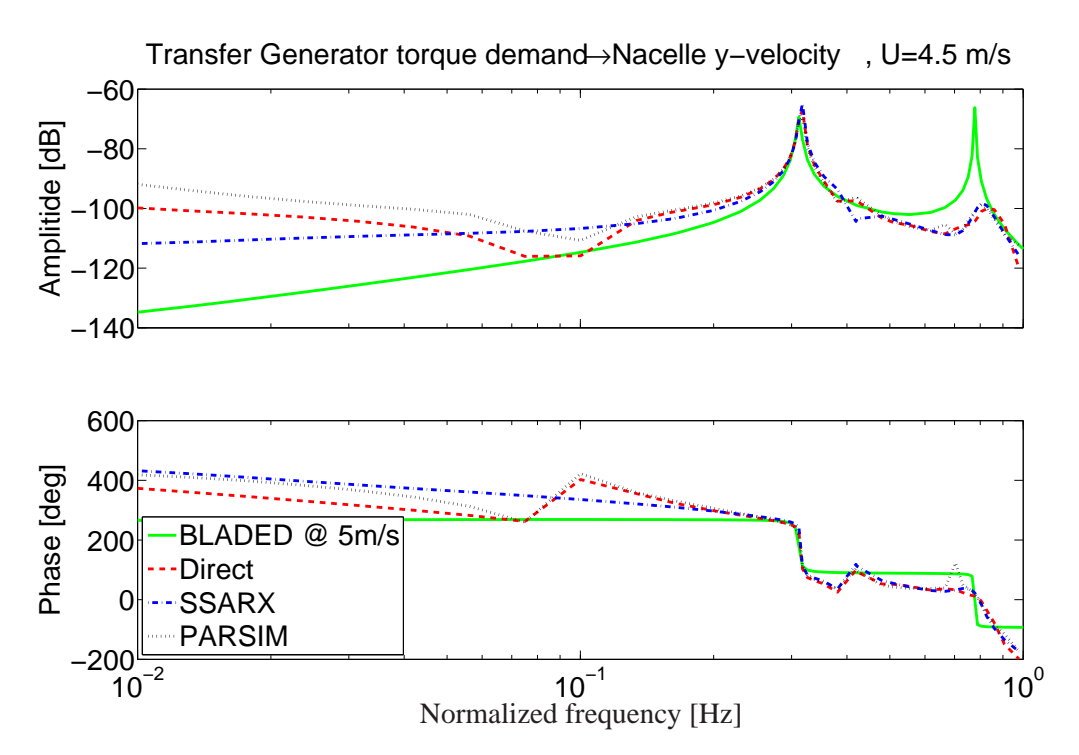


Figure 132 Bode plot of the identified tower sidewards models from 4.5 m/s nacelle wind speed, compared to BLADED model at 5 m/s undisturbed mean wind speed

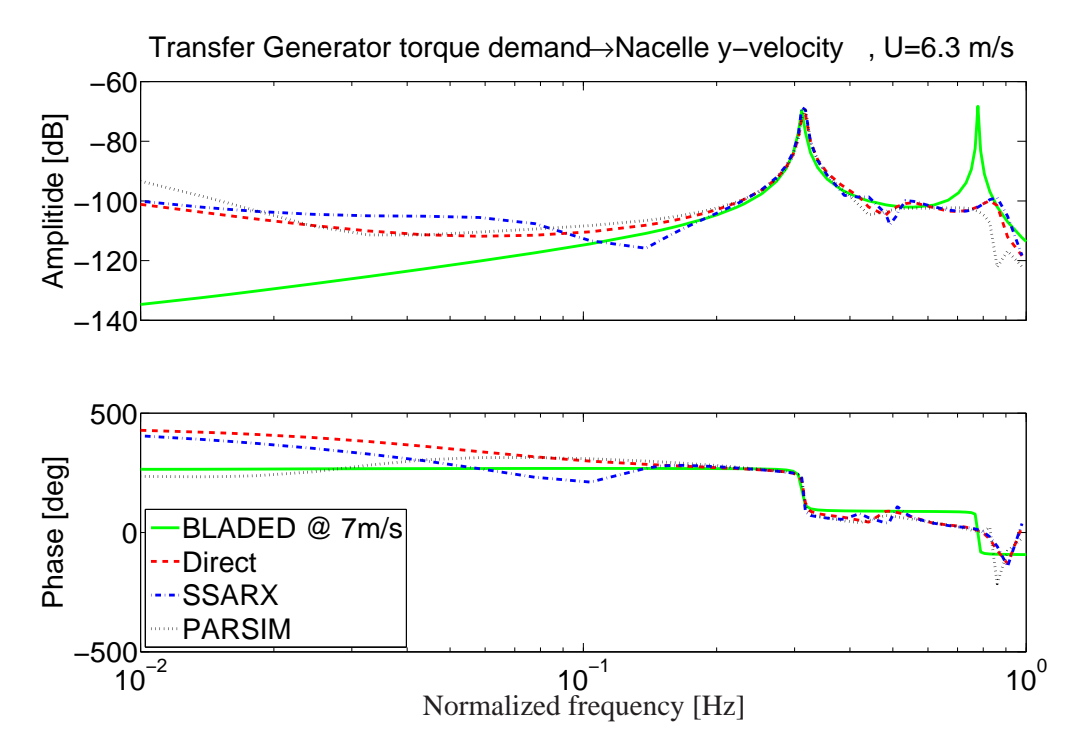


Figure 133 Bode plot of the identified tower sidewards models from 6.3 m/s nacelle wind speed, compared to BLADED model at 7 m/s undisturbed mean wind speed

resampled to 5 Hz. The validation results are given in Table 19. Again, the validation results indicate very high model accuracy. However, from Table 20 it becomes clear that a significant difference of about 10% is present between the identified drive-train frequency and the one obtained from the BLADED model. The excellent time-domain validation results in combination with reduced frequency domain accuracy implies that the drive-train frequency is not well present in the input-output data, as can happen due to the presense of a drive-train damping mechanism

in the controller.

wind [m/s]	Method	$R_{\epsilon}^{ ext{ix}}$	$R_{\epsilon u}^{ ext{ix}}$	VAF	PEC
4.5	Direct	0.0707	0.7321	99.98	6.797×10^{-3}
4.5	SSARX	0.0508	0.6704	99.98	6.731×10^{-3}
4.5	PARSIM	0.8471	0.856	99.96	1.004×10^{-2}
6.3	Direct	0.24	0.0996	100	5.97×10^{-3}
6.3	SSARX	0.181	0.2558	100	5.962×10^{-3}
6.3	PARSIM	0.13	0.4208	100	6.908×10^{-3}

Table 19 Validation results for identified models of the first drive-train mode

wind [m/s]	Method	Normalized freq. [Hz]	Log. decr. [%]
5	BLADED	0.7777	1.304
4.5	Direct	0.8773	14.12
4.5	SSARX	0.878	16.61
4.5	PARSIM	0.8261	6.877
7	BLADED	0.778	1.642
6.3	Direct	0.8496	1.499
6.3	SSARX	0.8534	1.822
6.3	PARSIM	0.8305	2.857

Table 20 Frequency and logarithmic decrement of the first drive-train mode computed from linearized BLADED model and identified models with methods Direct, SSARX and PARSIM

Figures 132-133 give Bode plots of the transfer functions $T_{\Omega T_{\rm g}}$, identified with methods Direct, SSARX and PARSIM, as compared to the one obtained from BLADED. As already mentioned, in both cases the identified drive-train frequency is about 10% higher than the one from BLADED. Comparing to BLADED, the PARSIM method should be labelled as best here, espessially for the test case at 4.5 m/s (Figure 132 and Table 20), where the other two methods have clearly more difficulty with proper estimation of the mode.

16.6 Conclusions and recommendations

Closed-loop system identification methods are applied to measurement data from a ALSTOM Wind Eco100 wind turbine. The measurement data is collected at below-rated wind speeds varying between 3 and 8 m/s, measured at nacelle. Filtered pseudo-random binary excitations are applied to both the pitch angle demand and the generator torque demand in order to make the identification of the transfer functions from these inputs to the outputs generator speed and tower top fore-aft and sidewards velocities possible. For evaluating the identified models, different time-domain validation criteria are used. The time-domain validation indexes indicate in all cases excellent model quality. Due to the lack of information about the excitation signals (only the excited inputs are given), no frequency-domain validation is possible by using closed-loop spectral analysis. However, frequency domain comparison is performed using BLADED models linearized at undisturbed mean wind speeds of 5 and 7 m/s. This comparison shows very good overlap around the first tower fore-aft and sidewards frequencies, but there is some discrepancy between the identified and the BLADED drive-train frequencies. This reduced frequency domain accuracy around the drive-train frequency, in combination with the excellent time-domain validation results, is a typical example of the effect of an active vibration damping loop on system identification. The drive-train damping loop in the torque controller suppresses vibrations around the first drive-train frequency, making it difficult for system identification to accurately identify the mode.

In order to improve the modeling around the drive-train frequency it is recommended to either

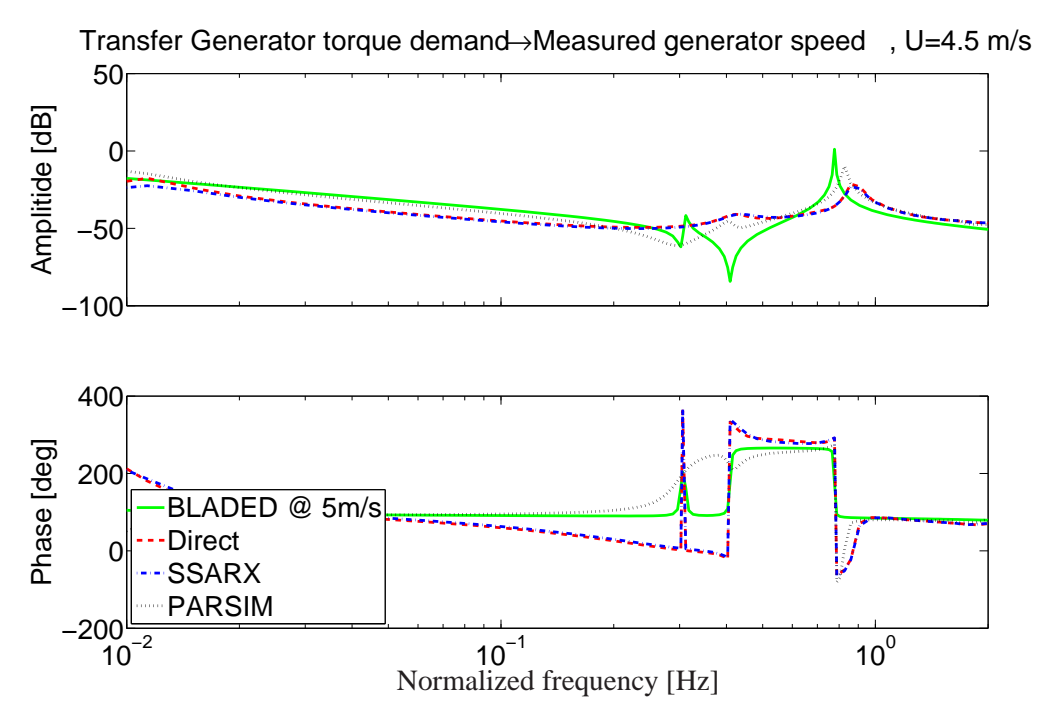


Figure 134 Bode plot of the identified drive-train models from 4.5 m/s nacelle wind speed, compared to BLADED model at 5 m/s undisturbed mean wind speed

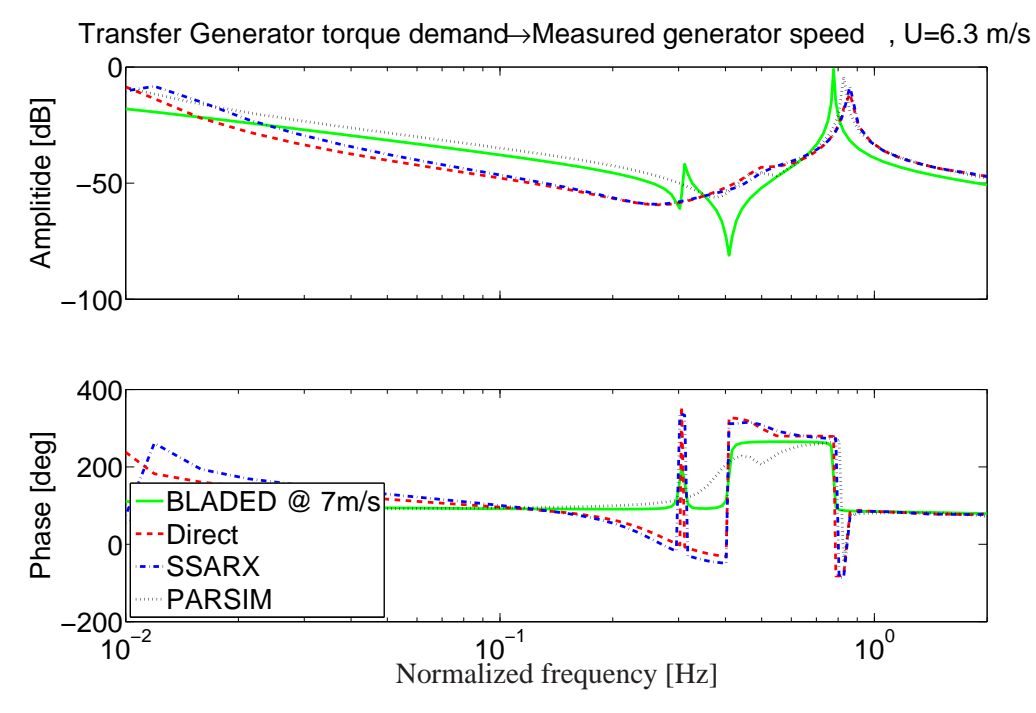


Figure 135 Bode plot of the identified drive-train models from 6.3 m/s nacelle wind speed, compared to BLADED model at 7 m/s undisturbed mean wind speed

increase the excitation around this frequency or to temporarily switch off the active damping loop during the identification experiment. It might also be beneficial to develop a "gray-box" identification algorithm that directly aims at estimating the parameters of a low order physical model of the relevant dynamics from input-output data collected under closed-loop.

Part VII

Integration of methods: Sustainable Control concept

Summary

Extreme environmental conditions, as well as system failure, are real-life phenomena. Especially offshore, extreme environmental conditions and system faults are to be dealt with in an effective way. Sustainable control (SusCon) is a concept for an integrated control platform. This platform accomplishes fault tolerant control in regular and extreme conditions during production operation and shutdown. It is built up of methods for the detection of extreme conditions and faults and from methods for operation and shut-down. These methods have been discussed in Parts II-V. In this section, the integration of the separate methods into the complete SusCon concept is considered.

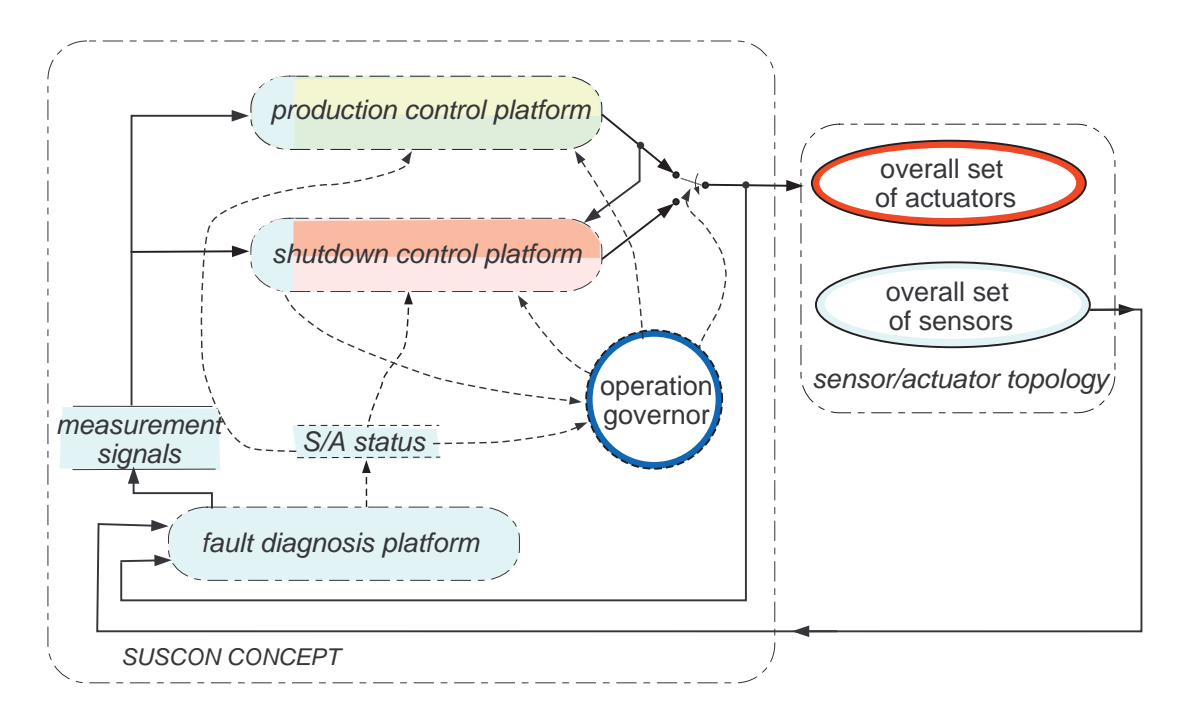


Figure 136 Functional layout SusCon concept

17 Introduction

The Sustainable control concept includes the development and integration of the following cornerstones that relate to wind turbine control in four different types of operating conditions:

- Optimized Feedback Control (OFC), for load reduction by advanced control methods during normal operating conditions (Part II),
- Fault Tolerant Control (FTC), for avoiding unnecessary standstill in cases of minor system failures by fault detection and controller reconfiguration (Part III),
- Extreme Event Control (EEC), for avoiding excessive loads and unnecessary shut-down under extreme conditions (Part IV),
- Optimal Shutdown Control (OSC), for avoiding excessive loads and serial damage after serious system failure or hyper-extreme conditions (Part V).

Figure 136 shows a functional layout of the SusCon concept. It includes platforms for production control, shutdown control and fault diagnosis. The dashed lines represent signals that govern the operation. The production and shutdown control platforms include monitoring and control methods; the fault diagnosis platform only monitoring methods. SusCon is achieved by synchronized alternate operation of the methods: a combination of active methods on the platform relates to one of the listed cornerstones.

It is clear that this approach basically differs from current isolated production and supervisory control.

The subsequent sections of this paper describe the different types of methods and the switching mechanisms, give a survey of conceived monitoring and control methods, address typicalities that relate to implementation, and show experimental and simulation results.

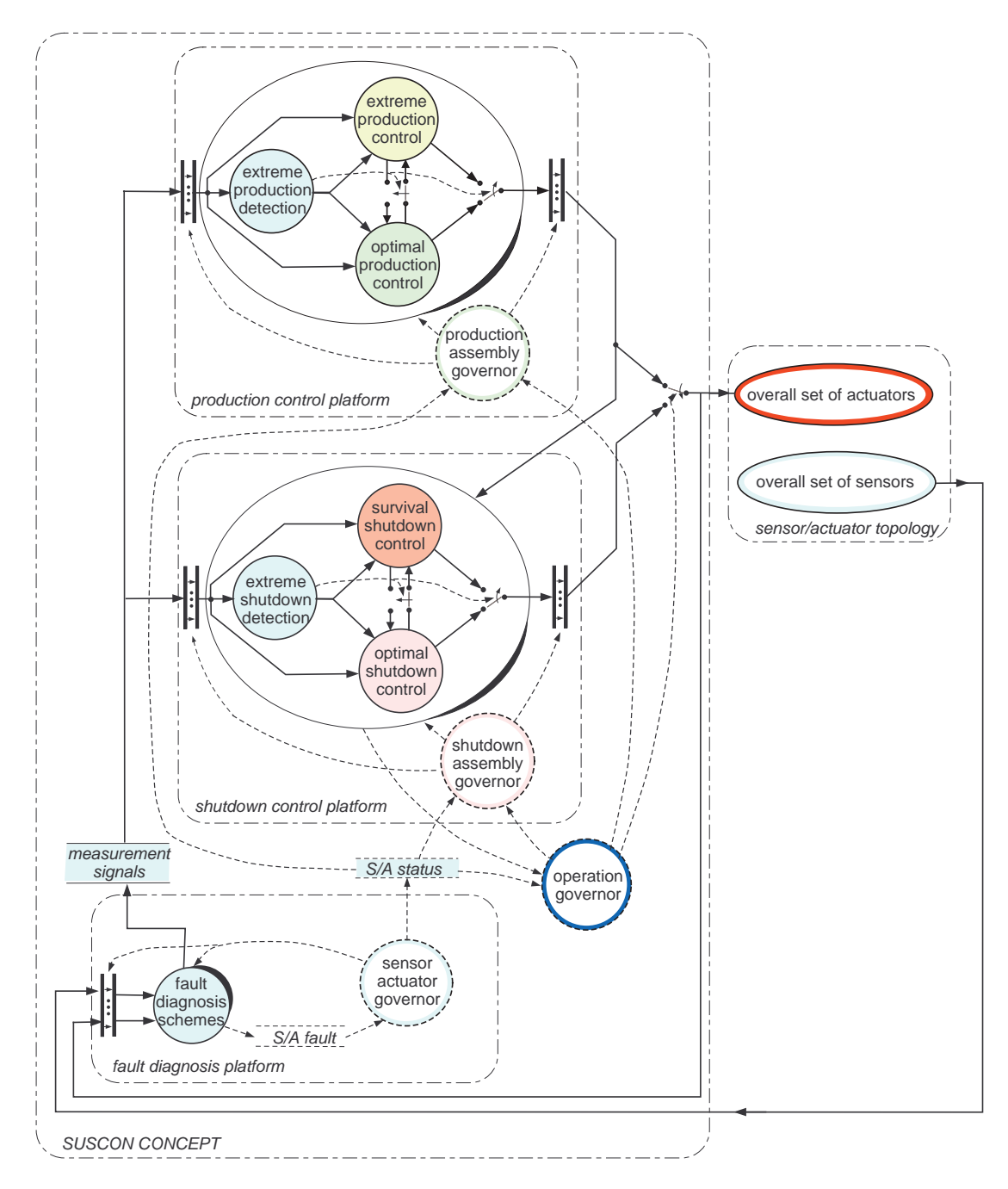


Figure 137 Detailed functional layout SusCon concept

18 Sustainable control

Figure 137 gives a more detailed view on the functional layout, in which a symbiosis of fault diagnosis, production control and shutdown control is pursued.

Assume that currently no severe failure has occurred and that no extreme condition applies that requires immediate shut-down (hyper extreme condition). The wind turbine will then run in production operation. The main arbiter, that is to say the *operation governor*, will retransmit the control signals from the production platform to the actuators. Further, the shutdown platform receives the current control signal values in order to tune its internal condition for smooth "take-over" when required.

All the time, the shutdown platform's unit for detection of hyper extreme conditions will be active.

Their detection is signaled to the operation governor. It will react by retransmitting the control signals from the shutdown platform instead of the production platform.

The subsequent subsections describe the internal working mechanism of the platforms for fault diagnosis and control. This includes the functionality of the methods that are part of the platforms. The working of the methods itself is explained in the next section.

18.1 Fault diagnosis platform

Sensor and actuator faults are identified with model-based fault detection and isolation (FDI) methods. The detection is based on the residues from Kalman filters. These filters are arranged such that the behavior of the residues in regular conditions can be distinguished from that in faulty conditions. The sensor/actuator governor translates a fault into the status of the sensor/actuator topology. This status is read out by the operation governor and the control platforms through the S/A-status flag. In case of a non-severe failure, the operation governor will take no action. However, the production assembly governor may reconfigure the active extreme detection method and or control methods as well as the retransmission of measurement signals.

A non-severe failure can be the drop-out of a redundant blade root moment sensor, or even the drop-out of a non-redundant blade root moment sensor. In the first case, only the retransmission of measurement signals is adapted; in the second case, the detection of extreme production conditions will no more be based on all blade root moments, and individual pitch control will be excluded from production control or based on other measurement signals.

Severe failures concern strongly deteriorated functioning of pitch and yaw actuators, grid drop-out and combinations of sensor faults. In that case, the operation governor will signal to the shutdown platform to take over the control. The shutdown assembly manager in turn will reconfigure the shutdown control methods for appropriate use of control signals.

18.2 Production control platform

The production assembly governor combines methods for detection of extreme events and production control as allowed by the current status of the sensor/actuator topology. Extreme events are detected from the outputs of Kalman filters that are arranged for this purpose.

Optimal production control includes collective pitch angle adjustment and generator torque setting. The control actions result from a trade-off between objectives for rotor speed regulation, optimal energy yield and damping of drive-train torsion and tower bending. Further, optimal production is pursued through cyclo-stochastic individual pitch control (IPC). This IPC is centered around one and two times the rotational frequency (1p, 2p). It reduces the loads on the blades around these frequencies as well as the loads on the nacelle and tower around 3p and in very low frequencies. In addition, very low-frequent IPC is added for the sake of aerodynamic rotor balancing. A prioritization algorithm divides available actuator capacity over collective and individual pitch control.

As long as the optimal production control unit applies, its internal condition is messaged to the unit for extreme production. The latter unit becomes active after the detection of an extreme event that still allows continuation of production operation. As from now, a completely different trade-off between control objectives will apply: extreme production control will focus on rotor speed limitation and reduction of extreme loads; energy yield and fatigue related damping are of minor importance. Further, the unit for extreme production control now messages its internal condition to the unit for optimal production control. This enables a smooth switch-back after the extreme conditions have ceased.

18.3 Shutdown control platform

The shutdown assembly governor combines methods for detection of hyper extreme events and shut down control as allowed by the current status of the sensor/actuator topology. Events that require shut down control are detected from gross values of direct measurement signals, the current status of sensors and actuators, and the residues of Kalman filters arranged for the detection of extreme (external) conditions.

Assume for instance that one actuator stucks while no other failure or extreme external conditions occurs. This is a severe failure that requires immediate turbine shut-down. Because of the remaining 'mild' conditions, the shutdown can be optimized despite of asymmetric rotor loading. The latter follows from the unbalanced aerodynamic pitch setting. The two valid pitch actuators and generator torque can be used such that smooth rotor deceleration is achieved while the effect on the tower by the asymmetric rotor loading is minimized. Even if also generator drop-out applies, this is still possible. For instance, non-linear model predictive control facilitates this.

Another severe failure could be 'free yawing' caused by free running yaw motor rotors. Under remaining mild conditions, this can also be processed through optimized turbine shut-down. Cyclic pitch angle adjusment allows for the generation of an aerodynamic yawing moment. An aerodynamic yaw servo system can be established on that principle. This allows for good yaw alignment in the first phase of turbine shutdown and steadily yawing out of the wind in the second phase.

During optimized tubine shutdown, the unit for survival shut-down will receive the belonging internal status. If for instance an extreme wind gust coincides with one stucking pitch actuator, it will be usually desired to shut-down the wind turbine as fast as possible. As from now, survival shut-down control will take-over optimal shut-down control. Again, the ceasing of the extreme condition could allow for optimized turbine shutdown. For this reason, the survival shutdown unit messages its condition to the optimal shutdown unit. Be aware that a 'moderate gust' from say 10 to 15 m/s may induce survival shutdown in case of large asymmetric rotor loading by actuator stuck.

Part VIII

Conclusions

To realize the ambitious goals, defined by the Dutch government, for the installation of 6000MW offshore wind energy by the year of 2020, it is inevitable that the price offshore of energy be significantly reduced. To this end, upscaling of the wind turbines to 10MW and more is required due to the high foundation and installation costs offshore. In addition, due to the bad accessibility offshore, the reliability should be strongly improved to achieve high enough availability. This means the the offshore wind energy generation should be able to keep on operating under most environmental conditions, and in spite of small defects. This project contributes significantly to achieving this goal by developing an innovative wind turbine control concept that integrates control, condition monitoring and supervisory control to enable, (a), significant extreme and fatigue loads reduction, and (b), adaptation of the operation to the changing conditions. This is realized by the development of an integrated approach for operating offshore wind turbines, referred to as "Sustainable Control". In this approach, the following four components can be distinguished, which will are made available in the form of methods:

- 1 Optimized Feedback Control (OFC), for reduction of the wind turbine costs and the limitations for upscaling by means of decreased wind turbine loads under normal operational conditions.
- 2 Fault Tolerant Control (FTC), for prevention of unnecessary standstill by means of an integration of self-adaptive controls and detection methods for component degradations.
- 3 Extreme Event Control (EEC), for reduction of turbine costs and increase of the certainty of electricity production by means of reduced turbine loads during extreme operating conditions,
- 4 Optimal Shutdown Control (OSC), for avoidance of accumulation of damage during shutdowns resulting from a serious defects by means of condition-specific shutdown control.

The core of this project consists of the technical development of above-mentioned four cornerstones of the control concept, and their validation based on PoP experiments. The results from the PoP experiments demonstrate that a reduction of fatigue loads on the blades of up to 17% can be realized with OFC, while the extreme loads in certain cases drop by as much as 50% with EEC and OSC.

The methods developed in this project, and the overall integrated control approach, "Sustainable Control", will be further developed after the termination of the project with the aim of creating a commercial product to be used to transfer knowledge to the industry. The focus lies on fine-tuning of the algorithms, software development and detailed prototype testing of a much larger duration than in this project. To this end, already before the actual termination of this project, two continuation projects have been defined within the "Far and Large Offshore Wind Innovation" programme (FLOW):

- "Control Design Tool Upgrade" (CDTup), number P201101-014-ECN: This project represents the first phase of a large-scale upgrade of the Control Design Tool (CDT) of ECN, a tool for the design of industrial wind turbine controllers. During this first phase, the algorithms OSC and EEC, as developed in the SusCon project, will be further improved and implemented into the CDT.
- "Improvement of advanced design tools", number P201203-006-ECN: In this continuation project, representing the second phase, the remaining SusCon algorithms (namely, OSC

and FTC) will be improved and added to the new tool, and the complete controller (incl. the whole SusCon concept) will be extensively tested on a 2-bladed prototype wind turbine of the Dutch wind turbine manufacturer 2-B Energy.

Furthermore, at the moment of writing of this report, it is being worked on a third related FLOW project with the wind turbine manufacturer XEMC-Darwind as partner. This project will aim at improvement of the new tool by means of verifying it on a 3-bladed wind turbine . The market introduction of the new control tool is expected in the year of 2013.

After that, the advantaged of "Sustainable Control" will be taken into consideration in the design of the new generation wind turbines, so that these are calculated for lower loads. This will firstly concern turbines of the current format, and after that much larger ones of up to the optimal for offshore wind energy generation size of 10 MW or larger.

References

- [1] Anderson, B. and J. Moore (1979): *Optimal Filtering*. Prentice-Hall, Englewood Cliffs, New Jersey, electrical engineering series edition.
- [2] Basseville, M. and V. Nikiforov (1993): Detection of Abrupt Changes Theory and Application. Prentice-Hall, Englewood Cliffs, N.J. URL http://www.irisa.fr/sisthem/kniga/.
- [3] Benasciutti, D. and R. Tovo (2005): Spectral methods for lifetime prediction under wide-band stationary random process. International Journal of Fatigue, 27.
- [4] Bianchi, F., H. De Battista and R. Mantz (2006): Wind Turbine Control Systems: Principles, Modelling and Gain-Scheduling Design (Advances in Industrial Control). Springer-Verlag London.
- [5] Bossanyi, E. (2003): *Individual Blade Pitch Control for Load Reduction*. Wind Energy, 6:119–128.
- [6] Bossanyi, E. (2004): *Developments in Individual Blade Pitch Control*. Proceedings of "the Science of Making Torque from Wind" Conference. pages 486–497.
- [7] Bossanyi, E. (2005): Further Load Reductions with Individual Pitch Control. Wind Energy, 8:481–485.
- [8] Boutayeb, M., R. Rafaralahy and M. Darouach (1997): Convergence Analysis of the Extended Kalman Filter Used as an Observer for Nonlinear Deterministic Discrete-Time Systems. IEEE Transactions on Automatic Control, 42(4):581–586.
- [9] Carcangiu, C., I.F. Balaguer, S. Kanev and M. Rossetti (2011): *Closed-Loop System Identification of Alstom 3MW Wind Turbine*. Proceedings of IMAC XXIX. Jacksonville-FL, USA.
- [10] Carcangiu, C., S. Kanev, M. Rossetti and I.F. Balaguer (2010): *System Identification on Alstom ECO100 Wind Turbine*. Proceedings of the POWER-GEN International Conference.
- [11] Caselitz, P. and J. Giebhardt (2005): *Rotor Condition Monitoring for Improved Operational Safety of Offshore Wind Energy Converters*. Journal of Solar Energy Engineering, 127(5):253–261.
- [12] Caselitz, P., J. Giebhardt, M. Mevenkamp and M. Reichardt (1997): *Application of Condition monitoring systems in wind energy converters*. Proceedings of European Wind Energy Conference. Dublin, pages 579–582.
- [13] Caselitz, P., W. Kleinkauf, T. Krüger, J. Petschenka, M. Reichardt and K. Störzel (1997): Reduction of Fatigue Loads on Wind Energy Converters by Advanced Control Methods. European Wind Energy Conference. Dublin Castle, Ierland, pages 555–558.
- [14] Chen, J. and R. Patton (1999): *Robust model-based fault diagnosis for dynamic systems*. Kluwer.
- [15] Chiuso, A. (2006): *Asymptotic Variance of Closed-Loop Subspace Identification Methods*. IEEE Transactions on Automatic Control, 51(8):1299–1314.
- [16] Chiuso, A. and G. Picci (2005): Consistency Analysis of Certain Closed-Loop Subspace Identification Methods. Automatica, 41(3):377–391.

- [17] Chowdhury, F. (2000): Ordinary and neural chi-squared tests for fault detection in stochastic systems. ÌEEE Transactions on Control Systems Technology, 8(2):372–379.
- [18] Coleman, R. and A. Feingold (1957): *Theory of Self-Excited Mechanical Oscillations of Helicopter Rotors with Hinged Blades*. Report NASA-TN 3844, NASA.
- [19] Donders, S. (2002): Fault Detection and Identification for Wind Turbine Systems: a Closed Loop Analysis. Master's thesis, University of Twente.
- [20] Dong, J. (2009): *Data driven fault tolerant control: a subspace approach*. Ph.D. thesis, Delft University of Technology.
- [21] Dragt, J. (1990): Atmospheric Turbulence Characteristics in the Rotating Frame of Reference of a WECS Rotor. in Proceedings of European Wind Energy Conference (EWEC). Madrid, Spain.
- [22] Font, I., S. Kanev and M. Rossetti (2010): *System identification on the ECO 100 wind turbine*. poster in the European Wind Energy Conference.
- [23] Font, I., S. Kanev, D. Tcherniak and M. Rossetti (2010): *System identification methods on Alstom ECO 100 wind turbine*. Proceedings of The Science of Making Torque from Wind Conference. FORTH, Heraklion, Crete, Greece.
- [24] Gahinet, P. and P. Apkarian (1994): A Linear Matrix Inequality Approach to \mathcal{H}_{∞} Control. International Journal of Robust and Nonlinear Control, 4:421–448.
- [25] George, K., M. Verhaegen and J. Scherpen (1999): A systematic and numerically efficient procedure for stable dynamic model inversion of LTI systems. Proceedings of the 38th Conference on Decision and Control. Pheonix, Arizona, USA, pages 1881–1886.
- [26] Gilson, M. and P. van den Hof (1996): *IV Methods for Closed-Loop System Identification*. Proceeding of the 13th Triennial World Congress of IFAC. San Fransisco, USA.
- [27] Gilson, M. and P. van den Hof (2001): On the relation between a bias-eliminated least-squares (BELS) and an IV estimator in closed-loop identification. Automatica, 37(10):1593–1600.
- [28] Goodwin, G., F. Graebe and M. Salgado (2001): *Control System Design*. Prentice Hall, Upper Saddle River, New Jersey.
- [29] Gustafsson, F. (1996): *The marginalized likelihood ratio test for detecting abrupt change*. IEEE Transactions on Automatic Control, 41(1):66–78.
- [30] Gustafsson, F. (2000): Adaptive Filtering and Change Detection. John Wiley & Sons Ltd.
- [31] Hammerum, K. (2006): A Fatigue Approach to Wind Turbine Control. Master's thesis, Technical University of Denmark.
- [32] Hansen, M. (2003): Aeroelastic Stability Analysis of Wind Turbines Using an Eigenvalue Approach. in Proceedings of European Wind Energy Conference (EWEC). Madrid, Spain.
- [33] Janssen, M. (2003): *Subspace identification and ARX modeling*. Proceedings of conference on System Indentification. Rotterdam, the Netherlands.
- [34] Jiang, B. and F. Chowdhury (2000): Fault estimation and accommodation for linear MIMO discrete-time Systems. IEEE Transactions on Control Systems Technology, 13(3):493–499.
- [35] Johnson (1980): Helicopter theory. Princeton University Press.

- [36] Julier, S., J. Uhlmann and H. Durrant-Whyte (1995): *A new approach for filtering nonlinear systems*. Proceedings of the American Control Conference. pages 1628–1632.
- [37] Kallesæ, B.S. (2006): A Low-order Model for Analysing Effects of Blade Fatigue Load Control. Wind Energy, 9:421–436.
- [38] Kanev, S. (2009): Dealing with actuator constraints in multi-mode blade load reduction control. Report ECN-Wind Memo-09-069, ECN Wind Energy.
- [39] Kanev, S. (2009): System identification from BLADED simulations with the Ecotècnia 100 wind turbine. Confidential report ECN-XŰ09-026, Energy Research Centre of the Netherlands (ECN).
- [40] Kanev, S. (2009): System identification from field measurements on Ecotècnia 100 wind turbine. Report ECN-X–09-089, Energy Research Center of the Netherlands.
- [41] Kanev, S. and T. van Engelen (2009): *Exploring the Limits in Individual Pitch Control*. Proceedings of the European Wind Energy Conference (EWEC). Marseille, France.
- [42] Kanev, S., J. Schuurmans and T. van Engelen (pending): *Apparatus and method for Individual Pitch control in Wind turbines*.
- [43] Kanev, S. and T. van Engelen (2008): Wind Turbine Extreme Gust Control. Report ECN-E-08-069, ECN Wind Energy. URL http://www.ecn.nl/docs/library/report/2008/e08069.pdf.
- [44] Kanev, S. and T. van Engelen (2010): *Wind Turbine Extreme Gust Control*. Wind Energy, 13(1):18–35.
- [45] Kanev, S. and M. Verhaegen (2005): *Two-Stage Kalman Filtering via Structured Square-Root*. Journal of Communications in Informations and Systems, 5(1):143–168.
- [46] Kay, S. (1998): Fundamentals of statistical signal processing: Detection Theory. Prentice-Hall.
- [47] Kendall, L., M. Balas, Y. Lee and L. Fingersh (1997): Application of proportional-integral and disturbance accommodating control to variable speed variable pitch horizontal axis wind turbines. Wind Engineering, 21:21–38.
- [48] Kodama, N. and T. Matsuzaka (2000): Power Variation Control of a Wind Turbine Generator using Probabilistic Optimal Control, including Feed-Forward Control from Wind Speed. Wind Engineering, 24(1):13–23.
- [49] Lindenburg, C. and G. Schepers (2001): *PHATAS-IV Aeroelastic modelling: Release* "*DEC-1999*" and "*NOV-2000*". Report ECN-CX-00-027, Energy Research Center of the Netherlands.
- [50] Ljung, L. (2005): System Identification Toolbox for use with Matlab. The MathWorks. URL http://www.mathworks.com/products/sysid/.
- [51] Ljung, L. and T. McKelvey (1996): Subspace Identification from Closed Loop Data. Signal Processing, 52:209–215. URL http://citeseerx.ist.psu.edu/viewdoc/download;jsessionid=FFE760D30EC067BB2A0491F829223437?doi=10.1.1.31.1305&rep=rep1&type=pdf. Technical report LiTH-ISY-R-1752.
- [52] Löfberg, J. (2004): YALMIP: A Toolbox for Modeling and Optimization in MATLAB. Proceedings of the CACSD Conference. Taipei, Taiwan. URL http://control.ee.ethz.ch/~joloef/yalmip.php.

- [53] Lorenzo, C. (1994): Continuum Fatigue Damage Modeling for Use in Life Extending Control. Technical Memorandum 106691, NASA.
- [54] Ma, X., M. Poulsen and H. Bindner (1995): Estimation of Wind Speed in Connection to a Wind Turbine. Report IMM-Technical report-1995-26, Technical University of Denmark. URL http://www2.imm.dtu.dk/pubdb/views/publication_details.php?id=2796.
- [55] Mangoubi, R. (1998): Robust Estimation and Failure Detection. Springer, London.
- [56] Mesic, S., V. Verdult, M. Verhaegen and S. Kanev (2003): Estimation and Robustness Analysis of Actuator Faults Based on Kalman Filtering. Proceedings of the 5th Symposium on Fault Detection, Supervision and Safety for Technical Processes (SAFEPROCESS'2003). Washington, D.C., USA.
- [57] Miner, M. (1945): Cumulative damage in fatigue. Journal of Applied Mechanics, 12:159–164.
- [58] Nijssen, R. (2006): Fatigue Life Prediction and Strength Degradation of Wind Turbine Rotor Blade Composites. Ph.D. thesis, Delft University of Technology.
- [59] Østergaard, K., P. Brath and J. Stoustrup (2007): *Estimation of effective wind speed*. Proceedings of the conference on the science of making torque from wind. Lyngby, Denmark. URL http://www.iop.org/EJ/article/1742-6596/75/1/012082/jpconf7_75_012082.pdf.
- [60] Qin, S. (2009): Data-driven Fault Detection and Diagnosis for Complex Industrial Processes. the Proceedings of the 7th IFAC Symposium on Fault Detection, Supervision and Safety of Technical Processes (SafeProcess09). Barcelona, Spain, pages 1115–1125.
- [61] Qin, S. and L. Ljung (2003): Closed-Loop Subspace Identification with Innovation Estimation. Proceedings of the 13th IFAC Symposium on System Identification (SysId). pages 887–892. Technical report LiTH-ISY-R-2563.
- [62] Ray, A. and M. Wu (1994): *Fatigue damage control of mechanical systems*. Smart Materials and Structtures, 3:47–58.
- [63] Ribrant, J. (2006): *Reliability performance and Maintainance: A survey of failure in wind power systems*. Report, KTH school of Electrical Engineering, Sweden.
- [64] Sbarbaro, D. and R. Peña (2000): A non-linear wind velocity observer for a small wind energy system. Proceedings of the 39th IEEE Conference on Decision and Control. Sydney, Australia, pages 3086–3087.
- [65] Selvam, K., S. Kanev, J.W. van Wingerden, T. van Engelen and M. Verhaegen (2009): Feedback-feedforward individual pitch control for wind turbine load reduction. International Journal of Robust and Nonlinear Control, 19(1):72–91.
- [66] Shinozuka, M. (1971): Simulation of multivariate and multidimensional random processes. Journal of the Acoustical Society of America, 49.
- [67] Snel, H. and G. Schepers (1994): *Joint Investigation of Dynamic Inflow Effects and Implementation of an Engineering Method*. Report ECN-C–94-107, Energy Research Center of the Netherlands (ECN).
- [68] Stol, K. and M. Balas (2003): *Periodic Disturbance Accommodating Control for Blade Load Mitigation in Wind Turbines*. Journal of Solar Energy Engineering, 125(4):379–385.

- [69] Thiringer, T. and A. Petersson (2005): Control of a Variable-Speed Pitch-Regulated Wind Turbine. Report, Chalmers University of Technology. URL http://www.vindenergi.org/Vindforskrapporter/VarvStyr_CTH_ Thiringer_hela.pdf?bcsi_scan_5AC5CC8B343D9567=0&bcsi_scan_filename=VarvStyr_CTH_Thiringer_hela.pdf.
- [70] van den Hof, P. and X. Bombois (2004): *System Identification for Control*. Lecture notes, Dutch Institute for Systems and Control (DISC).
- [71] van der Hooft, E., P. Schaak and T. van Engelen (2003): Wind turbine control algorithms. Report ECN-C-03-111, Energy Research Center of the Netherlands (ECN). URLhttp://www.ecn.nl/publicaties/default.aspx?nr=ECN-C--03-111. DOWEC-F1W1-EH-03-094/0.
- [72] van der Hooft, E. and T. van Engelen (2004): Estimated Wind Speed Feedforward Control for Wind Turbine Operation Optimization. Report ECN-C-04-126, Energy Research Center of the Netherlands (ECN). URL http://www.ecn.nl/publicaties/default.aspx?nr=ECN-RX--04-126.
- [73] van der Hooft, E., T. van Engelen, J. Pierik and P. Schaak (2007): *Real-time Process Simulator for Evaluation of Wind Turbine Systems: Modelling and Implementation*. Report ECN-E-07-046, Energy Research Center of the Netherlands (ECN).
- [74] van Engelen, T. (2001): *Development of Wind Turbine Control Algorithms for Industrial Use.* Proceedings of the European Wind Energy Conference. Copenhagen, Denmark.
- [75] van Engelen, T. (2006): Design model and load reduction assessment for multi-rotational mode individual pitch control (higher harmonics control). Proceedings of the European Wind Energy Conference. Athens, Greece. URL http://www.ecn.nl/publicaties/default.aspx?nr=ECN-RX--06-068.
- [76] van Engelen, T. (2007): Control design based on aero-hydro-servo-elastic linear models from TURBU (ECN). Proceeding of the European Wind Energy Conference. Milan, Italy. URL http://www.ecn.nl/publicaties/default.aspx?nr=ECN-M--07-054.
- [77] van Engelen, T. (2010): System and method for compensating rotor imbalance in a wind turbine.
- [78] van Engelen, T. and H. Braam (2004): *TURBU Offshore, Computer Program for Frequency Domain Analysis of Horizontal Axis Offshore Wind Turbines; Implementation.* Report ECN-C-03-138, ECN Wind Energy.
- [79] van Engelen, T., L. Machielse and S. Kanev (2010): *Method and system for wind gust detection in a wind turbine*.
- [80] van Engelen, T., H. Markou, T. Buhl and B. Marrant (2006): Morphological Study for Aeroelastic Control Concepts for Wind Turbines. Report ECN-E-06-056, Energy Research Center for the Netherlands (ECN). URL http://www.ecn.nl/publicaties/default.aspx?nr=ECN-E--06-056. Available for download at http://www.ecn.nl/publicaties/default.aspx?nr=ECN-E--06-056.
- [81] van Engelen, T. and P. Schaak (2007): *Oblique Inflow Model for Assessing Wind Turbine Controllers*. Proceedings of the 2nd Conference on The Science of Making Torque From Wind. Lyngby, Denmark.

- [82] van Engelen, T., J. Schuurmans, S. Kanev, J. Dong, M. Verhaegen and Y. Hayashi (2011): Fault tolerant wind turbine production operation and shutdown (Sustainable Control). Procedings of the EWEA Conference. Brussels, Belgium.
- [83] van Engelen, T. and E. van der Hooft (2003): *Individual Pitch Control Inventory*. Report ECN-C-03-138, Energy Research Center of the Netherlands (ECN). URL http://www.ecn.nl/publicaties/default.aspx?nr=ECN-C--03-138.
- [84] van Engelen, T. and E. van der Hooft (2004): *Dynamic inflow compensation for pitch controlled wind turbines*. Proceedings of the European Wind Energy Conference. London, UK. URL http://www.ecn.nl/publicaties/default.aspx?nr=ECN-RX--04-129.
- [85] Van Overschee, P. and B. De Moor (1993): Subspace algorithms for the stochastic identification problem. Automatica, 29(3):649–660. URL ftp://ftp.esat.kuleuven.ac.be/pub/SISTA/vanoverschee/reports/comb_ext2.ps.Z. Technical Report ESAT/SISTA 1992-34-I.
- [86] Van Overschee, P. and B. De Moor (1994): N4SID: Subspace Algorithms for Identification of Combined Deterministic-Stochastic Systems. Automatica, 30(1):75– 93. URL ftp://ftp.esat.kuleuven.ac.be/pub/SISTA/vanoverschee/ reports/comb_ext2.ps.Z. Technical Report ESAT/SISTA 1992-34-I.
- [87] Van Overschee, P. and B. De Moor (1997): *Closed-loop Subspace System Identification*. Proceedings of the 36th Conference on Decision and Control (CDC'97). San Diago, California, USA.
- [88] van Trees, H. (1968): *Detection, Estimation, and Modulation Theory*. John Wiley and Sons.
- [89] Verbruggen, T. (2003): Wind Turbine Operation and Maintenance based on Condition Monitoring. Report ECN-C-03-047, ECN Wind Energy.
- [90] Verdult, V. (2002): Feasibility Study on the Application of Model-Based Fault Detection and Controller Reconfiguration for Wind Turbines. Report, TU-Delft.
- [91] Verdult, V. and M. Verhaegen (2007): *Filtering and System Identification*. Cambridge University Press.
- [92] Verhaegen, M. (1993): Application of a Subspace Model Identification Technique to Identify LTI Systems Operating in Closed-Loop. Automatica, 29(4):1027–1040.
- [93] Verhaegen, M. (1994): *Identification of the deterministic part of MIMO state space models given in innovations form from input-output data*. Automatica, 30(1):61–74.
- [94] Wan, E. and R. van der Merwe (2000): *The Unscented Kalman Filter for Nonlinear Estimation*. Proceedings of the IEEE 2000 Adaptive Systems for Signal Processing, Communications, and Control Symposium. Lake Louise, Alberta, Canada.
- [95] Wang, J., G. Yang and J. Liu (2007): An LMI approach to \mathcal{H}_{-} index and mixed $\mathcal{H}_{-}/\mathcal{H}_{\infty}$ fault detection observer. Automatica, 43:1656 $\mathring{\mathbb{U}}$ -1665.
- [96] Wei, X. (2009): Fault Detection of Large Scale Off-shore Wind Turbine Systems. Report 09-044, Delft University of Technology.
- [97] Wei, X. and M. Verhaegen (2008): Fault Detection of Large Scale Wind Turbine Systems: A mixed H_infinity/H_ Index Observer Approach. Proceedings of the 16th Mediterranean Conference on Control and Automation. Ajaccio, France.

- [98] Wei, X. and M. Verhaegen (2008): *Mixed H_infinity/H_index Fault Detection Observer Design for LPV systems*. Proceedings of the 47th IEEE Conference on Decision and Control. Cancun, Mexico, pages 1073–1078.
- [99] Wei, X. and M. Verhaegen (2009): *Mixed H_/H_infinity Dynamic Observer Design for Fault Detection*. Proceedings of the European Control Conference. Budapest, Romania, pages 1913–1918.
- [100] Wei, X. and M. Verhaegen (2009): *Robust Fault Detection Observer Design for LTI Systems Based on GKYP Lemma*. Proceedings of the European Control Conference. Budapest, Romania, pages 1919–1924.
- [101] Wei, X. and M. Verhaegen (2009): *Robust Fault Detection Observer for LTI Systems with Additive Uncertainties*. Proceedings of the 7th IFAC Symposium on Fault Detection, Supervision and Safety of Technical Processes (SAFEPROCESS). Barcelona, Spain, pages 756–761.
- [102] Wei, X., M. Verhaegen and T. van Engelen (2008): Sensor Fault Diagnosis of Wind Turbines for Fault Tolerant Control. Proceedings of the 17th World congress of IFAC. Seoul, Korea, pages 3222–3227.
- [103] Wei, X., M. Verhaegen and T. van Engelen (2010): Sensor Fault Detection and Isolation for Wind Turbines Based on Subspace Identification and Kalman Filter Techniques. International Journal of Adaptive Control and Signal Processing, 24(8).
- [104] Willsky, A. and H. Jones (1976): A Generalized Likelihood Ratioi Approach to the Detection and Estimation of Jumps in Linear Systems. IEEE Transactions on Automatic Control, 1:108–112.
- [105] Winkelaar, D. (1992): SWIFT program for three-dimensional wind simulation: part 1: Model description and program verification. Report ECN-R-92-013, ECN Wind Energy. URL http://www.ecn.nl/docs/library/report/1992/r92013.pdf.
- [106] Zhou, K. and J. Doyle (1998): Essentials of Robust Control. Prentice-Hall.